

DISS. ETH NO. 27958

***The alkali-silica reaction damage in concrete at the mesoscale:
characterization by X-ray tomography***

A thesis submitted to attain the degree of

DOCTOR OF SCIENCES of ETH ZURICH

(Dr. sc. ETH Zurich)

presented by

MAHDIEH SHAKOORIOSKOOIE

M.Sc.

Sabancı University, Istanbul, Turkey

born on 21.03.1990

citizen of Iran

accepted on the recommendation of

Prof. Dr. Pietro Lura, examiner

Dr. Michele Griffa, co-examiner

Prof. Dr. Uli Angst, co-examiner

Prof. Dr. Peter Moonen, co-examiner

Prof. Dr. Jean-Francois Molinari, co-examiner

Prof. Dr. Ioannis Anastasopoulos, chair of the committee

2021

Dedication

To my dear husband for his immense love and patience during my PhD and to my dear parents and my lovely sister for their love and support

Acknowledgments

I would like to thank Professor Pietro Lura, Dr. Michele Griffa, Dr. Robert Zboray and Dr. Andreas Leemann for their exceptional support during my studies. Everything was generously available to me from high-quality education to the state-of-the-art research facilities. In addition to in-depth scientific education, they taught me a lot of life lessons with their noble behavior. The support that I received was beyond my imagination and words cannot express my gratitude!

I would also like to sincerely thank all the members of the Swiss National Science Foundation (SNF) Sinergia project (Nr. 171018, "Alkali-silica reaction in concrete", <http://p3.snf.ch/project-171018>) for many constructive discussions, guidance and passion for different collaborations to address important multidisciplinary questions regarding the ASR damage in concrete. More specifically I would like to express my gratitude to Prof. Karen Scrivener (at EPFL), Prof. Barbara Lothenbach (at Empa), Prof. Jean-François Molinari (at EPFL), Prof. Guoqing Geng (at NUS, Singapore), Dr. Mahsa Bagheri (at EPFL) and Emil Gallyamov (at EPFL), with whom I had the privilege of working closely on many collaborative projects.

I truly acknowledge the generous support of the SNF for financing my PhD project as well as the entire Sinergia project, which provided us a perfect opportunity to synergistically approach different complex and multidisciplinary aspects of the ASR damage.

I am very thankful to all the scientists, instrument specialists and members of the Concrete & Asphalt laboratory and Center for X-ray Analytics at Empa who selflessly helped and supported me during my studies. They never hesitated to help me in any aspect of my research. I owe a major part of my scientific achievements to their kind support.

Last but not least, I want to sincerely thank my dear husband, my parents and my lovely sister to whom I owe all my life and my achievements.

Dübendorf, 09 September 2021

Mahdiah Shakoorioskooie

Abstract

The alkali-silica reaction (ASR) is the source of one of the most deleterious durability issues of the worldwide concrete infrastructure. It consists of chemical reactions between aggregates and the alkaline pore solution. The ASR products lead to deformations and cracking and, consequently, extensive structural damage, causing major safety, economic and environmental issues. Since the first investigations (eight decades ago), some basic ASR (cracking) mechanisms have been discovered. However, a comprehensive understanding has not been achieved yet, due to its complex multiscale nature.

One of the major knowledge gaps stems from lack of characterization of the deformations and crack propagation at the mesoscale (few μm - few cm). Results from systematic non-destructive studies have been lacking, although they are necessary to track the ASR cracking. That is because the typical petrographic characterization techniques rely upon 2D microscopy (electron and optical), which require destructive specimen preparations. X-ray tomography (XT), as a non-destructive technique, has been recently adopted, although, so far only in limited cases, mainly for simplified model systems and exploited only for qualitative analysis.

During this PhD project, embedded within the framework of the Swiss National Science Foundation Sinergia project Nr. 171018 ("Alkali-silica reaction in concrete"), a comprehensive study of ASR cracking at the mesoscale was carried out using time-lapse XT and various image analysis approaches. The study involved mainly specimens undergoing ASR acceleration in the laboratory. Its key goal was to characterize, for the first time, the spatial-temporal evolution of both ASR products and cracks.

To achieve such goal, several challenges in the application of XT needed to be addressed. The result was the development of a new, integrated experimental and image analysis framework. One challenge consisted of enhancing the X-ray attenuation contrast between ASR products and the other material phases of concrete at the mesoscale, the former being normally undistinguishable from the latter in standard X-ray tomograms. Overcoming this challenge allowed analyzing both qualitatively and quantitatively their spatial-temporal distributions. Another challenge dealt with the contrast enhancement between aggregates and the cement paste, typically very low but needed to distinguish between products/cracks located either inside or outside aggregates. Finally, the qualitative and quantitative analysis of the tomographic time series required the implementation of distinct 3D image registration steps, to enable the time-lapse qualitative comparisons as well as the quantitative analysis. 3D image registration was additionally exploited both for estimating from the time series the global and local ASR-induced deformations and for increasing the robustness of the cracks and products detection (segmentation), compared with what achievable by conventional segmentation approaches.

The overall, new XT-based methodology was extensively validated, concerning any eventual spurious effect on the natural ASR (cracking) course. It was possible to show its applicability and it delivered both new information and respective quantitative data about the ASR crack networks, about the extent of ASR products transport along them and the associated cracking itself as well as about the localized deformations, which accompany the cracking. The obtained, 3D datasets about products, cracks and deformations provided a uniquely new integrated knowledge and data base for advancing the basic understanding of ASR (cracking) and for supporting the formulation and validation of respective computational models at the concrete mesoscale. In addition, the developed XT-based methodology could be immediately exploited by the ASR research community for investigations also at other space-time scales not addressed in this project, e.g., the early stages of products formation and cracking initiation.

Sommario

La reazione tra silice e alcali (in breve, secondo l'acronimo inglese, ASR, per "alkali-silica reaction") è la causa di uno dei maggiori problemi di durabilità dell'infrastruttura in calcestruzzo nel mondo. Questa reazione coinvolge gli aggregati e la soluzione alcalina presente nei pori del calcestruzzo. La formazione dei rispettivi prodotti di reazione dà luogo a deformazioni e rispettiva fratturazione. Ne consegue tipicamente un danneggiamento fino alla scala strutturale che causa problemi significativi, in termini di sicurezza, economici e di impatto ambientale dell'infrastruttura stessa. Oggigiorno, a circa 80 anni dai primi studi, alcuni dei meccanismi alla base della ASR e della rispettiva fratturazione nel calcestruzzo sono ben conosciuti. Tuttavia, non esiste ancora un complessivo quadro di conoscenze in merito a tutti i meccanismi, *in primis* a causa del coinvolgimento di processi a più scale spaziali, una caratteristica intrinseca della ASR e della fratturazione che ne consegue.

Una delle più importanti lacune conoscitive deriva dalla mancanza di caratterizzazione delle deformazioni e della rispettiva fratturazione ad una scala intermedia, definita qui come "mesoscala" e corrispondente approssimativamente all'intervallo tra alcuni micrometri e alcuni centimetri. In aggiunta, finora è sono mancate caratterizzazioni sistematiche e non distruttive, sebbene esse siano strettamente necessarie per seguire l'evoluzione della fratturazione da ASR. Tale mancanza deriva dal fatto che la caratterizzazione tipicamente eseguita si basa su microscopia bi-dimensionale (ad elettroni e ottica), la quale richiede una preparazione distruttiva dei campioni. La tomografia a raggi X (in breve, secondo l'acronimo inglese, XT, per "X-ray Tomography"), come metodica di caratterizzazione non distruttiva, è stata solo recentemente adottata e limitatamente allo studio di sistemi modello e per una caratterizzazione solo qualitativa.

In questo Dottorato, facente parte del progetto, di tipo Sinergia, No. 171018, intitolato "La reazione alcali-silice nel calcestruzzo" e finanziato dal Fondo Nazionale Svizzero per la Scienza, la fratturazione da ASR è stata studiata in modo esteso tramite l'uso di XT sequenziale (cioè a più stadi di evoluzione dei campioni) e di una varietà di metodiche di analisi delle rispettive immagini. Lo studio è stato effettuato principalmente su campioni soggetti ad accelerazione della ASR in laboratorio. L'obiettivo centrale dello studio è stato la caratterizzazione, per la prima volta, dell'evoluzione spazio-temporale sia dei prodotti di reazione che delle rispettive fratture.

Per raggiungere tale obiettivo, una serie di ostacoli nell'applicazione della XT sono stati affrontati e superati. Il superamento di tali ostacoli ha portato allo sviluppo di una nuova metodica, sia sperimentale che di analisi delle immagini, per la caratterizzazione della ASR e della rispettiva fratturazione. Uno degli ostacoli è consistito nella necessità di aumentare il contrasto di immagine, basato su assorbimento dei raggi X, tra i prodotti di reazione e le altre componenti del calcestruzzo. In tomografie a raggi X tradizionali, tali prodotti di reazione sono tipicamente non distinguibili da altre componenti del calcestruzzo. Un altro ostacolo da superare è consistito nella necessità di aumentare il contrasto tra gli aggregati e la matrice di pasta di cemento. Tale contrasto è anch'esso molto basso in tomografie standard. Tuttavia, è strettamente necessario per determinare se prodotti di reazione e fratture individuate si trovino entro aggregati o nella matrice cementizia. Infine, l'analisi sia qualitativa che quantitativa delle serie temporali di tomografie ha richiesto l'implementazione di diversi stadi di allineamento tridimensionale delle tomografie, come requisito fondamentale sia per la loro comparazione qualitativa che per la loro analisi quantitativa. In aggiunta, tale allineamento è stato utilizzato anche per stimare le deformazioni sia globali che locali indotte dalla ASR e per identificare prodotti di reazione e fratture con maggiore accuratezza in confronto a quanto ottenibile usando approcci tradizionali.

L'intera metodologia di studio basata su XT è stata validata in modo estensivo in merito alla minimizzazione di ogni suo eventuale effetto spurio sulla naturale progressione della ASR e della rispettiva fratturazione. È stato possibile dimostrare la sua applicabilità allo studio della ASR senza alterazioni

rispetto al corso naturale della stessa. Inoltre, ha fornito dati completamente nuovi in merito alla rete di fratture da ASR, al trasporto dei prodotti di reazione lungo tali fratture e alle rispettive conseguenze sulla propagazione di tali fratture e in merito alle deformazioni meccaniche che sono correlate a tali fratture. La base di dati tridimensionali, in merito ai prodotti di reazione, alle fratture e alle deformazioni, generata in questo Dottorato è un *unicum* ed una novità di estrema importanza per avanzare le conoscenze dei meccanismi alla base della fratturazione da ASR. In aggiunta è di fondamentale supporto alla formulazione e alla validazione di modelli matematici di tale fratturazione, in particolare alla mesoscala. In aggiunta, l'intera metodologia tomografica a raggi X sviluppata nel corso del Dottorato può essere immediatamente usata dalla comunità di ricerca su ASR per investigare altri meccanismi occorrenti a scale spazio-temporali diverse da quelle di indagine in questo Dottorato, per esempio la formazione dei primi prodotti di reazione e il corrispondente inizio della fratturazione.

List of publications and planned articles

In peer-reviewed scientific journals

Mahdieh Shakoorioskooie, Michele Griffa, Andreas Leemann, Robert Zboray, and Pietro Lura, "Alkali-silica reaction products and cracks: X-ray micro-tomography-based analysis of their spatial-temporal evolution at a mesoscale"- **Cement and Concrete Research** **150** (2021): **106593** (<https://www.sciencedirect.com/science/article/pii/S0008884621002428>)- **based on the results of Chapter 5**

Mahdieh Shakoorioskooie, Michele Griffa, Andreas Leemann, Robert Zboray, and Pietro Lura, "Comparison of alkali-silica-reaction cracking between laboratory and field-exposed samples studied by X-ray micro-tomography"- **To be submitted-** **based on the results of Chapter 4**

Mahdieh Shakoorioskooie, Michele Griffa, Andreas Leemann, Robert Zboray, and Pietro Lura, "Statistical evaluation of the spatial-temporal development of the alkali-silica reaction cracking in concrete"- **To be submitted-** **based on the results of second half of Chapter 6**

Mahdieh Shakoorioskooie, Michele Griffa, Andreas Leemann, Robert Zboray, and Pietro Lura, "Quantitative analysis of the spatial-temporal development of alkali-silica reaction products and cracks, by differentiating them within the aggregates and in the cement paste"- **To be submitted-** **based on the results of Chapter 6 and 7**

In peer-reviewed conference proceedings

Mahdieh Shakoorioskooie, Michele Griffa, Andreas Leemann, Robert Zboray, and Pietro Lura, "Evolution of alkali-silica reaction cracks and products in concrete at themeso-scale studied by X-ray micro-tomography", in First Book of Proceedings of the 16th international conference on Alkali-Aggregate Reaction in Concrete, (ICAAR2020-2022), April **2021**, pp. 1151–1162.

Mahdieh Shakoorioskooie, Andreas Leemann, Michele Griffa, Robert Zboray, and Pietro Lura. "Characterization of alkali-silica reaction damage in concrete by X-ray tomography." In Int. Conf. Tomogr. Mater. Struct. **2019**.

Leemann, Andreas, Ingmar Borchers, **Mahdieh Shakoorioskooie**, Michele Griffa, Christoph Müller, and Pietro Lura. "Microstructural analysis of ASR in concrete-accelerated testing versus natural exposure." In Proceedings of the International Conference on Sustainable Materials, Systems and Structures (SMSS2019), RILEM Publications SARL, Rovinj, Croatia. **2019**.

Table of contents

Chapter 1. Introduction and objectives	1
1.1. Background	1
1.2. Research objectives	5
1.3. Thesis outline	7
Chapter 2. Alkali-silica reaction (ASR) and respective damage in concrete: basics and state of the art in their characterizations	14
2.1. ASR chemistry and identified/proposed damage mechanisms	14
2.2. Reactive aggregates	19
2.3. Field examples of ASR damage	22
2.4. Laboratory characterizations of ASR and ASR damage in concrete	23
2.4.1. ASR acceleration for aggregate reactivity and concrete damage assessment: commonly used standardized protocols	23
2.4.2. Characterizations	24
2.4.2.1. Petrography by optical microscopy	24
2.4.2.2. Scanning electron microscopy (SEM) and energy-dispersive X-ray spectroscopy (EDX)	24
2.4.2.3. Mechanical and fracture properties characterization	26
2.4.2.4. Relative mass and length changes	28
2.4.2.5. Basics of X-ray tomography as applied for ASR (damage) characterization	29
2.4.2.5.1. Contrast enhancers for XT	38
2.4.2.5.2. Three-dimensional image registration	39
Chapter 3. Materials and methodology	60
3.1. Summary	60
3.2. Common materials and the basic concrete mix design	60
3.2. Characterizations	62
3.3. Analysis of the time-lapse X-ray tomograms	66
3.4. Contributions by others to the software and experimental efforts	81
Chapter 4. ASR crack networks: properties, evolution, and comparisons between laboratory and field specimens; A benchmark analysis	84
4.1. Summary	84
4.2. Experimental details specific for the benchmark campaign	84
4.2.1. Materials and specimens preparation	85
4.2.1.1. Laboratory-accelerated specimens	85
4.2.1.2. Field specimens	86
4.2.2. Characterizations	87
4.2.2.1. Laboratory-accelerated specimens	87
4.2.2.2. X-ray tomography	87
4.2.2.3. Time-lapse X-ray tomography analysis	84
4.3. Results	89
4.3.1. Laboratory-accelerated specimens	89

4.3.1.1. ASR-induced macroscopic dimensional changes	89
4.3.1.2. Chemical and morphological features of the ASR products	91
4.3.1.3. ASR cracking: time-lapse tomography qualitative analysis	93
4.3.2. Field specimens	96
4.3.2.1. ASR-induced macroscopic dimensional changes and morphological features of the ASR products	96
4.3.2.2. ASR cracking: X-ray tomography qualitative analysis	96
4.3.3. Quantitative comparison of the ASR cracking between laboratory and field specimens	98
4.3.4. Specimen size effect on the segmented crack network's features	103
4.4. Discussion	105
4.5. Conclusions	108
Chapter 5. ASR crack networks and ASR products: qualitative and quantitative analysis of their coupled properties and evolution	112
5.1. Summary	112
5.2. Experimental details specific for the Cs-based experimental campaign	112
5.2.1. Materials and experiments	113
5.2.2. Image analysis	114
5.3. Results	115
5.3.1. Increase in X-ray attenuation contrast for ASR products labelled with Cs	115
5.3.2. Chemical and morphological features of the ASR products	117
5.3.3. ASR-induced macroscopic dimensional changes and mechanical properties evolution	120
5.3.4. ASR cracking in the reference specimens: time-lapse XT, qualitative analysis	122
5.3.5. ASR cracking in the Cs-doped specimens: time-lapse XT, qualitative analysis	123
5.3.6. ASR crack networks: quantitative analysis	126
5.3.7. Local deformations analysis	129
5.4. Discussion	132
5.5. Conclusions	135
Chapter 6. Qualitative and quantitative analysis of ASR crack networks and their evolution in the concrete mesostructure context	138
6.1. Summary	138
6.2. Specific experimental and analysis details	138
6.2.1. Materials and specimen preparation	138
6.2.1.1. Specimens for the optimization of the BaSO ₄ concentration and assessment of its effects on the ASR (cracking)	138
6.2.1.2. Extensive quantitative analysis of specimens with optimal BaSO ₄ concentration	140
6.2.2. Characterizations	140
6.2.2.1. Measurements and analysis for the BaSO ₄ concentration optimization and for the assessment of its effects on the ASR (cracking)	140
6.2.2.2. Measurements and analysis on/of the specimens with optimal BaSO ₄ concentration	141
6.2.3. Analysis of the time-lapse X-ray tomograms	142
6.3. Results	143

6.3.1. BaSO ₄ concentration optimization	143
6.3.2. Influences of BaSO ₄ on the ASR (cracking)	146
6.3.2.1. Influence on the macroscopic dimensional changes induced by ASR	146
6.3.2.2. Influence on the Young's modulus evolution induced by ASR	148
6.3.2.3. Influence on the chemical composition and morphological features of the ASR products	149
6.3.2.4. Influence on the ASR cracking and respective local deformations	149
6.3.2.5. Influence on quantitative ASR crack features	155
6.3.3. Extensive experimental campaign with optimal BaSO ₄ concentration	161
6.3.3.1. ASR-induced macroscopic dimensional changes and mechanical properties evolution	161
6.3.3.2. Spatial-temporal evolution of ASR cracking	163
6.3.3.3. Quantitative analysis of the ASR crack networks	167
6.4. Discussion	171
6.5. Conclusions	173
Chapter 7. Qualitative and quantitative analysis of ASR crack networks and products in the concrete mesostructured context	176
7.1. Summary	176
7.2. Specific materials and methods	177
7.2.1. X-ray attenuation contrast enhancement between aggregates and cement paste and between the latter and ASR products	177
7.2.2. ASR characterization by XT and other methods	178
7.2.3. Analysis of the time-lapse X-ray tomograms	179
7.3. Results	180
7.3.1. BaSO ₄ concentration optimization: analysis of the tomographic contrast enhancement	180
7.3.2. Influence of the BaSO ₄ and CsNO ₃ presence on the ASR-induced macroscopic dimensional changes	182
7.3.3. Qualitative analysis of the ASR cracking and respective local deformations: in the presence of both BaSO ₄ and CsNO ₃	184
7.3.4. Quantitative analysis of the ASR cracking within aggregates and the cement paste	189
7.4. Discussion	195
7.5. Conclusions	197
Chapter 8. Conclusions and outlook	200
8.1. Synthesis of key achievements	200
8.2. Outlook	203
Appendix A	206
Appendix B	243
Appendix C	251
Appendix D	314
Appendix E	344

List of figures

Figure 1.1. Schematic illustration of some of the sequential processes constituting ASR: (a) highlight of key ASR actors, e.g., alkali cations (Na^+ and K^+) and hydroxyl (OH^-) anions in the pore space solution and certain types of silica (SiO_2) in the aggregates (black regions); (b) reaction between the alkaline pore solution and some of the aggregate silica; (c) cracking, induced by formation of ASR products (in yellow) within the aggregates, and their propagation into the cement paste (in grey). 2

Figure 1.2. Overview scheme representing the various sub-projects of the Swiss National Science Foundation (SNF) Sinergia project Nr. 171018, dedicated to ASR (damage), and of their interconnections, indicated by arrows. Sub-project V was the one concerning this PhD Thesis, with strong interconnection with sub-project VI, the latter related with multi-scale computational modeling of ASR cracking. The length scale(s) at which ASR (damage) was investigated in each sub-project is specified by the position on the axis of a corresponding sub-project's results, in the form of figures. The figures for each sub-project are adapted from: (I) [78]; (II) [79]; (III) [80]; (IV) [51]; (V) from the results presented in chapter 4 of this thesis; (VI) [61]. 6

Figure 2.1. (a). Quartz grains appearing (light) in greywacke coarse aggregate; (b) granite, consisting of coarse crystalline quartz (left), feldspar (right), and biotite mica (yellow); (c) microgranite, comprising of fine crystalline quartz (grey/white/black), feldspar (grey), muscovite mica (yellow/pink/blue) and biotite mica (brown/green); (d) granite cataclasite with a porphyritic texture containing porphyroclasts of feldspar (centre) set in a groundmass largely composed of finely crystalline quartz; (e) ultracataclasite, containing unfoliated groundmass of fine crystalline to cryptocrystalline silica, with rare strained porphyroclasts; (f) ultramylonite, comprised of foliated groundmass of fine crystalline to cryptocrystalline silica, with rare strained porphyroclasts. All insets were adapted from [72] and show optical, transmission micrographs obtained by cross-polarized light and a geometrical magnification factor of $\times 35$ 21

Figure 2.2. (a) Cherty quartzite, containing a combination of cryptocrystalline quartz (chert, top-right half) and interlocking, medium-grained quartz crystals (quartzite, left-bottom half); (b) diaquartzite, comprised of medium-grained quartz interlocking crystals; and (c) metaquartzite, with severely sheared and restructured quartz, including submicroscopic quartz. All insets were adapted from [72] and show optical micrographs obtained by cross-polarized light in a transmission mode, with a 150 times magnification. 21

Figure 2.3. (a) ASR cracks on a road over-pass pier in Canada [76], (b) ASR cracking in an elevated freeway structure in South Africa [76], (c) severe ASR damage to a railway arch bridge in Johannesburg [76], (d) ASR cracks with dark rims having a preferred orientation parallel to the compressive stress at the entrance of a tunnel in Switzerland [78], (e) ASR cracks on a supporting wall (in Switzerland) [78] and (f) ASR cracks on a supporting wall at the entrance of a gallery in Switzerland [78]. 23

Figure 2.4. (a) SEM-BSE image of a crack within an aggregate almost fully filled with ASR products. Most of the ASR products are observed with a plate-like morphology, which indicates the crystalline microstructure of the products. Small amounts of amorphous products (with no plate-like features) are shown with white arrows; (b) SEM-BSE image of a crack (within an aggregate) filled with a combination of amorphous and crystalline ASR products; and (c) scatter plot of $(\text{Na}+\text{K})/\text{Si}$ -ratio versus Ca/Si -ratio for both amorphous and crystalline ASR products, obtained by EDX point analysis. All insets were adapted from [92]. 25

Figure 2.5. (a) SEM-BSE image of a mortar specimen, accelerated at 40°C, showcasing extensive cracking within the aggregate and extending into the cement paste (adaptation from [95]); and (b) extremely fragmented ASR crack network in an aggregate in a mortar specimen, accelerated by ASTM C1260 (ASTM 2014b), at 80°C. In such cases crack propagation into the cement paste are less frequently observed (adaptation from [96]).	26
Figure 2.6. Evolution of Young modulus (reactive aggregate C reported in [77]), characterized at three acceleration temperatures and with two alkaline content levels.	27
Figure 2.7. Different modes of tensile testing of concrete.	27
Figure 2.7. (a) Time series of the relative length change at different acceleration temperatures. The markers show mean values while the error bars show standard deviations, both computed from a set of specimens. The number of specimens measured at each time point is indicated by the format of each marker: color filled markers correspond to three specimens; the white and black markers denote two and one specimen, respectively. The dashed lines show regression lines performed considering only data points with expansion values above 0.04%, their slopes are indicted with values next to each line. Both insets were adapted form [105].	29
Figure 2.8. Laboratory sized XT machine used in this study	32
Figure 2.9. Athematic illustration of 2D projections acquired form a 3D object, observed at distinct rotation angle θ of the object, with respect to a vertical axis z of rotation (adapted from [129]).	32
Figure 2.10. (a) Back-projection process, showing summing up over all possible orientation angles (smeared projections) after filtration; (b) examples of the projections at 0° and 90° and of the sum of their back-projections on a slice; and (c) an example demonstrating the effect of number of projections on the reconstructed slice. Adapted from [129].	35
Figure 2.11. Example slices of tomogram of a water-filled tube (as an object with spatially homogeneous attenuation coefficient): (a) generic spectral artifact in the reconstructed slice, with a distributed, speckle-like patter [142], and (b) beam hardening artifact, with a radial profile of the attenuation coefficient, higher values appearing towards the tube boundaries compared to its interior regions, also known as "cupping" [115].	37
Figure 2.12. Example slices showing common artifacts: (a) Ring artifact, (b) X-ray scatter artifact and (c) Beam hardening artifact [135].	38
Figure 2.13. Example slices from two concrete specimens: (a) reference specimen, without baryte addition and (b) specimen with a baryte content of 2.6 vol.-% (in respect of the total aggregate volume) [159].	39
Figure 2.14. Schematic illustration of the change of a fixed image (left) as a spatial mapping \vec{T} of its domain to another one (right), moved image domain. A certain feature indicated by the point \vec{p} in the fixed image domain is mapped by \vec{T} to a distinct point \vec{q} in the moved image domain as $\vec{q} = \vec{T}(\vec{p})$. The image registration processes is in fact about finding \vec{T} , such that the two images are matched [161].	41
Figure 2.15. General procedure of an image registration process [161].	42
Figure 2.16. Geometrical conventions in describing an image as data structure in the ITK libraries [161].	43

Figure 2.17. Example outputs of various transformations used for registering (a) fixed image and (b) moving image (with a distinct imaging modality): (c) results of a rigid body registration; (d) results of a global affine transformation; and (e) results of non-affine registration using a B-spline-based transformation model [161]. 45

Figure 2.18. Schematic illustration of a possible cost function surface (red mesh) with a global minimum (best solution of a registration problem). The optimization algorithm iteratively moves (arrows) the guess for the parameter vector \vec{m} according to certain criteria (e.g., along the direction of the gradient of the cost function but in the opposite sense) to find the solution [161]. 46

Figure 3.1. Two methods used for measuring of the relative length changes for various groups of specimens: (a) and (b) schematic illustration of the gauge (Rig) used for experimentally measuring the length change (dimensional change along the Z-axis) and (c) real mechanical gauges used in this study, referred to as "expansion measurement set-up1" throughout the thesis. (d) Schematic illustration of the Rig based on laser, custom designed and built during this PhD project for the purpose of automating the specimen longitudinal dimensional (relative) changes, entitled as "expansion measurement set-up2" throughout the thesis. 63

Figure 3.2. Two methods used for fixing the specimens to the rotating stage of the tomograph: (a) piezoelectric actuators and sample holder, called "holding set-up1" throughout the thesis; and (b) hexapod and sample holder, called "holding set-up2" throughout the thesis. 65

Figure 3.3. Example tomographic slices of one specimen from the experimental campaign described in Chapter 5. (a) and (b) show the slice, located at the same position, from the reference and deformed tomograms, respectively. The deformed tomogram of (b) is the one at about 195 days since start of the ASR acceleration and after the full chain of registrations. (c) and (d) show the results of the two distinct temporal subtractions, leading to the identifications of regions of empty cracks (inset (c)) and of pore space filled with ASR products (inset (d)), respectively 69

Figure 3.4. Comparison of empty crack segmentation results obtained by the black top-hat (BTH) transform + thresholding and by the temporal subtraction (TS) + thresholding procedures. (a): example ROI selected from one slice of a tomogram at a certain time t_i for one of the specimens of the experimental campaign described in Chapter 5, containing a partially empty crack; (b) the binary tomogram of empty cracks obtained from the BTH segmentation, superimposed on top of the same image as in (a) and rendered in semi-transparent red color; (c) binary tomogram of empty cracks obtained from the TS segmentation, superimposed on top of the subtraction image $\{I(\vec{x}_j, t_0)\}_{j=1,\dots,N} - \{\tilde{I}(\vec{x}_j, t_i)\}_{j=1,\dots,N}$. The comparison of (c) and (b) shows that the empty crack segmentation based upon the TS-based approached was less affected by artefacts and errors. 70

Figure 3.5. (a) 3D rendering of the segmented, total crack network (containing or not containing ASR products) of the U-Cs specimen (discussed in chapter 5), at 250 days. Each separated part (branch) of the crack network is rendered with a distinct color, just for the purpose of distinguishing them. The color assignment to each branch was random. (b)-(d) Three examples of separated branches of the crack network at 250 days, for the same specimen. The large parallelepiped box highlighted in orange delineates the tomographed volume. The smaller grey box shows a zoom-in view of the respective crack branch. The blue, parallelepiped box is the crack's bounding box oriented according to the three eigenvectors of the crack's shape tensor \mathbf{G} . Each eigenvector, located at the center of mass of the crack and scaled by half the lateral size of the bounding box along the same direction, is also rendered as a solid arrow. The red arrow refers to the eigenvector associated with the first eigenvalue. The green arrow to the second eigenvector and the blue one to the third. 75

Figure 3.6. Two examples of separate cracks (also called crack network branches) with rather folded surface, e.g., concave cracks. The large parallelepiped box highlighted in orange delineate the tomographed volume. The smaller, light grey box shows a zoom-in view of the respective crack network branch. The dark grey, parallelepiped box is the branch's bounding box oriented according to the three eigenvectors of the branch's shape tensor \mathbf{G} . Each eigenvector is also rendered as a solid arrow. It is located at the center of mass of the branch and scaled by half the lateral size of the bounding box along the same direction. The red arrow refers to the eigenvector associated with the first eigenvalue. The green arrow to the second eigenvector and the blue one to the third. 76

Figure 3.7. Description of the approach used for measuring/estimating the relative length change of the specimens by exploiting the results of 3D, global affine registration of the tomograms. (a) Rendering of the Z-component of the displacement vector field associated with the global affine registration results, $u_{Z,AFF}(\vec{x}, t_i)$, for a specimen at a given time point t_i , with $i \neq 0$. The color scale is in units of number of voxels. The units for the axes of the Cartesian frame of reference are also number of voxels. (b) The $u_{AFF,Z}(\vec{x})$ inside a 3D ROI spanning the entire volume along the Z-axis, with size $0.2 \times 0.2 \text{ mm}^2$ on the X – Y slices and centered in the middle of each such slice. (c) Schematic illustration of a specimen and of the axes of the respective Cartesian frame of reference. The indicative location of the volume investigated by XT is also specified. (d) Horizontal axis: values of $u_{Z,AFF}(\vec{x}, t_i)$ averaged over various 2D ROIs of distinct size located on slices orthogonal to the Z-axis and centered in the center of the slice itself, as a function of their Z-position (left vertical axis). Vertical axis on the right: size of the 2D X-Y ROIs over which $u_{Z,AFF}(\vec{x}, t_i)$ was averaged. The red line refers to the left vertical axis. The colored, circular markers refer to the right vertical axis and show the minimum and maximum values of $u_{Z,AFF}(\vec{x}, t_i)$ along the Z-axis, after averaging it over various 2D, rectangular ROIs. Circles of distinct colors show minimum and maximum values in correspondence of distinct ROI size. 79

Figure 4.1. Evolution of the relative change (with respect to the start of the ASR acceleration) in specimen length for the specimens cast with the three aggregate types (B, P and U) and with size of (a) $40 \times 40 \times 160 \text{ mm}^3$ and (b) $25 \times 25 \times 100 \text{ mm}^3$, respectively. The numbers 40 and 25 in the legends indicate the corresponding cross-sectional size of each specimen. Corresponding evolution of the relative change in specimen mass for the specimens with size of (c) $40 \times 40 \times 160 \text{ mm}^3$ and (d) $25 \times 25 \times 100 \text{ mm}^3$, respectively. In each plot, the marker indicates the average value from the set of six specimens cast for length and mass measurements. The error bar indicates the empirical standard deviation from the same set. 90

Figure 4.2. Examples of SEM-BSE micrographs of polished and epoxy-impregnated cross-sections from different specimens cast with B, P and U aggregates (within each column, highlighted with dotted boxes), acquired at (a) - (c) 50 days, (d) - (f) 150 days and (g) - (i) 500 days of ASR acceleration, respectively. 92

Figure 4.3. Energy-dispersive X-ray spectroscopy (EDX) analysis results, showing two atomic concentration ratios (alkalis over silicon and calcium over silicon) measured at more than 30 points located in regions of both crystalline (well inside the aggregates) and amorphous (at the aggregate boundaries and within the cement paste) ASR products. Each marker indicates the average value over the whole set of measuring points, while the error bar was defined as the empirical standard deviation of the same set. In addition to the results for the laboratory-accelerated specimens, cast with the three aggregate types, similar results are also shown for one of the field-exposed specimens, the B1(C+F) one. 92

Figure 4.4. Examples of tomographic slices from ROIs of the B40, P40 and U40 specimens, shown at three different time points to characterize qualitatively the ASR cracking. The first row shows always

the slice at the same position from the tomograms of a B40 specimen, acquired at (a) 50 days, (b) 150 days and (c) 500 days, respectively. The second row, insets (d) to (f), shows something similar but for a P40 specimen. The last row, insets (g) to (i), shows a similar example but for a U40 specimen. 93

Figure 4.5. (a)-(c): example of a slice from a ROI of an additional P40-2 specimen, obtained from its tomograms at three time points different from the ones used for XT on the other specimens, (a) 1 day, (b) 150 days, (c) 250 days, respectively, during ASR acceleration. The corresponding slice from the corresponding binary tomograms of the segmented cracks is superimposed over the respective X-ray tomogram's slice at (d) 1 day, (e) 150 days and (f) 250 days. The full binary tomograms of the segmented cracks are rendered in 3D in insets (g) to (i), for the three distinct time points, respectively. In each inset (g) to (i), the parallelepiped box surrounding the crack network indicates the specimen's tomographed volume. 95

Figure 4.6. 3D rendering of the segmented cracks binary tomograms (in dark red) at 500 days since ASR acceleration start, for the laboratory specimens (a) B40, (b) P40 and (c) U40. In each inset, a small part of the concrete was also rendered (in grey tones), while the most of it was corner-cut to reveal the segmented cracks inside it. 96

Figure 4.7. An example of a tomographic slice from each field-exposed specimen: (a) BF-40, (b) B1(C+NRF)-40 and (c) B1(C+F)-40 specimen, respectively. The rectangle in each inset indicates the smaller ROI which was cut out of the specimen in order to perform X-ray tomography with higher spatial resolution. Insets (d) to (f) show the same slices as in (a) to (c) but, in addition, overlapped on top of them, the corresponding slice taken at the same position from the binary tomogram of the segmented cracks. Such binary tomograms of the segmented crack networks are shown 3D rendered in (g) to (i), with part of the specimens also rendered in grey tones and partly not in order to allow viewing the segmented crack network inside them. 97

Figure 4.8. Quantitative comparison of the ASR cracking in different specimens based on the total crack volume fraction, \tilde{V}_{cracks} , as defined in Eq. (4.1), computed (a) for the laboratory specimens with size $40 \times 40 \times 160 \text{ mm}^3$, and (b) for the laboratory specimens with sizes $25 \times 25 \times 100 \text{ mm}^3$. The \tilde{V}_{cracks} values for both the laboratory (at the final time $t_f = 500$ days) and the field-exposed specimens. 99

Figure 4.9. Plots of the kernel density estimate (KDE) of the joint probability density function (PDF) of the two shape feature variables, the elongation E and the flatness F , computed from the shape tensor analysis of the segmented total crack network and interpreted as a bi-variate random variable, $(E; F)$. The statistical sample of such PDF was provided, for each specimen, by the set of values $\{(E_i; F_i)\}_{i=1, \dots, C}$ also plotted and obtained from the shape tensor analysis, where C indicates generically the total number of disconnected and independent cracks of a specimen at the chosen time point. (a) to (c): B40, P40 and U40 specimens, respectively, all at $t_f = 500$ days. (d) to (f): b25, p25 and u25, respectively, all at $t_f = 500$ days. (g) to (i): BF-40, B1(C+NRF)-40 and B1(C+F)-40, respectively. In all of the plots, the maximum value of the scale for the KDE estimates of the PDF is 3330. 100

Figure 4.10. (a) and (c): empirical (i.e., from the statistical sample) complementary cumulative distribution function (cCDF) of the bounding box length, L , $G_{\mathbb{L}}(L)$, in \log_{10} - \log_{10} scales (Zipf plot). Each separate crack contributed to one sampled value for L . (b) and (d): similar plots for the total crack network's local thickness, T_{local} , $G_{\mathbb{T}_{local}}(T_{local})$. Each voxel inside the total crack network provided a sampled value. (a) and (b): comparisons of the Zipf plots of $G_{\mathbb{L}}(L)$ and of $G_{\mathbb{T}_{local}}(T_{local})$, respectively, between the laboratory specimens, B40, P40 and U40, and the field ones, BF-40, B1(C+NRF)-40 and

B1(C+F)-40. (c) and (d): comparison of the Zipf plots of $G_L(L)$ and of $G_{T_{local}}(T_{local})$, respectively, for the b25, p25 and u25 specimens. 102

Figure 4.11. Visualization of the crack orientation analysis results. The crack orientation was operationally defined as the direction of the eigenvector \hat{u}_1 associated with the first and largest eigenvalue of the shape tensor \mathbf{G} . The segmented total crack network of a specimen corresponded to a set of \hat{u}_1 's, one for each independent crack. Each of these vectors are here plotted, after rescaling their magnitudes by a factor equal to 0.33, to make their projections on the planes of the Cartesian frame of reference more visible. The projections of \hat{u}_1 on the $X - Y$ plane are in violet, those on the $X - Z$ plane are in dark blue and those on the $Y - Z$ plane are in light blue. (a) to (c): B40, P40 and U40 specimens, respectively, all at $t_f = 500$ days. (d) to (f): b25, p25 and u25, respectively, all at $t_f = 500$ days. (g) to (i): BF-40, B1(C+NRF)-40 and B1(C+F)-40, respectively. 103

Figure 4.12. Example tomographic slices from a VOI of (a) the B40 specimen, (b) the corresponding binary tomogram of the segmented cracks overlapped on the same slice as in (a), and (c) the 3D rendering of the binary crack network. (d) to (f): the corresponding slices as in (a) to (c), respectively, but from the B40-cut-25 specimen, i.e., the sub-specimen obtained from B40 after cutting it to the cross-sectional size of $25 \times 25 \text{ mm}^2$, including the same VOI as shown for the original B40 specimen in insets (a) to (c). 104

Figure 4.131. Quantitative comparison of the specimen size effect on the crack network segmentation results, in terms of crack volume fraction, \tilde{V}_{cracks} . The specimen labels containing "cut" refer to sub-specimens cut out from the original corresponding specimen, including a region already part of the one tomographed in the original specimen, such that the crack network could be segmented for the same exact region at two distinct tomographic spatial resolution levels. 105

Figure 5.1. 2D ROIs selected on slices from the tomogram of a P-Ref specimen, showing the ASR-induced cracks and air voids filled with ASR products. 116

Figure 5.2. Examples of ROIs from tomograms of four distinct specimens cast with distinct alkali-doping. Each ROI was selected on a slice from the tomogram of a corresponding specimen. The common feature of each chosen ROI is the presence of air voids. At the late (20 weeks) stage of the used ASR acceleration, air voids were typically partially or almost completely filled with ASR products. The tomograms are ordered from left to right based upon the increasing atomic number of the alkalis (Na, K, Rb and Cs, respectively). ASR products labelled by Cs^+ cations increased their X-ray attenuation to a level above that of any other material phase in the specimens, except for some high density/high atomic number minerals in the aggregates. Thus, Cs-labelled ASR products were characterized on average by the highest X-ray attenuation contrast to any other material phase. 117

Figure 5.3. (a) and (b): examples of SEM-BSE micrographs of ASR products precipitated/accumulated inside the cracks of aggregates from a P-Ref specimen and a P-Cs one, respectively. 118

Figure 5.4. (a) to (c): SEM-BSE micrographs providing examples of the distribution of ASR products and cracks in the specimens cast with P aggregates and with CsNO_3 . The micrographs were acquired at 14, 80 and 120 days, respectively. In inset (b), ITZ means Interfacial Transition Zone. 119

Figure 5.5. Evolution of the relative dimensional change of the specimens cast with the P aggregates, with (blue shades and filled markers) and without (grey shades and hollow markers) Cs-doping. The label "digital" means the estimate was obtained for the tomographed volume of one specimen of each

type. The label "mechanical" means the estimate was obtained for the whole specimen volume, by experimental measurements with the gauge described in Section 3.2. (a) Results for the relative change in size along the Z-axis (i.e., length). The experimentally measured values were obtained, for each mix type, for six specimens (including the one being the subject of the tomography analysis). The marker shows the average of the six values. The error bar shows their empirical standard deviation. (b) and (c) Relative dimensional changes of the tomographed volumes, along the X, Y and Z axes for the P-Ref and P-Cs specimens, respectively. 121

Figure 5.6. The time series of the (a) quasi-static Young's modulus, (b) the flexural and (c) the compressive strength of specimens with and without Cs addition, cast with P aggregates. In each plot, the markers indicate the average of three values from three distinct specimens, while the error bar indicates the respective empirical standard deviation. In the case of the Young's modulus, the measurements were successively performed always on the same specimens, which were the same used also for XT. . . . 121

Figure 5.7. A slice from a ROI of the P-Cs specimen at four different time points. ASR products can be observed as very bright regions within cracks and near the aggregate boundaries. The four insets here are from the tomogram at (a) 1 day, (b) 85 days, (c) 145 days and (d) 250 days. 124

Figure 5.8. A slice from another ROI of the P-Cs specimen at four different time points. ASR products could be observed as filling up an air void a few mm away from the aggregate highlighted by the arrow, as a crack running through such aggregate evolved and propagating into the cement paste till the air void itself. The products were transported from such aggregates till the air void via the propagating cracks. The six insets shown here are from the tomogram at (a) 1 day, (b) 65 days, (c) 85 days, (d) 145 days, (e) 195 days and (f) 250 days. 125

Figure 5.9. Binary tomograms of the segmented empty cracks (in cyan) and of the ASR products (both inside and outside cracks, in yellow). Only a small VOI of the P-Cs specimen is shown. Such VOI contained cracks that were nucleated inside a single aggregate and propagated later into the surrounding cement paste. The insets from (a) to (f) correspond to different time points during the ASR acceleration, including 1 day, 65, 85, 145, 195 and 250 days, respectively. 126

Figure 5.10. Quantitative assessment of the ASR cracking in the P specimens by the total volume fraction of ASR-generated cracks (with or without ASR products), $\tilde{V}_{ASR\ cracks}$, as defined in Eq. (3.6). The total volume of ASR products (also normalized by the tomogram volume) is also shown by yellow markers 127

Figure 5.11. (a) and (b): empirical (i.e., from the statistical sample) complementary cumulative distribution function (cCDF) of the ASR crack bounding box length, L , $G_L(L)$, in \log_{10} - \log_{10} scales (Zipf's plot), for the P-ref and the P-Cs specimens, respectively. Each separate crack contributed to one sampled value for L . (c) and (d): corresponding Zipf's plots but for the ASR crack local thickness, T_{local} . In each Zipf's plot, the cCDF is shown at three distinct time points. 128

Figure 5.12. Visualization of the determinant of the Jacobian matrix ($J_{\vec{T}_{N-AFF}}(\vec{x}, t_i)$) of the transformation vector field $\vec{T}_{N-AFF}(\vec{x}, t_i)$ associated with the non-affine registration. This scalar field is used as a spatial map of the factor by which the volume locally expanded or contracted due to the spatially heterogeneous components of the ASR-induced displacement vector field. In this figure, only one slice from the tomographed volume is shown: (a) X-ray tomogram of the P-Ref specimen at the beginning of the ASR acceleration (at 1 day); (b) and (c) slices from the X-ray tomograms at 155 and 250 days, respectively; (d) and (e) the same slices as in (b) and (c), plus, overlapped on top of them semi-transparently and rendered according to the indicated color scale, the 2D cross-section, at the same position,

from $J_{\vec{T}_{N-AFF}}(\vec{x}, t_i)$, at the same corresponding time points. The scale bars of insets (d) and (e) have arbitrary units since $J_{\vec{T}_{N-AFF}}$ is a dimensionless variable. Values greater than 1 represent volumetric expansion, while values smaller than 1 indicate volumetric contraction. 131

Figure 5.13. Similar plots as in Figure 5.12 but for the P-Cs specimen. The chosen time points for the visualization are 30 days (insets (a) and (e)), 85 days ((b) and (f)), 145 days ((c) and (g)), 250 days ((d) and (h)). The first time point of visualization is here 30 days, instead of 1 day as in Figure 5.10. At such age, no ASR cracks could be resolved. Thus, the corresponding registered tomogram was essentially identical to the one at 1 day, providing a view of the reference cracking state. However, local deformations appeared already at 30 days, which motivates showing the $J_{\vec{T}_{N-AFF}}(\vec{x})$ scalar field already at such time point. 132

Figure 6.1. (a) to (e): examples of regions of interest (ROIs) on tomographic slices at 150 days of ASR acceleration, from the specimens cast with the U aggregates and with various BaSO₄ concentrations. (f) to (j): the same slices as in (a) to (e) but, additionally, with the corresponding slices from the binary tomograms of the segmented aggregates rendered as semi-transparent and in blue and overlaid on top of the tomographic slices. 145

Figure 6.2. Similar slices as shown in Figure 6.1 but for the specimens cast with the P aggregates. 145

Figure 6.3. Full tomogram voxel value histograms for the specimens cast with various BaSO₄ concentrations (0.25, 0.75, 1.5, 2.5 and 3 vol.%) and with (a) U and (b) P aggregates, respectively. Each histogram refers to the tomogram of a single specimen at 150 days of ASR acceleration. (c): volume fraction of segmented aggregates calculated based upon each tomogram whose voxel value histogram is shown in insets (a) and (b). The aggregate volume fraction was defined as the volume of segmented aggregates divided by the full volume of the tomogram. 146

Figure 6.4. (a) Evolution of the relative length change, along the specimen's longitudinal direction (Z-axis), for the specimens cast with the two aggregate types (blue shades for U, red shades for P) and with (filled markers) or without (hollow markers) BaSO₄. The markers indicate mean values while the error bars' size is the standard deviation of an ensemble of six distinct specimens, for each specimen batch. (b): evolution of the relative mass change of the same specimens as for (a). (c): evolution of the relative length change for the tomographed volume of one of the six U reference specimens and computed along each axis from the the global affine registration results (markers in grey tones). The relative length change along the Z-axis is compared with the corresponding experimental values from inset (a) (blue markers). (d): similar plot as in (c) but for the tomographed volume of one of the six P reference specimens. (e) and (f): similar plots as in (c) and (d) but for the tomographed volume of one of the six specimens cast with 2.5 vol.-% BaSO₄. 147

Figure 6.5. The time series of the quasi-static, compressive Young's modulus of specimens cast with both types of aggregates, without or with two BaSO₄ concentrations. The markers indicate mean values while the error bars size the standard deviation of an ensemble of three specimens (always the same at each time point), for each specimen batch. 149

Figure 6.6. Visualization of the evolution of ASR cracks and associated localized deformations for the U-Ref specimen. As an example, it is shown here only one small ROI on one slice from its tomographed volume, at multiple time points. The localized deformations are estimated by the determinant of the Jacobian matrix ($J_{\vec{T}_{N-AFF}}(\vec{x}, t_i)$) of the transformation vector field $\vec{T}_{N-AFF}(\vec{x}, t_i)$ associated with the

non-affine registration. Its values larger than 1 indicate local volumetric expansion. Its values smaller than 1 indicate volumetric shrinkage. (a) X-ray tomogram at 1 day since start of the ASR acceleration. (b) and (c): slice at the same position as in (a) but from the tomograms at 150 and 250 days, respectively. (d) and (e): the same slice as in (b) and (c), respectively, and, overlapped on top of them, semi-transparently, the slice at the same position but from $J_{\vec{T}_{N-AFF}}(\vec{x}, t_i)$ at the corresponding time points, respectively. The scale bars in (d) and (e) have, by definition of $J_{\vec{T}_{N-AFF}}$ (relative volume), no unit. 151

Figure 6.7. Similar visualization as in Figure 6.6 but for the U-2.5 vol.-% BaSO₄ specimen. The chosen time points for the visualization are 35 days (insets (a) and (e)), 55 days ((b) and (f)), 155 days ((c) and (g)), 250 days ((d) and (h)). The tomograms did not change significantly between 1 day and 35 days. Thus, the one at 35 days was representative of the reference tomogram at 1 day. 153

Figure 6.8. A small VOI of the binary tomograms of cracks inside aggregates (cyan) and in the cement paste (blue) is rendered at distinct time points for the U-2.5 vol.-% BaSO₄ specimen. Such VOI contained cracks, which were nucleated in an aggregate and further propagated into the surrounding cement paste. The insets from (a) to (d) correspond to different time points during the ASR acceleration, including 1 day, 55, 85 and 250 days, respectively. 154

Figure 6.9. Quantitative comparison of the ASR cracking in different specimens based on the estimates of two variables: (1) the total volume of ASR-induced cracks (filled grey markers for the U-2.5 Vol.% Ba and P-2.5 Vol.% Ba specimens and empty grey markers for the reference specimens) and those only in aggregates (lighter blue or red, filled markers, for U and P specimens, respectively) or cement paste (darker blue or red, filled markers, for U and P containing specimens, respectively), normalized by the tomogram volume, named as $\tilde{V}_{ASR,cracks,j}$, for the (a) U-2.5 Vol.% Ba and U-Ref and (b) P-2.5 Vol.% Ba and P-Ref specimens. 155

Figure 6.10. Correlation between the ASR cracks total volume fraction, $\tilde{V}_{ASR,cracks,tot}$, and the relative length changes along the X-, Y- and Z-axis and the relative volume change computed for the tomographed volumes of the specimens using the results of the global affine registration. The relative length changes are the $\frac{\Delta L_{AFF,k}}{L_{AFF,k}}$, with $k = X, Y, Z$, while the relative volume change was estimated approximately as $\sum_{k=X,Y,Z} \frac{\Delta L_{AFF,k}}{L_{AFF,k}}$. (a) U-2.5 vol.-% BaSO₄ specimen and (b) P-2.5 vol.-% BaSO₄ one. The dotted line indicates the $y = x$ line of the $\left(\tilde{V}_{ASR,cracks,tot}; \sum_{k=X,Y,Z} \frac{\Delta L_{AFF,k}}{L_{AFF,k}}\right)$ plane. 156

Figure 6.11. (a) and (b) complementary cumulative distribution function (cCDF) of the crack bounding box length, L , $G_{\mathbb{L}}(L)$, in \log_{10} - \log_{10} scale (Zipf's plot), for the specimen cast with U aggregates (with and without BaSO₄) and for the specimen cast with the P aggregates, respectively, at 250 days. (c) and (d) corresponding Zipf's plot for the crack local thickness, T_{local} 157

Figure 6.12. Plots of the kernel density estimate (KDE) of the joint probability density function (PDF) of the two shape feature variables, the elongation E and the flatness F , computed from the shape tensor analysis of the segmented total crack networks and treated as a bi-variate random variable, $(E; F)$. The statistical sample of such PDF was provided, for each specimen and at each time point, by the set of values $\{(E_i; F_i)\}_{i=1,\dots,C}$ obtained from the shape tensor analysis, where C indicates generically the total number of disconnected and independent branches of the segmented, total crack network of a specimen and at a certain time point. (a) and (b) U-Ref specimen, (c) and (d) P-Ref one, (e) and (f) U-2.5vol.% BaSO₄, and (g) and (h) P-2.5vol.% BaSO₄ specimens, at 1 day and 250 days, respectively. 158

Figure 6.13. Visualization of the crack orientation analysis results for the reference specimens and those cast with optimal BaSO₄ concentration value of 2.5 vol.-%. The crack orientation was operatively defined as the direction of the eigenvector \hat{u}_1 associated with the first and largest eigenvalue of the shape tensor \mathbf{G} . The segmented total crack network of a specimen corresponded to a set of \hat{u}_1 's, one for each independent crack (branch of the network). Each of these vectors are here plotted in green, after rescaling their magnitudes by a factor equal to 0.33, to make their projections on the planes of the Cartesian frame of reference more visible. The projections of \hat{u}_1 on the X – Y plane are in violet, those on the X – Z plane are in dark blue and those on the Y – Z plane are in light blue. : (a) and (b) U-Ref, (c) and (d) P-Ref, (e) and (f) U-2.5vol.% BaSO₄ and (g) and (h) P-2.5vol.% BaSO₄, at 1 day and 250 days, respectively. 160

Figure 6.14. (a): evolution of the longitudinal relative length change of u specimens, directly measured by the expansion measurement setup 2, shown in Figure 3.1 (3) and described in Section A4, on 10 specimens ($\frac{\Delta L_Z}{L_Z}$, blue markers) and indirectly estimated from the global affine registration results for 3 additional specimens for their tomographed volumes ($\frac{\Delta L_{AFF,Z}}{L_{AFF,Z}}$, red-pink markers). Each marker shows the average value, while the error bar was defined as the empirical standard deviation. (b): relative dimensional changes of the tomographed volumes along the X, Y and Z axes, $\frac{\Delta L_{AFF,k}}{L_{AFF,k}}$, with $k = X, Y$ and Z . The markers show the average of the values from the 3 tomographed specimens while the error bars the respective empirical standard deviation values. and (c): relative mass change time series of the 10 specimens whose $\frac{\Delta L_Z}{L_Z}$ is shown in inset (a). 162

Figure 6.15. Time series of the (a) quasi-static (longitudinal, compressive) Young's modulus, (b) flexural strength, and (c) (longitudinal) compressive strength of the U specimens. In each plot, the markers show the average and the error bar the empirical standard deviation of an ensemble of values from distinct specimens, the ensemble size being 3, 3 and 6 for insets (a), (b) and (c), respectively. For the Young's modulus measurements, the specimens were always the same at each time point. 163

Figure 6.16. Visualization of the determinant of the Jacobian matrix, $J_{\vec{T}_{N-AFF}}(\vec{x}, t_i)$, of the transformation vector field $\vec{T}_{N-AFF}(\vec{x}, t_i)$ associated with the non-affine registration, as computed from the tomographic time-series of the u_1 specimen. Only a few time points from the series are shown. $J_{\vec{T}_{N-AFF}}(\vec{x}, t_i)$ is used as a spatial map of the factor by which the volume locally expanded or shrunk due to the spatially heterogeneous components of the ASR-induced displacement vector field. (a) to (d): one slice from the specimen's fully registered X-ray tomogram at 56, 168, 224 and 404 days, respectively. (e) to (h): the same slices as in (a) to (d) but, in addition, overlapped on top of them, the corresponding slices from $J_{\vec{T}_{N-AFF}}(\vec{x}, t_i)$ are rendered semi-transparently and color-coded according to the indicated color scale. The scale bar of the insets (e) to (h) has no unit. $J_{\vec{T}_{N-AFF}}(\vec{x}, t_i)$ values greater than 1 represent volumetric expansion, values smaller than 1 indicate volumetric shrinkage. 164

Figure 6.17. Binary tomograms of cracks inside aggregates (in purple) and within the cement paste (in aquamarine), rendered for the u_2 specimen. Parts of the segmented aggregates are also rendered as solid, opaque regions in dark grey, at the bottom of the volume. The insets from (a) to (f) correspond to different time points during the ASR acceleration, including 1 day, 112, 140, 168, 224 and 404 days, respectively. 165

Figure 6.18. (a) to (c): 3D rendering of the binary tomogram of the segmented cracks at 404 days, with distinct colors distinguishing between aggregate (purple) and cement paste (aquamarine) regions, for

the u_1 , u_2 and u_3 specimens, respectively; (d) to (f): cumulative line projections of the total crack network volume shown in insets (a) to (c), respectively, on each of the three orthogonal plane of the Cartesian frame of reference; black pixels on such projection planes indicate absence of projection; (g) to (i): relative length changes time series of the tomographed volume along the X, Y and Z axes as computed from the results of the global affine registration, $\frac{\Delta L_{AFF,k}}{L_{AFF,k}}$, with $k = X, Y$ and Z , for the u_1 , u_2 and u_3 specimens, respectively. 166

Figure 6.19. (a) Time series of the ASR crack volume fractions, distinguishing between the volume fraction for all the cracks, $\tilde{V}_{ASR,cracks,tot}$, that for cracks just within the aggregates, $\tilde{V}_{ASR,cracks,agg}$ and that for those just in the cement paste, $\tilde{V}_{ASR,cracks,cem}(t_i)$, computed for the the tomographed regions of the u specimens; each marker indicates the average value from the three specimens, while the error bar indicates the standard deviation of the three values; (b) the $\tilde{V}_{ASR,cracks,tot}$ time series and the one for the relative volume change of the tomographed region, estimated by $\sum_{k=X,Y,Z} \frac{\Delta L_{AFF,k}}{L_{AFF,k}}$; for the latter time series, at each time point, the marker also indicates the average value from the three specimens while the error bar was computed as the square root of the sum of the variances of each $\frac{\Delta L_{AFF,k}}{L_{AFF,k}}$, based on the assumption that each of it was a Gaussian random variable; (c) empirical (i.e., statistical ensemble) complementary cumulative distribution function, $G_L(L)$, of the crack bounding box length, L , in \log_{10} - \log_{10} scales (Zipf's plot) for the u_1 specimen only and at three time points (168, 224 and 404 days); (d) Zipf's plot for the crack local thicknesses, T_{local} , also for the u_1 specimen and at the sametime points as in (c). 169

Figure 6.20. (a) to (c): kernel density estimate (KDE) of the joint probability density function (PDF) of the crack elongation E and flatness F , for the u_1 specimen at 168, 224 and 404 days, respectively. (d) to (f): visualization of the crack orientation analysis results for the u_1 specimen at 168, 224 and 404 days, respectively. Each point is the projection on the equatorial plane of the point on the unit sphere with spherical coordinates $(\theta; \varphi)$, $\theta \in [0^\circ; 360^\circ]$ and $\varphi \in [-90^\circ; 90^\circ]$, representing the first eigenvector \hat{u}_1 of the shape tensor \mathbf{G} of a crack. The radial distance of a point from the origin is mapped to the elevation angle φ axis according to the vertical scale, such that the distance between two successive circles in such polar coordinates framework corresponds to 10° distance on the φ axis. The X – and Y – axis of the specimen's Cartesian frame of reference are indicated in (d) to facilitate the interpretation of the crack orientation. 170

Figure 7.1. (a)-(e) Examples of ROIs on slices from the tomograms at 85 days of different specimens cast with U aggregates and distinct $BaSO_4$ concentrations but fixed $CsNO_3$ one (except for the specimen of (a), with no $CsNO_3$). 181

Figure 7.2. The tomographic contrast-to-noise ratio between the ASR products and aggregates (right vertical axis), the ASR products and the cement paste (left vertical axis) and between the aggregates and the cement paste (horizontal axis), as computed for the distinct specimens, cast with the distinct $BaSO_4$ concentration values and either without or with $CsNO_3$ at fixed concentration, from 40 voxel values for each material phase, sampled randomly from their tomograms at 85 days. 182

Figure 7.3. (a): evolution of the relative length change, along the specimen longitudinal direction (Z-axis) and measured experimentally ($\frac{\Delta L_z}{L_z}$), of distinct specimens cast with U aggregates, $CsNO_3$ and various $BaSO_4$ concentrations. The markers indicate averages while the error bars size is the standard deviation of six values from an ensemble of six distinct specimens, for each specimen set, i.e., $BaSO_4$

concentration. (b): comparison between the experimentally measured $\frac{\Delta L_z}{L_z}$ of the six specimens and the relative length change, along any axis of the Cartesian frame of reference and of another specimen, cast with 1.5 vol.-% BaSO₄, computed from the results of the affine registration (labelled as digital), $\frac{\Delta L_{AFF,k}}{L_{AFF,k}}, \forall k = X, Y, Z$ 183

Figure 7.4. Visualization of the evolution of ASR cracks and associated localized deformations for the U-Cs-1.5 vol.-% BaSO₄ specimen. As an example, it is shown here only one small ROI on one tomographic slice, at multiple time points. The localized deformations are estimated by the determinant of the Jacobian matrix ($J_{\vec{T}_{N-AFF}}(\vec{x}, t_i)$) of the transformation vector field $\vec{T}_{N-AFF}(\vec{x}, t_i)$ associated with the non-affine registration. Its values larger than 1 indicate local volumetric expansion. Its values smaller than 1 indicate volumetric shrinkage. (a) X-ray tomogram at 1 day since start of the ASR acceleration. (c) and (e): slices at the same position as in (a) but from the tomograms at 85 and 250 days, respectively. (b): slice at 55 days. (d) and (f): the same slices as in (b) and (e), respectively. In (b), (d) and (f), the slice at the same position but from $J_{\vec{T}_{N-AFF}}(\vec{x}, t_i)$ at the corresponding time points is rendered according to a color map and overlapped semi-transparently on top of the corresponding tomographic slice. The color scale bar has, by definition of $J_{\vec{T}_{N-AFF}}$ (relative volume), no unit. 185

Figure 7.5. 3D rendered volumes of interest (VOIs) from the binary tomograms of empty cracks either inside aggregates (cyan) or within the cement paste (blue) and of ASR products in the entire part of the pore space resolved in the tomograms (e.g., spherical air voids, porous patches and cracks), with distinction between regions inside (yellow) and outside (orange) of aggregates. The analyzed tomogram was the one of the U-Cs-1.5 vol.-% BaSO₄ at 250 days. (a): rendering of the VOI of all four types of binary tomograms (ASR products inside and outside aggregates and empty cracks inside and outside aggregates) together. (b): rendering of the VOI of only the two ASR products binary tomograms. (c): rendering of the VOI of only the two binary tomograms of empty cracks. 187

Figure 7.6. (a)-(d) combined 3D rendering of the binary tomograms of empty cracks inside aggregates (cyan), of those within the cement paste (blue), of ASR products in the entire pore space (i.e., in air voids, porous patches and cracks) inside aggregates (yellow) of ASR products outside of aggregates (orange). The binary tomograms are those of the U-Cs-1.5 vol.-% BaSO₄ specimen at 1 day, 55, 145 and 250 days, respectively. 189

Figure 7.7. (a) Volume fraction of ASR products or cracks, without or with distinction between aggregates and cement paste, at distinct time points, $\tilde{V}_{ASR,k,j}(t_i)$, plotted for the U-Cs-1.5 vol.-% BaSO₄ specimen. The markers in light and dark grey correspond to the total ASR products and cracks, all over the tomographed volume, respectively. The yellow markers represent the ASR products only inside the aggregates and those in orange refer to the ASR products in the cement paste, residing in any kind of pore space regions (cracks, air voids or porous patches). The cyan and blue markers refer to the cracks, either filled by ASR products or empty, inside the aggregates and the cement paste, respectively. (b) Correlation between the different volume fractions, $\tilde{V}_{ASR,k,j}$, values and the relative volume change of the tomographed region of the U-Cs-1.5 vol.-% BaSO₄ specimen, the latter estimated by its proxy variable being the sum of relative length changes along the three axes and computed from the results of the global affine registration, $\sum_{k=X,Y,Z} \frac{\Delta L_{AFF,k}}{L_{AFF,k}}$ 191

Figure 7.8. (a): complementary cumulative distribution function (cCDF) of the crack bounding box length, L , $G_{\mathbb{L}}(L)$, shown in the form of a Zipf's plot, for specimens cast with U aggregates (with and without

$\text{CsNO}_3+\text{BaSO}_4$), at 250 days. (b): cCDF of the crack local thicknesses, T_{local} . $G_{T_{\text{local}}}(T_{\text{local}})$, also shown in the form of a Zipf's plot, for the two same specimens as in (a) and also at 250 days. 192

Figure 7.9. Plots of the kernel density estimate (KDE) of the joint probability density function (PDF) of the two shape feature variables, the elongation E and the flatness F , computed from the shape tensor analysis of the segmented total crack network and treated as a bi-variate random variable, $(\mathbb{E}; \mathbb{F})$. (a) and (b): U-Ref specimen from the first experimental campaign described in Chapter 6. (c) and (d): U-Cs-1.5 -vol.% BaSO_4 specimen. 193

Figure 7.10. Visualization of the crack orientation analysis results. The crack orientation was operationally defined as the direction of the eigenvector \hat{u}_1 associated with the first and largest eigenvalue of the shape tensor \mathbf{G} . The segmented total crack network of a specimen corresponded to a set of \hat{u}_1 's, one for each independent crack (branch of the network). Each of these vectors are here plotted in red, after rescaling their magnitudes by a factor equal to 0.33, to make their projections on the planes of the Cartesian frame of reference more visible. The projections of \hat{u}_1 on the $X - Y$ plane are in violet, those on the $X - Z$ plane are in dark blue and those on the $Y - Z$ plane are in light blue. (a) and (b): U-Ref specimen of the first experimental campaign described in Chapter 6, at 1 and 250 days, respectively. (c) and (d): U-Cs-1.5 vol.-% BaSO_4 specimen, at 1 and 250 days as well, respectively. 194

List of tables

<i>Table 2.1. ASR- reactivity of various mineral, natural rocks or artificial aggregates (adapted from Ref. [72]).</i>	20
<i>Table 2.2. Classification of quartzite mineral groups ([75] and [72]).</i>	21
<i>Table 3.1. Generic mix composition of the specimens in units of $\text{kg}\cdot\text{m}^{-3}$ (mass per m^3 of cast material).</i>	61
<i>Table 3.2. Summary of spatial resolutions achieved in different conditions in the tomograms.</i>	65
<i>Table 4.1. Mix design of the laboratory-accelerated specimens, in units of $\text{kg}\cdot\text{m}^{-3}$ (mass per m^3 of cast material).</i>	86
<i>Table 5.1. Mix composition of the reference specimens (cast without CsNO_3) in units of $\text{kg}\cdot\text{m}^{-3}$ (mass per m^3 of cast material).</i>	114
<i>Table 5.2. Mix composition of the Cs-doped specimens in units of $\text{kg}\cdot\text{m}^{-3}$ (mass per m^3 of cast material).</i>	114
<i>Table 6.1. Mix composition of the BaSO_4 containing specimens in units of $\text{kg}\cdot\text{m}^{-3}$ (mass per m^3 of cast).</i>	139
<i>Table 6.2. Mix composition of the specimens with optimal BaSO_4 vol.% in units of $\text{kg}\cdot\text{m}^{-3}$ (mass per m^3 of cast).</i>	140
<i>Table 7.1. Mix composition of the specimens in units of $\text{kg}\cdot\text{m}^{-3}$ (mass per m^3 of cast).</i>	178

Chapter 1. Introduction and objectives

1.1 Background

Concrete is the most used construction material worldwide [1], owing to its low costs, versatility, durability in most environments and low specific carbon footprint compared to other construction materials such as steel, aluminum and wood. Additional advantages are high fire resistance [2] and high construction speed [3]. Nonetheless, like any other material, it also has durability issues, strongly related with its environmental boundary conditions. Several chemo-mechanical processes, which can degrade its mechanical properties and reduce the integrity and service life of structures made of it, involve its interactions with substances stemming from the surrounding environment. For example, the ingress of aqueous solutions, e.g., sea or ground or industrial waters, may trigger microstructural changes as a consequence of chemical reactions.

In the sea water case, its chloride ions content may trigger or accelerate corrosion of steel reinforcement bars (rebar) [4]. The corrosion products growth leads to local expansion, followed by cracking and, in certain cases, even surface spalling, in addition to the reduction in the rebars' cross-section size and to the loss of concrete-rebar bonding [5]. In the ground or industrial waters cases, sulfates react with some of the cement hydrates, leading to the formation of crystalline phases, e.g., ettringite and gypsum. Their crystal growth and associated stress development are considered among the main causes of the observed expansion and following cracking, a damage process frequently called sulfate attack [6], [7].

Other chemo-mechanical, deleterious processes are not based upon interactions with foreign substances, although they may still be modulated by the external environment. This PhD Thesis deals with one of them, the Alkali-Silica Reaction (ASR) and its associated damage [1], [8]. ASR (damage) is one of the most deleterious processes which can occur in concrete. It originates from an intrinsic chemical reaction between certain components of the aggregates (meta-stable silica) and hydroxyl ions and alkalis present in the concrete pore solution [9], [10]. The ASR products can lead to local expansions and cracking (see figure 1.1). The damage is twofold: not only the cracking but the deformations themselves may also impair the stability and functionality of a structure. The progressive cracking can degrade the mechanical properties and can additionally enhance the ingress of harmful substances, thus supporting other degradation processes, such as rebar corrosion [1].

The occurrence of ASR has been reported from every continent, both in the northern and in the southern hemispheres [11]. Switzerland is not an exception. One of the most important (Swiss) class of infrastructures suffering from ASR damage are dams, also due to their continuous contact with water. In 2017, the ASR working group of the Swiss Committee on Dams assessed the structural status and evolution (in terms of deformations) of 119 dams in Switzerland [12]. It found that about 50% of the Swiss dams were undergoing ASR and had developed permanent deformations. Only 38 dams exhibited just ASR tendencies, without structurally relevant deformations and changes. It was concluded that the concrete expansion had influenced 35% to 45% of the Swiss dams. Repair works have been conducted in a few cases, such as at the Illsee, Sera and Salanfe dams. Future repairs or replacements are expected.

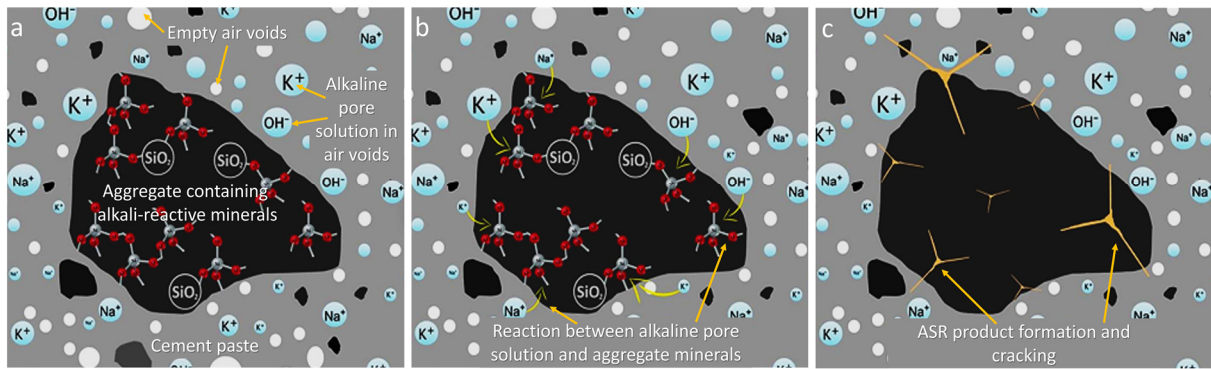


Figure 1.1. Schematic illustration of some of the sequential processes constituting ASR: (a) highlight of key ASR actors, e.g., alkali cations (Na^+ and K^+) and hydroxyl (OH^-) anions in the pore space solution and certain types of silica (SiO_2) in the aggregates (black regions); (b) reaction between the alkaline pore solution and silica in the aggregates; (c) cracking, induced by formation of ASR products (in yellow) within the aggregates, and propagation of cracks into the cement paste (in grey).

In general, alkali-reactive aggregates are found worldwide. Only few countries or regions have not reported ASR problems so far [11]. ASR damage in various structures imposes each year and in several countries a considerable amount of economic burden on society, due to the respective maintenance or replacement costs [11].

Since its first recognition in the 1940s by Stanton [13], extensive ASR research efforts have been invested for decades. On one side, methods have been developed for assessing, with laboratory tests, which aggregate and concrete types are more prone to ASR [11]. These efforts have provided engineers some pragmatic means to reduce the risk of extensive ASR damage in new concrete structures. However, they have been limited in scope and success, being also extremely time consuming and expensive. On the other side, more basic research efforts have increasingly adopted bottom-up, materials science-based approaches aiming directly at unveiling underlying mechanisms of ASR [14]–[17]. The belief is that such understanding of ASR chemo-mechanical mechanisms would constitute the basis for developing (1) laboratory-scale, experimental models able to mimic, within shorter time scales, the long-term performance of ASR-affected concrete structures [18]–[20], (2) optimized mix designs to avoid ASR in newly built structures and (3) repair approaches and tools to mitigate ASR in older structures [8], [21], [22].

The understanding of some ASR basic mechanisms has significantly advanced in the last three decades [8], [10], [23]–[29]. For example, various mechanisms at the basis of ASR (damage) have been investigated. As a consequence, partially predictive models both for laboratory-scale specimens [8], [29]–[33] and for actual structures have been developed [34]–[36]. This has occurred in parallel to the development of effective assessment procedures and experimental model systems to better monitor and characterize the ASR evolution [1], [32], [37]–[39].

Despite the mentioned efforts, the capability to fully explain, predict and avoid or mitigate ASR damage is far from being achieved [32], [40]–[43]. One of the reasons is that the governing chemo-mechanics is still characterized by many unknowns. Knowledge gaps still exist at multiple length and time scales and concerning the couplings between distinct types (i.e., chemical and mechanical) of involved processes [8].

ASR chemistry has been extensively studied. It is known that ASR is strongly dependent on several factors. The major ones include (i) the presence of enough reactive sites within the aggregates, (ii) the availability of a high concentration of hydroxyls and alkalis in the concrete pore solution, (iii) a source of soluble calcium and (iv) high moisture availability [8], [44], [45]. By eliminating any of such factors, ASR is significantly suppressed. In fact, several mitigation approaches consist of trying to exclude at least one of those factors [1], [18], [46], [47]. The ASR sequence has been typically described as consisting of four steps: (i) dissolution of meta-stable silica in the aggregates; (ii) formation of ASR products sol particles; (iii) formation of a ASR gel; (iv) swelling of the gel, with consequent local stress build-up within the aggregates, causing, in the long term, their cracking [8]. This paradigmatic description of ASR has been affected by many knowledge gaps and problems. Recent research results have been calling for its partial or complete revision.

The first area with knowledge gaps concerns the molecular nature of ASR products and its influence on the consequences of their formation, i.e., the local expansion and consequent cracking of the concrete micro- and, later on, mesostructure. It has been hypothesized that the ASR products, as gels, would expand as a consequence of two distinct evolution stages: (i) alkali-silica gel hydration and (ii) its volumetric increase and subsequent movement into the cement paste through the pore space, included newly created cracks inside the aggregates [1]. During the gel hydration, the difference between the chemical potential of the gel's solution and the one of the concrete pore solution would lead to water adsorption, accompanied by swelling, based on osmotic pressure [48]. Such hypothesized expansion mechanism has been recently challenged. First of all, more precise knowledge is available nowadays about the molecular nature of ASR products. As such, it is not possible anymore to consider them simply and rather abstractly as gels which interact with water. Early-age (or primary) products typically form within grain boundaries or intrinsic nano-/micro-cracks of aggregate minerals [49]. Such products are indeed often amorphous. However, later-stage (secondary) products within the bulk of aggregates are typically nano-crystalline [50].

Concerning the latter product types, micro-X-ray diffraction(XRD) and spectroscopic analysis has shown that they have molecular structure similar to that of a mineral called shlykovite [51]–[55]. The crystalline structure of different shlykovite variants is of monoclinic type with main structural units of "TOT blocks", comprising of tetrahedral Si (4- and 8-membered rings of SiO_4 -tetrahedra) layers (T) and an octahedral component (O), sandwiched between them [56]. Such layered atomic structures may differ, e.g., in terms of basal spacing value, depending upon whether the ASR products stemmed from laboratory-scale specimens or real concrete structures. Independently of such differences and despite the structurally possible water absorption/adsorption, distinct types of recent measurements showed both negligible absorption/adsorption capacity compared to common cement hydrates, e.g., calcium-silicate-hydrates (C-S-H), and the absence of significant dimensional changes even under significant relative humidity changes ("dry", i.e., $\approx 50\%$ relative humidity, RH, to moist, i.e., $\approx 100\%$ RH, conditions) [51], [57], [58]. In a more recent study by Geng *et al.* [59], based on *in situ* 3D micro-XRD, it was shown that moisture uptake did not result in swelling of crystalline ASR products retrieved from aggregate cracks. Thus, cumulating evidence points to no role by water adsorption/absorption in swelling of nano-crystalline products.

Concerning the early-age, amorphous products, less is known about their dimensional stability or changes upon water uptake. However, some recent experimental evidence supports the hypothesis of local expansion and consequent cracking due to local stress development upon the first crystallization stages of such amorphous products. Leemann and Münch [49] showed some examples of aggregate-

intrinsic cracks which opened up, likely due to localized crystal growth even before getting fully filled with ASR products.

The recent results reported above indicate that, despite the understanding of the ASR chemistry has steadily advanced, there still exists knowledge gaps about how the products' molecular properties influence the microscopic scale expansion and the associated cracking initiation. These knowledge gaps still hinder the development of bottom-up solutions to reduce the ASR risk in newly built concrete structures.

The ASR research has made far less progress on characterizing, thus on understanding, expansion and crack propagation at the mesoscale. By mesoscale, in this PhD thesis the length range from a few microns to a few centimeters is meant. Such characterization is indispensable in order to bridge between the sub-micron-scale information about the ASR chemo-mechanics and the macroscopic scale (tens of cm to m) observations of how concrete laboratory specimens and real world structures deform and crack.

Computational modeling of ASR damage in concrete structures needs such knowledge bridging. Indeed, most of the modeling work has focused so far on reproducing deformations observed at the macroscopic scale. It has relied upon either empirical or ad hoc model formulations strongly dependent on parameter calibration against specific experimental datasets, thus lacking universality [31], [35], [60], [61].

This research gap at the mentioned mesoscale stems, among others, from methodological gaps. Various studies focusing on characterizing ASR (cracking) at this length scale have already been reported in the literature. They were mainly based on optical [62], [63], scanning electron [63]–[66] and confocal scanning laser microscopy [67] of polished cross-sections of mortar and concrete specimens. All of these works were only observational, without quantitative characterization results. They identified various ASR-induced damage features mainly regarding secondary products, such as the filling of cracks and air voids by ASR products. The major drawback of the used microscopy techniques is that they do not allow actual time-lapse, thus consistent, monitoring of the ASR products and of the cracking of the same exact specimens, due to the intrinsic destructiveness of the respective specimen preparation. Thus, mesoscale computational modeling of ASR cracking lacks experimental observations, at the same length scale, which should guide its development and help with validating its results.

To address this limitation, X-ray tomography (XT) has been recently adopted. XT is significantly more limited than the mentioned microscopy techniques, in terms of spatial resolution achievable for a given specimen size. However, it offers the advantage of being completely non-destructive, thus enabling true time-lapse characterizations, in addition to being a 3D imaging technique. So far, only few ASR studies based upon XT have been published. Some of them have dealt only with mortar specimens [68]–[74] or model systems, e.g., glass particles-alkali solution mixtures [75]. Most of these studies mainly focused on rather idealized systems and did not track the ASR cracking using time-lapse XT. The ASR cracking was monitored in a time-lapse fashion only in two of them [72], [73]. However, in each of them either a mortar with fine sand (up to 1.18 mm sieve size) [72] or recycled glass fragments [73] were adopted as aggregates, instead of natural ones. Only two published articles so far reported investigations of ASR cracking in concrete specimens with actual aggregates [76], [77]. All of the X-ray tomography results available in the literature mainly concern the detection and characterization of ASR cracks and of their evolution, when tomographic time series were acquired. The characterization was prevalently qualitative, with the exception of the results reported in [74], where features of the pore space (statistics of volume, sphere-normalized surface/volume ratio and aspect ratio) were quantified. This analysis involved all of the pore space within the mortar specimens (cracks, inherent air voids and

regions in the sand particles dissolved due to ASR) and only at one time point (not time-lapse). None of the cited studies reported the characterization of the ASR products and of their evolution.

Systematic time-lapse studies of ASR products and cracks developments at the defined mesoscale would shed light on the fracture mechanics of concrete affected by ASR and how it affects, by any feedback loops, the ASR itself. The knowledge base accrued from such studies could then be used both for formulating and for validating mesoscale computational models of ASR damage taking into account the ASR chemistry, the multi-physics of ASR cracking and their couplings. The formulations of such mesoscale models could then be used, together with upscaling approaches, for developing macroscale models of significance for predicting, at the structural engineering level, ASR-induced deformations and changes of poro-mechanical properties. The latter remains a critical objective of the engineering community, motivated by the detrimental, socio-economic impacts of ASR damage on existing and future concrete infrastructure.

1.2 Research objectives

This project was part of a Swiss National Science Foundation (SNF) Sinergia project (Nr. 171018, "Alkali-silica reaction in concrete", <http://p3.snf.ch/project-171018>), which aimed at improving the basic understanding of the ASR chemo-mechanics, based on multidisciplinary and multiscale approaches. In this framework, six different sub-projects (see Figure 1.2) implemented techniques from different fields (chemistry and thermodynamic modelling, molecular structural analysis, 2D microscopy methods, time-lapse X-ray micro-tomography (XMT) with respective 3D image analysis and computational modelling) to achieve such general goal.

The main objective of this PhD project (sub-project V of the SNF Sinergia project, Figure 1.2) was to investigate the spatial-temporal evolutions of both ASR products and cracks and their eventual couplings at the mentioned mesoscale in concrete, using time-lapse XMT, and to assess their associated deformations and their degrading effects on the mechanical properties. Furthermore, the tomographic results from this project aimed at providing input for the development and validation of mesoscale computational models of ASR cracking and of their correspondingly up-scaled models, developed within sub-project VI at EPFL's Computational Solid Mechanics Laboratory (Figure 1.2).

To achieve the main objective, several challenges needed to be addressed, concerning the application of time-lapse XT to characterize simultaneously ASR products, respective local deformations and cracks. Among them, the following technical objectives were set.

- Developing an approach to enhance the X-ray tomographic contrast between ASR products and any other concrete material phase, as the first, needed step towards detecting and characterizing them with 3D image processing methods. Products are typically undistinguishable, in standard X-ray tomograms, from, e.g., cement hydrates or aggregate minerals.
- Developing and implementing an analysis methodology of the tomographic time series in order to make it possible to compare the tomograms at the distinct time points despite the deformations induced by ASR. At the same time, estimating, from the differing tomograms, such deformations, to create an experimental data basis for the validation of corresponding results from mesoscale simulations.
- Implementing an approach for simplifying the recognition of aggregates in X-ray tomograms, with the end goal of being able to perform quantitative analysis of products and cracks by distinguishing between their location in the mesostructure, i.e., inside aggregates or within

the cement paste. Real world aggregates exhibit, in X-ray tomograms, poor image contrast to the cement paste.

By addressing these challenges and sub-objectives, the project aimed at establishing, for the first time, an integrated experimental and analysis framework for studying the chemo-mechanics of ASR cracking at the mentioned concrete mesoscale, with specific optimization for what achievable by time-lapse X-ray tomography as a technique complementary to the 2D, destructive microscopy methods used so far more frequently in ASR research.

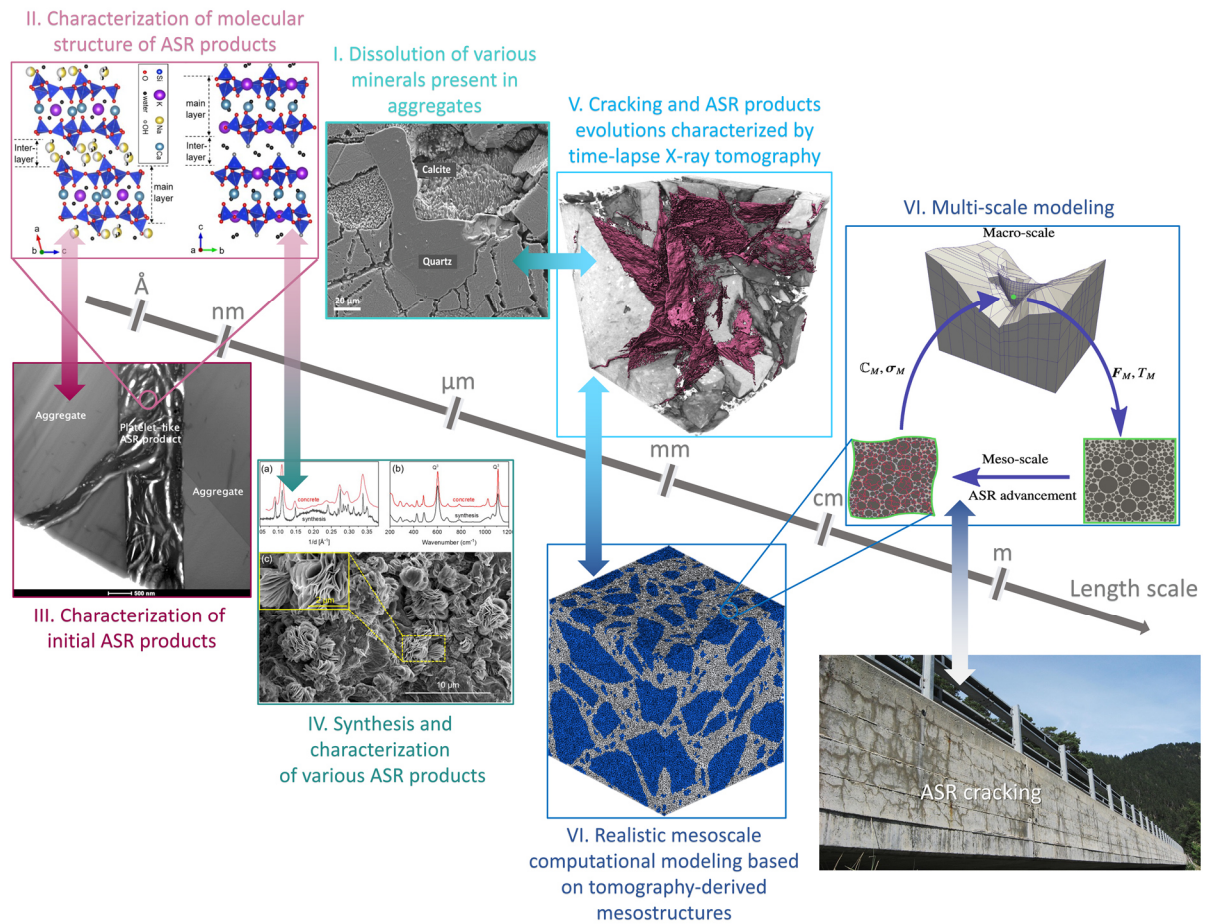


Figure 1.2. Overview scheme representing the various sub-projects of the Swiss National Science Foundation (SNF) Sinergia project Nr. 171018, dedicated to ASR (damage), and of their interconnections, indicated by arrows. Sub-project V was the one concerning this PhD Thesis, with strong interconnection with sub-project VI, the latter related with multi-scale computational modeling of ASR cracking. The length scale(s) at which ASR (damage) was investigated in each sub-project is specified by the position on the axis of a corresponding sub-project's results, in the form of figures. The figures for each sub-project are adapted from: (I) [78]; (II) [79]; (III) [80]; (IV) [51]; (V) from the results presented in chapter 4 of this thesis; (VI) [61].

1.3 Thesis outline

As mentioned in the previous Section, this PhD project aimed at advancing the basic understanding of some aspects, at the defined mesoscale, of the ASR chemo-mechanics and its associated cracking. This general goal was addressed by investigating the spatial-temporal evolution of both ASR products and cracks and their couplings, mainly using time-lapse XT and the respective image analysis. Several other destructive and non-destructive measurements were also carried out, to assess the associated bulk deformations and degradation of the mechanical properties in several specimens. Furthermore, the tomographic and non-tomographic results of this study aimed at creating a data- and knowledge-base also useful for the development and validation of mesoscale computational models of ASR cracking.

The objectives of this PhD project mentioned in Section 1.2 were addressed during the course of four different work packages with four respective specimen sets. One set included specimens belonging to a testing campaign started well before this PhD project and aiming at monitoring and characterizing ASR damage development under natural environmental conditions. The rest of the specimens were cast during the course of this PhD project, all of which with similar mix designs and identical aggregate types. By several characterization procedures, identical protocols and settings were implemented (otherwise explicitly mentioned). For the analysis of the tomographic results, similar workflows were used, to foster the results comparability across the different work packages.

Different Chapters and respective Appendices have been dedicated to discuss the basics and the implementation/technical details of different work packages as well as their corresponding outcomes.

The state-of-the-art background knowledge about ASR, its societal and economic impact and different approaches/methods to characterize it, along with the respective present knowledge gaps and research needs, are discussed and summarized in Chapter 2. Such a summary is inevitably more focused on aspects related with the work performed in this project, although an attempt was made to cover also more general aspects.

Chapter 3 and its dedicated Appendix (A) focuses on the detailed explanations of the raw materials and specimen preparation/casting, their boundary conditions for the experimental campaigns, the implementation of time-lapse XT, the respective image analysis workflows (image registration and segmentation and statistical analysis of distinct properties computed out of their results) as well as other characterization procedures. This Chapter provides all the general details. Other details about the campaign-specific adaptations of the materials and methods are provided additionally in each Chapter for the respective campaign.

Chapter 4 and its respective Appendix (B) report the results for the first specimen set. They were obtained from an XT campaign implemented both for laboratory-scale accelerated specimens and for field-exposed ones. These results include qualitative and quantitative assessments and comparisons of several features of the crack networks developed under the distinct boundary conditions, the laboratory and the field ones. This work package aimed at characterizing the propensity to ASR cracking of the chosen concrete mix designs (containing different alpine aggregate types) and at quantitatively assessing whether or not and how much/in what such cracking would be representative of that observed in concrete exposed to natural boundary conditions. The focus of this Chapter was on summarizing key similarities and differences between the specimens subjected to the two types of boundary conditions.

Chapter 5 and its Appendix (C) deal with results from a second experimental campaign during which a new XT methodology was developed with the purpose of investigating the coupled evolutions of ASR products and associated cracking. The methodology relied upon the addition of a source of caesium (Cs), i.e., CsNO_3 , to the concrete mix, acting as an XT contrast agent for ASR products. The experimental campaign addressed in details the question of whether such addition may spuriously alter the

ASR (cracking) or not and, if yes, in which way and how much. Finally, it allowed achieving a characterization of both the cracks spatial-temporal patterns and the ASR products ones.

Chapter 6 and its Appendix (D) report and discuss the results concerning a third specimen set, cast with another contrast agent, barium sulfate (BaSO_4), added to enhance the detection of the aggregates in the X-ray tomograms (otherwise often almost undistinguishable from the cement paste). The possibility to distinguish more easily and reliably between paste and aggregates enabled two key advancements in the ASR cracking characterization. First, it allowed and allows to sub-classify segmented features (e.g., cracks) based upon whether they were/are located within the aggregates or outside them. The latter sub-classification serves the purpose of analysing the ASR cracking with respect to the concrete mesoscale material phases (aggregate or paste). Second, the segmented aggregates lead to the partitioning of the investigated volume into the two mentioned main mesoscale phases, such that a realistic digital domain can be provided for mesoscale computational models. The optimization of this contrast agent's concentration in concrete specimens containing two aggregate types is presented in this Chapter. Also in this case, any eventual influence of its addition on the natural ASR (cracking) course was investigated in details and the results herein reported.

The implementation details and results of a fourth and final experimental campaign are provided in Chapter 7 and its Appendix (E). Here, the focus was on integrating the two experimental methodologies described in Chapters 5 and 6. The aim of this attempt was to enable the detection of both aggregates and ASR products in the X-ray tomograms, at the same time. This allowed and allows to characterize the spatial-temporal distributions of both ASR products and cracks with the additional possibility of identifying their location in the concrete mesostructure (i.e., inside or outside the aggregates). This achievement was possible thanks to the search of an optimal BaSO_4 concentration given a certain Cs one.

Finally, in Chapter 8, the significant conclusions, achievements and contributions of this project to addressing some of the knowledge gaps mentioned in Section 1.1 and goals stated in Section 1.2 are summarized and commented about. An outlook about how the outcomes of this project may impact the ASR research is also provided, with particular focus on their value for the development and validation of mesoscale computational modelling of ASR cracking and for the application of the developed XT methodologies and respective analysis workflow to the investigation of ASR cracking at other space-time scales not covered in this project, e.g., at very early stages and at the microscopic scale, when/where the first products precipitation and accumulation is accompanied by the initiation of the first cracks.

Bibliography

- [1] R. B. Figueira *et al.*, “Alkali-silica reaction in concrete: Mechanisms, mitigation and test methods,” *Construction and Building Materials*, vol. 222. Elsevier Ltd, pp. 903–931, 20-Oct-2019, doi: 10.1016/j.conbuildmat.2019.07.230.
- [2] T. Gernay, “Fire resistance and burnout resistance of reinforced concrete columns,” *Fire Saf. J.*, vol. 104, pp. 67–78, Mar. 2019, doi: 10.1016/j.firesaf.2019.01.007.
- [3] E. Henin and G. Morcous, “Non-proprietary bar splice sleeve for precast concrete construction,” *Eng. Struct.*, vol. 83, pp. 154–162, Jan. 2015, doi: 10.1016/j.engstruct.2014.10.045.
- [4] U. M. Angst, “Challenges and opportunities in corrosion of steel in concrete,” *Mater. Struct. Constr.*, vol. 51, no. 1, pp. 1–20, Feb. 2018, doi: 10.1617/s11527-017-1131-6.
- [5] L. Bertolini, “Steel corrosion and service life of reinforced concrete structures,” *Struct. Infrastruct. Eng.*, vol. 4, no. 2, pp. 123–137, Apr. 2008, doi: 10.1080/15732470601155490.
- [6] M. Santhanam, M. D. Cohen, and J. Olek, “Sulfate attack research - Whither now?,” *Cement and Concrete Research*, vol. 31, no. 6. Pergamon, pp. 845–851, 01-May-2001, doi: 10.1016/S0008-8846(01)00510-5.
- [7] A. Neville, “The confused world of sulfate attack on concrete,” *Cem. Concr. Res.*, vol. 34, no. 8, pp. 1275–1296, Aug. 2004, doi: 10.1016/j.cemconres.2004.04.004.
- [8] F. Rajabipour, E. Giannini, C. Dunant, J. H. Ideker, and M. D. A. Thomas, “Alkali-silica reaction: Current understanding of the reaction mechanisms and the knowledge gaps,” *Cem. Concr. Res.*, vol. 76, pp. 130–146, Jul. 2015, doi: 10.1016/j.cemconres.2015.05.024.
- [9] S. Chatterji, “Chemistry of alkali-silica reaction and testing of aggregates,” *Cem. Concr. Compos.*, vol. 27, no. 7–8, pp. 788–795, Aug. 2005, doi: 10.1016/j.cemconcomp.2005.03.005.
- [10] S. Diamond, “A review of alkali-silica reaction and expansion mechanisms 2. Reactive aggregates,” *Cem. Concr. Res.*, vol. 6, no. 4, pp. 549–560, Jul. 1976, doi: 10.1016/0008-8846(76)90083-1.
- [11] G. E. Blight and M. G. Alexander, *Alkali-Aggregate Reaction and Structural Damage to Concrete*. CRC Press, 2011.
- [12] F. Amberg, P. Droz, R. Leroy, J. Maier, B. Otto, and R. Bremen, “Concrete Swelling of Dams in Switzerland,” 2017.
- [13] T. E. Stanton, “Expansion of Concrete through Reaction between Cement and Aggregate,” (*No. SP-249-1*). [Online]. Available: <https://trid.trb.org/view/868520>. [Accessed: 20-Jan-2021].
- [14] S. Chatterji, “The role of Ca(OH)₂ in the breakdown of Portland cement concrete due to alkali-silica reaction,” *Cem. Concr. Res.*, vol. 9, no. 2, pp. 185–188, Mar. 1979, doi: 10.1016/0008-8846(79)90024-3.
- [15] T. C. Powers and H. H. Steinour, “An Interpretation of Some Published Researches on the Alkali-Aggregate Reaction Part 1-The Chemical Reactions and Mechanism of Expansion,” *ACI J. Proc.*, vol. 51, no. 2, pp. 497–516, Feb. 1955, doi: 10.14359/11691.
- [16] L. S. Dent Glasser and N. Kataoka, “The chemistry of ‘alkali-aggregate’ reaction,” *Cem. Concr. Res.*, vol. 11, no. 1, pp. 1–9, Jan. 1981, doi: 10.1016/0008-8846(81)90003-X.
- [17] A. B. Poole, “Introduction to alkali-aggregate reaction in concrete,” in *The Alkali-Silica Reaction in Concrete*, CRC Press, 1992, pp. 1–29.
- [18] J. Lindgård, Ö. Andiç-Çakir, I. Fernandes, T. F. Rønning, and M. D. A. Thomas, “Alkali-silica reactions (ASR): Literature review on parameters influencing laboratory performance testing,” *Cement and Concrete Research*, vol. 42, no. 2. Pergamon, pp. 223–243, 01-Feb-2012, doi: 10.1016/j.cemconres.2011.10.004.
- [19] M. Thomas, B. Fournier, K. Folliard, J. Ideker, and M. Shehata, “Test methods for evaluating preventive measures for controlling expansion due to alkali-silica reaction in concrete,” *Cem.*

- Concr. Res.*, vol. 36, no. 10, pp. 1842–1856, Oct. 2006, doi: 10.1016/j.cemconres.2006.01.014.
- [20] I. Sims and P. Nixon, “RILEM Recommended Test Method AAR-0: Detection of Alkali-Reactivity Potential in Concrete—Outline guide to the use of RILEM methods in assessments of aggregates for potential alkali-reactivity,” *Mater. Struct.*, vol. 36, no. 7, pp. 472–479, Aug. 2003, doi: 10.1007/bf02481527.
 - [21] M. D. A. Thomas, B. Fournier, and K. J. Folliard, “Report on Determining the Reactivity of Concrete Aggregates and Selecting Appropriate Measures for Preventing Deleterious Expansion in New Concrete Construction,” *Fed. Highw. Adm.*, Apr. 2008.
 - [22] B. Fournier, M.-A. Berube, K. J. Folliard, and M. Thomas, “Report on the Diagnosis, Prognosis, and Mitigation of Alkali-Silica Reaction (ASR) in Transportation Structures,” *Fed. Highw. Adm.*, Jan. 2010.
 - [23] S. Urhan, “Alkali silica and pozzolanic reactions in concrete. Part 1: Interpretation of published results and an hypothesis concerning the mechanism,” *Cem. Concr. Res.*, vol. 17, no. 1, pp. 141–152, Jan. 1987, doi: 10.1016/0008-8846(87)90068-8.
 - [24] S. Diamond, “A review of alkali-silica reaction and expansion mechanisms 1. Alkalies in cements and in concrete pore solutions,” *Cem. Concr. Res.*, vol. 5, no. 4, pp. 329–345, Jul. 1975, doi: 10.1016/0008-8846(75)90089-7.
 - [25] S. Chatterji, N. Thaulow, and A. D. Jensen, “Studies of alkali-silica reaction, part 6. Practical implications of a proposed reaction mechanism,” *Cem. Concr. Res.*, vol. 18, no. 3, pp. 363–366, May 1988, doi: 10.1016/0008-8846(88)90070-1.
 - [26] H. Wang and J. E. Gillott, “Mechanism of alkali-silica reaction and the significance of calcium hydroxide,” *Cem. Concr. Res.*, vol. 21, no. 4, pp. 647–654, Jul. 1991, doi: 10.1016/0008-8846(91)90115-X.
 - [27] Z. P. Bažant, G. Zi, and C. Meyer, “Fracture Mechanics of ASR in Concretes with Waste Glass Particles of Different Sizes,” *J. Eng. Mech.*, vol. 126, no. 3, pp. 226–232, Mar. 2000, doi: 10.1061/(asce)0733-9399(2000)126:3(226).
 - [28] E. Garcia-Diaz, J. Riche, D. Bulteel, and C. Vernet, “Mechanism of damage for the alkali-silica reaction,” *Cem. Concr. Res.*, vol. 36, no. 2, pp. 395–400, Feb. 2006, doi: 10.1016/j.cemconres.2005.06.003.
 - [29] P. Krivenko, R. Drochytka, A. Gelevera, and E. Kavalerova, “Mechanism of preventing the alkali-aggregate reaction in alkali activated cement concretes,” *Cem. Concr. Compos.*, vol. 45, pp. 157–165, Jan. 2014, doi: 10.1016/j.cemconcomp.2013.10.003.
 - [30] M. S. Islam and N. Ghafoori, “Evaluation of alkali-silica reactivity using ASR kinetic model,” *Constr. Build. Mater.*, vol. 45, pp. 270–274, Aug. 2013, doi: 10.1016/j.conbuildmat.2013.03.048.
 - [31] L. F. M. Sanchez, S. Multon, A. Sellier, M. Cyr, B. Fournier, and M. Jolin, “Comparative study of a chemo-mechanical modeling for alkali silica reaction (ASR) with experimental evidences,” *Constr. Build. Mater.*, vol. 72, pp. 301–315, Dec. 2014, doi: 10.1016/j.conbuildmat.2014.09.007.
 - [32] B. Li, L. Baingam, K. Kurumisawa, T. Nawa, and L. XiaoZhou, “Micro-mechanical modelling for the prediction of alkali-silica reaction (ASR) expansion: Influence of curing temperature conditions,” *Constr. Build. Mater.*, vol. 164, pp. 554–569, Mar. 2018, doi: 10.1016/j.conbuildmat.2018.01.007.
 - [33] R. Esposito and M. A. N. Hendriks, “A multiscale micromechanical approach to model the deteriorating impact of alkali-silica reaction on concrete,” *Cem. Concr. Compos.*, vol. 70, pp. 139–152, Jul. 2016, doi: 10.1016/j.cemconcomp.2016.03.017.
 - [34] R. Pignatelli, C. Comi, and P. J. M. Monteiro, “A coupled mechanical and chemical damage model for concrete affected by alkali-silica reaction,” *Cem. Concr. Res.*, vol. 53, pp. 196–210, Nov. 2013, doi: 10.1016/j.cemconres.2013.06.011.
 - [35] Y. Kawabata, J. F. Seignol, R. P. Martin, and F. Toutlemonde, “Macroscopic chemo-mechanical modeling of alkali-silica reaction of concrete under stresses,” *Constr. Build.*

- Mater.*, vol. 137, pp. 234–245, Apr. 2017, doi: 10.1016/j.conbuildmat.2017.01.090.
- [36] Q. Huang, P. Gardoni, D. Trejo, and A. Pagnotta, “Probabilistic model for steel-concrete bond behavior in bridge columns affected by alkali silica reactions,” *Eng. Struct.*, vol. 71, pp. 1–11, Jul. 2014, doi: 10.1016/j.engstruct.2014.03.041.
 - [37] X. X. Gao, S. Multon, M. Cyr, and A. Sellier, “Optimising an expansion test for the assessment of alkali-silica reaction in concrete structures,” *Mater. Struct. Constr.*, vol. 44, no. 9, pp. 1641–1653, Nov. 2011, doi: 10.1617/s11527-011-9724-y.
 - [38] H. W. Reinhardt and O. Mielich, “A fracture mechanics approach to the crack formation in alkali-sensitive grains,” *Cem. Concr. Res.*, vol. 41, no. 3, pp. 255–262, Mar. 2011, doi: 10.1016/j.cemconres.2010.11.008.
 - [39] L. Charpin and A. Ehrlacher, “A computational linear elastic fracture mechanics-based model for alkali-silica reaction,” *Cem. Concr. Res.*, vol. 42, no. 4, pp. 613–625, Apr. 2012, doi: 10.1016/j.cemconres.2012.01.004.
 - [40] K. E. Kurtis and P. J. M. Monteiro, “Chemical additives to control expansion of alkali-silica reaction gel: Proposed mechanisms of control,” *J. Mater. Sci.*, vol. 38, no. 9, pp. 2027–2036, May 2003, doi: 10.1023/A:1023549824201.
 - [41] V. E. Saouma, R. A. Martin, M. A. Hariri-Ardebili, and T. Katayama, “A mathematical model for the kinetics of the alkali-silica chemical reaction,” *Cem. Concr. Res.*, vol. 68, pp. 184–195, Feb. 2015, doi: 10.1016/j.cemconres.2014.10.021.
 - [42] J. R. Wright, S. Shafaatian, and F. Rajabipour, “Reliability of chemical index model in determining fly ash effectiveness against alkali-silica reaction induced by highly reactive glass aggregates,” *Constr. Build. Mater.*, vol. 64, pp. 166–171, Aug. 2014, doi: 10.1016/j.conbuildmat.2014.04.042.
 - [43] S. Poyet *et al.*, “Chemical modelling of Alkali Silica reaction: Influence of the reactive aggregate size distribution,” *Mater. Struct. Constr.*, vol. 40, no. 2, pp. 229–239, Mar. 2007, doi: 10.1617/s11527-006-9139-3.
 - [44] D. W. Hobbs, *Alkali-silica reaction in concrete*. Thomas Telford Publishing, 1988.
 - [45] M. A. Bérubé, J. Duchesne, J. F. Dorion, and M. Rivest, “Laboratory assessment of alkali contribution by aggregates to concrete and application to concrete structures affected by alkali-silica reactivity,” *Cem. Concr. Res.*, vol. 32, no. 8, pp. 1215–1227, Aug. 2002, doi: 10.1016/S0008-8846(02)00766-4.
 - [46] B. P. Gautam and D. K. Panesar, “The effect of elevated conditioning temperature on the ASR expansion, cracking and properties of reactive Spratt aggregate concrete,” *Constr. Build. Mater.*, vol. 140, pp. 310–320, Jun. 2017, doi: 10.1016/j.conbuildmat.2017.02.104.
 - [47] B. Fournier, J. H. Ideker, K. J. Folliard, M. D. A. Thomas, P. C. Nkinamubanzi, and R. Chevrier, “Effect of environmental conditions on expansion in concrete due to alkali-silica reaction (ASR),” *Mater. Charact.*, vol. 60, no. 7, pp. 669–679, Jul. 2009, doi: 10.1016/j.matchar.2008.12.018.
 - [48] J. Duchesne and M. A. Bérubé, “The effectiveness of supplementary cementing materials in suppressing expansion due to ASR: Another look at the reaction mechanisms part 2: Pore solution chemistry,” *Cem. Concr. Res.*, vol. 24, no. 2, pp. 221–230, Jan. 1994, doi: 10.1016/0008-8846(94)90047-7.
 - [49] A. Leemann and B. Münch, “The addition of caesium to concrete with alkali-silica reaction: Implications on product identification and recognition of the reaction sequence,” *Cem. Concr. Res.*, vol. 120, pp. 27–35, Jun. 2019, doi: 10.1016/j.cemconres.2019.03.016.
 - [50] E. Boehm-Courjault, S. Barbotin, A. Leemann, and K. Scrivener, “Microstructure, crystallinity and composition of alkali-silica reaction products in concrete determined by transmission electron microscopy,” *Cem. Concr. Res.*, vol. 130, p. 105988, Apr. 2020, doi: 10.1016/j.cemconres.2020.105988.
 - [51] Z. Shi, A. Leemann, D. Rentsch, and B. Lothenbach, “Synthesis of alkali-silica reaction product structurally identical to that formed in field concrete,” *Mater. Des.*, vol. 190, p.

- 108562, May 2020, doi: 10.1016/j.matdes.2020.108562.
- [52] R. Dähn *et al.*, “Application of micro X-ray diffraction to investigate the reaction products formed by the alkali-silica reaction in concrete structures,” *Cem. Concr. Res.*, vol. 79, pp. 49–56, Jan. 2016, doi: 10.1016/j.cemconres.2015.07.012.
 - [53] G. Geng *et al.*, “Atomistic structure of alkali-silica reaction products refined from X-ray diffraction and micro X-ray absorption data,” *Cem. Concr. Res.*, vol. 129, p. 105958, Mar. 2020, doi: 10.1016/j.cemconres.2019.105958.
 - [54] Z. Shi and B. Lothenbach, “The combined effect of potassium, sodium and calcium on the formation of alkali-silica reaction products,” *Cem. Concr. Res.*, vol. 127, p. 105914, Jan. 2020, doi: 10.1016/j.cemconres.2019.105914.
 - [55] A. Leemann, “Raman microscopy of alkali-silica reaction (ASR) products formed in concrete,” *Cem. Concr. Res.*, vol. 102, pp. 41–47, Dec. 2017, doi: 10.1016/j.cemconres.2017.08.014.
 - [56] N. V. Zubkova, Y. E. Filinchuk, I. V. Pekov, D. Pushcharovsky, and E. R. Yu. Gobechiya, “Crystal structures of shlykovite and cryptophyllite: comparative crystal chemistry of phyllosilicate minerals of the mountainite family,” *Eur. J. Mineral.*, vol. 22, no. 4, pp. 547–555, Sep. 2010, doi: 10.1127/0935-1221/2010/0022-2041.
 - [57] A. Leemann, Z. Shi, M. Wyrzykowski, and F. Winnefeld, “Moisture stability of crystalline alkali-silica reaction products formed in concrete exposed to natural environment,” *Mater. Des.*, vol. 195, p. 109066, Oct. 2020, doi: 10.1016/j.matdes.2020.109066.
 - [58] Z. Shi, G. Geng, A. Leemann, and B. Lothenbach, “Synthesis, characterization, and water uptake property of alkali-silica reaction products,” *Cem. Concr. Res.*, vol. 121, pp. 58–71, Jul. 2019, doi: 10.1016/j.cemconres.2019.04.009.
 - [59] G. Geng *et al.*, “An in-situ 3D micro-XRD investigation of water uptake by alkali-silica-reaction (ASR) product,” *Cem. Concr. Res.*, vol. 141, p. 106331, Mar. 2021, doi: 10.1016/j.cemconres.2020.106331.
 - [60] M. C. R. Farage, J. L. D. Alves, and E. M. R. Fairbairn, “Macroscopic model of concrete subjected to alkali-aggregate reaction,” *Cem. Concr. Res.*, vol. 34, no. 3, pp. 495–505, Mar. 2004, doi: 10.1016/j.cemconres.2003.09.001.
 - [61] E. R. Gallyamov, A. I. Cuba Ramos, M. Corrado, R. Rezakhani, and J. F. Molinari, “Multi-scale modelling of concrete structures affected by alkali-silica reaction: Coupling the mesoscopic damage evolution and the macroscopic concrete deterioration,” *Int. J. Solids Struct.*, vol. 207, pp. 262–278, Dec. 2020, doi: 10.1016/j.ijsolstr.2020.10.010.
 - [62] B. Fournier and M. A. Bérubé, “Alkali-aggregate reaction in concrete: A review of basic concepts and engineering implications,” *Can. J. Civ. Eng.*, vol. 27, no. 2, pp. 167–191, 2000, doi: 10.1139/199-072.
 - [63] A. Leemann and P. Lura, “E-modulus of the alkali-silica-reaction product determined by micro-indentation,” *Constr. Build. Mater.*, vol. 44, pp. 221–227, 2013, doi: 10.1016/j.conbuildmat.2013.03.018.
 - [64] M. Ben Haha, E. Gallucci, A. Guidoum, and K. L. Scrivener, “Relation of expansion due to alkali silica reaction to the degree of reaction measured by SEM image analysis,” *Cem. Concr. Res.*, vol. 37, no. 8, pp. 1206–1214, Aug. 2007, doi: 10.1016/j.cemconres.2007.04.016.
 - [65] Š. Lukschová, R. Přikryl, and Z. Pertold, “Petrographic identification of alkali-silica reactive aggregates in concrete from 20th century bridges,” *Constr. Build. Mater.*, vol. 23, no. 2, pp. 734–741, Feb. 2009, doi: 10.1016/j.conbuildmat.2008.02.020.
 - [66] A. Leemann and C. Merz, “An attempt to validate the ultra-accelerated microbar and the concrete performance test with the degree of AAR-induced damage observed in concrete structures,” *Cem. Concr. Res.*, vol. 49, pp. 29–37, 2013, doi: 10.1016/j.cemconres.2013.03.014.
 - [67] C. L. Collins, J. H. Ideker, and K. E. Kurtis, “Laser scanning confocal microscopy for in situ monitoring of alkali-silica reaction,” *J. Microsc.*, vol. 213, no. 2, pp. 149–157, Feb. 2004, doi: 10.1111/j.1365-2818.2004.01280.x.

- [68] S. Guo, Q. Dai, X. Sun, X. Xiao, R. Si, and J. Wang, “Reduced alkali-silica reaction damage in recycled glass mortar samples with supplementary cementitious materials,” *J. Clean. Prod.*, vol. 172, pp. 3621–3633, Jan. 2018, doi: 10.1016/j.jclepro.2017.11.119.
- [69] N. Marinoni, M. Voltolini, L. Mancini, P. Vignola, A. Pagani, and A. Pavese, “An investigation of mortars affected by alkali-silica reaction by X-ray synchrotron microtomography: A preliminary study,” *J. Mater. Sci.*, vol. 44, no. 21, pp. 5815–5823, Nov. 2009, doi: 10.1007/s10853-009-3817-9.
- [70] N. Marinoni *et al.*, “A combined synchrotron radiation micro computed tomography and micro X-ray diffraction study on deleterious alkali-silica reaction,” *J. Mater. Sci.*, vol. 50, no. 24, pp. 7985–7997, Dec. 2015, doi: 10.1007/s10853-015-9364-7.
- [71] M. Voltolini, N. Marinoni, and L. Mancini, “Synchrotron X-ray computed microtomography investigation of a mortar affected by alkali-silica reaction: A quantitative characterization of its microstructural features,” *J. Mater. Sci.*, vol. 46, no. 20, pp. 6633–6641, Oct. 2011, doi: 10.1007/s10853-011-5614-5.
- [72] D. Hernández-Cruz, C. W. Hargis, J. Dominowski, M. J. Radler, and P. J. M. Monteiro, “Fiber reinforced mortar affected by alkali-silica reaction: A study by synchrotron microtomography,” *Cem. Concr. Compos.*, vol. 68, pp. 123–130, Apr. 2016, doi: 10.1016/j.cemconcomp.2016.02.003.
- [73] S. Yang, H. Cui, and C. S. Poon, “Assessment of in-situ alkali-silica reaction (ASR) development of glass aggregate concrete prepared with dry-mix and conventional wet-mix methods by X-ray computed micro-tomography,” *Cem. Concr. Compos.*, vol. 90, pp. 266–276, Jul. 2018, doi: 10.1016/j.cemconcomp.2018.03.027.
- [74] M. Voltolini, N. Marinoni, and L. Mancini, “Synchrotron X-ray computed microtomography investigation of a mortar affected by alkali-silica reaction: A quantitative characterization of its microstructural features,” *J. Mater. Sci.*, vol. 46, no. 20, pp. 6633–6641, Oct. 2011, doi: 10.1007/s10853-011-5614-5.
- [75] T. Kim, M. F. Alnahhal, Q. D. Nguyen, P. Panchmatia, A. Hajimohammadi, and A. Castel, “Initial sequence for alkali-silica reaction: Transport barrier and spatial distribution of reaction products,” *Cem. Concr. Compos.*, vol. 104, p. 103378, Nov. 2019, doi: 10.1016/j.cemconcomp.2019.103378.
- [76] F. Weise, K. Volland, S. Pirskawetz, and D. Meinel, “Analyse AKR-induzierter Schädigungsprozesse in Beton: Einsatz innovativer Prüftechniken,” *Beton- und Stahlbetonbau*, vol. 107, no. 12, pp. 805–815, Dec. 2012, doi: 10.1002/best.201200049.
- [77] F. Weise and S. Pirskawetz, “Innovative measurement techniques for characterising internal damage processes in concrete due to ASR Materialien einer Gusswerkstatt von der Qubbet el-Hawa View project Dietmar Meinel Bundesanstalt für Materialforschung und-prüfung,” 2012.
- [78] M. Bagheri, “Aggregate dissolution in different pore solutions,” *thesis. EPFL*, 2021, doi: 10.5075/EPFL-THESIS-8882.
- [79] G. Geng, Z. Shi, B. Lothenbach, and A. Leemann, “A micro-XAS and XRD study of the crystalline alkali-silica reaction products,” in *First Book of Proceedings of the 16th international conference on Alkali-Aggregate Reaction in Concrete, (ICAAR2022)*, 2022, no. April 2021, pp. 15–23.
- [80] S. Barbotin-Albinski, Z. Shi, E. Boehm-Courjault, A. Leemann, and K. Scrivener, “Characterization of synthetic ASR products by TEM and preliminary comparison with on-field early stage products,” in *First Book of Proceedings of the 16th international conference on Alkali-Aggregate Reaction in Concrete, (ICAAR2022)*, 2022, no. April 2021, pp. 85–96.

Chapter 2. Alkali-silica reaction (ASR) and respective damage in concrete: basics and state of the art in their characterizations

2.1. ASR chemistry and identified/proposed damage mechanisms

The mechanisms involved in ASR have been extensively discussed in the literature [1]–[7]. Usually, the ASR (damage) sequence is synthetically described as the following: (I) dissolution of silica inside the aggregates; (II) nano-colloidal silica sol particles formation; (III) alkali-silica gel formation; (IV) water uptake by the alkali-silica gel; (V) volume increase of the gel, leading to local stress development and crack initiation/propagation [7], [8], which is accompanied by movement of the hydrated gel first towards, then throughout the cement paste. Such description has been based upon the key hypothesis of ASR products being hydrophilic gels characterized by the capability of large expansion upon water uptake. In what follows, a summary of the state-of-the-art knowledge about these five sequence stages is provided, along with a summary of key factors affecting it. Then, a survey of some of recently reported data is presented, focusing on some key results which have challenged some points or aspects of the standard sequence description summarized above, especially the mentioned key hypothesis.

(I). Silica dissolution inside the aggregates. Silica minerals are key constituents of many rock types, including those typically used as aggregates in concrete. They mainly consist of tetrahedral SiO_2 units (generically called silica). Each unit consists of one Si atom in the tetrahedron center and four oxygen atoms, two own, the other two from another surrounding unit [9]. These shared oxygen atoms are sometimes called as "bridging oxygens". They are part of what are called siloxane ($\equiv\text{Si}-\text{O}-\text{Si}\equiv$) bonds and contribute to the formation of long range chains of the mentioned tetrahedra. The bond angle of the $\text{O}-\text{Si}-\text{O}$ building block in a single tetrahedron is exactly equal to 109° . On the contrary, the bond angle of the $\text{Si}-\text{O}-\text{Si}$ blocks, connecting the distinct tetrahedra, can span the range $100^\circ - 170^\circ$ [10]. This variety is mirrored into a manifold of possible molecular structures for the chains of tetrahedra, from macro-crystalline to micro/nano-crystalline or even amorphous ones [11]. In addition to such conformational variety, the silica chains can also be impure, where H , K , Na and Ca may be connected to the oxygen atoms. All of these possible difference at the molecular structure level lead to a broadband spectrum of susceptibility to silica chain dissolution in certain chemical environments.

Here, for simplicity, only dissolution and ASR product formation from pure silica chains is considered. By exposure to an alkaline aqueous environment, OH^- (hydroxyl) anions decompose the silanol ($\equiv\text{Si}-\text{OH}$) groups, which constitute the interface between the solid silica chains and water. Thus, the silica network gets dissolved [12]:



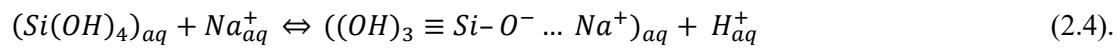
The formation of $\text{Si}(\text{OH})_4$ implies that three $\text{Si}-\text{O}^-$ groups remain on the solid surface of the of altered silica chain. The presence of such groups, not explicitly mentioned in Eq. (2.1), contributes to charge balance the left side of this equation. In addition to $\text{Si}(\text{OH})_4$, dissolution products might also be oligomers with the form $\text{Si}_n\text{O}_a(\text{OH})_b$, with $2a+b=4n$ [13].

The silica chain solubility increases as temperature increases or the silica crystallinity decreases [14]. Poorly crystalline or even amorphous silica chains are frequently termed metastable and are found in aggregates with high susceptibility to dissolution in aqueous alkaline environment, i.e., to ASR.

In alkaline environments, $\text{Si}(\text{OH})_4$ becomes ionized and gets converted into highly soluble ions [15]:

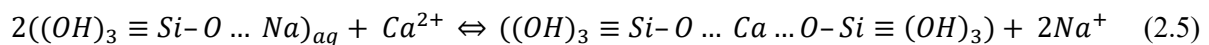


At $\text{pH} > 10 - 11$, reactions (2.1), (2.2) and (2.3) advance in the direction of H^+ production, thus leading to a pH reduction. Moreover, ion exchange can also happen, which can lower the pH even more:



In Eq. (2.4), the $\text{O}^- \dots \text{Na}^+$ block denotes a high likelihood that the formed bond is a strong Van der Waals one.

Some of the noteworthy consequences of the silica chain dissolution on the chemical and microstructural environment, both of the aggregates and of the concrete specimens, overall are the following ones. The silica chain dissolution has been shown, for some mineral types, to lead to a substantial increase in the local aggregate pore volume [6]. In addition, all of the mentioned reactions by which it can take place imply a local (i.e., in the dissolution region) reduction of the pH. This has an effect on the overall concrete environment. Indeed, when the gel formation takes place (from the alkali-silica sol, Eq. (2.4)), as explained below, Ca^{2+} cations, present in the concrete's pore solution, may replace alkalis being part of the gel structure, with their consequent release, Eq. (2.5), a process termed "alkali recycling" [16]. The decrease in the Ca^{2+} concentration in the pore solution stimulates additional dissolution of the portlandite in the cement paste. Thus, it leads to an increase in local pH (Eq. (2.6)):

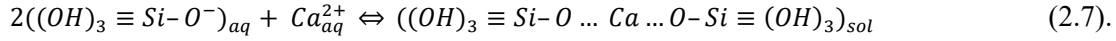


Thus, a negative feedback loop can get established, which supports the continuation of the metastable silica chain dissolution.

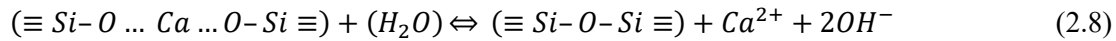
The silica dissolution picture drawn above concerns mainly the key chemical features. Not discussed here are the kinetic aspects and controls, which influence its rate, thus the entire ASR kinetics. It is just remarked that some studies have shown that the silica dissolution rate is greatly dependent on the pH and temperature [7], [17].

(II) and (III). Formation of colloidal silica sol particles and their gelation. The silica dissolution products would stay stably in the solution under two conditions: (1) in the absence of Ca^{2+} cations and in the absence of pH and temperature changes, which would lead to achieve the super-saturation of aqueous silica [18]. That would happen because, as shown with Eqs. (2. 2) and (2. 3), the dissolved silica

entities are negatively charged (at such high pH levels) and their mutual electrostatic repulsion would prevent their aggregation. Under such circumstances, the silica dissolution would simply slow down and ultimately stop when the silicon molar concentration in the pore solution, $[Si]_{aq}$, would reach its solubility limit [19]. Nevertheless, such situation does not happen in a concrete produced from Portland cement (PC): its pore solution always contains Ca^{2+} cations. Such cations contribute to link the dissolved silica entities together, with consequent formation of poly-metal silicates [20]:



Equation (2.7) describes a condensation process which creates the first precursors of sol particles. According to laboratory studies dealing with model systems of ASR products synthesized in conditions mimicking the chemical environment in a typical Portland cement-based concrete's pore solution, the Ca^{2+} cations might act as a catalyst in the reaction described in eg. (2.7) and might become liberated afterwards (Eq. (2.8)), forming siloxane bonds [21]:



As soon as a nucleus of the poly-metal silicates with a critical volume is formed, it can develop, via further condensation, into a nano-colloidal silica sol particle [22]. By aggregation of several of such colloidal particles, a continuous and space-filling ASR gel or a more compact macro-scale precipitate can form [21], [23], [24]. Such gel would be the first form of ASR products.

The proposed formation process for such initial ASR products is based upon the cumulated knowledge of the involved chemistry and of their chemical environment.

Based on the known chemistry, a significant amount of work has been dedicated to synthesize in the laboratory gels derived from similar chemical routes as the one described above, thus potentially acting as surrogate of ASR gels [25], [26].

Some of such synthesized phases have been found to be comprised of colloidal silica particle clusters surrounded by solution. The particles in such clusters have been characterized as having size of about 10-30 nm and the spacing from each other within the clusters seem to depend on the gel water content [27]. Such synthesized gels have been described as porous materials with very high surface area [28]. The rheological characterizations of some of such synthesized gels have suggested that ASR gels may be viscous fluids with a relatively high yield strength (up to 85 kPa) [29].

(IV) and (V). ASR gels water uptake and consequent expansion. Under the assumption that the early ASR products are highly porous gels, several mechanisms have been proposed concerning their hygroscopicity and corresponding dimensional changes. First of all, their molecular structure includes chemical groups, as $-OH$, $-O \dots Na$ and $-O^-$, which contribute to make their surface strongly hydrophilic, thus fostering adsorption of water. Different mechanisms have been then proposed which should promote water ingress into the gels by osmosis [30]. Finally, swelling has been also attributed to electrically repulsive forces inherently stemming from the structural surface charge of the gel's solid particles [31], [32].

The roles of alkalis and calcium: The hydration of Portland cement implies that the concrete pore solution contains potassium-, sodium- and calcium-hydroxide (KOH , $NaOH$ and $Ca(OH)_2$, respectively). Depending on the cement composition, distinct concentrations of K^+ , Na^+ , Ca^{2+} and OH^- ions can be achieved, i.e., the pore solution can achieve distinct alkalinity levels. Nevertheless, the pore solution is typically a highly alkaline liquid ($pH \sim 12.8$). In certain aggregate types, some of the minerals, e.g., micas and feldspars, can also act as additional sources of alkalis [33], [34]. Thus, the concrete pore solution provides, in general, a favorable chemical environment for ASR. An OH^- concentration above 0.2 M can actively trigger the dissolution of the metastable silicates in any reactive aggregate [35].

The understanding of the role of alkalis and of their concentrations on the formation of ASR products has gradually improved over time. A special focus of several research efforts has been dedicated to the role of Ca . Ca^{2+} cations seem to play key roles both in the formation, expansion and physical and mechanical properties of ASR products.

Under the gel model of such products, it has been shown in several studies that the presence of Ca^{2+} is crucial to form ASR gels: without Ca^{2+} , the dissolved silica species would remain in the solution without giving place to gelation [36]–[39].

It was believed by some scientists that Ca^{2+} concentration controls the formation of expansive alkali-silica complex or non-expansive lime-alkali-silica complex [40]. While others refused the non-expansiveness of the lime-alkali-silica complex and instead associated the role of Ca^{2+} concentration to controlling of the relative rates at which the silica ions diffuse in and out of the reactive grains [41]. In a later study, the idea of exchange between alkalis and Ca^{2+} in silica gel was introduced (leading to non-swelling lime-alkali-silica complex) and the fact that "alkali recycling" can also take place (further production of swelling alkali-silica complex) [5], [40], [42]. The concept of siloxane bond breakdown (adjacent to the silanol groups) was later introduced to cause local lattice stability reduction and thus allowing new bonds with alkalis [8]. The ASR products containing Ca^{2+} are stable in water, whereas without Ca^{2+} , silica ions can dissolve in water. The Ca^{2+} ions can react with dissolved silica to form ASR products, a process which would continue till its saturation [43]. The Ca^{2+} and alkalis diffuse from the pore solution to the aggregate interfaces or cracks, while the silicate ions dissolved from meta-stable silicate by OH^- , diffuse in opposite direction (out of aggregates) [44], [45]. Therefore, based on the few aspects (out of several research instances) explained here, the inevitable controlling role of Ca^{2+} and alkalis availability on the ASR mechanism becomes obvious [8].

The role of moisture. Water is essential for ASR from two perspectives: as a reactive agent and as a transport agent for other reactive entities [46]. Concrete cast with reactive aggregates typically develops ASR if exposed to environments with relative humidity (RH) not lower than 80% [47]. However, exceptions to this rule of thumb have been reported, consisting of observations of ASR cracking occurring in concrete exposed to drier environments [48]. These results have suggested that the ASR expansion may not be necessarily and strongly dependent upon continuous water uptake. In certain conditions, the moisture present since the beginning within the structure itself may suffice to support the expansion of the ASR products [49]. However, sufficient evidence has also been reported that any moisture increase can enhance the reaction rate [8].

The common view of ASR products (expansion) challenged by recent results. Both recent and less recent results reported in the literature suggest the existence of a wider variety of ASR products types

than just gels. As a consequence, the common view described above about the molecular scale mechanisms of the products' expansion is put into question. In what follows, a selection of such results and corresponding impacts is summarized.

First of all, optical microscopy and scanning electron microscopy (SEM) studies have shown that ASR products well within the aggregate interior typically exhibit morphologies characteristic of nano-crystalline platelets [50]–[52]. This is in contrast with products closer to the aggregate boundaries or inside cracks running through the cement paste, which typically appear, in the same types of images, featureless, i.e., amorphous [11]. The platelets-like inner products are frequently characterized by nanometer thickness and micron-sized width [50]–[52]. Their morphology can thus be undoubtedly distinguished from that of a gel [53]. Additional micro-XRD and various spectroscopic characterizations revealed the similarity between such nano-crystalline products and shlykovite, a layered silicate [25], [54]–[56]. Differences in the basal spacing values have been found for such nano-crystalline products, depending upon whether they were retrieved from real world-aged structures or they were synthesized in the laboratory [56]. Despite such differences, the common layered molecular structure has the capability of water absorption/adsorption. However, during water vapor sorption measurements, these products showed (1) no systematic and clear evidence of dimensional changes in correspondence of their interaction with water vapor molecules [57] and (2) smaller moisture adsorption/desorption capacity than the most abundant cement hydrates, i.e., calcium-silicate-hydrates (C-S-H) [58], [59]. The former results were obtained by *in situ* 3D micro-XRD measurements with synchrotron radiation. What such measurements showed was the presence of a dimensional change of the crystalline lattice upon a change in environmental relative humidity (RH) between 10% and about 40% for one type of nano-crystalline products but not for another type. In addition, the crack containing such products exhibited no resolvable dimensional changes, even in correspondence of a RH increase up to 97%. The sorption isotherms results reported in [58], [59] essentially suggest that the nano-crystalline ASR products should have lesser degree of interaction with water (vapor) than C-S-H, calling into question whether water uptake by the nano-crystalline products, even when occurring, could really be at the basis of the observed ASR-driven expansion. Thus, in summary, according to the most recently available data, the nano-crystalline ASR products typically found in the inner aggregate regions do not seem to strongly deform and expand upon water vapor uptake. Such results weaken the hypothesized role of expansion upon the products' water uptake in the ASR damage sequence.

In terms of temporal sequence, evidence has been reported of initial (i.e., early-age) ASR products within aggregate micro-cracks being mainly amorphous, while the nano-crystalline forms mentioned before appearing later and in larger cracks, when macroscopic scale expansion has already taken place [60]. A knowledge gap consists of the behavior of such initial amorphous products upon water uptake, i.e., whether they may swell or not. If not, another possible candidate as source of initial, localized aggregate expansion and correspondent crack opening is the evolution of the amorphous products into the mentioned nano-crystalline ones, with consequent development of local crystallization pressure. Some examples of opening of original grain boundaries and micro-cracks in aggregates as a consequence of localized crystal-growth, even before whole micro-crack were filled with products, are reported in [61]. These results support the hypothesis of product crystallization as a possible source of micro-crack opening. However, the experimental challenges of directly observing, at sub-micron scale, such crystallization and to measure any eventual crystallization pressure even in a physical model system representative enough of what happening in concrete have prevented so far to confirm definitely such hypothesis.

2.2. Reactive aggregates

The aggregates used for concrete production might be of sedimentary, igneous or metamorphic origin [62]. Generally, the ASR reactivity of an aggregate type relies on its mineralogy and texture [63]. Understanding the behavior of an aggregate type when exposed to the chemo-mechanical environment of a concrete (structure) is fundamental for improving our scientific understanding of ASR, thus for developing approaches to mitigate it.

There exists well standardized, laboratory tests for assessing the aggregate reactivity, for example the accelerated mortar bar test (AMBT, ASTM C1260 [64]) or the concrete prism test (CPT, ASTM C1293 [65]). However, they are not effective enough in capturing the impact of the aggregate composition and texture on the ASR rate. In addition, such tests, which focus mainly on assessing the macroscopic expansions of specimens cast with the investigated aggregates, do not allow assessing other features of how ASR develops, for a given aggregate type, e.g., whether it mainly involves or starts at the aggregate surface or more in internal regions and their inherent micro-cracks and grain boundaries [7], [66], [67]. Therefore, petrographic characterization, typically based upon optical microscopy, has been extensively used as a complementary method for attaining a primary insight into the ASR reactivity of an aggregate type.

As mentioned earlier, the silica dissolution kinetics is affected by the silica structure. Well crystallized (dense) forms of silica, such as quartz, usually are less prone to ASR [68]. The ingress rate of the alkali hydroxides (thus the ASR likelihood) increases with the decrease of the crystallinity degree of the silica minerals. As a consequence, cryptocrystalline or deformed and defective quartz exhibits higher propensity to ASR than pure quartz, since the surface area in the microstructure of the former is larger than that of the latter [47], [68], [69].

Amorphous silica-containing aggregates, e.g., opal and glass, are the most reactive types. The second most reactive class includes meta-stable, e.g., cristobalite and tridymite, micro-crystalline and other crystalline forms of silica with lattice defects or residual strains and internal micro-cracks.

It is worth noting that the ASR reactive minerals of an aggregate may occupy only about 1% of its total volume, typically being found in its interior [70], [71]. Despite this feature, such reactive minerals can get in contact with the pore solution either via a rather porous matrix of the whole aggregate, like in the case of chert, or via inherent grain boundaries and micro-cracks in the aggregates. The latter features of aggregates not only act as conveyors of the pore solution. They also provide a large surface area for the ASR initiation and advancement [7].

Aggregates are generally categorized as "slow" (also "low"), "normal" (or "intermediate") and "fast" (or "high") in terms of ASR reactivity, based on their composition/texture as assessed by petrographic analysis [7], [72]. For example, a certain type of aggregate is considered to have a low reactivity, if above 97% of its components are mineral with known low potential reactivity. On the other hand an aggregate would be classified as to have a high reactivity if it consists of above 10% crushed greywacke or recycled demolition waste. It is recommended that if aggregates contain measurable opal or opaline silica, they should not be classified and used (i.e., reactions are very fast) [72]. A list of common aggregate and mineral types, with their respective alkali-reactivity class, is provided in Table 2.1. The petrographic texture of some selected ones are also shown in Figure 2.1. For instance, crushed greywacke (Figure 2.1 (a)), which is a sandstone, is known to have a considerable high ASR reactivity [72]. On the contrary, granite, exemplified in Figure 2.1 (b), typically has low ASR reactivity. However, there are exceptions because of textural and mineralogical features. For example, a microgranite (Figure 2.1 (c)), which is a form of granite, can be more reactive than other granite types due to a higher content of disordered silica.

In general, shear banding can produce metamorphic variants such as cataclasite (Figure 2.1 (d)), ultracataclasite (Figure 2.1 (e)) and ultramylonite (Figure 2-1 (f)), which tend to have higher proportions of disordered quartz, thus to be more alkali-reactive [72], [73].

In terms of mineralogy of the rocks, two classes of minerals are considered highly ASR-reactive. They include metastable and disordered forms of quartz (e.g. opal, chalcedony, tridymite, cristobalite and aluminosilicate glasses in the matrix of intermediate to acid volcanic rocks) [72]. Natural rocks might have significantly diverse lithologies and thus ASR-reactive minor components (e.g. disordered or sub-microscopic forms of quartz) can exist within the aggregates that are classified as non-reactive. For instance, a granitic rock would be typically classified as an aggregate with a low reactivity, but in different shear zones the granite might have metamorphosed into cataclasite, ultracataclasite and ultramylonite. The main characteristics of these variations is that they all contain highly disordered quartz, which is ASR-reactive [72]. In general quartzite (metamorphic rock naturally produced from pure quartz sandstone), chert (fine-grained sedimentary rock composed of microcrystalline or cryptocrystalline quartz) and flint (sedimentary cryptocrystalline form of the mineral quartz) are the prevalent types of constituents found in most of the commonly used aggregates (in construction). To facilitate the classification of aggregates, a simple approach was proposed by Hunt [74], based on quartzite and chert content of the aggregates. It consists of characterizing and sorting their grains, as appearing inside aggregates, in terms of their texture, fabric and grain size, as shown in Table 2.2. According to this approach, examples of cherty quartzite, diaquartzite and metaquartzite are shown in Figure 2.2(a)-(c), respectively [72].

Table 2.1. ASR- reactivity of various mineral, natural rocks or artificial aggregates (adapted from Ref. [72]).

Low reactivity	Normal reactivity	High reactivity
Air-cooled blastfurnace slag	Arkose ⁴	Chalcedony or chalcedonic silica
Amphibolite ¹	Breccia	Cristobalite
Andesite ¹	Chert	Greywacke (crushed)
Basalt ¹	Conglomerate	Opal or opaline silica
Chalk	Flint	Tridymite
Diorite and microdiorite ¹	Granulite ¹	Recycled demolition waste
Dolerite ¹	Greywacke (uncrushed)	
Dolomite ²	Gritstone ⁴	
Expanded clay/shale/slate	Hornfels ¹	
Feldspar	Quartzite ⁴	
Gabbro ¹	Rhyolite ¹	
Gneiss ¹	Sandstone and siltstone ⁴	
Granite and microgranite ¹	Tuff ¹	
Limestone ²	Volcanic glass ⁵	
Marble ²		
Quartz ³		
Schist ¹		
Sintered pulverized-fuel ash		
Slate		
Syenite and microsyenite ¹		
Trachyte ¹		

1 Rock type generally not alkali-silica reactive but may occasionally contain reactive forms of silica (possibly including opal, chalcedony, tridymite, devitrified glass, microcrystalline or cryptocrystalline quartz, submicroscopic or disordered quartz).

2 Silicified limestones, dolomites, and marbles may be reactive due to the presence of disseminated microcrystalline or cryptocrystalline quartz.

3 Not quartzite, nor microcrystalline or cryptocrystalline quartz. In addition, highly disordered quartz and submicroscopic silica or is potentially reactive.

4 Sandstones may occasionally contain reactive forms of silica such as microcrystalline or cryptocrystalline quartz, strained or disordered quartz, opal, chalcedony. Greywacke can be highly alkali reactive (when crushed) and is considered separately from other sandstones.

5 Volcanic glass may be reactive if the noncrystalline glass has devitrified to become very finely crystalline.

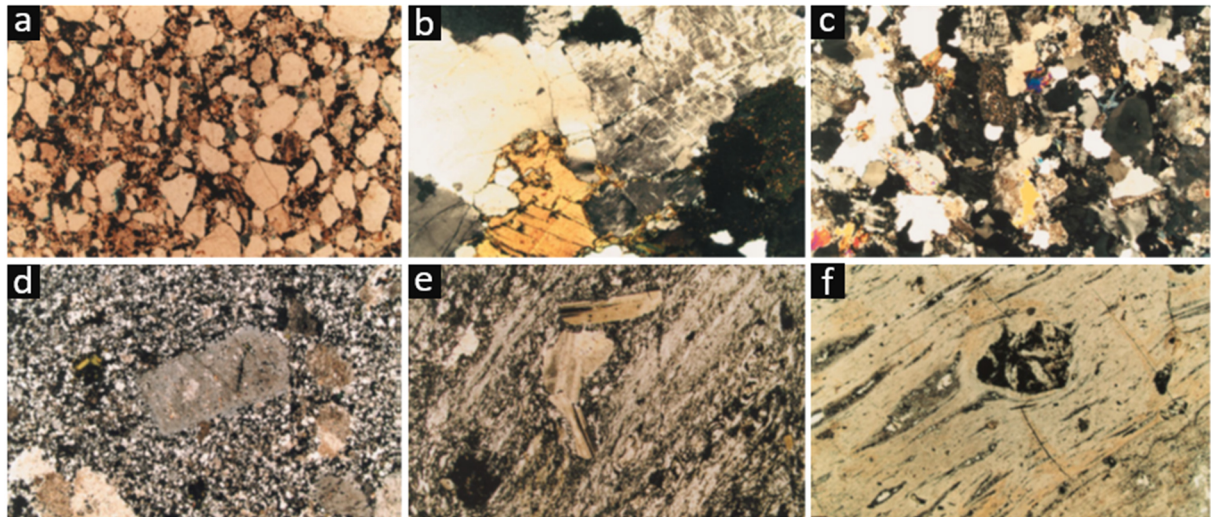


Figure 2.1. (a). Quartz grains appearing (light) in greywacke coarse aggregate; (b) granite, consisting of coarse crystalline quartz (left), feldspar (right), and biotite mica (yellow); (c) microgranite, comprising of fine crystalline quartz (grey/white/black), feldspar (grey), muscovite mica (yellow/pink/blue) and biotite mica (brown/green); (d) granite cataclasite with a porphyritic texture containing porphyroclasts of feldspar (centre) set in a groundmass largely composed of finely crystalline quartz; (e) ultracataclasite, containing unfoliated groundmass of fine crystalline to cryptocrystalline silica, with rare strained porphyroclasts; (f) ultramylonite, comprised of foliated groundmass of fine crystalline to cryptocrystalline silica, with rare strained porphyroclasts. All insets were adapted from [72] and show optical, transmission micrographs obtained by cross-polarized light and a geometrical magnification factor of $\times 35$.

Table 2.2. Classification of quartzite mineral groups ([75] and [72]).

FABRIC	TEXTURE			Content of nanocrystalline quartz (<2 μm)
	(Ortho)quartzite	Diaquartzite	Metaquartzite	
	Cherty quartzite	Cherty diaquartz	Cherty metaquartz	
	Quartzitic chert	Quartzitic diachert	Quartzitic metachert	
	Chert	Diachert	Metachert	
	Original grain structure visible	No original grain structure, interlocking crystals	Interlocking crystals, visible restructuring	
	INCREASING MATURITY			

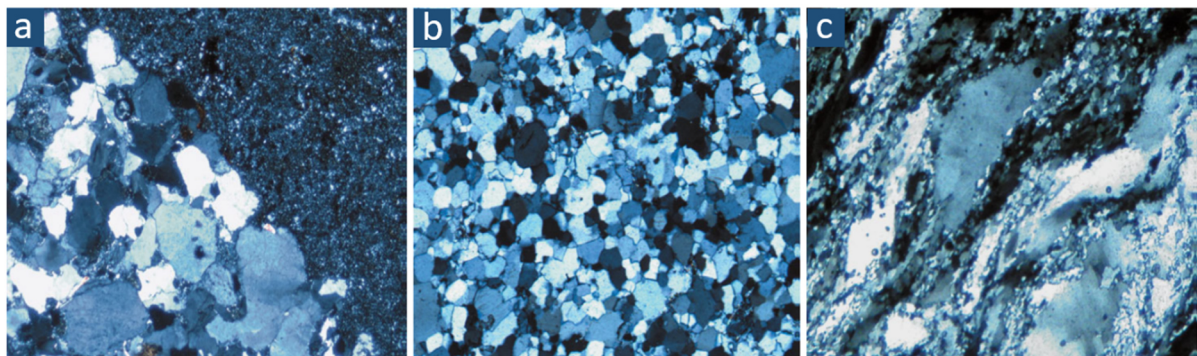


Figure 2.2. (a) Cherty quartzite, containing a combination of cryptocrystalline quartz (chert, top-right half) and interlocking, medium-grained quartz crystals (quartzite, left-bottom half); (b) diaquartzite, comprised of medium-grained quartz interlocking crystals; and (c) metaquartzite, with severely sheared and restructured quartz, including submicroscopic quartz. All insets were adapted from [72] and show optical micrographs obtained by cross-polarized light in a transmission mode, with a 150 times magnification.

2.3. Field examples of ASR damage

Deleterious effects of ASR on various civil structures have been identified in different countries around the world. It has always been a challenge for engineers in charge of operation and maintenance of such structures to assess their safety and performance and to protect them against ASR. Before conducting repairs on ASR damaged structures, a proper diagnosis of the damage type is necessary [76]. A comprehensive field survey is usually the ideal starting point for detecting ASR and its damage extent. ASR typically manifests itself with typical cracking patterns and moisture and/or ASR products leached out from those cracks (deposits) [77].

These crack patterns usually correspond to both shrinkage and ASR. During shrinkage, the surface layer of the concrete undergoes negative volume changes due to the loss of humidity, while in the interior parts a higher moisture content ASR is more favored. Therefore, the shrinkage cracks become wider and a different crack pattern can form (depending on other boundary conditions such as different restraints) [78].

The deposits usually form due to the wetting-drying cycles due to environmental changes. The silicon-rich pore solution reaches the concrete surface and amorphous silica containing minor amounts of calcium gets precipitated [78]. Furthermore, these deposits can form due to the penetration of considerable amount of water into the concrete and transporting dissolved ions to the concrete surface [78]. In this case portlandite and calcium carbonate precipitation (due to reacting with CO_2) may occur. Depending on the composition, the color of deposits might vary. They tend to appear white (if not contaminated by biological activities or organic materials) when formed by calcite [78].

Some examples of ASR cracking patterns, observable on the surfaces of structures worldwide, are shown in Figure 2.3. Figure 2.3 (a) shows a reinforced concrete foundation pier and Y-columns (20 years old) supporting a road overpass in Quebec City, Canada. The whitish stained region on the right hand-side of the image shows the leached ASR products from the respective cracks. Figure 2.3 (b) shows an elevated freeway structure (not repaired and 40 years old) in Port Elizabeth, South Africa. Figure 2.3 (c) shows another example of severe ASR cracking, including surface spalling, by the central abutment of a double arch railway bridge (not repaired and over 30 years old) in Johannesburg [76].

The first ASR-affected cases in Switzerland, reported in the literature, concerned the "Illsee dam" [78]. In Swiss structures (e.g. dams) the visual signs of significantly developed ASR occur as cracks. However, the pop-outs at the concrete surface (due to very fast and intense ASR), unlike the cases in some other countries, do not usually appear in Swiss structures. However, in some cases they might arise due to freeze-thaw damage [78]. Figure 2.3 (d)-(f) shows three examples of structural ASR damage found in Switzerland. The deposits (dark rims) caused by ASR can be observed along the crack edges.

The Swiss Committee on Dams released a report in 2017 about concrete swelling in Swiss dams [79], in which the results of several long-term studies on 11 Swiss dams monitored since their construction (up to 80 years of monitoring for some cases) was documented. The first deformations due ASR after construction was observed in different times at distinct dams, ranging from 5 - 27 years, with elongations of 300 - 400 $\mu\text{m}/\text{m}$ and elongation rates of 10 - 40 $\mu\text{m}/\text{m}/\text{year}$. The structural cracks were detected between 14 - 53 years in distinct dams. The crack width usually were estimated to be 100-1000 μm . The measured vertical displacement in the crest of a dam, over 60 years, showed a cumulated displacement of about 25 mm. Although such total displacement may not seem significantly high, but at critical locations in a structure, e.g., close to the gates of the dam, it can impair the functionality (e.g. disabling the gate operation).

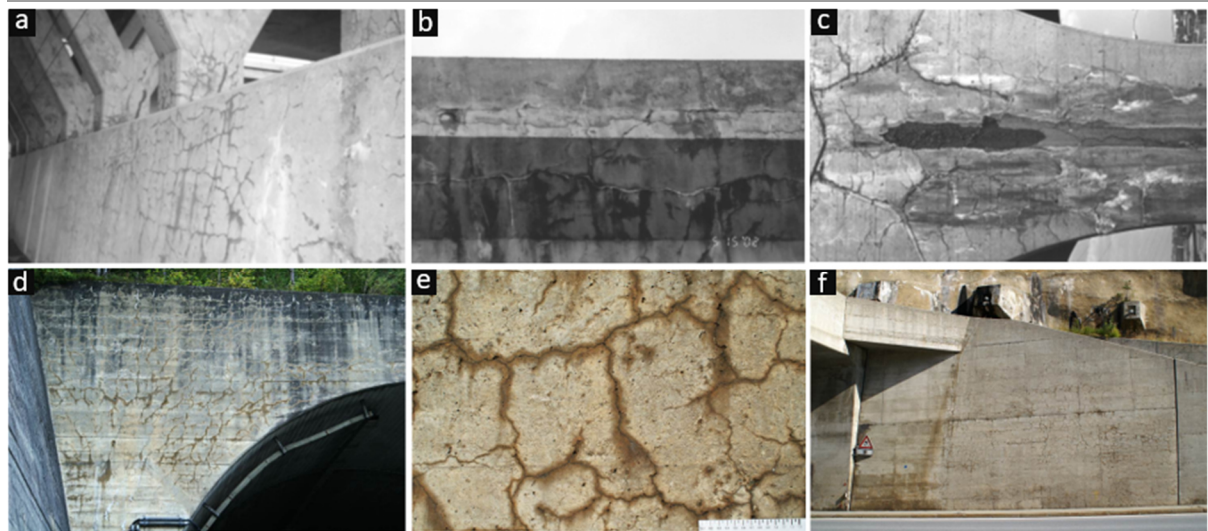


Figure 2.3. (a) ASR cracks on a road over-pass pier in Canada [76], (b) ASR cracking in an elevated freeway structure in South Africa [76], (c) severe ASR damage to a railway arch bridge in Johannesburg [76], (d) ASR cracks with dark rims having a preferred orientation parallel to the compressive stress at the entrance of a tunnel in Switzerland [78], (e) ASR cracks on a supporting wall (in Switzerland) [78] and (f) ASR cracks on a supporting wall at the entrance of a gallery in Switzerland [78].

2.4. Laboratory characterizations of ASR and ASR damage in concrete

2.4.1. ASR acceleration for aggregate reactivity and concrete damage assessment: commonly used standardized protocols

In order to assess the potential ASR reactivity of aggregates within shorter times (compared to those typically needed by real world structures to exhibit the common damage signs mentioned before), various laboratory standardized protocols for ASR acceleration and respective concrete damage assessment have been developed [80]–[86]. One of the most reliable for assessing ASR expansion of concrete is the already mentioned CPT protocol, consisting of storing the investigated mortar or concrete specimens in a controlled environment kept at $38 \pm 2^\circ\text{C}$ and RH above 95% [65]. The specimens need to be cast with a Portland cement of Type I and high in total alkali content (quantified by the Na_2O_{eq} , which is expressed as a fraction of the cement mass and should be 0.9 mass-%). NaOH needs to be added to the mixing water in an amount such that the total alkali content of the mix achieves the value of 1.25 mass-%. The expansion of the specimens are then regularly measured at specific time points until a specified age [65]. The CPT is commonly used as a reference standardized protocol to calibrate other similar techniques. By the CPT, the ASR reactivity of both fine and coarse (or of combinations thereof) aggregates can be assessed [87], [88]. Another standardized protocol, the AAR-3 [89], [90], was considered as a reference. However, it was superseded by other standards, specifically the AAR-2 and AAR-5 [90], similar to the already mentioned AMBT one, due its long term measurement requirements (12 months) [63]. An accelerated version of the AAR-3 protocol is the AAR-4.1, which requires storing the specimens at 60°C and a total testing time of 4 months [63], [90]. These latter acceleration and testing protocols are characterized by submerging the specimens in a highly alkaline solution rather than just exposing them to high relative humidity, as done during CPT. This restricts the alkali leaching out of the specimens during ASR acceleration tests.

2.4.2. Characterizations

2.4.2.1. Petrography by optical microscopy

One of the conventional, yet effective techniques to investigate the ASR reactivity, is assessing thin sections (sections with a thickness of 100-200 μm , cut from resin-impregnated samples) of samples by a polarized light microscope [91]. The optical microscope allows characterizing the structure at the mesoscale (few micrometers to few centimeters). Such investigations are often done with two main purposes. First, to characterize the texture of the aggregates themselves, as shown by some examples in Figure 2.1 and Figure 2.2. In this case, the thin sections were studied using polarized light, with crossed polarizers and, inserted, a gypsum plate. Various filters and apertures of a polarized light microscope help to identify the minerals regarding their texture and optical properties.

The second main application is to study the crack patterns developed in the concrete [78]. In this case, it is not necessarily needed to use thin section (transmission mode) and polarized light, an optical microscopy operating in reflection regime can also be used. In any case, it is important to use a fluorescent dye in the impregnation resin of these samples, so that the regions with cracks become evident under the light microscope. The cracks patterns are used to qualitatively or semi-quantitatively indicate the intensity of ASR in a certain type of aggregate [78].

2.4.2.2. Scanning electron microscopy (SEM) and energy-dispersive X-ray spectroscopy (EDX)

SEM, typically in back-scattered electron (BE) mode, is the other imaging technique frequently used for directly detecting the presence and evaluating the state of ASR, both in laboratory-based accelerated cases and for specimens obtained from the field.

As in the case of optical microscopy, SEM's main disadvantage in ASR-related applications consists not only of the two-dimensionality of the information provided but also in the destructiveness of the respective specimen preparation. However, SEM has proved to offer several advantages, among which a very broad spatial resolution range having a high overlap with the range of length scales of interest for characterizing ASR (from sub- μm to mm). Because of such advantage, the SEM characterization of ASR and ASR cracking has significantly contributed to the observation and understanding of several features and mechanisms.

SEM allowed observing that ASR products usually start forming as very thin (i.e., with sub- μm thickness) layers within the grain boundaries of different minerals [61]. At this stage, most of the products usually appear as amorphous, i.e., featureless, in the SEM images, at least at the smallest length scales resolvable by state-of-the-art electron microscopes. However, later on, when the first cracking already appeared, SEM observations could point out the existence of both crystalline and amorphous products [61].

The amorphous products have been often observed by SEM within cracks in the aggregates near the interfacial transition zone (ITZ), i.e., the cement paste region directly surrounding an aggregate and typically more porous than other, further away, paste regions. Such products not only typically look amorphous. They also have similar pixel values as the aggregate minerals. However, their recognition is supported by some typical features. For example, they frequently look like being accumulated as if forming a sort of plug inside the crack and close to the aggregate boundary. They are also predominantly observed close to a crack's boundaries, sometimes in the form of thin lining layers (Figure 2.4 (a) and (b)).

The crystalline products are characterized by a platelet-like morphology clearly visible in Figure 2.4 (a). That is the only feature which allows distinguishing them, in SEM-BSE micrographs, from amorphous products. They tend to form within cracks located in the interior regions of the aggregates. In most cases, they fill the cracks only partially (Figure 2-4 (a)).

SEM also allows observing ASR products extruded into ASR cracks propagated from an aggregate into the cement paste. Such products are typically looking as amorphous [61]. Such products extrusion has been observed in real world, ASR-affected concrete specimens as well as in lab-accelerated ones, where ASR cracks running through the cement paste are typically at the scale of tens to hundreds of μm in thickness. See Figure 2-5 (a) for an example. The exception concerns specimens whose ASR is the fastest accelerated in the lab, e.g., as by the protocols requiring 60°C or 80°C . In such cases, the ASR crack network inside an aggregate tends to be extremely fragmented and composed of narrower branches, instead of wide ones (Figure 2-5 (b)). Such narrower cracks typically do not propagate into the cement paste. Thus, in such cases, ASR products are typically observed in SEM-BSE as filling only the ITZ or the pore space around it [92].

Another key advantage of the SEM characterization consists of the possibility of performing, during the same imaging session, a local chemical characterization, in terms of elemental composition. This is possible because scanning electron microscopes are typically equipped also with point-wise X-ray detectors for EDX analysis. Thus, after having been imaged, a specific location of the investigated surface, e.g., a crack containing products, can be point-wise probed for its elemental (molar) concentration.

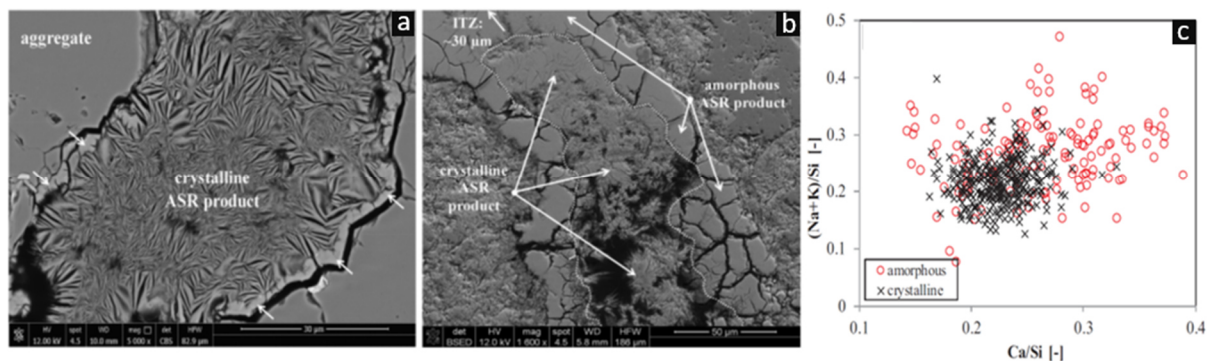


Figure 2.4. (a) SEM-BSE image of a crack within an aggregate almost fully filled with ASR products. Most of the ASR products are observed with a plate-like morphology, which indicates the crystalline microstructure of the products. Small amounts of amorphous products (with no plate-like features) are shown with white arrows; (b) SEM-BSE image of a crack (within an aggregate) filled with a combination of amorphous and crystalline ASR products; and (c) scatter plot of $(\text{Na}+\text{K})/\text{Si}$ -ratio versus Ca/Si -ratio for both amorphous and crystalline ASR products, obtained by EDX point analysis. All insets were adapted from [92].

EDX analysis of amorphous and crystalline ASR products has shown slight differences in their chemical compositions. The latter is typically analyzed in terms of Ca and alkali (mainly Na and K) concentrations, normalized by that of Si (the basic elemental species). Usually, the amorphous type has both greater variation as well as higher average values in the Ca/Si and $(\text{Na}+\text{K})/\text{Si}$ molar ratios, compared to the crystalline counterpart (Figure 2.4 (c)). Variations typically occur from one aggregate to another and also between amorphous products inside the aggregates and those in the cement paste. The products within the aggregates typically exhibit an average Ca/Si -ratio of about 0.25 and a $(\text{Na} + \text{K})/\text{Si}$ -ratio of 0.28. The products inside cracks through the cement paste typically show higher Ca/Si -ratio average

values, e.g., about 0.32, but lower average (Na + K)/Si-ratio values (~ 0.21) [53], [54], [93], [94]. The higher average Ca/Si-ratio value can be explained by the higher and more direct availability of Ca^{2+} cations in the cement paste, with their consequent easier and faster uptake by the products.

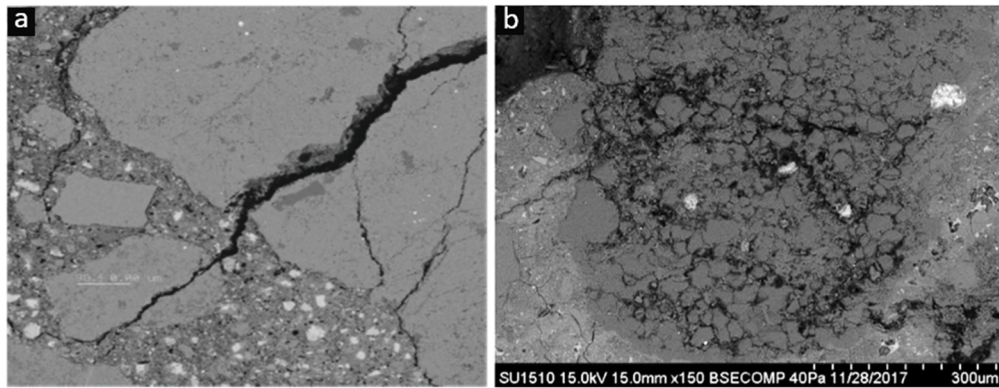


Figure 2.5. (a) SEM-BSE image of a mortar specimen, accelerated at 40°C, showcasing extensive cracking within the aggregate and extending into the cement paste (adaptation from [95]); and (b) extremely fragmented ASR crack network in an aggregate in a mortar specimen, accelerated by ASTM C1260 (ASTM 2014b), at 80°C. In such cases, crack propagation into the cement paste is less frequently observed (adaptation from [96]).

2.4.2.3. Mechanical and fracture properties characterization

A natural consequence of ASR cracking is the degradation of the mechanical and fracture properties. Tracking their evolutions may provide useful information on the damage state. Among several laboratory characterization techniques, measurements of the quasi-static Young's modulus, of the tensile and of the uniaxial compressive strengths have been frequently used [97].

Quasi-static Young's modulus. In structural engineering, the first important metric for load bearing capacity of concrete is its compressive strength. Nonetheless, in the case of ASR-damaged concrete, the usual positive correlations between tensile and compressive strengths and the Young's modulus do not hold, meaning, e.g., that a strong decrease in one variable is not always accompanied by a decrease in the other two. The Young's modulus typically has a clear sensitivity to ASR damage evolution. Reductions up to 65% in its value (after the first 28 days of hardening) have been observed [97], [98].

An example of Young's modulus evolution pattern during ASR is shown in Figure 2.6 for mortar specimens cast with a combination of several reactive aggregate types, each with distinct relative amount of phyllosilicates [77]. Such specimens were subjected to an adaptation of the French standard NF P18-585, where the change to the standard consisted in casting distinct specimens with distinct alkali contents for the mixing water and storing the specimens at distinct temperatures between 20° and 60°C. As visible in Fig. 2.6, independently of the specimen type, the Young's modulus increased up to about 25-28 days, after which it started to decrease (except for the specimens stored at the lowest temperature of 20°C). The initial increase was due to cement hydration. The decrease after 25-28 days was attributed to the ASR cracking, confirmed by SEM analysis of other specimens of the same types and following simultaneously the same protocols as those of Fig. 2.6 [77].

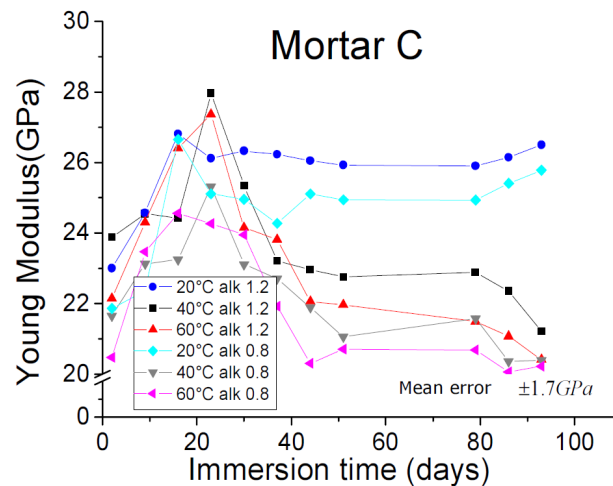


Figure 2.6. Evolution of Young's modulus (reactive aggregate C reported in [77]), characterized at three acceleration temperatures and with two alkaline content levels.

Tensile strength. This fracture property can be measured in three distinct ways (Figure 2.7), namely in direct (i.e., uniaxial), splitting or flexural mode. The tensile flexural strength is typically larger than the splitting one, which is larger than the direct one [97]. The tensile strength can be reduced up to 60% due to severe expansion, with respect to 28 day properties [98]. The direct tensile strength of concrete is typically not easily measured. The splitting or flexural mode measurements are routinely performed instead. The splitting test is very sensitive to the orientation of splitting and, as such, it is of limited value for evaluating the effects of the ASR damage. The flexural test provides a proxy measure of the actual tensile strength. Such proxy variable, called Modulus of Rupture (MR, expressed in MPa units), is proportional to the applied load at rupture and expresses the specimen's resistance to fail under bending. The common standards concerning the measurement of the flexural strength of concrete specimens are the ASTM C 78 [99] and ASTM C 293 [100].

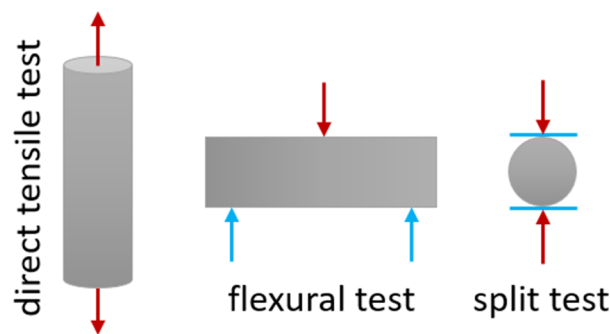


Figure 2.7. Different modes of tensile testing of concrete.

Uniaxial compressive strength. Decreases in this fracture mechanics property up to 40% have been reported in correspondence of very severe ASR damage [98]. This is a frequently reported result type: the uniaxial compressive strength starts to decrease only when the ASR cracking starts to be rather extended. Thus, as an ASR damage indicator, it is not as sensitive and indicative as the quasi-static Young modulus or the modulus of rupture are. Despite this fact, it is still frequently used because of the simple, well-established and diffused methods and equipment to measure it [101] and because the compressive strength is the fundamental concrete property based on which all other relevant engineering properties are calculated.

2.4.2.4. Relative mass and length changes

The relative mass and length changes (with respect to the beginning of testing, e.g., of an acceleration protocol) are the two most commonly measured variables during the ASR progress monitoring. The large expansions are usually associated with a high mass gain. The mass gain, in general, can be attributed to the water absorption by ASR products and water penetration into the internal micro-cracks and cracks, as they emerge due to ASR [102].

Despite being conceptually simple measurements, their implementation for ASR monitoring and characterization is not free of pitfalls. Concerning the length measurement of specimens subjected to the acceleration protocols requiring temperatures above the room one, temperature differences between the moment of actual measurement and the remaining storage time may introduce biases or may alter the specimens themselves. Thus, specific precautions need to be taken and sources of bias in the collected data need to be considered. When measuring on specimens stored at 40 °C, the minimization of the measurement time typically helps with reducing data bias from the eventual thermal shrinkage of the specimens [103]. The same does not hold anymore for specimens stored at higher temperatures, e.g., 60 °C. In such cases, the acceleration protocol typically indicate to move the specimens into an environment at room temperature 24 hours before the measurement. In addition to a reduction in the total acceleration time, such prescriptions implies cooling–heating cycles during the overall testing. Such cycles may cause ASR-unrelated, spurious deformations and associated cracking [103]. The inevitable drying due to the RH gradient between the specimen's pore space and measurement environment may eventually also trigger alkali transport, which can affect locally the ASR itself. These processes are among the drawbacks of the acceleration protocols requiring storage temperatures as high as 60 or 80 °C [103].

Some examples of expansion and mass increase are shown in Figure 2.7 (a) and (b), respectively. The reported data there concern specimens cast with highly reactive aggregates made of distinct minerals, including andesite, opal, cristobalite and volcanic glass. Protocols similar to the RILEM AAR-3 (at 38 °C) and the RILEM AAR-4 (at 60 °C) were used for the ASR acceleration. A difference consisted in the wrapping of the specimens in alkaline solutions-wet cloths, instead of submersion into the solutions [104].

Figure 2.7 (a) shows the time series for the relative length change, $\frac{\Delta L}{L_0}$, with qualitative features frequently observed. For the 60 °C case, $\frac{\Delta L}{L_0}$ exhibited initially, till 35 days, a higher rate than at lower temperatures. However, it later decreased. At 40 °C, the initial $\frac{\Delta L}{L_0}$ rate was lower compared at 60 °C and remained approximately constant till 140 days. Also at 40 °C, the $\frac{\Delta L}{L_0}$ rate decreased later on. However, the cumulative expansion exceeded at the end of the campaign that achieved at 60 °C. In the 20 °C case, $\frac{\Delta L}{L_0}$ exhibited initially delay, followed, since 35-50 days, by a linear increase till 140 days. Figure 2.7 (b) reports a scatter plot between the $\frac{\Delta L}{L_0}$ values and the corresponding relative mass change ones. It shows a strong, positive correlation between the two variables (at least at times when $\frac{\Delta L}{L_0}$ was greater than 0.04%). The linear regression results shown by the dashed lines show weaker correlation at lower temperatures. This implies that a larger amount of ASR products was probably produced at higher temperatures, leading to higher cumulative expansion.

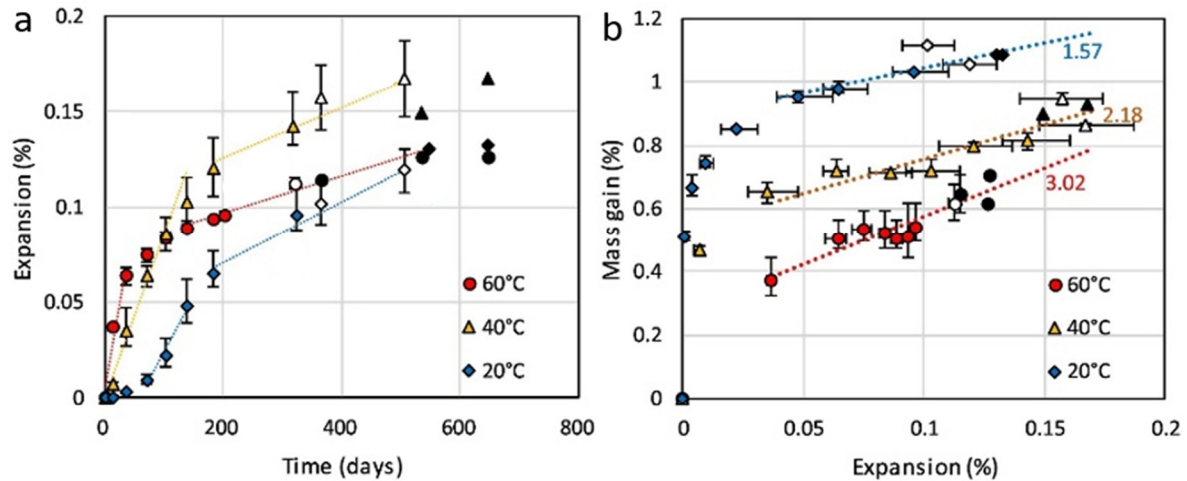


Figure 2.7. (a) Time series of the relative length change at different acceleration temperatures. The markers show mean values while the error bars show standard deviations, both computed from a set of specimens. The number of specimens measured at each time point is indicated by the format of each marker: color filled markers correspond to three specimens; the white and black markers denote two and one specimen, respectively. The dashed lines show regression lines performed considering only data points with expansion values above 0.04%, their slopes are indicted with values next to each line. Both insets were adapted from [105].

2.4.2.5. Basics of X-ray tomography as applied for ASR (damage) characterization

XT is nowadays used extensively both in Materials Science and Engineering [106]–[109], including in the field of concrete technology [110], as well as in the Earth and Environmental Sciences [111], [112], not to mention in the Biomedical Sciences and Engineering, where this 3D imaging technique stems from and where the strongest drives for new developments still exist [113]–[115].

There exists distinct types of XT. One way of distinguishing among them concerns from which main interaction processes between X-rays and matter the contrast in an X-ray tomogram (the created 3D image) stems. In this PhD project, X-ray attenuation contrast imaging (XACI) was used, whose principles are described below and which is the standard contrast mode. It relies on the transmission of an X-ray beam through the investigated specimens and its attenuation, in terms of the fraction of incident photons which actually emerges from the specimen's opposite side after their propagation through it. There exists other contrast modes for X-ray imaging, among which the two mostly developed are X-ray phase contrast imaging (XPCI) and X-ray dark-field contrast imaging (XDFCI). While XACI relies on the particle nature of X-rays as high energy photons, XPCI and XDFCI exploit their wave nature, as high frequency electromagnetic waves. The contrast in XPCI and XDFCI stems from other X-rays-matter interaction processes, mainly refraction and small angle scattering (SAS), respectively. Both XPCI and XDFCI have already found useful applications also in Materials Science and Engineering [109], [116], [117], including in the porous building materials fields [118]–[125]. However, they require either more specialized equipment and/or particular X-ray radiation characteristics which are not easily available for X-rays produced by laboratory-scale sources.

Another way of distinguishing between XT types actually relies upon the type of X-ray sources. In this PhD project, a laboratory source was used. Contrary to synchrotron radiation in the X-ray energy range, laboratory X-ray beams for tomography are highly polychromatic, have much lower brilliance/flux and much lower spatial coherence. The first characteristic makes discrimination between distinct material phases more difficult and introduces sources of artifacts. The second characteristics reduce the temporal

resolution of tomographic measurements. The third characteristic makes XPCI and XDPCI more complicated and typically requiring additional X-ray optics equipment and/or acquisition protocols and image formation approaches.

In the following, a brief review is provided about only those basic aspects of attenuation-contrast XT relevant to its use in this project. The review covers also some types of artifacts and some of the limitations which this project tried to address and to compound and reduce to achieve the set goals.

Basics of attenuation-contrast XT with laboratory sources. A laboratory-scale X-ray source for XT consists of a small linear accelerator of electrons. The respectively produced electron beam has energy typically in the range 20 – 300 keV. It is highly collimated and aimed at a small region (sub-mm to sub- μm) on a crystalline target typically made of high atomic number (Z) materials, e.g., tungsten. The strong deceleration the electrons experience while entering within the crystalline lattice of the target leads to the emission of bremsstrahlung radiation, in the form of X-ray photons, whose energy spans the full range up to the electron beam's incident energy. The emitted X-ray photons are typically contained within a conic volume whose aperture angle is the larger the smaller the target area irradiated by the electron beam (also called focal spot). The specimen to be tomographed is then irradiated by such a conic X-ray beam. Part of the beam is transmitted through the specimen, part not, due to different interaction processes. Thus, overall, the X-ray beam's intensity (i.e., number of photons per unit of time and unit of surface) is attenuated.

Within the photon energy range of 20–200 keV, the most probable photon-matter interaction processes are photoelectric absorption and Compton scattering. The first process contributes to remove from any linear trajectory (also called ray) from the source's focal spot to a location on the X-ray detector plane, past the specimen, a certain amount of photons. The second process alters the original trajectory of incident photons such that they may not end up on the detector plane anymore or they may be detected at other locations compared with the one intercepted on the detector's plane by the ray incident on the specimen.

Inside the specimen, at a generic position $\vec{x} = (x, y, z)$, its contribution to the X-ray beam attenuation along the rays passing at that position can be characterized by the local value of a scalar field indicated as $\mu(\vec{x})$ and called the X-ray mass attenuation coefficient (expressed in units of cm^2/g) [126]:

$$\mu(\vec{x}; E) = \alpha(\vec{x})f_p(E) + \beta(\vec{x})f_c(E) \quad (2.9)$$

where $f_p(E) \cong \frac{1}{E^{3.2}}$ is the photon energy (E) dependency of the photoelectric absorption cross-section while $f_c(E)$ is the photon energy dependency of the Compton scattering one (the so-called Klein–Nishina function, also monotonically decreasing with energy although slower than $f_p(E)$ for, e.g., $E > 50 \text{ keV}$). $\alpha(\vec{x})$ and $\beta(\vec{x})$ are characteristic coefficients of the material at location \vec{x} :

$$\alpha \approx K_1 Z^{3.8} \frac{\rho}{A} \quad (2-10)$$

$$\beta \approx K_2 Z \frac{\rho}{A} \quad (2-11)$$

where Z indicates the effective atomic number at the location \vec{x} , A is the corresponding atomic mass number, ρ the local mass density and K_1 and K_2 are constants. For many materials, the ratio $\frac{Z}{A}$ is practically constant in space. Therefore, α depends both on the spatial variations of both Z (thus of chemical species) and of ρ , with stronger influence by the former than the latter. On the contrary, β is chiefly determined by the spatial variation in ρ [127].

An X-ray attenuation contrast tomogram is essentially a reconstruction of the scalar field $\mu(\vec{x}; E)$ inside the volume of the irradiated specimen. For simplicity of presentation, it is hypothesized, in what follows, that a single photon energy E is used when irradiating the specimen. Equations 2.9-2.11 indicate that image contrast in such a type of tomogram depends essentially on a complicated contribution of local mass density and local chemical composition.

The basic tomographic imaging principle consists of the possibility of reconstructing $\mu(\vec{x}; E)$ starting from measurements of its line projections, $P_\mu(x', z', \theta, E)$ (also known as Radon transform):

$$P_\mu(x', z', \theta, E) = \int_{L(x', z', \theta)} \mu(\vec{x}; E) dl \quad (2.12),$$

where $\int_{L(x', z', \theta)} dl$ indicates the integration along the ray L connecting the X-ray source's focal spot with a point of coordinates (x', z') on the plane of the X-ray detector, when the specimen has a certain orientation angle θ around the vertical axis Z' of the detector, parallel to the vertical axis Z of the frame of reference attached to the specimen. Figure 2.8 shows a typical geometrical configuration of a laboratory-scale instrument for XT (also called tomograph) with the specimen located in between a 2D, pixelated X-ray detector and the X-ray source. The specimen is held on a stage which can rotate it.

For fixed θ , Eq. (2.12) represents a 2D (projection) image of the specimen. The cartoon in Figure 2.9 schematically shows examples of such 2D projection images. The link between them, at different θ values in the range $[0^\circ; 360^\circ]$, and $\mu(\vec{x}; E)$ is provided by the Fourier slice theorem [128]. Such theorem establishes that, at each vertical position z' and at each θ , the 1D Fourier transform of P_μ with respect to x' is equal to a radial cross-section, at angle θ , of the (2D) Fourier transform of the 2D cross-section of $\mu(\vec{x}; E)$ at vertical height $z = z'$. The latter 2D cross-section of $\mu(\vec{x}; E)$ is called a tomographic slice. A collection of P_μ 's, for distinct θ values, allows reconstructing, at each fixed $z = z'$, the Fourier transform of the slice of $\mu(\vec{x}; E)$ at such height $z = z'$. In principle, by inverse Fourier transform, such slice can thus be retrieved. A tomogram thus consists of a set of reconstructed slices, each orthogonal to the Z axis, which is the rotation axis of the specimen, parallel to the vertical axis of the detector.

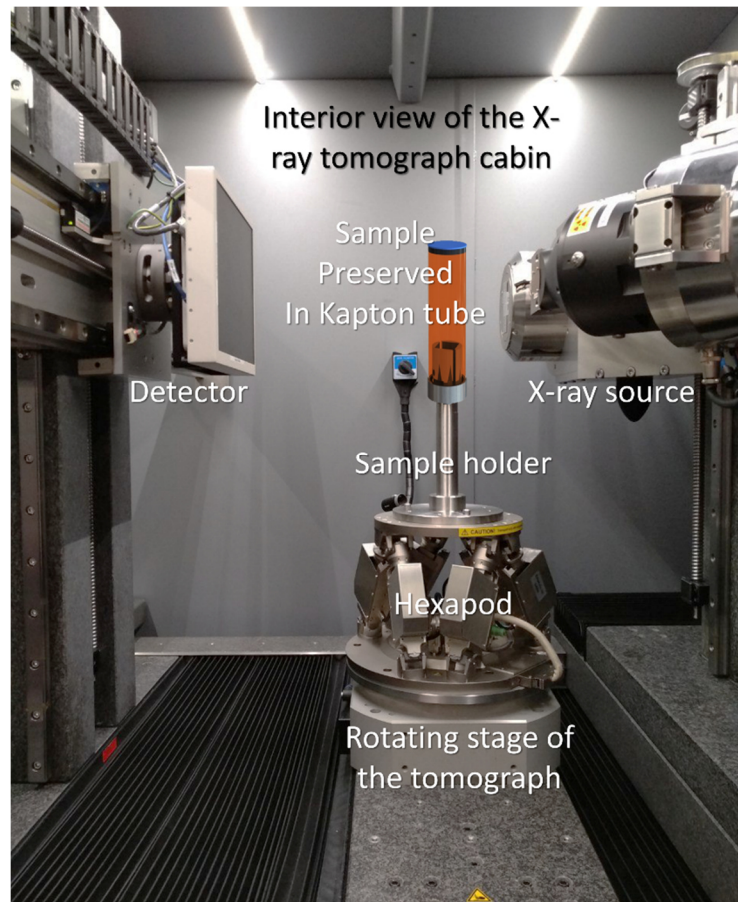


Figure 2.8. Laboratory sized XT machine used in this study.

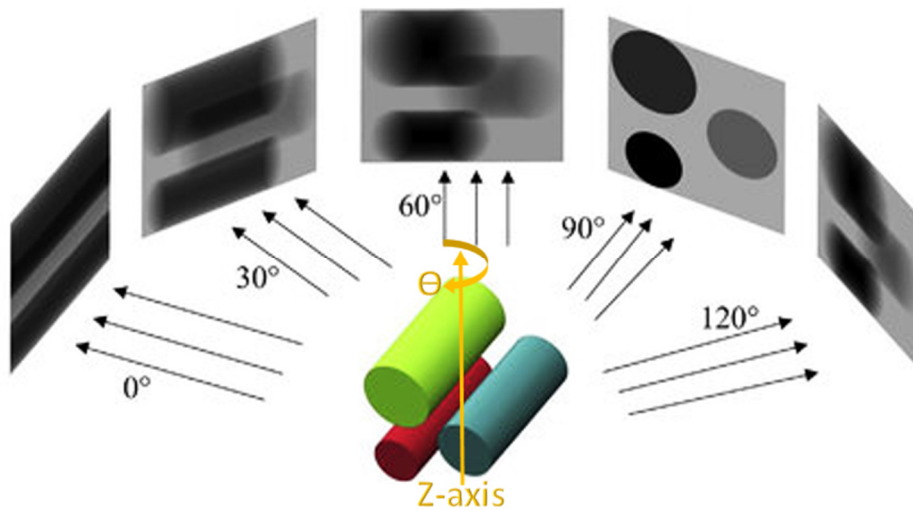


Figure 2.9. A schematic illustration of 2D projections acquired from a 3D object, observed at distinct rotation angle θ of the object, with respect to a vertical axis z of rotation (adapted from [129]).

Any XT measurement consists of two steps: a measurement one, needed to retrieve a collection of line projections of the specimen at distinct orientations θ ; a computational step (known as tomographic reconstruction), during which algorithms are used to retrieve $\mu(\vec{x}; E)$ from the set of line projections.

A physical model of how the intensity of the X-ray beam, transmitted through the specimen, is distributed on a plane past it provides a link between a measurable quantity (photon beam intensity I) and the line projections P_μ :

$$I(x', z', \theta, E) = I_0(x', z', E) \cdot e^{-\int_{L(x', z', \theta)} \mu(\vec{x}; E) dl} \quad (2.13),$$

where $I(x', z', \theta, E)$ is the transmitted X-ray beam intensity at position (x', z') for orientation θ of the specimen and $I_0(x', z', E)$ is the beam's intensity in the absence of the specimen.

Equation (2.13) is also known as Beer-Lambert law. Each 2D scalar field $I(x', z', \theta, E)$ is typically called a specimen radiograph. $I_0(x', z', E)$ is called a flat field (FF) radiograph, providing the intrinsic spatial distribution of the vertical cross-section of the X-ray conic beam which illuminates the specimen. Considering Eqs. (2.13) and (2.12) together, it follows that

$$P_\mu(x', z', \theta, E) = -\ln\left(\frac{I(x', z', \theta, E)}{I_0(x', z', E)}\right) \quad (2.14).$$

Thus, any XT measurement step consists in acquiring a set of specimen radiographs at distinct θ 's and at least one FF radiograph. In practice the FF radiograph in Eq. (2.14) is the result of pixel-wise averaging several of them, to increase the signal-to-noise ratio. In addition, a so called dark current (DC) radiograph is subtracted from each specimen radiograph and from the average FF one, being it the average of several radiographs acquired in the absence of the beam. The latter acquisition step allows to compensate for artifacts eventually arising from malfunctioning pixels of the detector providing a signal (thus a measured intensity) even in the absence of the beam.

One important concerns the limited validity of the Beer-Lambert law in describing the actual intensity of the transmitted beam as measurable past the specimen. Equation 2.13 is in principle valid only when the detector's plane with coordinates (x', z') lies immediately past the specimen. As shown in Fig. 2.8, this is not the case in standard, laboratory-scale XT measurements. A certain distance between the specimen and the detector always exists. It is actually exploited for taking advantage of the natural geometrical magnification of the projection images which derives from the conical shape of the emitted X-ray beam. The discrepancy between the physical model described by Eq. (2.13) and the physical reality may lead to so-called refraction artifacts. However, such artifacts have much less significance and negative impact when performing XT with laboratory X-rays than with synchrotron radiation, whose much higher spatial coherence implies that the refracted X-rays propagating from the exit plane of the specimen to the detector's plane can produce coherent interference patterns. The latter need to be taken into account in the physical model describing the relationship between $I(x', z', \theta, E)$ and $P_\mu(x', z', \theta, E)$ lest strong refraction artifacts impede a reliable and meaningful reconstruction of $\mu(\vec{x}; E)$.

Basics of tomographic reconstruction. Despite the Fourier slice theorem indicates that a 2D, inverse Fourier transform suffices for retrieving slices of $\mu(\vec{x}; E)$, actual reconstruction algorithms typically use other mathematical approaches to achieve such goal. That is commonly the case because of higher computational efficiency of the respective algorithms and/or smaller requirements in terms of data points and less numerical reconstruction artifacts. Several reconstruction algorithms have been proposed in this

regard. Hereby, only a few of the most used ones are briefly reviewed, with more elaboration on the family of filtered back-projection (FBP) ones, used in this PhD project.

Tomographic reconstruction techniques/approaches can be classified in two major groups, "exact" and "approximate".

An exact approach is based upon or at least inspired by a closed form, analytical solution of the continuous reconstruction inverse problem, where the scalar field to be reconstructed, $\mu(\vec{x}; E)$ in this context, is modelled as a continuous mathematical function. With such approaches, it is in principle possible to reconstruct $\mu(\vec{x}; E)$ as accurately as desired if a certain amount of noise-free line projections data are acquired. However, the actual numerical implementation of such analytical solutions always require numerical algorithms working with a space-discretized form of $\mu(\vec{x}; E)$, leading to approximate approaches and solutions. For instance, in the case of XT performed with a (almost) parallel beam, as it is the case with synchrotron radiation, the Fourier slice theorem provides the foundations for a class of algorithms working entirely within the Fourier space of the slices and with the respective inverse Fourier transformation [130], [131]. For cone beam XT, other closed form solutions and respective algorithmic implementations have been proposed. Three important algorithms are the Grangeat's formula for the inversion of the first derivative of the 3D Radon transform [132], the Katsevich's algorithm [133], [134] and the FBP approach described below. Due to intrinsic mathematical and computational issues, the actual algorithms stemming from all of these approaches lead intrinsically to approximate reconstructions, regardless of the data availability and measurement quality [135].

Another family of tomographic reconstruction approaches, falling under the umbrella name of algebraic reconstruction techniques (ART), also called iterative reconstruction techniques (IRT), are formulated mathematically since the start assuming that the scalar field to be reconstructed is spatially discretized [136]. By making no use of idealized mathematical hypothesis about the object scalar field, these approaches offer typically more robustness against different sources of artifacts, including paucity of acquired line projections data [136].

Reconstruction by filtered back-projection (FBP). The FBP is one of the most commonly used XT reconstruction methods. It is comprised of two steps: (i) filtering the line projections and (ii) back-projecting the corresponding out.

Figure 2. 10 schematically depicts the back-projection process, after the 2D projection images have been filtered. Distinct FBP implementations are characterized by distinct types of filter kernels. The results of the back-projection thus depends on the type of filter used. It is also strongly dependent upon the number of acquired 2D projection images over the θ range $[0^\circ; 360^\circ]$, since the back-projection consists in a pixel-wise sum of the version of such images smeared out through each slice's plane.

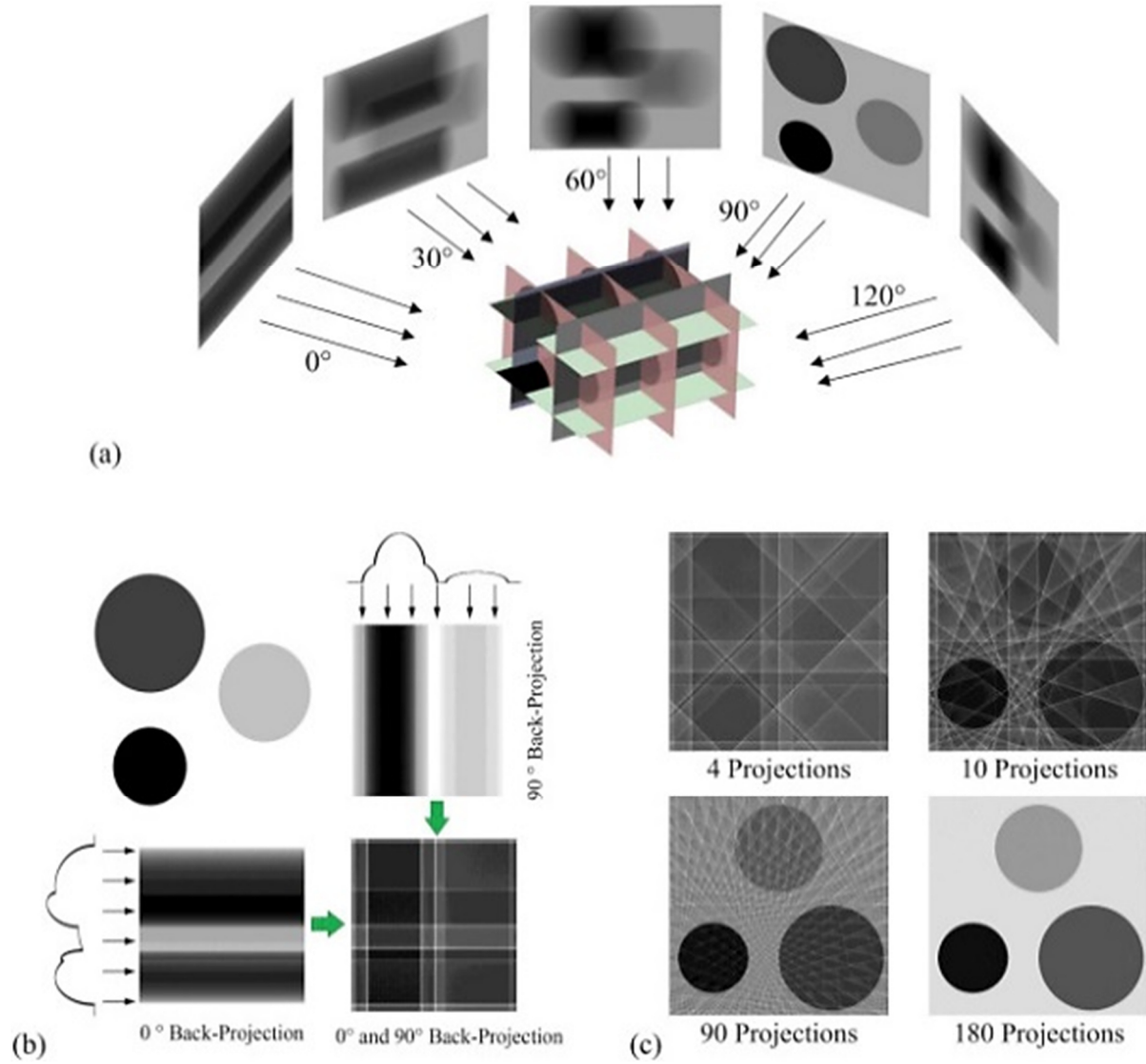


Figure 2.10. (a) Back-projection process, showing summing up over all possible orientation angles (smeared projections) after filtration; (b) examples of the projections at 0° and 90° and of the sum of their back-projections on a slice; and (c) an example demonstrating the effect of number of projections on the reconstructed slice. Adapted from [129].

Spatial resolution of X-ray tomograms. The spatial resolution of any image, including 3D ones as tomograms, can be defined as the minimum distance between two point-like features in the image below which they cannot be distinguished anymore as separate and point-like. In theory, it is an intrinsic property of the imaging system, being related with the characteristics of its total point spread function (PSF), and also called modulation transfer function (MTF). The latter represents, in the physical space or in the spatial Fourier domain, the response of the imaging system, i.e., the image, of a point-like specimen.

In the literature and for XT with laboratory sources, it is customary to provide the physical pixel size p of the 2D X-ray detector and the geometrical magnification factor M resulting from the conic geometry of the X-ray beam. The latter is defined as

$$M = \frac{d_{SD}}{d_{SS}} \quad (2.14)$$

where d_{SD} is the distance between the X-ray source (S) and the detector (D) while d_{SS} is the distance between the source and the specimen's (s) rotation axis. The actual size of a pixel in a radiograph is thus

$$\tilde{p} = \frac{p}{M} \quad (2.15)$$

as a consequence of the geometrical magnification. In cone beam XT, a voxel is typically isotropic (same size along each dimension) and with lateral size equal to \tilde{p} . This value is what is frequently and erroneously reported in the literature as spatial resolution of a tomogram. In reality, the effective spatial resolution, R_{eff} , is lower, meaning, it has a larger value. That occurs because of several effects, some of which are intrinsic to the tomograph, e.g., minimum noise level of the detector's pixels or focal spot size, others depend on the type of tomographed specimen. Some of the artifacts described below also contribute to lower the effective spatial resolution. A coarse approximate estimate of the effective spatial resolution can be provided by the following equation:

$$R_{eff} = \frac{\sqrt{p^2 + R_S^2}}{M} \quad (2.16)$$

where

$$R_S = f_s \cdot \frac{d_{SD}}{d_{SS}} \quad (2.17).$$

with f_s the source's focal spot size and d_{sd} the specimen-to-detector distance [137]. The definition of effective spatial resolution given in Eq. (2.16) takes into account the blur created in the radiographs by the focal spot size [137]. It considers the effects of only geometrical features of the measurement configuration in quantifying the effective spatial resolution.

Possible artifacts in X-ray tomograms. As mentioned before, laboratory-scale X-ray sources emit photons with energy spanning the range up to the corresponding voltage of the electron linear accelerator, indicated as E_{kVp} . The first consequence of such energy spectrum concerns the simplistic model of the relation between the measured transmitted intensity and the line projections of $\mu(\vec{x}; E)$ given by the Beer-Lambert law expressed in Eq. (2.13). Instead of Eq. (2.13) the following one should be considered in the model describing the transmitted intensity pattern being a radiograph:

$$I(x', z', \theta) = \int_0^{E_{kVp}} S(E) \cdot I_0(x', z', E) \cdot e^{-\int_{L(x', z', \theta)} \mu(\vec{x}; E) dl} dE \quad (2.18)$$

where $\int_0^{E_{kVp}} S(E) \cdot ? dE$ denotes the weighted integration over the photon energy range, from 0 to E_{kVp} , the source's energy spectrum, indicated by $S(E)$, providing the weighting function. Equation (2.18) is practically not usable, both from a mathematical point of view (highly ill-posed inverse problem for determining line projections) and also technically ($S(E)$ would need to be known for each measurement

settings). Thus, the model expressed by Eq. (2.13) is typically still used but by adopting specific corrections, frequently empirical ones [138]. The use of such corrections leads to artifacts falling in the class of spectral artifacts, some of which are exemplified in Figure 2.11.

Another source of artifacts, still related with the photon energy spectrum of the incident X-ray beam but, additionally, with the photon energy statistics of the transmitted beam, is beam hardening. The latter term refers to a shift of the average photon energy to higher values for the transmitted beam compared to the incident one. This occurs because, on average, photons with lower energy are more likely to be photoelectrically absorbed or (Compton) scattered. Along rays passing through thicker regions of a specimen with spatially constant $\mu(\vec{x})$, e.g., a cylinder filled with water (Figure 2.11 (b)), photoelectric absorption and Compton scattering events can occur more frequently than along thinner rays. Thus, along the former rays, the overall transmission is more strongly due to the higher energy photons, which are absorbed or scattered less per unit length (see Eq. (2.9), energy terms of the two contributors to $\mu(\vec{x})$, both decreasing with increasing E). The net result is that attenuation appears smaller in the thicker regions, leading to a spurious radial profile in any slice, with $\mu(\vec{x})$ decreasing towards the center. This artifact, sometimes called cupping, can be reduced by filtering out the lower energy part of the incident beam's spectrum by placing a certain thickness of a high Z material, e.g., Al or Cu, in front of the X-ray source. In addition or alternatively, the acquired radiographs can be pre-processed according to phenomenological models for compensating for the cupping [139], [140] or reconstruction methods, which take $S(E)$ into consideration in the image formation model have been also proposed [141].

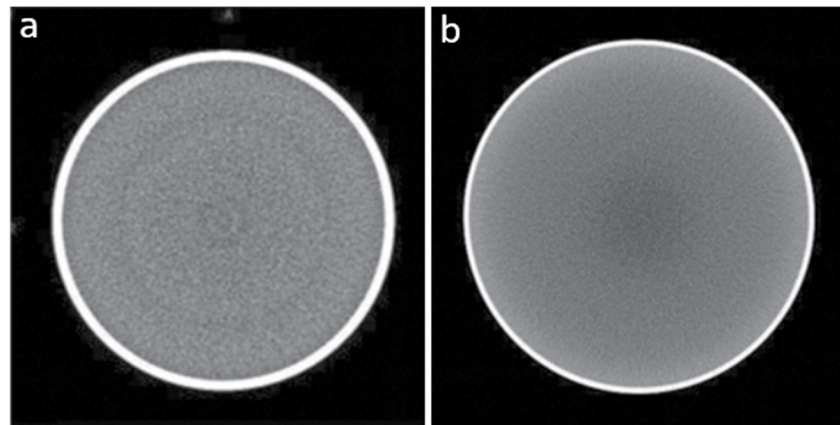


Figure 2.11. Example slices of tomogram of a water-filled tube (as an object with spatially homogeneous attenuation coefficient): (a) generic spectral artifact in the reconstructed slice, with a distributed, speckle-like pattern [142], and (b) beam hardening artifact, with a radial profile of the attenuation coefficient, higher values appearing towards the tube boundaries compared to its interior regions, also known as "cupping" [115].

Among several other types of artifacts [143]–[146], the following are acknowledged because of their universal occurrence in laboratory-scale XT.

Ring artifacts are exemplified in Figure 2.11 (a) and, even better, in Figure 2.12 (a). They appear as concentric rings in slices. They originate from the previously mentioned biased response of damaged detector pixels, even in the absence of an incident X-ray beam. When the dark current correction mentioned above does not suffice to subtract such spurious component of the pixel's response, each radiograph has at the damaged pixel location a constant response. This leads, after reconstruction, to a full circle with radius equal to the distance of that pixel from the center of the slice, since the attenuation

coefficient appears being the same along it (the respective projection value is always the same independently of θ). One way of reducing such artifacts is at the hardware level, by implementing robust offset-gain linearity correction based on the acquired dark current images. Another approach consists in applying specialized filters to the line projection images [147].

Finally, another artifact type is known as X-ray scatter artifact. It results from the presence of regions inside the specimen with very strong gradients in μ values. The end result is the appearance of cupping or low frequency "shading regions" and/or high μ streaks (also called metal artifacts), particularly in between heavily attenuating regions (Figure 2.12 (b)). These artifacts can be reduced by a minimized field of view or by the implementation of an anti-scattering hardware grids to be placed in front of the detector [148]–[151].

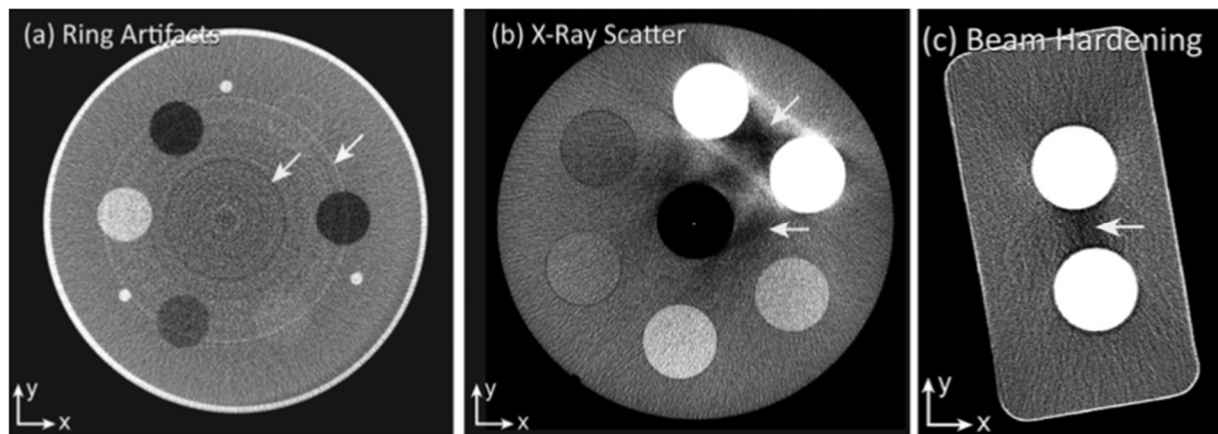


Figure 2.12. Example slices showing common artifacts: (a) Ring artifact, (b) X-ray scatter artifact and (c) Beam hardening artifact [135].

2.4.2.5.1. Contrast enhancers for XT

When a region of the specimen has μ values very close to those of surrounding regions, it is said that region of interest lacks X-ray attenuation contrast. A contrast agent for such specific feature/region is defined as a substance that, when added to the specimen, (1) it can localize itself into that region, e.g., by chemical binding, and (2) it offsets its μ values to enhance the region's attenuation contrast. Such a substance has usually a very high effective atomic number Z_{eff} relatively to the components of the surrounding regions, thus increasing the target's region average μ value well above that of the other regions [152].

The use of contrast agents in X-ray imaging has targeted a wide range of applications, starting from biomedical ones [152], materials engineering ones [153] and earth and environmental ones [154], [155]. In the biomedical realms, typically used contrast agents have been potassium iodide, iodine–potassium iodide, phosphotungstic acid, phosphomolibdic acid, osmium tetroxide, nanoparticle-based ones (e.g., gold, bismuth, tantalum, and gadolinium) [156]. In the materials engineering domains, extremely X-ray absorbing liquids as mercury have been used [153].

Suspensions of barium sulfate ($BaSO_4$, also called baryte) has been used for imaging-based diagnosis in certain medical areas [157]. Baryte is a white and inert powder, with high specific gravity and very low water solubility [158]. Its use as a attenuation contrast agent in medical X-ray imaging has been mainly motivated by the latter property as well as by the contribution by barium to increase the Z_{eff} , thus the μ one, of the region where the suspension cumulates, e.g., in the gastrointestinal tract. Thus, in

the barite suspension case, no specific chemical binding to certain target components of the specimens has been principally exploited. Based upon a similar principle, baryte has been proposed as an attenuation contrast agent in XT of concrete [159].

At the mesoscale as defined in this PhD Thesis, concrete has an extremely complex structure. However, its volumetrically more abundant mesoscale phases, i.e., the cement paste and aggregates, typically have similar μ values. Frequently, the mineralogical variety of aggregates used in concrete leads to have only parts of the aggregate set with sufficiently different average μ value. Thus both the visual and especially the algorithmic discrimination (also called segmentation in the image analysis and computer vision fields) of aggregates from the paste remain amongst the most challenging tasks in the analysis of attenuation contrast X-ray tomograms. Usual segmentation techniques such as voxel value range selection (also known as thresholding), gradient detection or pattern recognition have not been always successful or even applicable at all [160]. One approach to address this problem consists in adding into the concrete mix an inert contrast agent which would offset significantly the average μ value of the cement paste compared with that of aggregates. This is how baryte powder has been proposed to be used. It has been shown that its particles can be uniformly distributed throughout the paste, when they are fine enough ($\sim 1 \mu\text{m}$). The net result of such a uniform distribution is a sufficient increase in the paste's average μ value above typical values for many aggregate types [159]. Mechanical and isothermal calorimetric characterizations of the concrete cast with such barite addition showed no considerable alteration of the cement hydration and of the macroscopic mechanical properties. Figure 2.13 shows one slice from the X-ray tomogram of a reference specimen (inset (a)) and one slice from that of a specimen where 2.6 % of the total aggregate volume was substituted by baryte powder (inset (b)) [159]. In terms of mass ratio, in the case of the 2.6 vol.-% BaSO_4 mix, the BaSO_4 -to-cement mass ratio was 0.2, where the respective water-to-cement and total aggregate-to-cement ones were set to 0.5 and 4.46, respectively. In Figure 2.13 (a), the aggregate-to-paste contrast is clearly insufficient to distinguish between the two phases. On the contrary, the addition of baryte significantly enhanced their attenuation contrast, as visible in Figure 2.13 (b).

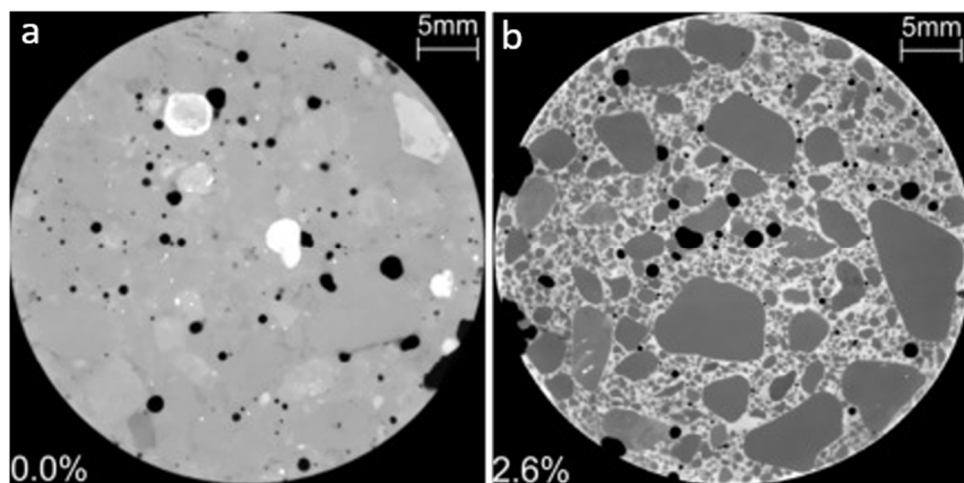


Figure 2.13. Example slices from two concrete specimens: (a) reference specimen, without baryte addition and (b) specimen with a baryte content of 2.6 vol.-% (in respect of the total aggregate volume) [159].

2.4.2.5.2. Three-dimensional image registration

Three-dimensional (3D) image registration is an image processing technique which does not apply only to X-ray tomograms and was not originally developed for assessing non-destructively (ASR) damage in

concrete. However, it can be considered as essential for its time-lapse characterization by XT. For this reason, it is presented upfront in this Section.

Time-lapse imaging and corresponding image registration are important tools in medical imaging, as, in several cases, images have to be acquired at distinct times to evaluate changes in a patient's condition [161]. In some cases, it is possible or needed to acquire, at the same time point, images with different modalities, for example, by XT and by magnetic resonance imaging (MRI). Images from different modalities may provide complementary information about different features, thanks to different types of image contrasts. In either case, the time-lapse single mode or the single time multi-mode (or even a combination of the two), the acquired images may not be immediately usable because of differences in the spatial locations of the same or corresponding features within a common frame of reference. That may occur because of simple specimen misalignment in between two distinct time points or because the frame of reference cannot be exactly the same, e.g., by multi-modal imaging with distinct instruments. Finding the spatial relations between pixels/voxels in two images is what enables comparison, both a qualitatively and quantitatively. In addition, such spatial relations may be one of the targets of the image analysis because it relates with deformations of features inside the specimens, as it is the case in this PhD project.

Image registration consists of finding an optimal (according to certain criteria) spatial mapping from pixels/voxels in one image to pixels/voxels in the other one, the two being, e.g., two points in a time series of images [162].

Image registration approaches and respective algorithms have been so far developed predominantly in the biomedical fields [162]–[168]. However, in the materials and mechanical engineering fields, a special type of image registration approach, called digital image correlation (DIC), sometimes explicitly called digital volume correlation (DVC) when applied to 3D images, has become a key methodology to measure indirectly strains from image time series of evolving specimens [169].

Mathematical formulation and solution of an image registration problem. Basics.

In any image registration problem, two images are considered: a reference image, also called the "fixed image", $I_F(\vec{x})$, and an image, also called "deformed image" or "moving image", $I_M(\vec{x})$, which is considered as the modified specimen's one. \vec{x} indicates a position in space, independently of being in 2D or 3D. In what followed, the 3D case is assumed. Both $I_F(\vec{x})$ and $I_M(\vec{x})$ are defined on a similar domain $D \subset \mathbb{R}^3$.

For simplicity, only scalar valued images (also called single channel images) are considered. As mentioned before, the difference between $I_F(\vec{x})$ and $I_M(\vec{x})$ may stem from something as simple as a misalignment of the imaged specimen or something as complex as an actual specimen deformation. In either case, one key assumption is that any given portion of the specimen located inside a certain voxel of the fixed image is contained also in the domain of the moving image, eventually just inside a voxel at another spatial position. Such assumption is often called the optical flow hypothesis or equation [170].

Under the optical flow hypothesis, registration tries to find the displacement vector field $\vec{u}(\vec{x})$, indicating where a certain voxel in the domain of the fixed image moved to in the domain of the moving image, or, also expressed by an equation,

$$I_M(\vec{x} + \vec{u}(\vec{x})) = I_F(\vec{x}) \quad (2.19).$$

In other words, Eq. (2.19) says that registration finds a mapping between (also called transformation or warping of, see Figure 2.14) the domains of the two images, $\vec{T}(\vec{x}) = \vec{x} + \vec{u}(\vec{x})$, which brings the two images to being identical to each other, thus correcting for the misalignment/deformation of the specimen [161]. $\vec{T}(\vec{x})$ is typically formulated and parametrized in a certain way, with a finite and discrete set of unknown parameters \vec{m} , thus it is frequently written as $\vec{T}_{\vec{m}}(\vec{x})$.

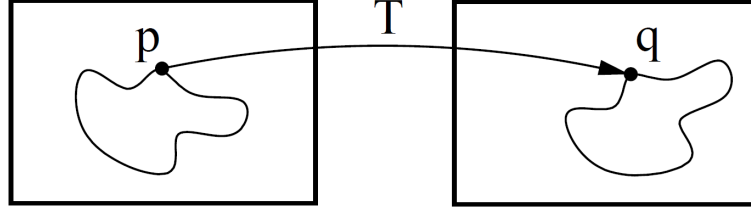


Figure 2.14. Schematic illustration of the change of a fixed image (left) as a spatial mapping \vec{T} of its domain to another one (right), moved image domain. A certain feature indicated by the point \vec{p} in the fixed image domain is mapped by \vec{T} to a distinct point \vec{q} in the moved image domain as $\vec{q} = \vec{T}(\vec{p})$. The image registration processes is in fact about finding \vec{T} , such that the two images are matched [161].

One important detail for understanding the results reported in Section 4 and its following ones is that, although the mapping \vec{T} goes from the fixed image domain to the moved image one, finding it allows morphing/transforming the moved image as such it gets to match (as well as possible) the fixed one. Indeed, Eq. (2.19), indicates that a new image can be created by taking the voxel value which the moved image has at the voxel of position $\vec{T}(\vec{x}) = \vec{x} + \vec{u}(\vec{x})$ and assign it to the voxel of position \vec{x} . The end goal of registration can be two-fold:

1. actually transform the moved image as such it matches the fixed one, once the mapping $\vec{T}(\vec{x})$ is found;
2. compute the displacement vector field $\vec{u}(\vec{x}) = \vec{T}(\vec{x}) - \vec{x}$ to quantify the misalignment/deformation.

The goal of point 1 is typical of cases where only misalignment occurred, e.g., in between two successive measurements and the two images need to be qualitatively and/or quantitatively compared. The goal of point 2 is typical of situations where the specimen actually deformed with time and the actual deformation is one target of the analysis.

The correctness of the registration is evaluated by a metric, indicated herein as \mathcal{S} and estimating an "image distance" or degree of image mismatch. Common formulations for \mathcal{S} are, e.g., a sum of squared differences (SSD), a normalized correlation coefficient (CC) or the mutual information (MI) of the two images [171]. The registration problem can thus be reformulated as an optimization problem where the global extremum of \mathcal{S} (minimum or maximum, depending on its definition), as a function of the mapping, i.e., of its parameters \vec{m} , is looked for. In the ideal case expressed by Eq. (2.19), the global extremum of $\mathcal{S}(\vec{m}; I_F, I_M)$ could in principle be found. This means that the moved image can be perfectly aligned/deformed, i.e., registered, to the fixed one. In the real world, the optical flow assumption of Eq. (2.19) does not hold because, at least, measurement noise and slight different imaging system performance at, e.g., two distinct time points contribute to create two distinct voxel values for the same fea-

ture/region in the specimen, left alone the eventual change in material properties because of, e.g., chemical reactions (as in the ASR case). As a consequence, in practical cases, the registration can only achieve a value close to the global extremum of $\mathcal{S}(\vec{m})$.

As any optimization problem, the registration one is typically ill-posed. Thus, a regularization (also called penalty, \mathcal{P}) term is usually introduced to constrain the possible range of \vec{m} values. The objective (also called cost) function $\mathcal{S}(\vec{m})$ is thus modified into a new one, $\mathcal{C}(\vec{m})$ [161]:

$$\mathcal{C}(\vec{m}; I_F, I_M) = -\mathcal{S}(\vec{m}; I_F, I_M) + \gamma \mathcal{P}(\vec{m}) \quad (2.20)$$

where γ weighs similarity between the two images against the regularity (sometimes in the form of smoothness) of the solution $\vec{T}_{\vec{m}}(\vec{x})$. Thus, the registration problem can finally be formulated, for example, as finding

$$\hat{m} = \arg \min_{\vec{m}} \mathcal{C}(\vec{m}; I_F, I_M) \quad (2.21),$$

then what is looked for is the global minimum of the cost function \mathcal{C} .

Any image registration procedure consists of a complicated workflow which goes beyond just the optimization problem synthesized in Eq. (2.21). The workflow has several pre- and post-optimization components which are schematically depicted in Figure 2.15 and are shortly described in the following paragraphs. The workflow considered here is specifically the one adopted by the 3D image registration software library Elastix [172], which has been used in this PhD project via its multi-language application programming interface (API), called SimpleElastiX [173], and which is based upon the open source image processing libraries ITK [174], [175], among the most popularly used in the biomedical sciences.

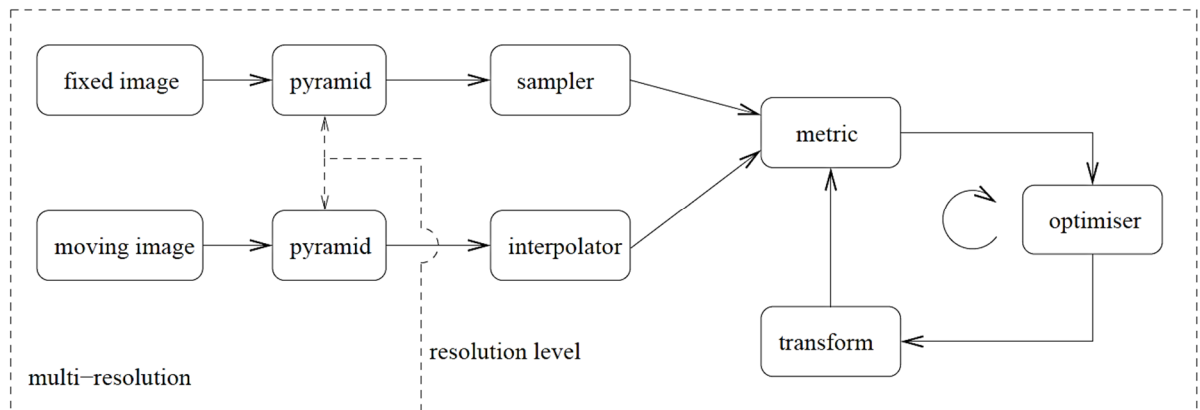


Figure 2.15. General procedure of an image registration process [161].

Image definition conventions. Figure 2.16 shows the conventions used in Elastix (thus in SimpleElastix) to define positions of pixels (coordinates), distance between them and size. These are the conventions inherited from the ITK libraries. Similar conventions are used for 3D images.

A circle indicates the center of a pixel/voxel. Its value (as a scalar field) is assumed to exist as a Dirac's delta function located within the circle. The distance between two pixels is measured between the pixel

centers and can be different along each dimension (anisotropic pixel size). The image origin is associated with the coordinates of the first pixel in the image. A pixel, being the rectangular region surrounding the pixel center, can be viewed as the Voronoi region of the image grid (Figure 2.16 (b)). Linear interpolation of image values in between pixels is performed inside the Delaunay region whose corners are pixel centers [161]. This is an essential operation in the image registration workflow (see below).

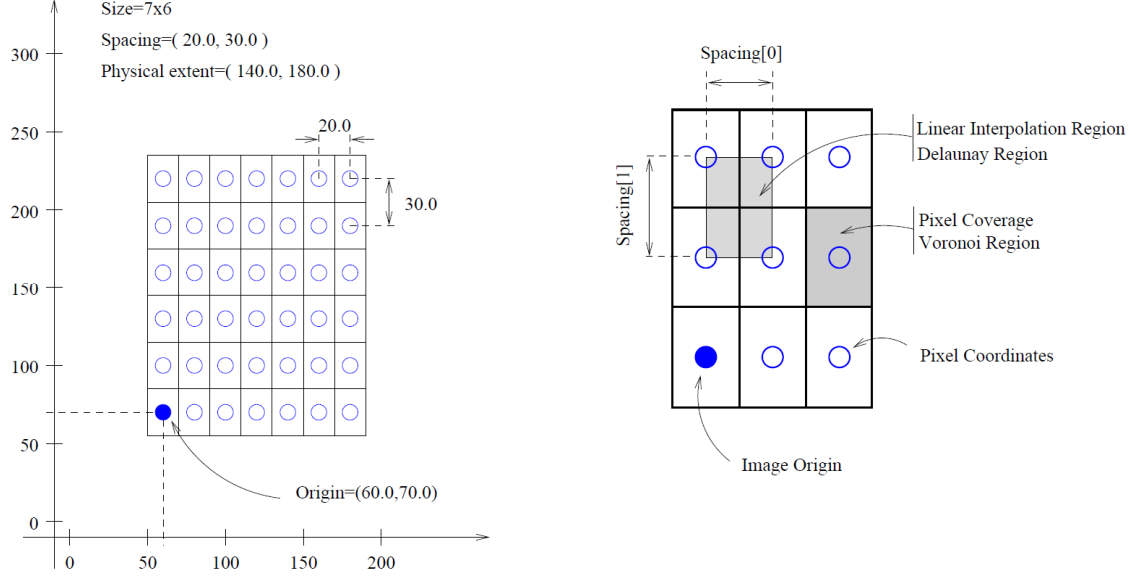


Figure 2.16. Geometrical conventions in describing an image as data structure in the ITK libraries [161].

Image distance metrics (or cost functions). As mentioned before, distinct definitions of the cost function $\mathcal{S}(\vec{m})$ (without the regularization term) have been formulated. The focus here is only on the one implemented in this project, the mutual Information or MI of the two images. It is quite a general metric with a proven good performance in many applications, empowering the registration of both mono-modal and multi-modal image pairs. If $I_F(\vec{x})$ and $I_M(\vec{x})$ are considered as being realizations of two distinct random variables (essentially two ergodic stochastic processes), they can be seen as samples from the two respective statistical ensembles and the respective (marginal) probability density functions (PDFs), $p_F(f)$ and $p_M(m)$, and their joint PDF, $p(f, m)$, can be estimated from them [176]–[178]. Here the symbols f and m indicate samples from the two random variables, i.e., generic voxel values from the two distinct images. The MI of the images/random variables is then defined as [161]

$$MI(\vec{m}; I_F, I_M) = \sum_{m \in L_M} \sum_{f \in L_F} p(f, m; \vec{m}) \log_2 \left(\frac{p(f, m; \vec{m})}{p_F(f) p_M(m; \vec{m})} \right) \quad (2.22)$$

where L_F and L_M are the regularly spaced sets of voxel values. To be noticed is that Eq. (2.22) considers the moving image after a certain transformation $T_{\vec{m}}$ has been applied to it.

The joint PDF is estimated using B-spline Parzen windows [161],

$$p(f, m; \vec{m}) = \frac{1}{|\Omega_F|} \sum_{\vec{x}_i \in \Omega_F} \omega_F \left(\frac{f}{\sigma_F} - \frac{I_F(\vec{x}_i)}{\sigma_F} \right) \times \omega_M \left(\frac{m}{\sigma_M} - \frac{I_M(T_{\vec{m}}(\vec{x}_i))}{\sigma_M} \right) \quad (2.23)$$

where ω_F and ω_M are fixed and moving B-spline Parzen windows. The scaling constants, σ_F and σ_M must equal the voxel value bin widths defined by L_F and L_M . These follow directly from the voxel value ranges of $I_F(\vec{x})$ and $I_M(\vec{x})$ and user-defined numbers of histogram bins, $|L_F|$ and $|L_M|$, respectively. Ω_F in Eq. (2.23) indicates the set of voxel positions of the fixed image.

With such a cost function, the registration consists in a maximization problem in respect to the unknown set of parameters \vec{m} .

Image sampler. Based on Eqs. (2.22) and (2.23), to solve the registration problem it is necessary to consider all the voxels (full sampling) of the fixed image ($\sum_{\vec{x}_i \in \Omega_F}()$). In practice, such full sampling is not crucial. A subset of its voxels might be sufficient. Such a subset can be sampled, among others, randomly on the image lattice, by a specific sampling algorithm [161].

Interpolators. Throughout the optimization procedure, the values of I_M need to be assessed at non-voxel positions $\vec{T}_{\vec{m}}(\vec{x})$, for which voxel value interpolation is required. Distinct interpolation techniques (with distinct quality and speed) are typically used, including nearest neighbor methods, linear interpolators and n-th order B-splines, in order of increasing accuracy and computational complexity [161].

Transformation. Depending on the registration problem, different parametrized transformation vector fields $\vec{T}_{\vec{m}}(\vec{x})$ can be adopted. The main types include rigid body, affine and non-affine transformations [161].

Rigid body transformations consists of the translation accompanied by a rotation [161]:

$$\vec{T}_{\vec{m}}(\vec{x}) = \mathbf{R} \cdot (\vec{x} - \vec{c}) + \vec{t} + \vec{c} \quad (2.24)$$

where \vec{t} denotes a translation vector, the \mathbf{R} indicates a proper and orthonormal rotation matrix (parametrized by the Euler angles) and \vec{c} stands for center of rotation. During a rigid body registration, the image is treated as a rigid body, which can translate and rotate but cannot be scaled/stretched. The parameter vector \vec{m} includes the three Euler angles (in rad) and the three components of the translation vector. The center of rotation is often considered as the center of the image [161].

A (global) affine transformation is defined as [161]:

$$\vec{T}_{\vec{m}}(\vec{x}) = \mathbf{R} \cdot \mathbf{G} \cdot \mathbf{S} \cdot (\vec{x} - \vec{c}) + \vec{t} + \vec{c} \quad (2.25)$$

where \mathbf{R} , \mathbf{G} and \mathbf{S} are rotation, shear and scaling matrices, respectively. The total number of parameters is 12 in this case.

Both a rigid body and a global affine transformations lead to displacement vector fields with constant first order derivatives, meaning, they lead to constant strain fields. Non-affine transformations are typically associated with more complicated and highly spatially dependent strain fields. One possible parametrization of such type of complicated transformation is by a set of B-spline functions, for example [161]

$$\vec{T}_{\vec{m}}(\vec{x}) = \vec{x} + \sum_{\vec{x}_k \in \mathcal{N}_{\vec{x}}} \vec{p}_k \beta^3\left(\frac{\vec{x} - \vec{x}_k}{\sigma}\right) \quad (2.26)$$

where the \vec{x}_k represent the B-spline control points, $\beta^3(\vec{x})$ shows a cubic multi-dimensional B-spline polynomial [179], \vec{p}_k denotes the B-spline coefficient vectors (the control point displacements), σ is the B-spline control point spacing, and $\mathcal{N}_{\vec{x}}$ the set of all control points within the compact support of the B-spline at \vec{x} . The control points, \vec{x}_k , are defined on a regular lattice, overlaid on that of the fixed image. The parameters of such a transformation are the \vec{p}_k . Thus, its total number is the triple of the number of control points. It can easily fall in the 10^6 range, indicating that the displacement vector field associated to the transformation of Eq. (2.26) may be capable of capturing extremely localized deformation, at the cost, though, of making the optimization problem extremely ill-posed. Figure 2.17 shows examples of the these various transformations in action [161].

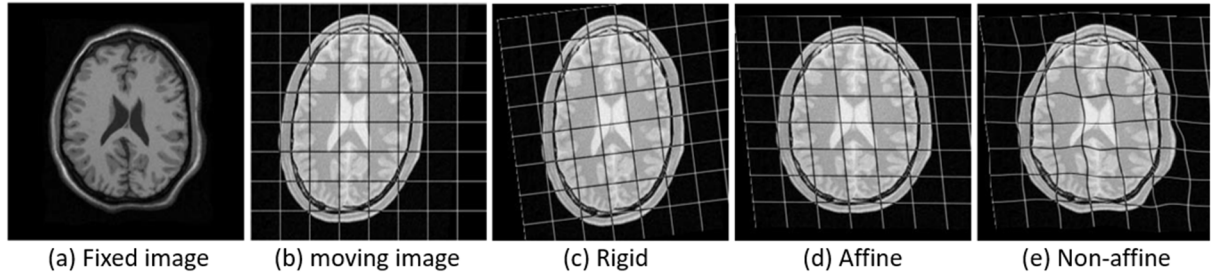


Figure 2.17. Example outputs of various transformations used for registering (a) fixed image and (b) moving image (with a distinct imaging modality): (c) results of a rigid body registration; (d) results of a global affine transformation; and (e) results of non-affine registration using a B-spline-based transformation model [161].

Optimizer Iterative approaches are typically used for solving numerically the optimization problem at the core of the registration workflow. This means that a finite difference evolution equation for the parameter vector \vec{m} is used [161]:

$$\vec{m}_{k+1} = \vec{m}_k + a_k \vec{d}_k \quad \text{with} \quad k = 0, 1, 2, \dots \quad (2.27)$$

where \vec{d}_k indicates the search direction in the parameter vector space at the k -th iteration step and a_k is a scalar gain factor controlling the step size along the search direction at such step. Figure 2.18 shows a cartoon which shows an ideal, complicated cost function surface in the parameter surface, the initial value of the parameter \vec{m} and its evolution through the vector space as such to approach iteratively the local minimum of the cost function, which in this case was formulated such that the registration problem would correspond to a minimization one. Iterative optimization approaches frequently used for image registration span a very broad range, from simpler ones as the quasi-Newton (QN) method, to more complicated ones, as the Robbins-Monro, passing through traditional and robust ones as gradient descent (GD) ones and nonlinear conjugate gradient (NCG) descent ones [180]. Amongst them, the GD approaches are probably the most frequently used. The GD method considers the search direction as the negative gradient of the cost function [161]:

$$\vec{m}_{k+1} = \vec{m}_k - a_k \vec{g}(\vec{m}_k) \quad (2.28)$$

in which the $\vec{g}(\vec{m}_k) = \partial C / \partial \vec{m}$ evaluated at the current position \vec{m}_k in the parameter vector space. Distinct approaches exist also for defining the gain factor values a_k , e.g., by a line search. A more advanced and robust version of the GD is the adaptive stochastic GD, which requires less parameters to be set and tends to be more robust to the presence of local minima/maxima of the cost function [161], [181].

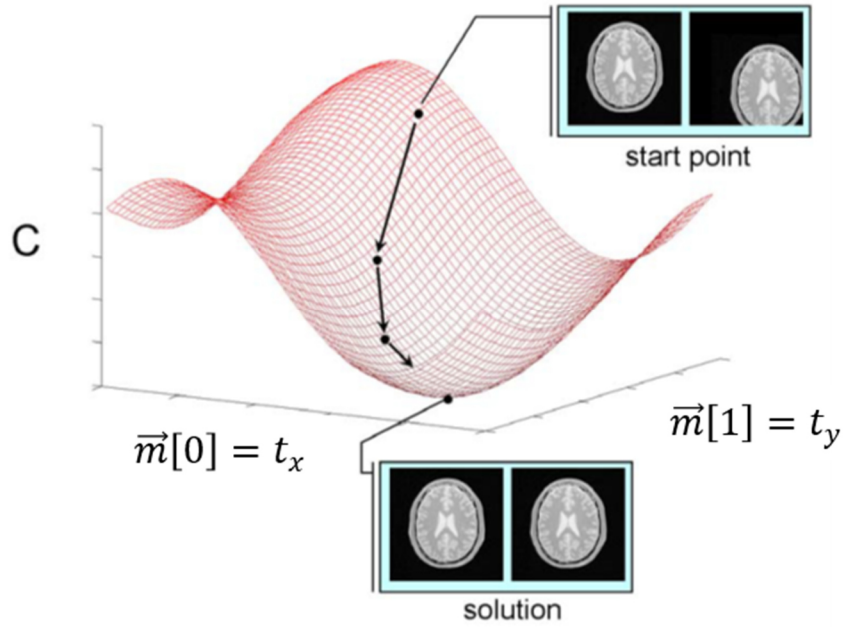


Figure 2.18. Schematic illustration of a possible cost function surface (red mesh) with a global minimum (best solution of a registration problem). The optimization algorithm iteratively moves (arrows) the guess for the parameter vector \vec{m} according to certain criteria (e.g., along the direction of the gradient of the cost function but in the opposite sense) to find the solution [161].

Hierarchical schemes for complexity reduction during registration. Generally, multi-resolution registration methods can be categorized in two main hierarchical procedures [164]. One procedure is motivated by "transformation complexity" while the other addresses "data complexity". The hierarchical approaches aim to reduce mentioned complexities [161]. In other words, to tackle the transformation complexity, the registration can be done in a stepwise manner, starting from rigid body registration, then doing a global affine registration and finally performing non-affine registration to registrar very fine (local) details. To overcome data complexity, during each of the registration steps, the processing of the images can be performed in a multi-resolution manner (going from low resolution to high resolution, to gradually increase the details).

Regarding data complexity, it is commonly recommended to start the registration not with the original images but with versions thereof with a lower degree of complexity, such as those obtained by some kind of smoothing or down-sampling. A set of images with increasing level of smoothing and generated from the same original image is known as a "scale space" of such image. Smoothed and down-sampled versions of an image have reduced complexity and (data) size. Such series of images can be thought of as a pyramid. Various types of pyramids (Gaussian and Laplacian pyramids, spline and wavelet pyramids) and scale spaces (e.g., a morphological scale space) exist, amongst which, the Gaussian pyramid is the most popular approach [161].

To reduce the transformation complexity, it is possible to start the registration with fewer degrees of freedom, i.e., with a smaller number of parameters. For instance, the registration can be carried out by

three successive stages, first according to a rigid body model, then according to an affine one and finally according to a more general non-affine model. Another approach consists of gradually increasing the number of degrees of freedom of a transformation model. For example, by a non-affine registration based upon a B-spline-based parametrization, it can be started with a coarser control points grid, then gradually repeated with finer grids [161].

Bibliography

- [1] S. Diamond, "A review of alkali-silica reaction and expansion mechanisms 1. Alkalies in cements and in concrete pore solutions," *Cem. Concr. Res.*, vol. 5, no. 4, pp. 329–345, Jul. 1975, doi: 10.1016/0008-8846(75)90089-7.
- [2] S. Diamond, "A review of alkali-silica reaction and expansion mechanisms 2. Reactive aggregates," *Cem. Concr. Res.*, vol. 6, no. 4, pp. 549–560, Jul. 1976, doi: 10.1016/0008-8846(76)90083-1.
- [3] S. Urhan, "Alkali silica and pozzolanic reactions in concrete. Part 1: Interpretation of published results and an hypothesis concerning the mechanism," *Cem. Concr. Res.*, vol. 17, no. 1, pp. 141–152, Jan. 1987, doi: 10.1016/0008-8846(87)90068-8.
- [4] S. Chatterji, N. Thaulow, and A. D. Jensen, "Studies of alkali-silica reaction, part 6. Practical implications of a proposed reaction mechanism," *Cem. Concr. Res.*, vol. 18, no. 3, pp. 363–366, May 1988, doi: 10.1016/0008-8846(88)90070-1.
- [5] H. Wang and J. E. Gillott, "Mechanism of alkali-silica reaction and the significance of calcium hydroxide," *Cem. Concr. Res.*, vol. 21, no. 4, pp. 647–654, Jul. 1991, doi: 10.1016/0008-8846(91)90115-X.
- [6] E. Garcia-Diaz, J. Riche, D. Bulteel, and C. Vernet, "Mechanism of damage for the alkali-silica reaction," *Cem. Concr. Res.*, vol. 36, no. 2, pp. 395–400, Feb. 2006, doi: 10.1016/j.cemconres.2005.06.003.
- [7] F. Rajabipour, E. Giannini, C. Dunant, J. H. Ideker, and M. D. A. Thomas, "Alkali-silica reaction: Current understanding of the reaction mechanisms and the knowledge gaps," *Cem. Concr. Res.*, vol. 76, pp. 130–146, Jul. 2015, doi: 10.1016/j.cemconres.2015.05.024.
- [8] R. B. Figueira *et al.*, "Alkali-silica reaction in concrete: Mechanisms, mitigation and test methods," *Construction and Building Materials*, vol. 222. Elsevier Ltd, pp. 903–931, 20-Oct-2019, doi: 10.1016/j.conbuildmat.2019.07.230.
- [9] A. Varshneya, *Fundamentals of inorganic glasses*. Elsevier, 2013.
- [10] *Fundamentals of Inorganic Glasses*. Elsevier, 1994.
- [11] J. E. Shelby, "Introduction to Glass Science and Technology," *R. Soc. Chem. 2nd Ed*, 2005. [Online]. Available: https://books.google.ch/books/about/Introduction_to_Glass_Science_and_Techno.html?id=s-kCEAAAQBAJ&redir_esc=y. [Accessed: 03-May-2021].
- [12] T. C. Powers and H. H. Steinour, "An Interpretation of Some Published Researches on the Alkali-Aggregate Reaction Part 1-The Chemical Reactions and Mechanism of Expansion," *ACI J. Proc.*, vol. 51, no. 2, pp. 497–516, Feb. 1955, doi: 10.14359/11691.
- [13] R. K. Iler, "The Chemistry of Silica: Solubility, Polymerization, Colloid and Surface Properties and Biochemistry of Silica," *Wiley, New York*, 1979. [Online]. Available: <https://www.wiley.com/en-us/The+Chemistry+of+Silica%3A+Solubility%2C+Polymerization%2C+Colloid+and+Surface+Properties+and+Biochemistry+of+Silica-p-9780471024040>. [Accessed: 03-May-2021].
- [14] V. S. Molchanov and N. E. Prikhidko, "Corrosion of silicate glasses by alkaline solutions - Communication 1. Breakdown of quartz, quartz glass, and some laboratory glasses by sodium hydroxide and sodium carbonate solutions," *Bull. Acad. Sci. USSR Div. Chem. Sci.*, vol. 6, no. 10, pp.

1179–1184, Oct. 1957, doi: 10.1007/BF01167384.

[15] S. Sjöberg, “Silica in aqueous environments,” *J. Non. Cryst. Solids*, vol. 196, pp. 51–57, Mar. 1996, doi: 10.1016/0022-3093(95)00562-5.

[16] J. and I. O. (Eds. . Skalny, J. Gebauer, “M.D.A. Thomas, The role of calcium hydroxide in alkali recycling in concrete, in: Materials Science of Concrete Special Volume on Calcium Hydroxide in Concrete,” *American Ceramic Society, Westerville*, 2001. [Online]. Available: <https://www.wiley.com/en-us/Materials+Science+of+Concrete%3A+Calcium+Hydroxide+in+Concrete%2C+Special+Volume-p-9781574981285>. [Accessed: 07-May-2021].

[17] H. Maraghechi, “DEVELOPMENT AND ASSESSMENT OF ALKALI ACTIVATED RECYCLED GLASS-BASED CONCRETES FOR CIVIL INFRASTRUCTURE A Dissertation in Civil and Environmental Engineering,” 2014.

[18] F. Gaboriaud, A. Nonat, D. Chaumont, and A. Craievich, “Aggregation and gel formation in basic silico-calco-alkaline solutions studied: A SAXS, SANS, and ELS study,” *J. Phys. Chem. B*, vol. 103, no. 28, pp. 5775–5781, Jul. 1999, doi: 10.1021/jp990151s.

[19] L. S. Dent Glasser and N. Kataoka, “The chemistry of ‘alkali-aggregate’ reaction,” *Cem. Concr. Res.*, vol. 11, no. 1, pp. 1–9, Jan. 1981, doi: 10.1016/0008-8846(81)90003-X.

[20] Iler and KR, “The chemistry of silica,” *Solubility, Polym. colloid Surf. Prop. Biochem. silica*, 1979.

[21] F. Gaboriaud, D. Chaumont, A. Nonat, B. Hanquet, and A. Craievich, “Study of the Influence of Alkaline Ions (Li, Na and K) on the Structure of the Silicate Entities in Silico Alkaline Sol and on the Formation of the Silico-Calco-Alkaline Gel,” *J. Sol-Gel Sci. Technol.*, vol. 13, no. 1–3, pp. 353–358, Jan. 1998, doi: 10.1023/a:1008644405473.

[22] S. L. Brantley, A. F. White, and J. D. Kubicki, *Kinetics of water-rock interaction*. 2008.

[23] G. W. Scherer, “Structure and properties of gels,” *Cem. Concr. Res.*, vol. 29, no. 8, pp. 1149–1157, Aug. 1999, doi: 10.1016/S0008-8846(99)00003-4.

[24] X. Hou, R. J. Kirkpatrick, L. J. Struble, and P. J. M. Monteiro, “Structural Investigations of Alkali Silicate Gels,” *J. Am. Ceram. Soc.*, vol. 88, no. 4, pp. 943–949, Apr. 2005, doi: 10.1111/j.1551-2916.2005.00145.x.

[25] Z. Shi, A. Leemann, D. Rentsch, and B. Lothenbach, “Synthesis of alkali-silica reaction product structurally identical to that formed in field concrete,” *Mater. Des.*, vol. 190, p. 108562, May 2020, doi: 10.1016/j.matdes.2020.108562.

[26] S. Barbotin-Albinski, Z. Shi, E. Boehm-Courjault, A. Leemann, and K. Scrivener, “Characterization of synthetic ASR products by TEM and preliminary comparison with on-field early stage products,” in *First Book of Proceedings of the 16th international conference on Alkali-Aggregate Reaction in Concrete, (ICAAR2022)*, 2022, no. April 2021, pp. 85–96.

[27] A. M. Buckley and M. Greenblatt, “The sol-gel preparation of silica gels,” *J. Chem. Educ.*, vol. 71, no. 7, pp. 599–602, 1994, doi: 10.1021/ed071p599.

[28] L. L. Hench and D. E. Clark, “Physical chemistry of glass surfaces,” *J. Non. Cryst. Solids*, vol. 28, no. 1, pp. 83–105, Apr. 1978, doi: 10.1016/0022-3093(78)90077-7.

[29] A. Gholizadeh Vayghan, F. Rajabipour, and J. L. Rosenberger, “Composition-rheology relationships in alkali-silica reaction gels and the impact on the Gel’s deleterious behavior,” *Cem. Concr. Res.*, vol. 83, pp. 45–56, May 2016, doi: 10.1016/j.cemconres.2016.01.011.

-
- [30] T. Ichikawa and M. Miura, "Modified model of alkali-silica reaction," *Cem. Concr. Res.*, vol. 37, no. 9, pp. 1291–1297, Sep. 2007, doi: 10.1016/j.cemconres.2007.06.008.
- [31] M. Prezzi, P. Monteiro, G. S.-A. materials journal, and undefined 1997, "The alkali-silica reaction: Part I. Use of the double-layer theory to explain the behavior of reaction-product gels," *ecn.purdue.edu*.
- [32] F. Rodrigues, P. Monteiro, G. S.-C. and C. Research, and undefined 1999, "The alkali-silica reaction: The surface charge density of silica and its effect on expansive pressure," *Elsevier*.
- [33] M. A. Bérubé, J. Duchesne, J. F. Dorion, and M. Rivest, "Laboratory assessment of alkali contribution by aggregates to concrete and application to concrete structures affected by alkali-silica reactivity," *Cem. Concr. Res.*, vol. 32, no. 8, pp. 1215–1227, Aug. 2002, doi: 10.1016/S0008-8846(02)00766-4.
- [34] J. H. P. van Aardt and S. Visser, "Formation of hydrogarnets: Calcium hydroxide attack on clays and feldspars," *Cem. Concr. Res.*, vol. 7, no. 1, pp. 39–44, Jan. 1977, doi: 10.1016/0008-8846(77)90006-0.
- [35] S. Diamond, "Effects of Microsilica (Silica Fume) on Pore-Solution Chemistry of Cement Pastes," *J. Am. Ceram. Soc.*, vol. 66, no. 5, pp. C-82–C-84, May 1983, doi: 10.1111/j.1151-2916.1983.tb10060.x.
- [36] S. Chatterji, "The role of $\text{Ca}(\text{OH})_2$ in the breakdown of Portland cement concrete due to alkali-silica reaction," *Cem. Concr. Res.*, vol. 9, no. 2, pp. 185–188, Mar. 1979, doi: 10.1016/0008-8846(79)90024-3.
- [37] D. W. Hobbs, "8 Minimizing the risk of expansion in new construction," in *Alkali-silica reaction in concrete*, Thomas Telford Publishing, 1988, pp. 155–174.
- [38] DIAMOND and S., "ASR-Another Look at Mechanisms," *Proc. 8th Intl. Conf. Alkali-Aggregate React.*, pp. 115–119, 1989.
- [39] R. F. Bleszynski and M. D. A. Thomas, "Microstructural studies of alkali-silica reaction in fly ash concrete immersed in alkaline solutions," *Adv. Cem. Based Mater.*, vol. 7, no. 2, pp. 66–78, Mar. 1998, doi: 10.1016/S1065-7355(97)00030-8.
- [40] J. Duchesne and M. A. Bérubé, "The effectiveness of supplementary cementing materials in suppressing expansion due to ASR: Another look at the reaction mechanisms part 1: Concrete expansion and portlandite depletion," *Cem. Concr. Res.*, vol. 24, no. 1, pp. 73–82, Jan. 1994, doi: 10.1016/0008-8846(94)90084-1.
- [41] S. Chatterji, N. Thaulow, and A. D. Jensen, "Studies of alkali-silica reaction. part 5. Verification of a newly proposed reaction mechanism," *Cem. Concr. Res.*, vol. 19, no. 2, pp. 177–183, Mar. 1989, doi: 10.1016/0008-8846(89)90081-1.
- [42] A. Sellier, E. Bourdarot, S. Multon, M. Cyr, and E. Grimal, "Combination of structural monitoring and laboratory tests for assessment of alkali-aggregate reaction swelling: Application to gate structure dam," *ACI Materials Journal*, vol. 106, no. 3, pp. 281–290, 01-May-2009, doi: 10.14359/56553.
- [43] A. Leemann, G. Le Saout, F. Winnefeld, D. Rentsch, and B. Lothenbach, "Alkali-Silica Reaction: the Influence of Calcium on Silica Dissolution and the Formation of Reaction Products," *J. Am. Ceram. Soc.*, vol. 94, no. 4, pp. 1243–1249, Apr. 2011, doi: 10.1111/j.1551-2916.2010.04202.x.
- [44] S. Rahimi-Aghdam, Z. P. Bazant, and F. C. Caner, "Diffusion-Controlled and Creep-Mitigated ASR Damage via Microplane Model. II: Material Degradation, Drying, and Verification," *J. Eng.*
-

Mech., vol. 143, no. 2, p. 04016109, Feb. 2017, doi: 10.1061/(ASCE)EM.1943-7889.0001185.

[45] Z. P. Bažant and S. Rahimi-Aghdam, “Diffusion-Controlled and Creep-Mitigated ASR Damage via Microplane Model. I: Mass Concrete,” *J. Eng. Mech.*, vol. 143, no. 2, p. 04016108, Feb. 2017, doi: 10.1061/(ASCE)EM.1943-7889.0001186.

[46] C. Larive, A. Laplaud, and O. Coussy, *The Role of Water in Alkali-Silica Reaction*. Quebec: 11th ICAAR, International Conference on Alkali Aggregate Reactions, 2000.

[47] M. A. Bérubé and B. Fournier, “Canadian experience with testing for alkali-aggregate reactivity in concrete,” *Cem. Concr. Compos.*, vol. 15, no. 1–2, pp. 27–47, Jan. 1993, doi: 10.1016/0958-9465(93)90037-a.

[48] S. Multon, “Evaluation expérimentale et théorique des effets mécaniques de l’alcali-réaction sur des structures modèles,” 2003.

[49] “theses.fr - Stéphane Multon, Experimental and theoretical evaluation of the mechanical effects of the alkali-reaction on model structures.” [Online]. Available: <http://www.theses.fr/2003MARN0181>. [Accessed: 02-May-2021].

[50] L. De Ceukelaire, “The determination of the most common crystalline alkali-silica reaction product,” *Mater. Struct.*, vol. 24, no. 3, pp. 169–171, May 1991, doi: 10.1007/BF02472981.

[51] K. Peterson, D. Gress, T. Van Dam, and L. Sutter, “Crystallized alkali-silica gel in concrete from the late 1890s,” *Cem. Concr. Res.*, vol. 36, no. 8, pp. 1523–1532, Aug. 2006, doi: 10.1016/j.cemconres.2006.05.017.

[52] A. Leemann and P. Lura, “E-modulus of the alkali-silica-reaction product determined by micro-indentation,” *Constr. Build. Mater.*, vol. 44, pp. 221–227, 2013, doi: 10.1016/j.conbuildmat.2013.03.018.

[53] A. Leemann and P. Lura, “E-modulus of the alkali-silica-reaction product determined by micro-indentation,” *Constr. Build. Mater.*, vol. 44, pp. 221–227, Jul. 2013, doi: 10.1016/j.conbuildmat.2013.03.018.

[54] A. Leemann, “Raman microscopy of alkali-silica reaction (ASR) products formed in concrete,” *Cem. Concr. Res.*, vol. 102, pp. 41–47, Dec. 2017, doi: 10.1016/j.cemconres.2017.08.014.

[55] Z. Shi and B. Lothenbach, “The combined effect of potassium, sodium and calcium on the formation of alkali-silica reaction products,” *Cem. Concr. Res.*, vol. 127, p. 105914, Jan. 2020, doi: 10.1016/j.cemconres.2019.105914.

[56] G. Geng *et al.*, “Atomistic structure of alkali-silica reaction products refined from X-ray diffraction and micro X-ray absorption data,” *Cem. Concr. Res.*, vol. 129, p. 105958, Mar. 2020, doi: 10.1016/j.cemconres.2019.105958.

[57] G. Geng *et al.*, “An in-situ 3D micro-XRD investigation of water uptake by alkali-silica-reaction (ASR) product,” *Cem. Concr. Res.*, vol. 141, p. 106331, Mar. 2021, doi: 10.1016/j.cemconres.2020.106331.

[58] Z. Shi, G. Geng, A. Leemann, and B. Lothenbach, “Synthesis, characterization, and water uptake property of alkali-silica reaction products,” *Cem. Concr. Res.*, vol. 121, pp. 58–71, Jul. 2019, doi: 10.1016/j.cemconres.2019.04.009.

[59] A. Leemann, Z. Shi, M. Wyrzykowski, and F. Winnefeld, “Moisture stability of crystalline alkali-silica reaction products formed in concrete exposed to natural environment,” *Mater. Des.*, vol. 195, p. 109066, Oct. 2020, doi: 10.1016/j.matdes.2020.109066.

[60] E. Boehm-Courjault, S. Barbotin, A. Leemann, and K. Scrivener, “Microstructure,

crystallinity and composition of alkali-silica reaction products in concrete determined by transmission electron microscopy,” *Cem. Concr. Res.*, vol. 130, p. 105988, Apr. 2020, doi:

10.1016/j.cemconres.2020.105988.

[61] A. Leemann and B. Münch, “The addition of caesium to concrete with alkali-silica reaction: Implications on product identification and recognition of the reaction sequence,” *Cem. Concr. Res.*, vol. 120, pp. 27–35, Jun. 2019, doi: 10.1016/j.cemconres.2019.03.016.

[62] “ASTM C294-12,” *Standard Descriptive Nomenclature for Constituents of Concrete Aggregates*, 2017. [Online]. Available: https://compass.astm.org/EDIT/html_annot.cgi?C294+19. [Accessed: 03-May-2021].

[63] R. B. Figueira *et al.*, “Alkali-silica reaction in concrete: Mechanisms, mitigation and test methods,” *Construction and Building Materials*, vol. 222. Elsevier Ltd, pp. 903–931, 20-Oct-2019, doi: 10.1016/j.conbuildmat.2019.07.230.

[64] “ASTM C1260 - 14 Standard Test Method for Potential Alkali Reactivity of Aggregates (Mortar-Bar Method),” *American Society for Testing and Materials, West Conshohocken, Pennsylvania*, 2014. [Online]. Available: <https://compass.astm.org/Standards/HISTORICAL/C1260-14.htm>. [Accessed: 03-May-2021].

[65] “ASTM C1293 - 20a Standard Test Method for Determination of Length Change of Concrete Due to Alkali-Silica Reaction,” *American Society for Testing and Materials, West Conshohocken, Pennsylvania*, 2008. [Online]. Available: <https://www.astm.org/DATABASE.CART/HISTORICAL/C1293-08B.htm>. [Accessed: 03-May-2021].

[66] F. Rajabipour, H. Maraghechi, and G. Fischer, “Investigating the Alkali-Silica Reaction of Recycled Glass Aggregates in Concrete Materials,” *J. Mater. Civ. Eng.*, vol. 22, no. 12, pp. 1201–1208, Dec. 2010, doi: 10.1061/(ASCE)MT.1943-5533.0000126.

[67] H. Maraghechi, S. M. H. Shafaatian, G. Fischer, and F. Rajabipour, “The role of residual cracks on alkali silica reactivity of recycled glass aggregates,” *Cem. Concr. Compos.*, vol. 34, no. 1, pp. 41–47, Jan. 2012, doi: 10.1016/j.cemconcomp.2011.07.004.

[68] M. A. T. M. Broekmans, “Structural properties of quartz and their potential role for ASR,” in *Materials Characterization*, 2004, vol. 53, no. 2–4, pp. 129–140, doi: 10.1016/j.matchar.2004.08.010.

[69] Š. Šachlová, A. Kuchařová, Z. Pertold, R. Příkryl, and M. Fridrichová, “Quantitative assessment of alkali silica reaction potential of quartz-rich aggregates: comparison of chemical test and accelerated mortar bar test improved by SEM-PIA,” *Bull. Eng. Geol. Environ.*, vol. 76, no. 1, pp. 133–144, Feb. 2017, doi: 10.1007/s10064-015-0812-z.

[70] A. B. Poole, “Introduction to alkali-aggregate reaction in concrete,” in *The Alkali-Silica Reaction in Concrete*, CRC Press, 1992, pp. 1–29.

[71] T. E. Stanton, “Expansion of Concrete through Reaction between Cement and Aggregate,” *Trans. Am. Soc. Civ. Eng.*, vol. 107, no. 1, pp. 54–84, Jan. 1942, doi: 10.1061/taceat.0005540.

[72] J. Ingham, *Geomaterials under the microscope*. Manson, 2013.

[73] B. J. Wigum and W. J. French, “Sequential examination of slowly expanding alkali-reactive aggregates in accelerated mortar bar testing,” *Mag. Concr. Res.*, vol. 48, no. 177, pp. 281–292, Dec. 1996, doi: 10.1680/mac.1996.48.177.281.

[74] J. M. Hunt, “Petroleum geochemistry and geology,” p. 743, 1996.

[75] L. Lonergan, “J. M. Hunt 1995. Petroleum Geochemistry and Geology, 2nd ed. xx + 743 pp.

New York: W. H. Freeman. Price £27.95 (hardcovers). ISBN 0 7167 2441 3.,” *Geol. Mag.*, vol. 133, no. 4, pp. 505–505, Jul. 1996, doi: 10.1017/s0016756800007755.

[76] G. E. Blight and M. G. Alexander, *Alkali-Aggregate Reaction and Structural Damage to Concrete*. CRC Press, 2011.

[77] M. Ben Haha, “mechanical effects of alkali silica reaction in concrete studied by sem-image analysis,” EPFL, 2006.

[78] A. Leemann, M. G.-R. of S. F. O. of E. P. SI, and undefined 2013, “Diagnosis of alkali-aggregate reaction in dams,” *Citeseer*, 2013.

[79] F. Amberg, P. Droz, R. Leroy, J. Maier, B. Otto, and R. Bremen, “Concrete Swelling of Dams in Switzerland,” 2017.

[80] M. Berra, T. Mangialardi, and A. E. Paolini, “Alkali-silica reactivity criteria for concrete aggregates,” *Mater. Struct.*, vol. 38, no. 3, pp. 373–380, Apr. 2005, doi: 10.1007/bf02479304.

[81] R. Johnson and M. H. Shehata, “The efficacy of accelerated test methods to evaluate Alkali Silica Reactivity of Recycled Concrete Aggregates,” *Constr. Build. Mater.*, vol. 112, pp. 518–528, Jun. 2016, doi: 10.1016/j.conbuildmat.2016.02.155.

[82] P. Nixon and I. Sims, “Testing aggregates for alkali-reactivity: Report of RILEM TC-106,” *Mater. Struct. Constr.*, vol. 29, no. 6, pp. 323–334, 1996, doi: 10.1007/BF02486340.

[83] V. Sirivivatnanon, J. Mohammadi, and W. South, “Reliability of new Australian test methods in predicting alkali silica reaction of field concrete,” *Constr. Build. Mater.*, vol. 126, pp. 868–874, Nov. 2016, doi: 10.1016/j.conbuildmat.2016.09.055.

[84] S. Chatterji, “Chemistry of alkali-silica reaction and testing of aggregates,” *Cem. Concr. Compos.*, vol. 27, no. 7–8, pp. 788–795, Aug. 2005, doi: 10.1016/j.cemconcomp.2005.03.005.

[85] L. F. M. Sanchez, B. Fournier, M. Jolin, and J. Bastien, “Evaluation of the Stiffness Damage Test (SDT) as a tool for assessing damage in concrete due to alkali-silica reaction (ASR): Input parameters and variability of the test responses,” *Constr. Build. Mater.*, vol. 77, pp. 20–32, Feb. 2015, doi: 10.1016/j.conbuildmat.2014.11.071.

[86] L. F. M. Sanchez, B. Fournier, M. Jolin, J. Bastien, and D. Mitchell, “Practical use of the Stiffness Damage Test (SDT) for assessing damage in concrete infrastructure affected by alkali-silica reaction,” *Constr. Build. Mater.*, vol. 125, pp. 1178–1188, Oct. 2016, doi: 10.1016/j.conbuildmat.2016.08.101.

[87] J. H. Ideker, B. L. East, K. J. Folliard, M. D. A. Thomas, and B. Fournier, “The current state of the accelerated concrete prism test,” *Cem. Concr. Res.*, vol. 40, no. 4, pp. 550–555, Apr. 2010, doi: 10.1016/j.cemconres.2009.08.030.

[88] S. Beauchemin, B. Fournier, and J. Duchesne, “Evaluation of the concrete prisms test method for assessing the potential alkali-aggregate reactivity of recycled concrete aggregates,” *Cem. Concr. Res.*, vol. 104, pp. 25–36, Feb. 2018, doi: 10.1016/j.cemconres.2017.10.008.

[89] O. behalf of the membership of R. T. 219-ACS, P. J. Nixon, and I. Sims, “RILEM recommended test method: AAR-2—Detection of potential alkali-reactivity—Accelerated mortar-bar test method for aggregates,” in *RILEM State-of-the-Art Reports*, vol. 17, Springer Netherlands, 2016, pp. 61–77.

[90] P. J. Nixon and I. Sims, *RILEM recommendations for the prevention of damage by alkali-aggregate reactions in new concrete structures: State-of-the-Art report of the RILEM technical committee 219-ACS*, vol. 17. Springer Netherlands, 2015.

-
- [91] I. Fernandes *et al.*, “Assessment of Concrete Aggregate for ASR Potential by Petrography. The Work Developed by RILEM TC-ACS (2007–2013),” *Eng. Geol. Soc. Territ. - Vol. 5 Urban Geol. Sustain. Plan. Landsc. Exploit.*, pp. 37–40, Jan. 2015, doi: 10.1007/978-3-319-09048-1_6.
- [92] A. Leemann, Z. Shi, and J. Lindgård, “Characterization of amorphous and crystalline ASR products formed in concrete aggregates,” *Cem. Concr. Res.*, vol. 137, p. 106190, Nov. 2020, doi: 10.1016/j.cemconres.2020.106190.
- [93] N. Thaulow, U. H. Jakobsen, and B. Clark, “Composition of alkali silica gel and ettringite in concrete railroad ties: Sem-edx and x-ray diffraction analyses,” *Cem. Concr. Res.*, vol. 26, no. 2, pp. 309–318, 1996, doi: 10.1016/0008-8846(95)00219-7.
- [94] I. Fernandes, “Composition of alkali-silica reaction products at different locations within concrete structures,” *Mater. Charact.*, vol. 60, no. 7, pp. 655–668, Jul. 2009, doi: 10.1016/j.matchar.2009.01.011.
- [95] P. Virmani, “Alkali-Silica Reaction Mechanisms and Detections: An Advanced Understanding,” *FHWA-HRT-14-079. United States. Fed. Highw. Adm.*, 2014.
- [96] O. Onuaguluchi and N. Banthia, “Alkali–Silica Reaction Resistance of Cementitious Material Containing CaCl₂-Blended Acrylic Polymer Emulsion,” *J. Mater. Civ. Eng.*, vol. 32, no. 3, p. 04019378, Mar. 2020, doi: 10.1061/(ASCE)MT.1943-5533.0003049.
- [97] I. Sims and A. B. Poole, *Alkali-aggregate reaction in concrete: A world review*. Taylor and Francis, 2017.
- [98] Institution of Structural Engineers (Great Britain) and Structural Engineers Trading Organisation., “Structural effects of alkali-silica reaction : technical guidance on the appraisal of existing structures.,” p. 45, 1992.
- [99] “ASTM C78- Standard test method for flexural strength of concrete.,” *American society for testing and materials*, 2002. .
- [100] “ASTM C293 / C293M - 16 Standard Test Method for Flexural Strength of Concrete (Using Simple Beam With Center-Point Loading).” [Online]. Available: <https://www.astm.org/Standards/C293>. [Accessed: 18-Jul-2021].
- [101] P. Mehta and P. Monteiro, *Concrete: microstructure, properties, and materials*. McGraw-Hill Education, 2014.
- [102] “Bridge Maintenance, Safety, Management, Life-Cycle Sustainability and Innovations,” *Bridg. Maintenance, Safety, Manag. Life-Cycle Sustain. Innov.*, Apr. 2021, doi: 10.1201/9780429279119.
- [103] W. Wallau, S. Pirskawetz, K. Volland, and B. Meng, “Continuous expansion measurement in accelerated concrete prism testing for verifying ASR-expansion models,” *Mater. Struct. Constr.*, vol. 51, no. 3, pp. 1–15, Jun. 2018, doi: 10.1617/s11527-018-1205-0.
- [104] Y. Kawabata, K. Yamada, Y. Sagawa, and S. Ogawa, “Alkali-Wrapped Concrete Prism Test (AW-CPT) – New Testing Protocol Toward a Performance Test against Alkali-Silica Reaction–,” *J. Adv. Concr. Technol.*, vol. 16, no. 9, pp. 441–460, Sep. 2018, doi: 10.3151/jact.16.441.
- [105] Y. Kawabata, C. Dunant, K. Yamada, and K. Scrivener, “Impact of temperature on expansive behavior of concrete with a highly reactive andesite due to the alkali–silica reaction,” *Cem. Concr. Res.*, vol. 125, p. 105888, Nov. 2019, doi: 10.1016/J.CEMCONRES.2019.105888.
- [106] J. Banhart, “Advanced tomographic methods in materials research and engineering,” *Oxford Univ. Press*, vol. 9780199213245, pp. 1–488, May 2008, doi:
-

10.1093/ACPROF:OSO/9780199213245.001.0001.

[107] E. Maire, “X-ray tomography applied to the characterization of highly porous materials,” *Annu. Rev. Mater. Res.*, vol. 42, pp. 163–178, Aug. 2012, doi: 10.1146/ANNUREV-MATSCI-070511-155106.

[108] E. Maire and P. J. Withers, “Quantitative X-ray tomography,” <https://doi.org/10.1179/1743280413Y.0000000023>, vol. 59, no. 1, pp. 1–43, Jan. 2014, doi: 10.1179/1743280413Y.0000000023.

[109] P. J. Withers *et al.*, “X-ray computed tomography,” *Nat. Rev. Methods Prim.* 2021 11, vol. 1, no. 1, pp. 1–21, Feb. 2021, doi: 10.1038/s43586-021-00015-4.

[110] S. Brisard, M. Serdar, and P. J. M. Monteiro, “Multiscale X-ray tomography of cementitious materials: A review,” *Cement and Concrete Research*, vol. 128. Elsevier Ltd, p. 105824, 01-Feb-2020, doi: 10.1016/j.cemconres.2019.105824.

[111] V. Cnudde and M. N. Boone, “High-resolution X-ray computed tomography in geosciences: A review of the current technology and applications,” *Earth-Science Rev.*, vol. 123, pp. 1–17, Aug. 2013, doi: 10.1016/J.EARSCIREV.2013.04.003.

[112] D. Wildenschild and A. P. Sheppard, “X-ray imaging and analysis techniques for quantifying pore-scale structure and processes in subsurface porous medium systems,” *Adv. Water Resour.*, vol. 51, pp. 217–246, Jan. 2013, doi: 10.1016/J.ADVWATRES.2012.07.018.

[113] W. A. Kalender, “X-ray computed tomography,” *Physics in Medicine and Biology*, vol. 51, no. 13. Phys Med Biol, 07-Jul-2006, doi: 10.1088/0031-9155/51/13/R03.

[114] T. M. Buzug, “Computed Tomography,” in *Springer Handbook of Medical Technology*, Berlin, Heidelberg: Springer Berlin Heidelberg, 2011, pp. 311–342.

[115] D. Jordan, “Handbook of X-ray Imaging: Physics and Technology. 1st Edition. Paolo Russo, Editor. Series in Medical Physics and Biomedical Engineering – CRC Press Taylor & Francis Group, Boca Raton, FL 2018. Hardcover: 1393pp. Price: \$416.00. ISBN: 9781498741521.” *Med. Phys.*, vol. 47, no. 6, pp. 2577–2578, Jun. 2020, doi: 10.1002/mp.14041.

[116] A. Sarapata, M. Ruiz-Yaniz, I. Zanette, A. Rack, F. Pfeiffer, and J. Herzen, “Multi-contrast 3D X-ray imaging of porous and composite materials,” *Appl. Phys. Lett.*, vol. 106, no. 15, p. 154102, Apr. 2015, doi: 10.1063/1.4918617.

[117] V. Revol *et al.*, “Sub-pixel porosity revealed by x-ray scatter dark field imaging,” *J. Appl. Phys.*, vol. 110, no. 4, p. 044912, Aug. 2011, doi: 10.1063/1.3624592.

[118] F. Yang *et al.*, “Dark-field X-ray imaging of unsaturated water transport in porous materials,” *Appl. Phys. Lett.*, vol. 105, no. 15, p. 154105, Oct. 2014, doi: 10.1063/1.4898783.

[119] F. Prade, M. Chabior, F. Malm, C. U. Grosse, and F. Pfeiffer, “Observing the setting and hardening of cementitious materials by X-ray dark-field radiography,” *Cem. Concr. Res.*, vol. 74, pp. 19–25, Aug. 2015, doi: 10.1016/J.CEMCONRES.2015.04.003.

[120] F. YANG *et al.*, “Visualization of water drying in porous materials by X-ray phase contrast imaging,” *J. Microsc.*, vol. 261, no. 1, pp. 88–104, Jan. 2016, doi: 10.1111/JMI.12319.

[121] F. Prade, K. Fischer, D. Heinz, P. Meyer, J. Mohr, and F. Pfeiffer, “Time resolved X-ray Dark-Field Tomography Revealing Water Transport in a Fresh Cement Sample,” *Sci. Reports* 2016 61, vol. 6, no. 1, pp. 1–7, Jun. 2016, doi: 10.1038/srep29108.

[122] F. Yang *et al.*, “Advancing the visualization of pure water transport in porous materials by fast, talbot interferometry-based multi-contrast x-ray micro-tomography,” in *Developments in X-Ray*

Tomography X, 2016, vol. 9967, p. 99670L, doi: 10.1117/12.2236221.

[123] F. Yang *et al.*, “X-ray dark-field contrast imaging of water transport during hydration and drying of early-age cement-based materials,” *Mater. Charact.*, vol. 142, pp. 560–576, Aug. 2018, doi: 10.1016/J.MATCHAR.2018.06.021.

[124] P. Trtik, A. Diaz, M. Guizar-Sicairos, A. Menzel, and O. Bunk, “Density mapping of hardened cement paste using ptychographic X-ray computed tomography,” *Cem. Concr. Compos.*, vol. 36, no. 1, pp. 71–77, Feb. 2013, doi: 10.1016/J.CEMCONCOMP.2012.06.001.

[125] J. C. da Silva *et al.*, “Mass Density and Water Content of Saturated Never-Dried Calcium Silicate Hydrates,” *Langmuir*, vol. 31, no. 13, pp. 3779–3783, Apr. 2015, doi: 10.1021/LA504478J.

[126] J. T. Bushberg, J. A. Seibert, E. M. Leidholdt, J. M. Boone, and E. J. Goldschmidt, “The Essential Physics of Medical Imaging,” *Med. Phys.*, vol. 30, no. 7, pp. 1936–1936, Jul. 2003, doi: 10.1118/1.1585033.

[127] E. Russo, Paolo, *Handbook of X-ray Imaging: Physics and Technology*. 2017.

[128] M. Born and E. Wolf, *Principles of optics: electromagnetic theory of propagation, interference and diffraction of light*. Elsevier, 2013.

[129] M. A. Ali, R. Umer, K. A. Khan, and W. J. Cantwell, “Application of X-ray computed tomography for the virtual permeability prediction of fiber reinforcements for liquid composite molding processes: A review,” *Composites Science and Technology*, vol. 184. Elsevier Ltd, p. 107828, 10-Nov-2019, doi: 10.1016/j.compscitech.2019.107828.

[130] B. Dowd, G. Campbell, ... R. M.-D. in X., and undefined 1999, “Developments in synchrotron x-ray computed microtomography at the National Synchrotron Light Source,” *spiedigitallibrary.org*, vol. 3772, no. 22, pp. 224–236, Sep. 1999, doi: 10.1117/12.363725.

[131] F. Marone, M. S.-J. of synchrotron radiation, and undefined 2012, “Regridding reconstruction algorithm for real-time tomographic imaging,” *scripts.iucr.org*, vol. 19, pp. 1029–1037, 2012, doi: 10.1107/S0909049512032864.

[132] P. Grangeat, “Mathematical framework of cone beam 3D reconstruction via the first derivative of the radon transform,” *Math. methods Tomogr. Springer, Berlin, Heidelb.*, pp. 66–97, 1991, doi: 10.1007/BFB0084509.

[133] A. Katsevich, “A general scheme for constructing inversion algorithms for cone beam CT,” *Int. J. Math. Math. Sci.*, vol. 2003, no. 21, pp. 1305–1321, 2003, doi: 10.1155/S0161171203209315.

[134] J. D. Pack, F. Noo, and R. Clackdoyle, “Cone-beam reconstruction using the backprojection of locally filtered projections,” *IEEE Trans. Med. Imaging*, vol. 24, no. 1, pp. 70–85, Jan. 2005, doi: 10.1109/TMI.2004.837794.

[135] E. Shaw, Chris C., “Cone Beam Computed Tomography,” *Taylor & Francis*, 2014. [Online]. Available:

[https://books.google.ch/books?hl=en&lr=&id=pqSNAgAAQBAJ&oi=fnd&pg=PP1&dq=Cone+Beam+Computed+Tomography&ots=tx7p5PjSgl&sig=kQB-](https://books.google.ch/books?hl=en&lr=&id=pqSNAgAAQBAJ&oi=fnd&pg=PP1&dq=Cone+Beam+Computed+Tomography&ots=tx7p5PjSgl&sig=kQB-A57wRsUAOdnbyrOg7COWPts#v=onepage&q=Cone+Beam+Computed+Tomography&f=false)

[A57wRsUAOdnbyrOg7COWPts#v=onepage&q=Cone Beam Computed Tomography&f=false](https://books.google.ch/books?hl=en&lr=&id=pqSNAgAAQBAJ&oi=fnd&pg=PP1&dq=Cone+Beam+Computed+Tomography&ots=tx7p5PjSgl&sig=kQB-A57wRsUAOdnbyrOg7COWPts#v=onepage&q=Cone+Beam+Computed+Tomography&f=false).

[Accessed: 03-May-2021].

[136] M. Beister, D. Kolditz, and W. Kalender, “Iterative reconstruction methods in X-ray CT,” *Phys. medica* 28, no. 2, pp. 94–108, 2012.

[137] M. Feser *et al.*, “Sub-micron resolution CT for failure analysis and process development,” *Meas. Sci. Technol.* 19(9), p. 094001, 2008, doi: 10.1088/0957-0233/19/9/094001.

-
- [138] T. M. Buzug, *Computed tomography : from photon statistics to modern cone-beam CT*. Section 9.6, Springer-Verlag, Berlin, 2008.
- [139] R. A. Brooks and G. Di Chiro, "Beam hardening in X-ray reconstructive tomography," *Phys. Med. Biol.*, vol. 21, no. 3, p. 390, May 1976, doi: 10.1088/0031-9155/21/3/004.
- [140] H. GT, "Correction for beam hardening in computed tomography," *Phys. Med. Biol.*, vol. 24, no. 1, pp. 81–106, 1979, doi: 10.1088/0031-9155/24/1/008.
- [141] C. H. Yan, R. T. Whalen, G. S. Beaupré, S. Y. Yen, and S. Napel, "Reconstruction algorithm for polychromatic CT imaging: application to beam hardening correction," *IEEE Trans. Med. Imaging*, vol. 19, no. 1, pp. 1–11, 2000, doi: 10.1109/42.832955.
- [142] D. D. Cody, D. M. Stevens, and L. E. Ginsberg, "Multi-detector row CT artifacts that mimic disease," *Radiology*, vol. 236, no. 3, pp. 756–761, Sep. 2005, doi: 10.1148/radiol.2363041421.
- [143] G. H. Glover and N. J. Pelc, "Nonlinear partial volume artifacts in x-ray computed tomography," *Med. Phys.*, vol. 7, no. 3, pp. 238–248, May 1980, doi: 10.1118/1.594678.
- [144] B. De Mm, J. Nuyts, P. Dupont, G. Marchai, and P. Suetttis, "Metal streak artifacts in x-ray computed tomography: A simulation study," *IEEE Trans. Nucl. Sci.*, vol. 46, no. 3 PART 2, pp. 691–696, 1999, doi: 10.1109/23.775600.
- [145] J. H. Siewerdsen and D. A. Jaffray, "A ghost story: Spatio-temporal response characteristics of an indirect-detection flat-panel imager," *Med. Phys.*, vol. 26, no. 8, pp. 1624–1641, Aug. 1999, doi: 10.1118/1.598657.
- [146] J. F. Barrett and N. Keat, "Artifacts in CT: Recognition and avoidance," *Radiographics*, vol. 24, no. 6. Radiological Society of North America Inc., 01-Nov-2004, doi: 10.1148/rg.246045065.
- [147] B. Münch, F. Marone, M. Stampanoni, and P. Trtik, "Stripe and ring artifact removal with combined wavelet — Fourier filtering," *Opt. Express*, Vol. 17, Issue 10, pp. 8567-8591, vol. 17, no. 10, pp. 8567–8591, May 2009, doi: 10.1364/OE.17.008567.
- [148] J. H. Siewerdsen and D. A. Jaffray, "Cone-beam computed tomography with a flat-panel imager: Magnitude and effects of x-ray scatter," *Med. Phys.*, vol. 28, no. 2, pp. 220–231, Feb. 2001, doi: 10.1118/1.1339879.
- [149] G. Jarry, S. A. Graham, D. J. Moseley, D. J. Jaffray, J. H. Siewerdsen, and F. Verhaegen, "Characterization of scattered radiation in kV CBCT images using Monte Carlo simulations," *Med. Phys.*, vol. 33, no. 11, pp. 4320–4329, Oct. 2006, doi: 10.1118/1.2358324.
- [150] W. Zbijewski and F. J. Beekman, "Efficient Monte Carlo based scatter artifact reduction in cone-beam micro-CT," *IEEE Trans. Med. Imaging*, vol. 25, no. 7, pp. 817–827, 2006, doi: 10.1109/TMI.2006.872328.
- [151] W. A. Kalender and Y. Kyriakou, "Flat-detector computed tomography (FD-CT)," *European Radiology*, vol. 17, no. 11. Springer Verlag, pp. 2767–2779, 23-Jun-2007, doi: 10.1007/s00330-007-0651-9.
- [152] S.-B. Y. and A. D. Watson*, "Metal-Based X-ray Contrast Media," *Chem. Rev.*, vol. 99, no. 9, pp. 2353–2377, Sep. 1999, doi: 10.1021/CR980441P.
- [153] H. E. Martz, C. M. Logan, D. J. Schneberk, and P. J. Shull, *X-Ray Imaging: Fundamentals, Industrial Techniques and Applications*. 2016.
- [154] D. Van Loo *et al.*, "Contrast agents for soil investigation with X-ray computed tomography," *Geoderma*, vol. 213, pp. 485–491, Jan. 2014, doi: 10.1016/J.GEODERMA.2013.08.036.
- [155] Y. Nakashima, "The use of sodium polytungstate as an X-ray contrast agent to reduce the
-

- beam hardening artifact in hydrological laboratory experiments,” *J. Hydrol. Hydromechanics*, vol. 61, no. 4, pp. 347–351, Dec. 2013, doi: 10.2478/JOHH-2013-0043.
- [156] M. M. Koç, N. Aslan, A. P. Kao, and A. H. Barber, “Evaluation of X-ray tomography contrast agents: A review of production, protocols, and biological applications,” *Microsc. Res. Tech.*, vol. 82, no. 6, pp. 812–848, Jun. 2019, doi: 10.1002/jemt.23225.
- [157] S. D. O’Connor and R. M. Summers, “Revisiting Oral Barium Sulfate Contrast Agents,” *Acad. Radiol.*, vol. 14, no. 1, pp. 72–80, Jan. 2007, doi: 10.1016/J.ACRA.2006.10.002.
- [158] P. Diós *et al.*, “Influence of barium sulfate X-ray imaging contrast material on properties of floating drug delivery tablets,” *Eur. J. Pharm. Sci.*, vol. 95, pp. 46–53, Dec. 2016, doi: 10.1016/j.ejps.2016.09.034.
- [159] P. Carrara *et al.*, “Improved mesoscale segmentation of concrete from 3D X-ray images using contrast enhancers,” *Cem. Concr. Compos.*, vol. 93, pp. 30–42, Oct. 2018, doi: 10.1016/j.cemconcomp.2018.06.014.
- [160] P. ; Carrara *et al.*, “Towards multiscale modeling of the interaction between transport and fracture in concrete,” *RILEM Tech. Lett.*, vol. 1, pp. 94–101, Dec. 2016, doi: 10.3929/ethz-b-000418713.
- [161] S. Klein and M. Staring, “Elastix, The Manual Elastix 4.9.0,” 2018. [Online]. Available: <https://usermanual.wiki/Document/elastix490manual.1389615963/html>. [Accessed: 03-May-2021].
- [162] B. Zitová and J. Flusser, “Image registration methods: A survey,” *Image Vis. Comput.*, vol. 21, no. 11, pp. 977–1000, Oct. 2003, doi: 10.1016/S0262-8856(03)00137-9.
- [163] J. B. A. Maintz and M. A. Viergever, “A survey of medical image registration,” *Med. Image Anal.*, vol. 2, no. 1, pp. 1–36, Mar. 1998, doi: 10.1016/S1361-8415(01)80026-8.
- [164] H. Lester and S. R. Arridge, “A survey of hierarchical non-linear medical image registration,” *Pattern Recognit.*, vol. 32, no. 1, pp. 129–149, Jan. 1999, doi: 10.1016/S0031-3203(98)00095-8.
- [165] E. Hajnal, Joseph V., and Derek LG Hill, “Medical Image Registration,” *CRC press*, 2001. [Online]. Available: https://books.google.ch/books?hl=en&lr=&id=2dtQNsk-qBQC&oi=fnd&pg=PP1&dq=Hajnal+et+al.+%5B2001%5D&ots=faAmJoEpe0&sig=ar1EDaf9zxU3NY81rzPnwvkirtw&redir_esc=y#v=onepage&q=Hajnal+et+al.+%5B2001%5D&f=false. [Accessed: 03-May-2021].
- [166] R. Sakamoto *et al.*, “Temporal subtraction of serial CT images with large deformation diffeomorphic metric mapping in the identification of bone metastases,” *Radiology*, vol. 285, no. 2, pp. 629–639, Nov. 2017, doi: 10.1148/radiol.2017161942.
- [167] E. Haber and J. Modersitzki, “Numerical methods for volume preserving image registration,” *Inverse Probl.*, vol. 20, no. 5, pp. 1621–1638, Aug. 2004, doi: 10.1088/0266-5611/20/5/018.
- [168] A. Sotiras, C. Davatzikos, and N. Paragios, “Deformable medical image registration: A survey,” *IEEE Trans. Med. Imaging*, vol. 32, no. 7, pp. 1153–1190, 2013, doi: 10.1109/TMI.2013.2265603.
- [169] H. Schreier, J. J. Orteu, and M. A. Sutton, “Image correlation for shape, motion and deformation measurements: Basic concepts, theory and applications,” *Image Correl. Shape, Motion Deform. Meas. Basic Concepts, Theory Appl.*, pp. 1–321, 2009, doi: 10.1007/978-0-387-78747-3.
- [170] F. Hild and S. Roux, “Digital Image Correlation: from Displacement Measurement to Identification of Elastic Properties – a Review,” *Strain*, vol. 42, no. 2, pp. 69–80, May 2006, doi: 10.1111/J.1475-1305.2006.00258.X.

-
- [171] B. Zitová and J. Flusser, “Image registration methods: A survey,” *Image Vis. Comput.*, vol. 21, no. 11, pp. 977–1000, 2003, doi: 10.1016/S0262-8856(03)00137-9.
- [172] S. Klein, M. Staring, K. Murphy, M. A. Viergever, and J. P. W. Pluim, “Elastix: A toolbox for intensity-based medical image registration,” *IEEE Trans. Med. Imaging*, vol. 29, no. 1, pp. 196–205, Jan. 2010, doi: 10.1109/TMI.2009.2035616.
- [173] K. Marstal, F. Berendsen, M. Staring, and S. Klein, “SimpleElastix: A User-Friendly, Multi-lingual Library for Medical Image Registration,” *IEEE Comput. Soc. Conf. Comput. Vis. Pattern Recognit. Work.*, pp. 574–582, Dec. 2016, doi: 10.1109/CVPRW.2016.78.
- [174] Y. TS *et al.*, “Engineering and algorithm design for an image processing Api: a technical report on ITK--the Insight Toolkit,” *Stud. Health Technol. Inform.*, vol. 85, pp. 586–592, Jan. 2002.
- [175] M. M. McCormick, X. Liu, L. Ibanez, J. Jomier, and C. Marion, “ITK: enabling reproducible research and open science,” *Front. Neuroinform.*, vol. 0, no. FEB, p. 13, Feb. 2014, doi: 10.3389/FNINF.2014.00013.
- [176] P. Viola and W. M. Wells, “Alignment by Maximization of Mutual Information,” *Int. J. Comput. Vis.*, vol. 24, no. 2, pp. 137–154, 1997, doi: 10.1023/A:1007958904918.
- [177] D. Mattes, D. R. Haynor, H. Vesselle, T. K. Lewellen, and W. Eubank, “PET-CT image registration in the chest using free-form deformations,” *IEEE Trans. Med. Imaging*, vol. 22, no. 1, pp. 120–128, Jan. 2003, doi: 10.1109/TMI.2003.809072.
- [178] P. Thévenaz and M. Unser, “Optimization of mutual information for multiresolution image registration,” *IEEE Trans. Image Process.*, vol. 9, no. 12, pp. 2083–2099, Dec. 2000, doi: 10.1109/83.887976.
- [179] M. Unser, “Splines: A Perfect Fit for Signal and Image Processing,” *IEEE Signal Process. Mag.*, vol. 16, no. 6, pp. 22–38, 1999, doi: 10.1109/79.799930.
- [180] S. Wright and J. Nocedal, “Numerical optimization,” *Springer Sci.* 35, pp. 67–68, 1999.
- [181] A. Klein *et al.*, “Evaluation of 14 nonlinear deformation algorithms applied to human brain MRI registration,” *Neuroimage*, vol. 46, no. 3, pp. 786–802, Jul. 2009, doi: 10.1016/j.neuroimage.2008.12.037.

Chapter 3. Materials and methodology

3.1. Summary

In Section 1.3, it has been mentioned that four sets of specimens have been cast and subjected to ASR acceleration and, in parallel, to time-lapse XT analysis and other characterizations, each set used for distinct goals. As also mentioned there, one of the sets included specimens not cast during this PhD project. They were previously cast and used within the framework of a testing campaign aiming at monitoring and characterizing ASR damage development under distinct, real world boundary conditions. For the specimens cast during the course of this PhD project, similar mix designs and identical aggregate types have been used. For what concerns all the distinct characterizations, including the XT analysis, identical or similar analysis workflows and settings/instruments have been developed and adopted for the four specimen sets. The present chapter is thus dedicated to describe and explain the identical or similar materials and methodologies (or parts thereof) used, independently of the specimen sets. Thus, this chapter reports the common material and methodological base for all the four experimental campaigns. Since each campaign required some specific adaptations, e.g., in terms of mix design, the additional material and methodological features specific of each single campaign are described at the beginning of each corresponding chapter.

The remainder of this Chapter is structured as in the following:

- Section 3.2 provides information about the common materials and the common aspects of the concrete mix design;
- Section 3.3 explain the characterization techniques and their implementations used in each experimental campaign, with focus on their common features/settings/approaches;
- Section 3.4 describes the custom 3D image analysis workflows developed in this project for analyzing in general the time-lapse tomograms acquired in any campaign.

3.2. Common materials and the basic concrete mix design

Two main types of aggregates have been used, originating from two distinct regions in central (canton Uri, or "U" aggregates) and Southwest (Praz, canton Valais, or "P" aggregates) Switzerland, respectively. Section A1.1 in the Appendix reports their chemical compositions, obtained by standardized X-ray fluorescence (XRF) analysis, and their mineralogical composition, obtained by powder X-ray diffraction (PXRD) analysis. The particle density of the U aggregates is $2667 \text{ kg} \cdot \text{m}^{-3}$ while the particle density of the P aggregates is $2651 \text{ kg} \cdot \text{m}^{-3}$, both measured according to the EN 1097-6:2000 standard [1]. While both aggregate types contain, for each mineral type, a similar amount of it, their differences stem from the minerals distribution and assemblage, i.e., from the mineralogical texture. The texture characterization was obtained with CP-OM. Section A1.1 of the Appendix reports its results, along with those of the chemical and mineralogical characterizations mentioned above.

The U aggregates are sedimentary rocks (impure sandstones), mainly constituted of microcrystalline quartz, including small amounts of amorphous SiO_2 , feldspar and calcite. Foliations, such as white mica flakes, are uniformly distributed in the interstitial regions between fine quartz grain boundaries. The

high specific surface area of their small grains (see Fig. A1 (b) and (d) in Appendix A), in addition to their mineral constituents (see note 4 in Table 2.2), make the U aggregates very reactive [2].

The P aggregates are metamorphic rocks (granitic) which are normally categorized as slow-reacting aggregates. Therefore, they should be expected to have lower reactivity than the U ones, because the U aggregates consist of diaquartzite, with a medium-grained quartz interlocking crystals. There are also several white mica platelets between its grains which facilitate the entrance of alkaline solution to the grain boundaries.

Unless stated differently in the following Chapters, the specimens cast during the course of this PhD project were prisms with size of 40 mm (*X*-axis), 40 mm (*Y*-axis) and 160 mm (*Z*-axis), respectively. Only in some cases, smaller specimens, with size of 25 mm (*X*-axis), 25 mm (*Y*-axis) and 100 mm (*Z*-axis), were cast. In the following, the *Z*-axis direction is called the specimen longitudinal direction, being the direction of largest specimen size. The maximum aggregate sieve size was always 11.25 mm. Such specimen size and aggregate sieve-size range was chosen in order to achieve a trade-off between the representativeness of the concrete volume undergoing ASR damage and the spatial resolution achievable in the X-ray tomograms.

As explained in Section 2.4.2.4, laboratory-scale X-ray tomographs, as the one used in this PhD project, exploits a conically emitted X-ray beam for the geometrical magnification of the projection images of the specimen. Equation (2.15) shows that M is inversely proportional to the source-to-specimen distance d_{ss} . Remembering that the latter distance refers to the source focal spot and the specimen's rotation axis, the finite specimen size limits from above the possible M values, thus the tomographic spatial resolution (see Eq. (2.17)), because there is a minimum d_{ss} value that can be achieved just based upon space constraint. It follows that the specimen size itself limits the effective spatial resolution. Additional constraints to increasing M may come from the need for the specimen projection, at any orientation angle θ , to fit completely within the horizontal field of view of the detector plane, in order to avoid tomographic reconstruction artifacts [3], [4]. Thus, overall, the maximum achievable spatial resolution is negatively correlated with the maximum lateral specimen size.

With such choice of specimen size, a spatial resolution of tens of microns was achieved, while imaging specimen regions containing at least several aggregates along each dimension of the volume. The latter feature is what determines the definition of concrete mesoscale in this PhD project. Such feature means that the investigated concrete volume was large enough for the ASR-induced stresses (and respective cracking) to stem from/to interact with a sufficient number of aggregates. In concrete structures, such interactions, in the presence of many aggregates, strongly drive/affect the cracking patterns. For this reason, it was important to have parts of such interactions also in the laboratory cast specimens used in this work, to achieve a minimum of ASR cracking representativeness.

The specimens were cast with a Portland cement of type CEM I 42.5 N with an alkali content (expressed as the Na₂O-eq.) of 0.79 mass-% of cement mass. That cement type's chemical composition, measured by XRF analysis as well, was the following (by mass-%): CaO 63.0, SiO₂ 20.1, Al₂O₃ 4.6, Fe₂O₃ 3.3, SO₃ 3.3, MgO 1.9, K₂O 0.96, TiO₂ 0.37, P₂O₅ 0.24, Na₂O 0.16, MnO 0.05, Cr₂O₃ 0.01, LOI 2.1. Table 3.1 below provides the basic mix composition which was the starting point for the mix design of each specimen type in each experimental campaign. NaOH was added in an amount leading to a Na₂O-eq. of 1.6 mass-%.

Table 3.1. Generic mix composition of the specimens in units of $\text{kg}\cdot\text{m}^{-3}$ (mass per m^3 of cast material).

Cement CEM I 42.5N	Aggregates			Deionized water	NaOH
	0 – 4 mm	4 – 8 mm	8 – 11.25 mm		
450	659	412	576	225	4.9

All types of specimens in each experimental campaign were subjected to the same laboratory ASR acceleration protocol. Such protocol was an adaptation of the SIA MB 2042 standard [6], typically used in Switzerland for assessing the degree of ASR reactivity of a certain concrete mix design. The protocol consisted of storing the specimens at 100% RH and $60 \pm 2^\circ\text{C}$ in a climatic chamber for 24 hours immediately after casting. They were then demolded and immersed in an alkaline solution (0.3 M KOH, 0.1 M NaOH) contained in boxes. Such a solution simulates the natural pore solution of concrete [7]. The boxes were tightly sealed and stored in an oven with a temperature of 40°C . Thus, the boundary conditions for the specimens were already accelerating the ASR kinetics, still closer to the natural condition of a field-exposed concrete when compared with those of some of the acceleration protocols described in Section 2.4.1, typically requiring storage at higher temperatures, e.g., at 60°C for the AAR-4.1 standard [8].

3.2. Characterizations

At distinct time points, different specimens were taken out of the sealed boxes to perform various characterizations and measurements on them. The measurements included mass and dimensional change (along the specimen longitudinal direction), quasi-static Young's modulus along the longitudinal direction (EN 12390-13:2013 standard [9]), flexural strength and compressive strength along the longitudinal direction (both according to the EN 196-1:2016 standard [10]), SEM-BSE, EDX and XT.

The strength measurements were carried out, at any stage of each campaign, on a distinct batch of one to six specimens. SEM-EDX was carried out on distinct batches of two specimens. The non-destructive measurements (length and mass changes, quasi-static Young's modulus and XT) were carried out on the same exact specimens (three in total) all along the duration of a campaign. Length and mass measurements were additionally performed also on a second batch of three other specimens. In the case of destructive measurements (SEM-EDX, compressive and flexural strengths), the specimens were randomly selected from additional batches distinct from those used for the non-destructive measurements.

Insets (a) and (b) in Figure 3.1 show cartoons illustrating the basic setup for the time-lapse measurements of size along the specimen's longitudinal direction (i.e., of length), $L_Z(t_i)$, $\forall i = 0, 1, \dots, N_t$. A mechanical displacement gauge (by Mitutoyo) with a resolution of $1\ \mu\text{m}$ was used (see Figure 3.1 (c)). This tool is called "expansion measurement set-up1" throughout the thesis. An Invar prism with nominal length of 160 mm or 100 mm (depending upon the nominal length of the cast specimens) was used for calibrating the gauge at each t_i . Invar is a Ni-Fe alloy with a considerably low thermal expansion coefficient. Care was taken to locate the specimen on the gauge such that, at each t_i , its pins were always positioned approximately the same, at the center of the specimen's ($X - Y$) lateral faces (Figure 3.1 (b)). The whole specimen-scale relative change in length, $\frac{\Delta L_Z}{L_Z}(t_i)$, $\forall i = 1, \dots, N_t$, was then computed to assess the specimen's global deformation.

Such mechanical gauge was used during the experimental campaigns described in Chapters 4, 5 and 7. Within the context of the experimental campaign described in Chapter 6, a distinct setup, custom de-

signed and developed within the context of this PhD project, was used in order to automate such measurements. This tool is called "expansion measurement set-up2" throughout the thesis (see for an example Figure 3.1 (e)). The developed setup is described in details in Section A4 of the Appendices. A statistical assessment of the measurement uncertainty and reproducibility of both measurement setups was performed. Its results are reported in Section A4 as well. It is shown there that the custom built setup allowed measuring ΔL_Z with a resolution of $1.1 \mu\text{m}$. On the other hand, no proper definition of the statistical uncertainty of the measurements performed with the mechanical gauge could be obtained.

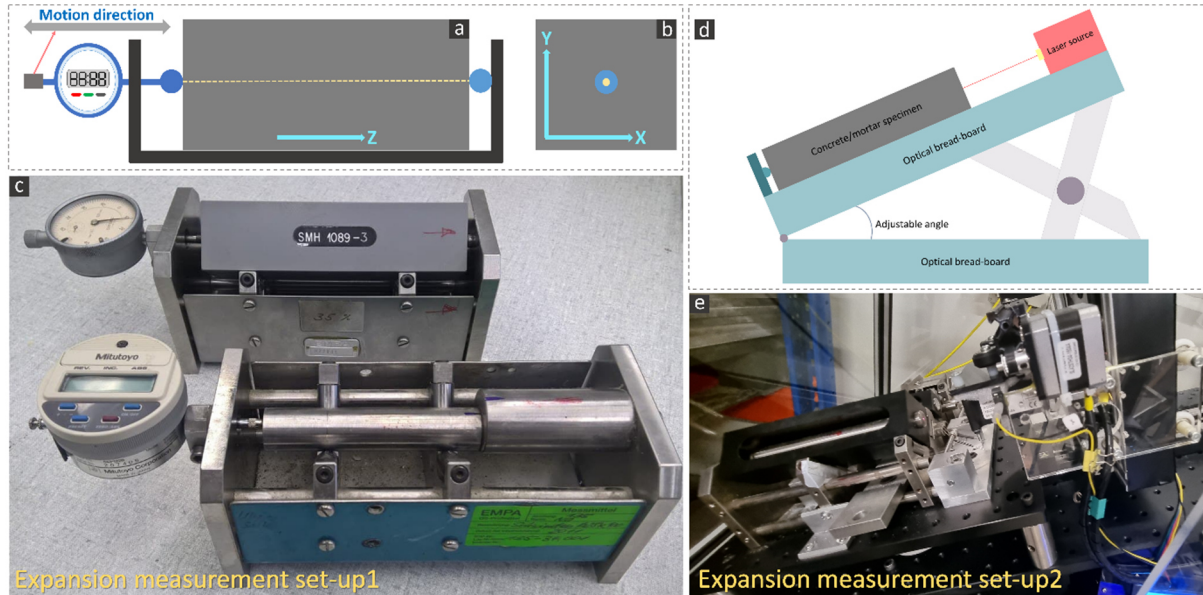


Figure 3.1. Two methods used for measuring of the relative length changes for various groups of specimens: (a) and (b) schematic illustration of the gauge (Rig) used for experimentally measuring the length change (dimensional change along the Z-axis) and (c) real mechanical gauges used in this study, referred to as "expansion measurement set-up1" throughout the thesis. (d) Schematic illustration of the Rig based on laser, custom designed and built during this PhD project for the purpose of automating the specimen longitudinal dimensional (relative) changes, entitled as "expansion measurement set-up2" throughout the thesis. (e) Real rig based on laser, custom designed and built during this PhD project.

SEM and EDX analyses were used (1) for imaging cracks and ASR products with higher spatial resolution than what achievable by XT, in order to characterize qualitative features of the ASR damage and the products' morphology, and (2) for characterizing their chemical composition, respectively. A FEI Quanta 650 environmental scanning electron microscope, by Thermo Fisher Scientific, equipped with an EDX detector (Thermo Noran Ultra Dry 60 mm^2) and the Pathfinder X-Ray Microanalysis software (also by Thermo Fisher Scientific), all available at Empa's Electron Microscopy Center (<https://www.empa.ch/web/s299/info>), were used for SEM and EDX analysis. The electron beam acceleration voltage for both the SEM and the EDX measurements was set to 20 kV .

The attenuation-contrast XT measurements were performed with two distinct X-ray sources for two distinct specimen size. For the sake of brevity, the XT settings are reported here only for the specimens with size $40 \times 40 \times 160 \text{ mm}^3$. The corresponding settings for the specimens with size $25 \times 25 \times 100 \text{ mm}^3$ are provided in Section A2.1. Here, it is only worth mentioning that the ball park estimate of the effective spatial resolution was approximately $70 \mu\text{m}$ for the $40 \times 40 \times 160 \text{ mm}^3$ specimens while it was improved to the value of about $30 \mu\text{m}$ for the $25 \times 25 \times 100 \text{ mm}^3$. Such estimates are based upon Eqs. 2.16 and 2.17 considering average values of the geometrical magnification M , of the

specimen-to-detector and source-to-specimen distances, d_{sd} and d_{ss} , respectively, and the X-ray sources' focal spot sizes at the used operational settings reported below and in Section A2.1.

Any XT measurement was performed using the EasyTomo XL-Ultra tomograph manufactured by RX Solutions, Chavanod, France, available at Empa's Center for X-ray Analytics. Such tomograph consists of a two interchangeable micro-focus X-ray sources and a flat panel X-ray detector. For the measurements on the larger specimens, the used X-ray source was a Hamamatsu L10801 (230 KeV source), which is a reflection-based source. The emitted X-ray beam geometry is a cone one, with a 30° opening angle. The X-ray detector (by Varian) consists of a 2D array of amorphous Si pixels (1920×1536), each with physical size $p = 127 \mu\text{m}$, covered with a thin layer of CsI (scintillator for the X-ray photons). The X-ray source voltage and current were set for all the measurements at about 90 kV and 150 μA , respectively. Thus, the corresponding X-ray photon energy range covered up to about 90 keV.

The source-to-specimen distance, d_{ss} , was about 114 mm and the source-to-detector distance, d_{sd} , was about 410 mm. Thus, the geometrical magnification M achieved in the radiographs was, according to Eq. (2.14), $M = 3.6$. The resulting effective voxel size for the final tomograms was $\tilde{p} = p/M \cong 35 \mu\text{m}$. At the operation voltage and current values mentioned above, the focal spot size f_s of the Hamamatsu L10801 X-ray source is of the order of $30 \mu\text{m}$, according to Hamamatsu's specifications. Thus, according to Eqs. (2.16) and (2.17), the effective spatial resolution estimate just based upon geometrical factors should be about $41 \mu\text{m}$. Thus, a ball park estimate of an upper bound of the actual effective spatial resolution was chosen as the double of \tilde{p} , i.e., as mentioned before, $70 \mu\text{m}$.

XT was always conducted only for the middle region along the longitudinal direction of each specimen (see Fig. 3.3 (e) below), covering a volume of interest (VOI) of $40 \times 40 \times 45 \text{ mm}^3$ (in comparison with the original specimen size of $40 \times 40 \times 160 \text{ mm}^3$). The rotation axis of the specimen stage was approximately parallel to the specimens' longitudinal direction. For each tomographic acquisition, 3600 radiographs were acquired over 360° of specimen rotation. Each acquired radiograph was the results of pixel-wise averaging of 10 radiographs at the same rotation angle. Each single radiograph for the averaging was obtained by exposing the X-ray detector for 227 ms to the X-ray beam. The tomographic reconstruction was carried out using a GPU-optimized cone beam filtered back-projection algorithm [11] provided by RX Solutions (XACT software, Ver. 1.1). Each tomogram, as a 3D image, was saved as a stack of 2D 16 bit unsigned integer TIFF images being the tomographic slices. The slices were equidistant from each other, i.e., the voxels were isotropic, with inter-slice distance equal to the voxel size \tilde{p} .

Two different set-ups were used to fix the specimens to the rotation stage of the tomograph. An example of each one of them is illustrated in Figure 3.2. The first set-up shown in Figure 3.2 (a), referred to in the following as "holding set-up1", was primarily used along with the piezoelectric actuators, for some measurements. Later, in order to have a more repeatable sample positioning during multiple time-lapse tomographies, an upgraded version of such sample holder was designed and manufactured, as shown in Figure 3.2 (b), and referred to as "holding set-up2". Furthermore, in order to have a reasonably correct repositioning of the specimens already at the tomography time (before rigid body registration), a semi-automatic repositioning procedure was developed. To do so, instead of piezoelectric actuators (with only 2 degrees of freedom), a hexapod by 6 degrees of freedom was attached to the rotating stage of the tomograph to position the sample holder (and the specimen gripped with it). The details of the design and implementation of holding set-up2 are provided in Section A2.2. The implementation of each method for holding the specimens will be specified in the corresponding following chapters.

In order to preserve the moisture and reduce the drying of the specimens during tomography, a hollow, cylindrical Kapton envelope was attached to the both sample holders. An example of such Kapton cylinder is shown for the case of the holding set-up2 in Figure 3.2 (b).

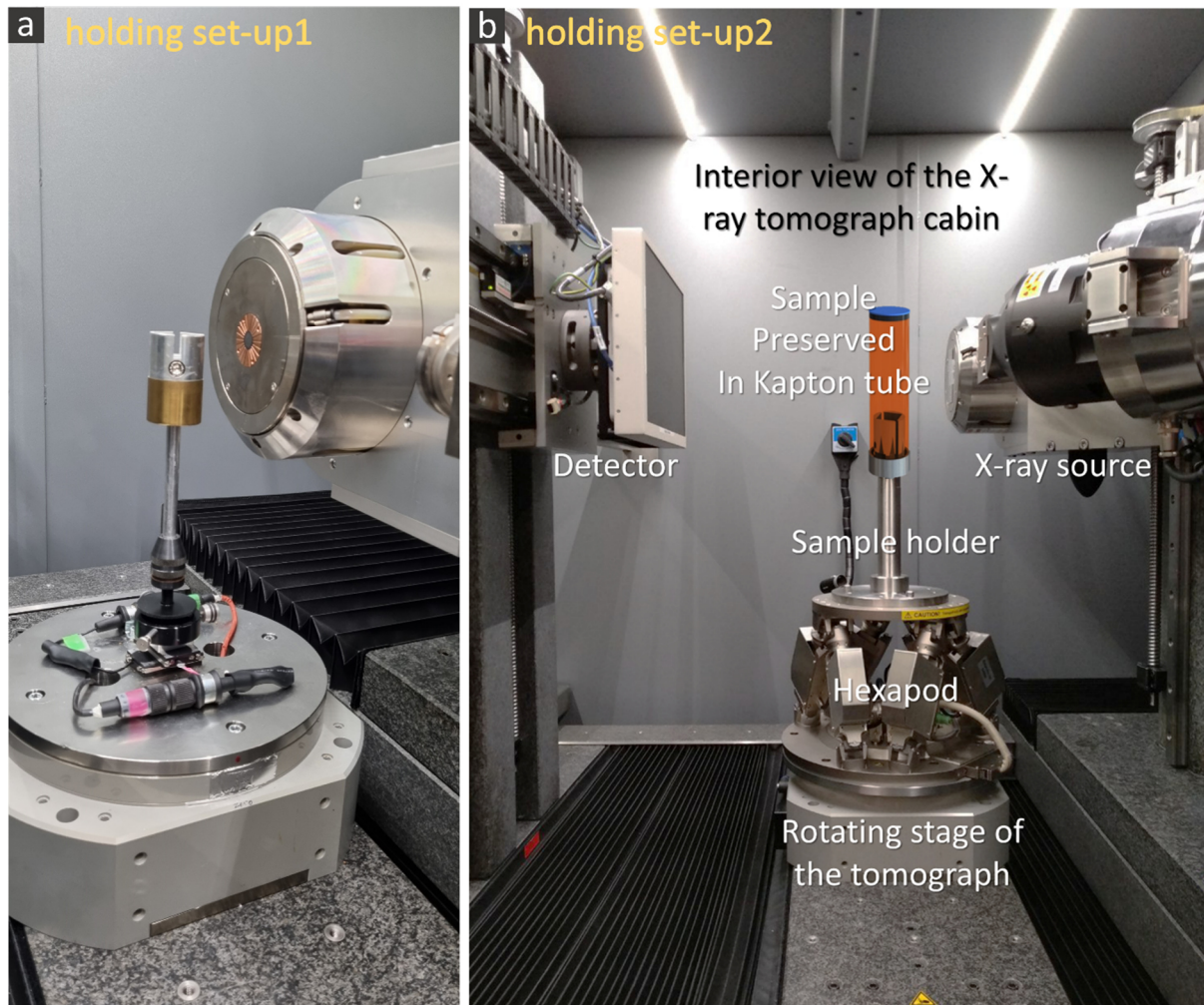


Figure 3.2. Two methods used for fixing the specimens to the rotating stage of the tomograph: (a) piezoelectric actuators and sample holder, called "holding set-up1" throughout the thesis; and (b) hexapod and sample holder, called "holding set-up2" throughout the thesis.

In summary, the range of spatial resolutions achieved in different conditions in the tomograms are listed in the table 3.2.

Table 3.2. Summary of spatial resolutions achieved in different conditions in the tomograms.

X-ray source	Specimen holder	Specimen size	Spatial resolution (μm)
Hamamatsu L10801 (230 KeV)	holding set-up1	$40 \times 40 \times 160 \text{ mm}^3$	~ 70
	holding set-up2	$25 \times 25 \times 100 \text{ mm}^3$	~ 50
Hamamatsu L10711-02 (160 KeV)	holding set-up1	$25 \times 25 \times 100 \text{ mm}^3$	~ 30
	holding set-up2	Diameter 15 mm	~ 20

3.3. Analysis of the time-lapse X-ray tomograms

A 3D image analysis workflow was implemented and applied, in each experimental campaign, to the tomograms of one out of the three tomographed specimens, of each type. The exception is the campaign described in Chapter 6, where the tomograms of all three specimens of each type were analyzed.

The workflow had a two-fold goal: on the one side, to simplify the qualitative comparison of the tomograms of a given specimen at the distinct time points, by making sure that the volumes would be aligned to a common frame of reference; on the other side, to go beyond a qualitative, visual comparison by performing a quantitative analysis which could actually take advantage of the 4D (space + time) information available.

In the following the steps of such workflow from a conceptual point of view are listed and described. The corresponding technical details about its actual software implementation and execution are reported in the Section A3 of the Appendixes. To be remarked is the fact that the symbol $I(\vec{x}_j, t_i)$ indicates in what follows the value of a voxel at position \vec{x}_j in the tomogram at the time point t_i in the series, with $i = 0, 1, \dots, N_t$. The index $j = 1, \dots, N$ enumerates the voxels in which the volume is discretized, N being the total number of voxels. The index i enumerates the time-points in a series, with a total number $N_t + 1$ differing between some of the experimental campaigns. The tomogram at t_0 was the one at a starting or reference state of a specimen. In the following, such reference state is meant to be the one exposed to the ASR acceleration protocol only for one day (when no potential ASR phenomenon, at least resolvable by XT could be expected). Such one day exposure is required to allow the solution adsorption to the concrete microstructure. If the reference tomogram was acquired before submerging the specimens into the alkaline solution (i.e., before exposure to the ASR acceleration protocol), the X-ray attenuation of the specimen and thus its voxel values could have been different with the tomograms at the other time points, where the specimens have a higher degree of water saturation in their pores (due to the immersion in alkaline solution).

(I) Image enhancement

Each tomogram was first of all enhanced, in terms of noise reduction. For each specimen and at each time point t_i in the series, the X-ray tomogram was firstly subjected to an edge-preserving noise-reduction step, with the goal of smoothing it without significant blurring of edges, e.g., boundaries between distinct material phases. A type of anisotropic diffusion filter [12] implemented in the Xlib library of plugins [13] for Fiji/ImageJ [14] developed and maintained at Empa's Concrete and Asphalt Laboratory. The name of the used plugin is "Anisotropic diffusion". Information about the whole Xlib library is available at <https://imagej.net/plugins/xlib>. See Section A3.1 for the detailed settings of the used "Anisotropic diffusion" plugin.

(II) Correction for specimen misalignments

Distinct time-lapse tomograms of the same specimen almost always exhibit specimen misalignment. This means that a reference point on the specimen surface, e.g., a corner, may be not located at the same position of a common and fixed frame of reference in two successive tomograms.

The tomographic measurements were designed and implemented in order to minimize upfront such misalignment. The same specimen holder was always used. Each specimen was positioned with a corner always at the same position on that holder. The holder itself was custom designed and manufactured in order to ease such positioning. Despite all these measures, misalignment was still unavoidable. That occurred and typically occurs because of limitations in the precision with which the same exact specimen can be mounted on the tomograph's specimen/rotation stage at the successive measurement time points.

It occurs also because the specimen stage itself can be moved to a nominal position only with a certain accuracy, which in the tomograph used in this study, is at the scale of few to tens of microns. For these reasons, the rigid body registration was additionally exploited to further reduce the misalignments between the time-lapse tomograms.

In each experimental campaign, the fixed, reference image was always the tomogram at the first time point, $\{I(\vec{x}_j, t_0)\}_{j=1, \dots, N}$, while the deformed or moved image was the tomogram at a successive time point, $\{I(\vec{x}_j, t_i)\}_{j=1, \dots, N}$, $\forall i = 1, \dots, N_t$. The tomogram obtained as output of the rigid body registration is indicated by $\{I_{RB}(\vec{x}_j, t_i)\}_{j=1, \dots, N}$, $\forall i = 1, \dots, N_t$. Such 3D image registration was carried out using the Python application programming interface (API) of the SimpleElastix image registration library [15]. SimpleElastix is an extension of the Elastix C++ image registration library [16]. The latter is based upon the Insight Segmentation and Registration Toolkit (ITK) library [17], [18]. SimpleElastix integrates Elastix with SimpleITK, the latter being a set of bindings to the ITK library offered in several programming languages [15].

The 3D rigid body registration used a multi-resolution scheme [16], [19] and an image similarity metric based on the mutual information of the two populations of voxel values [16], [19], one population corresponding to the reference tomogram at time t_0 , the second to the deformed specimen's tomogram, at time t_i . See Section A3.2 of the Appendixes for the details of the implementation of rigid body registration in SimpleElastix using its Python interface.

(III) Crack segmentation

To achieve the segmentation of empty cracks, a customized approach was used. By empty cracks, it is meant here cracks with either no ASR products at all or in a very small amount not sufficient to offset the crack voxel value above the typical values for empty regions.

The approach exploited the fact that ASR cracks were, for the tomogram at time t_i , a new feature, compared with the tomogram at t_0 . If cracks could appear in the hypothetical absence of any deformation of the specimen, the difference between the tomogram at t_0 and the tomogram at t_i should give as a result a tomogram where every voxel had value close to 0, except where changes appeared, i.e., where cracking occurred. Segmentation of crack voxels would then be feasible by selecting the voxels in such difference image with values in a certain interval (i.e., by the so called thresholding). Since cracking is actually a consequence of specimen deformation, the simple difference mentioned above is, in this case, not useful. Regions at time t_i , not containing cracks, thus unchanged, were not exactly located at the same positions as at t_0 . Such regions have, in the difference tomogram, voxel value very different from zero. This limitation was addressed by performing 3D, non-rigid image registration between the output of the processing step described in step (II) above, at t_i , $\forall i = 1, \dots, N_t$, and the tomogram at t_0 .

Such non-rigid registration was performed in two successive steps. The first step consisted of global affine registration, to compensate for bulk and coarse volumetric changes. The output tomogram of such step was the input for the second step. The latter consisted of non-affine registration, to try to compensate for spatially heterogeneous deformations. The finally registered tomogram was then subtracted from the tomogram at t_0 . This difference tomogram was then segmented by voxel value thresholding.

The details of all these steps are described in the following sub-sections.

3D, global affine registration. The output tomograms of the 3D rigid body registration described at the step (II) above, $\{I_{RB}(\vec{x}_j, t_i)\}_{j=1, \dots, N_t}$, $\forall i = 1, \dots, N_t$, were subjected to 3D, global affine registration. Each $\{I_{RB}(\vec{x}_j, t_i)\}_{j=1, \dots, N_t}$, $\forall i = 1, \dots, N_t$, was registered against the reference tomogram $\{I(\vec{x}_j, t_0)\}_{j=1, \dots, N_t}$. The affine mapping vector field, $\vec{x}' = \vec{T}_{AFF}(\vec{x})$, was modelled as the combination of a rotation, a shear transformation, isotropic scaling and a translation (Eq. (2.25)):

$$\vec{x}' = \vec{T}_{AFF}(\vec{x}) = \mathbf{R} \cdot \mathbf{G} \cdot \mathbf{S} \cdot (\vec{x} - \vec{c}) + \vec{t} + \vec{c} \quad (3.1)$$

where

$$\mathbf{G} = \begin{pmatrix} 1 & G_{12} & G_{13} \\ G_{21} & 1 & G_{23} \\ G_{31} & G_{32} & 1 \end{pmatrix} \quad (3.2),$$

$$\mathbf{S} = \begin{pmatrix} S_1 & 0 & 0 \\ 0 & S_2 & 0 \\ 0 & 0 & S_3 \end{pmatrix} \quad (3.3)$$

and

$$\mathbf{R} = \mathbf{R}_z(\alpha) \mathbf{R}_y(\beta) \mathbf{R}_x(\gamma) \begin{pmatrix} \cos \alpha & -\sin \alpha & 0 \\ \sin \alpha & \cos \alpha & 0 \\ 0 & 0 & 1 \end{pmatrix} \begin{pmatrix} \cos \beta & 0 & \sin \beta \\ 0 & 1 & 0 \\ -\sin \beta & 0 & \cos \beta \end{pmatrix} \begin{pmatrix} 1 & 0 & 0 \\ 0 & \cos \gamma & -\sin \gamma \\ 0 & \sin \gamma & \cos \gamma \end{pmatrix} \quad (3.4)$$

are 3×3 , real-valued matrices with elements independent of \vec{x} (i.e., global affine transformation) representing the shear, scaling and rotation transformations, respectively. Eq. (3.4) defines an intrinsic rotation whose Euler angles are α , β , γ around the intrinsic Z , Y and X axes, respectively. The term \vec{t} in Eq. (E3.1) stands for the translation vector (see Eq. (2.25)). Since the input to this global affine registration step was a tomogram already rigidly registered against the reference tomogram, the matrix \mathbf{R} and the vector \vec{t} in Eq. (E3.1) were essentially estimated as the identity matrix and the null vector, respectively, from the affine registration procedure.

In the following, $\{I_{AFF}(\vec{x}_j, t_i)\}_{j=1, \dots, N_t}$, $\forall i = 1, \dots, N_t$, indicates the tomogram obtained as output of this global affine registration. Its algorithmic implementation was done also in this case by using the Python API of SimpleElastix. As for the rigid body registration, the image similarity metric was based on the mutual information of the two voxel populations. A multi-resolution scheme was also used. The details of the software implementation of this registration step are provided in Section A3.3 of the Appendices.

3D, non-affine registration. The tomograms $\{I_{AFF}(\vec{x}_j, t_i)\}_{j=1, \dots, N_t}$, $\forall i = 1, \dots, N_t$, were registered against $\{I(\vec{x}_j, t_0)\}_{j=1, \dots, N_t}$ according to a non-affine transformation model, $\vec{x}' = \vec{T}_{N-AFF}(\vec{x})$, parametrized by using the multi-dimensional cubic B-spline model described by Eq. (2.26). As a reminder, such registration allows compensating for spatially varying deformations, thus for the part of the ASR-induced deformations being spatially heterogeneous, e.g., highly localized. The output of such registration was the set of tomograms $\{\tilde{I}(\vec{x}_j, t_i)\}_{j=1, \dots, N_t}$, $\forall i = 1, \dots, N_t$.

The Python API of SimpleElastix was used to program also this type of registration, still using a multi-resolution scheme and an image similarity metric based upon the mutual information of the two voxel populations. Also for this registration step, the software details are provided in Section A3.3 of the Appendices.

Empty crack segmentation. Each tomogram $\{\tilde{I}(\vec{x}_j, t_i)\}_{j=1, \dots, N}$, $\forall i = 1, \dots, N_t$ (Figure 3.3 (b)), is a version of the original one, $\{I(\vec{x}_j, t_i)\}_{j=1, \dots, N}$, but deformed as such both the misalignment due to the specimen repositioning at each measurement time point t_i and the deformations induced by ASR are compensated for. Thus, each of them approximately matches the reference tomogram, except at locations where the ASR cracks appeared between the reference time t_0 and time t_i . As mentioned above, the developed analysis workflow used the voxel-wise difference between $\{I(\vec{x}_j, t_0)\}_{j=1, \dots, N}$ and $\{\tilde{I}(\vec{x}_j, t_i)\}_{j=1, \dots, N}$ as a 3D spatial map of a (sort of) "likelihood" for the voxel to be inside a (empty or filled by a small amount of ASR products) crack (Figure 3.3 (c)).

This approach to identify and select regions where changes happened is a relatively well-established method in quantitative medical diagnosis based on time-lapse X-ray or Magnetic Resonance (MRI) imaging. It is usually named as Temporal Subtraction (TS) [20]–[22]. By the choice of a "likelihood" range, that 3D scalar field of likelihood was converted into a binary one (also called a binary tomogram), coded using 8-bit unsigned integer numbers and a value of 0 for a voxel outside a crack and of 255 otherwise.

Due to noise and partial volume effects in $\{I(\vec{x}_j, t_0)\}_{j=1, \dots, N}$ and $\{\tilde{I}(\vec{x}_j, t_i)\}_{j=1, \dots, N}$, each of such binary tomogram for ASR-related cracks still contained artefacts, in the form of small and rather spherical sets of connected voxels ("clusters") which did not actually fall within newly formed cracks. These clusters were algorithmically selected by computing, for each set of connected voxels in the binary tomogram, a feature variable SD :

$$SD = \frac{S_{sphere}}{S_{\partial\Omega}} \quad (3.5)$$

where S_{sphere} is the surface area of a sphere with volume equal to the total volume of the voxel set and $S_{\partial\Omega}$ is its actual boundary surface ($\partial\Omega$) area. SD measures the sphericity degree of the voxel cluster [23]. Clusters with SD values close to 1 are highly spherical. Clusters corresponding to the actual cracks had SD values much smaller than 1. That should be expected, since cracks are 3D objects with high shape anisotropy. All the clusters with $SD > 0.4$ were selected and excluded from the previous binary tomogram, obtaining a new one called, in what follows, as $\{\tilde{I}_{ASR\ crack}^B(\vec{x}_j, t_i)\}_{j=1, \dots, N}$. This binary tomogram acted as the final spatial map of the voxels identified as belonging to (empty) ASR crack volume newly formed at time t_i compared with time t_0 . In order to be able to compute the total volume of cracks, including what already existed in the tomogram at t_0 , thus not due to ASR, an additional crack segmentation workflow, consisting of the following steps, was implemented.

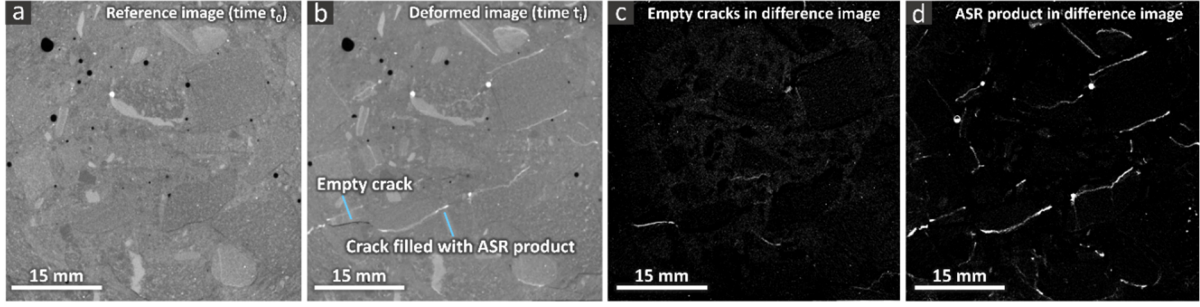


Figure 3.3. Example tomographic slices of one specimen from the experimental campaign described in Chapter 5. (a) and (b) show the slice, located at the same position, from the reference and deformed tomograms, respectively. The deformed tomogram of (b) is the one at about 195 days since start of the ASR acceleration and after the full chain of registrations. (c) and (d) show the results of the two distinct temporal subtractions, leading to the identifications of regions of empty cracks (inset (c)) and of pore space filled with ASR products (inset (d)), respectively.

A black top-hat (BTH) transform was applied to $\{I(\vec{x}_j, t_0)\}_{j=1,\dots,N}$. It is a mathematical morphology operator acting on binary as well as grey-level images. When applied to grey-level images (like the tomograms in this PhD project), it produces a new grey-level image as output, with pixel/voxel value having the meaning of likelihood that a certain object's area/volume includes, in the input image, that pixel/voxel. The object has a specific shape and must have on average lower pixel/voxel value than in its surroundings. Thus, such transform allows mapping out regions (1) containing local minima and (2) being specifically shaped [24]. By thresholding the transform's output, it is possible to obtain a binary image segmenting the chosen type of objects out of the original image. The predefined shape of the object is determined by choosing the structuring element (SE) of the morphological operation used in the transform (a morphological opening). As SE, a 3D thin disk, with size of $S_{BTH} = 3$ voxels was used. Such choice was motivated by the fact that empty cracks are (1) 3D regions with high shape anisotropy (i.e., high aspect ratios), in addition to (2) containing local minima of the original grey-level image. The actual software implementation of such transform was based on the module "Edit New Label Field" (in the Segmentation tab) of Avizo 3D, an image processing software suite by Thermo Fisher Scientific.

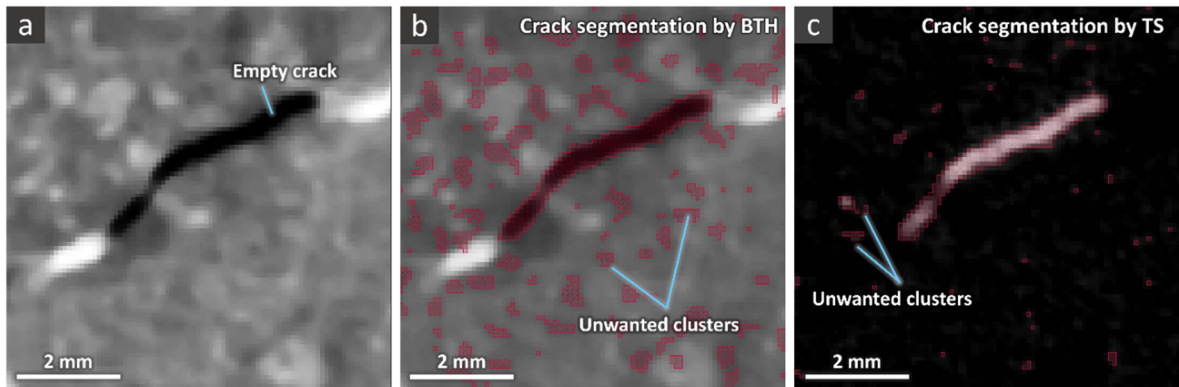


Figure 3.4. Comparison of empty crack segmentation results obtained by the black top-hat (BTH) transform + thresholding and by the temporal subtraction (TS) + thresholding procedures. (a): example ROI selected from one slice of a tomogram at a certain time t_i for one of the specimens of the

experimental campaign described in Chapter 5, containing a partially empty crack; (b) the binary tomogram of empty cracks obtained from the BTH segmentation, superimposed on top of the same image as in (a) and rendered in semi-transparent red color; (c) binary tomogram of empty cracks obtained from the TS segmentation, superimposed on top of the subtraction image $(\{I(\vec{x}_j, t_0)\}_{j=1,\dots,N} - \{\tilde{I}(\vec{x}_j, t_i)\}_{j=1,\dots,N})$. The comparison of (c) and (b) shows that the empty crack segmentation based upon the TS-based approach was less affected by artefacts and errors.

The result of the sequence BTH transform \rightarrow thresholding was a binary tomogram, which was subjected to the same sphericity-based filtering described above, to exclude clusters of voxels not belonging to actual cracks. In comparison with the binary tomograms obtained by the registration \rightarrow temporal subtraction \rightarrow thresholding procedure, those produced by the BTH transform \rightarrow thresholding contained by far much more artefacts due to noise and partial volume effect. See Figure 3.4 for a comparison. Due to this reason, the BTH empty crack segmentation procedure was used only at t_0 .

The resulting binary tomogram, called $\{I_{crack}^B(\vec{x}_j, t_0)\}_{j=1,\dots,N}$, was then Boolean-added, by a Boolean OR operator, to each $\{\tilde{I}_{ASR\ crack}^B(\vec{x}_j, t_i)\}_{j=1,\dots,N}$, $\forall i = 1, \dots, N_t$, to obtain at each t_i a binary tomogram of total crack volume (called $\{I_{crack}^B(\vec{x}_j, t_i)\}_{j=1,\dots,N}$), independently of whether generated by ASR or pre-existing it.

It is need to remark again that the latter binary tomograms provide an identifying (or label) map of voxels contained in empty crack regions. The adjective "empty" is used not with absolute meaning. It rather means that such segmented crack regions either contained no ASR products at all or contained them in low enough volume fraction and/or with low enough concentration of bound Cs^+ ions such that their X-ray attenuation was extremely small, similar to that of empty air. Crack regions containing ASR products in large enough volume fraction and with large enough Cs concentration (see Chapter 5) were characterized by voxel values very large compared with the surrounding. Thus, they were segmented according with the procedure described at the point (IV) described below and generically defined as "ASR products regions".

Figure 3.4 above exemplifies some of the advantages brought by the TS-based approach to the segmentation of empty crack. However, in principle, the TS-based approach implies one specific type of disadvantage: the tomogram at time t_i , $\forall i = 1, \dots, N_t$, gets deformed by the overall image registration workflow. As a consequence, each segmented crack may have size (volumetric or linear, e.g., thickness), shape, orientation and location modified compared the ground truth in the unregistered tomogram at t_i itself.

In order to assess how and how much the cracks segmented by the TS-based approach differed from ground truth, the TS-based approach performance was compared with that of a more conventional approach, e.g., the BTH-based one, both applied to a set of toy cases with both actual and surrogate cracks in the tomographic images and in model images. The details of such comparative analysis are fully reported in Section A3.3 of the Appendices. The overall result was that the overall registration workflow did not deform a single crack much in terms of shape, orientation and volume, rather it just displaced it at the scale of a few voxels. Such a result indicates that the TS-based crack segmentation approach does not seem to introduce any systematic error in the quantification of crack size and orientation, which are key targets of the analysis in this project. However, it does introduce a systematic spatial displacement of the cracks in the frame of reference common to all the tomograms of a time series. The latter bias implies that the TS-based approach should not be used in the cases where the position of the crack in

respect to the common frame of reference is one of the wanted output from the image analysis, which was not the case in this project.

(IV) ASR products segmentation

The ASR products were segmented by subtracting the reference tomogram, $\{I(\vec{x}_j, t_0)\}_{j=1,\dots,N}$, from each B-spline registered tomogram, $\{\tilde{I}(\vec{x}_j, t_i)\}_{j=1,\dots,N}$, $\forall i = 1, \dots, N_t$, the resulting tomogram having large and positive voxel values only where the products appeared between the times t_0 and t_i , given that the products provided their voxels extremely high values compared to voxels where most of the other material phases were contained (at least for specimens cast with the addition of Cs, see Chapter 5). It was thus possible to choose a range of voxel values (thresholding) to select the products' voxels in such difference tomogram.

In order to further distinguish between products in cracks from those in other types of pores, e.g., air voids, the same type of sphericity-based filter was used. Clusters of products' voxels with sphericity SD (see Eq. (3.5) above) smaller than 0.4 were classified as belonging to cracks, while those with SD larger than 0.4 were classified as belonging to other pore types. Thus two disjoint binary tomograms were created, called $\{\tilde{I}_{ASR\ prod.-crack}^B(\vec{x}_j, t_i)\}_{j=1,\dots,N}$ and $\{\tilde{I}_{ASR\ prod.-void}^B(\vec{x}_j, t_i)\}_{j=1,\dots,N}$, $\forall i = 1, \dots, N_t$, respectively.

The union, by a Boolean OR operator, of $\{\tilde{I}_{ASR\ prod.-crack}^B(\vec{x}_j, t_i)\}_{j=1,\dots,N}$ and $\{\tilde{I}_{ASR\ crack}^B(\vec{x}_j, t_i)\}_{j=1,\dots,N}$ led to the creation of a new binary tomogram, called $\{\tilde{I}_{ASR\ crack-tot}^B(\vec{x}_j, t_i)\}_{j=1,\dots,N}$, $\forall i = 1, \dots, N_t$, classifying voxels exhibiting changes to ASR, in comparison to the reference tomogram at t_0 . The respective change was due to the appearance of a crack, either containing products with high Cs concentration or no products or with low Cs concentration.

(V) Aggregate segmentation

In specimens containing $BaSO_4$ in the cement paste, the aggregates were segmented by manually selecting a corresponding range of voxel value (thresholding). As explained in Section 1.2, the main motivation for segmenting the aggregates was to differentiate between ASR cracks and products in the aggregates and those in the cement paste. This goal was achieved by exploiting the segmented aggregate binary tomogram as a mask to select only the features spatially overlapping with it. The features falling outside of the aggregate mask were labeled as belonging to the cement paste. Furthermore, as mentioned in Section 1.2, the segmented aggregate binary tomograms supported the mesoscale computational modeling of ASR cracking in concrete performed within sub-project VI of the SNF Sinergia project by EPFL's Computational Solid Mechanics Laboratory. The support consisted of the fact that such binary tomograms provided the basis for creating a finite element method mesh of the spatial domain of the simulation where the aggregates, as one component of the domain (or material phase) had realistic shape and volume, instead of being represented as idealized spherical regions with distinct radii (a frequently needed simplification to cope with computational issues [25]).

(VI) Quantitative characterization of the crack network

By crack network, it is meant in the following the sets of interconnected clusters of voxels classified by steps (III) and (IV) as belonging to cracks, either original or ASR-induced and either containing ASR products with high Cs concentrations or not (labelled as empty). In addition to quantifying the volume of such crack network several feature variables of the crack network were computed at the distinct time

points t_i , to quantitatively characterize the temporal evolution of the network itself. Such quantitative analysis complemented the qualitative one obtained by the 3D rendering of the network's binary tomogram.

The following paragraphs introduce the definition of the feature variables used, their meaning and how their values are reported in the following chapters for the data derived from each experimental campaign.

ASR cracks' or products' volume fraction. In order to quantify the ASR damage density, the volume fraction of cracks (with and without products) and of ASR products (when possible) were computed. In the cases where the aggregates were segmented, such volume fraction values were computed twice, differentiating between cracks and products within the aggregates and within the cement paste. In each chapter dedicated to certain type of specimen groups, the details of the computed quantities will be further clarified.

The volume fraction of the ASR cracks (or products) was computed, at any time point t_i , $\forall i = 1, \dots, N_t$, by normalizing the volume of the crack network (of products) by the total volume of the tomogram ($V_{tomogram}$):

$$\tilde{V}_{ASR,k,j}(t_i) = \frac{V_{k,j}(t_i) - V_{k,j}(t_0)}{V_{tomogram}} \cdot 100 [\%] \quad (3.6)$$

In Eq. (3.6), there are two indexes/labels, k and j . k indicates the ASR feature, i.e., either ASR product or ASR crack. j indicates the location of the feature in either main material phase of the concrete mesostructure, i.e., aggregates or cement paste. The index j appears only in Chapters 6 and 7, reporting the results from the experimental campaigns where BaSO₄ was used as contrast agents between aggregates and paste, thus, where it was possible to perform the aggregate segmentation. In those Chapters, when referring to the specimens containing BaSO₄, j has value "Agg" for the features within the aggregates and "Cem" for those within the cement paste. In the other Chapters as well as in Chapters 6 and 7 (when considering reference specimens not containing BaSO₄) the variable of Eq. (3.6), simply called $\tilde{V}_k(t_i)$, will refer to the total volume fraction of the features k all over the tomographed volume, without distinction between aggregate and cement paste volume. $V_{k,j}(t_0)$ in Eq. (3.6) means the total volume of features k at the reference time point, t_0 (e.g., original cracks). The difference between the crack network's volume at any time point t_i and the original's one, $V_{cracks,j}(t_i) - V_{cracks,j}(t_0)$, provides the volume of cracks exclusively generated by ASR. The same difference but for $k = \text{products}$ was simply equivalent to $V_{products,j}(t_i)$, since there were no ASR products at t_0 , thus $V_{products,j}(t_0)=0$.

The main rationale for reporting time series of $\tilde{V}_{k,j}$ and not directly of $V_{k,j}(t_i) - V_{k,j}(t_0)$ is to provide values which could be directly comparable with each other independently of the actual size of the tomographed volume.

Shape tensor analysis. Each binary tomogram of cracks, with or without ASR products and ASR-induced or not, $\{\tilde{I}_{ASR\ crack-tot}^B(\vec{x}_j, t_i)\}_{j=1,\dots,N}$, $\forall i = 1, \dots, N_t$, and $\{I_{crack}^B(\vec{x}_j, t_0)\}_{j=1,\dots,N}$, was first of all subjected to labelling: each set of interconnected, segmented voxels (a cluster) was identified and assigned a digital label to identify it as a distinct 3D object. Each cluster was thus treated as a distinct part (or branch) of the crack network and it is simply called in the following as crack. Each of those binary tomograms thus provided, at any given time point in the series, including the reference time t_0 , a statistical *ensemble* of cracks. The labelling was performed with the module "Label Analysis" of the Avizo 3D software.

The same module of Avizo 3D was used to compute, for each distinct labelled crack, its shape tensor \mathbf{G} . The shape tensor $\mathbf{G} = \{G_{ij}\}_{i,j=1,2,3}$ of a geometrical, 3D object is an analogue of the moment of inertia tensor of a physical body [26], [27]. Its elements are defined as

$$G_{ij} \equiv \int_{\Omega} (x_i - x_{i,CM})(x_j - x_{j,CM}) d\vec{x}, \quad \forall i, j = 1, 2, 3 \quad (3.7)$$

where Ω means the 3D region occupied by the single crack as a 3D object, $\vec{x}_{CM} \equiv \frac{1}{V_{\Omega}} \int_{\Omega} \vec{x} d\vec{x}$ is the crack's center-of-mass (CM) position vector, V_{Ω} means the crack volume and the indexes i and j just enumerates the three Cartesian components of a position vector inside Ω . In Avizo 3D, \mathbf{G} is also called as "variance-covariance matrix" because it has the form of the covariance matrix of a random vector, being it in this case the position vector for the points inside Ω . The same software module computed the *eigenvalues* $\lambda_1 \geq \lambda_2 \geq \lambda_3$ and the respective *eigenvectors*, $(\hat{u}_1; \hat{u}_2; \hat{u}_3)$ of \mathbf{G} . The *eigenvectors'* directions indicate the principal axes (called in short *eigendirections* in what follows) of the crack. The *eigendirection* associated with the largest *eigenvalue* is the direction along which the branch is the most elongated.

A parallelepiped with sides oriented along the three *eigendirections* and circumscribing the object (called bounding box in the following) allows characterizing its characteristic sizes, shape and orientation in space [26]–[30]. The three lateral sizes of such bounding box were used as definitions of length (L), height (or equivalently called width, H) and thickness (T) of the crack, corresponding to the largest, mid and smallest size of the parallelepiped box, respectively ($L \geq H \geq T$) [29]. L , H and T were actually computed, with the aid of the same Avizo 3D module, by using two feature variables associated with the direction of each *eigenvector*. These feature variables are called in such module "ExtentMaxi" and "ExtentMini", where $i = 1, 2, 3$ enumerates the *eigenvectors*. ExtentMaxi is always a positive number while ExtentMini is always negative. ExtentMaxi is computed as the distance between the crack's CM and the plane tangent to the crack's boundary surface, on the side pointed at by \hat{u}_i , and orthogonal to the *eigenvector* \hat{u}_i . ExtentMini is computed similarly as ExtentMaxi but for the plane also tangent to the crack's boundary surface, also orthogonal to the \hat{u}_i but on the side in the opposite direction of \hat{u}_i , thus being assigned a negative value. The final, feature variable ExtentToti = ExtentMaxi – ExtentMini was computed, it being equal to the size of the bounding box along the i -th direction.

Three crack's boundary box size measures were defined as in the following:

- length $L = \text{ExtentTot1}$
- height (or width) $H = \text{ExtentTot2}$
- thickness $T = \text{ExtentTot3}$.

It has to be noted that L , H and T correspond to the Feret (or caliper) diameters along the directions of \hat{u}_1 , \hat{u}_2 and \hat{u}_3 , respectively. L and T are not necessarily equal to the maximum and minimum Feret diameter of a crack, respectively, although they may be close to, depending upon the crack's surface shape.

Insets (a) in Figure 3.5 show 3D renderings of the segmented, total crack network (with or without ASR products) of the U-Cs specimen (specimen with Cs-doping) at 250 days. Distinct, disconnected cracks are rendered with distinct colors. Figure 3.5 (b) to (d) show the 3D renderings of three individual cracks selected from the population shown in Figure 3.5 (a). These cracks were selected as examples because they have, from (b) to (d), increasingly complex morphology, e.g., surface folding and fragmentation. While the large, orange box in each inset indicates the tomographed volume, the small blue box is the bounding box of the individual crack, as computed by its shape tensor analysis. Such box is oriented

along the three *eigenvectors* of the shape tensor \mathbf{G} of the crack. The *eigenvectors* are rendered as solid arrows, starting from the center of mass of the crack itself.

Such type of visual analysis allowed validating qualitatively the shape tensor analysis results. The size of an object along the direction of one *eigenvector* of \mathbf{G} may not necessarily provide useful, quantitative information about the object itself. The shape tensor analysis, in this regard, may be hindered or biased just as it happens with other approaches to estimate size and orientation of a 3D object. That is because the definition of size and orientation is an ill-posed problem for 3D highly convoluted and irregularly shaped objects, as separated cracks are. Indeed, there is no unique and unequivocal definitions of size and main orientation of an object with arbitrary shape.

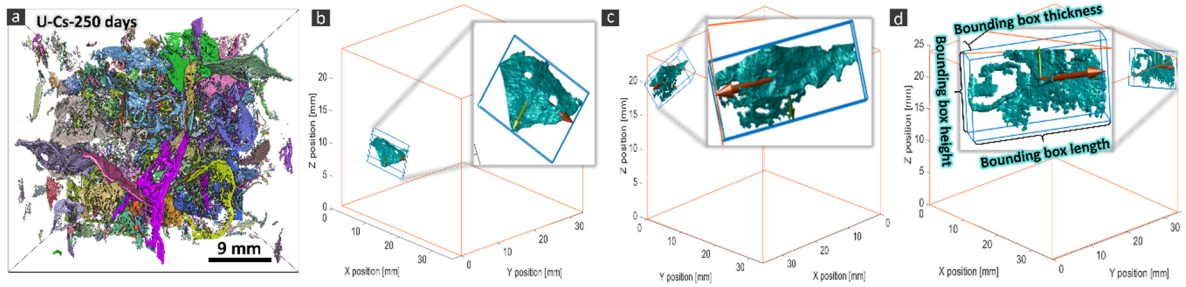


Figure 3.5. (a) 3D rendering of the segmented, total crack network (containing or not containing ASR products) of the U-Cs specimen (discussed in chapter 5), at 250 days. Each separated part (branch) of the crack network is rendered with a distinct color, just for the purpose of distinguishing them. The color assignment to each branch was random. (b)-(d) Three examples of separated branches of the crack network at 250 days, for the same specimen. The large parallelepiped box highlighted in orange delineates the tomographed volume. The smaller grey box shows a zoom-in view of the respective crack branch. The blue, parallelepiped box is the crack's bounding box oriented according to the three eigenvectors of the crack's shape tensor \mathbf{G} . Each eigenvector, located at the center of mass of the crack and scaled by half the lateral size of the bounding box along the same direction, is also rendered as a solid arrow. The red arrow refers to the eigenvector associated with the first eigenvalue. The green arrow to the second eigenvector and the blue one to the third.

In our specific case, the type of visual analysis mentioned above showed that the directions of the three *eigenvectors* of \mathbf{G} provided, for most of the cracks, the right information about the directions of maximum, intermediate and minimum spatial extent of the crack, despite its eventual complex morphology. Correspondingly, the lateral sizes of the mentioned crack bounding boxes (length L , height H and thickness T) could be, for a majority of the cracks, meaningfully used for a quantitative assessment of the crack sizes. That was valid for both the reference and the Cs-doped specimens and for each aggregate type. The exceptions consisted of cracks with rather folded surface, e.g., concave cracks as those shown in Figure 3.6. For such cracks, the bounding box thickness T achieved values which significantly overestimated the scale of an actual crack thickness. In order to avoid the statistics of an indicative crack thickness being spuriously biased by such overestimated boundary box thickness values, this feature variable was not adopted as indicative crack thickness. Instead, the statistics of the crack network's local thickness field, $T_{local}(\vec{x})$ was analyzed.

Finally it has to be remarked that estimates of crack length and crack height/width more accurate than the computed L and H would need to take into account the actual curvature field of the 3D object, e.g., of its tortuosity [36]. Achieving such more accurate estimates requires more advanced approaches and respective computational techniques and it still presents several challenges. See for example Section 2.6

in [36] and [37] for a description of the open problems and respective approaches. The adoption of such approaches in our work extended beyond the focal points and target of our work, i.e., obtaining meaningful and representative quantitative estimates of crack size even though not the most possible accurate.

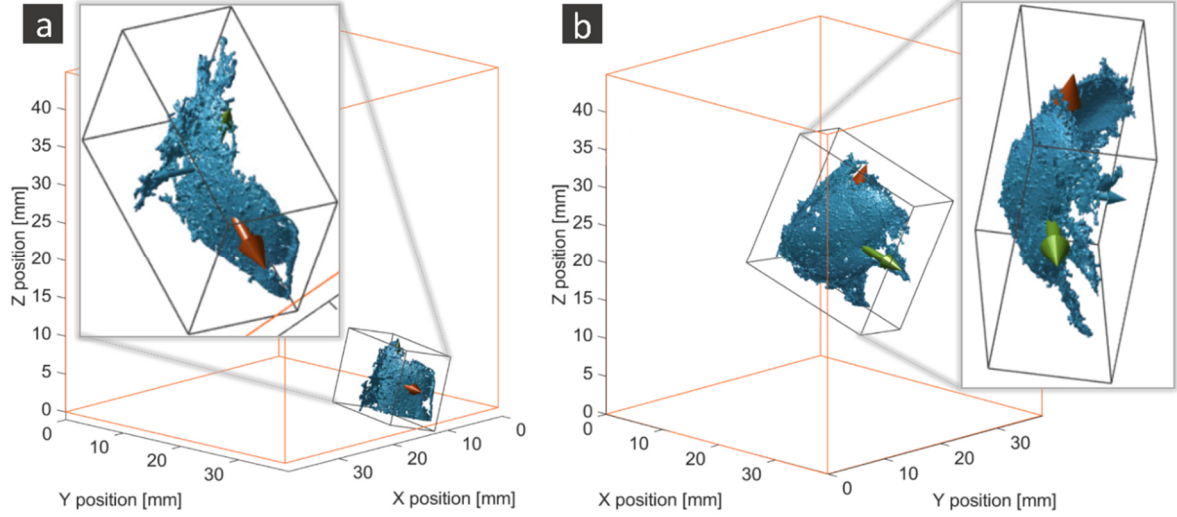


Figure 3.6. Two examples of separate cracks (also called crack network branches) with rather folded surface, e.g., concave cracks. The large parallelepiped box highlighted in orange delineate the tomographed volume. The smaller, light grey box shows a zoom-in view of the respective crack network branch. The dark grey, parallelepiped box is the branch's bounding box oriented according to the three eigenvectors of the branch's shape tensor \mathbf{G} . Each eigenvector is also rendered as a solid arrow. It is located at the center of mass of the branch and scaled by half the lateral size of the bounding box along the same direction. The red arrow refers to the eigenvector associated with the first eigenvalue. The green arrow to the second eigenvector and the blue one to the third.

Ratios of the *eigenvalues* of \mathbf{G} allow a coarse classification of shape, even when the 3D object is very irregularly shaped. Specifically, two variables (also called shape anisotropy degrees [31]) were used in this PhD project:

$$E = 1 - \frac{\lambda_3}{\lambda_1} \quad (3.8)$$

and

$$F = 1 - \frac{\lambda_3}{\lambda_2} \quad (3.9).$$

E is an **elongation** parameter while F is a **flatness** one. Each independent crack was mapped to a point in the $(E; F)$ 2D plane. The analysis of the distribution of $(E; F)$ points allowed comparing crack shapes across specimens.

Finally, the distribution of the direction of the *eigenvector* of \mathbf{G} associated with the first *eigenvalue*, $\hat{\mathbf{u}}_1$, was analysed to assess the crack orientations. The direction of $\hat{\mathbf{u}}_1$ was expressed in spherical coordinates, $(\varphi_1; \theta_1)$, and mapped on one hemisphere of a 3D sphere of radius equal to one, for better visualization of the orientation distribution.

Local thickness analysis. At any time point t_i , a scalar field called local thickness, in short $T_{local}(\vec{x})$, was computed at any position \vec{x} inside the region Ω of any segmented crack by using the binary tomograms $\{\tilde{I}_{ASR\ crack-tot}^B(\vec{x}_j, t_i)\}_{j=1, \dots, N_t}$, $\forall i = 1, \dots, N_t$.

The mathematical definition of $T_{local}(\vec{x})$ is the one proposed by Hildebrand and R  egsegger [32]. $T_{local}(\vec{x})$ is there defined as the diameter of the largest sphere which (1) contains \vec{x} and (2) is contained within the region Ω . The actual computation of $T_{local}(\vec{x})$ was performed with Avizo 3D's module "Thickness Map", with its option "Boundary Voxels" set to "included", by which Hildebrand and R  egsegger's algorithm was implemented with additional "inclusion" of the voxels belonging to the boundary of Ω .

$T_{local}(\vec{x})$ provides a spatial distribution of crack thickness. As a thickness metric, it is advantages and disadvantages:

- its definition is independent from using a specific geometrical model to describe approximately a 3D object, as done in the shape tensor analysis with the use of the bounding box; as a consequence, a complicated shape of the crack due to, e.g., high curvatures, introduces less bias in the final estimates of the $T_{local}(\vec{x})$ values, compared with what happens on the contrary with the estimates of the bounding box thickness T ;
- while each crack can be characterized by a single and unique T value, it has a whole distribution of T_{local} values; when the statistics of thickness for the whole crack network needs to be analyzed, an intermediate analysis step is needed, consisting of computing first statistical metrics of the distribution of T_{local} values for each single crack, then analyzing the distribution of such metrics over the whole *ensemble* of cracks.

(VII) Global and local deformations analysis

Global analysis

The dimensional changes of the tomographed portion of the specimen (also called volume of interest, VOI, in Figure 3.7 (e)) could be quantified based upon the results of the global affine registration and compared, for the specimen longitudinal direction (Z-axis), with those obtained by the experimental measurements with the whole specimen, described in Section 3.2. Such comparison allowed assessing whether or not the length change of the VOI approximated well that of the whole specimen, thus, in such a case, signaling whether the VOI was a representative or unrepresentative volume for what concerned the macroscopic dimensional changes.

Since the global affine registration model is based upon the assumption of a linear mapping vector field (see Eq. 3.1 above), the corresponding displacement vector field, $\vec{u}_{AFF}(\vec{x})$, is also linearly dependent on \vec{x} ,

$$\vec{u}_{AFF}(\vec{x}, t_i) \equiv \vec{x}'(t_i) - \vec{x} = \vec{T}_{AFF}(\vec{x}, t_i) - \vec{x} = (\mathbf{R}(t_i) \cdot \mathbf{G}(t_i) \cdot \mathbf{L}(t_i) - \mathbb{I}_3) \cdot \vec{x} + \vec{t}(t_i) + (\mathbb{I}_3 - \mathbf{R}(t_i) \cdot \mathbf{G}(t_i) \cdot \mathbf{L}(t_i)) \cdot \vec{c}, \forall i = 1, \dots, N_t \quad (3.10)$$

where \mathbb{I}_3 is the 3×3 identity matrix. Inset (c) in Figure 3.7 shows the plot of $u_{Z,AFF}(\vec{x}, t_i)$ inside the tomographed volume of a specimen at a given time point t_i , with $i \neq 0$, showing how it depends mainly on z , as it should be expected based upon the theoretical model expressed by Eq. (3.10). Inset (f) in Figure 3.7 shows with two distinct vertical axes the changes of three variables. The red line in the plot is associated with the left vertical axis. It shows on the horizontal axis the values of $u_{Z,AFF}(\vec{x}, t_i)$ averaged over various 2D ROIs, each located on a slice orthogonal to the Z -axis (Figure 3.7 (d)) and centered in the center of the slice itself. This is the first variable, shown by the red line as a function of the slice's Z -position (shown on the left vertical axis). Such a plot was repeated for a distinct size of the 2D ROIs (from $0.175 \times 0.175 \text{ mm}^2$ to $10.5 \times 10.5 \text{ mm}^2$). The results were independent from the ROI size. The vertical axis on the right hand-side shows all those $X - Y$ ROI size values. At each position along such right vertical axis, the corresponding minimum and maximum values of the averaged $u_{Z,AFF}(\vec{x}, t_i)$ (the other two variables) are plotted with circular markers with distinct colors for the distinct ROI size. Such double vertical axes plot shows that (1) $u_{Z,AFF}(\vec{x})$ clearly varied linearly with z , (2) the X - Y -averaged $u_{Z,AFF}(\vec{x})$ is independent of the $X - Y$ ROI size and (3) the tomographed portion of the specimen, centered about its mid, got deformed along the specimen's longitudinal direction from the center off (negative displacement values below the center, positive ones above).

Based upon such properties of $u_{Z,AFF}(\vec{x})$, it was possible to compute

the relative change in size of the tomographed volume along the Z direction, $\frac{\Delta L_{AFF,Z}}{L_{AFF,Z}}(t_i), \forall i = 1, \dots, N_t$, as the absolute value of the difference between the maximum and the minimum value of $u_{AFF,Z}(\vec{x})$ inside a 3D ROI spanning the entire volume along the Z -axis, with size $0.2 \times 0.2 \text{ mm}^2$ on the $X - Y$ slices and centered in the middle of each such slice (Figure 3.7 (d)). Another adopted approach to compute $\frac{\Delta L_{AFF,Z}}{L_{AFF,Z}}(t_i)$ consisted of first averaging $u_{AFF,Z}(\vec{x})$ on 2D, centered ROIs located on $X - Y$ slices, then of computing the minimum and maximum values of the resultant function of z over the whole range of Z slices and finally computing the absolute value of their difference. Both approaches led to almost identical final values of $\frac{\Delta L_{AFF,Z}}{L_{AFF,Z}}$.

Similar properties characterized $u_{X,AFF}(\vec{x})$ and of $u_{Y,AFF}(\vec{x})$, which resulted to depend mainly on x and y , respectively. As a consequence, it was possible to adopt the same procedure to compute $\frac{\Delta L_{AFF,X}}{L_{AFF,X}}$ and $\frac{\Delta L_{AFF,Y}}{L_{AFF,Y}}$, i.e., to estimate the longitudinal strains along the X - and Y -axis, respectively, at least for the tomographed volume, entirely based upon the results of the global affine registration.

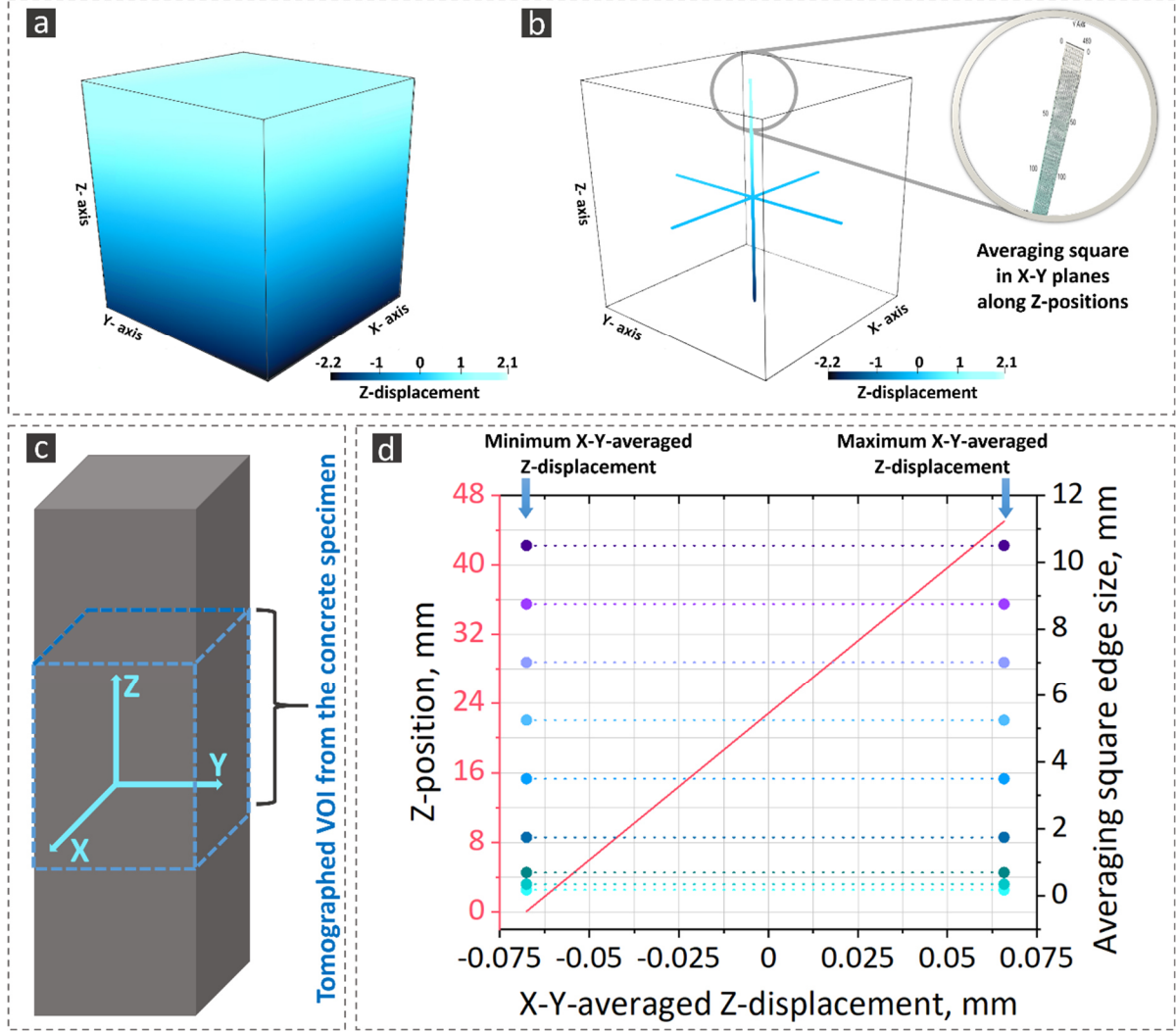


Figure 3.7. Description of the approach used for measuring/estimating the relative length change of the specimens by exploiting the results of 3D, global affine registration of the tomograms. (a) Rendering of the Z-component of the displacement vector field associated with the global affine registration results, $u_{Z,AFF}(\vec{x}, t_i)$, for a specimen at a given time point t_i , with $i \neq 0$. The color scale is in units of number of voxels. The units for the axes of the Cartesian frame of reference are also number of voxels. (b) The $u_{AFF,Z}(\vec{x})$ inside a 3D ROI spanning the entire volume along the Z-axis, with size $0.2 \times 0.2 \text{ mm}^2$ on the X – Y slices and centered in the middle of each such slice. (c) Schematic illustration of a specimen and of the axes of the respective Cartesian frame of reference. The indicative location of the volume investigated by XT is also specified. (d) Horizontal axis: values of $u_{Z,AFF}(\vec{x}, t_i)$ averaged over various 2D ROIs of distinct size located on slices orthogonal to the Z-axis and centered in the center of the slice itself, as a function of their Z-position (left vertical axis). Vertical axis on the right: size of the 2D X-Y ROIs over which $u_{Z,AFF}(\vec{x}, t_i)$ was averaged. The red line refers to the left vertical axis. The colored, circular markers refer to the right vertical axis and show the minimum and maximum values of $u_{Z,AFF}(\vec{x}, t_i)$ along the Z-axis, after averaging it over various 2D, rectangular ROIs. Circles of distinct colors show minimum and maximum values in correspondence of distinct ROI size.

Local analysis

The results of the non-affine registration were exploited to compute 3D scalar fields providing information about the spatial distribution of ASR-induced deformations.

One such scalar field is the Euclidean norm (i.e., magnitude) of the displacement vector field associated with the vector field of the non-affine mapping,

$$\|\vec{u}_{N-AFF}(\vec{x}, t_i) \equiv \|\vec{x}'(t_i) - \vec{x}\| = \|\vec{T}_{N-AFF}(\vec{x}, t_i) - \vec{x}\|, \forall i = 1, \dots, N_t \quad (3.11).$$

It provides the spatial map of a sort-of "intensity" or "degree" of the local deformations.

The second scalar field is the determinant of the Jacobian matrix of the mapping vector field $\vec{T}_{N-AFF}(\vec{x}, t_i)$, in short called the Jacobian of the mapping:

$$J_{\vec{T}_{N-AFF}}(\vec{x}, t_i) \equiv \det\left(\frac{\partial \vec{T}_{N-AFF}}{\partial \vec{x}}\right)(\vec{x}, t_i), \quad \forall i = 1, \dots, N_t \quad (3.12),$$

where

$$\frac{\partial \vec{T}_{N-AFF}}{\partial \vec{x}} \equiv \begin{pmatrix} \frac{\partial T_{N-AFF,1}}{\partial x_1} & \frac{\partial T_{N-AFF,1}}{\partial x_2} & \frac{\partial T_{N-AFF,1}}{\partial x_3} \\ \frac{\partial T_{N-AFF,2}}{\partial x_1} & \frac{\partial T_{N-AFF,2}}{\partial x_2} & \frac{\partial T_{N-AFF,2}}{\partial x_3} \\ \frac{\partial T_{N-AFF,3}}{\partial x_1} & \frac{\partial T_{N-AFF,3}}{\partial x_2} & \frac{\partial T_{N-AFF,3}}{\partial x_3} \end{pmatrix} \quad (3.13)$$

is the Jacobian matrix of the mapping vector field $\vec{T}_{N-AFF}(\vec{x}, t_i)$, $x_1 = x$, $x_2 = y$ and $x_3 = z$.

It is reminded that (see [33])

$$d\vec{x}' = \frac{\partial \vec{T}_{N-AFF}}{\partial \vec{x}} \cdot d\vec{x} \quad (3.14)$$

such that

$$dV_{\vec{x}'}(\vec{x}, t_i) = J_{\vec{T}_{N-AFF}}(\vec{x}, t_i) \cdot dV_{\vec{x}} \quad (3.15),$$

where $dV_{\vec{x}}$ indicates the volume of an infinitesimal region about the position \vec{x} at the reference time t_0 and $dV_{\vec{x}'}$ indicates the volume of the corresponding region at time t_i around the position \vec{x}' in the tomographed volume being the landing position after the non-affine mapping of \vec{x} .

Equation (3.15) indicates that the Jacobian of the non-affine transformation provides a spatial map of the ratio between the local volume at time t_i and the local volume at time t_0 of the same infinitesimal region after and before the local deformations, respectively [33]. Values larger than 1 indicate a local volumetric expansion while values smaller than 1 a local contraction. Both $\vec{u}_{AFF}(\vec{x}, t_i)$ and $\frac{\partial \vec{T}_{N-AFF}}{\partial \vec{x}}(\vec{x}, t_i)$ were computed as outputs of the respective registration workflows implemented by the use of the SimpleElastix image registration library.

3.4 Contributions to software and experimental efforts

Some visualizations and plots in different Chapters were performed with software developed by Dr. Michele Griffa (Empa). All specimens used for OM and SEM were prepared by Boris Ingold (Empa). The compressive and flexural strength and Young's modulus measurements on some of the specimens described in Chapter 6 (see Figure 6.15 and Figure D16) were performed by Daniel Käppeli (Empa). All of the rest of specimen preparation, measurements and 3D image analysis (including workflow implementation) were performed by myself.

Bibliography

- [1] “CEN, Prüfverfahren für mechanische und physikalische Eigenschaften von Gesteinkörnungen – Teil 6: Bestimmung der Rohdichte und der Wasseraufnahme, EN 1097-6:2001 D.” [Online]. Available: <https://www.beuth.de/de/norm/din-en-1097-6/34244218>. [Accessed: 07-May-2021].
- [2] I. Fernandes, M. A. T. M. Broekmans, M. dos A. Ribeiro, and I. Sims, “Sedimentary Rocks,” in *Petrographic Atlas: Characterisation of Aggregates Regarding Potential Reactivity to Alkalis*, Dordrecht: Springer Netherlands, 2016, pp. 43–101.
- [3] G. JC and L. S, “The reconstruction of objects from incomplete projections,” *Phys. Med. Biol.*, vol. 25, no. 1, pp. 129–136, 1980, doi: 10.1088/0031-9155/25/1/012.
- [4] A. Kyrieleis, V. Titarenko, M. Ibison, T. Connolley, and P. J. Withers, “Region-of-interest tomography using filtered backprojection: Assessing the practical limits,” *J. Microsc.*, vol. 241, no. 1, pp. 69–82, Jan. 2011, doi: 10.1111/j.1365-2818.2010.03408.x.
- [5] P. Mehta and P. Monteiro, *Durability. Alkali-Aggregate Reaction. Section 5.14., in: Concrete: microstructure, properties, and materials- 3rd edition*. McGraw-Hill, New York, 2006.
- [6] “SIA MB 2042, Vorbeugung von Schäden durch die Alkali-Aggregat-Reaktion (AAR) bei Betonbauten, Schweizerischer Ingenieur- und Architektenverein (2012).” [Online]. Available: <https://www.sia.ch/de/dienstleistungen/artikelbeitraege/detail/article/neues-merkblatt-sia-2042/>.
- [7] B. Lothenbach and F. Winnefeld, “Thermodynamic modelling of the hydration of Portland cement,” *Cem. Concr. Res.*, vol. 36, no. 2, pp. 209–226, Feb. 2006, doi: 10.1016/j.cemconres.2005.03.001.
- [8] P. Nixon, ... I. S.-R. for the P. of D. by, and undefined 2016, “RILEM Recommended Test Method: AAR-4.1—Detection of Potential Alkali-Reactivity—60° C Test Method for Aggregate Combinations Using Concrete Prisms,” *Springer*.
- [9] “CEN, Prüfung von Festbeton – Teil 13: Bestimmung des Elastizitätsmoduls unter Druckbelastung (Sekantmodul), EN 12390-13:2013 D.” [Online]. Available: <https://www.beuth.de/de/norm/din-en-12390-13/187189769>. [Accessed: 11-Jan-2021].
- [10] “DIN EN 196-1: 2016 DE - Test method for cement - Part 1: Determination of strength; German version EN 196-1: 2016 (Foreign Standard).” [Online]. Available: <https://webstore.ansi.org/standards/din/dinen1962016de>. [Accessed: 11-Jan-2021].
- [11] L. A. Feldkamp, L. C. Davis, and J. W. Kress, “Practical cone-beam algorithm,” *J. Opt. Soc. Am. A*, vol. 1, no. 6, p. 612, Jun. 1984, doi: 10.1364/josaa.1.000612.
- [12] D. Tschumperlé and R. Deriche, “Anisotropic Diffusion Partial Differential Equations for Multichannel Image Regularization: Framework and Applications,” *Advances in Imaging and Electron Physics*, vol. 145, no. SUPPL. pp. 149–209, 2007, doi: 10.1016/S1076-

- 5670(06)45004-7.
- [13] B. Münch, “Xlib (ImageJ / Fiji plugins),” *ImageJ*, 2019. [Online]. Available: <https://imagej.net>.
 - [14] C. A. Schneider, W. S. Rasband, and K. W. Eliceiri, “NIH Image to ImageJ: 25 years of image analysis,” *Nature Methods*, vol. 9, no. 7. Nat Methods, pp. 671–675, Jul-2012, doi: 10.1038/nmeth.2089.
 - [15] K. Marstal, F. Berendsen, M. Staring, and S. Klein, “SimpleElastix: A User-Friendly, Multilingual Library for Medical Image Registration,” *IEEE Comput. Soc. Conf. Comput. Vis. Pattern Recognit. Work.*, pp. 574–582, Dec. 2016, doi: 10.1109/CVPRW.2016.78.
 - [16] S. Klein, M. Staring, K. Murphy, M. A. Viergever, and J. P. W. Pluim, “Elastix: A toolbox for intensity-based medical image registration,” *IEEE Trans. Med. Imaging*, vol. 29, no. 1, pp. 196–205, Jan. 2010, doi: 10.1109/TMI.2009.2035616.
 - [17] Y. TS *et al.*, “Engineering and algorithm design for an image processing Api: a technical report on ITK--the Insight Toolkit.,” *Stud. Health Technol. Inform.*, vol. 85, pp. 586–592, Jan. 2002.
 - [18] M. M. McCormick, X. Liu, L. Ibanez, J. Jomier, and C. Marion, “ITK: enabling reproducible research and open science,” *Front. Neuroinform.*, vol. 0, no. FEB, p. 13, Feb. 2014, doi: 10.3389/FNINF.2014.00013.
 - [19] A. Nan, M. Tennant, U. Rubin, and N. Ray, “DRMIME: Differentiable Mutual Information and Matrix Exponential for Multi-Resolution Image Registration,” PMLR, Sep. 2020.
 - [20] M. Tsuchiya *et al.*, “Temporal subtraction of low-dose and relatively thick-slice CT images with large deformation diffeomorphic metric mapping and adaptive voxel matching for detection of bone metastases: A STARD-compliant article,” *Med. (United States)*, vol. 99, no. 12, 2020, doi: 10.1097/MD.00000000000019538.
 - [21] R. Sakamoto *et al.*, “Temporal subtraction of serial CT images with large deformation diffeomorphic metric mapping in the identification of bone metastases,” *Radiology*, vol. 285, no. 2, pp. 629–639, Nov. 2017, doi: 10.1148/radiol.2017161942.
 - [22] K. Onoue *et al.*, “CT temporal subtraction improves early detection of bone metastases compared to SPECT,” *Eur. Radiol.*, vol. 29, no. 10, pp. 5673–5681, Oct. 2019, doi: 10.1007/s00330-019-06107-w.
 - [23] I. Cruz-Matías *et al.*, “Sphericity and roundness computation for particles using the extreme vertices model,” *J. Comput. Sci.*, vol. 30, pp. 28–40, Jan. 2019, doi: 10.1016/j.jocs.2018.11.005.
 - [24] E. R. Dougherty and R. A. Lotufo, *Hands-on Morphological Image Processing*. SPIE, 2003.
 - [25] A. I. Cuba Ramos, C. Roux-Langlois, C. F. Dunant, M. Corrado, and J. F. Molinari, “HPC simulations of alkali-silica reaction-induced damage: Influence of alkali-silica gel properties,” *Cem. Concr. Res.*, vol. 109, pp. 90–102, Jul. 2018, doi: 10.1016/j.cemconres.2018.03.020.
 - [26] M. R. Teague, “IMAGE ANALYSIS VIA THE GENERAL THEORY OF MOMENTS.,” *J. Opt. Soc. Am.*, vol. 70, no. 8, pp. 920–930, Aug. 1980, doi: 10.1364/JOSA.70.000920.
 - [27] H. Goldstein, C. P. Poole, and J. L. Safko, “The Rigid Body Equations of Motion: Classical Mechanics, 3rd ed.,” *Pearson*, 2013. .
 - [28] D. N. Theodorou and U. W. Suter, “Shape of Unperturbed Linear Polymers: Polypropylene,” *Macromolecules*, vol. 18, no. 6, pp. 1206–1214, 1985, doi: 10.1021/ma00148a028.
 - [29] S. T. Erdoğan, E. J. Garboczi, and D. W. Fowler, “Shape and size of microfine aggregates: X-ray microcomputed tomography vs. laser diffraction,” *Powder Technol.*, vol. 177, no. 2, pp. 53–63, Aug. 2007, doi: 10.1016/j.powtec.2007.02.016.

- [30] M. Zemp, O. Y. Gnedin, N. Y. Gnedin, and A. V. Kravtsov, “On determining the shape of matter distributions,” *Astrophys. Journal, Suppl. Ser.*, vol. 197, no. 2, p. 30, Dec. 2011, doi: 10.1088/0067-0049/197/2/30.
- [31] M. C. Cavalli, M. Griffo, S. Bressi, M. N. Partl, G. Tebaldi, and L. D. Poulikakos, “Multiscale imaging and characterization of the effect of mixing temperature on asphalt concrete containing recycled components,” *J. Microsc.*, vol. 264, no. 1, pp. 22–33, Oct. 2016, doi: 10.1111/jmi.12412.
- [32] T. Hildebrand and P. Rügsegger, “A new method for the model-independent assessment of thickness in three-dimensional images,” *J. Microsc.*, vol. 185, no. 1, pp. 67–75, 1997, doi: 10.1046/j.1365-2818.1997.1340694.x.
- [33] M. H. Protter and B. Charles Jr, *Intermediate Calculus*. 2012.

Chapter 4. ASR crack networks: properties, evolution, and comparisons between laboratory and field specimens; A benchmark analysis

4.1. Summary

This Chapter presents the results of a XT campaign involving both laboratory-scale accelerated specimens and field-exposed ones. The XT analysis aimed at qualitatively and quantitatively characterizing and comparing various features of the crack networks developed under the influence of the distinct boundary conditions (and respective time scales) within which the two sets of specimens developed ASR cracks. The rationale at the basis of such campaign was manifold. On the one side, there was the need to characterize the propensity to ASR cracking of the chosen concrete mix design(s), including the distinct aggregate types, and to characterize it, in order to create a first benchmark dataset. This was a first necessary step in the original plan of this PhD project. On the other side, it was important to address the omnipresent questions of how, how much and with which ASR (cracking) features are specimens accelerated in the laboratory representative, in comparison with specimens affected by ASR developed under real world boundary conditions.

Section 4.2 describes those experimental procedures' details specific of and/or additional for this experimental campaign, in comparison with the general procedures explained in Chapter 3. Section 4.3 reports the most important results from the time-lapse XT measurements on both sets of specimens (laboratory and field ones), as well as results from other measurement types. Additional results are provided in Appendix B. In Section 4.4, the key similarities and differences between the two specimen classes are summarized and their relevance is discussed upon from the point of view of addressing (some of) the questions mentioned above. Finally, Section 4.5 synthesizes the most important conclusions that can be drawn from this benchmark experimental campaign.

4.2. Experimental details specific for the benchmark campaign

Concerning ASR (cracking) induced in the laboratory, the benchmark experimental campaign comprised of the following steps:

1. casting of concrete specimens containing three distinct aggregate types and with two distinct size values optimally chosen for achieving, on the one side, sufficient mesoscale representativeness (see Section 3.2 for its definition) and, on the other side, spatial resolution sufficient to detect a significant part of ASR cracking;
2. application of the laboratory ASR acceleration protocol described in Section 3.2;

3. during the acceleration, non-destructive measurements, including XT ones, were performed on the same exact specimens along with other destructive measurements performed on other specimens;
4. three specimens were cored from field-exposed blocks derived from another project; such blocks were cast years earlier than this PhD project and according to another mix design; the cores had size comparable with that of the laboratory-accelerated specimens;
5. XT was performed on such cores;
6. all the tomograms of any specimen were analyzed according to the same workflow having as target the crack network characterization and the comparison of its features for the distinct specimen types.

The following sub-sections detail these six steps.

4.2.1. Materials and specimens preparation

4.2.1.1. Laboratory-accelerated specimens

Three aggregate types were used to cast three distinct specimen sets. Two of the three were the aggregate types already mentioned in Section 3.2 (labelled as U, for Uri, and P, for Praz, aggregates). The third aggregate type used in this experimental campaign originates from Northeast Switzerland, in Brienz (Canton Bern), thus labelled as "B" aggregates. The same XRF and PXRD analyses mentioned in Section 3.2 and detailed in Appendix A1.1 were performed on the B aggregates as well. Compared with the U and P aggregates, the B ones had lower quartz content (26 mass-% *versus* about 50 mass-%) but higher feldspars content (50 mass-% *versus* 25 and 16 mass-% for U and P aggregates, respectively).

In terms of mineralogical textures, the B aggregates exhibited similar features as the ones described in Section 3.2 and in Section A1.1 of Appendix A for the P aggregates, thus classifying as metamorphic rocks as the P ones. Thus, such an aggregate is expected to present a rather slower reaction than the U one. An example of their mineralogical texture, compared with those of U and P aggregates, is provided in Figure B1 (in Appendix B), in the form of CP-OP micrographs of thin sections.

The mix design used to cast all the laboratory accelerated specimens is summarized in Table 4.1. See Section 3.2 for the details about the cement type used and its composition and Na₂O-eq value.

Prismatic specimens both with size of 40×40×160 mm³ and of 25×25×100 mm³ were cast in number of 30 for each size, in order to look for an optimal trade-off between the specimen volume's mesoscale representativeness and a sufficient spatial resolution in the tomograms.

By casting specimens of distinct size, special attention was dedicated to assess how and how much the ASR development differed. It has been reported in the literature that the ASR-induced maximum macroscopic expansion positively correlates with the specimen size, for specimens subjected to acceleration conditions including high relative humidity and temperature [1]. However, other reported results indicated that such positive correlation may hold only up to a certain specimen size. For instance, by changing the prism size from 50×50×281 mm³ to 75×75×281 mm³, no significant difference in the macroscopic expansion was observed for specimens subjected to ASR acceleration by immersion in a 1M NaOH solution stored at 60°C [2].

The specimens with size $40 \times 40 \times 160 \text{ mm}^3$ and containing B, P and U aggregates are in the following referred to as "B40", "P40" and "U40", respectively, while those with size $25 \times 25 \times 100 \text{ mm}^3$ are called "b25", "p25" and "u25", respectively.

All the cast specimens were subjected to the ASR acceleration protocol detailed in Section 3.2, for a total of 500 days.

Table 4.1. Mix design of the laboratory-accelerated specimens, in units of $\text{kg} \cdot \text{m}^{-3}$ (mass per m^3 of cast material).

Cement CEM I 42.5N	Aggregates			Deionized water	NaOH
	0 – 4 mm	4 – 8 mm	8 – 11.25 mm		
450	659	412	576	225	4.9

4.2.1.2. Field specimens

Three specimens of distinct concrete types and exposed to real world environmental boundary conditions were investigated.

The first specimen was cored out of a concrete wall with an approximate age of 40 years, located along a mountain road at about 1000 m on the sea level (Brünigpass, in central Switzerland). The exact mix design for such structure is unknown. What was known is that it was cast with the B aggregate type. In addition, considering its environmental exposure class (exposure to frost and de-icing salts), it is expected to have been cast with a water-to-cement ratio (by mass, w/c) ≤ 0.50 and a cement content $\geq 300 \text{ kg} \cdot \text{m}^{-3}$. Such specimen is, in the following, referred to as "BF-40".

The second and third specimens were cast in 2004 within the framework of the PARTNER European project [3], which aimed at comparing different standards (a RILEM one *versus* European regional ones) for assessing ASR propensity of very different aggregates types from distinct regions in Europe with distinct climates (from Iceland to Greece). The two specimens were those labelled as "B1(C+NRF)-40" and "B1(C+F)-40" within such project. Their mix designs differed only in the utilized fine aggregate types. They were concretes cast with a CEM I 42.5 R (Norcem) cement with a $\text{Na}_2\text{O}_{\text{eq}}$ of 1.26 mass-%. The cement content used in the mix was $440 \text{ kg} \cdot \text{m}^{-3}$ and the w/c was adjusted to 0.50. The B1(C+NRF)-40 specimen was cast with its fine aggregate fraction made up of non-reactive, natural gravel/sand from a glacio-fluvial deposit in south-western Norway, originally composed of Precambrian crystalline rocks (mainly granites and gneisses). On the contrary, the B1(C+F)-40 was cast with a fine fraction consisting of highly reactive rocks. The latter originated from western Belgium, and were crushed silicified, dark-grey argillaceous limestone with fossil debris (in short siliceous limestone or SLS). Their main reactive mineral was crypto-/micro-crystalline quartz (with some fibrous habit) [3]. Such aggregates had already led to catastrophic ASR damages in several concrete structures such as bridges and water management ones.

The original specimens of both types were cast as cubes with size of $300 \times 300 \times 300 \text{ mm}^3$. They were exposed to the open environment in Valencia (Spain) for 13 years. No mechanical load was applied to them, such that they could expand freely, as happening for laboratory-accelerated specimens. In 2017, both specimens were cut (as cylinders with different lengths, L_{field} , in the range of ~ 50 -70 mm, and with a diameter of ~ 40 mm) to sample out at locations of interest, mainly from interior parts, to avoid collecting samples affected by carbonation. These specimens were first tomographed as they were received. Later smaller rectangular sub-specimens were carefully cut (with a diamond saw), with sizes of $15 \times 15 \times L_{field} \text{ mm}^3$ (where L_{field} was the longitudinal size of the specimen, in the range ~ 20 -30 mm). Two sub-specimens were derived from each specimen and tomographed. Before cutting these smaller sub-specimens, the larger cores were first impregnated in the epoxy resin, in order to stabilize them as much as possible and to avoid introducing any damage propagations due to the cutting stress and vibrations.

4.2.2. Characterizations

4.2.2.1. Laboratory-accelerated specimens

At 18 distinct time points over the course of 500 days, six specimens (always the same ones), for each aggregate type and of each size, were taken out of the oven used for the ASR acceleration, to measure their mass and length (size along the specimen longitudinal direction) changes. The SEM-BSE measurements were carried out on all types of lab specimens cast with B, P and U aggregates at 50, 150 and 500 days to identify the morphology of the ASR products. The EDX analysis was also performed on all of these specimens only at 150 days to assess the chemical composition of the ASR products.

4.2.2.2. X-ray tomography

For the laboratory-acceleration case, time-lapse XT was carried out at three time points (50, 150 and 500 days after ASR acceleration onset) on the same exact specimen (one of the six specimens on which the length and mass measurements were performed), for each size and each aggregate type. The XT was not performed earlier than 50 days because relevant expansion was measured for similar test specimens only after about 40-60 days. Therefore, it was assumed that, given the XT configuration and the consequent spatial resolution, ASR cracks would become resolvable only starting about that time. Nevertheless, the XT was performed also at 1 day just for one different specimen cast with P aggregates. The same specimen was additionally tomographed at 150 and 250 days.

The XT on the B40, P40 and U40 specimens as well as the larger field specimens (40 mm in diameter) was carried out with the same settings as described in Section 3.2. The b25, p25 and u25 specimens were also tomographed with the same settings as the larger specimens, except for the source-to-specimen distance d_{ss} , which could be reduced from 113.62 mm for the latter to 71.38 mm for the former. As a consequence, the effective spatial resolution for such small, field-exposed specimens could be raised to 50 μm .

The field-exposed sub-specimens (those with cross-section of size $15 \times 15 \text{ mm}^2$), were tomographed with a different configuration. The second X-ray source available on the tomograph was adopted, a Hamamatsu L10711-02, which is, contrary to the other source described in Section 3.2, a direct transmission

micro-focus source. The L10711-02 is equipped with a LaB₆ filament and a 1 µm-thick W target deposited on a 500 nm-thick diamond support. This filament and target combination allows reducing significantly the source's focal spot size f_s , which, according to Hamamatsu specifications, is in the range of about 2-3 µm at the voltage and current levels it was operated (140 kV and 180 µA). Thus, with this source, higher spatial resolution for the smaller specimens could be achieved than for the larger specimens tomographed with the other source, at the cost of longer measurement time, since the latter is characterized by higher X-ray photon flux. The same detector as described in Section 3.2 was used to tomograph any specimen and each acquisition consisted of 3600 radiographs as well. The effective spatial resolution achieved for the smaller specimens was ~ 0.02 mm.

In order to achieve a preliminary assessment of the specimen size's influence on the resolvable ASR cracks' size, the larger laboratory-accelerated specimens were carefully cut to smaller size, then tomographed again. This means, for example, that, after the last tomography on the B40 specimen, it was cut to a cross-sectional size of 25×25 mm² (new specimen B40-cut-25). Such sub-specimens were tomographed with the same settings as for the 25×25×100 mm³ specimens.

The holding set-up 1 described in Chapter 2 was used for all the specimens.

4.2.2.3. Time-lapse X-ray tomography analysis

Steps (I) and (II) (image enhancement and specimen misalignment correction) of the time-lapse tomograms analysis workflow described in Section 3.3 were applied for any laboratory-accelerated specimen. The crack network segmentation did not follow the TS-based workflow described in Section 3.3, since such workflow was developed later than the acquisition and analysis of most of the tomograms in this experimental campaign. That segmentation was carried out according to the more time consuming workflow based on the black top-hat morphological transform (BTH, see Section 3.3, step (III), the subsection titled as "Empty crack segmentation"), for any specimen type. Once the cracks were segmented, they were digitally labelled and some of the quantitative characterizations described in Section 3.3, step (IV), was applied to the crack networks. Specifically, the following crack network feature variables were computed.

Only for one specimen the TS-based workflow described in Section 3.3 was implemented. This specimen was an additional specimen produced by P aggregates, which was tomographed from one day after exposure to the ASR acceleration protocol, and at two additional time points, 155 and 250 days. The results of this specimens are shown in Figure 4.5.

Cracks' volume fraction

The first quantitative characterization and comparison of the ASR cracking in distinct specimen types was carried out based on the total volume fraction of the segmented cracks, defined as

$$\tilde{V}_{cracks}(t_i) = \frac{V_{cracks}(t_i)}{V_{tomogram}} \cdot 100 [\%] \quad (4.1).$$

Equation (4.1) is similar to (3.6) in Section 3.3, with $V_{tomogram}$ indicating the total volume of any tomogram and $V_{cracks}(t_i)$ the total volume of cracks segmented in the whole tomogram at any time point t_i , $\forall i = 1, \dots, N_t$, independently of whether they were located inside aggregates or inside the cement paste. The only difference between the volume fraction defined in Eq. (4.1) and the one defined in

Eq. (3.6) is that the latter refers only to ASR-generated cracks, since the volume of segmented cracks at the reference time point t_0 is subtracted from the corresponding volume at t_i . Due to the systematic lack of tomograms at t_0 in this experimental campaign, both for the laboratory-accelerated and for the field specimens, the crack volume fraction of Eq. (4.1) includes the contribution of cracks already existing at t_0 , i.e., at the ASR acceleration onset (1 day after casting).

The quantitative comparison of \tilde{V}_{cracks} values between the laboratory and the field specimens involved, for the laboratory specimen, only the value at last time point $t_{N_t} = 500$ days.

Local thickness and shape tensor analysis

The local thickness, $T_{local}(\vec{x})$, was computed within the region occupied by each segmented crack at t_{N_t} , for the laboratory specimens. It was also computed for the region of each segmented crack in the tomograms of the field specimens. See Section 3.3, step (VI) of the image analysis workflow, for its definition and meaning. By comparing the distribution of T_{local} values for crack networks of the two distinct specimen types, a comparison between them in terms of crack thickness could be performed.

In terms of crack length, the crack networks were compared based upon the definition of crack length L also provided at step (VI) of the image analysis workflow described in Section 3.3 and based upon the size of the bounding box along the direction of the *eigenvector* \hat{u}_1 of the shape tensor \mathbf{G} (see Eq. (3.7)) associated with its first and largest *eigenvalue* λ_1 .

The crack orientation was defined as the orientation of \hat{u}_1 , represented by its spherical coordinates $(\varphi_1; \theta_1)$ on the unit sphere, as defined at step (VI) in Section 3.3. as well. In order to qualitatively classify and compare the crack shape, the elongation E and the flatness F feature variables, defined by Eqs. (3.8) and (3.9), respectively, were computed based upon the calculation of the *eigenvalues* of \mathbf{G} . The statistical *ensembles* of $(E; F)$ values for the laboratory specimens and the field ones were then compared with each other. An example of the bounding box of an individual crack segmented from one tomogram of a laboratory specimen is provided by Figure B6 in Appendix B.

4.3. Results

4.3.1. Laboratory-accelerated specimens

4.3.1.1. ASR-induced macroscopic dimensional changes

The relative changes (with respect to the value at t_0) in specimen length and mass are shown in Figure 4.1, for any specimen type. The specimens cast with the U aggregates achieved the highest level of expansion, at any time point (Figure 4.1 (a) and (b)). The P aggregates had the lowest maximum temporal expansion. These results were independent of the specimen size. The latter mainly influenced the range of relative length change values: the larger specimens expanded maximally (in time) between 2 and 3 times more than the smaller ones, depending of the aggregate type.

From a qualitative point of view, the expansion of any specimen type could be described approximately as piece-wise linear. The specimens cast with the U aggregates exhibited an expansion rate which was

higher within the first 100 days and similar afterwards, compared with the rate of the two other specimen types. This expansion patterns was observed independently of the specimen size. It confirmed the expected "fast-reacting" nature of the U aggregates, given their mineralogical texture [4], [5]. The specimens cast with the two other aggregate types exhibited similar expansion patterns and levels, which could also be ascribed to their similar mineralogical textures, both belonging to the category of metamorphic rocks [5].

The mass increased with a similar trend for any specimen type, the smaller specimens achieving gaining slightly less mass compared to the larger ones (Figure 4.1 (b) and (a), respectively). The specimens cast with U aggregates gained the highest mass at almost all time points. The mass increase can be attributed to the uptake of the alkaline solution the specimens were immersed into.

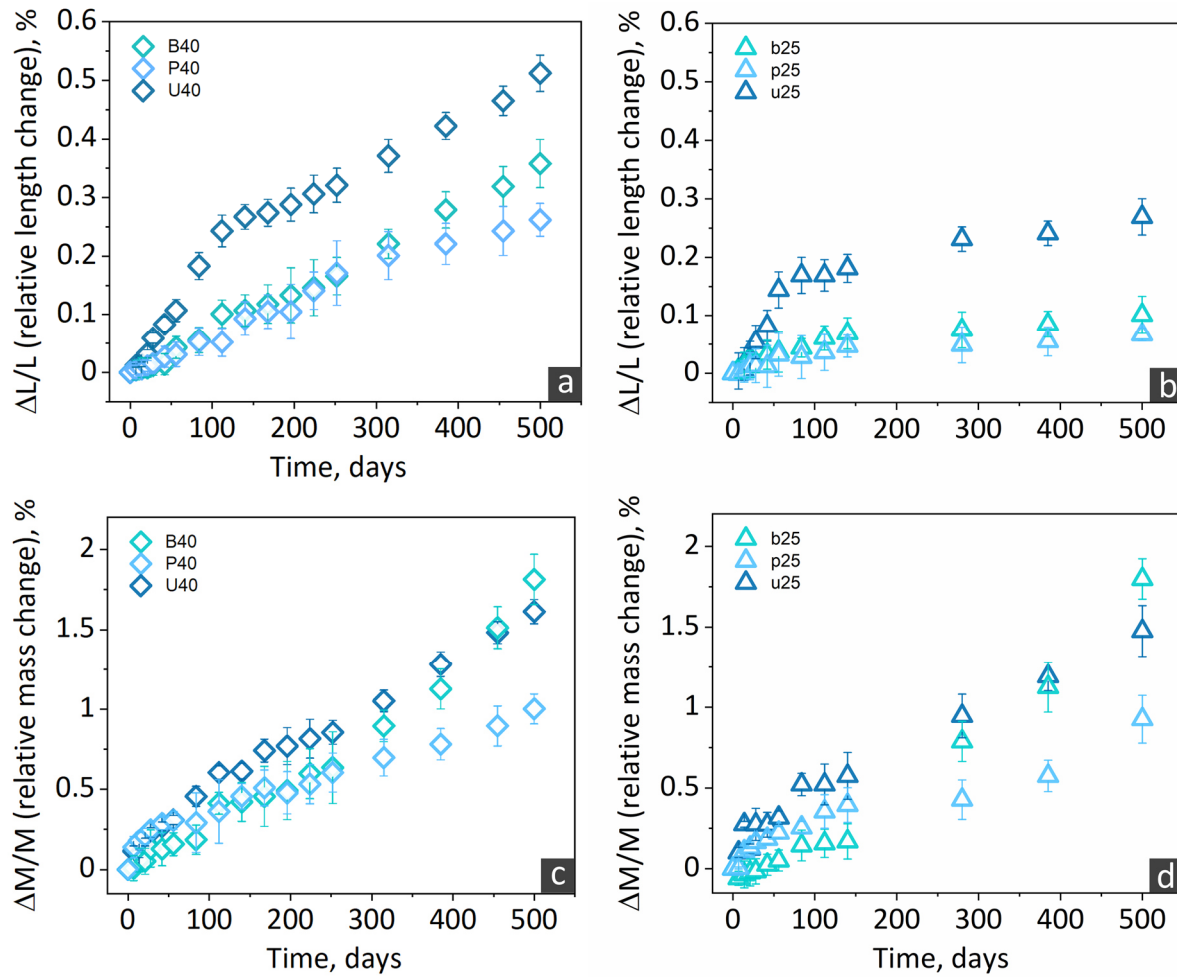


Figure 4.1. Evolution of the relative change (with respect to the start of the ASR acceleration) in specimen length for the specimens cast with the three aggregate types (B, P and U) and with size of (a) $40 \times 40 \times 160 \text{ mm}^3$ and (b) $25 \times 25 \times 100 \text{ mm}^3$, respectively. The numbers 40 and 25 in the legends indicate the corresponding cross-sectional size of each specimen. Corresponding evolution of the relative change in specimen mass for the specimens with size of (c) $40 \times 40 \times 160 \text{ mm}^3$ and (d) $25 \times 25 \times 100 \text{ mm}^3$, respectively. In each plot, the marker indicates the average value from the set of six specimens cast for length and mass measurements. The error bar indicates the empirical standard deviation from the same set.

4.3.1.2. Chemical and morphological features of the ASR products

Figure 4.2 shows SEM-BSE micrographs of polished cross-sections of epoxy-impregnated specimens sacrificed at distinct time points for different purposes. At 50 and 150 days, the goal was to characterize the morphology of ASR products inside cracks. At 500 days, the goal was to gain an overview of the ASR crack patterns. The micrographs belonging to the same column refer to cross-sections from specimens cast with the same aggregate type, sacrificed at the distinct time points.

The ROIs shown in insets (a) to (f) were in the aggregates' interiors. There, ASR products with typical platelet-like morphology could be clearly identified within veins with μm -scale thickness (Figure 4.2 (a) to (f)), in agreement with what already reported extensively in the literature (see Section 2.4.2.2). Other ROIs, closer to the aggregates' boundaries, exhibited veins also filled with ASR products but they were feature-less (amorphous), as also already reported extensively in the literature.

Insets (g) to (i) of Figure 4.2 show the micrographs of ROIs from 500 day-old specimens. At such time, even wider cracks, only partly filled, could be observed spanning a long distance within aggregates and, for some of them, continuing as cracks within the cement paste. Big chunks of products were also identifiable in cracks within the cement paste, while others among such cracks were also empty.

It has to be noted that the time at which the micrographs were acquired allowed mainly to observe (micro-)cracks. Some of them may have originated from grain boundaries which, with time, filled up with products, opened up and propagated further as cracks. However, there was no possibility to distinguish between a crack propagated from a filled grain boundary and a crack evolved from a smaller one existing already at the beginning of the ASR acceleration. As shown in [6], grain boundaries filled with ASR products are typically at the hundreds nm-scale and are typically observed at the beginning of the ASR acceleration, after which they evolve into propagating cracks.

The EDX (point-)analysis results for the formed ASR products are summarized in Figure 4.3, showing the characterization of their chemical composition in terms of two typical atomic concentration ratios mentioned in Section 2.4.2.2, i.e., alkalis over Si and Ca over Si, respectively. The point analysis were carried out on two different cross-sections from each specimen, at 150 days. In addition to the data for laboratory specimens cast with any aggregate type, similar results for one of the field specimens, B1(C+F), are also shown in the same Figure, for easier comparison between specimens subjected to distinct boundary conditions.

Figure 4.3 shows that, for any given specimen type, the ASR products exhibited atomic concentration ratios values in ranges typically reported in the literature (see Section 2.4.2.2). Products within/from U and P aggregates exhibited very similar concentrations, in agreement with the XRF and PXRD results mentioned in Section 3.2 and reported in Section A1.1 of the Appendices, which already indicated very similar chemical compositions. The specimens cast with the B aggregates exhibited systematically lower Ca/Si ratio values compared to the other two types of aggregates. When comparing laboratory-accelerated and field-exposed specimens, the products' composition was, for the analysed specimens, quite similar only in the case of the laboratory specimens cast with the B aggregates. Such a chemical composition similarity between some laboratory-accelerated and some field-exposed specimens, including some from the same exposure site the specimens here analysed came from, was already reported by Leemann *et al.* [7]. Via Raman spectroscopy, they additionally showed that laboratory specimens accelerated via the CPT protocol exhibited products with molecular structure similar to that of products found in the field specimens, mainly consisting of SiO_2 -tetrahedra sheets [7].

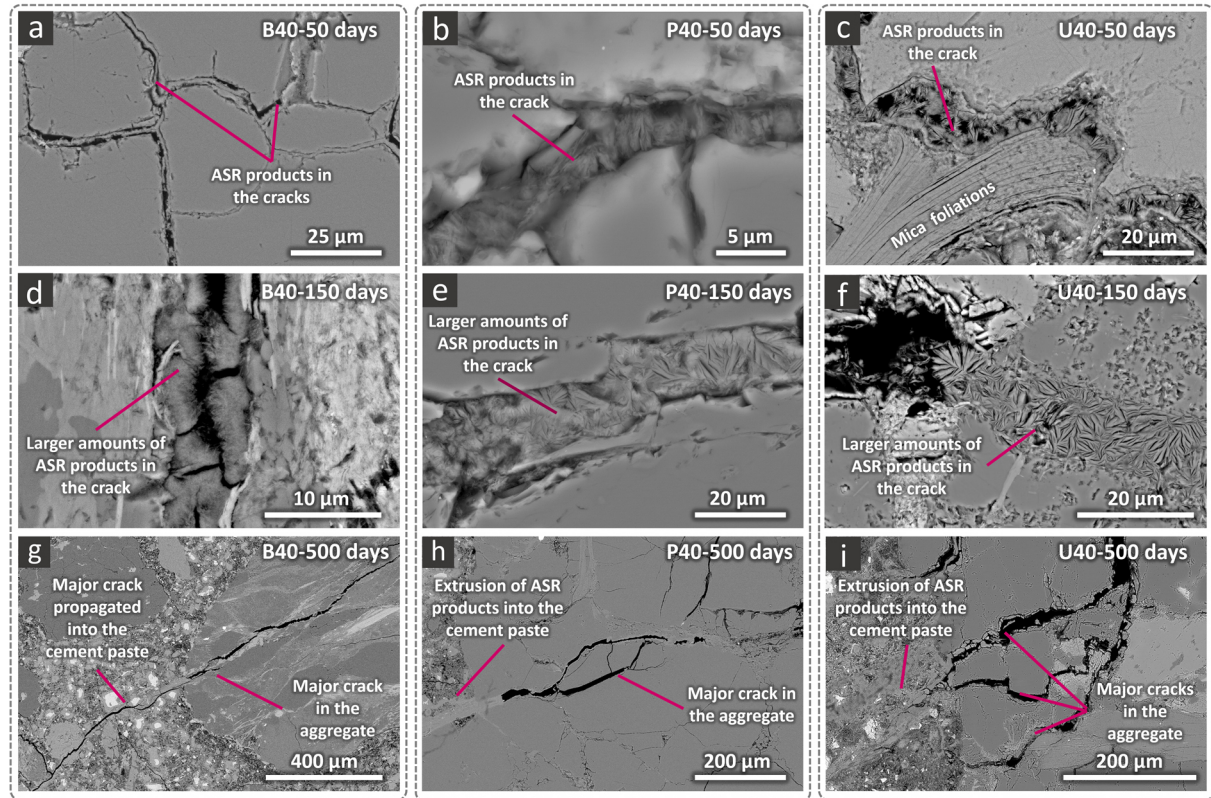


Figure 4.2. Examples of SEM-BSE micrographs of polished and epoxy-impregnated cross-sections from different specimens cast with B, P and U aggregates (within each column, highlighted with dotted boxes), acquired at (a) - (c) 50 days, (d) - (f) 150 days and (g) - (i) 500 days of ASR acceleration, respectively.

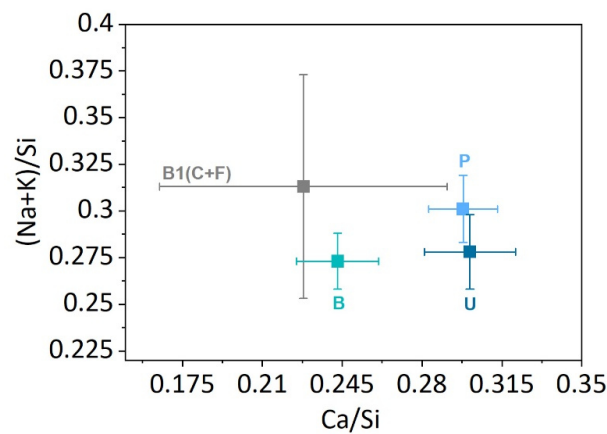


Figure 4.3. Energy-dispersive X-ray spectroscopy (EDX) analysis results, showing two atomic concentration ratios (alkalis over silicon and calcium over silicon) measured at more than 30 points located in regions of both crystalline (well inside the aggregates) and amorphous (at the aggregate boundaries and within the cement paste) ASR products. Each marker indicates the average value over the whole set of measuring points, while the error bar was defined as the empirical standard deviation of the same set. In addition to the results for the laboratory-accelerated specimens, cast with the three aggregate types, similar results are also shown for one of the field-exposed specimens, the B1(C+F) one.

4.3.1.3. ASR cracking: time-lapse tomography qualitative analysis

Figure 4.4 provides, for any specimen type and with size $40 \times 40 \times 160 \text{ mm}^3$, an example of a 2D tomographic slices from a ROI at multiple time points. Similar examples but for the corresponding specimens of size $25 \times 25 \times 100 \text{ mm}^3$ are provided in Figure B2 in Appendix B, Section B2.1. As already mentioned in Section 4.2.2.2, the starting point of each XT time series was at 50 days since starting the ASR acceleration protocol. However, in order to evaluate the original state of the aggregates before ASR acceleration, an additional specimen cast with P aggregates was tomographed immediately one day after ASR acceleration start, then at 150 and 250 days. A slice from the time-lapse tomograms of this specimen is shown in Figure 4.5, at each of the three time points. It has to be noted that, for any given specimen, a slice time series shows exactly same ROI. That is because the time-lapse tomograms were registered using the full registration workflow described in Section 3.3.

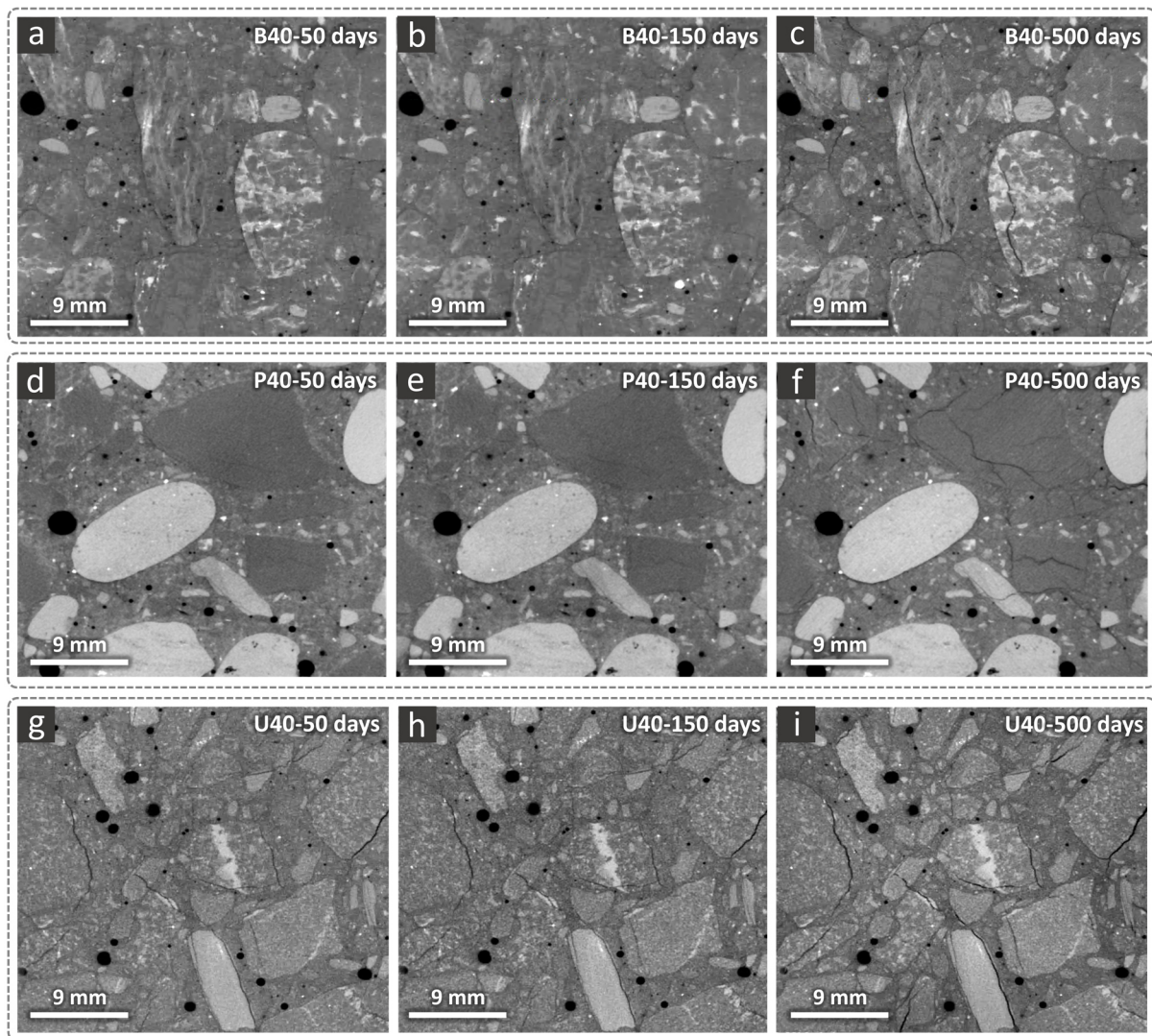


Figure 4.4. Examples of tomographic slices from ROIs of the B40, P40 and U40 specimens, shown at three different time points to characterize qualitatively the ASR cracking. The first row shows always the slice at the same position from the tomograms of a B40 specimen, acquired at (a) 50 days, (b) 150 days and (c) 500 days, respectively. The second row, insets (d) to (f), shows something similar but for a P40 specimen. The last row, insets (g) to (i), shows a similar example but for a U40 specimen.

The visual inspection of the tomographic slices from the tomogram at 1 day of such additional P40 specimen, as shown in Figure 4.5 (a) by one single example, indicated the presence inside the aggregates of (micro-)cracks, large enough to be resolved, which were inherent features. Such (micro-)cracks as well as smaller ones, not resolvable in the acquired tomograms, and even smaller inherent aggregate features, such as mineral grain boundaries (existing at length scale of tens/hundreds of nm), are known to play a significant role in the initiation and development of ASR cracking [8]. Due to the spatial resolution limitations of the performed XT measurements, the detection of the finer aggregate structural features, i.e., grain boundaries and sub- μm - and μm -scale cracks, was not feasible in the experimental campaigns of this PhD project. This implies that it was not possible to resolve ASR cracking since its very early stages, when, likely, opening up grain boundaries and micro-cracks and nucleating the first new micro-cracks. However, it was still possible to observe ASR cracking in action at least when involving the larger inherent cracks with size above the tomographic spatial resolution, as exemplified by comparing Figure 4.5 (a), (b) and (c). In Figure 4.5 (b), it can be clearly seen that the inherent crack highlighted in inset (a) propagated further and its thickness increased with time. Such crack also advanced through the cement paste and joined another crack evolving within another aggregate.

Not all the resolved and segmented cracks originated from inherent ones with size above the spatial resolution. Several cracks appeared at certain point in the tomographic series. The lack of higher spatial resolution did not allow tracing back their origin. However, they typically followed a temporal pattern as the one described above: since the time point they could be resolved in a tomogram, they were observed propagating further through the aggregate volume, some of them even beyond it, through the cement paste, increasing both in length and thickness, as clearly showcased by the examples in Figure 4.5 (b) and (c). The 3D rendering of the segmented crack network, shown at distinct time points in Figure 4.5 (d) – (f), suggest that the cracks were distributed rather homogeneously inside the tomographed volume and their network consisted of a rather dense combination of long and shorter ones.

The crack network's qualitative evolution exhibited by the additional P40 specimen was similarly followed by the other specimens, independently of aggregate type and specimen size. However, one key difference was observed between the specimens cast with the U aggregates and those cast with the two other aggregate types. While at 50 days very few cracks with thickness just above the tomographic spatial resolution were detected in specimens cast with the B and P aggregates, independently of the specimen size, such thin cracks were detected in the U40 (Figure 4.4 (g)) and u25 (Figure B2 (g)) specimens. Such an observation correlates well with the macroscopic length change shown in Figure(a) and (b). Indeed, regardless of their size, the specimens cast with the U aggregates expanded at a higher rate at the beginning of the ASR acceleration and reached, at 50 days, larger length change values, compared with the specimens cast with the B and P aggregates. At 150 days, the specimens with B and P aggregates exhibited qualitatively a similar cracking extent as at 50 days, with no clear evidence of a strong dependence on the specimen size, especially for the specimens with the B aggregates. On the contrary, further crack propagation and widening could be already observed between those two time points for the specimens with U aggregates. For any specimen type and size, the crack network evolution between 250 and 500 days was extremely clearly characterized by the appearance of new cracks and the increase in the length and thickness of those already observed at 250 days. Cracking through the cement paste was also systematically observed.

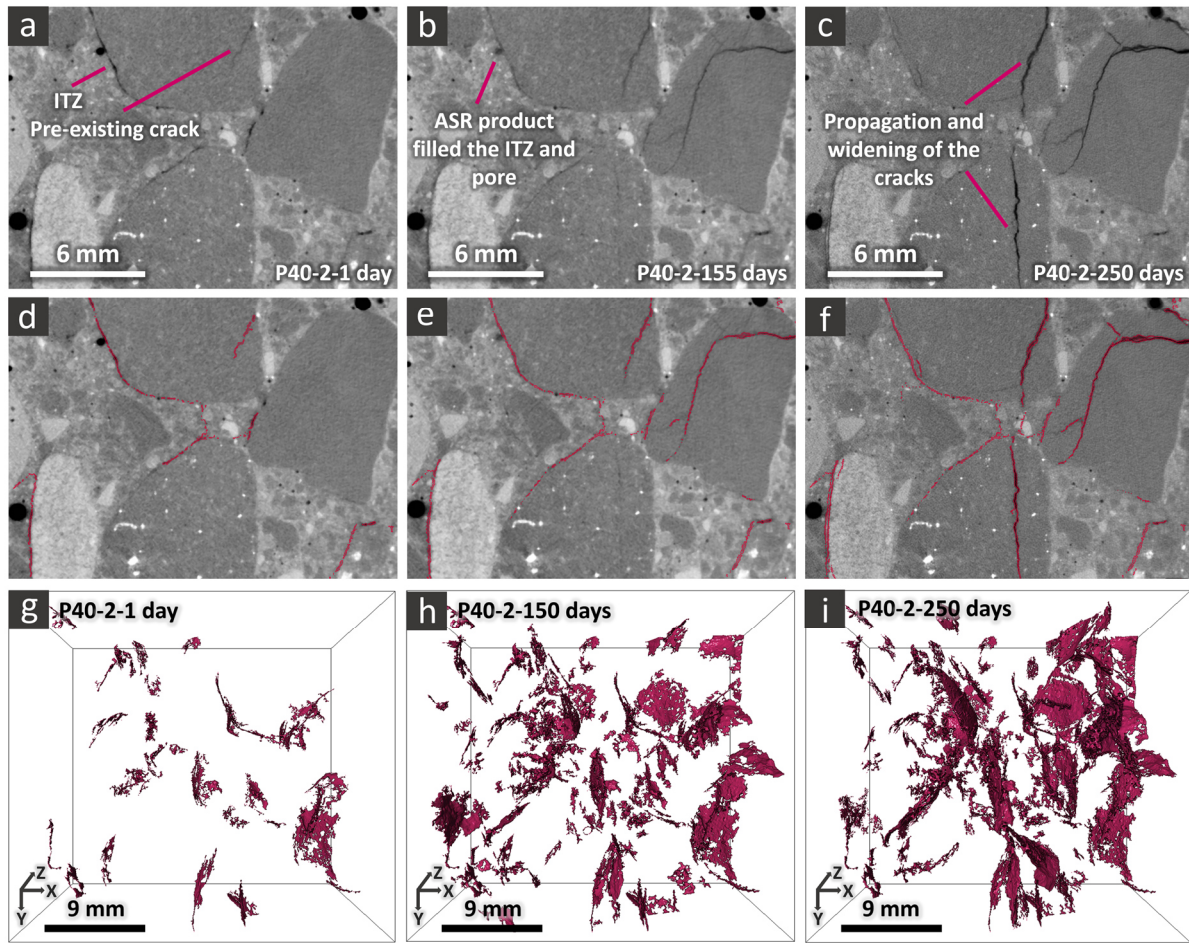


Figure 4.5. (a)-(c): example of a slice from a ROI of an additional P40-2 specimen, obtained from its tomograms at three time points different from the ones used for XT on the other specimens, (a) 1 day, (b) 155 days, (c) 250 days, respectively, during ASR acceleration. The corresponding slice from the corresponding binary tomograms of the segmented cracks is superimposed over the respective X-ray tomogram's slice at (d) 1 day, (e) 150 days and (f) 250 days. The full binary tomograms of the segmented cracks are rendered in 3D in insets (g) to (i), for the three distinct time points, respectively. In each inset (g) to (i), the parallelepiped box surrounding the crack network indicates the specimen's tomographed volume.

In order to compare (qualitatively) the cracks spatial distribution, the crack networks segmented in the tomogram at 500 days were 3D rendered as solid objects. They are shown in Figure 4.6 for the larger specimens. Analog 3D renderings but for the smaller specimens are additionally shown in Figure B3 in the Appendix B.. Regardless of the aggregate type and specimen size, the 3D rendering allowed assessing qualitatively that the cracks were distributed homogeneously. The 3D rendering also allowed confirming, although still only qualitatively, that the specimens with U aggregates developed more extensively cracks.

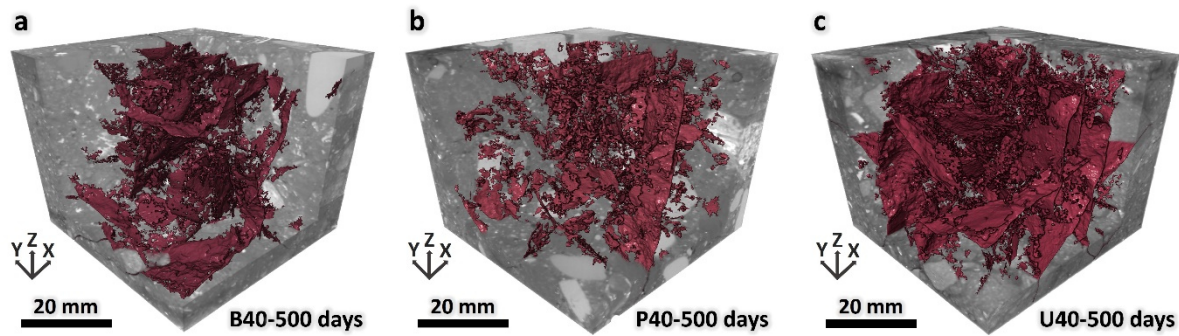


Figure 4.6. 3D rendering of the segmented cracks binary tomograms (in dark red) at 500 days since ASR acceleration start, for the laboratory specimens (a) B40, (b) P40 and (c) U40. In each inset, a small part of the concrete was also rendered (in grey tones), while the most of it was corner-cut to reveal the segmented cracks inside it.

4.3.2. Field specimens

4.3.2.1. ASR-induced macroscopic dimensional changes and morphological features of the ASR products

No data were obviously available for the BF-40 specimens, since it was directly derived from coring out of an aged structure and not subjected to further ASR acceleration in the laboratory. On the contrary, the relative length change of the B1(C+NRF)-40 and B1(C+F)-40 specimens were measured within the context of the EU PARTNER project [3]. Such measurements indicated a continuous expansion with approximately constant rate. The B1(C+NRF)-40 and B1(C+F)-40 specimens reached the maximum expansion of 0.352 % and 0.356 %, respectively, after 13 years. The slightly lower final expansion level of B1(C+F) was attributed to the dissolution of its finer reactive aggregates (the sand particles). It was hypothesized that the alkalis involved in the finer aggregates' dissolution led to a reduction in alkalinity of the pore solution. The latter limited the expansion and cracking of the larger aggregates.

SEM-BSE micrographs acquired from the B1 (C+F) specimen showed that most of the ASR products in the aggregate interior regions were crystalline while those at the aggregate edges and detected in the cement matrix were amorphous [7], as commonly reported in the literature.

4.3.2.2. ASR cracking: X-ray tomography qualitative analysis

The tomograms of the field-exposed specimens are showcased in three distinct columns in Figure 4.7, each corresponding to a distinct one. The first row, Figure 4.7 (a)-(c), shows in each inset a slice from the tomogram. The second row, Figure 4.7 (d)-(f), show again the same slice with, in addition and overlapped on top of it, the slice taken at the same position from the binary tomogram of the segmented crack network, rendered in color, in order to showcase such segmentation results. Finally, the last row, Figure 4.7 (g)-(i), show the 3D rendering of the whole binary tomogram of the segmented crack network as well as the 3D rendering of the specimen's tomogram itself, mostly cut away to allow seeing the crack network inside the volume.

The visual inspection of the tomographic slices from all the specimens, Figure 4.7 (a)-(f), suggests similar ASR crack patterns as already observed for the laboratory-accelerated specimens (compare Figure 4.7 with Figure 4.4). Indeed, cracks were detected both inside the aggregates and in the cement paste. When comparing the B1 (C+NRF) and B1 (C+F) specimens, Figure 4.7 (b) and (c) respectively, it was qualitatively observed that the extent of the crack network was slightly smaller in the latter specimen as well as its cracks were slightly thinner. Such a qualitative observation correlates well with the relative length change results for both specimen types: a smaller expansion was measured for the B1 (C+F) specimen than for the B1 (C+NRF) one.

The 3D rendered crack network binary tomograms, Figure 4.7 (g)-(i), better allowed comparing the crack spatial distribution for the different specimens. Similar to what observed in the laboratory specimens case (Figure 4.6), the cracks were distributed homogeneously and consisted of larger and smaller branches were observed. They looked like having a broad range of curvatures and degrees of fragmentation. As expected, in comparison with the B1 (C+NRF) specimen, a relatively lower crack network volumetric density can be hypothesized for the B1 (C+F) specimen based upon the comparison of the 3D renderings (Figure 4.7 (h) *versus* Figure 4.7 (i)).

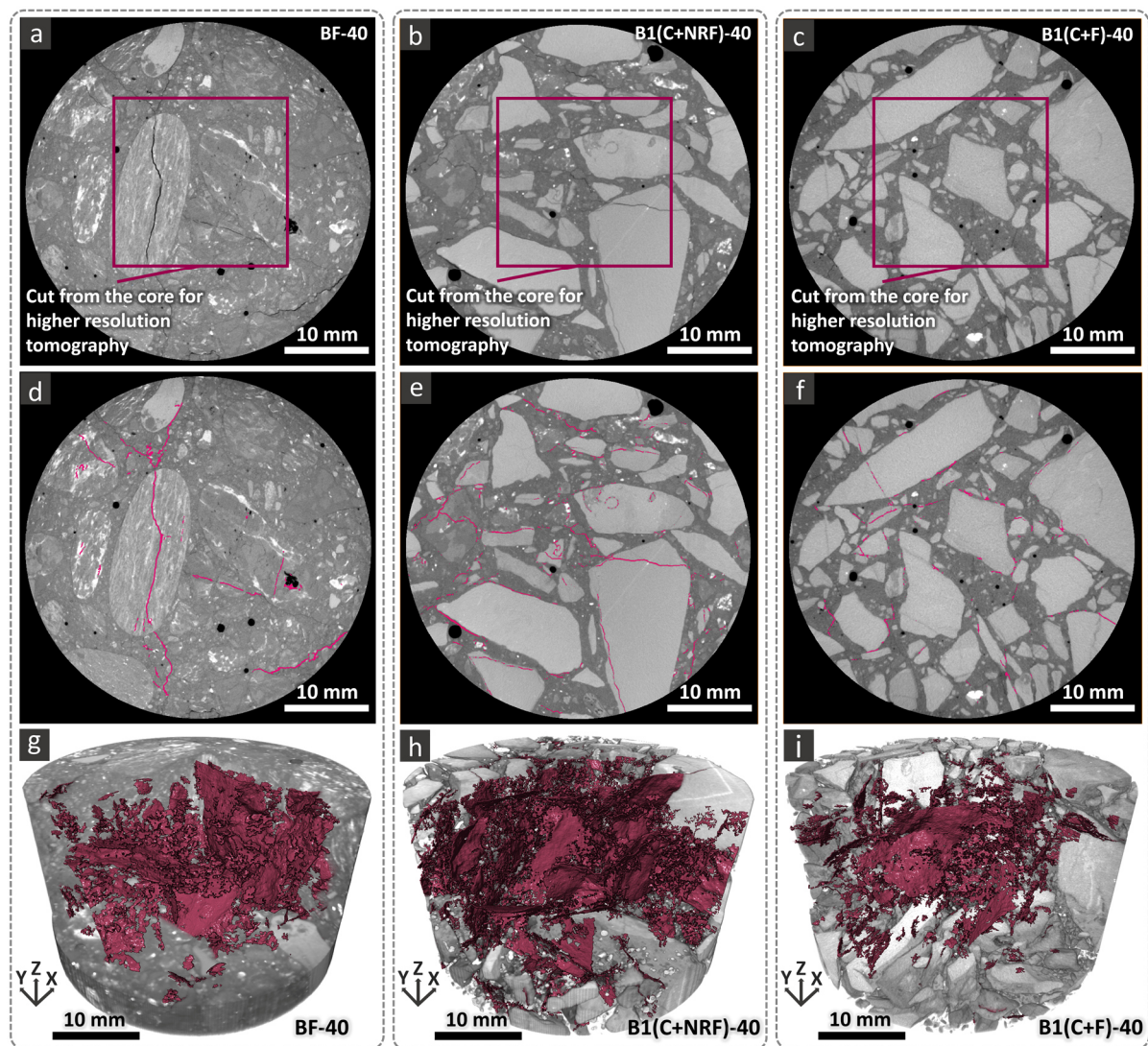


Figure 4.7. An example of a tomographic slice from each field-exposed specimen: (a) BF-40, (b) B1(C+NRF)-40 and (c) B1(C+F)-40 specimen, respectively. The rectangle in each inset indicates the smaller ROI which was cut out of the specimen in order to perform X-ray tomography with higher spatial resolution. Insets (d) to (f) show the same slices as in (a) to (c) but, in addition, overlapped on top of them, the corresponding slice taken at the same position from the binary tomogram of the segmented cracks. Such binary tomograms of the segmented crack networks are shown 3D rendered in (g) to (i), with part of the specimens also rendered in grey tones and partly not in order to allow viewing the segmented crack network inside them.

4.3.3. Quantitative comparison of the ASR cracking between laboratory and field specimens

As the first feature variable of the quantitative tomographic analysis, the time series of the segmented crack volume fraction, $\tilde{V}_{cracks}(t_i)$, $\forall i = 1, \dots, N_t$, are compared for the distinct specimen types in Figure 4.8. The evolution of \tilde{V}_{cracks} for the laboratory specimens of both size value ($40 \times 40 \times 160 \text{ mm}^3$ and $25 \times 25 \times 100 \text{ mm}^3$) over the five time points up to 500 days are shown in Figure 4.8 (a) and (b), respectively. Their \tilde{V}_{cracks} at the final point $t_{N_t} = t_f$ is plotted again in Figure 4.8 (c) along with the \tilde{V}_{cracks} value for the three field-exposed specimens.

Concerning the laboratory specimens, Figure 4.8 (a) and (b), the total crack volume fraction (Eq. (4.1)) correlated positively with the macroscopic length changes shown in Figure: independently of the specimen size, the specimens with the U aggregates exhibited the highest \tilde{V}_{cracks} values, at any time point. The specimens with the B aggregates reached slightly larger $\tilde{V}_{cracks}(t_f)$ values just as they achieved a slightly larger final expansion level, with respect to those with the P aggregates. Given any aggregate type, the \tilde{V}_{cracks} values were smaller for the smaller specimens, at any time point. For example, at the final time point $t_f=500$ days, the B40, P40 and U40 specimens reached about 0.34%, 0.33% and 0.39% larger $\tilde{V}_{cracks}(t_f)$ values than the b25, p25 and u25 ones did, respectively (see Figure 4.8 (c) for the comparison).

The \tilde{V}_{cracks} value for the BF40 specimen was closer to the $\tilde{V}_{cracks}(t_f)$ value of the B40 specimen than of the b25 one. The B1(C+NRF)-40 and B1(C+F)-40 specimens exhibited a \tilde{V}_{cracks} value in the same range as the $\tilde{V}_{cracks}(t_f)$ values of the larger laboratory specimens. The $\tilde{V}_{cracks}(t_f)$ value for the B1(C+NRF)-40 specimen was about 20% higher than that of the B1(C+F)-40 one, confirming what could be only hypothesized from the qualitative inspection of the 3D renderings of the segmented crack networks (Figure 4.7, inset (h) versus (i)).

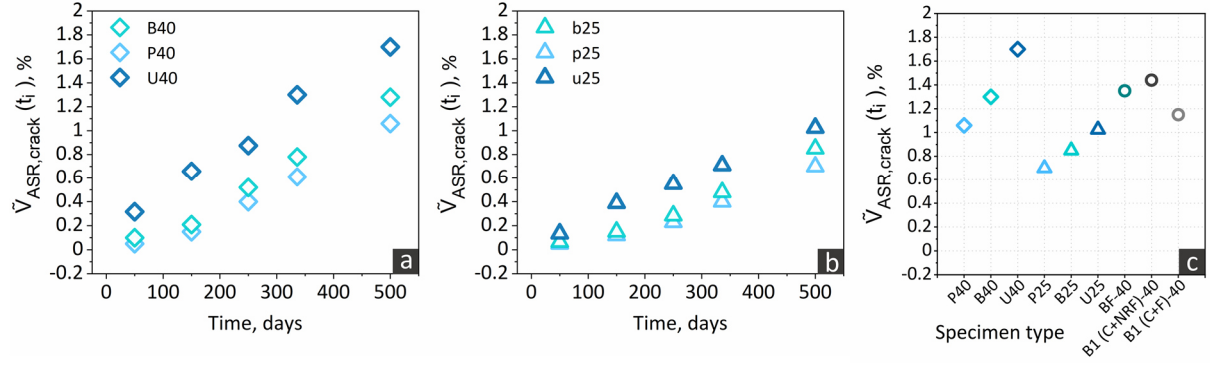


Figure 4.8. Quantitative comparison of the ASR cracking in different specimens based on the total crack volume fraction, \tilde{V}_{cracks} , as defined in Eq. (4.1), computed (a) for the laboratory specimens with size $40 \times 40 \times 160 \text{ mm}^3$, and (b) for the laboratory specimens with sizes $25 \times 25 \times 100 \text{ mm}^3$. The \tilde{V}_{cracks} values for both the laboratory (at the final time $t_f = 500$ days) and the field-exposed specimens.

Concerning the crack shape, Figure 4.9 shows the crack elongation *versus* flatness plane, ($E; F$), where each separated crack is mapped onto as a single point and the whole crack network corresponds to a cloud of points. For the laboratory specimens, only the crack networks at 500 days were considered, in order to compare them against the field-exposed specimens'. In such plane, acting as a crack shape phase diagram of sorts, points close to the $[1; 1]$ corner corresponds to 3D objects with shape of a very thin plate. Pseudo-cylindrical objects would be located closer to the $[1; 0]$ corner, while almost spherical ones would be found close to the origin of that Cartesian coordinate system. Any point in the middle would correspond to objects with more complicated and irregular shape.

The cloud of points corresponding to the crack network was interpreted as a statistical *ensemble* of sampled values for a corresponding bi-variate random variable ($\mathbb{E}; \mathbb{F}$). Its joint PDF was then estimated based upon such *ensemble*, using a kernel density estimate (KDE) approach implemented in the "2D Kernel Density" module of the software Origin Pro® 2020b (Ver. 9.7.5.184, by OriginLab®, Northampton, MA; USA). The KDE estimate of the joint PDF of ($\mathbb{E}; \mathbb{F}$) allows locating the regions in the ($E; F$) plane with higher occurrence of points than just the 2D scatter plot itself. Each point in the cloud is colored in Figure 4.9 according to a corresponding scale of values of the PDF.

Figure 4.9 shows that, regardless of the aggregate type, specimen size and boundary conditions, the majority of cracks were located towards the top-right corner, indicating that they could be approximately described as curved, thin plates similar to the single examples shown in Figures 3.5 and 3.6.

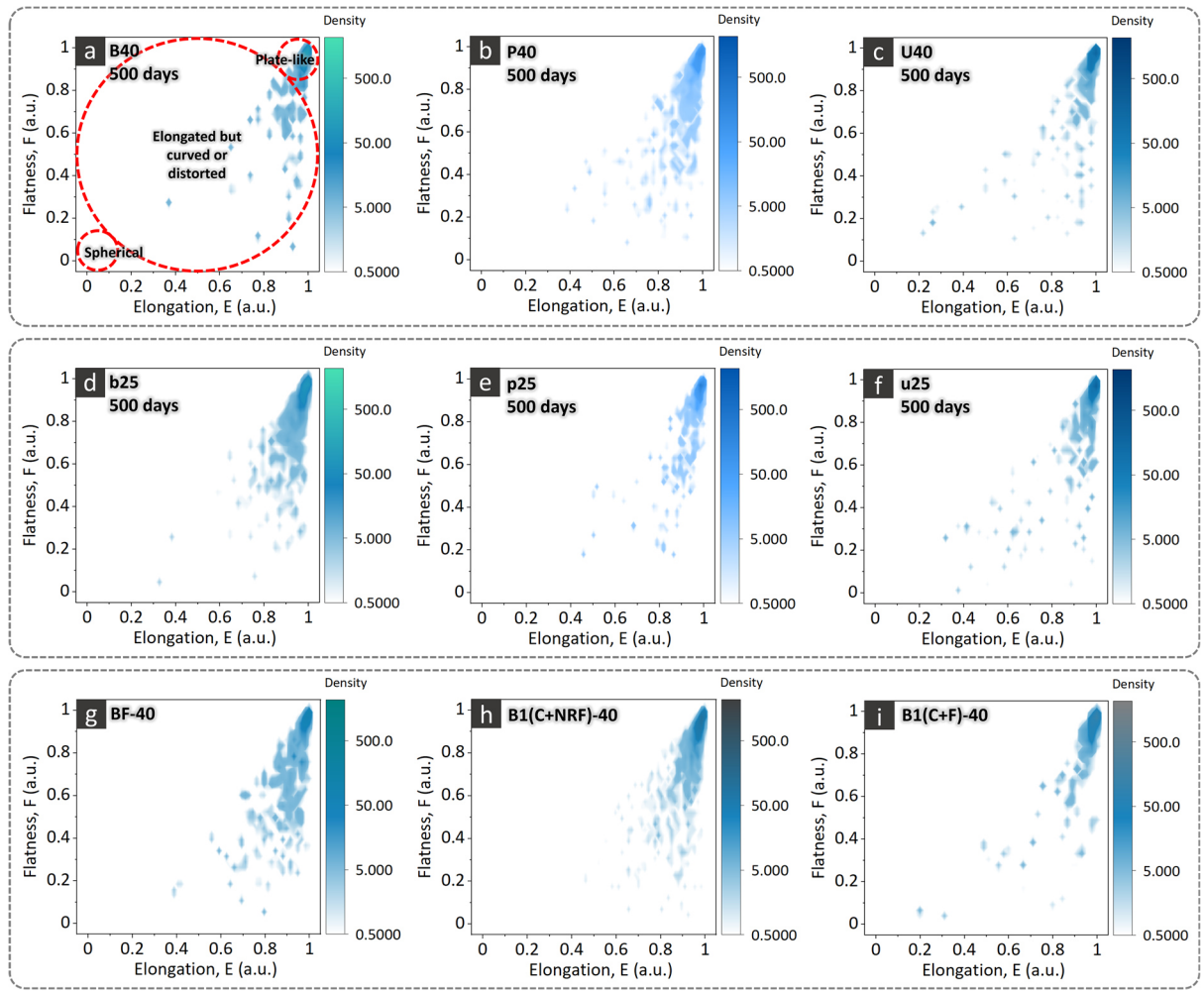


Figure 4.9. Plots of the kernel density estimate (KDE) of the joint probability density function (PDF) of the two shape feature variables, the elongation E and the flatness F , computed from the shape tensor analysis of the segmented total crack network and interpreted as a bi-variate random variable, $(\mathbb{E}; \mathbb{F})$. The statistical sample of such PDF was provided, for each specimen, by the set of values $\{(E_i; F_i)\}_{i=1, \dots, C}$ also plotted and obtained from the shape tensor analysis, where C indicates generically the total number of disconnected and independent cracks of a specimen at the chosen time point. (a) to (c): B40, P40 and U40 specimens, respectively, all at $t_f = 500$ days. (d) to (f): b25, p25 and u25, respectively, all at $t_f = 500$ days. (g) to (i): BF-40, B1(C+NRF)-40 and B1(C+F)-40, respectively. In all of the plots, the maximum value of the scale for the KDE estimates of the PDF is 3330.

Figure 4.10 (a) and (c) compares the distribution of crack bounding box length, L , values of all specimens, while Figure (4.11) (b) and (d) does the same for the local thickness, T_{local} , ones. Again, for the laboratory specimens, only the values at 500 days were considered. The distributions are presented in the form of a Zipf's plot, which typically shows the statistical *ensemble* estimate of the complementary cumulative distribution function (cCDF), $G_X(x)$, of a random variable X , in \log_{10} - \log_{10} scales [9]–[11]. The main reason for choosing such type of plot is that both L and T_{local} displayed, independently of the specimen type, right-skewed and long-tailed empirical PDFs. For a distribution with such properties, the Zipf's plot magnifies useful features in the long tail of the PDF. More importantly, it allows assessing whether the analyzed random variable may be distributed according to a power law PDF model or another type of long tailed PDF, e.g., an exponential or stretched exponential (also called Weibull) or gamma model [10], [12], [13]. In the case of a power law distribution, the data in the Zipf's plot should

be approximately located along a line while, in the case of the other long tailed distributions, the distribution should deviate from a line for a slight amount of downward curvature.

The distributions of crack size variables, especially length and thickness, for cracking in brittle materials have been extensively shown to be rather well described by one of such theoretical PDF models [14]. This is in agreement with the hypothesis that cracking in such materials may belong to a large class of processes characterized by (1) criticality and (2) (certain degrees of) scale invariance [15], two properties that lead to such types of distributions [12], [15]. Thus, crack size variables should be expected to follow qualitatively such types of distributions for cracking unperturbed by spurious damage sources, e.g., internal blast, superficial impact or fragmentation led by chemical attacks.

The larger laboratory specimens and the field ones exhibited very similar distributions of L values (Figure 4.10 (a)), with the only exception of the B40 specimen, which had slightly higher fractions of cracks at intermediate length values (between 5 and 10 mm). The T_{local} distributions (Figure 4.10 (b)) were also rather similar except for the two field specimens B1(C+F)-40 and B1(C+NRF)-40, which had significantly lower fraction for $T_{local} > 0.16$ mm. Particularly remarkable is the similarity of the T_{local} distributions for the B40 and BF-40 specimens, cast with the same aggregate type but subjected to completely different boundary conditions and aging time periods. The smaller laboratory specimens exhibited L and T_{local} ranges shifted towards lower values compared with the ranges for the larger respective specimens. While the aggregate type seemed not to have influenced the L values, it seems it played a more significant role in the distribution of T_{local} values, with the u25 specimen having significantly higher fractions of thicker cracks compared with the two other specimens of the same size.

Figure 4.11 shows the distribution of \hat{u}_1 for a given crack network. Each \hat{u}_1 is not only graphically rendered. Its projections on the planes of the Cartesian coordinate systems are also shown, to support the visualization. Each row in that Figure refers to a different specimen type and, inside a row, each inset shows the set of \hat{u}_1 's associated with the crack network at a fixed time point (500 days for the laboratory specimens).

On average, every laboratory specimen (first and second rows in Figure 4.11), exhibited a rather isotropic distribution of orientations. The B40, b25, U40 and u25 exhibited, compared with the P40 and p25, a slight preferential crack orientation (i.e., a small orientation anisotropy degree) along the Z axis and in one of the lateral directions Y or X . For instance, for the U40 specimen, the majority of the cracks were aligned prevalently along the Z direction and a bit more in the Y direction than in the X one. A slightly more frequent orientation along a specific direction implies that the direction of largest crack extent is spatially inclined (fully or partially) along that direction. Given that, according to the shape analysis results reported above, the majority of cracks had the shape of thin, curved plates, a slight preferential orientation in one direction implies that the crack thickness could contribute to the macroscopic dimensional changes preferentially in a direction orthogonal to the orientation direction. Concerning the field specimens (Figure 4.11 (g)-(i)), no sign of even a slight orientation anisotropy could be observed.

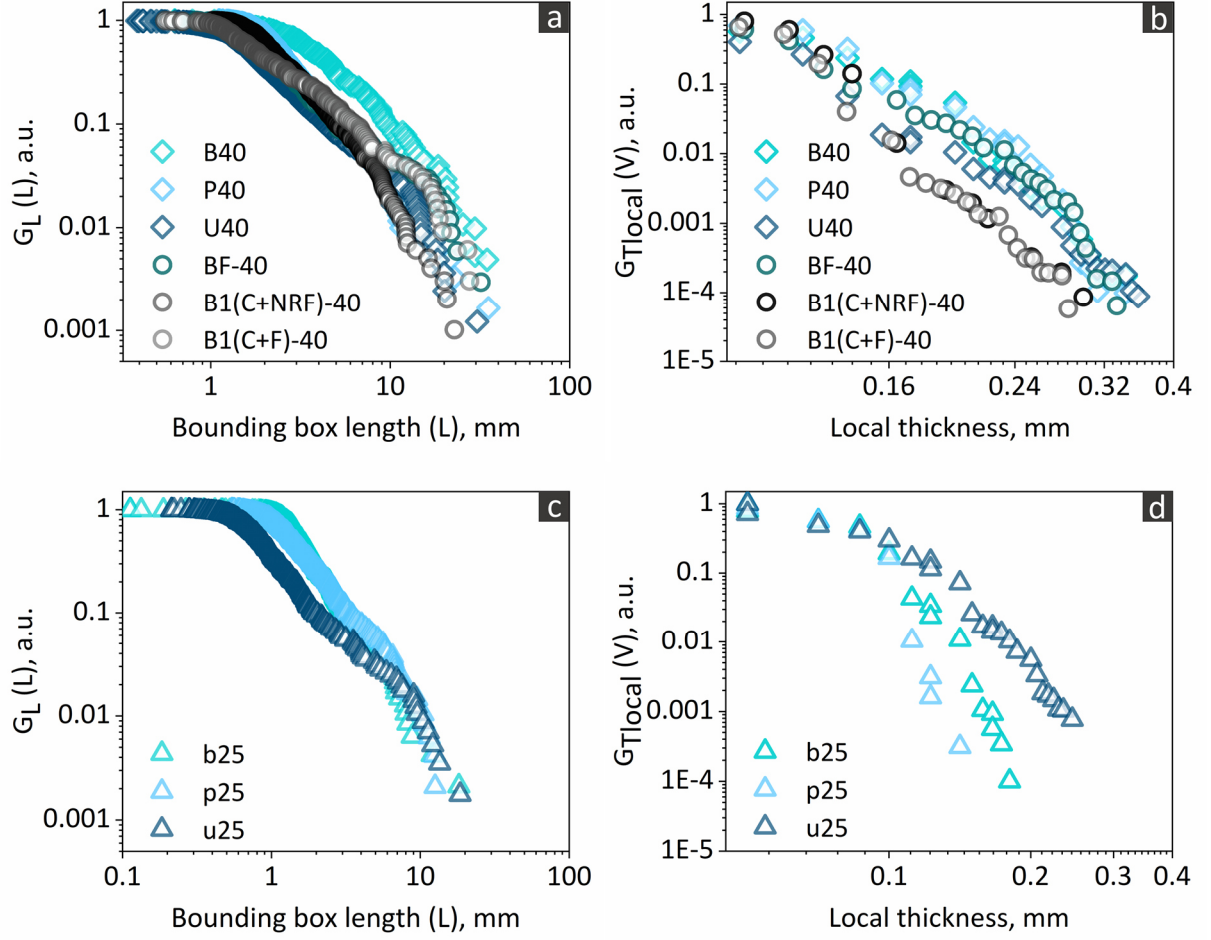


Figure 4.10. (a) and (c): empirical (i.e., from the statistical sample) complementary cumulative distribution function (cCDF) of the bounding box length, L , $G_L(L)$, in \log_{10} - \log_{10} scales (Zipf plot). Each separate crack contributed to one sampled value for L . (b) and (d): similar plots for the total crack network's local thickness, T_{local} , $G_{T_{local}}(T_{local})$. Each voxel inside the total crack network provided a sampled value. (a) and (b): comparisons of the Zipf plots of $G_L(L)$ and of $G_{T_{local}}(T_{local})$, respectively, between the laboratory specimens, B40, P40 and U40, and the field ones, BF-40, B1(C+NRF)-40 and B1(C+F)-40. (c) and (d): comparison of the Zipf plots of $G_L(L)$ and of $G_{T_{local}}(T_{local})$, respectively, for the b25, p25 and u25 specimens.

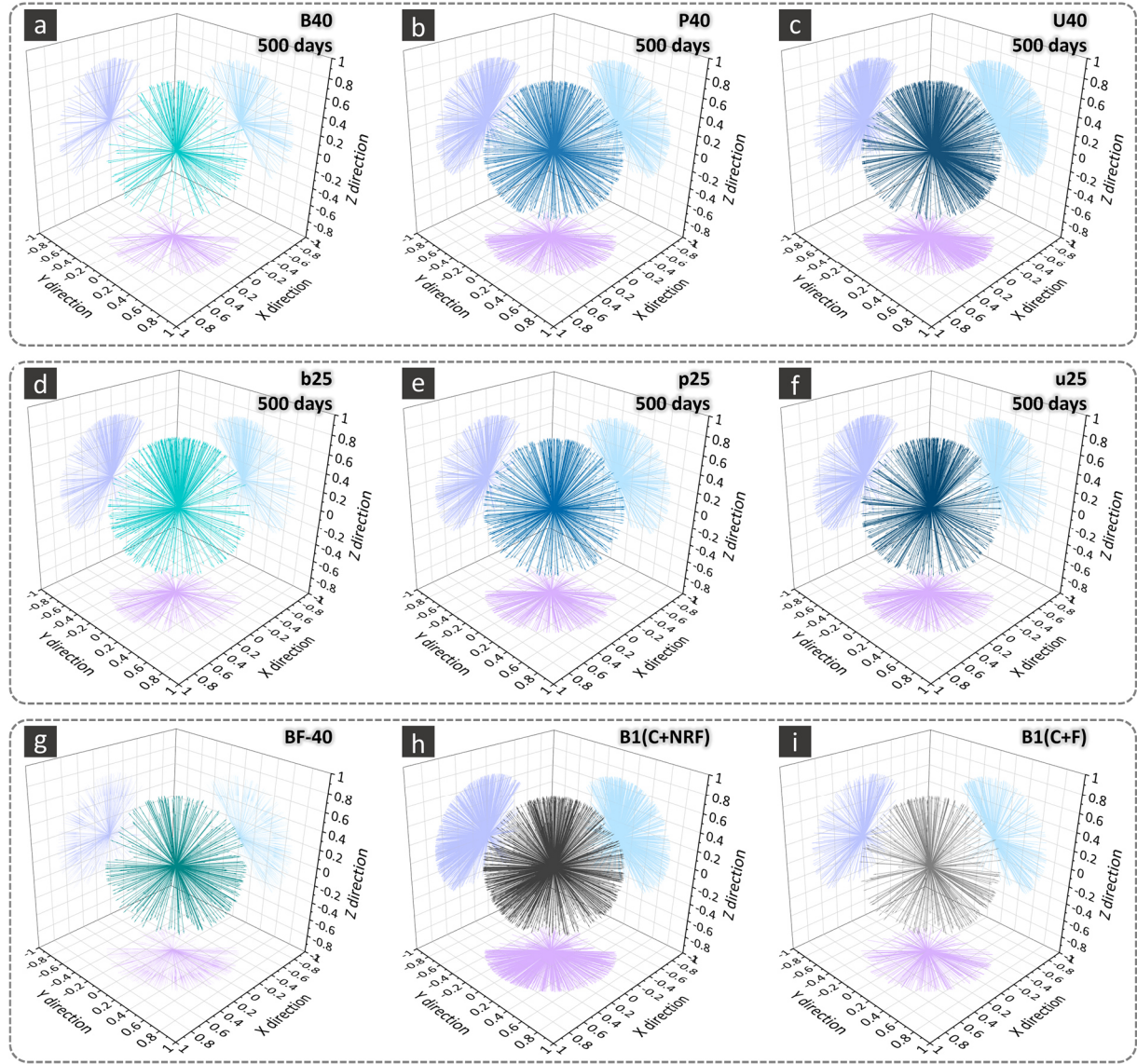


Figure 4.11. Visualization of the crack orientation analysis results. The crack orientation was operatively defined as the direction of the eigenvector \hat{u}_1 associated with the first and largest eigenvalue of the shape tensor \mathbf{G} . The segmented total crack network of a specimen corresponded to a set of \hat{u}_1 's, one for each independent crack. Each of these vectors are here plotted, after rescaling their magnitudes by a factor equal to 0.33, to make their projections on the planes of the Cartesian frame of reference more visible. The projections of \hat{u}_1 on the X – Y plane are in violet, those on the X – Z plane are in dark blue and those on the Y – Z plane are in light blue. (a) to (c): B40, P40 and U40 specimens, respectively, all at $t_f = 500$ days. (d) to (f): b25, p25 and u25, respectively, all at $t_f = 500$ days. (g) to (i): BF-40, B1(C+NRF)-40 and B1(C+F)-40, respectively.

4.3.4. Specimen size effect on the segmented crack network's features

In order to evaluate the specimen size effect, thus the tomographic spatial resolution, on the crack detection in the tomograms, a VOI of the B40 laboratory specimen at 500 days (labelled in the following as B40-cut-25), which was already part of the tomographed volume of that specimen, was cut out with size of $25 \times 25 \times 100$ mm³ and tomographed again (approximately at the middle of the specimen) at higher

spatial resolution. Figure 4.12 (a) shows a slice belonging to such VOI before it was cut out, i.e., still taken from the tomogram of the original B40 specimen. The corresponding region tomographed in the B40-cut-25 sub-specimen is shown in Figure 4.12 (d). With the increase in spatial resolution, it is clearly observable that the many features recognizable in both tomograms are clearly better resolved in the B40-cut-25 tomogram than in the B40 one. The higher spatial resolution implied larger portion of the crack network could be segmented. This result can be appreciated by comparing Figure 4.12 (b) and (e), where the same slices as in (a) and (d) are shown but with the corresponding slices from the respective crack network binary tomograms overlapped on them and colored. The whole crack network binary tomograms are 3D rendered in Figure 4.12 (c) and (f), respectively. Both the slices in insets (b) and (e), with a magnified ROI, and the 3D rendering in insets (c) and (f) show how the increase in the spatial resolution allowed refining parts of the crack network from the B40 specimen and contributed to add new, smaller regions to the network. The computed $\tilde{V}_{cracks}(t_f)$ values for both tomogram confirmed the latter qualitative observation: approximately 9% more crack volume fraction (Figure 4.13) was detected in the B40-cut-25 tomogram than in the B40 one.

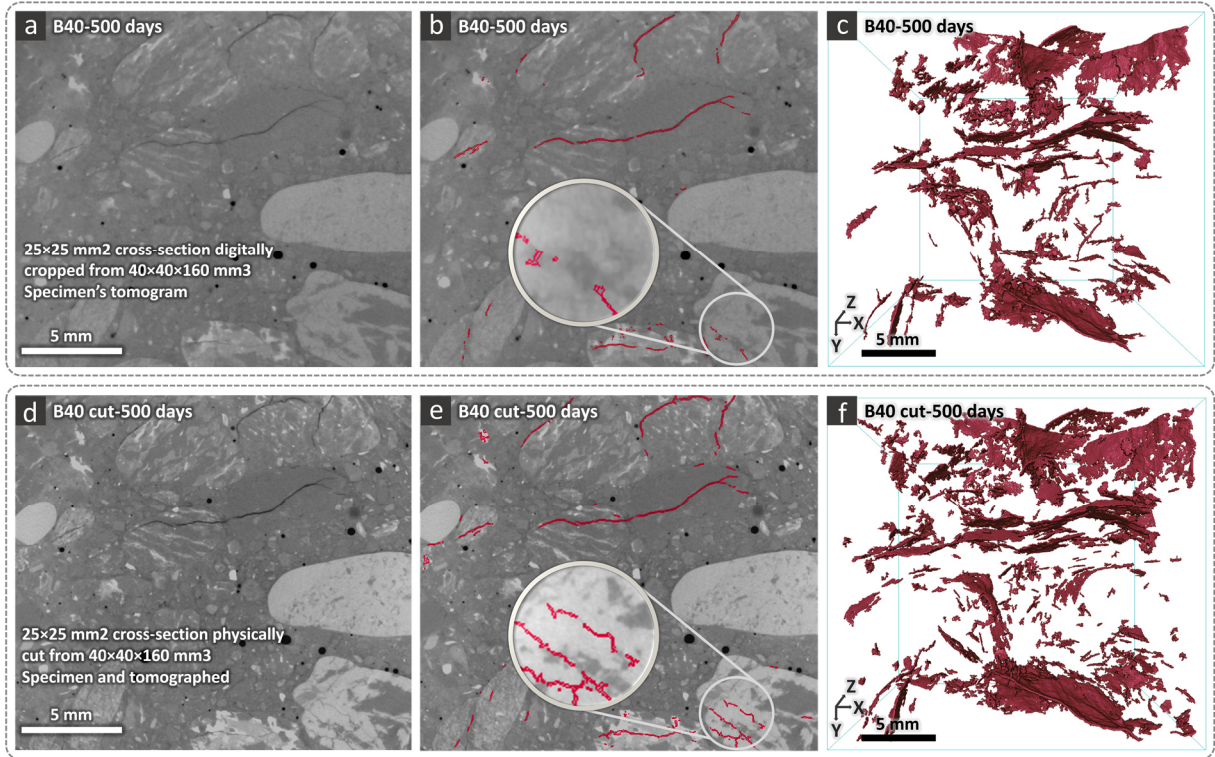


Figure 4.12. Example tomographic slices from a VOI of (a) the B40 specimen, (b) the corresponding binary tomogram of the segmented cracks overlapped on the same slice as in (a), and (c) the 3D rendering of the binary crack network. (d) to (f): the corresponding slices as in (a) to (c), respectively, but from the B40-cut-25 specimen, i.e., the sub-specimen obtained from B40 after cutting it to the cross-sectional size of $25 \times 25 \text{ mm}^2$, including the same VOI as shown for the original B40 specimen in insets (a) to (c).

A similar experimental assessment was performed for each field specimen. Slices from the tomograms of the smaller, cut sub-specimens and from the corresponding crack network binary tomograms are showcased in Figure B4. The computed \tilde{V}_{cracks} values for the tomograms of the original specimens and

of their sub-specimens are shown altogether in Figure 4.13 as well. The relative increase in \tilde{V}_{cracks} was for all the specimens in the range 12-14%.

The \tilde{V}_{cracks} values of the cut sub-specimens were, independently of the specimen type, higher than the $\tilde{V}_{cracks}(t_f)$ values of the b25, p25 and u25 specimens, which were tomographed at similar or slightly smaller spatial resolution. For example, the B40-cut-25 sub-specimen had a $\tilde{V}_{cracks}(t_f)$ value $\sim 58\%$ higher than the B25 specimen, even though the two differed exclusively in terms of original specimen size.

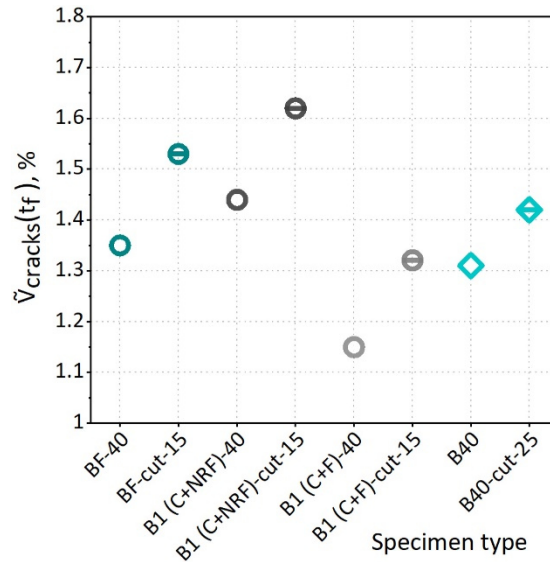


Figure 4.131. Quantitative comparison of the specimen size effect on the crack network segmentation results, in terms of crack volume fraction, \tilde{V}_{cracks} . The specimen labels containing "cut" refer to sub-specimens cut out from the original corresponding specimen, including a region already part of the one tomographed in the original specimen, such that the crack network could be segmented for the same exact region at two distinct tomographic spatial resolution levels.

4.4. Discussion

The laboratory specimens, accelerated with the chosen protocol, exhibited, independently of the aggregate type, both a significant propensity to ASR cracking and typical features of it, when compared with other concrete types also subjected to laboratory acceleration protocols.

At the whole specimen size, the propensity is testified by the levels of expansions achieved, independently of the aggregate type, the relative length changes systematically increased over time and reached to 0.25-0.5% expansion after 500 days (Figure 4.1). At the microscopic scales, the SEM/EDX analysis of the reaction products, both inside aggregates and inside the cement paste, showed they had typically observed morphological features (platelet-like structure, inside the aggregates, amorphous inside the cement paste) and typically reported chemical composition (Figures 4.3 and 4.4). At the mesoscopic scale, time-lapse XT and the respective image analysis allowed observing the evolution of several cracks, some of which were the continuation of others which were already observed at the first point in the tomographic time series. It was possible to observe several cracks increasing both in length

and in thickness. The observation of cracks also inside the cement paste was consistent with what systematically reported within the literature.

The comparison of all these features and properties between the laboratory and the field-exposed specimens allowed addressing some of the questions mentioned in Section 4.1 and concerning the representativeness of the laboratory-accelerated ASR cracking when compared with that occurring in the real world at much longer time scales and under distinct boundary conditions changing seasonally and daily. Instead of answering such questions only based upon typical petrographic analysis with optical microscopy and/or SEM/EDX and upon expansion measurements, the quantitative analysis of X-ray tomograms, specifically of the segmented crack network, allowed addressing those questions in broader terms and with novel quantifications.

At 500 days of ASR acceleration, the larger laboratory specimens achieved relative length change values in a not too broad range which included the values of the two types of field specimens for which such measurement results were also available (the B1(C+NRF) and B1(C+F) specimens). The U40 specimen's value was about 47% higher than the field specimens' values. The P40 specimen's value was about 29% lower. The B40 specimen's value was about the same. Results more useful for addressing the representativeness questions were provided by the segmented crack network analysis. The crack volume fraction values for both the larger laboratory specimens and for the field ones (Figure 4.8 (c)) fell all within the range 1 – 1.7 vol.-%. More interesting, the two specimens cast with the B aggregate type, one laboratory-accelerated (B40), the other from the field (BF-40), had crack volume fraction values differing in absolute value of about 4% (the BF-40 value was that much larger than the B40 one) and showed distributions of crack length and crack thickness rather overlapping with each other (Figure 4.10 (b)). These quantitative results suggest that the crack networks in the laboratory specimens were characterized, at 500 days, already by some features also observable in the field specimens. It has to be reminded that the latter conclusions can be drawn only for the larger laboratory specimens because they shared with the field specimens the same horizontal (i.e., X and Y , see Figure 3.7) size, which is the size parameter constraining the tomographic spatial resolution. A similar level of spatial resolution could not be exactly achieved for the tomograms of the smaller laboratory specimens and the field-exposed cut-out sub-specimens, thus making a complete comparison of crack volume fraction and size distribution not feasible. The latter specimens had lateral size of 15 mm instead of 25 mm.

Concerning the representativeness of the range of values of the crack volume fraction and crack length and thickness, for both the laboratory and the field specimens, there is lack of comparable data in the literature, especially obtained from measurements in 3D. An example of literature data is provided in Table 1 of [16], which reports the percentage of the pore volume (3.5%) due to its regions classified as cracks in one mortar specimen with a porosity of 12 vol.-% and subjected to ASR acceleration by submersion in a 1M NaOH solution at 80°C. Such specimens had size of 25×25×28.5 mm³ and were tomographed at 14 days of ASR acceleration with synchrotron radiation, which allowed achieving much higher spatial resolution (the voxel size was 9×9×9 μm³) than in the tomograms of the smaller laboratory specimens in this project. Despite the identical lateral specimen size and the higher spatial resolution, the computed crack volume fraction was 0.42 vol.-% (assuming that their specimen occupied in the X - Y plane the whole tomogram volume). Such smaller value compared with those reported in Figures 4.9 and 4.13 may be attributed not only to an earlier acceleration time at which the specimen was tomographed but also to the spurious perturbation to the ASR cracking process by the higher temperature (80°C instead of 40°C). Such higher temperature led to extreme aggregate dissolution, including formation of new aggregate pore space in the form of small spherical pores, which constituted about 82%

of the whole segmented pore space of the specimen (see still Table 1 in [16]). Such dissolution pores are not observed at all in real world concrete affected by ASR and clearly bias the occurrence of ASR cracking itself. Thus, X-ray tomography data of crack volume fraction from laboratory specimens accelerated at 80°C cannot be considered representative of real world ASR cracking, contrary to the data reported in this Chapter, which are likely the first ones to be directly validated against corresponding values from real world concrete.

The crack length and thickness distributions shown in Figure 4.10 were right-skewed and with long tails for both the laboratory and the field specimens. Their shapes in the Zipf's plots shown in such Figure remind of typical distributions of similar feature variables extensively observed and reported in the literature for crack networks in brittle materials, e.g., rocks [14], [17]. As mentioned in Section 4.3, one proposed explanation for the widespread observations of such types of distributions for such variables relates with cracking in such materials sharing many common features with other physical processes characterized by scale invariance and criticality [13], [14], [18]. A detailed and thorough assessment of whether the distributions in Figure 4.10 may be better described by a power law model or, e.g., by a stretched exponential/Weibull one may allow further characterization of the ASR cracking process based upon physical models [18]. However, such statistical modelling was considered not feasible since the range of values for both the crack length and the crack thickness was not broad enough. This is a common problem in the analysis of crack networks in brittle materials, whose length and thickness typically span several orders of magnitude but whose detection and analysis is typically confined to only a narrow range of values, when using a single measurement technique. A fully multi-scale crack segmentation from images at multiple spatial resolution ranges would be needed for collecting data in a broader enough range to perform reliable statistical modelling. This is a well-known and debated problem in the literature [17]. Even in the absence of a conclusive assessment of whether such distribution could be better modelled by a power law distribution or by a stretched exponential one, the key conclusions that can be drawn from Figure 4.10, especially its inset (b), is that

- (1) the ASR cracking process in all the laboratory specimens was very likely not spuriously perturbed by the ASR acceleration, which in other conditions, e.g., at 80°C, may lead to the extreme aggregate dissolution mentioned above, leading to the formation of additional, respective pores strongly impairing the cracking process itself [16], [19]–[21] and,
- (2) the ASR cracking process in the larger laboratory specimens led additionally to crack size features similarly distributed as in the field-exposed specimens, which, as expected, also exhibited right-skewed, long-tailed distributions for such features.

The crack networks in the laboratory specimens exhibited one geometrical difference compared with those in the field specimens: their orientations (as defined in this project) tended to be slightly more frequently along the specimen's longitudinal (i.e., Z-)axis, Figure 4.11. As mentioned in the previous Section, this implies that crack width increase contributed slightly more to expansion along a direction orthogonal to such axis. This slight difference may be attributed to the specimens' aspect ratio, which was 4:1 (Z-axis *versus* X- or Y-axis), implying a smaller gradient in moisture and alkali contents along the X- and Y-axis than along the Z-axis. The crack orientation in the field specimens results more isotropically distributed since such specimens were obtained from either larger ones (the case for the two specimens from the EU PARTNER project) or from an actual concrete structure, in either case from a larger volume of concrete with much smaller aspect ratio (1:1 in the PARTNER project specimens case), thus likely less affected by anisotropy of gradients in the moisture and alkali content scalar fields.

More extensive comparative studies as performed in this experimental campaign would be needed to validate the observed and quantified similarities between laboratory-accelerated and real world specimens and to assess the statistical robustness and significance of such similarities.

The size of the laboratory specimens played a significant role in the ASR cracking representativeness. The smaller laboratory specimens achieved slightly smaller crack length and thickness values and significantly smaller macroscopic expansion levels and final crack volume fraction values, compared with the larger laboratory specimens and the field ones. The smaller crack length and thickness values alone could not explain the smaller crack volume fraction ones. The 3D rendering of the segmented crack networks confirmed qualitatively that the smaller laboratory specimens (Figure B3) exhibited less extensive cracking than the larger specimens (Figure 4.6). This difference could be attributed to a less representative volume of concrete, in terms of ASR expansion and cracking. As mentioned in Section 3.2, cracking in concrete is strongly influenced by the interactions between the developed internal stresses and the aggregates. A smaller number of aggregates along any direction may inhibit cracking or alter its patterns. Further investigations would be needed also in this case to assess with sufficient statistical robustness the effects of specimen size and aspect ratio on the ASR cracking. However, it has to be remarked that correspondingly derived optimal specimen size and aspect ratio may impose constraints on which parts of the crack networks and at which time could be analysed with XT. Larger specimens may develop more representative ASR crack networks, as the results reported in this Chapter seem to indicate. However, parts of such more representative crack networks may not be resolved in the corresponding X-ray tomograms, meaning that earlier ASR stage cracks may not be resolved as well.

This issue points out a key limitation of studying ASR by XT. As mentioned already in Sections 2.4.2.5 and 3.2, independently of the X-ray source type (laboratory scale or an electron synchrotron), the smaller the specimen size, the higher the tomographic spatial resolution achievable. Thus, when smaller parts of the ASR crack networks want to be investigated by XT, one is limited to work with either smaller, thus less representative concrete volume or only with parts thereof obtained from larger volume (typically with consequent perturbation of the original state of the specimen) or with model systems.

The impact of the specimen size on the spatial resolution level, thus on quantitative features of the segmented crack network, was assessed by focusing on comparing the crack volume fraction of the same VOI of a specimen when tomographed in the original specimen and after cutting it to a smaller size sufficient to include such VOI. The effect of specimen size was examined, by cutting a smaller 80 % volume reduction. Independently of the aggregate type and boundary conditions (i.e., laboratory acceleration or field-exposure), the crack volume fraction of the resolved and segmented cracks increased between 9 and 14 %. This quantification was used in the part of the project where the ASR cracking evolution also at earlier stages wanted to be investigated (see Chapter 6) by using the smaller specimen size, at the cost of slightly reduced cracking representativeness.

4.5. Conclusions

The most important conclusions that could be drawn from the first experimental campaign conducted in this PhD project and presented in this chapter can be shortlisted as following ones.

- (a) The laboratory-accelerated specimens developed extensive ASR expansion. The ASR products were characterized, in terms of morphology and chemical composition, by typical properties repeatedly reported in the literature and also measured for the field-exposed specimens investigated.
- (b) Similar cracking patterns were qualitatively observed in the tomograms of the laboratory specimens, regardless of the type of aggregates, at 500 day after ASR acceleration, and in the tomograms of the field-exposed specimens.
- (c) The ASR-induced macroscopic expansion and the total crack volume fraction for the laboratory specimens reached, at 500 days of acceleration, values rather comparable with those for the field specimens.
- (d) Crack shape and size features did not differ much between the laboratory and field specimens, at least when considering the larger specimen size. A slight difference was though observed for the crack orientation, which was slightly anisotropic in the laboratory specimens compared with the field ones.
- (e) The specimen representativeness, in terms of ASR cracking, turned out to be clearly influenced by the specimen. The larger specimens ($40 \times 40 \times 160 \text{ mm}^3$), independently of the aggregate types, exhibited dimensional and crack network geometric properties more similar to the corresponding ones of the field specimens.
- (f) By cutting sub-specimens from the original ones, after having tomographed them, till including only a smaller volume 80% smaller than the previously tomographed one and by repeating tomography at higher spatial resolution the crack volume fraction increased between 9- and 14 % (depending on the specimen). Such quantitative assessment of the specimen size effect on the tomographic spatial resolution, thus on the resolution of additional parts of the crack network, should allow choosing an optimal specimen size depending upon the ASR analysis targets and depending upon whether more importance wants to be given to the specimen representativeness in terms of developed ASR cracking or possibility to analyse smaller parts of the crack networks, eventually at earlier ASR stages.

Bibliography

- [1] J. Lindgård, E. J. Sellevold, M. D. A. Thomas, B. Pedersen, H. Justnes, and T. F. Rønning, “Alkali-silica reaction (ASR) - Performance testing: Influence of specimen pre-treatment, exposure conditions and prism size on concrete porosity, moisture state and transport properties,” *Cem. Concr. Res.*, vol. 53, pp. 145–167, Nov. 2013, doi: 10.1016/j.cemconres.2013.05.020.
- [2] E. Latifee, “Miniature Concrete Prism Test - a New Test Method for Evaluating the ASR Potential of Aggregates, the Effectiveness of ASR Mitigation and the Job Mixture,” *All Diss.*, Aug. 2013.
- [3] J. Lindgård *et al.*, “The EU ‘PARTNER’ Project - European standard tests to prevent alkali reactions in aggregates: Final results and recommendations,” *Cem. Concr. Res.*, vol. 40, no. 4, pp. 611–635, Apr. 2010, doi: 10.1016/j.cemconres.2009.09.004.
- [4] I. Fernandes, M. A. T. M. Broekmans, M. dos A. Ribeiro, and I. Sims, “Sedimentary Rocks,” in *Petrographic Atlas: Characterisation of Aggregates Regarding Potential Reactivity to Alkalis*, Dordrecht: Springer Netherlands, 2016, pp. 43–101.
- [5] I. Fernandes *et al.*, “Alkali-silica reactivity of some common rock types. A global petrographic atlas,” *Q. J. Eng. Geol. Hydrogeol.*, vol. 46, no. 2, pp. 215–220, May 2013, doi: 10.1144/qjegh2012-065.
- [6] A. Leemann and B. Münch, “The addition of caesium to concrete with alkali-silica reaction: Implications on product identification and recognition of the reaction sequence,” *Cem. Concr. Res.*, vol. 120, pp. 27–35, Jun. 2019, doi: 10.1016/j.cemconres.2019.03.016.
- [7] P. Leemann, A. Borchers, I. Shakoorioskooie, M. Griffa, M. Müller, C., & Lura, “MICROSTRUCTURAL ANALYSIS OF ASR IN CONCRETE-ACCELERATED TESTING VERSUS NATURAL EXPOSURE,” in *Proceedings of the International Conference on Sustainable Materials, Systems and Structures (SMSS2019)*, RILEM Publications SARL, Rovinj, Croatia, 2019, pp. 222–229.
- [8] C. Röbller, B. Möser, C. Giebson, and H. M. Ludwig, “Application of Electron Backscatter Diffraction to evaluate the ASR risk of concrete aggregates,” *Cem. Concr. Res.*, vol. 95, pp. 47–55, May 2017, doi: 10.1016/j.cemconres.2017.02.015.
- [9] P. Cirillo, “Are your data really Pareto distributed?,” *Phys. A Stat. Mech. its Appl.*, vol. 392, no. 23, pp. 5947–5962, Dec. 2013, doi: 10.1016/j.physa.2013.07.061.
- [10] M. Newman, “Power laws, Pareto distributions and Zipf’s law,” *Contemp. Phys.*, vol. 46, no. 5, pp. 323–351, Sep. 2005, doi: 10.1080/00107510500052444.
- [11] G. K. Zipf, *Human Behaviour and the Principle of Least Effort*. Reading, MA: Addison-Wesley, 1949.
- [12] D. Sornette, “Probability Distributions in Complex Systems,” *R.A. Meyers (Ed.), Encycl.*

- Complex. Syst. Sci. Springer New York, New York, NY*, pp. 7009–7024, 2009, doi: 10.1007/978-0-387-30440-3_418.
- [13] A. Clauset, C. R. Shalizi, and M. E. J. Newman, “Power-law distributions in empirical data,” *SIAM Review*, vol. 51, no. 4. Society for Industrial and Applied Mathematics, pp. 661–703, 06-Nov-2009, doi: 10.1137/070710111.
- [14] E. Bonnet *et al.*, “Scaling of fracture systems in geological media,” *Rev. Geophys.*, vol. 39, no. 3, pp. 347–383, Aug. 2001, doi: 10.1029/1999RG000074.
- [15] D. Sornette, *Critical phenomena in natural sciences: chaos, fractals, selforganization, and disorder: concepts and tools*, 2nd ed. New York: Springer, Berlin, 2004.
- [16] M. Voltolini, N. Marinoni, and L. Mancini, “Synchrotron X-ray computed microtomography investigation of a mortar affected by alkali-silica reaction: A quantitative characterization of its microstructural features,” *J. Mater. Sci.*, vol. 46, no. 20, pp. 6633–6641, Oct. 2011, doi: 10.1007/s10853-011-5614-5.
- [17] P. Adler and J. Thovert, *Fractures and fracture networks, Chapter 5*. Dordrecht: Springer, 1999.
- [18] D. Sornette, *Critical Phenomena in Natural Sciences*. Berlin, Heidelberg: Springer Berlin Heidelberg, 2000.
- [19] N. Marinoni, M. Voltolini, L. Mancini, P. Vignola, A. Pagani, and A. Pavese, “An investigation of mortars affected by alkali-silica reaction by X-ray synchrotron microtomography: A preliminary study,” *J. Mater. Sci.*, vol. 44, no. 21, pp. 5815–5823, Nov. 2009, doi: 10.1007/s10853-009-3817-9.
- [20] N. Marinoni *et al.*, “A combined synchrotron radiation micro computed tomography and micro X-ray diffraction study on deleterious alkali-silica reaction,” *J. Mater. Sci.*, vol. 50, no. 24, pp. 7985–7997, Dec. 2015, doi: 10.1007/s10853-015-9364-7.
- [21] N. Marinoni, M. Voltolini, L. Mancini, and F. Cella, “Influence of aggregate mineralogy on alkali-silica reaction studied by X-ray powder diffraction and imaging techniques,” *J. Mater. Sci.* 2011 476, vol. 47, no. 6, pp. 2845–2855, Nov. 2011, doi: 10.1007/S10853-011-6114-3.

Chapter 5. ASR crack networks and ASR products: qualitative and quantitative analysis of their coupled properties and evolution

5.1. Summary

In this Chapter, a methodology, developed in this PhD project to investigate the coupled evolution of ASR products and associated cracking, is presented. The methodology is based on XT and the addition of caesium (Cs) to the concrete mix as a XT contrast agent. See Section 2.4.2.5.1 for the meaning of contrast agent for attenuation-contrast XT.

The methodology allowed and allows achieving a time-lapse visualization and characterization of the spatial-temporal patterns of not only the ASR cracks but also the ASR products.

In Section 5.2, the additional experimental settings and details specifically used in the methodology and the associated experimental campaign to test it is summarized. Section 5.3 reports the most significant results, while additional results are included in the Appendix C. Section 5.4 synthesizes and discusses the relationships between all of the made observations and quantitative results. Finally, Section 5.5 lists the most important findings.

5.2. Experimental details specific for the Cs-based experimental campaign

The methodology mentioned above was developed during an experimental campaign consisting of the following steps:

- concrete specimens, with and without a source of Cs, were cast in either case with two of the three reactive aggregates mentioned in Chapter 4 and with the larger size of those mentioned there for achieving cracking representativeness;
- the specimens were subjected to the same ASR acceleration protocol in the laboratory;
- at multiple and successive time points during the acceleration, non-destructive measurements on the same exact specimens were performed;
- other destructive measurements or measurements that might have perturbed the ASR development were performed on separate specimens at different acceleration times.

The following Sub-sections report the details of these steps.

5.2.1. Materials and experiments

The specimens were prisms with size 40 mm (X -axis), 40 mm (Y -axis) and 160 mm (Z -axis), respectively. Distinct specimens, with and without Cs, were cast with the U and P aggregates described in details in Section 3.2 and in Appendix A1.1. Table 5.1 provides the mix composition of the reference specimens, cast without Cs. It is the same mix composition as for the specimens of the experimental campaign described in Chapter 4 and reported in Table 3.1. The specimens with Cs were cast with an identical mix design (Table 5.2) except for the addition of CsNO_3 as the Cs source. In order to keep the Na_2O -eq value of the concrete the same as for the reference specimens, NaOH was added to the mix in a smaller amount (Table 5.2), because of the additional contribution of CsNO_3 to the alkalinity of the pore solution. Such reduction was assumed (and verified by the obtained results shown in Section 5.3) not to hinder the ASR development, as the added CsNO_3 counterbalanced the unavoidable drop in the pore solution alkalinity due to the smaller NaOH content. With the added amount of CsNO_3 , the alkali molar ratio of the concrete $[\text{Cs}]/[\text{Na}+\text{K}]$ was 0.43.

Cs was chosen as an optimal tracer of ASR products. Its choice was made in terms of their increased visibility in X-ray tomograms, when containing Cs. The choice was based upon the results of a preliminary experimental campaign, which is described in full details in Section C2 of the Appendix C. In this campaign, distinct specimens cast with distinct additional sources of alkali ions (Na^+ , K^+ , Rb^+ and Cs^+) were investigated. All such ions were expected to (1) get embedded within ASR products and (2) increase their X-ray attenuation coefficient, μ , because of their similar or higher atomic number compared with that of the most abundant atomic species composing ASR products. As expected from the work of Leemann and Münch [1], Cs^+ ions did get incorporated in the ASR products. In the preliminary experimental campaign, including XT measurements it was possible to confirm that the incorporated Cs also determined the largest increase in X-ray attenuation by the products, as visible in the tomograms, compared with the other alkali ions (see Section 5.3.1 below).

Both the specimens with and those without Cs-doping, independently of the aggregate type, were subjected to the same laboratory ASR acceleration protocol as discussed in Section 3.1. At distinct time points, the specimens were taken out of the sealed boxes to perform various characterisations and measurements on them. The measured variables included mass and length, quasi-static Young's modulus along the longitudinal direction, flexural strength and compressive strength along the longitudinal direction, SEM-BSE, EDX and XT. The strength measurements were carried out, at each stage of the campaign, on a distinct batch of three specimens. SEM-EDX was carried out on distinct batches of two specimens. The non-destructive measurements (length and mass, quasi-static Young's modulus and XT) were carried out on the same exact specimens (three in total) all along the campaign. The analysis of the tomograms was performed only for one of the three specimens. Length and mass measurements were additionally performed also on a second batch of three other specimens. In the case of destructive measurements (SEM-EDX, compressive and flexural strengths), the specimens were randomly selected from additional batches distinct from those used for the non-destructive measurements.

All the measurement types were performed on both the Cs-doped specimens, named in the following as "P-Cs" and "U-Cs" for the two distinct aggregate types, respectively, and the specimens without any doping, used as reference counterparts and named as "P-Ref" and "U-Ref", respectively. The specimens subjected to XT were measured only up to 250 days. Within such period, the tomographic time series consisted of $N_t = 3, 12$ and 8 time points for the P-Ref/U-Ref, P-Cs and U-Cs specimens, respectively.

SEM and EDX analyses were used for imaging cracks and ASR products with higher spatial resolution than what achievable by XT, in order to characterize qualitative features of the ASR damage and the products' morphology and to characterize their chemical composition, respectively. Section C1.2 provides the details about the latter measurements. The XT measurements were performed according to the settings described in Section 3.2.

Table 5.1. Mix composition of the reference specimens (cast without CsNO_3) in units of $\text{kg}\cdot\text{m}^{-3}$ (mass per m^3 of cast material).

Specimen label	Cement CEM I 42.5N	Aggregates			Deionized water	NaOH
		0 – 4 mm	4 – 8 mm	8 – 11.25 mm		
P-Ref/U-Ref	450	659	412	576	225	4.9

Table 5.2. Mix composition of the Cs-doped specimens in units of $\text{kg}\cdot\text{m}^{-3}$ (mass per m^3 of cast material).

Specimen label	Cement CEM I 42.5N	Aggregates			Deionized water	NaOH	CsNO_3
		0 – 4 mm	4 – 8 mm	8 – 11.25 mm			
P-Cs/U-Cs	450	659	412	576	225	1.8	13.5

5.2.2. Image analysis

The 3D image analysis consisted of all the steps (I) to (VI) presented and detailed in Section 3.3.

ASR cracks and ASR products segmentation. Crack regions, being either empty or filled by ASR products with very low Cs concentration, were clearly identifiable visually (see Figure 5.7 for some examples). At the first time point, the original cracks¹ were segmented using the BTH procedure, while at all the other time points they were segmented by TS-based methodology. The ASR products were segmented according to the procedure based on the TS approach, as described in Section 3.3 as well.

Quantitative crack network analysis. In addition to computing the volume (fraction) of the ASR crack networks (computed for the ASR products as well), other crack feature variables were computed to

¹ Here and in what follows, the term "original cracks" or "original pores" is used to indicate cracks/pores not generated by ASR, for example cracks existing intrinsically in the aggregates. Such cracks/pores are those detected already in the tomograms at the reference time point $t_0 = 1$ day, before the start of the ASR acceleration protocol.

quantitatively characterize the crack networks' temporal evolution. Using the shape tensor analysis as described at step (VI) in Section 3.3, the crack's bounding box length (L) and height (also called width, H) were computed. In addition, the crack shape and orientation analysis described in Sections 3.3 (point (VI)) and 4.2.2.3 were also performed, based on the shape tensor calculations.

Local thickness analysis. The segmented crack local thickness scalar field, $T_{local}(\vec{x})$, was computed based on the procedure explained in Section 3.3. The visualization of $T_{local}(\vec{x})$ allowed getting qualitative insights into the spatial-temporal distribution of the cracking. The $T_{local}(\vec{x})$ values were assembled together from all the crack network branches to create a whole statistical *ensemble*. Then, as already done for the experimental campaign described in Chapter 4, the statistics of such *ensemble* and, additionally, its temporal evolution were analyzed in order to assess quantitative features of the cracking.

Global and local deformations analysis. As mentioned in Section 3.3, the outputs of both the global affine and of the non-affine registration steps (performed to achieve the ASR crack segmentation), are distinct displacement vector fields, $\vec{u}(\vec{x}, t_i)$, at each time point t_i , $\forall i = 1, \dots, N_t$. In the case of the affine registration, such vector field is linearly dependent in \vec{x} , while the respective field associated with the non-affine registration can exhibit strong spatial variations. The global affine displacement vector field was used to compute the bulk, relative size change of the tomographed volume along the axes $k = X, Y$ or Z , as described at point (VII) in Section 3.3. Among the three of them, the relative size change computed along the Z -axis (thus a relative longitudinal length change) was compared with the experimentally measured one, $\frac{\Delta L_Z}{L_Z}(t_i)$, obtained via the mechanical length gauge described in Section 3.2 and shown in Figure 3.1 (c). Finally, the non-affine registration results were used to map out the local deformations and to investigate their eventual correlations with the ASR cracks and reaction products. For this purpose, both $\|\vec{u}(\vec{x}, t_i)\|$, $\forall i = 1, \dots, N_t$, and the determinant of the Jacobian matrix of the non-affine mapping vector field, $J_{\vec{T}_{N-AFF}}(\vec{x}, t_i)$, $\forall i = 1, \dots, N_t$, were implemented.

5.3. Results

In this Section only the results for the specimens cast with the Praz (P) aggregates are reported, given the fact that for the specimens cast with the Uri (U) aggregates, overall very strong similarities in their results. However, such similar results are reported in details in the Appendix C. The most significant difference among specimens cast with the two aggregate types consisted of a faster ASR reactivity for the U specimens.

5.3.1. Increase in X-ray attenuation contrast for ASR products labelled with Cs

The increase in X-ray attenuation for producted labelled by Cs was large enough to offset their average voxel value well above that of any other material phase inside the aggregates or inside the cement paste, with the exception of some mineral inclusions in the aggregates with high metallic content, which occurred in any case only rarely. Thus, the tomographic (i.e., voxel value) contrast between Cs-labelled products and any other material phase increased significantly. An example of such a significant contrast increase is provided by Figures 5.1 and 5.2 (d). Figure 5.1 shows tomographic slices from a P-Ref specimen, with focus on ROIs where a significant accumulation of products was present, e.g., inside air voids. Despite their accumulation in such regions, the X-ray attenuation contrast between the unlabeled

products and the surrounding material phases was not very large. Figure 5.2 shows one slice from the tomograms of the distinct specimens cast with the distinct alkalis during the preliminary experimental campaign described in Section C2 of Appendix C. With increasing atomic number of the alkalis (from Na to Cs), the X-ray attenuation contrast between the products embedding them and the surrounding material phases increased till its maximum achieved in the Cs case.

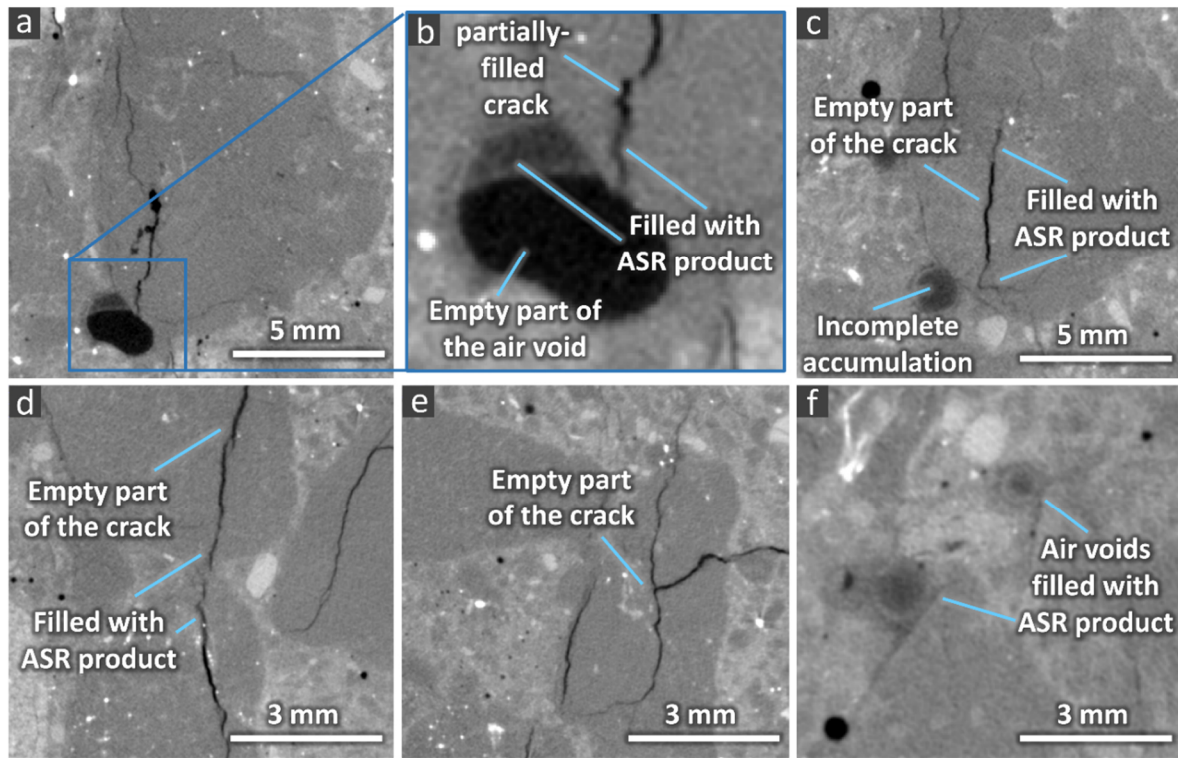


Figure 5.1. 2D ROIs selected on slices from the tomogram of a P-Ref specimen, showing the ASR-induced cracks and air voids filled with ASR products.

Figures 5.2 (a) and (b) show no significant contrast enhancement obtained by using Na- and K-doping. Rb-doping (Figure 5.2 (c)) already allowed visualizing more clearly the ASR products. However, only Cs-doping (Figure 5.2 (d)) allowed achieving extremely high X-ray attenuation contrast levels, needed not only to make the products recognizable by a human observer but also to make them identifiable by a segmentation algorithm.

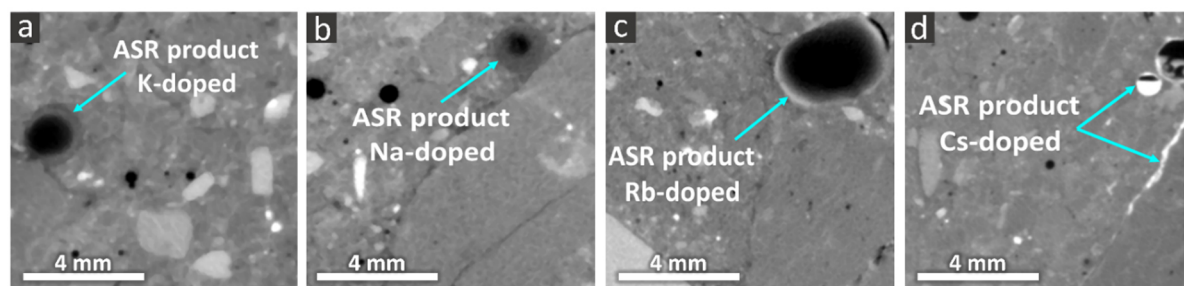


Figure 5.2. Examples of ROIs from tomograms of four distinct specimens cast with distinct alkali-doping. Each ROI was selected on a slice from the tomogram of a corresponding specimen. The common feature of each chosen ROI is the presence of air voids. At the late (20 weeks) stage of the used ASR acceleration, air voids were typically partially or almost completely filled with ASR products. The tomograms are ordered from left to right based upon the increasing atomic number of the alkalis (Na, K, Rb and Cs, respectively). ASR products labelled by Cs^+ cations increased their X-ray attenuation to a level above that of any other material phase in the specimens, except for some high density/high atomic number minerals in the aggregates. Thus, Cs-labelled ASR products were characterized on average by the highest X-ray attenuation contrast to any other material phase.

5.3.2. Chemical and morphological features of the ASR products

Figures 5.3 (a) and (b) show SEM-BSE micrographs of ASR products inside cracks from a P-Ref specimen and a P-Cs one, respectively. These micrographs were acquired at 120 days of ASR acceleration time and, for both specimens, from interior regions of the aggregates, where the ASR products are usually rather crystalline [2]. The ASR products developed in the P-Cs case presented a significantly higher image (i.e., pixel value) BSE contrast than the ones formed in the P-Ref case, in agreement with what already reported in [1]. As already shown in [1] and [2], in the absence of Cs-doping, the ASR products exhibited similar SEM-BSE pixel value as the surrounding material phases (Figure 5.3 (a)). Therefore, they could be distinguished only based on their typical morphological features and chemical composition (when performing additional EDX analysis). For crack regions in the aggregate interior, such features consist of the plate-like morphology already mentioned in Section 2.4.2.2 [2]. In the presence of Cs-doping, the products identification could rely not only on such morphological features but also on the significantly enhanced BSE-contrast, confirming that Cs was incorporated in the products. The latter result was confirmed by EDX analysis (see Section C1.2 for the details). Such analysis also showed no evidence of significant compositional differences in the products, with or without embedded Cs, except for its presence.

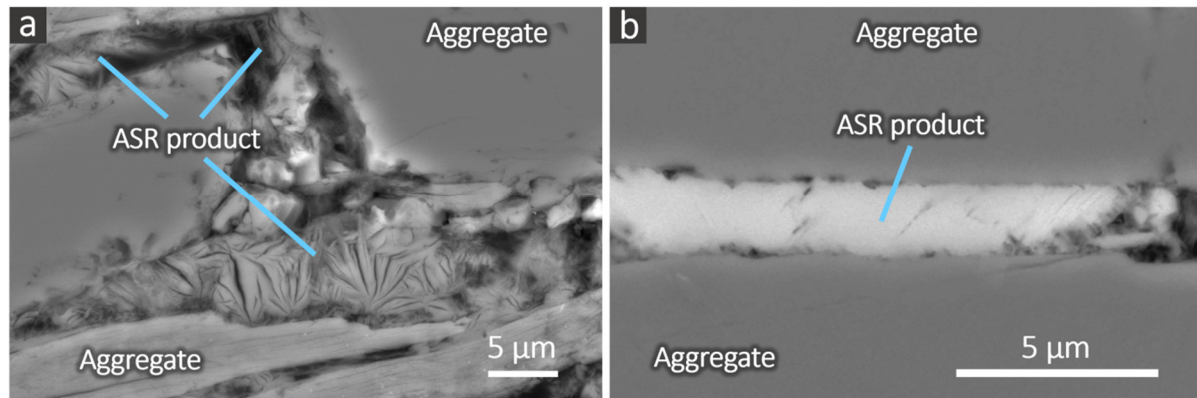


Figure 5.3. (a) and (b): examples of SEM-BSE micrographs of ASR products precipitated/accumulated inside the cracks of aggregates from a P-Ref specimen and a P-Cs one, respectively.

Cs-doping also allowed confirming the observation, in SEM-BSE micrographs of distinct specimens at distinct time points, of a specific spatial-temporal distribution pattern of ASR products, already reported in [1]. Figure 5.4 exemplifies such pattern for P-Cs specimens. Results for the other specimen types are available in Section C1.2.

At 14 days, Cs-containing products could be seen at inter-granular quartz regions close to the aggregate edges and in cracks at the sub-micron and micron scales, in cracked or un-cracked aggregates or in both. Such products are the initial ASR products [1] and could not be detected by XT, as performed in this study, due to insufficient spatial resolution. At 80 days, more products could be seen in internal regions than close to the edges. This is in agreement with the observations reported in [1] of a sort of ASR reaction/product front moving from the aggregate boundaries towards the inner regions. At 120 days, such front advanced inside the aggregates, while the cracks were on average wider. Although most of the cracks within the aggregates themselves were found empty, some large chunks of products could also be found. They filled part of the cracks in the aggregates (highlighted in the micrograph in Figure 5.4 (c)).

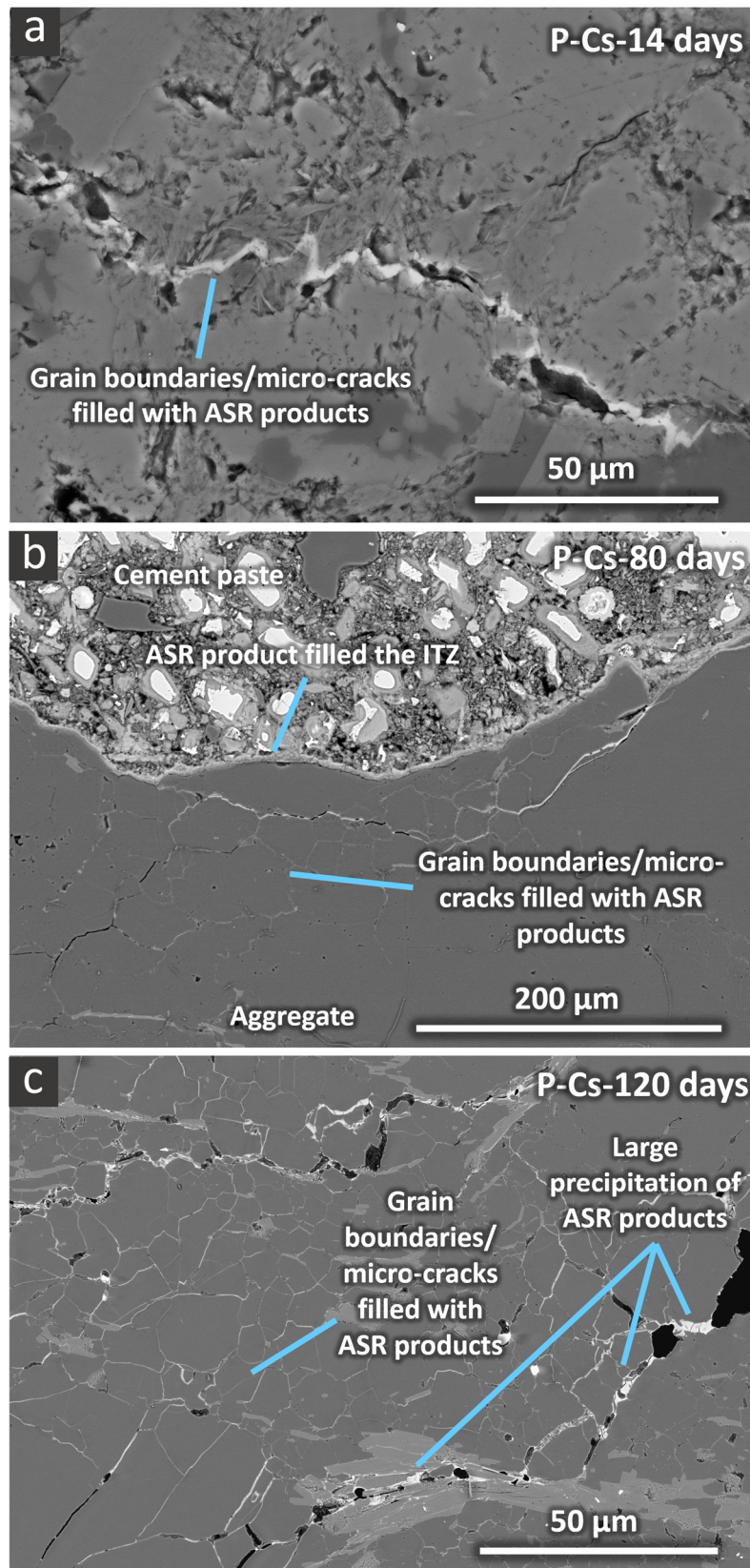


Figure 5.4. (a) to (c): SEM-BSE micrographs providing examples of the distribution of ASR products and cracks in the specimens cast with P aggregates and with CsNO_3 . The micrographs were acquired at 14, 80 and 120 days, respectively. In inset (b), ITZ means Interfacial Transition Zone.

5.3.3. ASR-induced macroscopic dimensional changes and mechanical properties evolution

The relative length change evolution, both of the whole specimens (experimentally measured by the mechanical gauge) and for the tomographed volumes (measured from the global affine registration results) is shown in Figure 5.5 (a). Corresponding results for the specimens cast with U aggregates can be found in Section C4.1. All the specimens expanded along the Z-axis approximately in a linear fashion but with distinct and slightly different rates. Detailed quantitative analysis of such rates can be found in Section C4.2.

At early age (7 – 14 days), the Cs-doped specimens expanded longitudinally with rates similar to those of their corresponding reference specimens. However, at about 20 days, the doped specimens started to exhibit higher expansion rates. The maximum expansion of the doped specimens was at least about 30% larger than what attained by the corresponding reference specimens. This expansion boosting effect was also observed for the specimens of the preliminary study by which the doping alkali was chosen and it was already reported in [1]. The other alkalis had qualitatively a similar effect as Cs did.

As already observed in [1], the main influence of Cs-doping consisted in an increase in ASR kinetics. This result is supported not only by the observed faster expansion but also by a faster mass increase, due to the uptake of the alkaline solution in which the specimens are submerged. A faster/higher uptake correlates well with higher expansion. Cs-doping was accompanied by a faster/higher mass increase, with a maximum value in time about 25 - 40% higher for the doped specimens than for the reference ones. The detailed results about the mass evolution are available in Section C4.3 of Appendix C.

The relative length changes of the tomographed volumes differed significantly from the respective changes measured experimentally for the full specimen volume only up to 21 days. See Section C4.2 for the statistical analysis of the relevance of such differences. After 21 days, the minimum and the maximum values of the relative difference between the estimated relative length changes were 0.00042% and 0.0325%, respectively, for all specimen types. This result suggests that, after 21 days, the deformations occurring in the tomographed volume were representative of those at the length scale of the full specimen, despite the fact that only about 30% of the whole specimen volume was tomographed.

Figure 5.5 (b) and (c) compare the relative length changes with the respective relative changes in size of the tomographed volume along the two other axes, X and Y . For both the reference and the Cs-doped specimens, the maximum expansion was larger in the lateral directions (X and Y) than in the longitudinal direction (Z). Similar results for the U specimens are reported in Section C4.1.

This difference is likely due to the aspect ratio of the specimens (1:4). Because of the latter, the near-surface zone (with higher moisture and alkali content, thus prone to expansion) contributes to a higher proportion of the size in the X and Y directions than in the Z direction (see also [3], [4]).

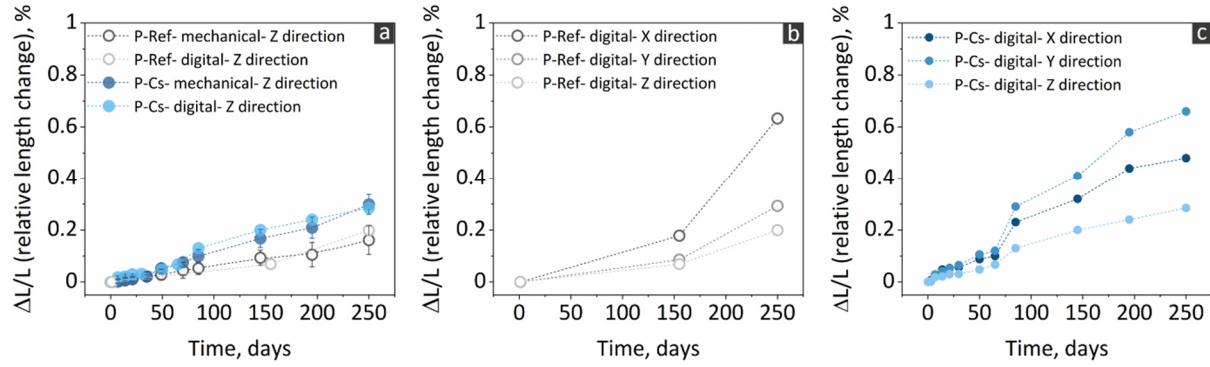


Figure 5.5. Evolution of the relative dimensional change of the specimens cast with the P aggregates, with (blue shades and filled markers) and without (grey shades and hollow markers) Cs-doping. The label "digital" means the estimate was obtained for the tomographed volume of one specimen of each type. The label "mechanical" means the estimate was obtained for the whole specimen volume, by experimental measurements with the gauge described in Section 3.2. (a) Results for the relative change in size along the Z-axis (i.e., length). The experimentally measured values were obtained, for each mix type, for six specimens (including the one being the subject of the tomography analysis). The marker shows the average of the six values. The error bar shows their empirical standard deviation. (b) and (c) Relative dimensional changes of the tomographed volumes, along the X, Y and Z axes for the P-Ref and P-Cs specimens, respectively.

The time series of the quasi-static Young's modulus and of the flexural and compressive strengths are shown in Figure 5.6 (a) to (c), respectively. The temporal evolution of each of these mechanical properties was characterized by an increase up to about 30 to 70 days since the ASR acceleration started, which is attributable to the ongoing cement hydration. Although ASR cracking was likely already occurring during this time period (see the expansion in Figure 5.5), the positive effect of cement hydration on the mechanical properties was prevalent in this initial period. While both the flexural and the compressive strength peaked at about 70 days and slightly decreased (flexural strength) or remained approximately constant (compressive strength) afterwards, the Young's modulus peaked earlier (about 30 days), after which it monotonically and strongly decreased.

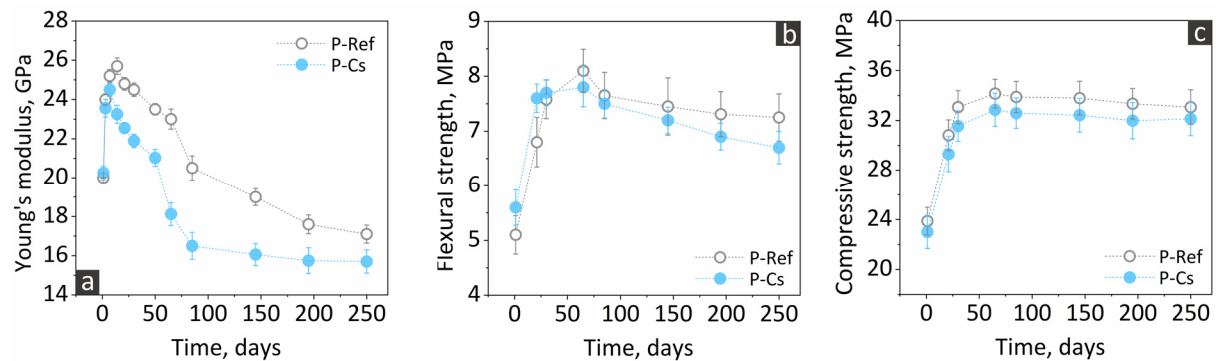


Figure 5.6. The time series of the (a) quasi-static Young's modulus, (b) the flexural and (c) the compressive strength of specimens with and without Cs addition, cast with P aggregates. In each plot, the markers indicate the average of three values from three distinct specimens, while the error bar indicates the respective empirical standard deviation. In the case of the Young's modulus, the measurements were successively performed always on the same specimens, which were the same used also for XT.

The effect of Cs-doping on the mechanical properties was quite clear. The Young's modulus developed at early ages rather similarly, up to the peak. After that, the Cs-doped specimens exhibited a much faster drop than their corresponding reference specimens and achieved a plateau, while the reference specimens' modulus was still decreasing at the end of the measuring campaign. A similar but less remarked effect of Cs-doping is visible in the evolution of the flexural and compressive strengths (Figure 5.6 (b) and (c), respectively). In summary, the higher levels of expansion due to Cs-doping were mirrored by lower values of macroscopic mechanical properties. Similar results for the U specimens are reported in Section C6.

5.3.4. ASR cracking in the reference specimens: time-lapse XT, qualitative analysis

Due to similar X-ray attenuation, ASR products, aggregates and hydrated cement phases attained very similar voxel values. Thus, the only visible change due to ASR consisted of the cracks. No ASR products within the cracks could be as easily resolved as in the SEM-BSE micrographs of Figures 5.3 (b) and 5.4. XT can only identify ASR cracks with thickness larger than the spatial resolution of the acquired tomogram, which is typically several tens of microns for cm-scale specimens, at least when working with state-of-the-art laboratory-scale tomographs. However, at the early ASR stages, the ASR products precipitate and accumulate within aggregate grain boundaries and micro-cracks, which are intrinsic aggregate features with thickness in part below the spatial resolution of the performed XT [1].

Later stage products typically appear within cracks of thickness larger than tens of microns [5], [6] and can in principle be resolved in X-ray tomograms. However, they bear low image contrast to the other material phases (see Figure 5.1), e.g., cement hydrates and aggregate minerals. Such low image contrast stems from similar elemental composition and mass density for products and the other material phases in the aggregates and cement paste. The lack of X-ray attenuation contrast makes the systematic and reliable identification of the products extremely difficult, limiting, e.g., the successful application of image analysis algorithms for quantitative analysis. As a result of the mentioned issues, it has not yet been possible to take advantage of the non-destructiveness of XT for unequivocally, reliably and systematically visualizing ASR products.

In all the tomograms of the reference specimens, it was observed that ASR cracks originated always inside the aggregates, then propagated into the cement paste, as already shown in the literature at multiple length scales [7], [8]. The cracks also increased, in a step-wise manner, in length and width. Furthermore, the ASR cracks propagated in some cases starting from cracks that were already evident at 1 day. In addition to being locations of stress localization, such original cracks inside aggregates have been identified, along with grain and sub-grain boundaries, in the literature as loci of enhanced ASR product precipitation and accumulation [1], [9]. Such regions are also more prone to coalesce with propagating cracks. The spatial resolution in the tomograms (about $70\ \mu\text{m}$) was not sufficient to resolve actual grain boundaries, which are typically tens of nm in width [1]. Thus, in the tomograms mainly original cracks were resolved.

At any time point, the cracks were distributed rather homogeneously in the inspected volumes. This could be observed in the binary tomograms of the segmented cracks. The segmented crack networks appeared to be similar, independently of the aggregate type. The crack networks consisted of rather densely interconnected long and short branches. Details about qualitative features of the crack networks as discerned from 3D rendering of the binary tomograms are available in Section C6.

5.3.5. ASR cracking in the Cs-doped specimens: time-lapse XT, qualitative analysis

Cs-doping clearly allowed tracing the accumulation of ASR products, thus providing important information about the spatial-temporal ASR evolution. This result is exemplified in Figure 5.7 and Figure 5.8 for the analyzed P-Cs specimen.

Figure 5.7 shows a slice parallel to the $X - Y$ plane from a VOI of the P-Cs specimen at four different time points. ASR products are evident as very bright regions within cracks and near the aggregate boundaries, especially after 145 days. The aggregate highlighted in Figure 5.7 (a) contained cracks with size close to the tomographic spatial resolution already at 1 day (original cracks). At 85 days (Figure 5.7 (b)), the main ASR effect was the filling of pores close to the aggregate boundaries, particularly in the ITZ. After 145 days, the ASR products were extruded towards/into the cement paste via newly created cracks or extremely widened grain boundaries (Figure 5.7 (c)). In addition to filling in the cracks present in the cement paste on the left-hand side of the central aggregate, the ASR products also filled, at 250 days, the more delaminated ITZ of another adjacent aggregate at its right /bottom side (Figure 5.7 (d)). At 250 days, it can be also observed that cracks propagated further (top-left corner of Figure 5.7 (d)), they widened up and formed a continuous crack path by connecting with the other cracks in the cement paste. The movie MC1 in Section C7 shows the complete time series of one slice from a larger VOI containing the one used for Figure 5.7.

The extrusion of ASR products from an aggregate (where they were first detected) into the surrounding cement paste was systematically observed also in other Cs-doped specimens, either along a propagating crack or into other pores, e.g., in the ITZ. Cracks that were initially filled with ASR products emptied when the cracks propagated further, while the ASR products were extruded further away in the process.

In some cracks, ASR products were present only on their internal surfaces, while the center was empty. The cracks appeared to have enlarged, with the ASR products splitting and remaining attached to the edges. The opening tip of those cracks was instead filled with a considerable amount of ASR products. See Figure 5.7 (d) and movie MS1 in Section C7.

In some cases, the ITZ, original pores and air voids at a distance from a cracking aggregate became gradually filled up with ASR products. Figure 5.8 shows an example of this observation for a different VOI compared with the one of Figure 5.7. See the movie MS2 in Section C7 for the full time series of which Figure 5.8 is only a subset. Figure 5.8 shows an air void located about 3 mm from an aggregate that got split by one ASR crack. The crack propagated further into the cement paste and through the air void. The crack within the aggregate emptied of ASR products and the products were transported along the crack through the cement paste and accumulated into the air void. The accumulation progressed steadily, first with the formation of a meniscus at 65 days. Then, the void became filled at 85 days. Later, at about 145 days, by opening another crack in the cement paste (lower left of the air void) part of the air void was depleted of the ASR products and the X-ray attenuation of the remaining products within the void appeared to increase (indicated by the increase in brightness of the voxels within the void), possibly due to Ca^{2+} ions uptake [10], [11]. At 195 and 250 days, the cracks in the cement paste and aggregate extensively widened.

The ASR products extrusion into the cement paste (1) was spatially widespread, (2) it happened in a rather isotropic fashion and not only along the cracks and (3) it led to a widespread filling of pores (not only air voids) in the cement paste around the cracks.

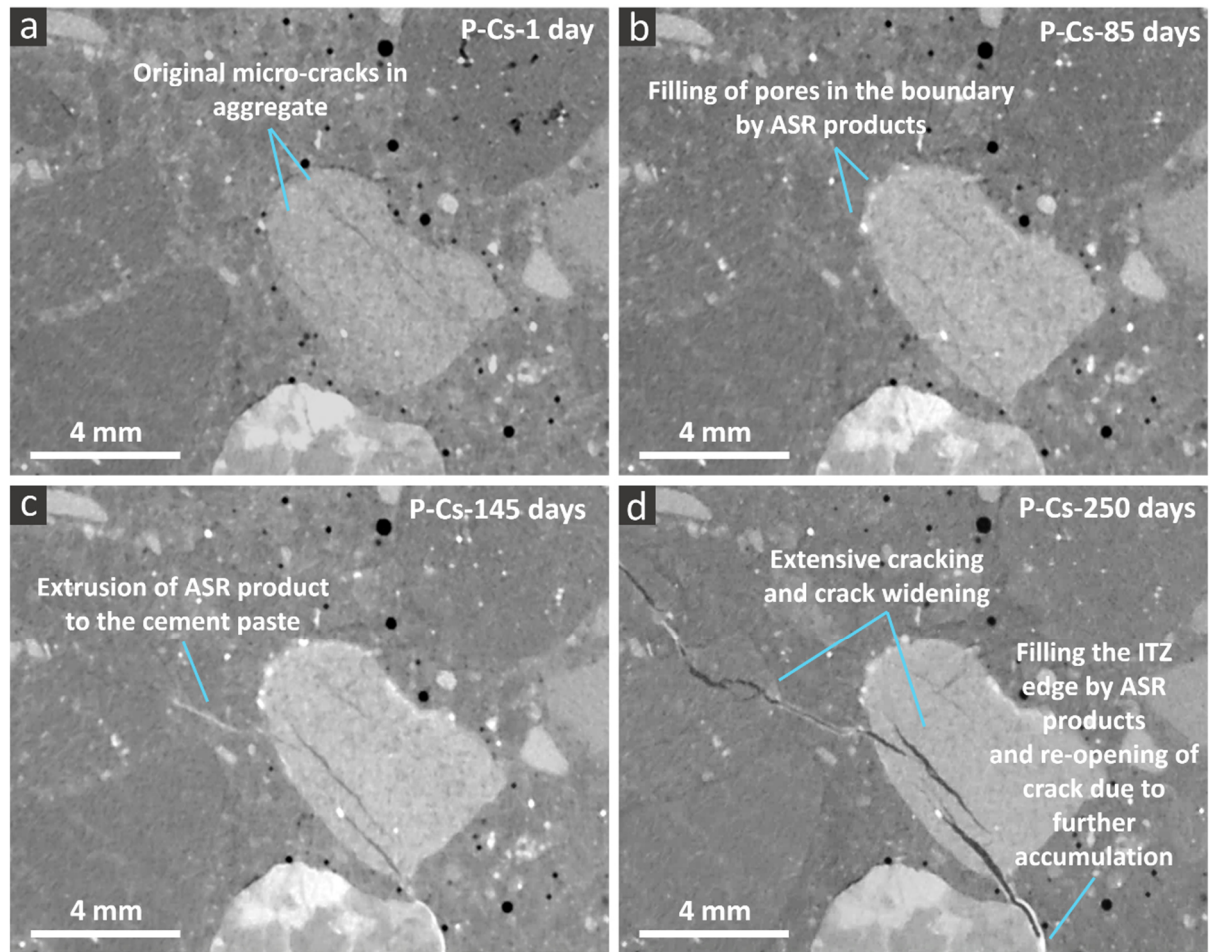


Figure 5.7. A slice from a ROI of the P-Cs specimen at four different time points. ASR products can be observed as very bright regions within cracks and near the aggregate boundaries. The four insets here are from the tomo-gram at (a) 1 day, (b) 85 days, (c) 145 days and (d) 250 days.

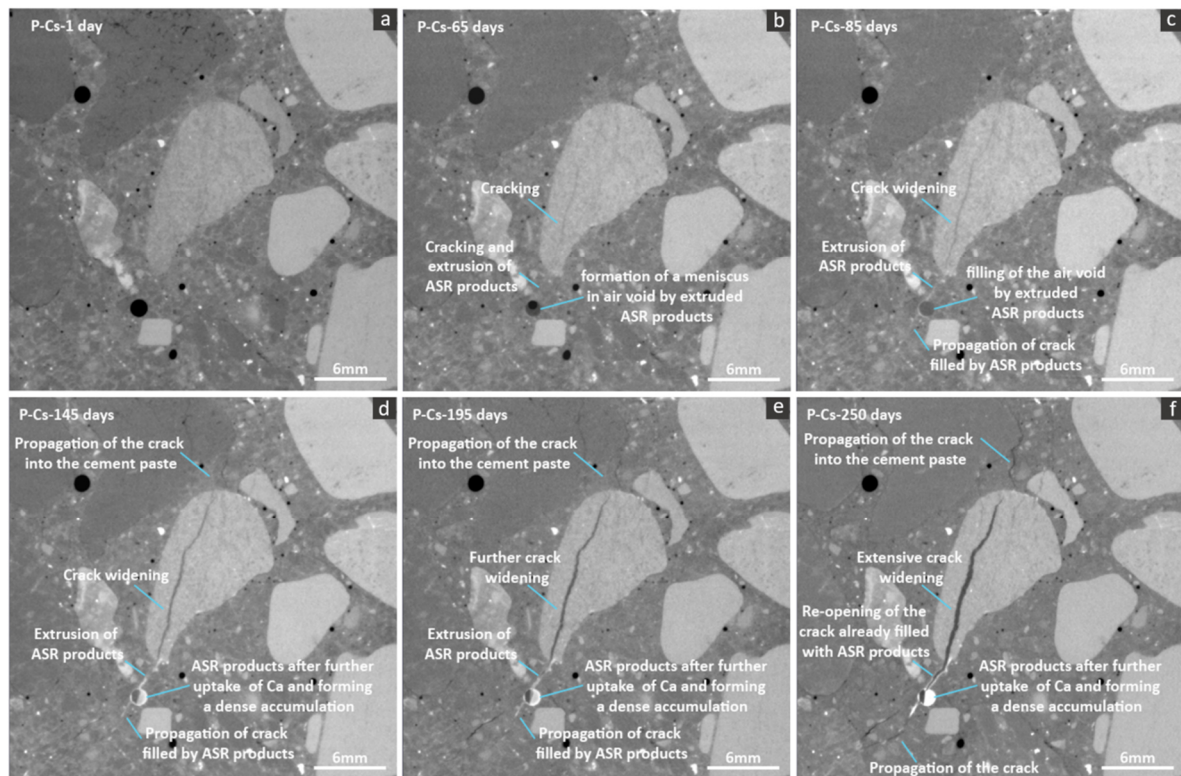


Figure 5.8. A slice from another ROI of the P-Cs specimen at four different time points. ASR products could be observed as filling up an air void a few mm away from the aggregate highlighted by the arrow, as a crack running through such aggregate evolved and propagating into the cement paste till the air void itself. The products were transported from such aggregates till the air void via the propagating cracks. The six insets shown here are from the tomogram at (a) 1 day, (b) 65 days, (c) 85 days, (d) 145 days, (e) 195 days and (f) 250 days.

Figure 5.9 exemplifies such three features by the rendering, at multiple time points, of a small VOI for two types of binary tomograms: the one of empty cracks and that of ASR products (both inside and outside cracks). Details about the 3D rendering approach are available in Section C7. The chosen VOI contained a single large aggregate. Figure 5.9 shows that the ASR cracks started their development from original cracks/pores in the aggregate (inset (a)) and gradually propagated with time. The cracks inside the aggregate remained mainly empty, while those in the cement paste became partially or completely filled with products. This can be appreciated mainly at later times (insets (e) and (f)): products regions with the typical features of cracks, e.g., a high degree of shape anisotropy, evolved in distinct parts of the VOI along any possible direction. The small and isolated regions occupied by the products corresponded to other types of pores, e.g., porous patches or ITZ, mainly in the cement paste. Three air voids which became completely filled are observable already at early times (inset (b)). No large crack completely crossed their volumes, as, on the contrary, it happened in the example of Figure 5.8. Rather, they were in the nearby of crack network branches not propagating towards them. The latter example showcases the second feature mentioned above for the products extrusion, i.e., an isotropic distribution of products through the pore space of the cement paste. Additional qualitative evidence of such and of other features of the products extrusion, as well as of the crack propagation, is provided in Section C7.

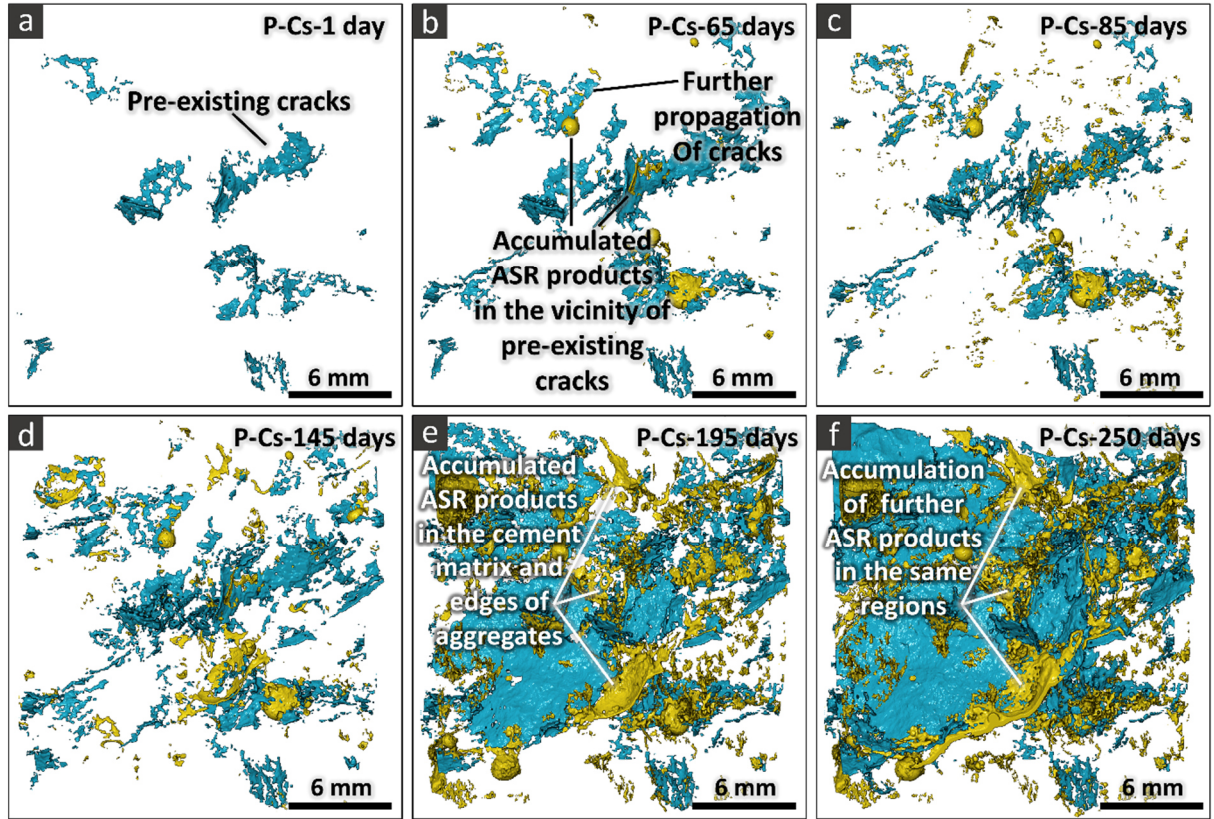


Figure 5.9. Binary tomograms of the segmented empty cracks (in cyan) and of the ASR products (both inside and outside cracks, in yellow). Only a small VOI of the P-Cs specimen is shown. Such VOI contained cracks that were nucleated inside a single aggregate and propagated later into the surrounding cement paste. The insets from (a) to (f) correspond to different time points during the ASR acceleration, including 1 day, 65, 85, 145, 195 and 250 days, respectively.

5.3.6. ASR crack networks: quantitative analysis

Figure 5.10 shows the time series of ASR cracks total volume fraction values, $\tilde{V}_{ASR\ cracks}(t_i)$, $\forall i = 1 \dots, N_t$, as defined in Eq. (3.6) with $k = ASR\ cracks$ and independently of the crack location, inside aggregates or the cement paste, for both the P-Ref and the P-Cs specimens. It has to be reminded that contrary to Chapter 4, where the volume fraction could be estimated only for the total amount of cracks, either original or ASR-generated, in this Chapter the results refer only to ASR-induced cracks because of the availability of the tomograms at the reference time $t_0 = 1$ day. Figure 5.10 also shows the volume of ASR products (also normalized by $V_{tomogram}$) independently of the type of pore space they occupied (cracks, air-voids, ITZ and porous patches). The comparison of Figure 5.5 with Figure 5.10 shows a feature which was observed independently of the specimen type: a positive correlation between the normalized volume of ASR-generated cracks and the longitudinal expansion. The P-Cs specimens achieved, at 250 days, almost double longitudinal expansion compared with the P-Ref (see Figure 5.5). The tomographed P-Cs specimen exhibited almost three times larger volume of ASR-generated cracks (see Figure 5.10). Additional details about such positive correlation can be found in Section C8.

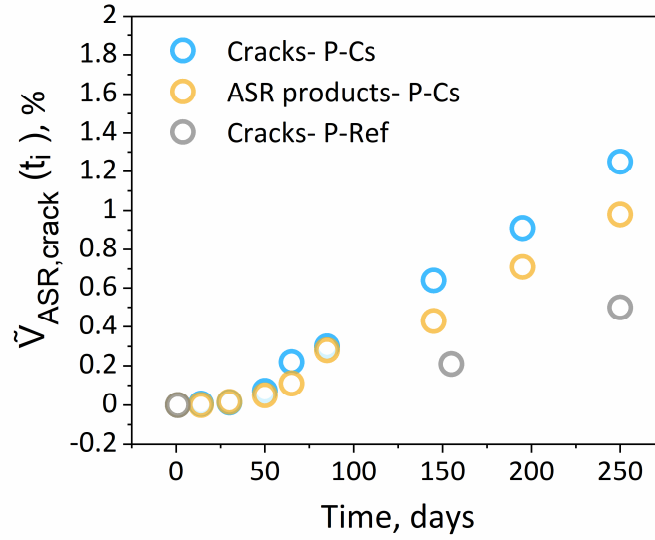


Figure 5.10. Quantitative assessment of the ASR cracking in the P specimens by the total volume fraction of ASR-generated cracks (with or without ASR products), $\tilde{V}_{ASR, cracks}$, as defined in Eq. (3.6). The total volume of ASR products (also normalized by the tomogram volume) is also shown by yellow markers.

Figure 5.10 also shows that the total volume of ASR products (inside or outside cracks) evolved synchronously with the total volume of ASR cracks and was at most about 16% smaller than it (at 250 days). With the possibility of distinguishing between products inside and outside cracks, the fraction of filled ASR crack volume was computed, which achieved a maximum value of 30% for the tomographed P-Cs specimen. Section C8 reports the full time series of such fraction of filled ASR crack volume. These results mirror what observable in the 3D renderings of the same type as the one shown in Figure 5.9: a significant accumulation of ASR products outside of the ASR cracks. This is in agreement with the qualitative observation mentioned before of extensive detection of products in pores other than cracks, the majority of which located in the cement paste.

Concerning the ASR crack size analysis, of the three size definitions obtained from the shape tensor (\mathbf{G}) analysis, i.e., the bounding box's length L , its height (or width) H and its thickness T , the latter did not provide meaningful estimates. That is because of the characteristic geometrical features of the crack network branches as 3D objects. They had high aspect ratios and an indicative shape of thin, curved and fragmented plates, similarly as for the cracks of the laboratory accelerated and field-exposed specimens analyzed in Chapter 4 (see specifically Figure 4.10). This feature was independent of (1) the aggregate type, (2) the presence or absence of Cs-doping and (3) of time. The detailed results the latter statement is based upon are provided in Section C9.1. As already mentioned at point (VI) in Section 3.3 and in correspondence of the examples shown in Figure 3.6, such curved shape impaired the meaningfulness of the T values. On the contrary, L maintained a high degree of representativeness for the maximum size of a crack. The detailed confirmation of such results, based on the shape tensor analysis, as well as the qualitative (i.e., visual) and quantitative assessments of the reliability and meaningfulness of the L , H and T values are provided in Section C9.1 as well. Instead of the T values, the statistics of the computed local thickness field $T_{local}(\vec{x})$ were considered for the quantitative analysis of crack thickness.

Figure 5.11 shows the distributions of L and of $T_{local}(\vec{x})$ values for the P-Ref (insets (a) and (c)) and P-Cs (insets (b) and (d)) specimens. Only three time points from the whole time series are shown for both the P-Ref and the P-Cs specimens, chosen such that they are at similar times as for P-Ref specimen. The distributions are shown in the form of Zipf's plots, analogously as done in Section 4.3.3, Figure 4.1.

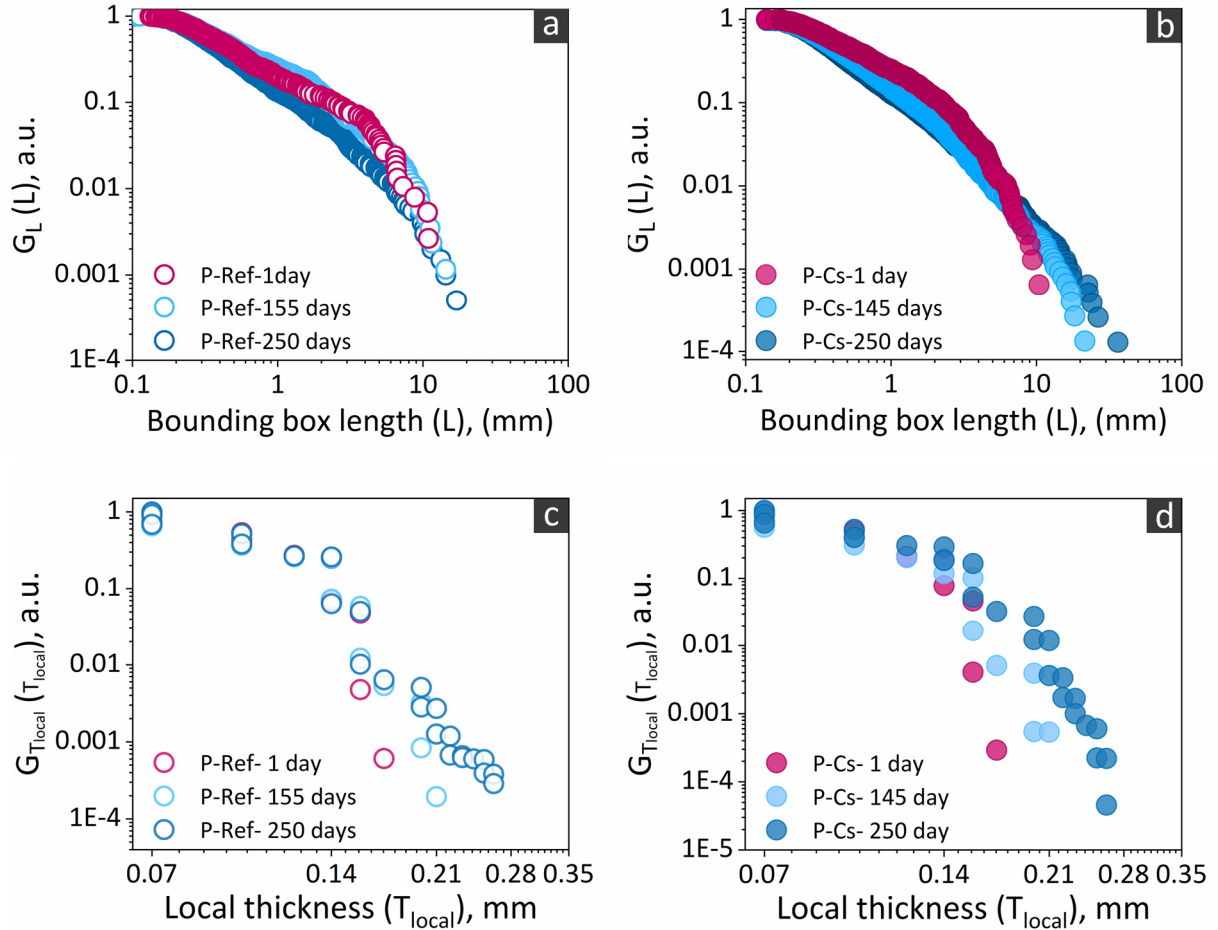


Figure 5.11. (a) and (b): empirical (i.e., from the statistical sample) complementary cumulative distribution function (cCDF) of the ASR crack bounding box length, L , $G_L(L)$, in \log_{10} - \log_{10} scales (Zipf plot), for the P-ref and the P-Cs specimens, respectively. Each separate crack contributed to one sampled value for L . (c) and (d): corresponding Zipf's plots but for the ASR crack local thickness, T_{local} . In each Zipf's plot, the cCDF is shown at three distinct time points.

The first important observation is that, also in this case, right-skewed and long-tailed PDFs were observed for L and T_{local} . Additional results, showing long-tailed PDFs for other crack size metrics (H and the crack network branch volume, V_{crack}), are reported in Section C9.1. The fact that L and T_{local} exhibited right-skewed and long-tailed distributions at any time during the cracking process and, more importantly, independently of Cs-doping, indicates the absence of spurious effects on the ASR cracking by the doping. Similar results for the U specimens are available in Section C9.1. The consequences of ASR kinetics acceleration by Cs-doping significantly concerned the tails of the distributions of L and T_{local} . For example, at 250 days, the maximum L values reached about 40 mm for the P-Cs specimen

(Figure 5.11 (b)) while only about 20 mm for the P-ref one (Figure 5.11 (a)). Similar results obtained for the U specimens are provided in Section C9.1.

Overall, independently from the absence or the presence of Cs-doping, the ASR cracking was accompanied by more significant changes to the overall distribution of T_{local} than to that of L . In Figure 5.11, clearly detectable temporal changes are indeed observable only at the very end of the right side tail of the L distribution. On the contrary, cracking brought a more evident shift of the overall T_{local} distribution towards larger values. $T_{local}(\vec{x})$, as a scalar field, showed, at any given time point, a rather homogenous distribution. Detailed results of the spatial analysis of $T_{local}(\vec{x})$ are reported in Section C9.2.

In terms of crack orientation, no influence of Cs-doping and of the aggregate type was observed. All the specimens showed a slight preferential tendency to be the most elongated along the Z axis. Section C9.1 provides the results of the detailed and quantitative analysis of crack orientation based upon the shape tensor analysis implemented as explained in Sections 3.3 (point (VI)) and 4.2.2.3. As already noticed for the laboratory-accelerated specimens of the experimental campaign described in Chapter 4, a slightly preferential elongation in the Z direction was observed. The detailed results are reported in Figures C36 to C38 in Section C9.1. This feature is in good agreement with the results about the macroscopic expansion along the three axes, as estimated based upon the affine registration procedure. Recalling from Figure 5.5, insets (b) and (c), it was observed that the expansion along the X and Y axes were larger than or at least equal to the one along the Z axis. Section C4.1 reports corresponding and similar results for the U specimens. As already explained in Section 4.4, a slightly preferential crack orientation along the Z axis implies that the crack thickness increase shown in Figure 5.11 for the P specimens (in Figures C41 and C42, analogously, for the U specimens) predominantly contributed to expansion along a direction orthogonal to the Z axis, making it larger along the X and Y axes than along the Z one.

5.3.7. Local deformations analysis

In order to characterize the cracking in the distinct specimens, the determinant of the Jacobian matrix, $J_{\vec{T}_{N-AFF}}(\vec{x}, t_i)$, associated with the transformation vector field of the final non-affine registration step, $\vec{T}_{N-AFF}(\vec{x}, t_i)$, was visualized at distinct time points t_i , $\forall i = 1, \dots, N_t$. See Eq. (3.12) for its exact definition. The results for the P specimens are shown here, focusing on features which were commonly observed also for the U specimens. The results for the U specimens, as well as additional results based upon the magnitude of the displacement vector field associated with the non-affine deformation are shown in Section C10.

The $J_{\vec{T}_{N-AFF}}(\vec{x}, t_i)$ scalar field is shown, at specific time points, in Figure 5.12 and Figure 5.13 for the P-Ref and P-Cs specimens, respectively. In each of these figures, only one slice from the specimen's tomographed volume is shown (insets in the first row or first two rows). The slice at the same position but from the 3D distribution of $J_{\vec{T}_{N-AFF}}$ values is rendered, in the last row, semi-transparently according to a color scale and overlapped on top of the respective tomogram's slice.

Figures 5.12 (d) and (e) showcase some features of the ASR-induced deformations that were observed as systematically accompanying cracking, independently of the aggregate type. First of all, regions where newly formed ASR cracks appeared were systematically characterized by local expansion. These are the yellow to red regions in Figure 5.12 (d) and (e). There, $J_{\vec{T}_{N-AFF}}$ achieved values larger than one, corresponding to local volumetric increase compared with the reference time point t_0 . With time, the

local expansion became larger and also covered a larger area around the crack. This was consistently observed for all the newly formed cracks. An enlargement, far away from the cracks, of zones of high expansion (marked in red) in the $J_{\vec{T}_{N-AFF}}$ map was observed in particular for cracks that opened up (see, e.g., the cracks pointed at by lines in Figure 5.12 (d) and (e), features (I) and (II)). Regions of local volumetric contraction (blue/cyan in Figure 5.12 (d) and (e), with $J_{\vec{T}_{N-AFF}}$ values smaller than 1) were systematically observed to evolve, both in spatial extent and in intensity, in between regions of local volumetric expansion. The observed alternation of expansion zones to contraction ones, with high degree of localization of extreme values (minima and maxima of $J_{\vec{T}_{N-AFF}}$), is to be expected from cracking in concrete, because of its high degree of spatial heterogeneity/disorder (both in terms of physical properties and geometrical/size ones of its distinct material phases) and its brittleness.

In Figure 5.12, another feature is notable: some original cracks or more porous regions at the aggregate boundaries did not evolve into an opening and lengthening crack, rather they either remained the same or gradually closed or filled up. See as examples the features labelled as (III) in Figure 5.12. The $J_{\vec{T}_{N-AFF}}$ typically had, in the proximity of such regions, values smaller than or equal to 1 (Figure 5.12 (d) and (e)), confirming that local volumetric contraction occurred at these locations. According to what observed, ASR cracking did not always nucleate and advance from any resolved original crack or highly porous region. Rather some of these regions even contracted due to the spatially heterogeneous distribution of deformations accompanying the ASR cracking. These observations cannot however exclude that ASR cracks may nucleate and propagate preferentially from original cracks or highly porous regions that are smaller than $70 \mu m$, the approximate spatial resolution in these tomograms.

The development of regions of local volumetric expansion exactly where ASR cracks appeared was a feature systematically observed also for Cs-doped specimens. The evolution of such regions followed temporal patterns which were similar to those observed for the reference specimens. The first yellow/red spots (where $J_{\vec{T}_{N-AFF}} > 1$) appeared in the Cs-doped specimen already after 30 days (Figure 5.13 (e)). However, such first expansion hotspots appeared when no ASR crack could be actually resolved in the corresponding tomograms. These zones of localized expansion might precede ASR cracking or might indicate that cracks are already present but smaller than the spatial resolution of the tomograms.

With time, the expansion regions increased both in extent, all around the respectively developing ASR cracks, and in intensity (i.e., $J_{\vec{T}_{N-AFF}}$), see Figure 5.13 (f)-(h). Regions of high local contraction also appeared around those of local expansion. Thus, from a qualitative point of view, the reference and the Cs-doped specimens exhibited similar spatial-temporal $J_{\vec{T}_{N-AFF}}$ maps. The [minima, maxima] values of $J_{\vec{T}_{N-AFF}}$, for the Cs-doped specimen and at 250 days, reached higher values ([0.8, 1.12]) compared to those achieved by the reference specimen ([0.8, 1.09]).

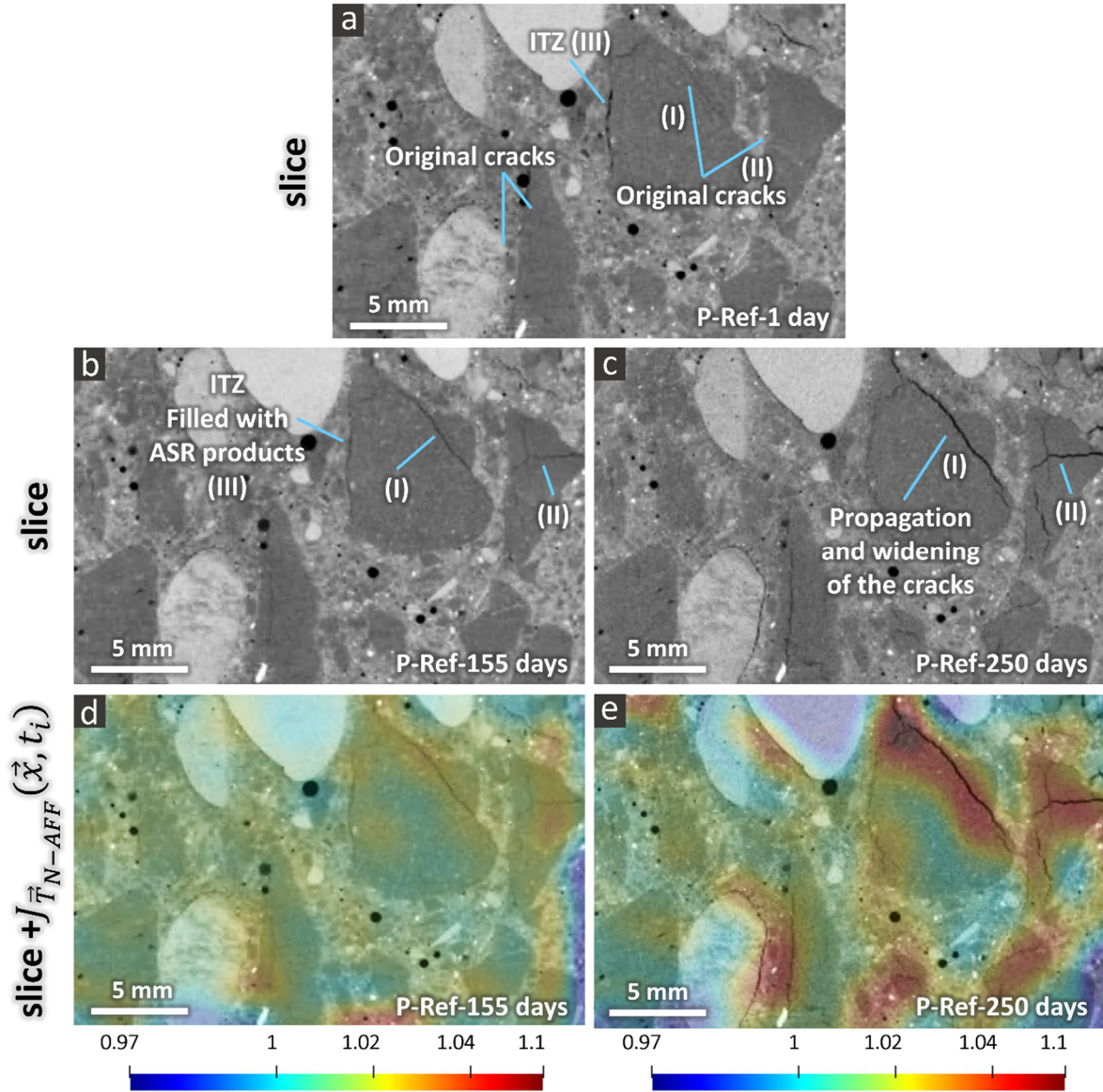


Figure 5.12. Visualization of the determinant of the Jacobian matrix ($J_{\vec{T}_{N-AFF}}(\vec{x}, t_i)$) of the transformation vector field $\vec{T}_{N-AFF}(\vec{x}, t_i)$ associated with the non-affine registration. This scalar field is used as a spatial map of the factor by which the volume locally expanded or contracted due to the spatially heterogeneous components of the ASR-induced displacement vector field. In this figure, only one slice from the tomographed volume is shown: (a) X-ray tomogram of the P-Ref specimen at the beginning of the ASR acceleration (at 1 day); (b) and (c) slices from the X-ray tomograms at 155 and 250 days, respectively; (d) and (e) the same slices as in (b) and (c), plus, overlapped on top of them semi-transparently and rendered according to the indicated color scale, the 2D cross-section, at the same position, from $J_{\vec{T}_{N-AFF}}(\vec{x}, t_i)$, at the same corresponding time points. The scale bars of insets (d) and (e) have arbitrary units since $J_{\vec{T}_{N-AFF}}$ is a dimensionless variable. Values greater than 1 represent volumetric expansion, while values smaller than 1 indicate volumetric contraction.

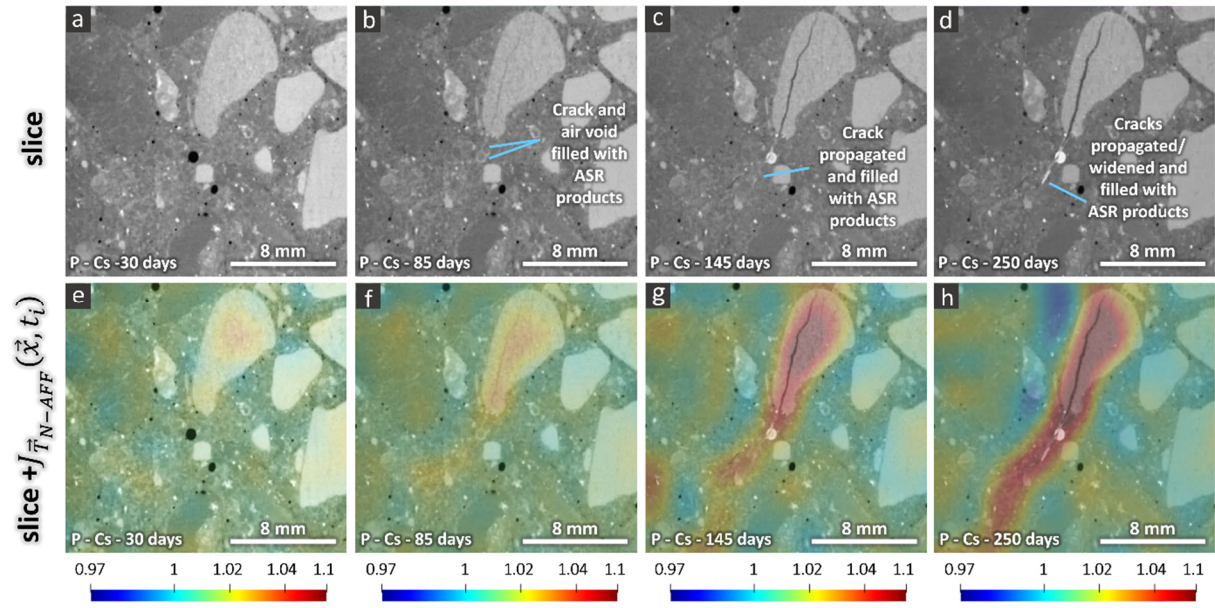


Figure 5.13. Similar plots as in Figure 5.12 but for the P-Cs specimen. The chosen time points for the visualization are 30 days (insets (a) and (e)), 85 days ((b) and (f)), 145 days ((c) and (g)), 250 days ((d) and (h)). The first time point of visualization is here 30 days, instead of 1 day as in Figure 5.10. At such age, no ASR cracks could be resolved. Thus, the corresponding registered tomogram was essentially identical to the one at 1 day, providing a view of the reference cracking state. However, local deformations appeared already at 30 days, which motivates showing the $J_{T_{N-AFF}}(\vec{x})$ scalar field already at such time point.

5.4. Discussion

No significant differences due to the Cs-doping were detected for the cracking (Figure 5.11) and for the spatial-temporal patterns of the associated local deformations (Figure 5.12 and Figure 5.13), except for time lags due to the faster ASR kinetics in the presence of Cs. This experimental campaign thus provided extensive evidence, complementary to that in [1], that Cs-doping can be used for the visualization of ASR products by, e.g., electron microscopy or XT, without perturbing the ASR (damage) evolution in laboratory- accelerated specimens.

More importantly, the results presented in this Chapter provide several useful insights into general features of ASR and its associated cracking. It has to be remarked that most of the features described and shown in Section 5.3 were observed not only in the specimens with Praz aggregates, whose results are reported in Section 5.3, but also in the specimens with the Uri aggregates, whose results are reported only in the Appendix C. In the following, these features are summarized and contextualized within the existing knowledge framework about the chemo-mechanics of ASR. With such a summary, some perspectives are provided on how the work presented in this Chapter could be extended in the future to advance the understanding of ASR cracking.

As described in Section 2.1, ASR starts with dissolution of reactive silica in the aggregates. The dissolved silica leads to the formation of an alkali-silica sol. When the concentration in the sol reaches supersaturation ASR products are formed. The silica dissolution does not occur with any preference at specific locations within the aggregates. However, at the early ages, the formation of ASR products

occurs first at the periphery of the aggregates, close to the cement paste, where alkali and Ca^{2+} ions are more available. With time, they progressively precipitate/accumulate from the boundaries to the interior of the aggregates, forming a so called advancing ASR front [1]. This process, observed both in SEM-BSE images for the early ASR products (Figure 5.4 (b)) and in those reported by [1], occurs thanks to the transport of the mentioned ions along grain boundaries and original cracks.

Therefore, the associated early stage cracking is also expected to advance from the boundaries to the aggregates' inner regions. However, the size of the early stage cracks are much smaller than the spatial resolution achieved in the tomograms collected during this PhD project, as confirmed by the SEM-BSE images. Higher spatial resolution (i.e., tens/hundreds nm length scale) XT on Cs-doped specimens may be extremely useful for actually observing sequentially, on the same exact specimen, the spatial-temporal pattern of the ASR reaction front and the associated early cracking. Until now, the very early cracking stages have only been observed in 2D, non-time-lapse datasets, i.e., SEM observations on distinct specimens at distinct times [3].

The XT observations reported in this Chapter suggest that large amounts of ASR products accumulated preferentially at few specific locations at the aggregate boundaries. For example, large ($>70\text{ }\mu\text{m}$) original cracks or delaminated ITZs were systematically observed to fill up with ASR products (see the examples of delaminated ITZs in Figure 5.7, top-left corner of the central aggregate). This can be easily understood considering (1) the higher likelihood of high Ca^{2+} concentration in such regions and (2) the fact that such regions could act as reservoirs where transported products can accumulate. With ongoing time, such accumulation can lead to widening of the cracks and their further propagation, even into the cement paste (see Figure 5.7 (c) and (d) and the associated movie MS1 in Section C7, which shows more time frames than what shown in Figure 5.7).

In addition, it was observed that, along some cracks, the ASR products were transported at distances of up to several mm, as reported in Section 5.3.5. Both Figure 5.7 and Figure 5.8 (and the respective movies MS1 and MS2 in Section C7, which complement them) show two clear examples of such process, occurring gradually up to a certain point at later times. The ASR products were systematically observed to accumulate in cement paste cracks, ITZs and natural air voids in the cement paste. Such an accumulation, even at several mm from the aggregate where the products formed, can happen due to the extrusion of ASR gel (as a less viscous phase) outside of the aggregates. The occurrence of such extrusion and the corresponding filling of, e.g., air voids, even up to several mm away from ASR-cracking aggregates have been already inferred before from observations in optical and electron micrographs reported in the literature [5], [12], [13]. However, to my knowledge, those in this Chapter are the first ever reported direct, time-lapse and non-destructive *in situ* 3D observations of such transport process.

Figure 5.8 and the associated movie MS2 in Section C7 provides a clear visual evidence of the described mm-scale transport and accumulation of real-world ASR products. There, the bottom air void was reached, after 55 days, by a crack stemming from the aggregate on its top-right side and propagating through the cement paste. ASR products moved through the evolving crack and gradually accumulated in the air void (compare the voxel value increase inside the air void between 75 and 250 days, which stems partly from an increase in volumetric concentration of products). Additional products reached the air void via the connecting crack and accumulated on top of the older products. Simultaneously, the average voxel value of the previously accumulated products increased in time and was larger than that of the newly accumulating products (compare the frame at 150 days with the one at 200 days in the movie MS2). The latter feature could be explained as an effect of Ca^{2+} ions absorption by the already accumulated products [14]. Experimental work on synthesized ASR products [15] has confirmed an hypothesis [10] according to which the products' stiffness may increase as a consequence of Ca^{2+} ions

absorption. Based upon such results, reported in the literature, and what observable, for example, in Figure 5.8 and in the respective movie MS2, it can be concluded that the products transport characteristics and its spatial-temporal extent may be strongly influenced by the local supply of Ca^{2+} ions and the corresponding evolution of the products' mechanical properties. Thus, taking into account couplings between Ca^{2+} ions transport/uptake and temporal changes in the products' mechanical properties may be a key and necessary ingredient of computational models of ASR cracking working at the microstructure and mesostructure length scales. Although there is lack of data about mechanical properties in the literature, e.g., elastic moduli [6], [16] and viscosity, of ASR products extracted from real world concrete, the data measured for their laboratory synthesized analogs and reported in [15] constitute a good starting point for the development of fully chemo-mechanical computational models taking into account reactive transport of Ca^{2+} ions.

The ASR product transport and accumulation were observed to occur more frequently towards the outer boundary of the aggregates. This could be explained, on the one side, by the tendency of the silica-rich thick solution and of the alkalis to become inter-dispersed more homogeneously. Due to the presence of a concentration gradient (more silica-rich solution within the aggregate and more alkalis and Ca^{2+} in the cement paste), the silica-rich solution moves out and forms stiffer products by Ca^{2+} uptake of. on the contrary, alkalis move inwards (i.e. within the cracks in aggregates) and lead to further silica dissolution. On the other side, products formed and accumulated at the aggregate boundaries may be already stiffer than those formed more inside the aggregate, because of the higher likelihood of Ca^{2+} ions uptake at the boundaries than inside.

Despite the products accumulation in cracks, both inside and outside the aggregates, aggregate dissolution and product accumulation continued (Figure 5.7 and Figure 5.8). Further accumulation was frequently accompanied by widening of the cracks and breakdown of the previously formed ASR products. This was evidently observed both by SEM-BSE (Figure 5.4) and by XT (for example, Figure 5.7 (d)) results, in the form of broken ASR products sticking to the inner surfaces of widened cracks. Thus, complete crack filling and clogging by products was not frequently observed. Such result is confirmed quantitatively by the computed ASR crack filling ratio (reported in Section C8, Figure C22), whose maximum value was 30% for the P-Cs specimen. The new products usually further precipitated/accumulated within the same cracks, which became wider.

The spatial-temporal maps of $J_{\vec{T}_{N-AFF}}$ shown in Section 5.3.7 (Figure 5.12 and Figure 5.13) indicate the existence of spatial correlations between localized deformations, mainly expansion, and cracks. In addition, as mentioned in Section 5.3.7, localization of expansion before crack appearance (see Figure 5.13) was observed for certain aggregates. The latter feature might indicate the presence of cracks smaller than the spatial resolution of the tomograms. An increase in both the temporal and the spatial resolutions of XT might help not only with investigating the ASR reaction front and the associated early cracking mentioned above. It might also allow investigating the causal relationships between the measured local deformations and the resolved cracking.

The temporal resolution increase is mainly limited by instrument access. On the contrary, the spatial resolution increase is more fundamentally limited by the intrinsic, negative correlation with the specimen size (higher spatial resolution is achievable only for smaller specimens).

Local tomography [17] may help, for cm-scale specimens as used in this PhD project, to improve the spatial resolution by a factor of two to three. However, that will not suffice for resolving early stage products accumulation and respective initial crack propagation. The latter targets could be resolved us-

ing the approaches presented in this work together with acquiring datasets with tomographic microscopes based upon synchrotron radiation. The latter measurements would be feasible only for extremely simplified model systems whose realization is extremely challenging and whose representativeness of ASR in actual concrete would need to be carefully assessed and proven.

5.5. Conclusions

In synthesis, the most significant conclusions that can be drawn from the results reported in this Chapter are the following ones.

- a) ASR cracks were first generated in the aggregates and later propagated into the cement paste. Along with crack propagation, it was possible to observe, for the first time in a time-lapse manner, the extrusion of ASR products into the cement paste.
- b) The extrusion suggests that, at early stages, the ASR products may be a low-viscosity gel which can move away from the originating aggregate and can accumulate later elsewhere as a more stiff phase upon uptake of Ca. Progressive accumulation of ASR products within cracks and air voids in the paste, with following Ca uptake from them, thus their stiffening, was observed in this work. Successive extrusions of low-viscosity, lower Ca-content products being added in time were also observed.
- c) The accumulation of ASR products in air voids and cracks in the cement paste or in the ITZ of aggregates surrounding those from which the products originated was observed systematically. Significant portions of the ASR-generated crack volume remained at later ages empty of ASR products.

In the future, the workflow for 3D image analysis and product tracing developed in this PhD project could be directly implemented with XT characterized by higher spatial resolution, for investigating the early stages of ASR products formation and respective cracking. This could be done, e.g., by exploiting local tomography approaches or by using synchrotron radiation-based XT on smaller model systems. This could help with shedding light on some of the chemo-mechanical coupled phenomena at the basis of the early ASR cracking.

Bibliography

- [1] A. Leemann and B. Münch, “The addition of caesium to concrete with alkali-silica reaction: Implications on product identification and recognition of the reaction sequence,” *Cem. Concr. Res.*, vol. 120, pp. 27–35, Jun. 2019, doi: 10.1016/j.cemconres.2019.03.016.
- [2] A. Leemann, “Raman microscopy of alkali-silica reaction (ASR) products formed in concrete,” *Cem. Concr. Res.*, vol. 102, pp. 41–47, Dec. 2017, doi: 10.1016/j.cemconres.2017.08.014.
- [3] C. Merz and A. Leemann, “Assessment of the residual expansion potential of concrete from structures damaged by AAR,” *Cem. Concr. Res.*, vol. 52, pp. 182–189, Oct. 2013, doi: 10.1016/j.cemconres.2013.07.001.
- [4] J. Lindgård, E. J. Sellevold, M. D. A. Thomas, B. Pedersen, H. Justnes, and T. F. Rønning, “Alkali-silica reaction (ASR) - Performance testing: Influence of specimen pre-treatment, exposure conditions and prism size on concrete porosity, moisture state and transport properties,” *Cem. Concr. Res.*, vol. 53, pp. 145–167, Nov. 2013, doi: 10.1016/j.cemconres.2013.05.020.
- [5] V. Jensen, “Alkali-aggregate reaction in Southern Norway,” *Dr. thesis, Tech. Univ. Trondheim, NTH, Norw.*, p. pp 265 +10 Appendices, 1993.
- [6] A. Leemann and P. Lura, “E-modulus of the alkali-silica-reaction product determined by micro-indentation,” *Constr. Build. Mater.*, vol. 44, pp. 221–227, Jul. 2013, doi: 10.1016/j.conbuildmat.2013.03.018.
- [7] E. Boehm-Courjault, S. Barbotin, A. Leemann, and K. Scrivener, “Microstructure, crystallinity and composition of alkali-silica reaction products in concrete determined by transmission electron microscopy,” *Cem. Concr. Res.*, vol. 130, p. 105988, Apr. 2020, doi: 10.1016/j.cemconres.2020.105988.
- [8] P. Rivard, B. Fournier, and G. Ballivy, “The damage rating index method for ASR affected concrete - A critical review of petrographic features of deterioration and evaluation criteria,” *Cem. Concr. Aggregates*, vol. 24, no. 2, pp. 81–91, Dec. 2002, doi: 10.1520/cca10531j.
- [9] C. Rößler, B. Möser, C. Giebson, and H. M. Ludwig, “Application of Electron Backscatter Diffraction to evaluate the ASR risk of concrete aggregates,” *Cem. Concr. Res.*, vol. 95, pp. 47–55, May 2017, doi: 10.1016/j.cemconres.2017.02.015.
- [10] S. Urhan, “Alkali silica and pozzolanic reactions in concrete. Part 1: Interpretation of published results and an hypothesis concerning the mechanism,” *Cem. Concr. Res.*, vol. 17, no. 1, pp. 141–152, Jan. 1987, doi: 10.1016/0008-8846(87)90068-8.
- [11] F. Rajabipour, E. Giannini, C. Dunant, J. H. Ideker, and M. D. A. Thomas, “Alkali-silica reaction: Current understanding of the reaction mechanisms and the knowledge gaps,” *Cem. Concr. Res.*, vol. 76, pp. 130–146, Jul. 2015, doi: 10.1016/j.cemconres.2015.05.024.

- [12] T. Knudsen and N. Thaulow, “Quantitative microanalyses of alkali-silica gel in concrete,” *Cem. Concr. Res.*, vol. 5, no. 5, pp. 443–454, Sep. 1975, doi: 10.1016/0008-8846(75)90019-8.
- [13] A. D. Jensen, S. Chatterji, P. Christensen, and N. Thaulow, “Studies of alkali-silica reaction - part II effect of air-entrainment on expansion,” *Cem. Concr. Res.*, vol. 14, no. 3, pp. 311–314, May 1984, doi: 10.1016/0008-8846(84)90046-2.
- [14] M. D. A. Thomas, “The role of calcium hydroxide in alkali recycling in concrete, in: Materials Science of Concrete Special Volume on Calcium Hydroxide in Concrete,” *Am. Ceram. Soc. Westerv. (OH), USA*, pp. 269–280, 2001.
- [15] A. Gholizadeh-Vayghan, F. Rajabipour, M. Khaghani, and M. Hillman, “Characterization of viscoelastic behavior of synthetic alkali-silica reaction gels,” *Cem. Concr. Compos.*, vol. 104, p. 103359, Nov. 2019, doi: 10.1016/j.cemconcomp.2019.103359.
- [16] G. Geng *et al.*, “Mechanical behavior and phase change of alkali-silica reaction products under hydro-static compression,” *urn:issn:2052-5206*, vol. 76, no. 4, pp. 674–682, Jul. 2020, doi: 10.1107/S205252062000846X.
- [17] A. Kyrieleis, V. Titarenko, M. Ibison, T. Connolley, and P. J. Withers, “Region-of-interest tomography using filtered backprojection: Assessing the practical limits,” *J. Microsc.*, vol. 241, no. 1, pp. 69–82, Jan. 2011, doi: 10.1111/j.1365-2818.2010.03408.x.

Chapter 6. Qualitative and quantitative analysis of ASR crack networks and their evolution in the concrete mesostructure context

6.1. Summary

In this Chapter, the implementation and concentration-optimization of a contrast agent for enhancing the visibility of natural aggregates in the X-ray tomograms (otherwise almost undistinguishable) within the cement paste has been explained. Section 6.2 describes the exclusive/additional experimental procedure (in addition to the general procedure explained in chapter 3), which was carried out for the specific specimens discussed in this chapter. Section 6.3 illustrates the most important findings and the rest of the results are framed as Appendix D dedicated to this chapter. Section 6.4 discusses and synthesizes the important remarks concerning all the observations. Finally, section 6.5 highlights the most important conclusions.

6.2. Specific experimental and analysis details

The overall experimental and analysis workflow of this part of the PhD project consisted of three major steps:

- (1) optimization of the XT contrast between aggregates and cement paste;
- (2) assessment of contrast agent's effects on the ASR (cracking) development;
- (3) extensive quantitative analysis of specimens cast with the optimized mix design including the contrast agent, in order to characterize ASR cracking in respect of the concrete mesostructure.

These three steps are explained in the following sub-sections.

6.2.1. Materials and specimen preparation

6.2.1.1. Specimens for the optimization of the BaSO₄ concentration and assessment of its effects on the ASR (cracking)

Reference specimens

Specimens without BaSO₄ and with size 40×40×160 mm³ were cast according with the basic mix composition reported in Table 3.1 and with the same aggregate sieve size and cement type described in Section 3.1. Such specimens were cast with the U and P aggregates and are named hereafter as "U-Ref" and "P-Ref", respectively, as done in Chapter 5. They played the role of reference specimens, not being

affected by any eventual side effect of $BaSO_4$. All of these reference specimens, as well as those cast with $BaSO_4$, were subjected to the same ASR acceleration protocol detailed in Section 3.1.

Specimens with $BaSO_4$

The X-ray attenuation contrast between aggregates and the cement paste was optimized by casting several distinct batches of specimens $40 \times 40 \times 160 \text{ mm}^3$ in size and according with the same reference mix composition of Table 3.1 except for replacing a fraction of the aggregate total volume (regardless of the sieve size) by an equal volume of $BaSO_4$. Different concentrations (i.e., fractions of total aggregate volume replaced) were tested: 0.25, 0.75, 1.5, 2.5 and 3 vol.-%. Table 6.1 shows the mix compositions and the respective specimen labels.

As mentioned in Section 2.4.2.5.1, $BaSO_4$ (also known as baryte or barite) is typically available in the form of a fine, white powder. The average particle size was estimated, by SEM-BSE imaging, to be at the scale of a few μm . Some examples of SEM-BSE micrographs of the used powder's grain are provided in Section D1.1 of Appendix D (Figure D1 (a)). The $BaSO_4$ grains could be uniformly distributed through the cement paste independently of the concentration value, within the tested range, as assessed by SEM-BSE as well (see Figure D1 (c) and (d) for some examples). Therefore, its X-ray attenuation was expected to be monotonically increased with increasing concentration. It has to be noticed that the $BaSO_4$ replacement of a volumetric fraction of aggregates implied an increase in the specimen mass, given $BaSO_4$ higher mass density ($4480 \text{ kg} \cdot \text{m}^{-3}$ [1]) compared with that of each aggregate type ($2667 \text{ kg} \cdot \text{m}^{-3}$ and $2651 \text{ kg} \cdot \text{m}^{-3}$, for the U and P aggregates, respectively, see Section 3.2). In correspondence of the maximum $BaSO_4$ concentration of 3 vol.-%, the relative mass increase was 1.44% and 1.46% for the specimens cast with U and P aggregates, respectively.

Table 6.1. Mix composition of the $BaSO_4$ containing specimens in units of $\text{kg} \cdot \text{m}^{-3}$ (mass per m^3 of cast).

Specimen label	Cement CEM I 42.5N	Aggregates			Deionized water	NaOH	$BaSO_4$
		0 – 4 mm	4 – 8 mm	8 – 11.25 mm			
<i>U – 0.25 vol. % $BaSO_4$</i>	450	656	410	574	225	4.9	7
<i>U – 0.75 vol. % $BaSO_4$</i>	450	650	406	569	225	4.9	21
<i>U – 1.5 vol. % $BaSO_4$</i>	450	641	401	561	225	4.9	43
<i>U – 2.5 vol. % $BaSO_4$</i>	450	630	394	552	225	4.9	70
<i>U – 3 vol. % $BaSO_4$</i>	450	625	390	547	225	4.9	84
<i>P – 0.25 vol. % $BaSO_4$</i>	450	656	410	574	225	4.9	7
<i>P – 0.75 vol. % $BaSO_4$</i>	450	650	406	569	225	4.9	21
<i>P – 1.5 vol. % $BaSO_4$</i>	450	641	401	561	225	4.9	43
<i>P – 2.5 vol. % $BaSO_4$</i>	450	630	394	552	225	4.9	70
<i>P – 3 vol. % $BaSO_4$</i>	450	625	390	547	225	4.9	84

6.2.1.2. Extensive quantitative analysis of specimens with optimal BaSO₄ concentration

Once an optimal BaSO₄ concentration value was chosen (see 6.3.1 for how this choice was achieved), a new batch of specimens were cast according with the same mix composition shown in Table 6.2, with the optimal concentration and with both aggregate types and they subjected to the same ASR acceleration protocol described in Section 3.1. The specimens were cast with distinct size values for different characterization purposes. Those used for XT analysis and for relative mass and length change measurements were cast with size of $25 \times 25 \times 100 \text{ mm}^3$. As shown in Chapter 4, this size may have led to slightly less representative ASR cracking but it allowed resolving the part of the crack network characterized by smaller size features, e.g., narrower thickness, which implies resolving cracks also at earlier stages. The specimens for the characterization of the mechanical properties had larger size of $40 \times 40 \times 160 \text{ mm}^3$, being it a more standardized size for the types of measurements performed, listed in Section 6.2.2.2. Note that, in the following, the specimens cast with size of $25 \times 25 \times 100 \text{ mm}^3$ are labelled with small starting letters of their corresponding aggregate (e.g., *u*, for Uri aggregates) while those with size of $40 \times 40 \times 160 \text{ mm}^3$ are denoted with capital letters (e.g., *U*, still for Uri aggregates). This naming pattern also applies to the previous groups of the specimens mentioned in section 6.2.1.1. Table 6.2 shows the mix composition and the specimen labels.

Table 6.2. Mix composition of the specimens with optimal BaSO₄ vol.% in units of $\text{kg}\cdot\text{m}^{-3}$ (mass per m^3 of cast)

Specimen label	Cement CEM I 42.5N	Aggregates			Deionized water	NaOH	BaSO ₄
		0 – 4 mm	4 – 8 mm	8 – 11.25 mm			
<i>U</i> or <i>u</i>	450	630	394	552	225	4.9	70
<i>P</i> or <i>p</i>	450	630	394	552	225	4.9	70

6.2.2. Characterizations

6.2.2.1. Measurements and analysis for the BaSO₄ concentration optimization and for the assessment of its effects on the ASR (cracking)

At different time points, the specimens described in Section 6.2.1.1, were taken out of the alkaline solution to be characterized with various methods. The non-destructive measurements were repeatedly performed on average, nine successive time points within the total duration of the experimental campaign and on three specimens of each set (the reference set and the BaSO₄ ones). Such measurements, in addition to XT, also included those of mass and length changes and the quasi-static (compressive) Young's modulus measured along the specimen longitudinal direction following the standard mentioned in Section 3.2. The length change measurements were performed with the mechanical displacement gauge described in Section 3.2 (shown in Figure 3.1 (c)). The Young's modulus was the only mechanical parameter measured. The compressional and flexural strengths were not measured in this campaign,

since, as shown by the results reported in Chapter 5 and Appendix C, they were much less sensitive than the Young's modulus to the ASR progression, after the first fifty days of ASR acceleration (see Figure 5.6 for the specimens with the P aggregates and Figure C10 for those with U aggregates). The goal of such measurements, additional to XT, was to assess any eventual, undesired influence of BaSO₄ on the expansion and mechanical properties.

The only destructive measurements performed on some of these specimens consisted of SEM and EDX analysis performed at one time point (150 days and Figure D3 shows EDX point analysis results obtained at 150 days) on polished cross-sections from parts of two distinct additional specimens. EDX point analysis was used to characterize the chemical composition of the ASR products, in order to assess whether the use of BaSO₄ could have any effect on the ASR. XT was performed with the basic settings described in Section 3.2 characterized by maximum X-ray photon energy of 90 keV and an upper bound of the effective spatial resolution of approximately 70 μm .

6.2.2.2. Measurements and analysis on/of the specimens with optimal BaSO₄ concentration

The experimental campaign described in Section 6.2.1.2 aimed at optimizing the BaSO₄ concentration and included already specimens with what was chosen as its optimal value. However, it was designed to be neither time resolved nor extensive, because of the need to characterize many specimens, with distinct BaSO₄ concentrations.

The successive experimental campaign, described here, was on the contrary only focused on characterizing ASR cracking in specimens with the optimal BaSO₄ concentration with higher temporal resolution, especially at the earlier ASR ages, and with a larger number of specimens.

The time-lapse measurements performed on its specimens, described in Section 6.2.1.2, regarded, in addition to the XT analysis, the mass and length changes of ten specimens with size $25 \times 25 \times 100 \text{ mm}^3$, for each aggregate type, not including the 3 specimens subjected to XT, the quasi-static (compressive) Young's modulus (on 3 specimens, for each aggregate type), flexural strength (on 3 specimens, for each aggregate type) and longitudinal compressive strength (on 6 specimens, for each aggregate type), all performed since the start of the ASR acceleration. It is reminded that all the mechanical characterization measurements were performed on specimens with size $40 \times 40 \times 160 \text{ mm}^3$. The length change measurements were performed with the expansion measurement setup 2 mentioned in Section 3.2 and shown in Figure 3.1 (e), relying on an optical approach instead of a purely mechanical one and allowing a higher degree of measurement automation without sacrificing the measurement resolution and repeatability (see Section A4 of the Appendices).

Time-lapse XT was performed with the holding setup 2 described in Section 3.2 and only on the specimens cast with the U aggregates and with size $25 \times 25 \times 100 \text{ mm}^3$, on a total of 3 different specimens of the same batch. Due to time and tomograph accessibility constraints, it was not possible to run an analogous time-lapse XT campaign on specimens cast with the P aggregates.

The original motivation for using $25 \times 25 \times 100 \text{ mm}^3$ specimens instead of $40 \times 40 \times 160 \text{ mm}^3$ for such XT study with higher temporal resolution was to be able to resolve cracks at earlier stages than what was feasible by working with the larger specimens. According to the specimen labelling scheme mentioned in Section 6.2.1.2, such XT specimens were named as u_i , with $i = 1, 2, 3$. The XT and the

relative mass and length change measurements were conducted at 18 distinct time points, within the total duration of 404 days. Thus, the time-lapse campaign was not only overall longer than the one used for the BaSO₄ concentration optimization. It was also characterized by a higher density of time points within the first two month since ASR acceleration start. The mechanical characterization included an additional time point (i.e., 19 measuring points) at 557 days, in order to assess the mechanical properties evolution in the very long-term. In the case of the non-destructive measurements (XT and Young's modulus), the same specimens were measured at every time point, belonging to two distinct and dedicated batches for the two distinct measurement types, respectively. For XT, the 160 kV source was used with voltage and current set to 98 kV and 100 μ A, respectively. The spatial resolution of the tomograms was estimated to be approximately 35 μ m.

6.2.3. Analysis of the time-lapse X-ray tomograms

Image enhancement

To minimize the noise in the tomograms without smoothing edges, the same anisotropic diffusion filtering as described at the point (I) in Section 3.3 was used.

Correction for the specimen misalignments

In order to achieve (quantitative and qualitative) comparability between the time-lapse tomograms, the tomogram at each time point $t_i, \forall i = 1, \dots, N_t$, was rigidly registered to the reference one (the tomogram at time $t_0=1$ day). The rigid body registration procedure was the same as described at point (II) in Section 3.3.

Crack segmentation

The cracks were segmented using the TS-based procedure described at point (III) in Section 3.3, with the exception of the tomogram at the reference time point, for which the segmentation was performed with the approach relying upon the BTH transform (also described at point (III) in Section 3.3).

For the quantitative analysis of the crack features mentioned below and only for the specimens with optimal BaSO₄ concentrations mentioned in Section 6.2.2.2, the ASR crack segmentation was repeated with a modification to the TS-based approach, which avoids introducing any small displacement of such cracks. The results of such segmentation were the ones used for the crack feature analysis of such specimens. The modified TS-based segmentation approach is described in details in Section D2.5 of the Appendices, along with a comparison of its results against those from the standard TS-based approach explained in Section 3.3.

Aggregate segmentation

In the specimens containing BaSO₄, the aggregates were segmented by manual selection of a corresponding voxel value range ("thresholds selection").

Global and local deformations analysis

The displacement vector fields, $\vec{u}(\vec{x}, t_i)$ output from the affine and non-affine registration steps of the TS-based crack segmentation workflow were used to quantify the global and local deformations induced by ASR. As mentioned at point (VII) in Section 3.3, the affine registration displacement vector field, $\vec{u}_{AFF}(\vec{x}, t_i)$, was used to compute the relative size changes, $\frac{\Delta L_{AFF,k}}{L_{AFF,k}}(t_i)$, with $k = X, Y$ and Z indicating the axes of the Cartesian frame of reference. The global affine registration-based relative length change, $\frac{\Delta L_{AFF,Z}}{L_{AFF,Z}}(t_i)$, was compared with the experimentally measured $\frac{\Delta L_Z}{L_Z}(t_i)$ values. As mentioned in Section 3.3, the $\frac{\Delta L_{AFF,Z}}{L_{AFF,Z}}(t_i)$ indicates the relative length change only for the specimen's tomographed portion,

while the $\frac{\Delta L_Z}{L_Z}(t_i)$ refers to the full specimen. As mentioned already in Section 5.3.3., comparing these variables allows evaluating the representativeness of the tomographed region, in terms of the ASR-induced deformations. In addition to $\frac{\Delta L_{AFF,Z}}{L_{AFF,Z}}(t_i)$, the relative length changes computed along X and Y directions, provided complementary and unique information about the bulk deformations in the lateral directions, which were not measured experimentally.

Lastly, the non-affine registration displacement vector field, $\vec{u}_{N-AFF}(\vec{x}, t_i)$, was used to map the local deformations. As described at point (VII) in Section 3.3, and shown already in use in Sections 5.3.7 and C10, two scalar fields were computed based upon $\vec{u}_{N-AFF}(\vec{x}, t_i)$, its magnitude (i.e., its Euclidean norm), $\|\vec{u}_{N-AFF}\|(\vec{x}, t_i)$, and the determinant of the Jacobian matrix of the non-affine mapping vector field, $J_{\vec{T}_{N-AFF}}(\vec{x}, t_i)$. It is reminded that $J_{\vec{T}_{N-AFF}}(\vec{x}, t_i)$ maps the local relative volume (volume at t_i divided by volume at t_0). Its values larger than 1 denote a volumetric expansion while those smaller than 1 correspond to a volumetric shrinkage.

Shape tensor and local thickness analyses

From the shape tensor \mathbf{G} , the bounding box length L of each crack was computed and its statistics were analyzed.

Similar to what was presented in Section 4.3.3, the statistics of the crack shape was analysed based upon the joint distribution of values of the crack elongation, E , and crack flatness, F , defined by Eqs. (3.8) and (3.9), respectively. Their joint distribution was presented in the form of the KDE of their joint PDF, $f_{(E;F)}(E; F)$, which was obtained via the same software described in Section 4.3.3

The crack orientation analysis was also performed in the form of assessing qualitatively the distribution of the direction of the first *eigenvector* of \mathbf{G} , \hat{u}_1 , as also shown done in Chapters 4 and 5.

Finally, the crack thickness analysis was based upon the computation of the local crack thickness, $T_{local}(\vec{x})$.

6.3. Results

6.3.1. BaSO₄ concentration optimization

The aggregate-to-cement paste X-ray attenuation contrast enhancement by BaSO₄ and its optimization were investigated by considering the tomograms, at 150 days, of different specimens, each cast with a different concentration. Examples of ROIs on slices from such tomograms are shown in the first rows of Figure 6.1 and Figure 6.2 for the specimens with U and P aggregates, respectively. Larger ROIs on the same slices are additionally reported in Figure D5 and Figure D6, respectively. The aggregate-to-cement paste contrast was enhanced by increasing, above the value of 0.25 vol.-%, the BaSO₄ concentration. Below that value, the contrast remained poor and at similar levels as in the reference specimen tomograms. A qualitative comparison of X-ray attenuation contrast between aggregates and cement paste in specimens cast without and with 0.25 vol.-% BaSO₄, is provided in Section D1.3. It has to be underlined that such a BaSO₄ concentration value cannot be used as an absolute threshold value, above which the contrast started to increase, given the limited number of distinct BaSO₄ concentration values

which were tested. However, it can be stated that concentrations smaller than or equal to 0.25 vol.-% provided no contrast enhancement, while at 0.75 vol.-% the enhancement was already clearly evident. Thus, a lower bound for the BaSO₄ concentration may lay in between those two values, for the purpose of achieving contrast enhancement. It must be reminded that this result may not apply universally to any X-ray tomograms, even of the same specimens, rather it may depend upon the X-ray tomograph used and its measurement settings, especially acceleration voltage and current.

Figure 6.3 (a) and Figure 6.3 (b) show the full tomogram's voxel value distributions of the reference specimens and of those cast with different BaSO₄ concentrations, for the U and P aggregates, respectively. For each specimen type, the tomogram of one specimen at 150 days of ASR acceleration was used. For both aggregate types, the voxel value distributions remained prevalently unimodal when using the smallest BaSO₄ concentration, 0.25 vol.-%. This feature indicates little voxel value differences between aggregates and cement paste, the two main mesoscopic scale phases, volume-wise. Slightly less unimodal was the distribution for the P aggregate tomograms than for the U ones. This difference is due to the higher mineralogical heterogeneity in the P case. Despite such higher voxel value heterogeneity, the segmentation of voxels of the paste or of the aggregates remained extremely challenging also in such P tomograms, when using approaches relying only on the distribution of voxel values, because of the high degree of overlapping of the voxel value ranges for paste and aggregates. Figure 6.1(f) and Figure 6.2(f) show, for example, the results of the aggregate segmentation based upon thresholds selection in the 0.25 vol.-% case. There, the same ROIs from the corresponding segmented aggregate binary tomograms were overlaid on top of those of Figure 6.1 (a) and Figure 6.2 (a) and rendered in semi-transparent blue and red, respectively. Many regions of the cement paste were included by such segmentation in the aggregates class, because of sharing the same voxel values.

The aggregate-to-cement paste contrast enhancement by increasing the BaSO₄ vol.-% is mirrored into the voxel value distributions' evolution visible in Figure 6.3 (a) and (b). From being mostly unimodal, they gradually became multi-modal and with decreasing overlapping of the corresponding peaks. In each of such distributions corresponding to higher BaSO₄ vol.-% values, the left-most, well-defined peak corresponded to most of the aggregate voxels, while the right-most peak to the cement paste. With increasing BaSO₄ vol.-%, the separation of the peaks increased, thus, correspondingly, also the accuracy of the aggregate segmentation by thresholds selection, as qualitatively evident in Figure 6.1 (f)-(j) and Figure 6.2 (f)-(j).

In order to assess more quantitatively the effect of the BaSO₄ concentration increase on the aggregate segmentation accuracy increase and to choose an optimal value for it, the following approach was considered. At each BaSO₄ concentration, the difference between the mix design's nominal aggregate vol.-% for the full specimen and the corresponding one obtained from the aggregate segmentation for the tomographed volume was computed. Figure 6.3(c) shows that, independently of the aggregate type, the increase in BaSO₄ concentration led to higher volume fraction of segmented aggregates, converging towards the mix design's nominal value. Such value (~ 62 vol.-%) was approached starting from about 1.5 vol.-%. An increase above 2.5 vol.-% provided no significant improvement. Thus, the range between the 1.5 vol.-%. and 2.5 vol.-% was chosen as the one where an optimal BaSO₄ concentration value would be located, leading to a minimum in the difference between the nominal and computed aggregate fraction. The main reason for not considering values higher than 2.5 vol.-% was that it was observed that they actually hindered the reliability of the ASR crack segmentation, especially for cracks with thickness close to the tomographic spatial resolution, due to partial volume effect [2].

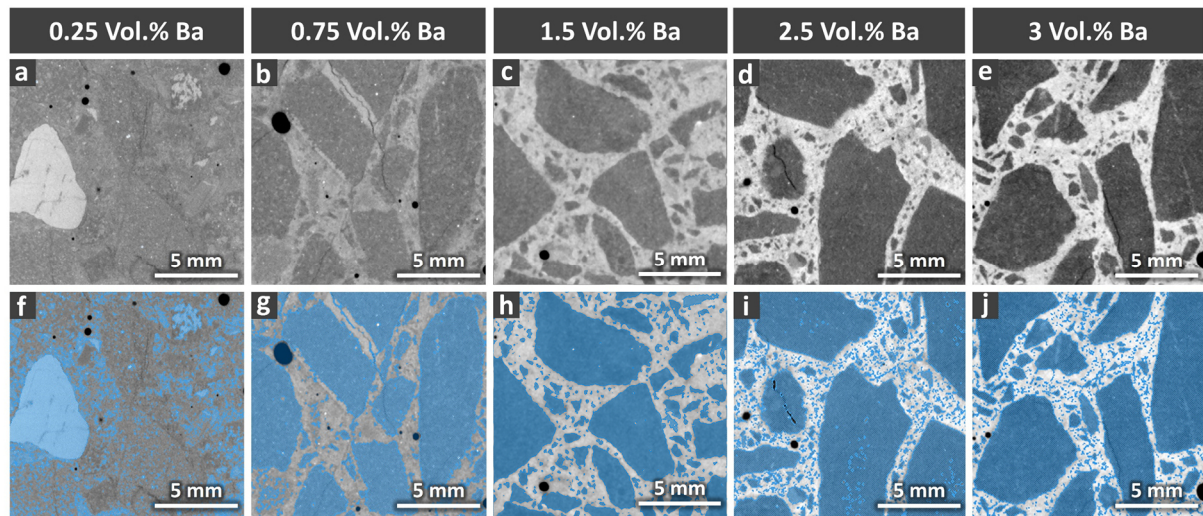


Figure 6.1. (a) to (e): examples of regions of interest (ROIs) on tomographic slices at 150 days of ASR acceleration, from the specimens cast with the U aggregates and with various BaSO_4 concentrations. (f) to (j): the same slices as in (a) to (e) but, additionally, with the corresponding slices from the binary tomograms of the segmented aggregates rendered as semi-transparent and in blue and overlaid on top of the tomographic slices.

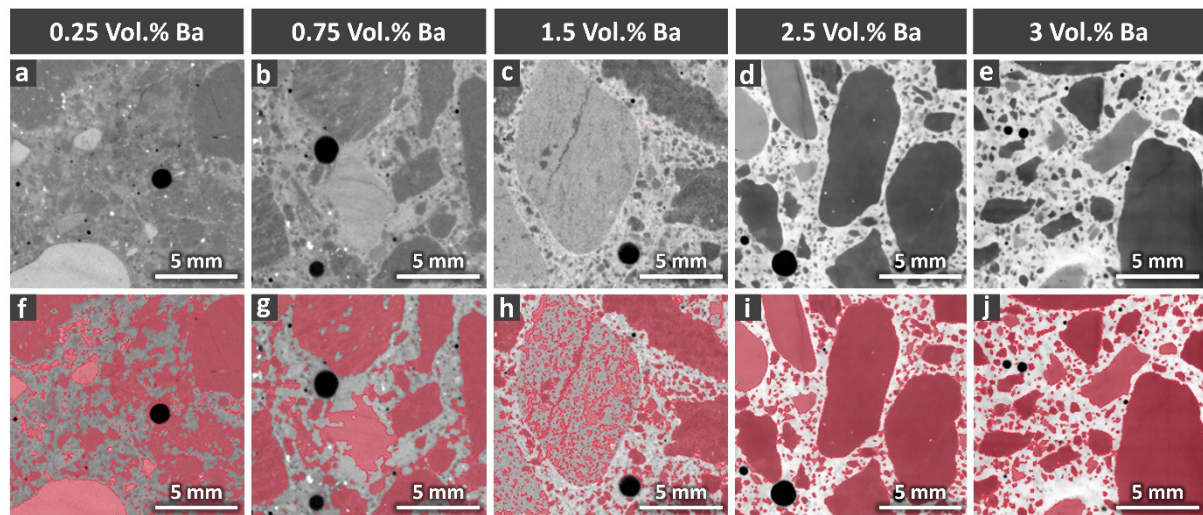


Figure 6.2. Similar slices as shown in Figure 6.1 but for the specimens cast with the P aggregates.

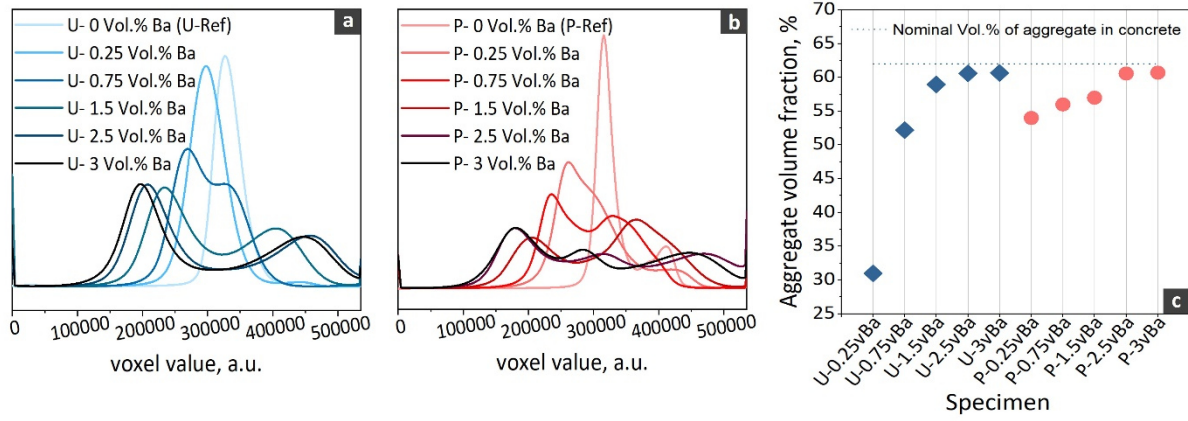


Figure 6.3. Full tomogram voxel value histograms for the specimens cast with various BaSO_4 concentrations (0.25, 0.75, 1.5, 2.5 and 3 vol.%) and with (a) U and (b) P aggregates, respectively. Each histogram refers to the tomogram of a single specimen at 150 days of ASR acceleration. (c): volume fraction of segmented aggregates calculated based upon each tomogram whose voxel value histogram is shown in insets (a) and (b). The aggregate volume fraction was defined as the volume of segmented aggregates divided by the full volume of the tomogram.

6.3.2. Influences of BaSO_4 on the ASR (cracking)

6.3.2.1. Influence on the macroscopic dimensional changes induced by ASR

The time series of relative length change (along the specimen longitudinal direction, i.e., Z-axis, $\frac{\Delta L_Z}{L_Z}$) values, measured with the displacement gauge, is shown in Figure 6.4 (a) for specimens cast with the two aggregate types and either without or with the distinct BaSO_4 concentrations.

For any of the two aggregate types, the ASR expansion along the Z-axis proceeded rather similarly, independently of the BaSO_4 presence or absence in the mix design. At any time point, a different BaSO_4 concentration led to distinct values in $\frac{\Delta L_Z}{L_Z}$. However, such variations were with amplitude well within the data scatter range associated with distinct specimens, as the error bars overlapping indicates (Figure 6.4(a)). The specimens which underwent XT exhibited $\frac{\Delta L_Z}{L_Z}$ time series which strongly overlapped with those of the other respective specimens. A similar influence by BaSO_4 was also observed for the relative mass change time series, as seen in Figure 6.4(b).

In addition to the experimental measurements with the displacement gauge mentioned above, such time series were also obtained directly from the tomographic time series, based on the global affine registration results ($\frac{\Delta L_{AFF,k}}{L_{AFF,k}}$ time series, with $k = X, Y$ and Z). Similar features in terms of size changes along the three directions was observed in the specimens with BaSO_4 (Figure 6.4(e) and (f)) compared to their corresponding reference specimens (Figure 6.4(c) and (d)), regardless of the type of aggregates. For instance, the expansion in one of the lateral directions of the specimens (X- or Y-axis) was larger than that along the longitudinal (Z-axis) direction). Thus, overall, the addition of BaSO_4 did not perturb the ASR-induced expansion.

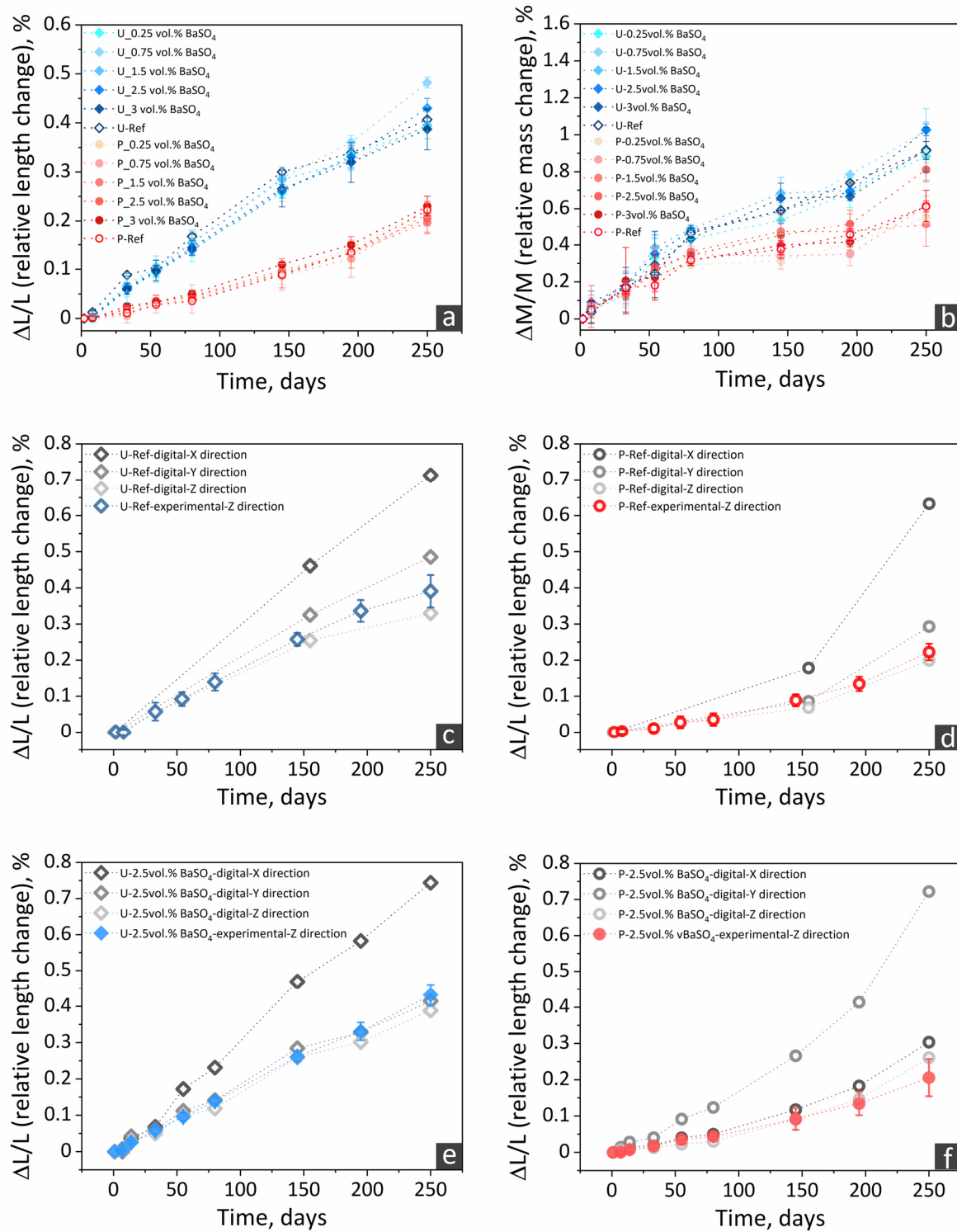


Figure 6.4. (a) Evolution of the relative length change, along the specimen's longitudinal direction (Z-axis), for the specimens cast with the two aggregate types (blue shades for U, red shades for P) and with (filled markers) or without (hollow markers) $BaSO_4$. The markers indicate mean values while the error bars' size is the standard deviation of an ensemble of six distinct specimens, for each specimen batch. (b): evolution of the relative mass change of the same specimens as for (a). (c): evolution of the relative length change for the tomographed volume of one of the six U reference specimens and computed along each axis from the the global affine registration results (markers in grey tones). The relative length change along the Z-axis is compared with the corresponding

experimental values from inset (a) (blue markers). (d): similar plot as in (c) but for the tomographed volume of one of the six P reference specimens. (e) and (f): similar plots as in (c) and (d) but for the tomographed volume of one of the six specimens cast with 2.5 vol.-% BaSO₄.

The specimens produced with U aggregates expanded faster than those with P aggregates, as already reported in Section 4.3.1.1 (Figure 4.1) and in Section C4.1 (Figure C8). The former specimens reached a maximum expansion level almost double the one of the latter, at 250 days. As mentioned already in Chapters 4 and 5, the higher expansion rates for the specimens cast with U aggregates than for those cast with P aggregates are attributed to their differences in the mineralogical texture. As sedimentary rocks, the U aggregates contains higher volume fraction of grain boundaries, which can facilitate silica dissolution, thus increasing the ASR rates and the corresponding expansion.

In each of insets (c) to (f) of Figure 6.4, the $\frac{\Delta L_Z}{L_Z}$ time series is plotted along with the $\frac{\Delta L_{AFF,Z}}{L_{AFF,Z}}$ one in order to assess the representativeness of the tomographed volume's deformations in respect of the whole specimen's ones. Independently of the aggregate type and of the presence or absence of BaSO₄, the two time series were rather overlapped, signalling that, at least along the Z-axis, the expansion of the tomographed volume occurred rather similarly as for the whole specimen.

6.3.2.2. Influence on the Young's modulus evolution induced by ASR

The Young's modulus evolution for some of the BaSO₄ containing specimens and for their corresponding reference specimens is presented in Figure 6.5. The qualitative pattern of the evolution was the same as already reported in Figure 5.6 and in Figure C10 for specimens cast with and without CsNO₃. It was characterized, for all specimens, by the achievement of a peak value at about 15-20 days, similarly to what observed for the P and U specimens of the experimental campaign described in Chapter 5 (see Figure 5.6 (a) and Figure C10 (a), respectively). As already mentioned in Section 5.3.3, such an increase within the first 20 days could be attributed to the cement paste hardening because of cement hydration. Even if ASR cracking might have already happened during this period, the microstructure formation due to cement hydration compensated its degradation effects. After about 20 days, the Young's modulus started to strongly and monotonically decline. After 150 days, the decrease rate slowed down, except for the P-ref specimens. The latter was a different feature of the Young's modulus time series, when compared with the analogous one shown in Figure 5.6 (a). The temporal evolution pattern characterized all the specimen types. The specimens cast with BaSO₄ followed an analogous evolution as their respective reference ones. At any time point and for any aggregate type, the differences between reference and BaSO₄-doped specimens were at a scale comparable with the data scatter range due to material heterogeneity. The P specimens exhibited smaller differences than the U ones, when comparing the results without and with BaSO₄.

As mentioned in Section 6.2.1.1, the replacement by BaSO₄ of an equivalent volume of aggregates led to a slight increase in specimen mass, for example a 1.44% and 1.46% mass increase at 3 vol.-% replacement, for the U and P aggregates respectively. In addition, since BaSO₄ resulted being well dispersed throughout the cement paste, as shown both in Figures 6.1 and 6.2 and in Figure D1, there exists the possibility of a stiffening effect of the cement paste. The Young's modulus time series in Figure 6.5 provide no systematic evidence of such a stiffening by the BaSO₄ addition: at any time point and for a given aggregate type, no systematic increase in Young's modulus was observed in correspondence of

the increase in BaSO_4 concentration. The range of Young's modulus values, in the absence or in the presence of BaSO_4 , was also similar to the range obtained in the experimental campaigns described in Chapters 4 and 5, except for the an increase of about 4 GPa in the plateau value achieved after about 150 days, which was about 21 GPa for the specimens cast with BaSO_4 while it was about 17 GPa for those without it (compare Figure 6.5 with Figures 5.6 (a) and C10 (a)).

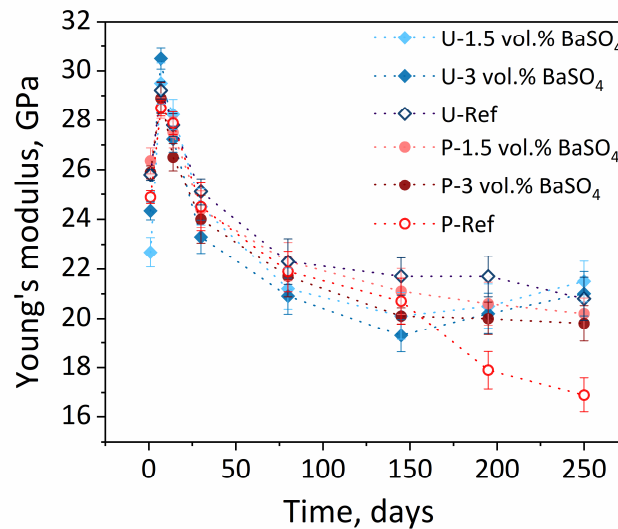


Figure 6.5. The time series of the quasi-static, compressive Young's modulus of specimens cast with both types of aggregates, without or with two BaSO_4 concentrations. The markers indicate mean values while the error bars size the standard deviation of an ensemble of three specimens (always the same at each time point), for each specimen batch.

6.3.2.3. Influence on the chemical composition and morphological features of the ASR products

The analysis of qualitative features of the ASR products by SEM-BSE micrographs showed no evidence of differences induced by the addition of BaSO_4 to the concrete mix. Such result was confirmed also in terms of the products' chemical composition, as analyzed by EDX. Detailed results of both analysis types are available in Section D1.

6.3.2.4. Influence on the ASR cracking and respective local deformations

Independently of the absence or the presence of BaSO_4 and of the aggregate type, the ASR cracking and its associated deformations were characterized by common qualitative features.

First of all, the ASR cracks gradually grew in length and thickness. Second, in many cases, cracks were observed to grow from regions, which already contained crack-like parts of the pore space, e.g., thin and short original cracks or delaminations in ITZs. Finally, the coalescence of shorter/narrower cracks led to the formation of longer/wider ones, giving rise to branching networks which, at the end of the measurement campaign (250 days), typically percolated the whole tomographed volume, at least along one dimension.

The first two qualitative features could be easily detected by visual inspection, at successive time points, of both slices from the registered tomograms and of 3D renderings of the binary tomograms of segmented cracks. Figure 6.6 (a)-(c) and Figure 6.7 (a)-(d) provide examples of such features as visible in slices from the U-Ref specimen and the U-2.5 vol.-% BaSO₄ one, respectively. Similar examples but for the corresponding P specimens are available in Section D1.4 of Appendix D. The comparison of Figure 6.6 (a)-(c) with Figure 6.7 (a)-(d) also allows clearly appreciating the advantage of aggregate-to-cement paste contrast enhancement by the use of BaSO₄. In its absence (Figure 6.6 (a)-(c)), the recognition of when the cracks propagated beyond an aggregate volume into the cement paste was extremely challenging, even for a human being, let alone for algorithms. On the contrary, that was completely feasible for the specimen with the optimal BaSO₄ concentration (Figure 6.7 (a)-(d)).

3D rendering of the whole crack network binary tomograms, as exemplified in Figure 6.8 for the U-2.5 vol.-% BaSO₄ specimen, allowed not only tracking the lengthening and widening of the cracks. It also allowed observing the coalescence of initially independent cracks and the percolation of the resultant network. The latter is an intrinsic 3D process, thus not observable by the mere slice inspection. Examples of crack network percolation for the other specimens are additionally available in Section D1.4.

The feasibility of a comprehensive aggregate segmentation, when using BaSO₄, thus of reliably distinguishing between aggregate and cement paste regions, also allowed observing that the crack propagation through the paste played a significant role in the crack network percolation. This feature can be appreciated when observing the crack evolution throughout the paste from 85 days to 250 days in Figure 6.8 (c) and (d), respectively.

Crack growth from/around pre-existing, crack-like pores could be very well observed in the slices as well as by the 3D rendering of the crack binary tomograms. For example, the delaminations in the ITZs highlighted in Figure 6.6 (a) were observed to not only to widen, but they also propagated further along the aggregate boundaries (Figure 6.6 (b) and (c)). Figure 6.7 (a)-(d) show that a pre-existing crack in one aggregate (left side of each inset) propagated both upward and downward inside the aggregate and also into the cement paste (bottom side of the aggregate), in addition to widening up.

Concerning the localized deformations accompanying the ASR cracking, Figure 6.6 (d)-(e) and Figure 6.7 (e)-(h) exemplify the evolution of the determinant of the Jacobian matrix of the non-affine transformation vector field, $J_{\vec{T}_{N-AFF}}(\vec{x}, t_i)$, for the U-Ref and U-2.5 vol.-% specimens, respectively. Similar results were obtained for the corresponding P specimens, reported in Section D1.4 (Figures D7 and D10, respectively).

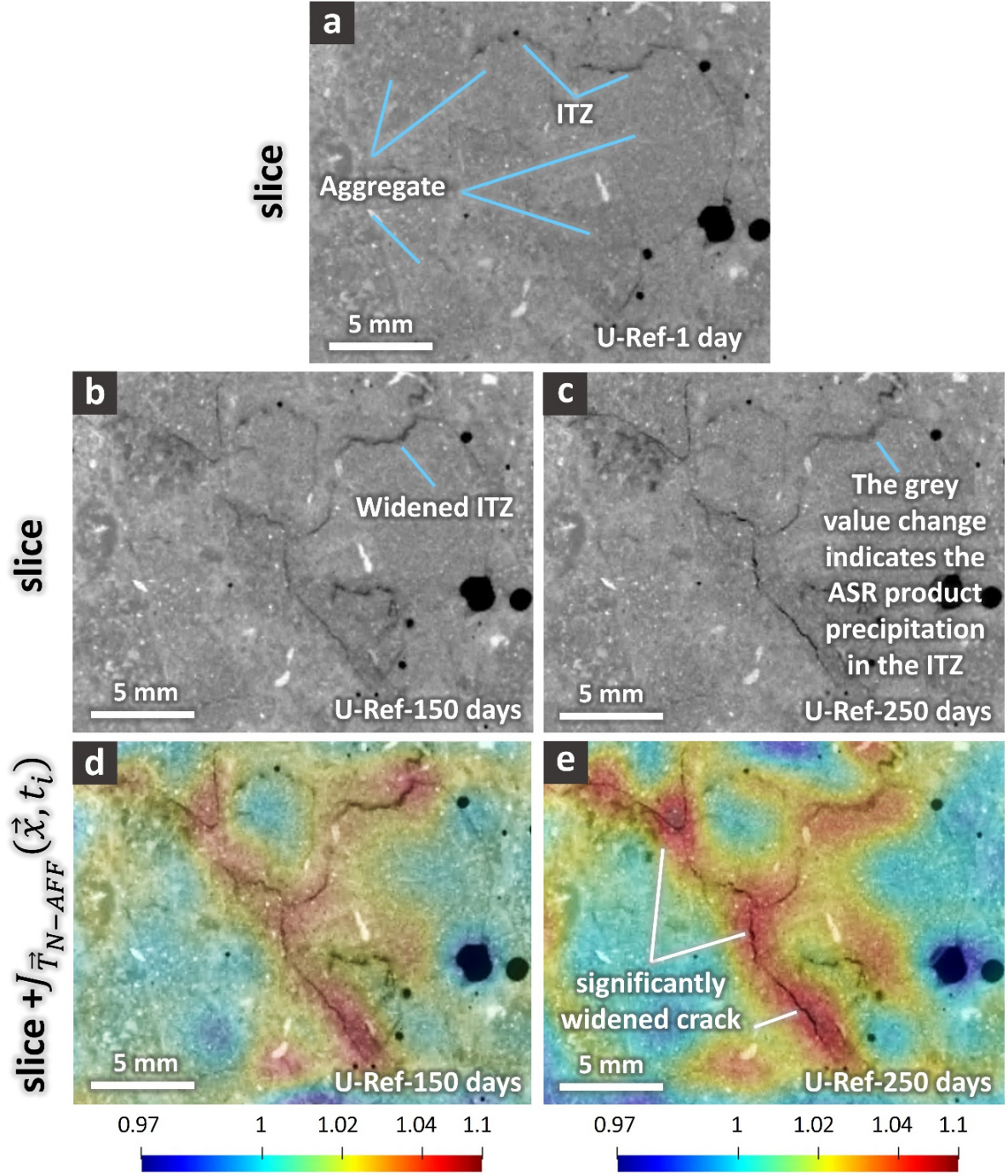


Figure 6.6. Visualization of the evolution of ASR cracks and associated localized deformations for the U-Ref specimen. As an example, it is shown here only one small ROI on one slice from its tomographed volume, at multiple time points. The localized deformations are estimated by the determinant of the Jacobian matrix ($J_{\tilde{T}_{N-AFF}}(\vec{x}, t_i)$) of the transformation vector field $\tilde{T}_{N-AFF}(\vec{x}, t_i)$ associated with the non-affine registration. Its values larger than 1 indicate local volumetric expansion. Its values smaller than 1 indicate volumetric shrinkage. (a) X-ray tomogram at 1 day since start of the ASR acceleration. (b) and (c): slice at the same position as in (a) but from the tomograms at 150 and 250 days, respectively. (d) and (e): the same slice as in (b) and (c), respectively, and, overlapped on top of them, semi-transparently, the slice at the same position but from $J_{\tilde{T}_{N-AFF}}(\vec{x}, t_i)$ at the corresponding time points, respectively. The scale bars in (d) and (e) have, by definition of $J_{\tilde{T}_{N-AFF}}$ (relative volume), no unit.

For each specimen, only the slice from $J_{\vec{T}_{N-AFF}}(\vec{x}, t_i)$ at the same position as the one from the tomogram is shown at each time point, overlapped semi-transparently and rendered with a color scale on top of the corresponding tomogram's slice. Such overlapping allows observing the correlations between cracks and localized deformations. What was systematically observed, independently of the use or not of BaSO₄, was localized volumetric expansion (reddish, "hot" colors in Figure 6.6 (d)-(e) and Figure 6.7 (e)-(h), corresponding to $J_{\vec{T}_{N-AFF}}$ values larger than one) which often preceded crack appearance in the tomograms. Over time, as cracking progressed, such localized expansion regions grew both in "intensity" (maximum value) and in extent around the associated cracks. Regions of local volumetric shrinkage, corresponding to bluish, "cold" colors in both figures and associated with $J_{\vec{T}_{N-AFF}}$ values smaller than 1, also appeared and evolved in terms of extent and intensity, intercalated between the "hot" zones. Such a high degree of localization of extreme (minima and maxima) $J_{\vec{T}_{N-AFF}}$ values is expectable for cracking in highly heterogeneous materials as concrete. In addition to common qualitative features, the specimens, with either aggregate type and without or with BaSO₄, exhibited similar ranges of volumetric deformation values, for instance at the latest time point (250 days). The [minima, maxima] values of $J_{\vec{T}_{N-AFF}}$ were [0.9, 1.12] and [0.89, 1.09] for the U-Ref and P-Ref specimens, respectively, while they were [0.9, 1.1] and [0.8, 1.1] for the U-2.5 vol.-% and P-2.5 vol.-% BaSO₄ ones, respectively.

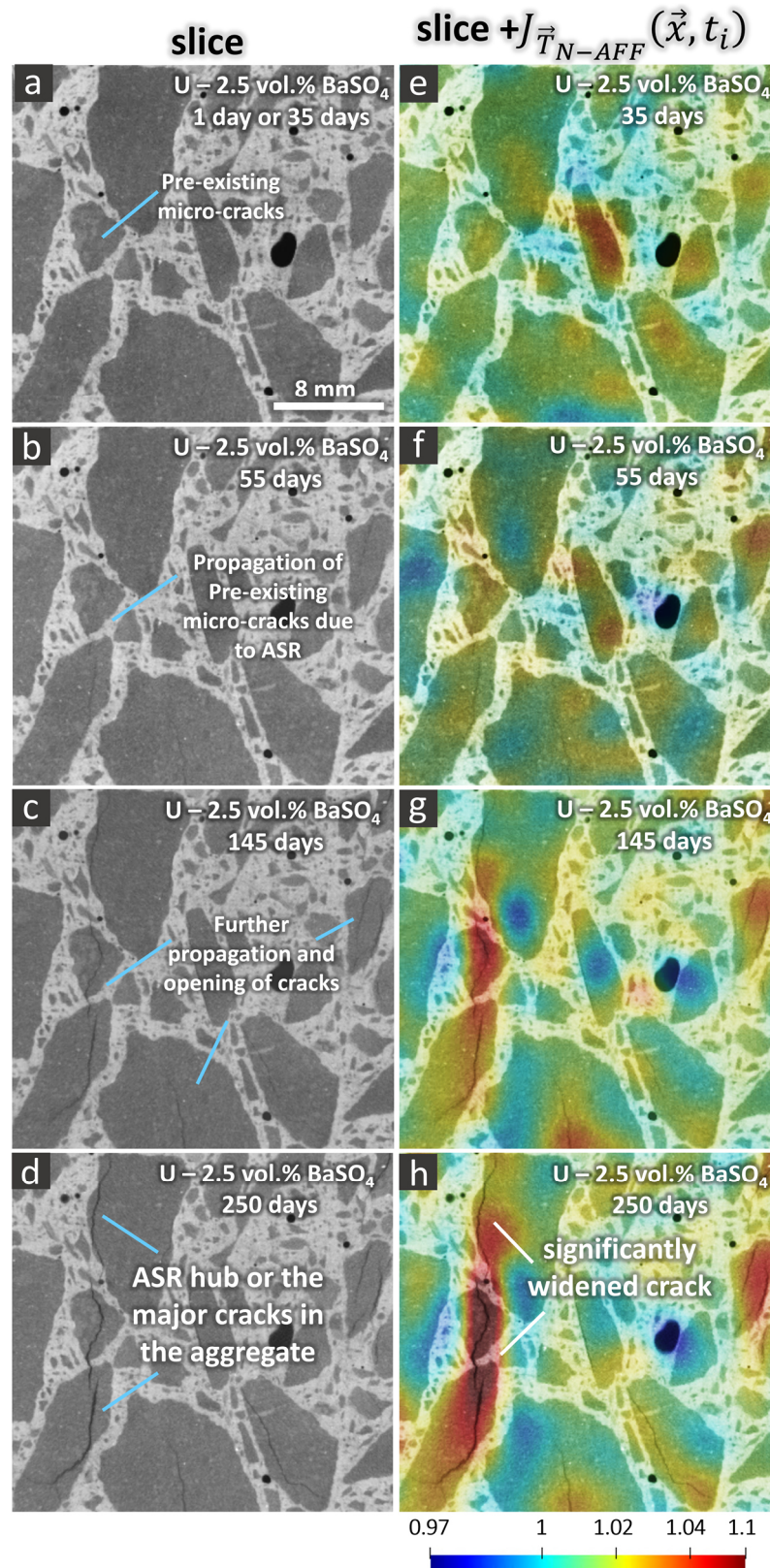


Figure 6.7. Similar visualization as in Figure 6.6 but for the U-2.5 vol.-% BaSO₄ specimen. The chosen time points for the visualization are 35 days (insets (a) and (e)), 55 days ((b) and (f)), 155 days ((c) and (g)), 250 days ((d) and (h)). The tomograms did not change significantly between 1 day and 35 days. Thus, the one at 35 days was representative of the reference tomogram at 1 day.

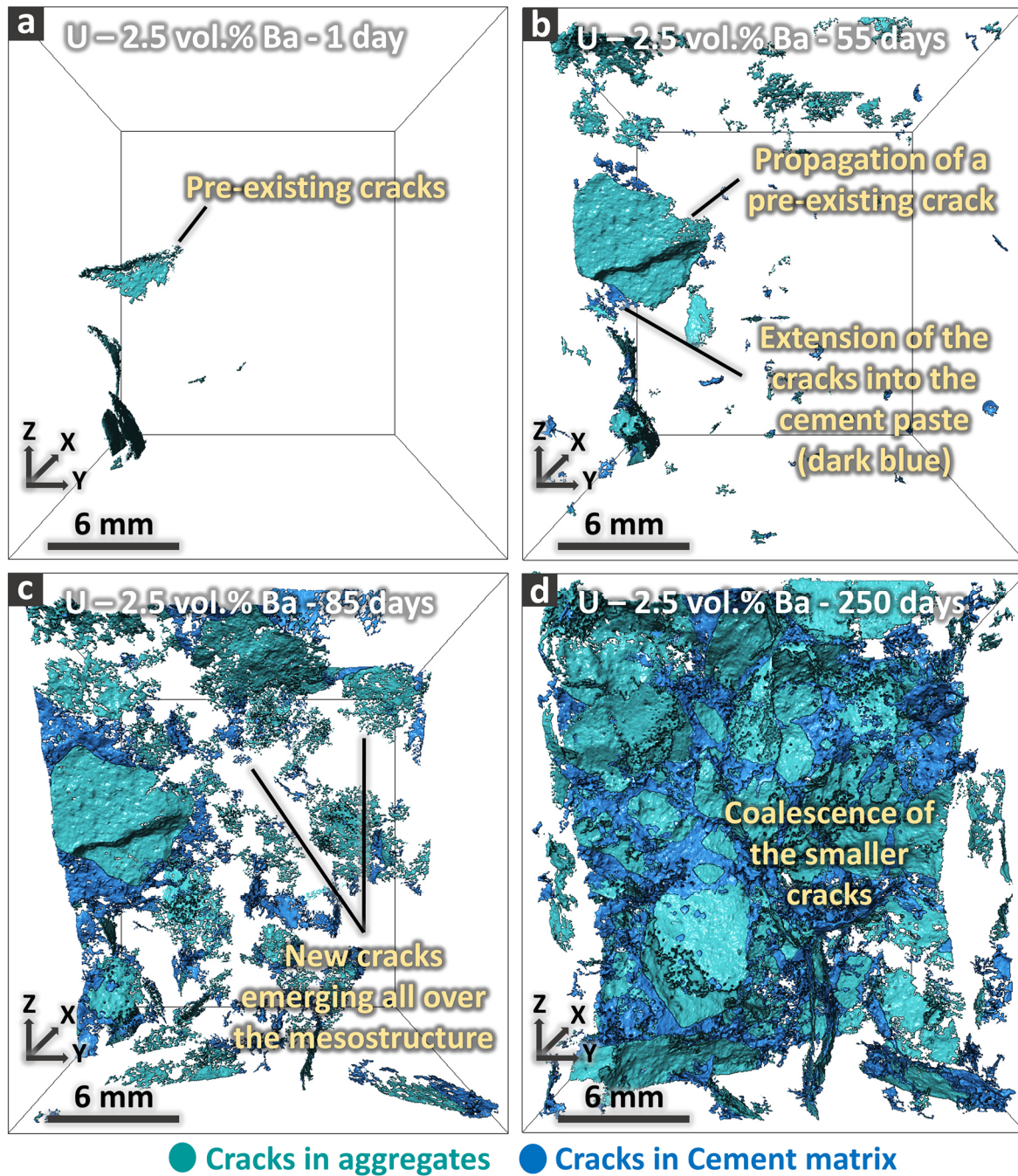


Figure 6.8. A small VOI of the binary tomograms of cracks inside aggregates (cyan) and in the cement paste (blue) is rendered at distinct time points for the U-2.5 vol.-% BaSO₄ specimen. Such VOI contained cracks, which were nucleated in an aggregate and further propagated into the surrounding cement paste. The insets from (a) to (d) correspond to different time points during the ASR acceleration, including 1 day, 55, 85 and 250 days, respectively.

6.3.2.5. Influence on quantitative ASR crack features

In order to quantify the bulk cracking extent within the imaged volume of the different specimens (with or without BaSO₄), the time series of ASR-induced cracks volume fraction values, $\tilde{V}_{ASR,cracks,j}(t_i)$, $\forall i = 1, \dots, N_t$, were computed in the solid phase j ($= Aggr$ or Cem , for aggregates and cement paste, respectively), as defined in Eq. (3.6). In addition, the two time series were time-wise summed up ($j = tot$), to provide the overall ASR cracks volume fraction, independently of whether located inside aggregates or inside the cement paste.

Figure 6.9 (a) and (b) show that, regardless of the aggregate type, the specimens cast with BaSO₄ achieved slightly higher $\tilde{V}_{ASR,cracks,tot}$ values. Except for this slight difference, BaSO₄ seems not to have altered the general pattern of the bulk cracking. The specimens with U aggregates exhibited more cracking than those with P aggregates, as already observed in the experimental campaigns described in Chapters 4 and 5 (Figure 4.9 and Figure C20). At the last time point (250 days), the value for the U-2.5 vol.-% BaSO₄ specimen was about 22% higher than the value for the corresponding P specimen (1.41% for U-2.5Vol.-% BaSO₄ and 1.15% for P-2.5Vol.-% BaSO₄).

A strong positive correlation between $\tilde{V}_{ASR,cracks,tot}$ and the relative volume change of the tomographed region was observed for each specimen (Figure 6.10 (a) and (b)). The volumetric expansion of the tomographed region of each specimen was estimated, at each time point, approximately by summing up the three relative length changes computed from the results of the global affine registration, i.e., it was estimated by $\sum_{k=X,Y,Z} \frac{\Delta L_{AFF,k}}{L_{AFF,k}}(t_i)$, in analogy with the fact that the trace of the strain tensor provides the relative volumetric change of a solid. The ASR cracks volume fraction and the relative volume change were not only positively correlated. They were linearly correlated with a slope almost equal to 1, suggesting that the tomographed region's volume change was mostly due to the ASR cracking itself.

Whether the use of BaSO₄ affected the volumetric partitioning of cracks between aggregates and the cement paste could not be assessed because of the intrinsic difficulties in segmenting aggregates in the reference specimens, especially the U one. What could be only observed, in the specimens with BaSO₄, was a difference due to the aggregate type. In the U-2.5 vol.-% BaSO₄ specimen, more extensive cracking within the aggregates than in the cement paste was measured, especially after 90 days (Figure 6.9 (a)). On the contrary, no significant difference in ASR cracks volume fraction was observed inside and outside the aggregates for the P-2.5 vol.-% BaSO₄ specimen.

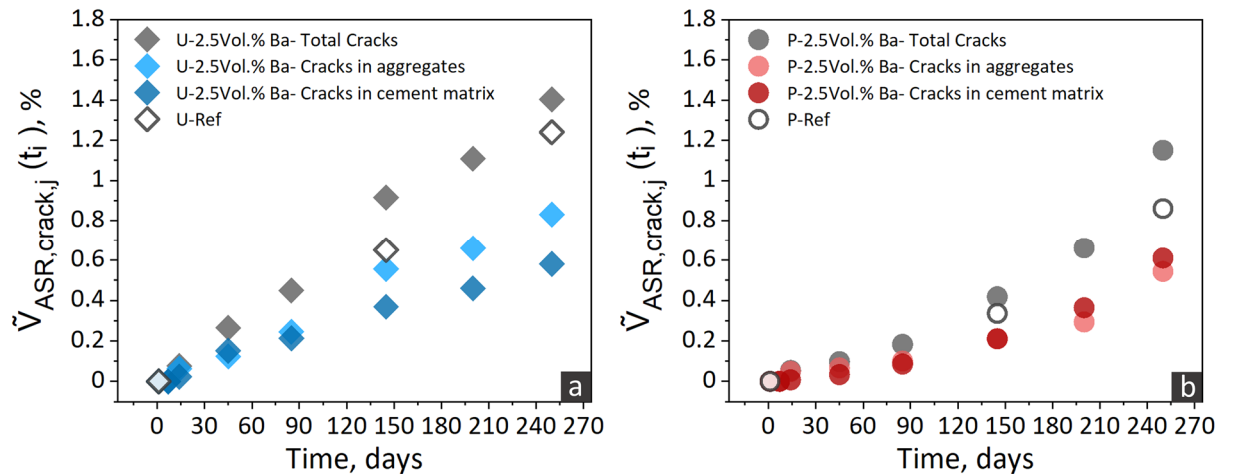


Figure 6.9. Quantitative comparison of the ASR cracking in different specimens based on the estimates of two variables: (1) the total volume of ASR-induced cracks (filled grey markers for the U-2.5 Vol.% Ba and P-2.5 Vol.% Ba specimens and empty grey markers for the reference specimens) and those only in aggregates (lighter blue or red, filled markers, for U and P specimens, respectively) or cement paste (darker blue or red, filled markers, for U and P containing specimens, respectively), normalized by the tomogram volume, named as $\tilde{V}_{ASR,cracks,j}$, for the (a) U-2.5 Vol.% Ba and U-Ref and (b) P-2.5 Vol.% Ba and P-Ref specimens.

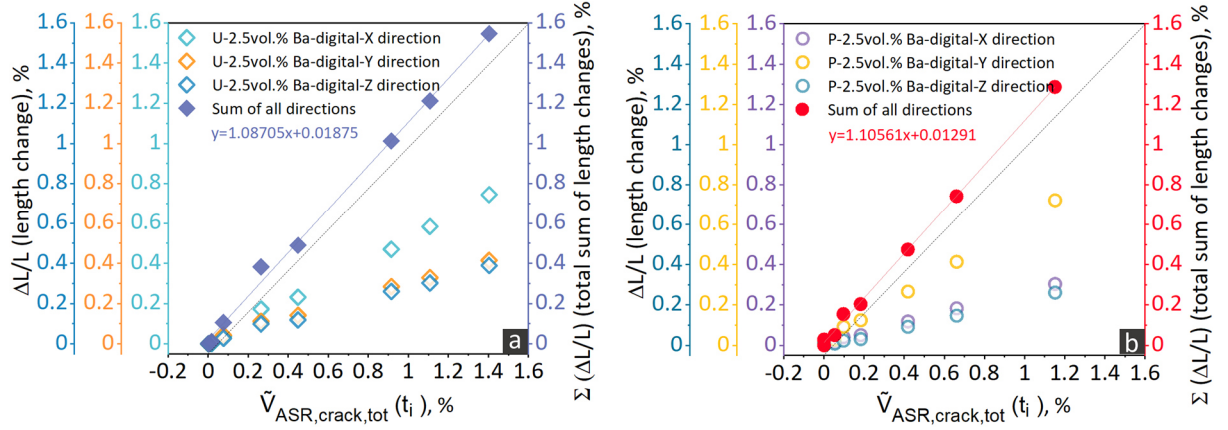


Figure 6.10. Correlation between the ASR cracks total volume fraction, $\tilde{V}_{ASR,cracks,tot}$, and the relative length changes along the X-, Y- and Z-axis and the relative volume change computed for the tomographed volumes of the specimens using the results of the global affine registration. The relative length changes are the $\frac{\Delta L_{AFF,k}}{L_{AFF,k}}$, with $k = X, Y, Z$, while the relative volume change was estimated approximately as $\Sigma_{k=X,Y,Z} \frac{\Delta L_{AFF,k}}{L_{AFF,k}}$. (a) U-2.5 vol.-% BaSO₄ specimen and (b) P-2.5 vol.-% BaSO₄ one. The dotted line indicates the $y = x$ line of the $(\tilde{V}_{ASR,cracks,tot}; \Sigma_{k=X,Y,Z} \frac{\Delta L_{AFF,k}}{L_{AFF,k}})$ plane.

The shape tensor analysis was used to obtain a quantitative estimate of the crack bounding box length L . Its distribution (again the statistical *ensemble* estimates of the complementary cumulative distribution functions, $G_L(L)$, presented in the form of a Zipf's plot), for the U-2.5 vol.-% BaSO₄ and P-2.5 vol.-% BaSO₄ specimens, along with for the corresponding reference specimens, U-Ref and P-Ref, at 250 days, is shown in Figure 6.11 (a) and (b), respectively. It is observed that, regardless of the aggregate type, the overall L distributions and their maximum values are comparable for the BaSO₄-containing specimen and the corresponding reference one.

The local thickness field, $T_{local}(\vec{x})$, analysis results for the same specimens at 250 days are also presented in insets (c) and (d) of Figure 6.11. These plots are analogous to the plots shown in Figure 6.11 (a) and (b), but the $G_{T_{local}}(T_{local})$ shows the statistical *ensemble* estimate of the cCDF for the local thicknesses. Similar to the results obtained for the L distributions, T_{local} also showed comparable and comparably distributed values for both the BaSO₄-containing specimens and the reference ones.

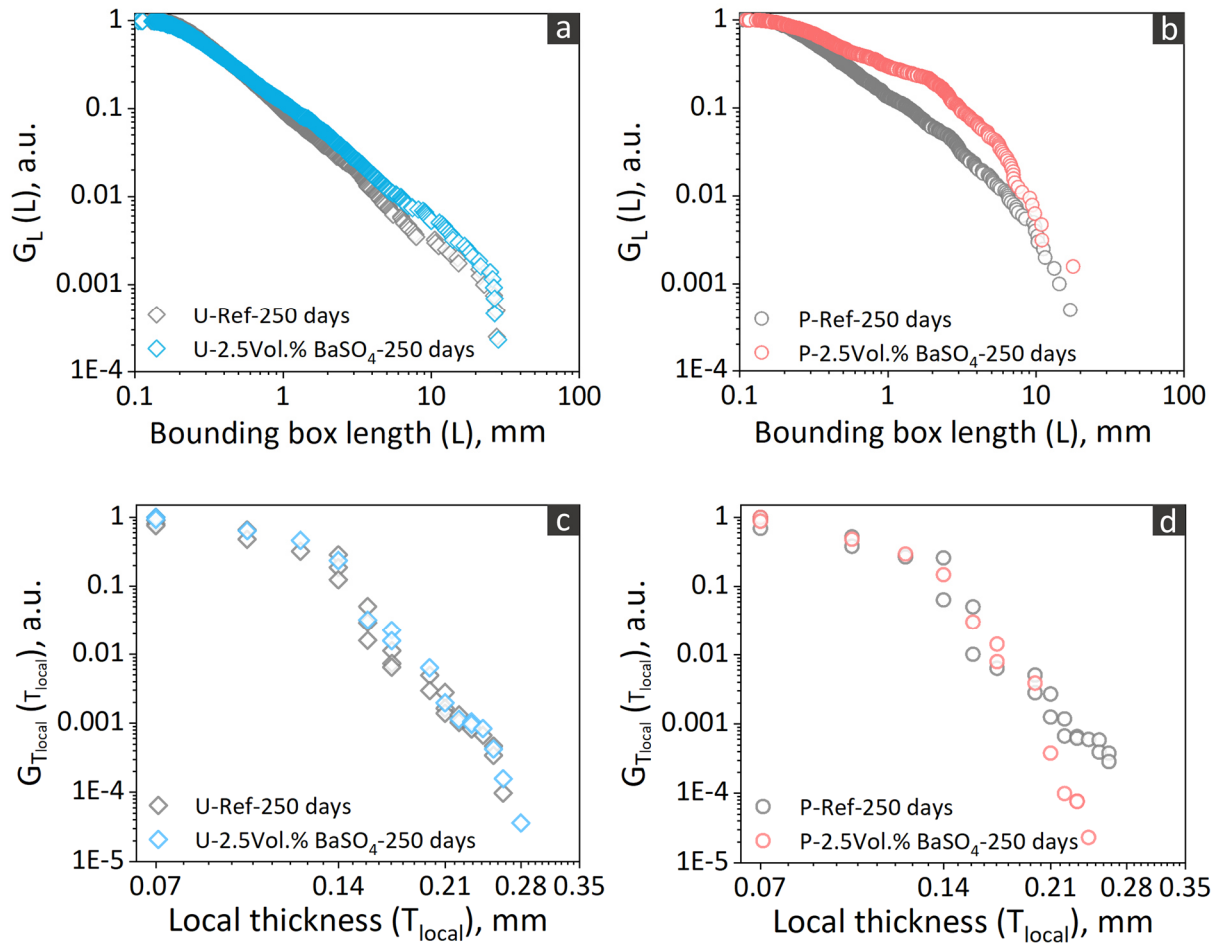
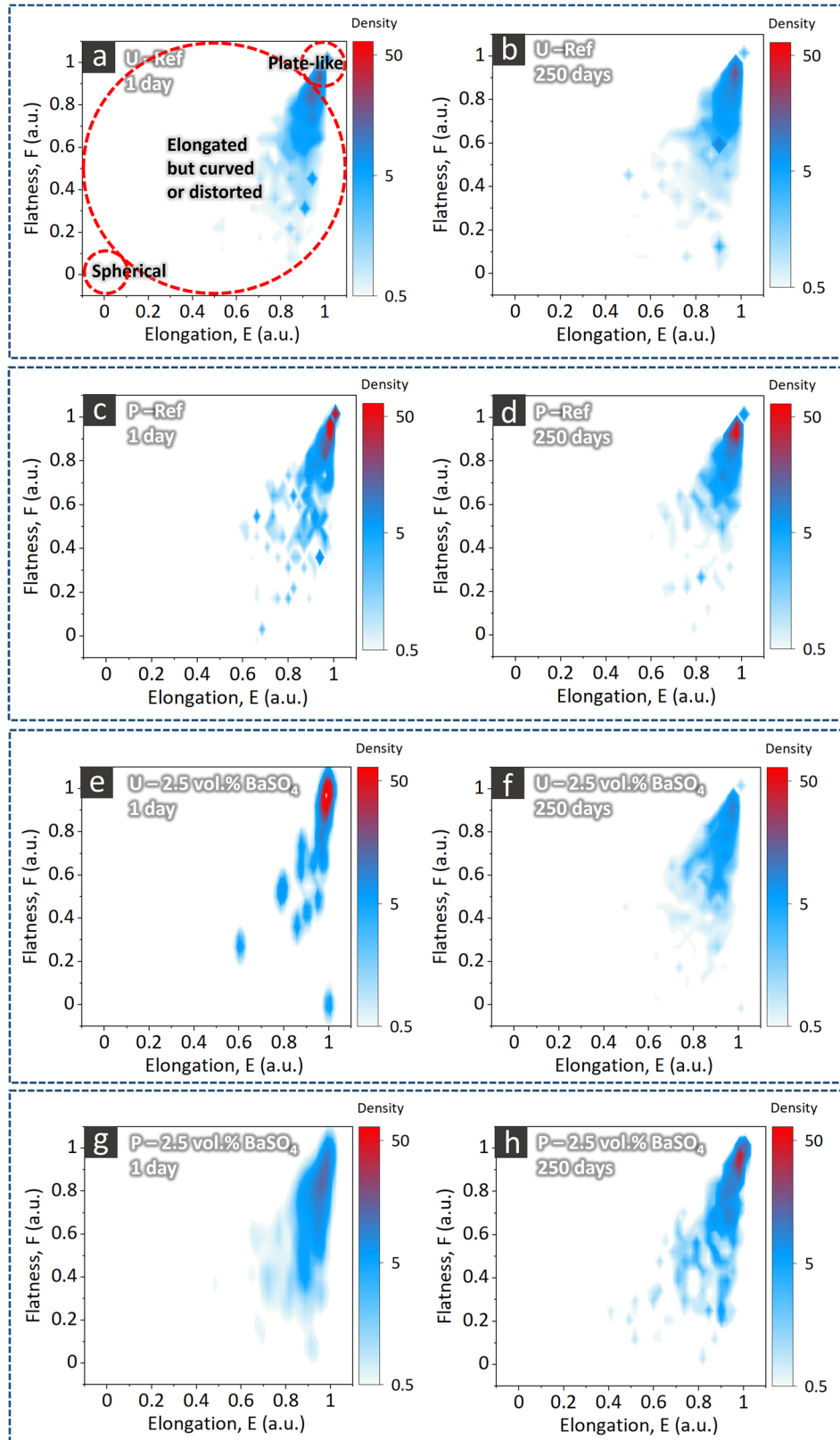


Figure 6.11. (a) and (b) complementary cumulative distribution function (cCDF) of the crack bounding box length, L , $G_L(L)$, in \log_{10} - \log_{10} scale (Zipf's plot), for the specimen cast with U aggregates (with and without BaSO₄) and for the specimen cast with the P aggregates, respectively, at 250 days. (c) and (d) corresponding Zipf's plot for the crack local thickness, T_{local} .

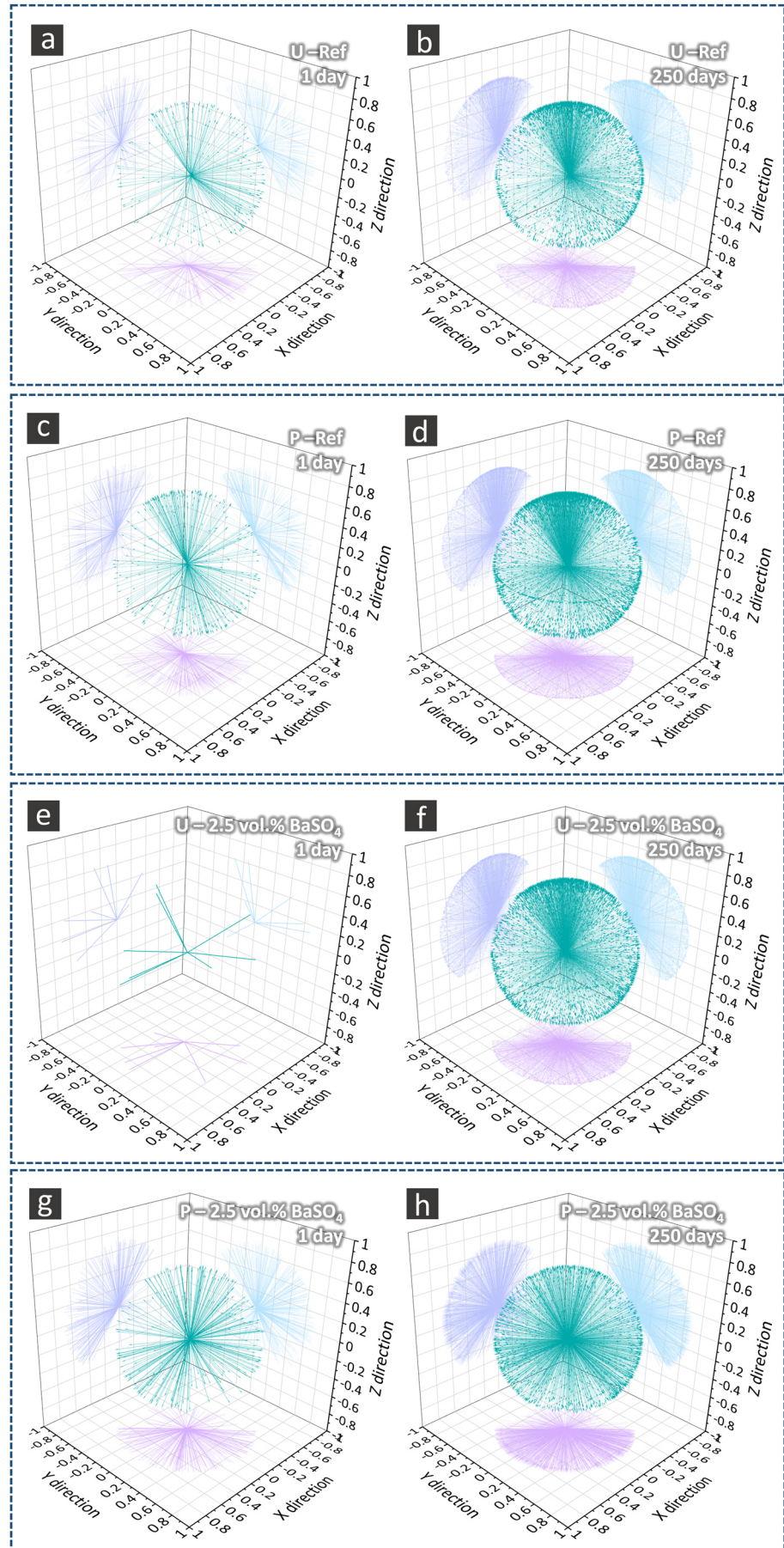
Figure 6.12. Plots of the kernel density estimate (KDE) of the joint probability density function (PDF) of the two shape feature variables, the elongation E and the flatness F , computed from the shape tensor analysis of the segmented total crack networks and treated as a bivariate random variable, $(E; F)$. The statistical sample of such PDF was provided, for each specimen and at each time point, by the set of values $\{(E_i; F_i)\}_{i=1, \dots, C}$ obtained from the shape tensor analysis, where C indicates generically the total number of disconnected and independent branches of the segmented, total crack network of a specimen and at a certain time point. (a) and (b) U-Ref specimen, (c) and (d) P-Ref one, (e) and (f) U-2.5vol.% BaSO_4 , and (g) and (h) P-2.5vol.% BaSO_4 specimens, at 1 day and 250 days, respectively.



The BaSO₄ addition did not seem to perturb the crack shape, as assessed by the analysis of the joint PDF of the crack elongation E and crack flatness F , $f_{(\mathbb{E};\mathbb{F})}(E; F)$. Figure 6.12 shows the KDE of $f_{(\mathbb{E};\mathbb{F})}(E; F)$ for the reference specimens and for the U-2.5vol.% BaSO₄ and P-2.5vol.% BaSO₄ ones. For each specimen, the results are shown only at 1 day and 250 days. At both time points and for all the specimens, the cracks were predominantly mapped to the top-right corner of the shape phase diagram, meaning that they had a plate-like. For a clear example of the plate-like morphology of the cracks, the reader is invited to look at the 3D rendering of the segmented crack network of the U-Ref specimen at 250 days in Figure D14 (a).

The distribution of the first eigenvector, \hat{u}_1 , of the shape tensor \mathbf{G} of each crack is shown in Figure 6.13 for the reference specimens and the U-2.5vol.% BaSO₄, and P-2.5vol.% BaSO₄ ones, at 1 day and 250 days for each specimen. For any specimen, at the first time point (i.e., when only original cracks could be present and segmented), the crack orientation distribution was rather uniform, in some cases very sparse. However, at 250 days, a tendency for preferential orientation towards the Z-axis could be observed for all the specimens except for the P-2.5vol.% BaSO₄. The latter is a feature which was already observed for the U and P specimens of Chapters 4 and 5. The addition of BaSO₄ thus seemed not to have any significant influence on the crack orientation.

Figure 6.13. Visualization of the crack orientation analysis results for the reference specimens and those cast with optimal BaSO_4 concentration value of 2.5 vol.-%. The crack orientation was operatively defined as the direction of the eigenvector \hat{u}_1 associated with the first and largest eigenvalue of the shape tensor \mathbf{G} . The segmented total crack network of a specimen corresponded to a set of \hat{u}_1 's, one for each independent crack (branch of the network). Each of these vectors are here plotted in green, after rescaling their magnitudes by a factor equal to 0.33, to make their projections on the planes of the Cartesian frame of reference more visible. The projections of \hat{u}_1 on the $X - Y$ plane are in violet, those on the $X - Z$ plane are in dark blue and those on the $Y - Z$ plane are in light blue. : (a) and (b) U-Ref, (c) and (d) P-Ref, (e) and (f) U-2.5vol.% BaSO_4 and (g) and (h) P-2.5vol.% BaSO_4 , at 1 day and 250 days, respectively.



6.3.3. Extensive experimental campaign with optimal BaSO₄ concentration

6.3.3.1. ASR-induced macroscopic dimensional changes and mechanical properties evolution

The time series of the longitudinal relative length change, $\frac{\Delta L_Z}{L_Z}$, of the u specimens, measured with the optical displacement gauge (see the label "u-laser-z direction") is shown in Figure 6.14 (a). The reader is reminded that these were 10 specimens with identical size ($25 \times 25 \times 100 \text{ mm}^3$) as for the 3 specimens subjected to XT, the latter being distinct specimens. Up to about 2 months from ASR acceleration start; these 10 specimens were measured much more frequently than what done in all the other experimental campaigns so far described. During about the first 25 days, a contraction instead of an expansion was observed, in strong contrast with what observed for the $40 \times 40 \times 160 \text{ mm}^3$ specimens cast with the same mix design, including the same BaSO₄ concentration of 2.5 vol.-% (see Figure 6.4 (a)). This result was also in contrast with any other $\frac{\Delta L_Z}{L_Z}$ measurements done on specimens cast with U or any other aggregate type, as shown in Chapters 4 and 5. After about 25 days, the specimens exhibited monotonic expansion, as originally expected. The initial longitudinal contraction characterized also the 3 specimens undergoing XT, which were measured exactly at the same times, belonged to the same batch of cast material and followed exactly the same history, except for remaining for longer time outside of the alkaline solution for acceleration because the XT measurement obviously required longer time than the length one. For the 3 XT specimens, the relative length change was the one estimated only for the tomographed volume and obtained from the results of the global affine registration, i.e., $\frac{\Delta L_{AFF,Z}}{L_{AFF,Z}}$ (see the time series labelled as "u-affine-Z direction in Figure 6.14 (a) as well). By comparing the two time series in such plot, it can be seen that the $\frac{\Delta L_Z}{L_Z}$ time series and the $\frac{\Delta L_{AFF,Z}}{L_{AFF,Z}}$ followed qualitatively a similar evolution, the $\frac{\Delta L_{AFF,Z}}{L_{AFF,Z}}$ values being slightly smaller than the $\frac{\Delta L_Z}{L_Z}$ ones between about 50 and 250 days, otherwise the two being rather the same also in terms of values. This result indicated that the deformations inside the tomographed volume were very likely rather representative of those happening in the full specimen volume. The relative mass change time series evolved monotonically during the whole campaign, with a change of growth rate after 110 days (Figure 6.14 (c)). Figure 6.14 (b) compares the relative length changes along all the X , Y and Z directions of the tomographed specimens, as obtained from the results of the global affine registration of their tomographed volumes. The overall expansion extent in the two lateral directions (X and Y) was higher compared to the longitudinal (Z -axis) one, similarly to what observed not only for the larger U specimens with the same BaSO₄ concentration but also for corresponding specimens cast with P aggregates (see Figure 6.4 (e) and (f)).

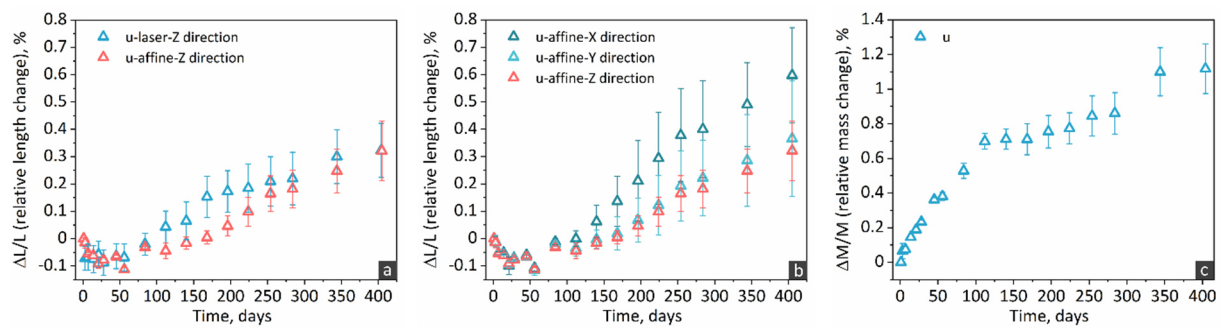


Figure 6.14. (a): evolution of the longitudinal relative length change of u specimens, directly measured by the expansion measurement setup 2, shown in Figure 3.1 (3) and described in Section A4, on 10 specimens ($\frac{\Delta L_Z}{L_Z}$, blue markers) and indirectly estimated from the global affine registration results for 3 additional specimens for their tomographed volumes ($\frac{\Delta L_{AFF,Z}}{L_{AFF,Z}}$, red-pink markers). Each marker shows the average value, while the error bar was defined as the empirical standard deviation. (b): relative dimensional changes of the tomographed volumes along the X, Y and Z axes, $\frac{\Delta L_{AFF,k}}{L_{AFF,k}}$, with $k = X, Y$ and Z . The markers show the average of the values from the 3 tomographed specimens while the error bars the respective empirical standard deviation values. and (c): relative mass change time series of the 10 specimens whose $\frac{\Delta L_Z}{L_Z}$ is shown in inset (a).

The temporal evolution of the mechanical properties followed patterns similar to what already observed for specimens cast with U and P aggregates. However, the availability of data at later times compared to what acquired in the experimental campaign described in Chapter 5, provided also some new insight. The time series of the quasi-static (compressional) Young's modulus, the flexural and the compressive strengths are shown in Figure 6.15 (a) to (c), respectively, only for the U specimens. Corresponding time series for the P ones are additionally provided in Section D2.2 (Figure D16) of the Appendices.

For the U specimens as well as for the P ones, both the Young's modulus and the flexural strength were sensitive proxy variables of ASR cracking. On the contrary, the compressive strength was much less sensitive to the ASR progression, as already noted in Section 5.3.3 and reported in the literature (see Section 2.4.2.3). For all the specimens, the temporal evolution of all three mechanical properties was characterized by an increase up to about 30 (Young's modulus and flexural strength) to 70 (compressive) days, again most probably associated with the ongoing cement hydration. After such increase, a monotonic decline followed, except for the compressive strength, which shortly decreased, then remained approximately constant.

While the P specimens showed a monotonic decrease in Young's modulus and flexural strength till the very last time point of 557 days, the U specimens seemed to have achieved a minimum at about 224 days, after which, at 404 days (the next time point), they exhibited for those two parameters higher values. At 557 days, the flexural strength was approximately at the same value, whereas the Young's modulus exhibited consistently still an increase.

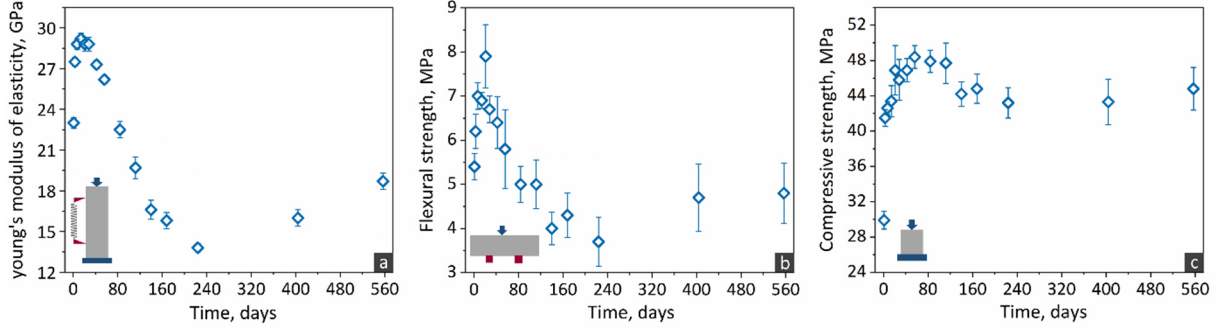


Figure 6.15. Time series of the (a) quasi-static (longitudinal, compressive) Young's modulus, (b) flexural strength, and (c) (longitudinal) compressive strength of the U specimens. In each plot, the markers show the average and the error bar the empirical standard deviation of an ensemble of values from distinct specimens, the ensemble size being 3, 3 and 6 for insets (a), (b) and (c), respectively. For the Young's modulus measurements, the specimens were always the same at each time point.

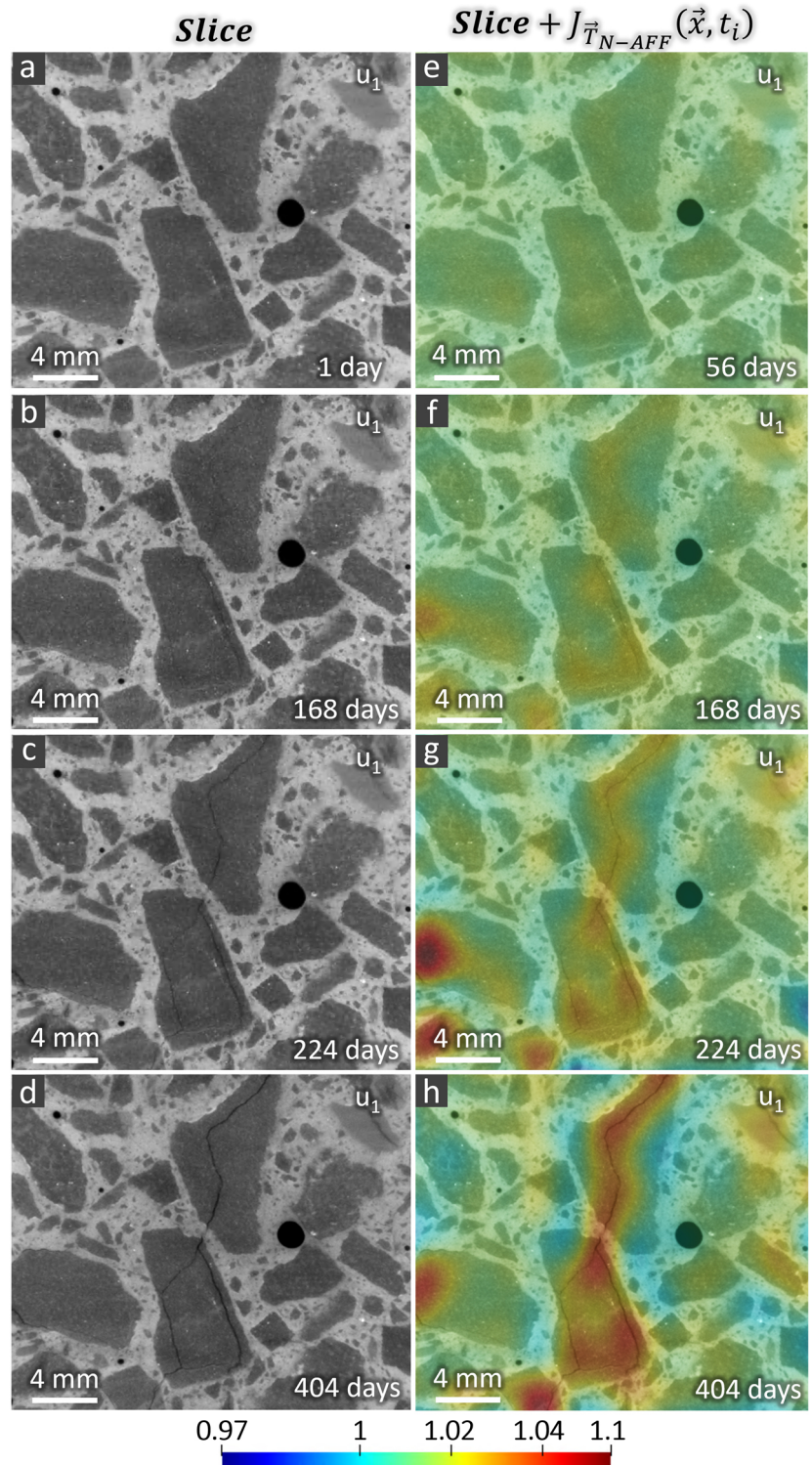
6.3.3.2. Spatial-temporal evolution of ASR cracking

In Figure 6.16, the insets (a) to (d) show a small ROI on a slice taken from the tomograms of one of the three specimens, u_1 . Only 4 of the 18 tomograms are considered there, specifically those at 56, 168, 224 and 404 days, respectively. The tomogram at 56 days shown in inset (a) was very similar to those at preceding time points, suggesting that any ASR crack formed and propagating within this time period had size below the tomographic spatial resolution. A confirmation of such detail can be obtained by comparing inset (a) in Figure 6.16 with inset (a) of Figure D16, where the same ROI on the same slice is shown at additional time points, including at the reference one, $t_0 = 1$ day. The ASR cracking which could be resolved in such tomographic time series and in those for the other two u specimens exhibited the same qualitative features already observed with lower temporal resolution for the specimens cast with the U and P aggregates and the same BaSO_4 concentration during the experimental campaign for its optimization, as well as observed also for the corresponding reference specimens in that campaign and for all the specimens of the experimental campaign described in chapter 5. The cracks were first observed inside the aggregates volume and in their ITZs. Gradually, they became longer and thicker. Some of them propagated further into the cement paste. Specifically for the u specimens, the first cracks were resolved in the tomograms at times between 84 and 112 days.

Insets (e) to (h) in Figure 6.16 show the same slices shown in (a) to (d) with the additional overlapping on top of them of the corresponding slices of $J_{\vec{T}_{N-AFF}}(\vec{x}, t_i)$, rendered semi-transparently and color coded. As already shown in Figures 6.6 and 6.7, a spatial correlation between local volumetric expansion (hot colors in the $J_{\vec{T}_{N-AFF}}$ field, associated with values greater than 1) and the appearance and evolution of cracks was often observed. The same visualization as in insets (e) to (h) but with two additional time points is provided in Figure D16, which, even more clearly, showcases such correlation. Additional evidence of the correlation is provided by the 3D rendering of both the segmented cracks and of $J_{\vec{T}_{N-AFF}}(\vec{x})$, performed for the u_1 specimen at four distinct time points and shown in Figure D21. This is the same type of correlation already observed for the specimens of the Cs-doping experimental campaign (see Figures 5.12 and 5.13). The first zones of local volumetric expansion appeared in all 3 u specimens between 45 and 56 days. At those times, no cracks could be yet resolved in the tomograms

of any specimen. Although at times later than 56 days there were slight variations in the hot zones distribution, most of them consistently increased in extent and intensity. The decay or complete disappearance of a few hot zones was also observed along with the consistent development of local volumetric contraction zones (cold-colored regions, with $J_{\vec{T}_{N-AFF}}$ values <1) was also observed alongside that of expansion zones. Some of them continuously advanced both in extent as well as in intensity, as already observed for other specimens in Sections 5.3 and C10. The [average minima \pm standard deviation, average maxima \pm standard deviation] values of $J_{\vec{T}_{N-AFF}}$, for all 3 specimens and at 440 days, were $[0.89 \pm 0.026, 1.12 \pm 0.046]$.

Figure 6.16. Visualization of the determinant of the Jacobian matrix, $J_{\vec{T}_{N-AFF}}(\vec{x}, t_i)$, of the transformation vector field $\vec{T}_{N-AFF}(\vec{x}, t_i)$ associated with the non-affine registration, as computed from the tomographic time-series of the u_1 specimen. Only a few time points from the series are shown. $J_{\vec{T}_{N-AFF}}(\vec{x}, t_i)$ is used as a spatial map of the factor by which the volume locally expanded or shrunk due to the spatially heterogeneous components of the ASR-induced displacement vector field. (a) to (d): one slice from the specimen's fully registered X-ray tomogram at 56, 168, 224 and 404 days, respectively. (e) to (h): the same slices as in (a) to (d) but, in addition, overlapped on top of them, the corresponding slices from $J_{\vec{T}_{N-AFF}}(\vec{x}, t_i)$ are rendered semi-transparently and color-coded according to the indicated color scale. The scale bar of the insets (e) to (h) has no unit. $J_{\vec{T}_{N-AFF}}(\vec{x}, t_i)$ values greater than 1 represent volumetric expansion, values smaller than 1 indicate volumetric shrinkage.



Among the 3 u specimens, for one of them, u_2 , original cracks could be resolved within the aggregates at the reference time point $t_0=1$ day, because of their size being enough above the tomographic spatial resolution. In such a case, it was possible to observe and assess the role of original cracks as preferential nucleation sites of the whole crack network. Figure 6.17 showcases such role as observed from the tomographic volume of u_2 by the 3D rendering at 6 out of the 18 points of the time series of the crack network binary tomograms, distinguishing by colors those inside aggregates (in purple) from those in the cement paste (in aquamarine). The same rendering but at additional time points is provided in Figure D22. A small region of original crack is shown in Figure 6.17 (a), which refers to the starting state of the crack network, at 1 day. At 112 days (Figure 6.17 (b)), the original crack region appeared already significantly more extended. New cracks also appeared in another region of the volume. However, the most extensive cracking developed around the original crack. With time, the crack network extended itself in all directions, far from the original region (insets (c) to (e)). The cracks propagated increasingly not only through aggregate regions but also through the cement paste. At 404 days (Figure 6.17 (f)), the network almost percolated through the volume. This time-lapse observation in 3D of an example of an original, mesoscopic scale crack as a preferential region for the onset of ASR cracking supports and confirms non-time-lapse observations, reported in previous studies and performed with SEM-BSE at much smaller length scales, of mineral grain boundaries and original micro-cracks acting as well as preferential regions/features for ASR crack nucleation [3]. Since such structural features are at the scale of tens/hundreds of nanometers to a few microns, they fell outside the spatial resolution range of these tomograms (about 35 μm), thus a similar time-lapse tracking of ASR cracks from such smaller features as the one shown in Figure 6.17 for a larger original crack could not be performed.

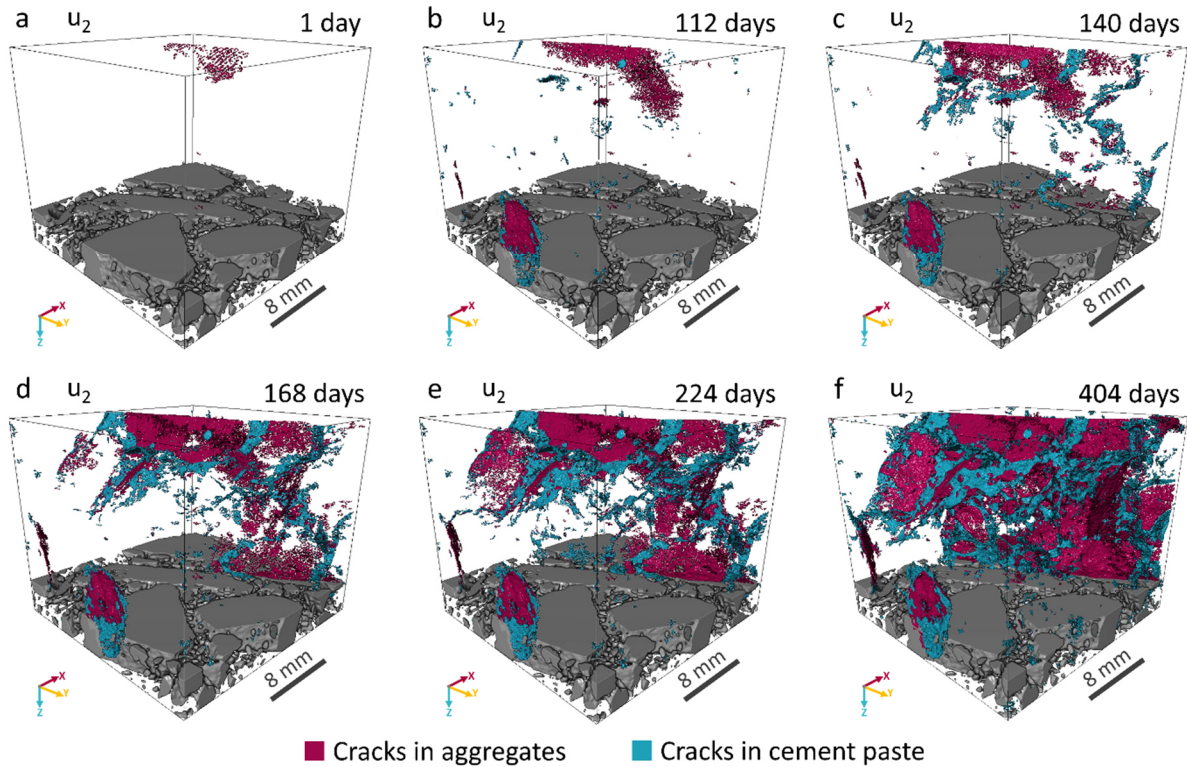


Figure 6.17. Binary tomograms of cracks inside aggregates (in purple) and within the cement paste (in aquamarine), rendered for the u_2 specimen. Parts of the segmented aggregates are also rendered as solid, opaque regions in dark grey, at the bottom of the volume. The insets from (a) to (f) correspond to different time points during the ASR acceleration, including 1 day, 112, 140, 168, 224 and 404 days, respectively.

Two of the specimens (u_2 and u_3) had cracks propagating with orientation preferentially aligned along the Z-axis, while the third specimen, u_1 , had cracks slightly more isotropically oriented. This feature could be identified already qualitatively by the visual inspection of the 3D rendered binary tomograms of the segmented cracks, e.g., at 404 days, shown in Figure 6.18 (a) to (c). In order to make the preferential orientation visually more clear, the cumulative orthogonal projection of the total crack network on each of the three planes of the Cartesian frame of reference are shown for each specimen, in insets (d) to (f). The higher proportion of empty (black) regions on the $X - Y$ projection plane than on the other planes, in insets (e) and (f) compared with inset (d), indicates that the cracks extended preferentially along directions at small angle to the Z-axis.

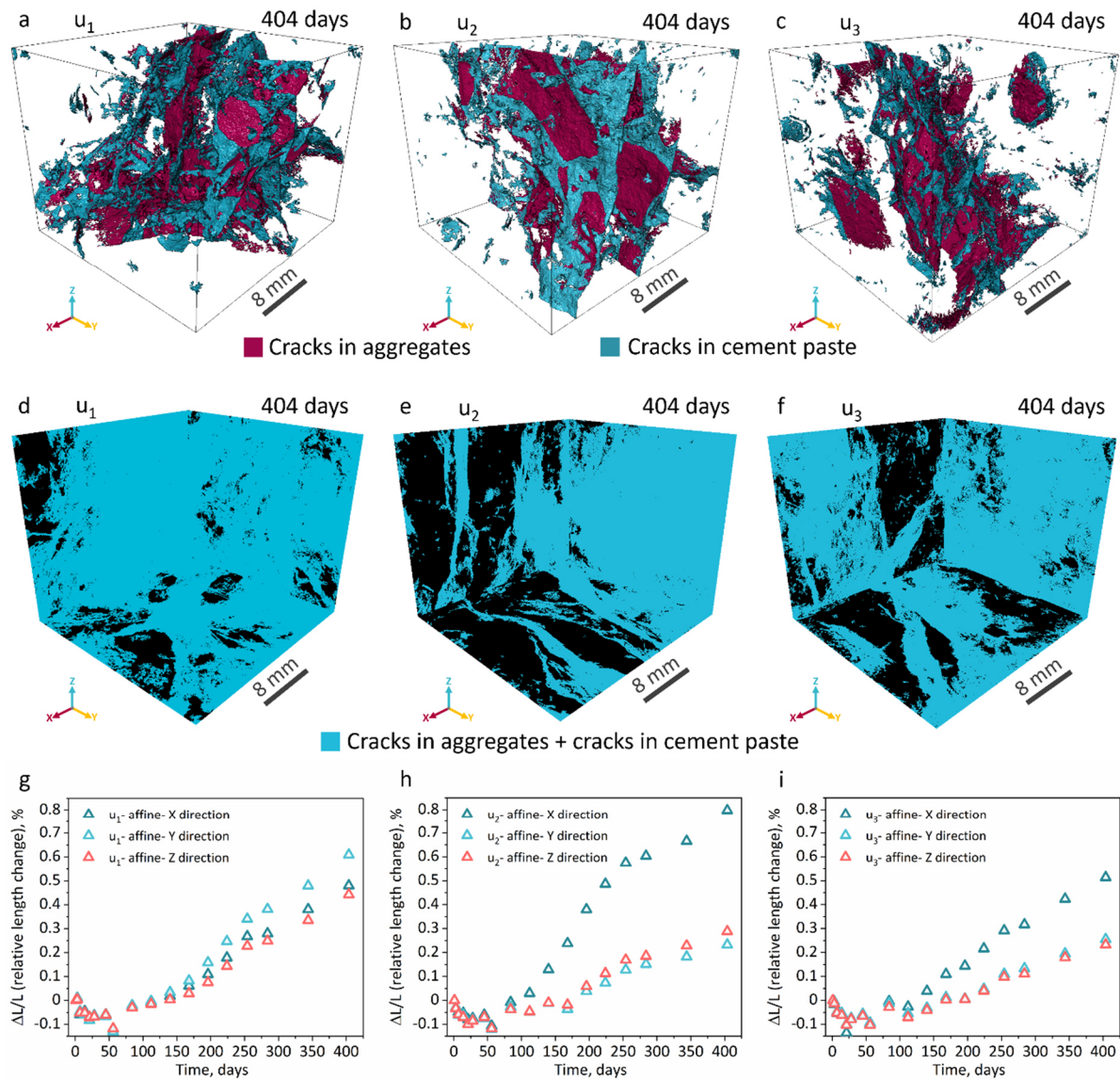


Figure 6.18. (a) to (c): 3D rendering of the binary tomogram of the segmented cracks at 404 days, with distinct colors distinguishing between aggregate (purple) and cement paste (aquamarine) regions, for the u_1 , u_2 and u_3 specimens, respectively; (d) to (f): cumulative line projections of the total crack network volume shown in insets (a) to (c), respectively, on each of the three orthogonal plane of the Cartesian frame of reference; black pixels on

such projection planes indicate absence of projection; (g) to (i): relative length changes time series of the tomographed volume along the X , Y and Z axes as computed from the results of the global affine registration, $\frac{\Delta L_{AFF,k}}{L_{AFF,k}}$, with $k = X, Y$ and Z , for the u_1 , u_2 and u_3 specimens, respectively.

This qualitative difference, captured by the visualizations in insets (a) to (f), is mirrored by the relative length changes results for the tomographed volumes along all the X , Y and Z directions, as computed from the affine registration results. Figure 6.18 (g) to (h) unbundles the data already reported in Figure 6.14 (b), where, for each $k = X, Y, Z$, only the average $\frac{\Delta L_{AFF,k}}{L_{AFF,k}}$ over the 3 specimens is shown. The $\frac{\Delta L_{AFF,k}}{L_{AFF,k}}$ time series of the u_1 specimen (Figure 6.18 (g)) were quite similar, independently of the direction along which they were computed. Whereas, in the u_2 case (Figure 6.18 (h)), there was a significant difference between the expansion along the Z -axis and that along the two other ones. The u_3 specimen exhibited also a difference between the expansion along the Z and the two other axes, although smaller than in the u_2 case. Correspondingly, the orthogonal, line projection of the segmented crack network onto the $X - Y$ plane was only for the u_1 specimen as much plane-filling as the two other orthogonal projections. This result is a direct consequence of the crack orientation anisotropy degree: smaller expansion along the Z -axis can result from the thickness of the cracks being more often aligned along a direction at a certain angle from the Z -axis. The smaller the crack orientation anisotropy degree, the more randomly the crack orientation, thus also the crack thickness direction, with consequent more equal contribution of the crack thickness growth to the expansion in any direction.

6.3.3.3. Quantitative analysis of the ASR crack networks

The temporal evolution of the volume of segmented ASR cracks could be assessed both for the crack network of the whole tomographed region and separately for the aggregate and the cement paste regions, given the aggregate segmentation made possible by the use of the $BaSO_4$.

The 3 u specimens exhibited similar patterns of total crack volume fraction growth with time, as shown by the $\tilde{V}_{ASR,cracks,tot}$ time series shown in Figure 6.19 (a), (navy blue markers). The time series is shown only from 112 days, since, as mentioned in the previous Section, the first ASR cracks which could be resolved appeared between 84 and 112 days, for any specimen. Till about 175 days, the 3 specimens achieved very similar $\tilde{V}_{ASR,cracks,tot}$ values, after which they exhibited different values but, at any time point, within 47% (relative range of the three specimens' values). In terms of partition between aggregate and cement paste regions, the cracks volume were almost equally distributed between the two material phases till 284 days, after which the crack networks grew, on average, slightly faster within the cement paste (see the two last time points, 314 and 404 days), as shown by the $\tilde{V}_{ASR,cracks,agg}$ (purple markers) and by the $\tilde{V}_{ASR,cracks,cem}$ (sky blue markers) time series also shown in Figure 6.19 (a).

A strong linear correlation between the relative volume change of the tomographed region and the total ASR cracks volume fraction, $\tilde{V}_{ASR,cracks,tot}$, was observed for the two specimens cast with the same $BaSO_4$ optimal concentration value and with the two aggregate types, respectively, and used in the experimental campaign for the $BaSO_4$ concentration optimization (see Figure 6.10). Such a linear correlation could be more robustly confirmed from the analysis of the u specimens' tomograms. Figure 6.19 (b) shows that the time series of $\tilde{V}_{ASR,cracks,tot}$ and that of $\sum_{k=X,Y,Z} \frac{\Delta L_{AFF,k}}{L_{AFF,k}}$, the proxy variable of the

relative volume change of the tomographed region, overlapped on top of each other. This result actually indicates an almost 1:1 relationship between the two variables, suggesting that the new generated ASR crack volume could account for a majority of the estimated volumetric change of the tomographed regions of the 3 specimens.

The qualitative observation of crack lengthening and widening with increasing time supported by the slice time series in Figure 6.18 and by the time series of 3D rendering of the crack network in Figure 6.19 could be validated by the analysis of the temporal evolution of the distribution of values for the crack bounding box length L , shown in Figure 6.19 (c), and for the crack local thickness T_{local} , shown in Figure 6.19 (d). Both figures showcase the distributions only for the u_1 specimen and only at 3 time points, to avoid cluttering the plots. Similar plots for the two other specimens are provided in Figure D26.

The crack lengthening was, on average, less clear as the crack widening. Every specimen exhibited an increase in the maximum L value. For example, for the u_1 specimen, the maximum L value was 8.035 mm at 168 days. It then reached 20.213 mm and 24.510 mm at 224 days and 404 days, respectively. At the same time points, the other two specimens evolved from 15.747 mm and 13.060 mm at 168 days to 23.548 mm and 24.672 mm, in the case of u_2 specimen, and 18.522 mm and 28.122 mm in the case of the u_3 one, respectively (see Figure 6.19 (c) and Figure D26 (b) and (c) for the corresponding Zipf's plots). However, a clear and systematic shift of the overall distribution of L towards larger values with increasing time was not observed for every specimen. Such a shift was, for example, more clear for the u_3 specimen while being completely absent for the u_2 one (). The ranges of L values for the three specimens overlapped with each other significantly, especially at the last time point when the tomography analysis was performed, i.e., at 404 days.

The local thickness distributions were characterized by a more remarked rightward shift with time than those of L . Such a shift is showcased in Figure 6.19 (d) for the u_1 specimen, while the corresponding Zipf's plots for the two other specimens are reported in Figure D26 (e) and (f). The maximum T_{local} values at 168 days, 224 days and 404 days for the different specimens were the following: u_1 : 0.2 mm, 0.269 mm and 0.295 mm; u_2 : 0.2 mm, 0.2915 mm and 0.296 mm; u_3 : 0.25 mm, 0.259 mm and 0.282 mm, respectively. Thus, also in the case of T_{local} , the maximum value consistently increased as the ASR cracking advanced.

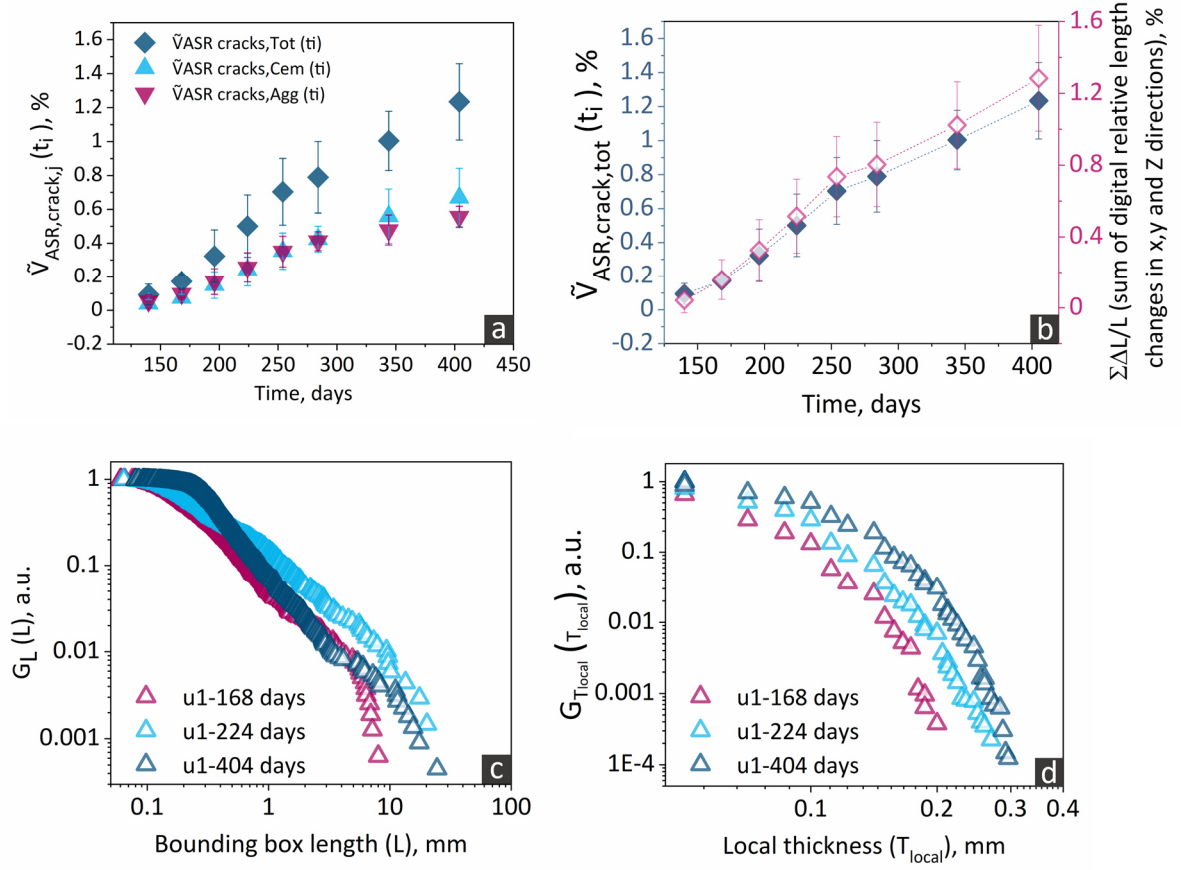


Figure 6.19. (a) Time series of the ASR crack volume fractions, distinguishing between the volume fraction for all the cracks, $\tilde{V}_{ASR,cracks,tot}$, that for cracks just within the aggregates, $\tilde{V}_{ASR,cracks,agg}$ and that for those just in the cement paste, $\tilde{V}_{ASR,cracks,cem}(t_i)$, computed for the the tomographed regions of the u specimens; each marker indicates the average value from the three specimens, while the error bar indicates the standard deviation of the three values; (b) the $\tilde{V}_{ASR,cracks,tot}$ time series and the one for the relative volume change of the tomographed region, estimated by $\sum_{k=X,Y,Z} \frac{\Delta L_{AFF,k}}{L_{AFF,k}}$; for the latter time series, at each time point, the marker also indicates the average value from the three specimens while the error bar was computed as the square root of the sum of the variances of each $\frac{\Delta L_{AFF,k}}{L_{AFF,k}}$, based on the assumption that each of it was a Gaussian random variable; (c) empirical (i.e., statistical ensemble) complementary cumulative distribution function, $G_L(L)$, of the crack bounding box length, L , in \log_{10} - \log_{10} scales (Zipf's plot) for the u_1 specimen only and at three time points (168, 224 and 404 days); (d) Zipf's plot for the crack local thicknesses, T_{local} , also for the u_1 specimen and at the sametime points as in (c).

The separated cracks had also in this case the shape of curved and fragmented thin-plates, with a broad range of curvatures. The 3D rendering in Figure 6.17 and Figure 6.18 of the crack networks provide only a qualitative indication of such shape type. The shape tensor analysis allowed confirming more quantitatively such indication. Insets (a) to (c) in Figure 6.20 show the mapping of each disconnected crack to a point in the elongation vs flatness, $(E; F)$, plane, for the u_1 specimen and at three consecutive time points of 168, 224 and 404 days, respectively. The corresponding results for the two other specimens are additionally provided in Figure D27. At any time point and for all specimens, the majority of

the cracks were mapped in a region close to the top-right corner ($[1; 1]$) of the $(E; F)$ plane. No significant difference in shape distribution was observed among the three specimens. Such shape distributions did not also evolve considerably with time.

The qualitative observation that the cracks in the u_1 specimen were slightly more isotropically oriented than those in the other two specimens (see Figure 6.18) found confirmation from the quantitative crack orientation analysis based upon the shape tensor one. Insets (d) to (f) in Figure 6.20 show a slightly different presentation of the orientation analysis results, than as shown in Sections 4.3.3, Section C9 and Section 6.3.2.5. There, the eigenvector \hat{u}_1 of each independent crack is plotted as an arrow (rescaled by a certain factor), with the head of the arrow essentially identifying a point on a sphere. In Figure 6.20 (d) to (f), the projection of each point on the sphere onto its equatorial plane, corresponding to the $X - Y$ plane of the specimen's frame of reference, is shown instead. The scales of the two spherical angular coordinates, $\theta \in [0^\circ; 360^\circ]$ and $\varphi \in [0^\circ; 180^\circ]$, identifying univocally each eigenvector \hat{u}_1 , are reported. The distance between each concentric circle in the polar plot corresponds to 10° along the φ axis. The plots in Figure 6.22 (d) to (f) refer to the u_1 specimen at three consecutive time points, 168, 224 and 404 days, respectively. The corresponding plots for the two other specimens are shown in Figure D28. Any of the three specimens exhibited at any time point cracks oriented along any direction. However, over time, the density of the points on the equatorial plane increased more towards its center, indicating a preferential orientation of the cracks along the Z -axis, as showcased in Figure 6.18 (d) to (f) for the u_1 specimen. When comparing such plots for the three specimens at 404 days, it is possible to observe the u_1 specimen having a higher density of points also at larger radial distances than the two other specimens (see Figure D28 (c), (f) and (i) for the u_1 , u_2 and u_3 specimens, respectively). Higher density of points at larger radial distance implies higher fraction of cracks oriented further away from the Z -axis, i.e., a smaller degree of orientation anisotropy towards the Z -axis, as qualitatively observed from the 3D rendering in Figure 6.18.

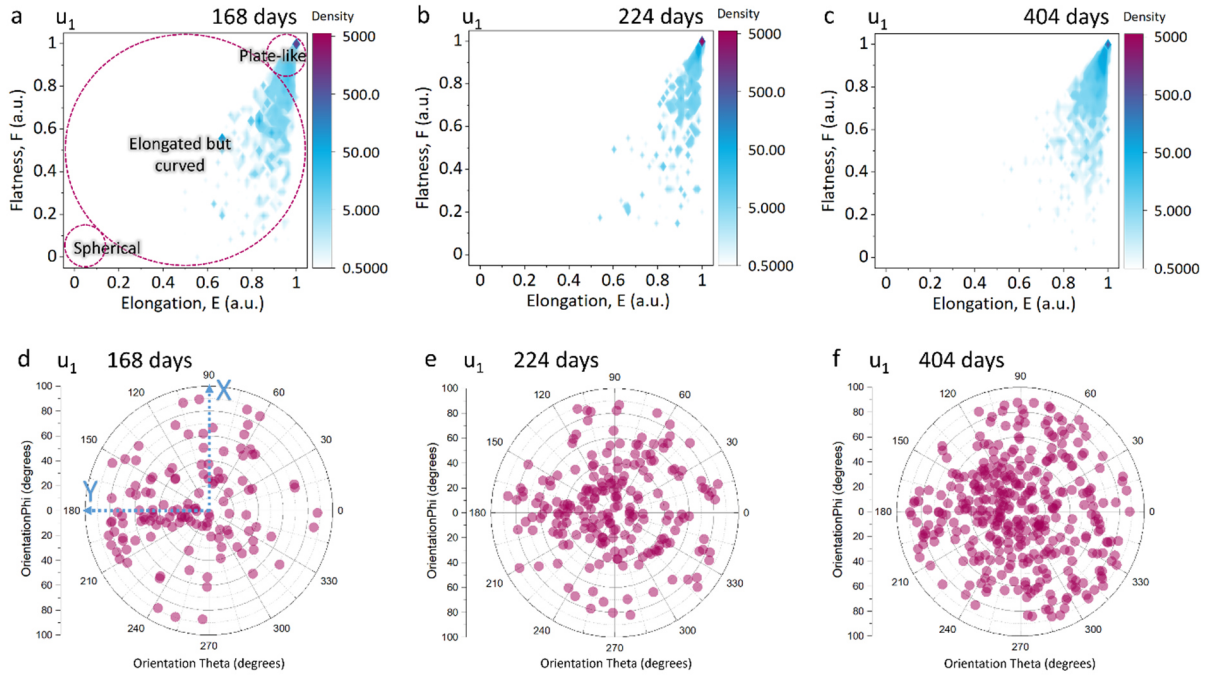


Figure 6.20. (a) to (c): kernel density estimate (KDE) of the joint probability density function (PDF) of the crack elongation E and flatness F , for the u_1 specimen at 168, 224 and 404 days, respectively. (d) to (f): visualization of

the crack orientation analysis results for the u_1 specimen at 168, 224 and 404 days, respectively. Each point is the projection on the equatorial plane of the point on the unit sphere with spherical coordinates $(\theta; \varphi)$, $\theta \in [0^\circ; 360^\circ]$ and $\varphi \in [-90^\circ; 90^\circ]$, representing the first eigenvector \hat{u}_1 of the shape tensor \mathbf{G} of a crack. The radial distance of a point from the origin is mapped to the elevation angle φ axis according to the vertical scale, such that the distance between two successive circles in such polar coordinates framework corresponds to 10° distance on the φ axis. The X – and Y –axis of the specimen's Cartesian frame of reference are indicated in (d) to facilitate the interpretation of the crack orientation.

6.4. Discussion

The first experimental campaign described in this Chapter and dedicated to the optimization of the contrast enhancement by BaSO_4 addressed a substantial and omnipresent issue for the application of standard XT in concrete science and technology. As mentioned in Section 2.4.2.5.1, the solid material phases of concrete typically bear little to no X-ray attenuation contrast between each other because of similar chemical composition and mass density, thus similar X-ray attenuation coefficient values. Thus, their segmentation is typically very challenging and time consuming. The lack of voxel value contrast in standard X-ray tomograms can be addressed by using other X-ray image contrast mechanisms and respective imaging modalities already mentioned in Section 2.4.2.5. X-ray phase contrast imaging (XPCI) has been shown particularly successful in addressing the issue of enhancing the contrast between the cement paste and aggregates. However, XPCI remains till nowadays expensive to be implemented at the laboratory scale and still affected by several limitations impacting its use with concrete specimens at the mesoscale, e.g., its difficult implementation with photon energy above 100 keV. Thus, the possibility of addressing such image contrast issue still when using standard, i.e., attenuation contrast-based, XT represents a step forward.

The substantial advancement for ASR research brought by the work reported in this Chapter consisted of identifying a range of BaSO_4 concentration (above 0.75 vol.-% and less than 3 vol.-%) and an optimal value (2.5 vol.-%) which simultaneously allowed (1) achieving a reliable segmentation of the aggregates used (2) without any significant perturbation to the ASR (cracking). The latter feature and result was extensively assessed both in terms of macroscopic, i.e., specimen scale, expansion and mechanical properties evolution and in terms of ASR cracking features, including associated local deformations, as well in terms of ASR products' chemical composition and morphology.

The possibility to segment the cement paste from aggregates empowered and empowers obtaining new quantitative insight about ASR (cracking). One key type of obtained result consisted, for the specimens examined, of the observation of ASR cracking being as much extensive inside the aggregates as throughout the cement paste. Such result was assessed both qualitatively, by the 3D rendering of the segmented crack networks shown in Figures 6.8, 6.17, 6.18 (a)-(c) and, more extensively, in Figures D20, D21, D22, D23 and D24, and quantitatively, by the evaluation of the crack volume fractions (see Figure 6.9 and Figure 6.19 (a)). The detection and quantification of such ASR cracking characteristic could not be easily obtained by, e.g., traditional petrographic analysis, given the intrinsic 3D nature of crack networks: many thin sections at different, successive depths of the same region would need to be acquired and analysed, which would require an extensive effort compared to that of a XT measurement.

The type of quantitative assessment of ASR cracks inside aggregates and through the cement paste shown in this Chapter should act as a key information/criterion for the validation of computational models of ASR cracking, along with the possibility of modelling such process in realistic, mesoscopic scale geometrical domains obtained from the binary tomograms of the aggregates, the other key value of the reported work for computational modelling efforts.

The extensive experimental campaign with optimal BaSO₄ concentration of 2.5 vol.-% allowed providing more robust confirmation of certain ASR cracking features already reported in the previous Chapters, as well as it allowed assessing more robustly other ones. The robustness came both from larger specimen sets, e.g., three for XT analysis and ten specimens for length and mass measurements, as well as from a higher number of points in the time series, including, for the mechanical properties, at very late stages (560 days), not explored in all the other experimental campaigns.

One feature of the ASR expansion and associated cracking which could be robustly confirmed is the anisotropy of expansion and the associated slight anisotropy in crack orientation. The qualitative and quantitative crack orientation analysis results shown in Figures 6.20 (a)-(f) and Figure 6.20 or Figure D28 (d),(f) and (i) confirm a slight preferential crack orientation towards the Z-axis, which implies the crack thickness increase with time preferentially contributed to expansion along directions orthogonal to the Z-axis. Indeed, most of the specimens exhibited larger relative length changes along the X- or Y-axis than along the Z one (see Figure 6.4 (c)-(f) and Figure 6.18 (g)-(i), Figure 5.5 (b)-(c) and Figure C5 (b)-(c)), suggesting that crack widening had a key contribution in the macroscopically measured expansion. As already discussed in Section 4.4, one of the possible sources of the larger expansion orthogonally to the Z-axis may consists of the smaller gradient in moisture and alkali contents along the X- and Y-axes than along the Z one, given that any specimen used in this PhD project was elongated in that direction, mostly with an aspect ratio of 4:1 (Z versus X or Y axes). Although this explanation is physically plausible, a systematic study investigating ASR expansion and cracking in isotropic specimens (e.g., cubes) would be still required to confidently validate it. Imaging the distribution of moisture and alkali, e.g., by MRI, along with XT, both performed at the same time points, would allow assessing the correlation degree between water and alkali content gradients and local deformations and cracking. Such correlation degree remains to date poorly characterized, despite its relevance for computational modeling of ASR (cracking) in real world structures.

Among all the results reported in this Chapter, two of them, not exclusively related with the possibility of distinguishing cracks as inside aggregates or the cement paste, are particularly noteworthy.

The first one consists of the observed strong linear correlation (almost 1:1 relationship) between the ASR cracks volume fraction, $\tilde{V}_{ASR,cracks,tot}$, and the relative volume change of the tomographed volume (see Figures 6.10 and Figure 6.19 (b)). Despite the latter was estimated just by a proxy variable, $\sum_{k=X,Y,Z} \frac{\Delta L_{AFF,k}}{L_{AFF,k}}$, and only for the tomographed volume, not for the whole specimen, the strong overlapping between the $\frac{\Delta L_Z}{L_Z}$ and the $\frac{\Delta L_{AFF,Z}}{L_{AFF,Z}}$ time series (see Figures 6.4 (c)-(f) and 6.14 (a)) strongly support the hypothesis of such proxy estimate being indicative of the actual relative volume change for the whole specimen. If completely confirmed, the almost 1:1 relationship mentioned above would indicate that crack lengthening and widening may account for the majority of the measured macroscopic expansion, at least for specimens under free boundary conditions as those investigated in this project.

The second noteworthy result consists in the observation, in the very long term, of a recovery of the quasi-static Young modulus and flexural strength of the specimens cast with U aggregates and not for those cast with the P ones (see Figure 6.15).

Such a recovery could be related, on the one side, with the stiffening of the ASR products mentioned in Sections 5.4 and 5.5, contributed by the Ca^{2+} uptake. In addition, evidence exists in the literature about ASR products found in cracks inside decade-old structures having chemical composition rather similar to C-S-H [4]. Thus, the observed recovery could be thought of as a partial crack healing process. On the other side, the continuous crack filling by products (see for example Figure C20) could also contribute to such a partial crack healing process. The reason why such a recovery was not equally observed for the specimens cast with the P aggregates may reside in their distinct reactivity degree due to their textural differences. As reported in Chapter 5, a more extensive ASR products accumulation within the cracks was detected for the specimens cast with the U aggregates than with the P ones (Figure C20). Consequently, a recovery of mechanical properties because of the crack filling by products becoming stiffer and stiffer should be more likely and expected for the specimens with more extensive crack filling, although also with more extensive cracking itself. The actual occurrence of a sort of partial crack healing at late age and its dynamic equilibrium with new cracking would require systematic evaluation and confirmation in future research works.

6.5. Conclusions

Among the results from the two experimental campaigns addressed by this Chapter and respective conclusions which can be drawn, the following ones are especially noteworthy.

- a) BaSO_4 , added to the concrete mix as an X-ray attenuation contrast agent, did not noticeably affect the natural ASR behaviour of the specimens, in terms of dimensional changes, mass increase, mechanical properties, morphological and chemical properties of the ASR products, quantified crack features, based on the comparison with corresponding reference specimens cast without it.
- b) A useful range of BaSO_4 concentration for enhancing the X-ray attenuation contrast between aggregates and the cement paste at the point of making the aggregate segmentation relatively simple and reliable was 0.75 vol.-% to 3 vol.-% BaSO_4 , regardless of the aggregate type.
- c) Also for the specimens cast with BaSO_4 , ASR cracks developed in the form of fragmented and curved, plate-like 3D objects, whose length and thickness steadily increased over time, a typical cracking pattern observed already for the specimens of the other experimental campaigns described in Chapters 4 and 5.
- d) The ASR crack volume fraction increased monotonically in time and, when partitioned for cracks inside aggregates *versus* cracks within the cement paste, it was observed that, almost at any time, an equivalent crack volume fraction existed in both material phases of the concrete mesostructured, an observation uniquely empowered by time-lapse XT and by the implemented methodology for the aggregate segmentation.
- e) The macroscopic expansion could be mostly attributed to ASR crack volume formation, as evinced from the almost 1:1 relationship between ASR crack volume fraction and relative volume change of the tomographed regions of the specimens.

- f) A recovery of the Young's modulus and of the flexural strength was observed in specimens cast with the U aggregates at late time, while they continued decreasing for the corresponding specimens cast with the P aggregates, likely due to their different degrees of crack filling by ASR products, attributable to their distinct reactivity degrees, and to the stiffening of the products themselves with ongoing time.

Bibliography

- [1] Hanor J S 2000 Barite–Celestine Geochemistry and Environments of Formation *Rev. Mineral. Geochemistry* **40** 193–275
- [2] Ketcham R A and Mote A S 2019 Accurate Measurement of Small Features in X-Ray CT Data Volumes, Demonstrated Using Gold Grains *J. Geophys. Res. Solid Earth* **124** 3508–29
- [3] Leemann A and Münch B 2019 The addition of caesium to concrete with alkali-silica reaction: Implications on product identification and recognition of the reaction sequence *Cem. Concr. Res.* **120** 27–35
- [4] Rajabipour F, Giannini E, Dunant C, Ideker J H and Thomas M D A 2015 Alkali-silica reaction: Current understanding of the reaction mechanisms and the knowledge gaps *Cem. Concr. Res.* **76** 130–46

Chapter 7. Qualitative and quantitative analysis of ASR crack networks and products in the concrete mesostructure context

7.1. Summary

This Chapter reports and describes the results of an experimental campaign which aimed at integrating together and harmonizing the two experimental methodologies described in Chapters 5 and 6. The problem to be addressed by such an integration was making both aggregates and ASR products segmentable in attenuation contrast X-ray tomograms such that ASR cracking could be investigated at the chosen mesoscale by fully characterizing the products and cracks spatial-temporal distributions with the possibility of discriminating between their location in the concrete mesostructure (i.e., inside aggregates or within the cement paste). Such problem could not be addressed simply by blindly adopting the optimal BaSO₄ concentration obtained in the first experimental campaign described in Chapter 6

As shown in Chapter 5, the extrusion of ASR products into the cement paste was observed to take place consistently. When occurring in specimens cast with both CsNO₃ and BaSO₄, the extruded Cs-labelled ASR products may bear similar X-ray attenuation as the BaSO₄-labelled cement paste, thus making the segmentation of products inside the paste not possible. To avoid this problem, the optimization of the concentration of either contrast agent needs to be adapted to the presence and concentration of the other.

Section 7.2 describes the experimental and analysis details additional to those of the general procedure described in Chapter 3) and specifically needed for the investigation target mentioned above. Section 7.3 reports the most important findings from the experimental campaign and respective tomographic analysis. Additional and complementary results are provided in the Appendix E. Section 7.4 synthesizes the important results and discusses about what could be learnt about ASR cracking at the chosen mesoscale with the newly integrated methodologies. The main highlights of this experimental campaign and of the impact of the methodological integration are provided in the conclusive Section 7.5.

7.2. Specific materials and methods

The full experimental and analysis workflow mainly consisted of two steps:

1. the simultaneous optimization of the BaSO_4 and CsNO_3 concentrations in the concrete mix composition to enable the visualization and segmentation in the tomograms of both aggregates and ASR products;
2. the characterization with the approaches already used in the experimental campaigns described in the previous Chapters of the evolution of the ASR products and cracks while being able to take into account and discern their position within the mesostructure.

7.2.1. X-ray attenuation contrast enhancement between aggregates and cement paste and between the latter and ASR products

An experimental parametric analysis with respect to the BaSO_4 concentration was performed with the goal of maximizing synergistically both the aggregate-to-cement paste and the cement paste-to-ASR products tomographic contrast. In order to minimize the optimization parameters, and since the CsNO_3 concentration already implemented in the previous study (discussed in chapter 6) allowed reasonably high X-ray attenuation for the ASR products, its concentration was kept fixed and only BaSO_4 concentration was adjusted.

The X-ray attenuation contrast between aggregates and the cement paste was optimized by casting specimens according with the same approach described in Chapter 6, i.e., specimens following the reference mix composition reported in Table 6.1 except for replacing a fraction of the aggregate total volume (regardless of the sieve-size range) with a corresponding volume fraction of BaSO_4 . The replacement volume fractions were 0.75, 1.5, 2 and 3 vol.-%. These concentration values were inspired by the results obtained from the sets of specimens of the BaSO_4 concentration optimization experimental campaign described in Chapter 6, where also other values were considered. Compared with that experimental campaign, the investigated BaSO_4 concentration range was narrower, starting at 0.75 vol.-%, because it was observed in the previous campaign that the only smaller value tested, 0.25 vol.-%, was almost ineffective in enhancing the aggregate-to-cement paste contrast. The optimal value of 2.5 vol.-% was not included in this new optimization campaign because in the previous campaign the corresponding contrast enhancement was only slightly smaller than what achieved with using 3 vol.-%. Instead, the value of 2 vol.-%, intermediate to values already explored in the previous campaign, was now investigated, with the goal of finding an optimal trade-off between contrast enhancement maximization and BaSO_4 content minimization. Indeed, although the results presented in Chapter 6 showed no significant negative

or spurious influence of BaSO_4 , at the tested concentrations, on ASR (cracking), its content minimization given the achievement of a target contrast enhancement level should always be sought after, since it is a filler which makes the specimen mix composition depart from the original one.

The ASR products tomographic visibility and segmentability was made possible by adding into the concrete mixing water CsNO_3 in the same amount as done for the experimental campaign described in Chapter 5, i.e., 30 g per 1 kg of cement, resulting in a molar ratio to the alkalis contained in the cement ($[\text{Cs}]/[\text{Na}+\text{K}]$) of 0.43.

Specimens with size $40 \times 40 \times 160 \text{ mm}^3$ were cast only with the U aggregate type, because by being more reactive it can lead to relatively faster evaluation of ASR cracking behaviour while optimizing the best BaSO_4 concentration. Table 7.1 provides the details of the mix composition and the respective specimen labels. The same laboratory ASR acceleration protocol described in Section 3.2 was adopted.

Table 7.1. Mix composition of the specimens in units of $\text{kg}\cdot\text{m}^{-3}$ (mass per m^3 of cast)

Specimen label	Cement CEM I 42.5N	Aggregates			Deionized water	NaOH	CsNO_3	BaSO_4
		0 – 4	4 – 8	8 – 11.25				
		mm	mm	mm				
<i>U – Cs – 0.75 vol. % BaSO_4</i>	450	650	406	569	225	1.8	13.6	21
<i>U – Cs – 1.5 vol. % BaSO_4</i>	450	641	401	561	225	1.8	13.6	43
<i>U – Cs – 2 vol. % BaSO_4</i>	450	636	397	556	255	1.8	13.6	57
<i>U – Cs – 3 vol. % BaSO_4</i>	450	625	390	547	225	1.8	13.6	84

7.2.2. ASR characterization by XT and other methods

As done in the other experimental campaigns, the specimens were taken out of the oven at successive time points to be characterized with various methods. The non-destructive measurements were repeatedly performed at eight successive time points within the total duration of the experimental campaign, all on three distinct specimens, except for the XT which was performed on one specimen of each set (the reference specimens one, with CsNO_3 but without BaSO_4 , and one set for each distinct BaSO_4

concentration). Such measurements, in addition to XT (using the holding setup 1 shown in Figure 3.2 (a)), included mass and length relative changes on three distinct specimens (the latter with the expansion measurement setup 1 shown in Figure 3.1 (c)), since the start of the ASR acceleration, along with the quasi-static (compressive) Young's modulus, measured along the specimen longitudinal direction, all following the same procedures already explained in Section 3.2.

Two important details about the XT measurements are the maximum X-ray photon energy used (90 keV) and the tomograms' effective spatial resolution (approximately 70 μm). The former parameter value indicates the X-ray energy range for which the voxel value contrast between the distinct material phases was optimized. The same BaSO_4 and CsNO_3 amounts may not be contrast-optimal for X-ray tomograms of larger specimens acquired at much higher photon energies, e.g., at several hundreds of keV. That is because X-ray attenuation decreases nonlinearly with increasing photon energy. The X-ray source used in this experimental campaign was the one described in Section 3.2.

7.2.3. Analysis of the time-lapse X-ray tomograms

The same workflow described in Section 6.3.2 was applied in this experimental campaign as well to characterize the ASR cracking in the specimen with the BaSO_4 concentration considered as optimal. The two only differences in the workflow implementation for this experimental campaign were the following:

- (1) given the presence of CsNO_3 , an additional segmentation task regarded the ASR products, which were segmented based upon the procedure described at point (IV) in Section 3.3;
- (2) where present, BaSO_4 allowed the segmentation of the aggregates (also in this case by thresholds selection) and the respective binary tomograms were used as masks to discriminate between regions both of the segmented products and of the cracks belonging to aggregates and respective regions belonging to the cement paste. In other words, every sub-region of the segmented entity (a crack or a products region) falling within such an aggregate mask was labelled as being within aggregates, while each one falling outside of such a mask was labelled as existing within the cement paste. The actual implementation of such discrimination consisted of applying to the binary tomogram of the aggregates and to that of empty cracks (products, respectively) a voxel-wise Boolean AND operator. The output was a new binary tomogram identifying voxels belonging to crack (products) and at the same time to aggregates. The same procedure was followed for the cement paste binary tomogram and the empty cracks (products) one. Overall, as a result, four binary tomograms were obtained, partitioning the empty cracks (products) regions between those inside aggregates and those inside the cement paste.

For the cracks (original and ASR ones) segmentation, the same workflow mentioned in Section 6.2.3 was used, exploiting the direct TS-based approach.

7.3. Results

7.3.1. BaSO₄ concentration optimization: analysis of the tomographic contrast enhancement

Figure 7.1 shows examples of ROIs on slices from the tomograms at 85 days of five distinct specimens cast with the chosen, fixed CsNO₃ concentration but with varying BaSO₄ ones. In the absence of BaSO₄ (inset (a)) or at a low concentration, e.g., 0.75 vol.-% (inset (b)), the ASR products-cement paste contrast is high enough to support the products segmentation but the aggregates-paste contrast is not sufficient for an easy aggregate segmentation. Whereas, at higher BaSO₄ concentrations, e.g., 2 or 3 vol.-%, insets (d) and (e) respectively, the Cs-labelled products were poorly discernible from the cement paste, because of too similar X-ray attenuation levels by both of them.

In order to quantitatively find an optimal BaSO₄ concentration, the contrast-to-noise ratio (CNR) between aggregates and the cement paste was compared with the CNRs between the ASR products and aggregates and between the ASR products and the cement paste. The CNR was defined as

$$CNR_{i,j} = \frac{|\mu_i - \mu_j|}{\sqrt{\sigma_i^2 + \sigma_j^2}} \quad (7.1)$$

where the indexes i and j are labels indicating the two material phases for which the contrast was computed, e.g., cement paste *versus* aggregates, μ_i and σ_i indicate the average and the standard deviation of voxel values from a statistical sample for the material phase i . For each material phase, forty locations were randomly chosen to build up the statistical sample.

Figure 7.2 shows the computed CNR values for the three couples of material phases mentioned before. A useful trade-off in terms of enough contrast between products and cement paste and between aggregate and cement paste was achieved at 1.5 vol.-% of BaSO₄ concentration. The (segmented) aggregate volume fraction for the 1.5 vol.-% BaSO₄ specimen was computed to be ~ 58 vol.-%, which is slightly

smaller than the nominal aggregate volume fraction as computed from the corresponding mix composition (~ 62 vol.-%).

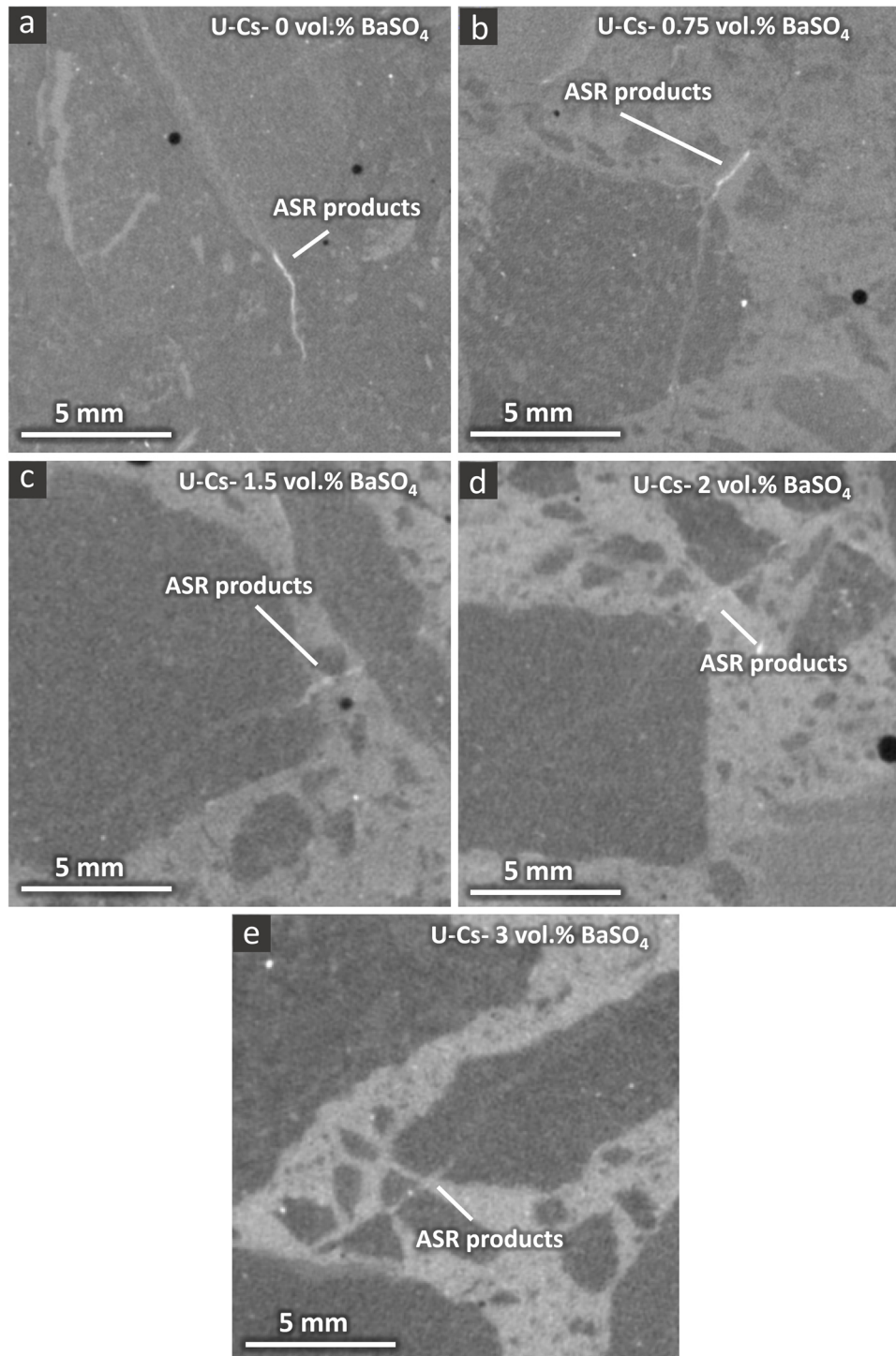


Figure 7.1. (a)-(e) Examples of ROIs on slices from the tomograms at 85 days of different specimens cast with U aggregates and distinct BaSO_4 concentrations but fixed CsNO_3 one (except for the specimen of (a), with no CsNO_3).

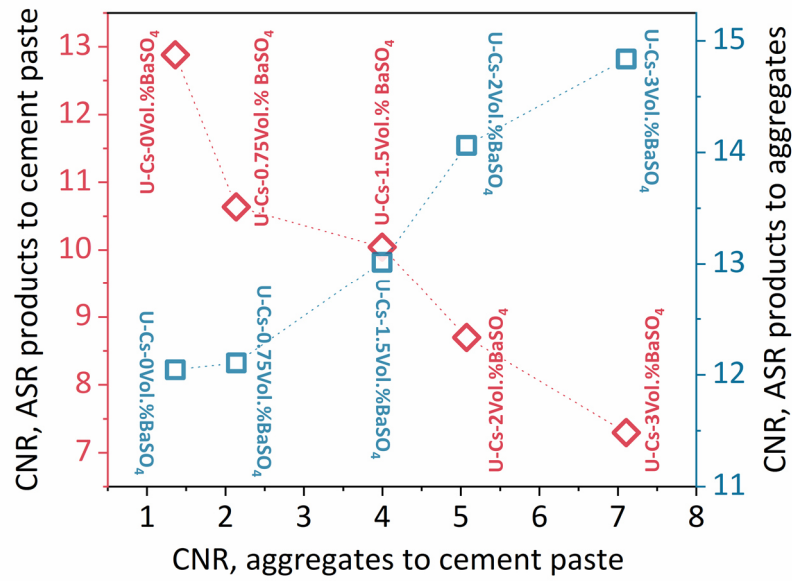


Figure 7.2. The tomographic contrast-to-noise ratio between the ASR products and aggregates (right vertical axis), the ASR products and the cement paste (left vertical axis) and between the aggregates and the cement paste (horizontal axis), as computed for the distinct specimens, cast with the distinct BaSO_4 concentration values and either without or with CsNO_3 at fixed concentration, from 40 voxel values for each material phase, sampled randomly from their tomograms at 85 days.

7.3.2. Influence of the BaSO_4 and CsNO_3 presence on the ASR-induced macroscopic dimensional changes

The BaSO_4 addition (at different concentrations) had a very small effect on the expansion along the Z-axis consisting in slightly higher average $\frac{\Delta L_z}{L_z}$ values, starting from about 140 days, compared with the specimens cast with no BaSO_4 , as observable in Figure 7.3 (a). However, the difference in the average value at each time point was smaller or of the same magnitude as the error bars. When comparing the specimens cast with distinct BaSO_4 concentrations, no systematic variation of the $\frac{\Delta L_z}{L_z}$ time series with the increasing BaSO_4 concentration could be observed, as it was already the case for the specimens cast without CsNO_3 discussed in Chapter 6 (see Figure 6.4 (a)). At any time point, $\frac{\Delta L_z}{L_z}$ fluctuated randomly with BaSO_4 concentration and with the fluctuation amplitudes were significantly smaller than the range defined by the computed error bars. The maximum average expansion of the BaSO_4 -free specimens of this group, labelled as U-Cs 0 vol.-% Ba in Figure 7.3 (a), was about 13% larger than the one achieved by the U-Ref specimens of the first experimental campaign described in Chapter 6 (see Figure 6.4 (a)).

Such expansion boosting effect by the CsNO_3 presence was already observed in the experimental campaigns described in Chapter 5 (see Figure 5.5 (a) and Figure C5 (a)). There, it was already shown that the main Cs-doping influence was an increase in the ASR kinetics, which manifested itself as a faster expansion.

Along the two lateral (i.e., X - and Y -) axis, the expansion was larger than or similar to the one along the Z -axis, as showcased for one specimen, U-Cs-1.5 vol.% BaSO_4 , in Figure 7.3 (b), estimated based upon the results of the affine registration. This result mirrors what already systematically observed in the other experimental campaigns, including for specimens cast only with BaSO_4 (see the example in Figure 6.4 (e) for a specimen cast with 2.5 vol.-% BaSO_4 and no CsNO_3).

The relative mass changes of the same six specimens of Figure 7.3 (a) also did not considerably vary by different BaSO_4 concentrations and in the presence of CsNO_3 . See Figure E1, in the Appendices for the additional data. Therefore, the concurrent presence of CsNO_3 and BaSO_4 seems not to have perturbed, within the used range of BaSO_4 concentrations, the previously observed ASR expansion for specimens cast with CsNO_3 and the effects of the latter on expansion itself

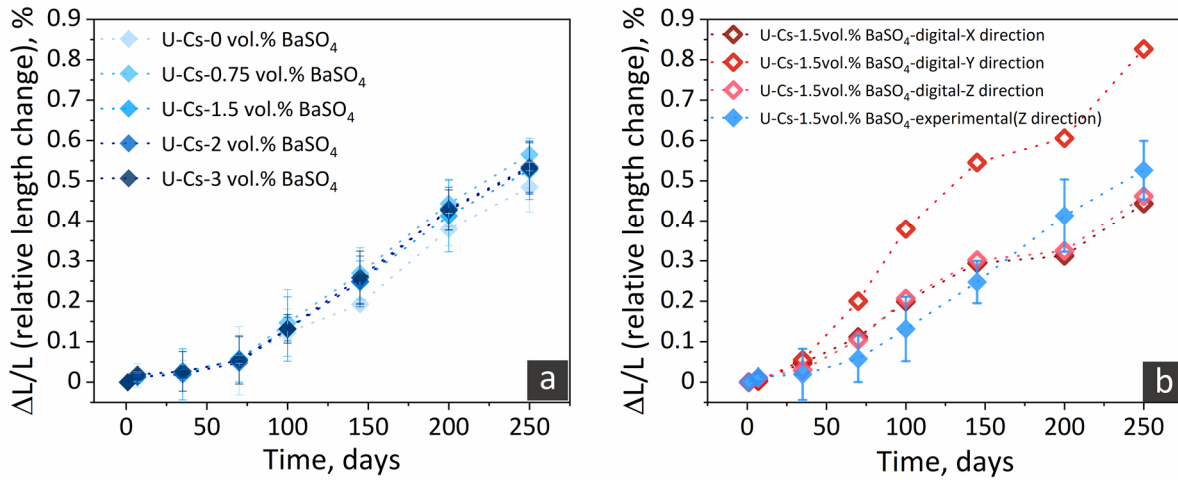


Figure 7.3. (a): evolution of the relative length change, along the specimen longitudinal direction (Z -axis) and measured experimentally ($\frac{\Delta L_z}{L_z}$), of distinct specimens cast with U aggregates, CsNO_3 and various BaSO_4 concentrations. The markers indicate averages while the error bars size is the standard deviation of six values from an ensemble of six distinct specimens, for each specimen set, i.e., BaSO_4 concentration. (b): comparison between the experimentally measured $\frac{\Delta L_z}{L_z}$ of the six specimens and the relative length change, along any axis of the Cartesian frame of reference and of another specimen, cast with 1.5 vol.-% BaSO_4 , computed from the results of the affine registration (labelled as digital), $\frac{\Delta L_{AFF,k}}{L_{AFF,k}}, \forall k = X, Y, Z$.

7.3.3. Qualitative analysis of the ASR cracking and respective local deformations: in the presence of both BaSO₄ and CsNO₃

The chosen BaSO₄ concentration of 1.5 vol.-%, as an optimal trade-off value to enhance contrast between the three couples of material phases mentioned in Section 7.3.1, made the ASR products within cracks, both inside aggregates and within the cement paste, clearly discernible, especially after 85 days, as it can be seen in Figure 7.4 (c) and (e). One of the aggregates highlighted in Figure 7.4 (a), contained a relatively large cavity in it as resolved in its tomogram at 1 day (an original crack). At 55 days, shown in Figure 7.4 (b) the ASR products fill this cavity. As this cavity was located almost in the middle of the aggregate (almost), the accumulation of the ASR products there, indicates that the different alkalis and even Ca could easily reach to the interior regions of the U aggregates (as a sedimentary rock) to form a dense ASR product. Such easier outreach of the ions into the aggregates is also evident in the density of the accumulated ASR products inside the aggregate cracks in the concrete produced by U aggregates. Whereas, in the case of P aggregates, the ASR products are usually detected in the edges of the aggregates or in the cement paste. As already observed in Figure D17 and quantified in Figure C20, there is a significantly higher cracks filling ratio by ASR products in the concrete produced by U aggregates compared to the one produced by P aggregates. Furthermore, the accumulation of the ASR products in the cavity (Figure 7.4 (a)) did not lead to propagation of a crack (at least not resolvable) from that aggregate, probably due to the adequate capacity of the cavity to accommodate the ASR products, similar to the air voids in the cement paste.

Crack generation was detected already at 55 days at other regions of the specimen as seen in Figure 7.4 (b), while the ASR products were not visible yet. At 85 days (Figure 7.4 (c)) the ASR products filled part of the further propagated cracks. The products were clearly detectable inside the aggregates, within cracks propagated into the cement matrix and also in the ITZ of some aggregates. At 250 days, further ASR products were found accumulated within the same regions where they were already observed, in smaller amounts, at the previous time points. The accumulation of further ASR products went on systematically hand-in-hand with the crack widening. The extrusion of ASR products from the aggregates into the cement paste (either along a propagating crack or into other types of pores, e.g., ITZ or air voids) was a feature systematically observed in several specimens belonging to other experimental campaigns. Additional examples of cracking features similar to those described here (e.g., products accumulation in cracks and in other pore types, e.g., air voids, within the cement paste) but from distinct ROIs on other slices from the tomograms of the same specimen are provided in Figure E2 and Figure E3.

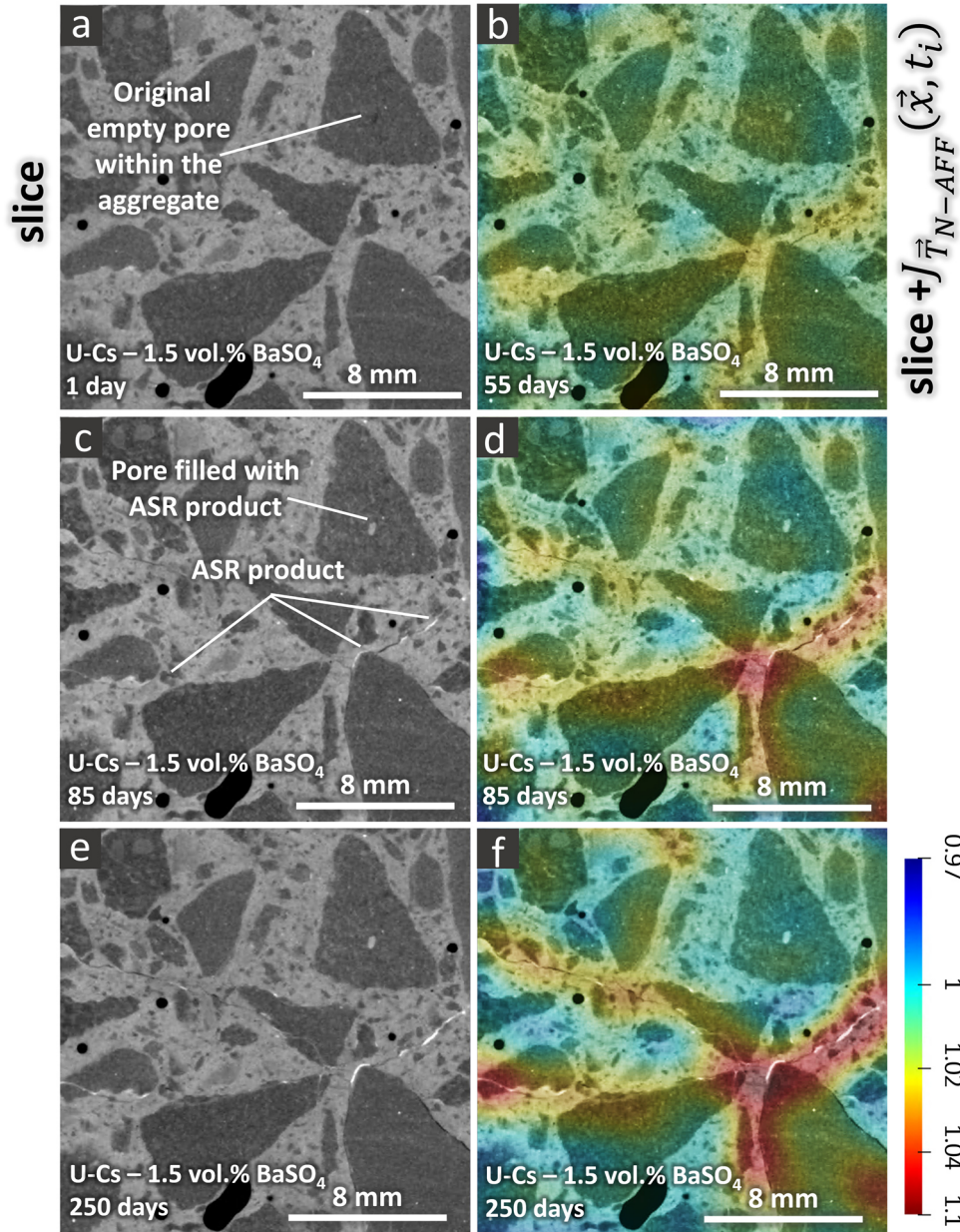


Figure 7.4. Visualization of the evolution of ASR cracks and associated localized deformations for the U-Cs-1.5 vol.-% BaSO₄ specimen. As an example, it is shown here only one small ROI on one tomographic slice, at multiple time points. The localized deformations are estimated by the determinant of the Jacobian matrix ($J_{\tilde{T}_{N-AFF}}(\vec{x}, t_i)$) of the transformation vector field $\tilde{T}_{N-AFF}(\vec{x}, t_i)$ associated with the non-affine registration. Its values larger than 1 indicate local volumetric expansion. Its values smaller than 1 indicate volumetric shrinkage. (a) X-ray tomogram at 1 day since start of the ASR acceleration. (c) and (e): slices at the same position as in (a) but from the tomograms at 85 and 250 days, respectively. (b): slice at 55 days. (d) and (f): the same slices as in (b) and (e), respectively. In (b), (d) and (f), the slice at the same position but from $J_{\tilde{T}_{N-AFF}}(\vec{x}, t_i)$ at the corresponding time points is rendered according to a color map and overlapped semi-transparently on top of the corresponding tomographic slice. The color scale bar has, by definition of $J_{\tilde{T}_{N-AFF}}$ (relative volume), no unit.

The development of local volumetric expansion regions overlapping with the cracked regions of the U-Cs-1.5 vol.-% BaSO₄ specimen was systematically observed, as it was for the specimens of the campaigns described in Chapters 5 and 6. The slice from $J_{\vec{T}_{N-AFF}}$, at the same position and same time as the tomographic one in Figure 7.4 (c) and (e), is shown in Figure 7.4 (d) and (f), respectively. Except for the Figure 7.4 (b) which shows both the slice and transparently superimposed $J_{\vec{T}_{N-AFF}}$ map at 55 days. At 55 days, several yellow/red zones (i.e., with $J_{\vec{T}_{N-AFF}} > 1$) appeared (with no detectable cracks yet) along with the first visible cracks, with thickness above the tomographic resolution (Figure 7.4 (b)). The spatial extent and intensity of the expansion zones increased over time in parallel to the lengthening and widening of the ASR cracks, an evolution pattern already reported in Chapters 5 and 6. This is another example of spatial correlations between cracks and local expansion zones. As already observed in the previous Chapters, expansion zones were alternated to local volumetric contraction ones (blue shades). The [minima, maxima] values of $J_{\vec{T}_{N-AFF}}$, for the analyzed specimen, at 250 days, were [0.9, 1.07].

Overall, the simultaneous presence of BaSO₄ and CsNO₃ seemed not to have altered many of the qualitative features of the spatial-temporal distributions of cracks and products already observed from the analysis of the tomographic time series belonging to the experimental campaigns described in the two previous Chapters. However, they extended the analysis range because of the possibility of locating cracks and products in either major material phase of the mesostructure (aggregates or cement paste).

A qualitative overview about the spatial distribution and spatial correlations between cracks and products and about their partitioning between cement paste and aggregates could be obtained already by rendering in 3D the four binary tomograms mentioned in Section 7.2.3. Figure 7.5 showcases such rendering for the tomogram at 250 days. While in inset (a) there, all four binary tomograms are shown together, each rendered with a distinct color, insets (b) and (c) show separately the binary tomograms of products and of empty cracks, respectively. These distinctly rendered binary tomograms allowed noticing several qualitative features. From Figure 7.5 (b), it could be already inferred that ASR products likely existed in almost equal amounts within the aggregates and within the cement paste. Much of the ASR products within the cement paste were accumulated inside large air voids (Figure 7.5 (b)).

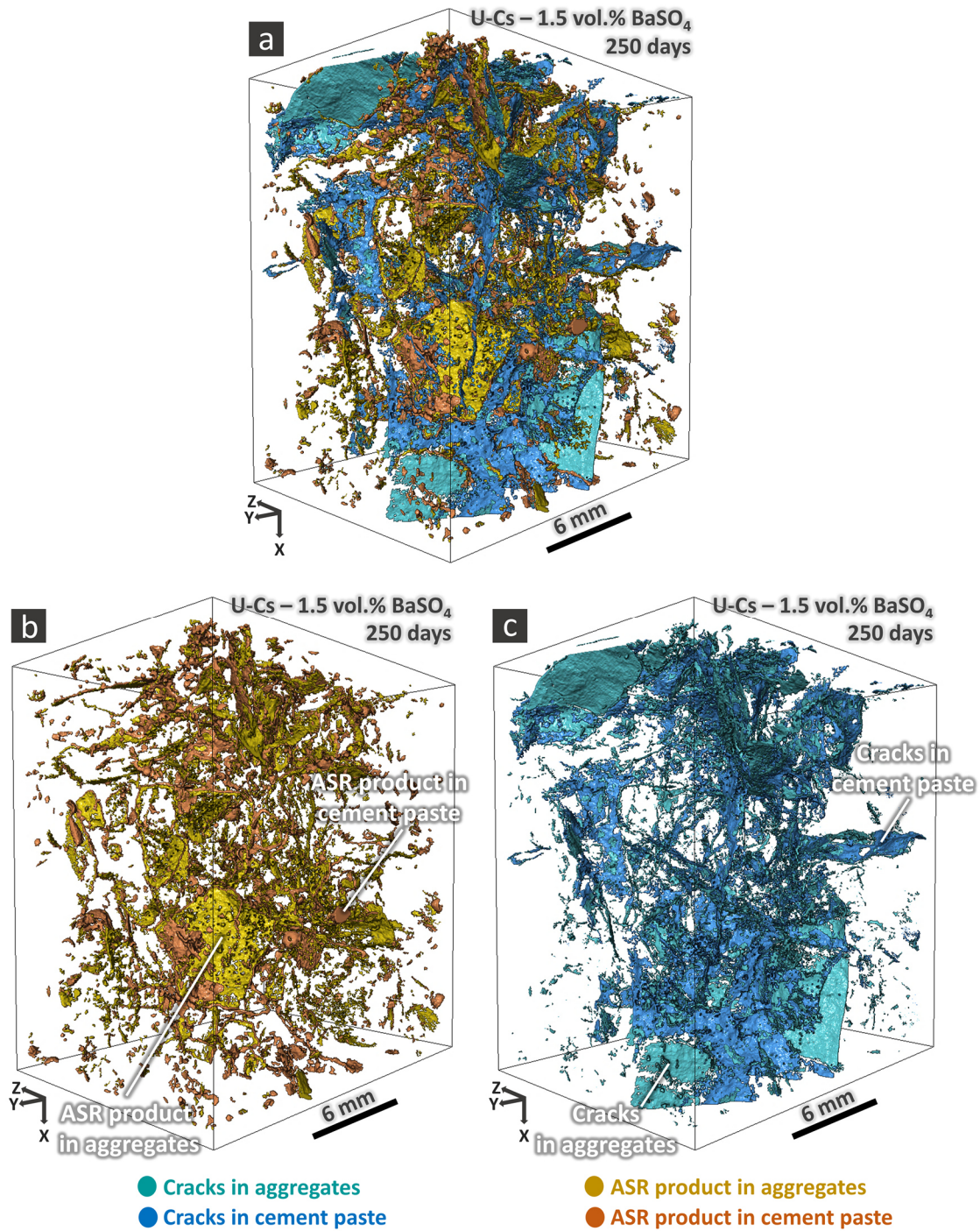


Figure 7.5. 3D rendered volumes of interest (VOIs) from the binary tomograms of empty cracks either inside aggregates (cyan) or within the cement paste (blue) and of ASR products in the entire part of the pore space resolved in the tomograms (e.g., spherical air voids, porous patches and cracks), with distinction between regions inside (yellow) and outside (orange) of aggregates. The analyzed tomogram was the one of the U-Cs-1.5 vol.-% BaSO₄ at 250 days. (a): rendering of the VOI of all four types of binary tomograms (ASR products inside and outside aggregates and empty cracks inside and outside aggregates) together. (b): rendering of the VOI of only the two ASR products binary tomograms. (c): rendering of the VOI of only the two binary tomograms of empty cracks.

When inspecting the rendering similar to the one in Figure 7.5 (a) but for the tomograms at multiple time points, it was possible to observe that the products were transported rather isotopically throughout the mesostructure, without any sign of preferential directionality, e.g., along the gravity field. An example of such time series of 3D rendering is additionally provided in Figure 7.6. Such an isotropic redistribution of the products was already observed for the two specimens, with U and P aggregates, respectively, of the experimental campaign described in Chapter 5 (see for example Figure 5.9, for the P-Cs specimen, and Figures C16 and C17 for the U-Cs one). Most of the cracks inside the aggregates were empty, only a few of them were almost fully filled with products. This feature could be recognized by comparing the volume rendered in yellow in Figure 7.6 (b) (products inside aggregates) with the one rendered in cyan in Figure 7.6 (c). In Figure 7.6 (b), the yellow regions with higher aspect ratio correspond to cracks filled with products. The cracks in the cement paste were only partially filled as well.

The spatial-temporal distribution of both products and cracks could be more extensively characterized, although still on a qualitative basis, than what was possible with the results presented in Chapter 5, where the distinction between aggregate and cement paste regions was not possible. Since 55 days (Figure 7.6 (b)), a significant accumulation of products directly inside or in the vicinity of original pore space could be observed. At 145 days (Figure 7.6 (c)), a significant larger amount of products could be detected and this occurred both inside the aggregates and in the cement paste. Such significant increase in products accumulation was accompanied by a considerable amount of cracking. Finally, at 250 days (Figure 7.6 (d)), the overall ASR products volume could be found almost in every region of the tomographed volume, as long as the crack network percolated the volume itself.

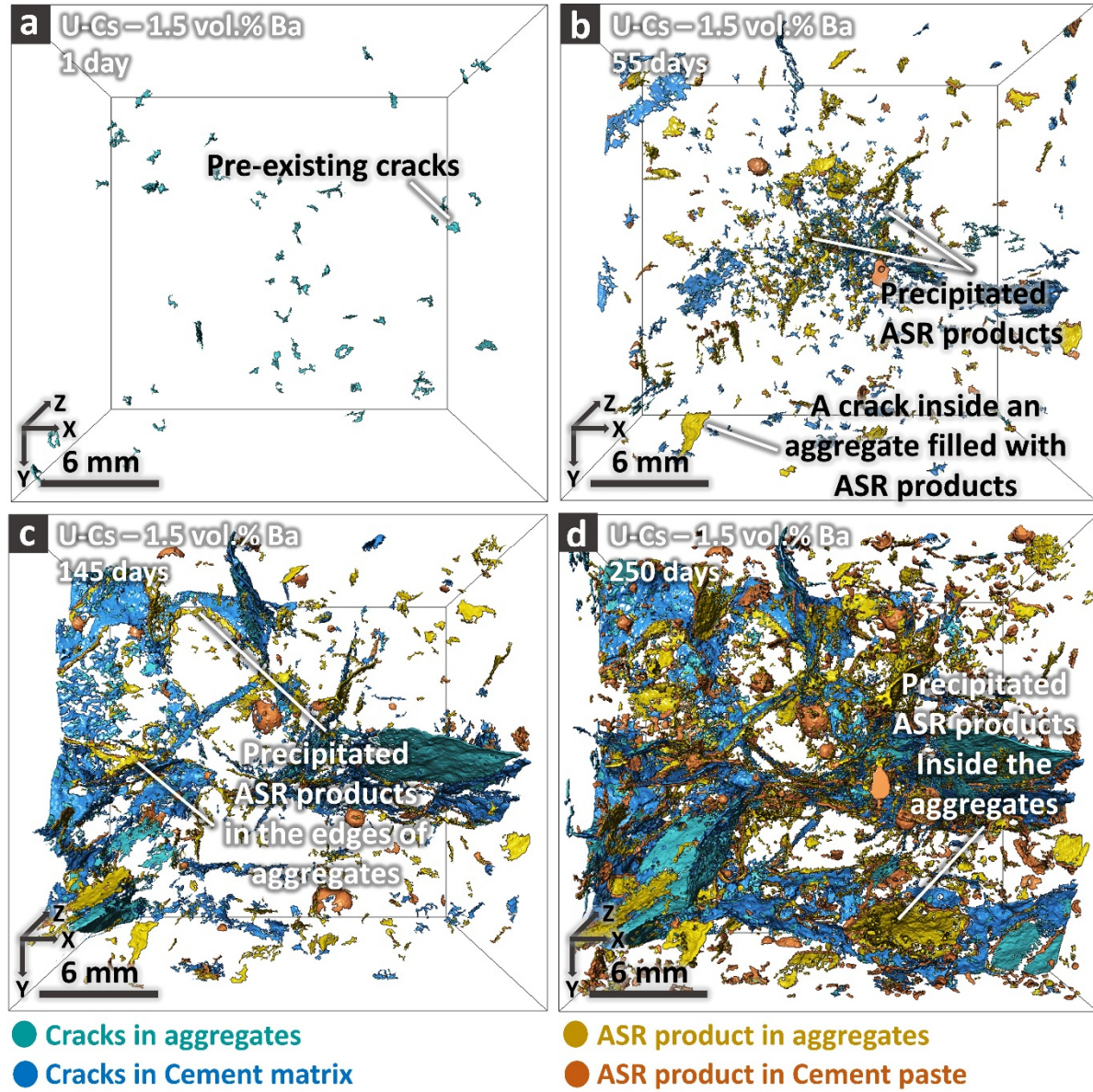


Figure 7.6. (a)-(d) combined 3D rendering of the binary tomograms of empty cracks inside aggregates (cyan), of those within the cement paste (blue), of ASR products in the entire pore space (i.e., in air voids, porous patches and cracks) inside aggregates (yellow) of ASR products outside of aggregates (orange). The binary tomograms are those of the U-Cs-1.5 vol.% BaSO₄ specimen at 1 day, 55, 145 and 250 days, respectively.

7.3.4. Quantitative analysis of the ASR cracking within aggregates and the cement paste

The aggregate (and consequently) cement paste segmentations allowed quantifying the ASR cracks and products volume fractions both independently of their location with respect to the mesostructure (as already achieved in the previously reported experimental campaigns) and with separate reference to aggregates and cement paste. Thus, distinct time series of volume fractions $\tilde{V}_{ASR,k,j}(t_i)$, $\forall i = 1, \dots, N_t$,

with the index $k = \text{cracks}$ or products while the index $j = \text{Agg}$ or Cem or tot (the latter indicating no mesoscale phase distinction) were computed according to Eq. (3.6). All such time series are shown in Figure 7.7 (a).

The maximum $\tilde{V}_{ASR,crack,tot}$ value, achieved at 250 days, was 1.73%, higher than the corresponding values reached by the U-2.5 vol.-% BaSO₄ (1.41%, see Figure 6.9 (a)) and U-Ref (1.19%, see Figure C18 (c)) specimens, respectively. This difference is in agreement with the accelerated ASR kinetics in the presence of CsNO₃, as reported and discussed in Chapter 5. Indeed, the relative length change, measured experimentally along the specimen longitudinal direction, $\frac{\Delta L_z}{L_z}$, was also larger for the U-Cs-1.5 vol.-% BaSO₄ (see Figure 7.3 (a)) specimen than for those two other specimens (see Figure 6.4 (a), Figure C5 (a) and Figure 4.1 (a)). The U-Cs-1.5 vol.-% BaSO₄ specimen also showed higher $\tilde{V}_{ASR,crack,tot}$ value at 250 days than the corresponding specimen in the absence of BaSO₄ (about 1.6%, see Figure C18 (c)). This difference cannot be directly attributed to the BaSO₄ presence, since, as shown by the $\frac{\Delta L_z}{L_z}$ time series in Figure 7.3 (a), the BaSO₄ presence or absence as well as its concentration seemed not to have altered significantly the longitudinal expansion, which is positively correlated with $\tilde{V}_{ASR,crack,tot}$ (as shown in Figure C19) both in the absence and in the presence of CsNO₃. The U-Cs specimen investigated by XT in the campaign described in Chapter 5 achieved at 250 days a smaller $\frac{\Delta L_z}{L_z}$ value (about 0.4%, Figure C5 (a)) than the U-Cs-1.5 vol.-% BaSO₄ specimen (about 0.45%, Figure 7.3 (a)), which agrees with a smaller $\tilde{V}_{ASR,crack,tot}$ value of the former compared with the value of the latter, independently of the presence of BaSO₄. Larger ASR cracks volume fraction values were estimated inside aggregates than inside the cement paste, starting from about 35/55 days.

When considering the ASR products, their total volume fraction, $\tilde{V}_{ASR,products,tot}(t_i)$, was always smaller than the cracks' one, as already observed for the U-Cs specimen of Chapter 5 (see Figure C18 (c)). The main difference between the two specimens was that such difference was smaller for the U-Cs specimen of Chapter 5.

The differentiation between ASR products within the aggregates and within the cement paste showed that $\tilde{V}_{ASR,products,Agg}$ was slightly higher than, $\tilde{V}_{ASR,products,Cem}$ at earlier ages, e.g., up to about 100 days. However, afterwards, slightly more products seemed to have accumulated within the paste than within aggregates. However, the statistical significance of such difference could not be assessed given only one specimen was tomographically analyzed.

A strong positive correlation between $\tilde{V}_{ASR,cracks,tot}$ and the relative volume change of the tomographed region of the specimen was observed (Figure 7.7 (b)). The latter variable was estimated as

$\sum_{k=X,Y,Z} \frac{\Delta L_{AFF,k}}{L_{AFF,k}}$, as already explained in Section 6.3.2.5. Compared with the results shown in Figures 6.10 and Figure 6.25 (b), such a positive correlation between the two variables was not anymore of the type of a linear relationship or even almost a 1:1 one.

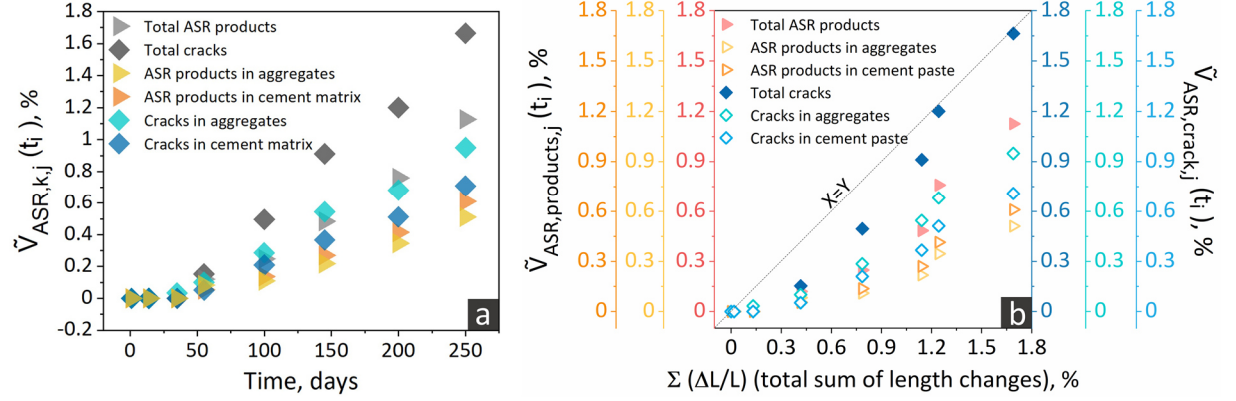


Figure 7.7. (a) Volume fraction of ASR products or cracks, without or with distinction between aggregates and cement paste, at distinct time points, $\tilde{V}_{ASR,k,j}(t_i)$, plotted for the U-Cs-1.5 vol.-% $BaSO_4$ specimen. The markers in light and dark grey correspond to the total ASR products and cracks, all over the tomographed volume, respectively. The yellow markers represent the ASR products only inside the aggregates and those in orange refer to the ASR products in the cement paste, residing in any kind of pore space regions (cracks, air-oids or porous patches). The cyan and blue markers refer to the cracks, either filled by ASR products or empty, inside the aggregates and the cement paste, respectively. (b) Correlation between the different volume fractions, $\tilde{V}_{ASR,k,j}$, values and the relative volume change of the tomographed region of the U-Cs-1.5 vol.-% $BaSO_4$ specimen, the latter estimated by its proxy variable being the sum of relative length changes along the three axes and computed from the results of the global affine registration, $\sum_{k=X,Y,Z} \frac{\Delta L_{AFF,k}}{L_{AFF,k}}$.

The shape tensor analysis was used to assess quantitatively the distribution of crack length values, in terms of crack bounding box length, L , as done already for the tomograms of the other experimental campaigns. The statistical *ensemble* estimates of the complementary cumulative distribution function, $G_L(L)$, of L is shown in the form of a Zipf's plot in Figure 7.9 (a) for the tomograms at 250 days of two specimens, the U-Cs-1.5 vol.-% $BaSO_4$ specimen and the U-Ref specimen of the experimental campaign described in Chapter 6 and used there for the optimization of the $BaSO_4$ concentration in the absence of $CsNO_3$. The distribution of the L values and its maxima are within similar ranges, suggesting that the presence of both $BaSO_4$ and $CsNO_3$ may have not had any spurious effect on the crack length. Lack of influence of $CsNO_3$ alone on the distribution and maxima of L was already shown in Chapter 5 (compare Figure C29 (c) *versus* (d), for what concerns a U-Ref specimen *versus* a U-Cs one). It has to

be remarked that the range of L values for the U-Cs-1.5 vol.-% BaSO₄ specimen was similar to the one for the U-Cs specimen (thus cast without BaSO₄) of Chapter 5, as seen from Figure C29 (d).

In terms of local thickness, T_{local} , values, the U-Cs-1.5 vol.-% BaSO₄ exhibited a distribution which was comparable to the one of the U-Ref specimen of Chapter 6 only at the lower values, while it departed from it at the higher values, with much larger maximum, as seen in the tails of the distributions (Figure 7.8 (b)). Such a difference in the T_{local} distributions, in the absence and in the presence of CsNO₃, was already observed between the U-Ref and U-Cs specimens of Chapter 5 (compare Figure C39 (c) and (d)) and, as mentioned in Chapter 5, could be attributed mainly to the accelerated ASR kinetics in the presence of CsNO₃.

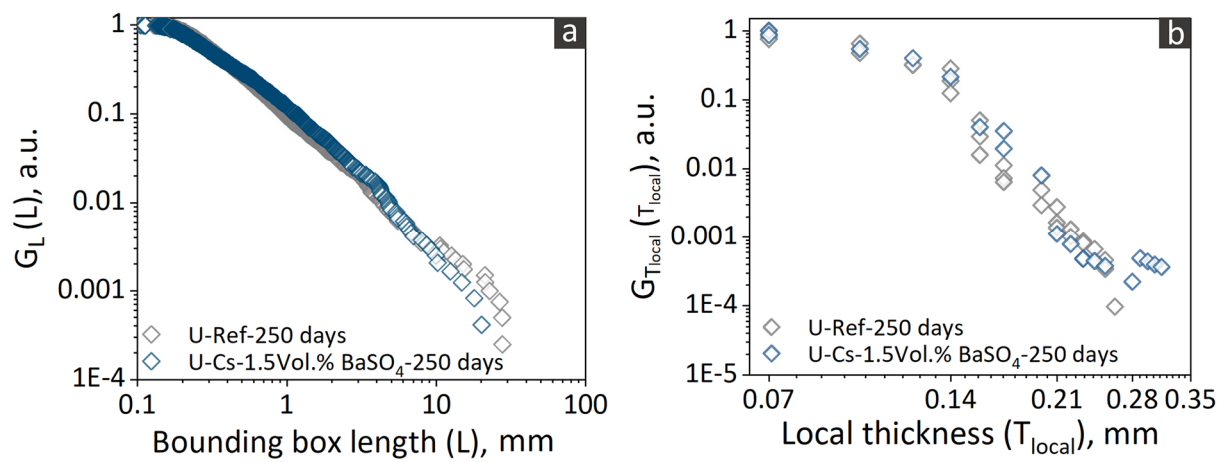


Figure 7.8. (a): complementary cumulative distribution function (cCDF) of the crack bounding box length, L , $G_L(L)$, shown in the form a Zipf's plot, for specimens cast with U aggregates (with and without CsNO₃+BaSO₄), at 250 days. (b): cCDF of the crack local thicknesses, T_{local} , $G_{T_{local}}(T_{local})$, also shown in the form of a Zipf's plot, for the two same specimens as in (a) and also at 250 days.

The elongation, E , versus flatness, F , plots at the first and last (250 days) time points of both the same U-Ref specimen mentioned in Chapter 6 and of the U-Cs-1.5 vol.-% BaSO₄ specimens (Figure 7.9) showed that the presence of both CsNO₃ and of BaSO₄ did not have any kind of significant influence on the crack shape, which remained prevalently that of a thin, curved plate, as observed for all the specimens of any experimental campaign.

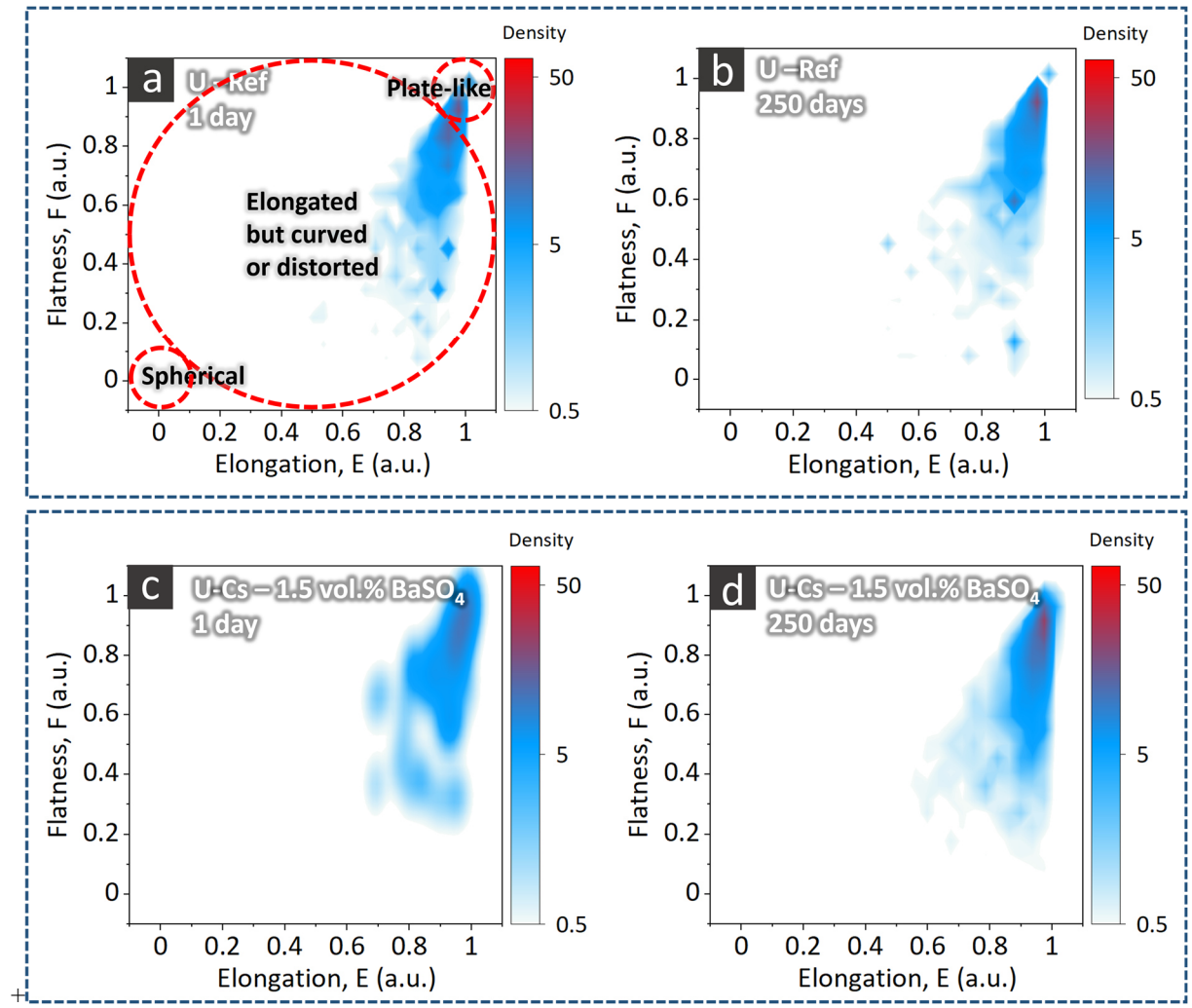


Figure 7.9. Plots of the kernel density estimate (KDE) of the joint probability density function (PDF) of the two shape feature variables, the elongation E and the flatness F , computed from the shape tensor analysis of the segmented total crack network and treated as a bi-variate random variable, $(E; F)$. (a) and (b): U-Ref specimen from the first experimental campaign described in Chapter 6. (c) and (d): U-Cs-1.5 -vol.% BaSO₄ specimen.

The 3D distribution of the first *eigenvector*, \hat{u}_1 , of the shape tensor \mathbf{G} for the same two specimens as for the shape analysis of Figure 7.9 and at the first and last time points as well (Figure 7.10) confirmed that the simultaneous presence of CsNO₃ and BaSO₄ in the mix designed seemed not to have altered the typical crack orientation features systematically observed across the distinct experimental campaigns and for distinct specimen types. For both specimens, at the first time point (i.e., in the presence of only original cracks), a rather uniform and relatively sparse crack orientation distribution could be observed. However, at the last time point, the crack networks of both specimens exhibited a slight tendency for being aligned along the Z-axis. As remarked in the previous Chapters, even a slight preferential crack orientation along the specimen longitudinal direction (the Z-axis), automatically implies that the crack

thickness increase with time contributed more to the specimen dimensional changes in directions orthogonal to that axis than along it, which is exactly what was observed for both specimens (see Figure 6.4 (c) for the U-Ref specimen and Figure 7.3 (b) for the U-Cs-1.5 vol.-% BaSO₄ one).

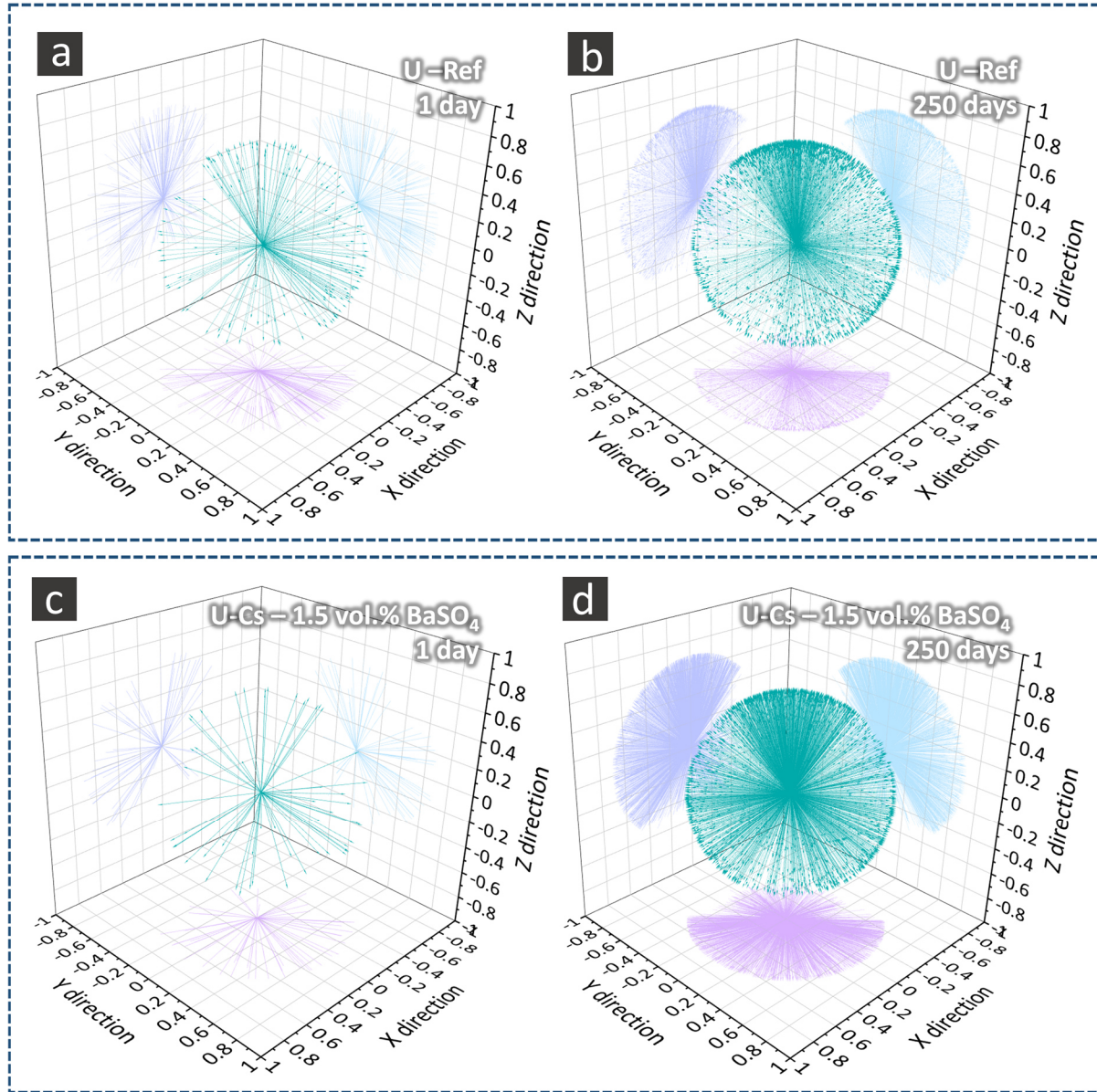


Figure 7.10. Visualization of the crack orientation analysis results. The crack orientation was operatively defined as the direction of the eigenvector \hat{u}_1 associated with the first and largest eigenvalue of the shape tensor \mathbf{G} . The segmented total crack network of a specimen corresponded to a set of \hat{u}_1 's, one for each independent crack (branch of the network). Each of these vectors are here plotted in red, after rescaling their magnitudes by a factor equal to 0.33, to make their projections on the planes of the Cartesian frame of reference more visible. The projections of \hat{u}_1 on the X – Y plane are in violet, those on the X – Z plane are in dark blue and those on the Y – Z plane are in light blue. (a) and (b): U-Ref specimen of the first experimental campaign described in Chapter 6, at 1 and 250 days, respectively. (c) and (d): U-Cs-1.5 vol.-% BaSO₄ specimen, at 1 and 250 days as well, respectively.

7.4. Discussion

The problem of enhancing simultaneously the voxel value contrast between aggregates and the cement paste, aggregates and ASR products and, finally, between products and the cement paste was the one which needed and needs to be addressed in order to achieve the goal of segmenting all the material phases of interest to fully investigate ASR (cracking) at the concrete mesoscale defined in this PhD project. Such goal was finally achieved in this project by searching for a trade-off between enhancing the aggregate-to-cement paste contrast (by BaSO_4 , Chapter 6) and enhancing the aggregate-to-products contrast (by CsNO_3 , Chapter 5) while simultaneously limiting the inevitable reduction in products-to-cement paste contrast, as shown in Figure 7.2. A key detail of the trade-off which was found and which corresponds to optimal concentrations of both CsNO_3 and BaSO_4 needs to be again reminded and strongly remarked: such optimal concentrations of the two distinct contrast agents are valid (1) for the type of concrete mix design used (meaning, mainly, for the aggregate type used) and (2) for the X-ray photon energy range of the performed XT measurements. While the latter parameter may find a broad applicability also for concrete specimens of other mix designs, as long as the specimen size would remain similar, the results shown in Figure 7.2 may very likely not be valid anymore for other mix designs with aggregates having very different X-ray attenuation properties compared with those of the aggregates used in this project. Thus, the key remark concerns the need to find the optimal trade-off specific for the concrete mix design used, although the contrast agents' concentration values used in the presented work may provide already some useful initial guesses for the trade-off search.

No qualitative and quantitative major differences were found between the specimen with the optimal mix design and reference specimens, in terms of whole specimen dimensional changes (Figure 7.3), spatial-temporal patterns of cracking and correlated local deformations (Figure 7.4), chemical and morphological properties of the ASR products (Section E2 of the Appendices), crack size, shape and orientation (Figures 7.7, 7.8 and 7.9, respectively). The major difference, already observed and remarked in Chapter 5, consisted of the faster expansion and ASR cracking for the specimen with the contrast agents. However, they could be essentially ascribed only to the CsNO_3 presence, confirming similar results reported in Chapter 5. Thus, the presence of both CsNO_3 and BaSO_4 seems not to introduce any spurious perturbation of the ASR (cracking), based upon the results reported herein. Instead, such simultaneous use of both contrast agents allowed expanding significantly the ASR (cracking) observational and quantification possibilities by XT.

While the spatial-temporal accumulation patterns of ASR products inside aggregate and cement paste cracks could be characterized qualitatively (i.e., visually) already by using CsNO_3 only (see Chapter 5),

the optimal mix design containing both contrast agents opened and opens up new quantitative characterizations.

With the results of this Chapter, it was possible to confirm what already observed in those reported in Chapter 5: the systematic transport and accumulation of ASR products in the pore space of/surrounded by the cement paste, including cracks, which originated inside aggregates and later propagated into the paste, and air voids. However, the possibility of quantifying their volume fractions also separately for aggregate and paste regions contributed to a major new result: at any time point, the products were observed to be in almost equal amounts both inside aggregates and within the cement paste (see Figure 7.7 (a)). This result confirmed quantitatively what could be observed only qualitatively by rendering in 3D the binary tomograms of products inside aggregates and paste, at multiple time points (see Figure 7.6). What these results suggest is a continuous accumulation of ASR products within the cement paste, leading to their presence in such part of the mesostructure as extensively as inside the aggregates, where products actually originate. Although the presence of products inside pore space of/surrounded by the cement paste is a very well and since decades known ASR (cracking) feature, as remarked in Section 5.4, the XT methodology developed in this PhD project allowed for the first time a truly quantitative and non-destructive assessment of how extensive and at which stages such presence occurred. This result suggests that the ASR products transport investigated and extensively described in Chapter 5 may take place already at very early ASR stages and likely via ASR cracks formed at multiple length scales, including those below the spatial resolution limits of the tomograms acquired in this project. Thus, the need for time-lapse XT at higher spatial resolution, commented about in Section 5.4, acquires even more importance at the light of the results reported in this Chapter.

The volume fraction results reported in Figure 7.7 (a), both for the products and for the cracks, are also relevant for the validation of computational models of ASR cracking, as they provide a quantitative example of how much extensive cracking throughout the cement paste could be, compared with the cracking inside aggregates. Figure 7.7 (a) shows that the volume fraction of the total crack network inside aggregates was larger than the corresponding volume fraction inside the cement paste at any time point and reached a maximum value of 34% at 250 days.

The almost equal partitioning of ASR products volume between aggregates and the cement paste suggests that their transport was rather extensive. The qualitative examples of Chapter 5 (see Figures 5.8, 5.9 and the respective movies mentioned in Section C7) already showed that such transport occurred as well at the length scale of several mm far away from the originating aggregates. This quantitative and qualitative evidence of the products transport calls for a better understanding of the temporal evolution of the viscoelastic properties of the ASR products. As mentioned in Section 5.4, it has been shown that the Ca^{2+} ions uptake by products does occur, with consequent exchange of alkali ions [1], and typically

leads to a stiffening of the products themselves, although the latter has been predominantly observed for laboratory-synthesized products [2]. Since higher stiffness would hinder their transport, it follows to hypothesize that the products transport may prevalently occur before their extensive uptake of Ca^{2+} ions. The latter may happen predominantly or earlier for the products which have reached the paste regions and only much later and much more slowly for products inside the aggregates. Less extensive transport into the paste regions could on the contrary suggest that significant Ca^{2+} diffusion into the aggregates occurred, with consequent products stiffening and transport stopping. The latter process has been extensively shown not to take place, based upon the observation of much lower Ca content for products in inner aggregate regions than in the cement paste [3].

The chemo-mechanical couplings between Ca^{2+} uptake by products in the cement paste regions and their mechanical properties are still missing in most of computational modelling of ASR cracking. The results presented in Chapter 5 and in this Chapter strongly call for taking them more in consideration in future models. Further experimental, multi-scale and multi-disciplinary investigations would still be needed to better resolve, especially in time, the evolution of the products' viscoelastic properties.

7.5. Conclusions

The key conclusions that can be summarized for the experimental campaign presented in this Chapter are the following ones:

- a) an optimal BaSO_4 concentration was found for enhancing the aggregate-to-cement paste X-ray attenuation contrast in the presence of CsNO_3 , without decreasing too much the same contrast between the ASR products and the cement paste; such optimal BaSO_4 concentration was found to be 1.5 vol.-% for the types of aggregates used in this project; this may not be as much optimal in the case of specimens with other aggregate types, however, the proposed procedure presented herein could be adapted to find a respective optimal value;
- b) the addition of both contrast agents (BaSO_4 and CsNO_3) to the concrete mix did not affect the natural ASR (cracking) of the specimens, as assessed in terms of morphological and chemical properties of the ASR products, full specimen-scale dimensional changes and overall ASR cracking properties;
- c) it was confirmed that the presence of CsNO_3 only accelerated the ASR kinetics, resulting into slightly higher bulk expansion and higher crack volume fraction values;

- d) the added possibility of distinguishing both cracks and products based upon their location in the mesostructure, i.e., either inside aggregate or outside them, empowered a quantitative analysis that showed that the volume of produced products was equipartitioned between aggregate and cement paste regions, thus providing a quantitative basis to the qualitative observations already reported in Chapter 5 of extensive ASR products extrusion outside of the aggregates.

Bibliography

- [1] F. Rajabipour, E. Giannini, C. Dunant, J. H. Ideker, and M. D. A. Thomas, “Alkali-silica reaction: Current understanding of the reaction mechanisms and the knowledge gaps,” *Cem. Concr. Res.*, vol. 76, pp. 130–146, Jul. 2015, doi: 10.1016/j.cemconres.2015.05.024.
- [2] A. Gholizadeh-Vayghan, F. Rajabipour, M. Khaghani, and M. Hillman, “Characterization of viscoelastic behavior of synthetic alkali–silica reaction gels,” *Cem. Concr. Compos.*, vol. 104, p. 103359, Nov. 2019, doi: 10.1016/j.cemconcomp.2019.103359.
- [3] T. Katayama, “ASR gels and their crystalline phases in concrete - universal products in alkali-silica, alkali-silicate and alkali-carbonate reactions,” in: *Proceedings of the 14th International Conference on the Alkali-Aggregate Reaction, Austin (Texas), USA, 2013.* .

Chapter 8. Conclusions and outlook

8.1. Synthesis of key achievements

This project aimed at addressing, by the use of XT, the following, very specific research needs to fill particular knowledge gaps about ASR (cracking) in concrete (see also section 1.1 for details):

1. the lack of truly time-lapse experimental data about the spatial-temporal evolution of (I) ASR products, (II) local deformation and (III) cracks at the concrete mesoscale;
2. the corresponding lack of data and thus of understanding about the possible couplings between the spatial-temporal evolutions of ASR products and cracks.

Some important points are mentioned in Section 1.1 about these two knowledge gaps and, especially, about their relevance:

- i. a lot of information about ASR cracking features at the mesoscale has been already available in the literature since years or even decades, thanks to the use of traditional optical and electron microscopy techniques. One example mentioned in Chapter 5 is the presence of ASR products inside the pore space outside of aggregates, surrounded by the cement paste, e.g., in the air voids. However, all of these data are not truly time-lapse because of the intrinsic destructiveness of the respective specimen preparation, with consequent limitations, both in terms of data representativeness (features at distinct time points observed and characterized from distinct specimens) and of data availability (very limited datasets given the need to have a distinct specimen for the investigation at each distinct time point);
- ii. physics- and chemistry-based computational models of ASR (cracking) at the mesoscale require, for their development and validation, experimental data about the spatial-temporal evolutions mentioned above. Such models are needed in order to realize, by following upscaling approaches, macroscopic scale models with predictive capabilities about deformations and damage of structural engineering interest. On the contrary, most of the ASR damage modeling work of the past has been performed at the macroscopic scale and based upon phenomenological and/or *ad hoc* approaches. These past approaches cannot be generalized and need to be substituted by true material-science based models;
- iii. XT had been so far adopted to investigate ASR only in limited cases, mainly not in time-lapse mode and mainly for simplified model systems and in a qualitative manner [1–4]. Standard XT, i.e., attenuation contrast-based, had several limitations, in particular it did not allow to distinguish the ASR products from the other material phases.

This PhD project has achieved several key results on two distinct levels, which are condensed and highlighted here in the following, while some of their longer-term impact on ASR (cracking) research as

well as some of their limitations are summarized and discussed in the next Section. The first level at which key results/advancements were obtained concerns the XT methodology for the characterization of the three ASR features mentioned above: products, induced deformations and cracks.

One key methodology advancement consisted in developing and validating experimental protocols to overcome the intrinsic limitations of standard XT in detecting ASR products or aggregates or both of them. The use of CsNO_3 and of BaSO_4 , added to the concrete mix design for the purpose of contrast enhancement in distinct image types, was proposed already independently of this PhD project. The use of CsNO_3 was proposed for enhancing the electron back-scattering contrast between products and the other material phases in SEM micrographs [5]. The use of BaSO_4 was proposed to enhance the X-ray attenuation contrast between aggregates and the cement paste in tomograms [6]. The new advancement brought by this PhD project consisted (1) in optimizing their applications for XT of ASR-affected specimens and (2) assessing, for the first time and extensively, which kind of perturbations they could cause to the ASR (cracking) itself. The only significant perturbation which was observed came from the ASR kinetics acceleration caused by CsNO_3 addition, while no effects were noticed for BaSO_4 . Thus, this PhD work could show that (1) the needed X-ray contrast enhancement between products and aggregates (Chapters 5 and 7), products and cement paste (Chapters 5 and 7) and aggregates and cement paste (Chapters 6 and 7) can be achieved and (2) it seems to alter only one ASR feature (the time scale), which can be taken into account in advance in the experiment design, leaving all the other features essentially unperturbed.

The extensive search for and assessment of any eventual spurious impact of either contrast agents on ASR (cracking) was possible only because in this project the mentioned XT methodology was actually developed in parallel to the implementation of a comprehensive and customized 3D image analysis workflow. The latter allows achieving many targets at once, among which the quantitative characterization of several crack features (overall volume fraction, statistics of crack length, thickness, orientation and shape). Without such quantitative crack features characterizations, it would have not been possible to assess whether and how much the use of one or of both contrast agents affected the ASR cracking.

The development and implementation of such workflow addressed, among others, the need of comparing, first of all qualitatively, e.g., by visual comparisons, the distinct tomograms acquired at the successive time points. This was achieved by an image registration methodology that was developed and implemented for this specific purpose. Addressing this need led to the possibility of quantifying and monitoring both the global and the localized deformations associated with the ASR cracking (point (1) of the knowledge gaps list mentioned above), via the global affine and non-affine registration steps described in Section 3.3. The implemented registration workflow methodology also had an outcome not envisaged at the beginning of the project: the simplification and robustness increase of the crack and products segmentation based upon the (direct or inverse) temporal subtraction (TS) approach. This outcome can be also considered as a key, new methodological advancement contributed by this PhD project and Thesis: although the TS approach to segmentation of objects in tomograms was not new, its application to the segmentation of cracks and the quantitative assessment of its robustness and limitations (Chapter 5 and the respective Appendix C) can be considered as a novelty.

The developed crack segmentation and features analysis workflow enabled the quantitative comparison of ASR crack networks developed in specimens with distinct mix designs and, more importantly, very different boundary conditions (free expansion under laboratory-scale ASR acceleration *versus* free expansion under outside field exposure, Chapter 4). The availability of digitized models of parts of the

crack networks (those parts included in the tomograms) and the computation of statistics of a few geometrical and dimensional features significantly extended and complemented more traditional ways of comparing the ASR behavior of distinct concrete specimens, e.g., by longitudinal expansion measurement. Because of this complementary analysis, several similarities were found between the ASR cracking in the laboratory-accelerated specimens and in the field-exposed ones, even for specimens not cast with the same exact aggregate type. Thus, it was possible to assess, more in depth than what traditionally possible, how much the cracking observed in the specimens accelerated with the chosen protocol was representative of real-world ASR cracking. The methodological advancement was in this case two-fold: on the one side, it could be concluded that the acceleration protocol led to rather representative ASR crack networks, for the chosen mix designs; on the other side, it was chosen how the 3D image analysis workflow helped and could help better comparing such complex 3D objects as crack networks, which is an essential step towards more reliable comparability of ASR (cracking) degrees across specimens and specimens' types.

Overall, this Thesis contributes to expand significantly the applicability of standard, i.e., attenuation contrast-based, XT to ASR (damage) research. This overall result was extensively confirmed by the outcomes of the distinct experimental campaigns performed in this project. Such outcomes belong to the second level of the project's achievements, i.e., filling up the mesoscale ASR (cracking) knowledge gaps themselves. In the following, a short-list of observations and ASR (cracking) features is provided, focusing on those which were significantly new, decisively enabled by the developed XT methodology, and with a strong potential of contributing not only to fill the mentioned knowledge gaps but also to advance the computational modeling of ASR cracking at the mesoscale.

- a) Along with the crack propagation, for the first time in a time-lapse manner, the extrusion of ASR products into the cement paste was visualized.
- b) The extrusion suggests that, at early stages, the ASR products may be a low-viscosity gel which can move away from the originating aggregate and can accumulate later elsewhere as a stiffer phase upon uptake of Ca. Progressive accumulation of ASR products within cracks and air voids surrounded by the cement paste, with following Ca uptake from them, thus their stiffening, was observed in this work. Successive extrusions of low-viscosity, lower Ca-content products being added in time were also observed.
- c) The accumulation of ASR products in the air voids and cracks in the cement paste or in the ITZ of aggregates surrounding those from which the products originated was observed systematically. Significant portions of the ASR-generated crack volume remained at later ages empty of ASR products.
- d) The volume fraction of the cracks increases monotonically over time and a significant amount of cracking in the cement paste is observed;
- e) The ASR products were systematically observed to be present extensively outside of aggregates.

8.2. Outlook

As mentioned in the previous Section, the developed XT methodology significantly extended the range of ASR cracking features, at the mesoscale, which could be observed (some for the first time) and quantified/monitored in time, contributing to fill up some of the knowledge gaps mentioned in Section 1.1. The immediate relevance of some of the key results for the mesoscale computational modeling of ASR cracking was also mentioned in the previous Section. More in general, one way some knowledge gaps will be filled by the work presented in this Thesis is by the planned, open sharing of the actual tomographic datasets themselves (both the raw tomographic time series and the outputs of the 3D image analysis workflow). Sharing such datasets will further support both the development and the validation of more realistic computational models in several ways.

One direct contribution to such support comes from the binary tomograms of the aggregates and of the parts of the pore space surrounded by the cement paste and not being cracks, e.g., air voids and porous patches. The binary tomograms of the latter pore types were not directly used in this project. However, they can be easily obtained from the raw tomograms and from the binary tomograms which were used in this project (cracks, products and cement paste). The aggregate and pore space binary tomograms provide realistic geometrical models of the computational domains, at the mesoscale. The creation of computational meshes from such binary tomograms could complement algorithmically generated concrete mesostructure [7], the latter being easier and cheaper to generate but still not reproducing all the mesoscale geometrical and spatial distribution features.

Furthermore, as mentioned in the previous Section, the quantified volume fractions of ASR products and cracks, both outside and inside aggregates, provide key data for the validation of the modeling results.

Finally, the local displacement vector field, $\vec{u}_{N-AFF}(\vec{x}, t)$, obtained from the output of the non-rigid registration could be used for the validation of modeling results as well as an initial (in time) condition for simulations. In the latter case, the corresponding strain tensor field would need to be computed as well as a stress tensor field. The latter could be computed from the strain tensor field once assigning to each mesoscale material phase (visco-)elastic properties obtained, e.g., from direct measurements on aggregates and on model mortar matrix specimens.

As mentioned already in the previous Section, the correspondingly developed and validated mesoscale models could then be used, together with upscaling approaches, for developing macroscale ones [8], essential for predicting at the macroscopic scale the ASR-induced deformations and the mechanical properties degradation and for structural design-optimization tasks.

Another potential area of significant impact of the work presented in this PhD Thesis concerns a completely different spatial-temporal scale range than the one investigated in this project. Indeed, the overall experimental and 3D image analysis methodology could be directly exploited for investigating the formation of ASR products and the associated cracking at (a) much earlier ASR stages (thus at much smaller length scales than those covered in this project) and (b) with much higher temporal resolution. This would be an extension of the work performed in this project which could shed light on some of the chemo-mechanical coupled phenomena at the basis of the early ASR cracking, an area where many basic knowledge gaps still remain, as described in Section 1.1.

In this project, the time-lapse 3D information about mesoscale ASR cracking obtained was first of its kind. However, it was not possible in any datasets to obtain a complete picture about, e.g., the full propagation of a single ASR crack, because sometimes the tomograms were acquired at points when the crack propagation had already advanced significantly. Decreasing the sampling time, i.e., performing XT more frequently would not only be extremely resource-intensive but, at the mesoscale, it may not necessarily help because of the unpredictability of the evolution of the crack network, covering it already significant volumetric ranges, thus with the possibility of branching and other complex evolutionary modalities.

Time-lapse XT tomography with much higher temporal and spatial resolution, e.g., performed with synchrotron radiation, applied to very small (mm scale) and very simplified systems may allow to track down the evolution of analogues of first ASR cracks related with early stage ASR product formation. What is meant here as a small and simplified model system could be, e.g., a small portion of a single aggregate surrounded some thin layers of cement paste, fixed inside a customized cell heated up at 40°C and filled up with the same alkaline solution used in this PhD project. Such model system could then be tomographed for 2-3 consecutive days, starting from about 14-21 days (based upon the experience made in this project, including the acquired SEM datasets) since the start of the immersion of the model system within the cell. Such an investigation with the described model system could be performed also with a laboratory-scale tomograph, by adopting local tomography approaches, although, obviously, at significantly smaller spatial and temporal resolutions.

The XT measurement and analysis methodology proposed in this Thesis would find immediate applicability to the tomographic time-series obtained from such measurements. More challenging would be the design and implementation of a model system, inside which the first ASR product formation and the related ASR cracking, at a scale smaller than tens of μm , could be representative of those occurring in much larger model systems or even actual laboratory-scale specimens, where the chemical environment of the pore solution and the mechanical boundary conditions would be more complicated.

Despite the mentioned challenges in extending at the microscopic scale and early ASR stages the type of investigation performed in this project at the mesoscale, the developed methodology proposed in this Thesis will contribute to enable new investigations about basic chemo-mechanical processes involved in ASR (cracking), thus to partly fill the knowledge gaps which still do not allow to develop and support, at the real-world scale, preventive and interventional engineering measures/approaches to reduce ASR's negative impact on the world-wide concrete infrastructure.

Bibliography

- [1] Marinoni N, Voltolini M, Mancini L, Vignola P, Pagani A and Pavese A 2009 An investigation of mortars affected by alkali-silica reaction by X-ray synchrotron microtomography: A preliminary study *J. Mater. Sci.* **44** 5815–23
- [2] Marinoni N, Voltolini M, Broekmans M A T M, Mancini L, Monteiro P J M, Rotiroti N, Ferrari E and Bernasconi A 2015 A combined synchrotron radiation micro computed tomography and micro X-ray diffraction study on deleterious alkali-silica reaction *J. Mater. Sci.* **50** 7985–97
- [3] Kim T, Alnahhal M F, Nguyen Q D, Panchmatia P, Hajimohammadi A and Castel A 2019 Initial sequence for alkali-silica reaction: Transport barrier and spatial distribution of reaction products *Cem. Concr. Compos.* **104** 103378
- [4] Yang S, Cui H and Poon C S 2018 Assessment of in-situ alkali-silica reaction (ASR) development of glass aggregate concrete prepared with dry-mix and conventional wet-mix methods by X-ray computed micro-tomography *Cem. Concr. Compos.* **90** 266–76
- [5] Leemann A and Münch B 2019 The addition of caesium to concrete with alkali-silica reaction: Implications on product identification and recognition of the reaction sequence *Cem. Concr. Res.* **120** 27–35
- [6] Carrara P, Kruse R, Bentz D P, Lunardelli M, Leusmann T, Varady P A and De Lorenzis L 2018 Improved mesoscale segmentation of concrete from 3D X-ray images using contrast enhancers *Cem. Concr. Compos.* **93** 30–42
- [7] Holla V, Vu G, Timothy J J, Diewald F, Gehlen C and Meschke G 2021 Computational Generation of Virtual Concrete Mesostructures *Mater. 2021, Vol. 14, Page 3782* **14** 3782
- [8] Gallyamov E R, Cuba Ramos A I, Corrado M, Rezakhani R and Molinari J F 2020 Multi-scale modelling of concrete structures affected by alkali-silica reaction: Coupling the mesoscopic damage evolution and the macroscopic concrete deterioration *Int. J. Solids Struct.* **207** 262–78

Appendix A

Dedicated supporting information for chapter 3

A1. Materials characterizations

A1.1 ASR-reactive aggregates: chemical and mineralogical characterizations

Table TA1 provides the chemical composition of both the U and the P aggregates, as obtained by X-ray fluorescence (XRF) analysis, which was performed by an external, analytics company, on sintered powder according to the standard DIN EN 196-2 [1]. The aggregate powder was obtained by grinding one kg of aggregates in the sieve size range 0 – 4 mm with a planetary ball-milling machine. The size range < 63 µm was used for analysis. Table TA1 shows that silica (SiO₂) is the predominant chemical species of both aggregate types. The other minerals had similar content in both types of aggregates.

Mineralogical information about each aggregate type was obtained by powder X-ray diffraction (PXRD) analysis, which was performed by Dr. Frank Winnefeld of the Empa's Concrete and Asphalt Laboratory using Cu-K α X-rays and a Bragg-Brentano geometrical configuration. The scattering angle (2θ) range covered by the X-ray detector was [7°; 70°]. The measurement was performed with a Malvern Panalytical X'Pert Pro MPD diffractometer. The analysis of the PXRD pattern indicated that both the P and the U aggregates consist of about 50 mass-% quartz. The feldspars (with Na content > K content) in these aggregates differs slightly, 25 mass-% in U and 16 mass-% in P. Carbonates (with more calcite than dolomite) are about 14 mass-% in U and 20 mass-% in P aggregates. The remaining mineral phases are layer silicates such as clinochlore, muscovite and biotite. Nevertheless, the differences in the mineralogical compositions are almost negligible.

Table TA1. Chemical composition obtained by X-ray fluorescence (XRF) analysis performed according to the DIN EN 196-2:2013 standard. ♥ LOI: Loss on Ignition. † TC: Total Carbon content, measured according to the ISO 10694 standard [2]. ‡ TOC: Total Organic Carbon content. ♠ TIC: Total Inorganic Carbon content, obtained as the difference between the TC and TOC values. ♦ CO₂: total CO₂ content obtained from the TC value.

Chemical species	Uri ("U")	Praz ("P")
	Content (mass-%)	Content (mass-%)
SiO ₂	64.3	67.98
Al ₂ O ₃	8.79	7.16
CaO	8.66	8.86
Fe ₂ O ₃	2.02	1.38
MgO	2.06	1.91
K ₂ O	2.1	2.17
TiO ₂	0.346	0.201
Cr ₂ O ₃	0.006	0.005
MnO	0.048	0.03
P ₂ O ₅	0.079	0.064
Na ₂ O	1.65	1.37
SO ₃	0.39	0.09
LOI♥	9.45	8.68
Total	99.89	99.9
TC†	2.14	2.15
TOC‡	0.18	0.05
TIC♠	1.96	2.1
CO ₂ ♦	7.18	7.7

Regardless of relatively similar compositions, there are major differences between the size distributions of the minerals (i.e., texture) of the two aggregates (Figure A1). The P aggregates (Figure A1 (a) and (c)) are characterized by elongated, highly undulated quartz grains presumably created by tectonic processes [3]. They are metamorphic rocks (granitic) of alluvial origin, mainly consisting of gneiss and quartzite. A bimodal grain size distribution was observed, consisting of a fine grained matrix of micro-crystalline quartz and muscovite and coarse, highly undulated quartz grains (Figure A1 (c)). The matrix consisted of a mixture of mica and micro-crystallized quartz. The U aggregates, on the other hand, were identified as sedimentary aggregates consisting of several equi-sized quartz grains (Figure A1 (b)).

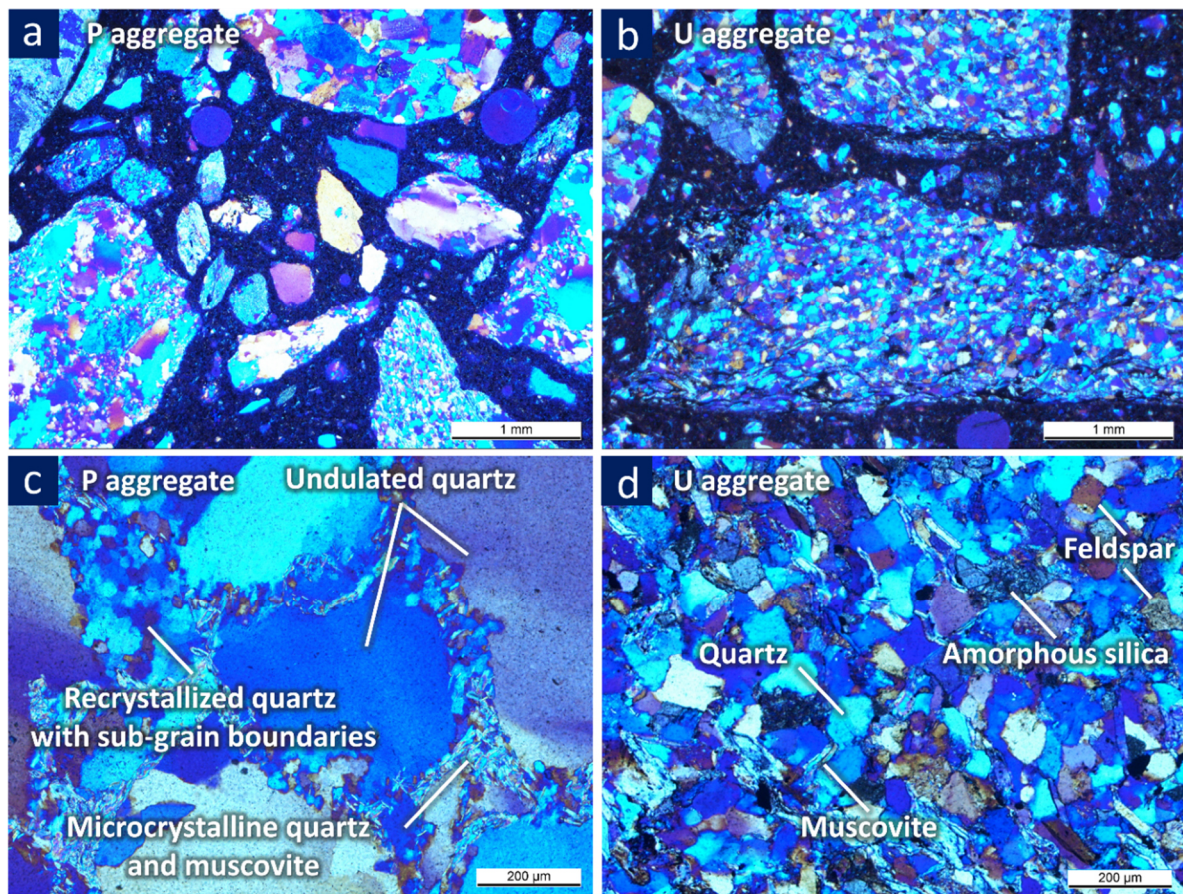


Figure A1. Examples of mineral textures of both P and U aggregate types, the main ones used in this PhD project, characterized by optical microscopy performed with cross-polarized light (CP-OM): (a) and (c) thin-section image from specimens containing P aggregates, at lower and higher magnifications, respectively; (b) and (d) the same for U aggregates.

A2. Time-lapse X-ray tomography (XT)

A2.1 Experimental settings for the measurements on the $25 \times 25 \times 100 \text{ mm}^3$ specimens

The second X-ray source of the same tomograph described in Section 3.2 is a Hamamatsu L10711-02 (160 KeV source). It is a micro-focus source as well but based upon the direct transmission geometrical configuration. In the tomograph used within this project, this source was equipped with a LaB₆ filament and a 1 μm -thick W target deposited on a 500 nm-thick diamond support, which allows achieving sub-micron focal spot size at certain operational voltage and current values. The emitted X-ray beam geometry is a cone one also in this case but with an opening angle up to 140°, compared with the 30° of the other source. The X-ray source voltage and current were set to about 100 kV and 50 μA , respectively. With such settings, the focal spot size f_s is estimated to be approximately 2 μm , based upon the manufacturer's technical specifications. The source-to-specimen distance, d_{ss} was about 33 mm and the source-to-detector distance, d_{sd} , was about 166 mm, leading to a geometrical magnification $M \cong 5$. The resulting effective voxel size for the tomograms was $\tilde{p} = p/M \cong 25 \mu\text{m}$. As already done for the tomograms of the larger specimens, Eqs. (2.16) and (2.17) were used to estimate the effective spatial resolution only when considering geometrical factors. The result of the estimate using the formula for R_{eff} in Eq. (2.16) is 25.45 μm . Thus, a ball park estimate of the upper bound of the actual effective spatial resolution is 30 μm .

For these, smaller specimens, XT was conducted as well only for their middle region along the specimen longitudinal direction, covering a volume of interest (VOI) of $25 \times 25 \times 30 \text{ mm}^3$. The rest of the XT settings was the same as for the measurements performed on the larger specimens, described in Section 3.2.

A2.2. Time-lapse X-ray micro-tomography

Specimen holder used for time-lapse X-ray tomography. During the time-lapse tomography measurements, the ASR accelerated specimens had to be manually fixed onto an holder (Figure A2 and A3) at each measuring time point (usually every 2-4 weeks) over the course of a measurement campaign (between 250 and 404 days, depending on the campaign). For a truly time-lapse investigation, the same volume of interest (VOI) should be tomographed at each time point t_i , $\forall i = 1, \dots, N_t$, as it was done at the first (reference) time point t_0 . Some of the tomographs, like the one used in this project, provide a specimen holder mounted on a stack of two linear stages controlled by piezoelectric actuators. Corresponding software allows setting at t_i the holder's reference position (the one at t_0) as well as the same values for the other settings of the tomograph. These other settings include the spatial positions of the source and detector, the X-ray beam's properties, the X-ray detector's parameters and tomographic acquisitions settings, e.g., number of radiographs acquired.

Despite the possibility of using at each measurement time the same exact settings, the linear stages, on which the specimen holder sits and located on top of the rotation stage (Figure A2 (d)), have limited accuracy in achieving a wanted position, at the scale of tens of μm for the tomograph used in this project. This implies that, by successive displacements, the errors in position cumulates with time, increasing the inaccuracy in repositioning the holder at the same nominal location, unless the calibration of such stages is always repeated between two successive measurements, which was not possible for this project.

In addition, the specimens are typically fixed to the holder manually and human errors in doing so are another source of inaccuracy. Furthermore, in the case of specimens undergoing ASR-induced expansion, the VOI can also slightly shift. Overall, these factors contribute to specimen misalignment in between t_0 and t_i , $\forall i = 1, \dots, N_t$, which needs to be corrected for by rigid-body registration and which makes the registration itself more challenging (the larger and more complex the misalignment, the more ill-posed the registration problem).

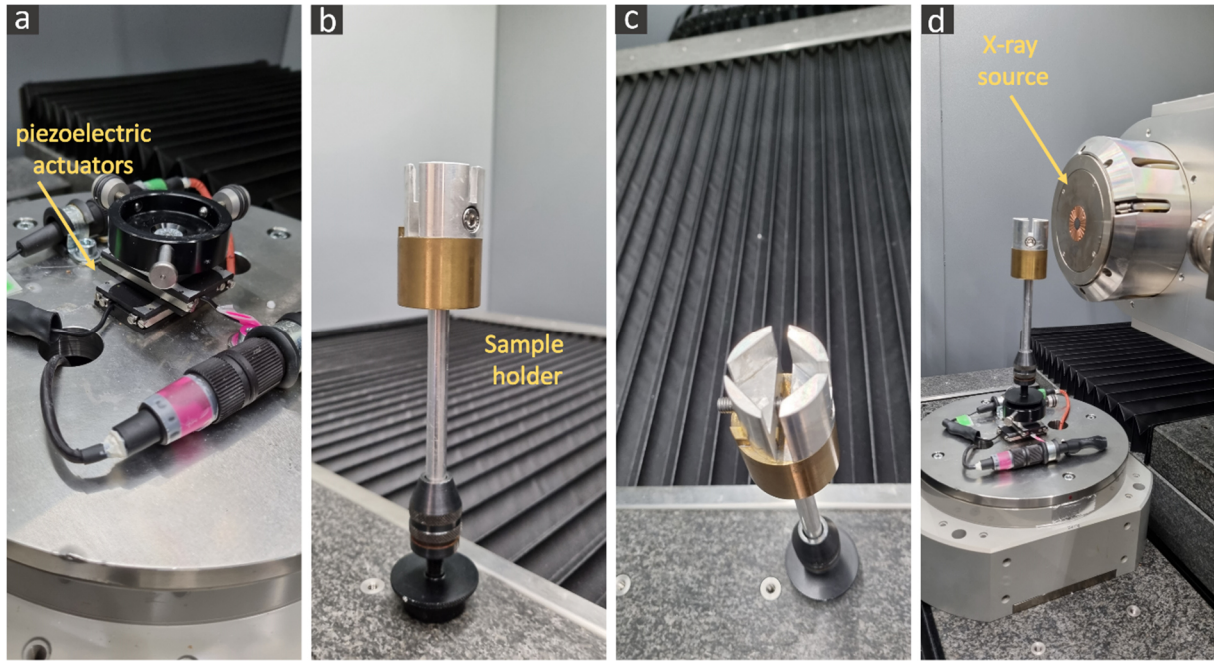


Figure A2. (a) Piezoelectric actuators attached to the rotating stage of the tomograph, (b) and (c) sample holder and (d) sample holder fixed to the piezoelectric actuators, called "holding set-up1" throughout the thesis.

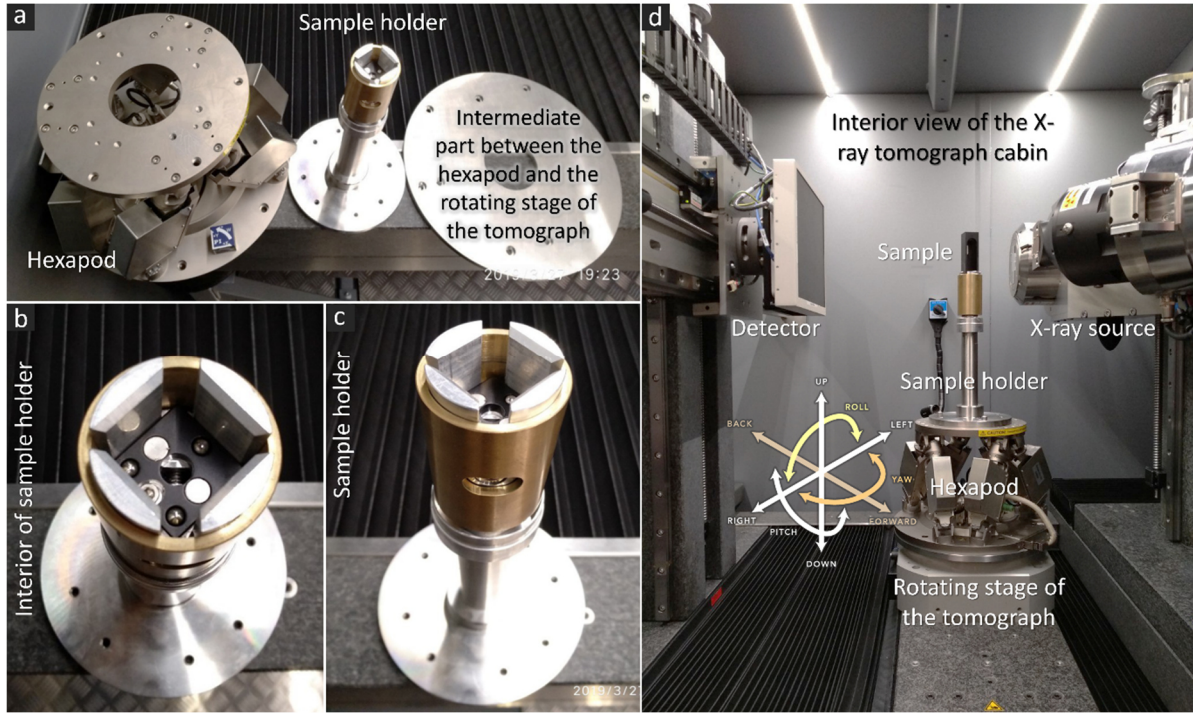


Figure A3. (a) Hexapod and sample holder to fix the specimens during tomography, called "holding set-up2" throughout the thesis, (b) and (c) photos of sample holder from different angles, and (d) tomography setting.

To address already experimentally the specimen repositioning issue, in some experimental campaigns, the stack of two linear stages was replaced by an hexapod (Figure A3 (a) and (d)), a moving platform with 6 degrees of freedom (DOF, shown in Figure A3 (d)), and a semi-automated repositioning workflow was developed and programmed into Python scripts to maximize and speed up restoring the specimen position at each time point t_i with respect to the reference position at t_0 .

The 6 DOF (3 translations and 3 Euler rotations) of an hexapod allow 3D rigid body positioning of the specimen, compared with the planar translation allowed by the stack of two linear stages. The hexapod used was an H-824 6-Axis (by PI, Karlsruhe, Germany) with a repeatability accuracy of $\pm 0.1 \mu\text{m} / \pm 2 \mu\text{rad}$ operated by a C-887.52x hexapod motion controller (by PI, Karlsruhe, Germany). The problem of a single 3D repositioning was broken down into several, iterative simpler steps of specimen's 2D projection-based position recovery.

As an example of such iterative workflow, consider first the simple case of the specimen being, at t_i , tilted around its Z-axis and translated along its Z-axis. Such rotation + translation misalignment thus consists overall by a rigid body movement on a plane parallel to the detector's plane. As a consequence, the specimen's radiograph, acquired at $\theta_z = 0^\circ$, reveals immediately the misalignment and its type (Figure A4 (b)) when compared with the radiograph acquired at the same angle at t_0 (assuming that the specimen was ideally straight, as shown in Figure A4 (a)). The rotation and translation parameters, with respect to the reference position, can then be computed by a rigid body registration (Figure A4 (c)). See Section 2.4.5.2 for the definition of a rigid body registration. By moving the specimen according to these rotation and translation but in inverse direction/with the opposite rotation angle, the specimen can be repositioned as in the reference case at t_0 .

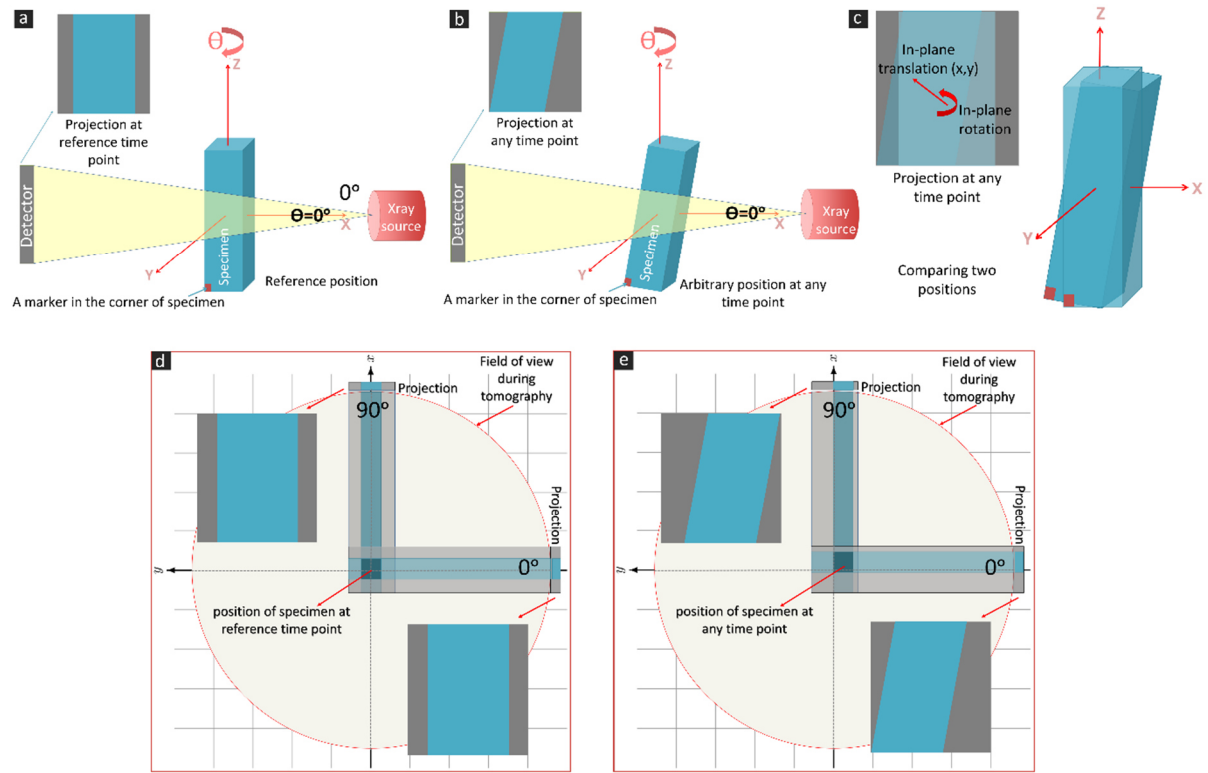


Figure A4. Schematic illustration of fundamentals of projection and repositioning of the specimen to its reference position, at any given time point: (a) a projection at reference time point; (b) a projection at any time point, where the sample could be dispositioned due to human or other sources of error; (c) comparing the specimen position and one of their corresponding projections at a certain angle; (d) and (e) how two 2D projections at 0° and 90° can tell (reconstruct) the position of specimen in 3D, at reference or any other given time point, respectively.

In general, the actual specimen misalignment does not happen solely on a plane parallel to the detector's. A general misalignment may consist of movements according to all the six DOF (three translational and three rotational). In order to correct for a general misalignment, the iterative workflow consisted of following steps and was supported by the following components.

First of all, the holder was optimally designed to grip the specimen tightly. Furthermore, each specimen was marked since t_0 in one corner (see Figure A4 (a)-(c)), in order to place it on the holder always, approximately, at the same position (e.g., with the marker always pointing towards the detector). These experimental measures already helped in reducing the misalignment. What still remained of it was corrected for by the iterative workflow. The latter, in a general case, consisted first of all of acquiring two radiographs, one at $\theta = 0^\circ$, the other at $\theta = 90^\circ$, at t_0 (Figure A4 (d) and (e)). At any following time point t_i , $\forall i = 1, \dots, N_t$, the iterative procedure consisted of the following steps (see Figure A5).

The first step aimed at finding the optimal orientation of the specimen around the vertical, Z-axis ($\theta_z = \theta$), where optimal refers to the minimization of the misalignment.

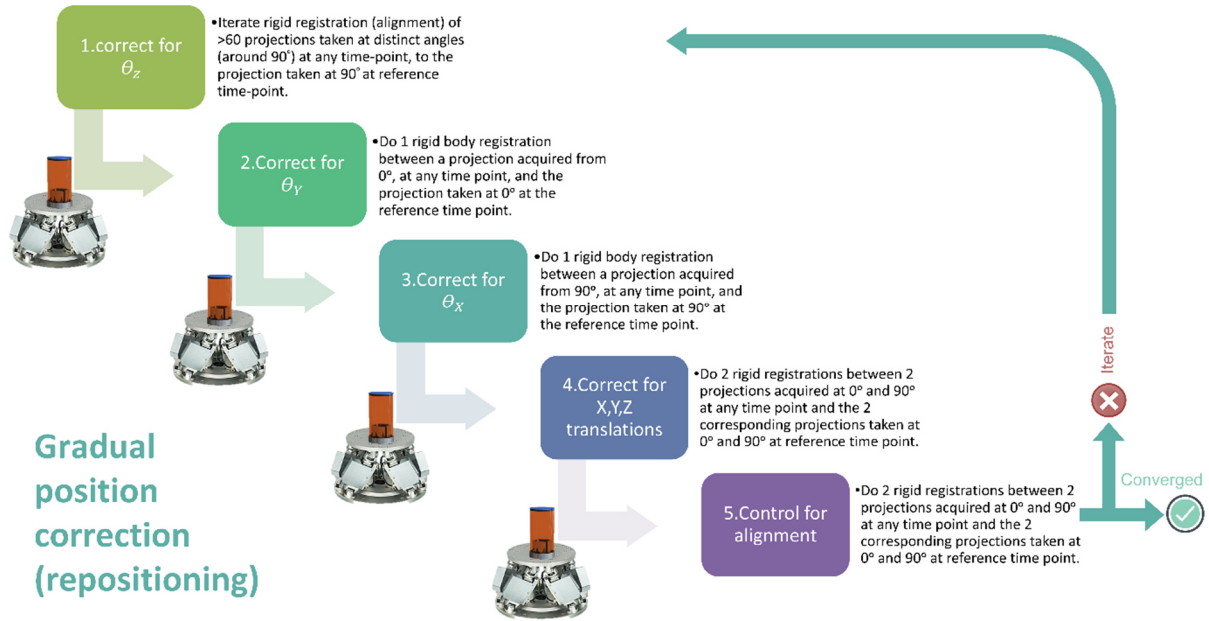


Figure A5. Workflow of the gradual sample repositioning.

Several radiographs were acquired around $\theta = 90^\circ$, for instance between 70° - 110° with increasing steps of 0.5° . Each of them was then registered according to the rigid body model against the radiograph at 90° acquired at t_0 .

The SimpleElastix Python script to perform such set of rigid body registration was the following:

```
import SimpleITK as sitk

import pims

elastixImageFilter = sitk.SimpleElastix()

outdir = "C:/ElasticFiles/WinPython-64bit-3.4.4.2/ResultFolder/Hex-21.18.2019/90-(1,1,1,1,1)"

elastixImageFilter.LogToConsoleOn()

elastixImageFilter.LogToFileOn()

elastixImageFilter.SetOutputDirectory(outdir)

elastixImageFilter.SetFixedImage(sitk.ReadImage("C:/ElasticFiles/WinPython-64bit-3.4.4.2/Result-Folder/Hex-21.18.2019/90-(1,1,1,1,1)/90.tiff"))

vector = sitk.VectorOfImage()
```

```
population = pims.ImageSequence("C:/ElasticFiles/WinPython-64bit-3.4.4.2/ResultFolder/Hex-21.18.2019/ref/Proj/*.tif")
```

```
for i in population:
```

```
    elastixImageFilter.SetMovingImage(sitk.GetImageFromArray(i))
```

```
    parameterMapVector = sitk.VectorOfParameterMap()
```

```
    parameterMapVector.append(elastixImageFilter.ReadParameterFile("C:/ElasticFiles/WinPython-64bit-3.4.4.2/ResultFolder/Hex-Pivot290/Parameters_Rigid_2D.txt"))
```

```
    elastixImageFilter.SetParameterMap(parameterMapVector)
```

```
    elastixImageFilter.Execute()
```

```
    # Transform label map using the deformation field from above
```

```
    elastixImageFilter.GetTransformParameterMap()
```

```
    vector.push_back(elastixImageFilter.GetResultImage())
```

The SimpleElastix parameter file for such rigid body registration, containing the settings for the registration algorithm itself, was the following:

```
(FixedInternalImagePixelType "float")
```

```
(FixedImageDimension 2)
```

```
(MovingInternalImagePixelType "float")
```

```
(MovingImageDimension 2)
```

```
(Registration "MultiResolutionRegistration")
```

```
(Interpolator "LinearInterpolator")
```

```
(ResampleInterpolator "FinalBSplineInterpolator")
```

```
(Resampler "DefaultResampler")
```

```
(FixedImagePyramid "FixedRecursiveImagePyramid")
```

```
(MovingImagePyramid "MovingRecursiveImagePyramid")
```

```
(Optimizer "AdaptiveStochasticGradientDescent")
```

```
(Transform "EulerTransform")
```

(Metric "AdvancedMattesMutualInformation")

(AutomaticScalesEstimation "true")

(AutomaticTransformInitialization "true")

(HowToCombineTransforms "Compose")

(NumberOfHistogramBins 32)

(ErodeMask "false")

(NumberOfResolutions 10)

(MaximumNumberOfIterations 1000)

(NumberOfSpatialSamples 10000)

(ImageSampler "RandomCoordinate")

(NewSamplesEveryIteration "true")

(BSplineInterpolationOrder 1)

(FinalBSplineInterpolationOrder 3)

(DefaultPixelValue 0)

(WriteResultImage "false")

(ResultImagePixelType "float")

(ResultImageFormat "tif")

The results from each registration were saved into a log-file, which was then used to search which one of them achieved the best match with the radiograph at $\theta = 90^\circ$ acquired at t_0 . The best match was looked for by considering the rigid body registration's objective function, which was also in this case based upon the mutual information of the two registered images. The registration whose final value of such objective function was the smallest (due to the definition of the mutual information metric [4], that we used in our registrations, described in section 3.3 of chapter 3) meant the registration was the most successful. However, we multiplied this value to a minus (-minima) to achieve a positive value, just to make the plots more intuitive to the user (Figure A6). This result was assumed to indicate that the radiograph at t_i and at the θ value between 70° and 110° which was the most successfully registered to the radiograph at 90° at t_0 indicated which $\theta_Z = \theta$ was the closest to the original orientation of the specimen at t_0 . An example of the registration's objective function value as a function of the specimen's $\theta_Z = \theta$ value is shown in Figure A6. This example indicates that, among all the radiographs acquired between about 70° and 110° , the one at 89° could be the most successfully registered. Therefore, by rotating the

specimen around the Z-axis of -1° (i.e., $\theta_Z = -1^\circ$, where the minus sign indicates a backward rotation), the specimen misalignment around such axis could be minimized.

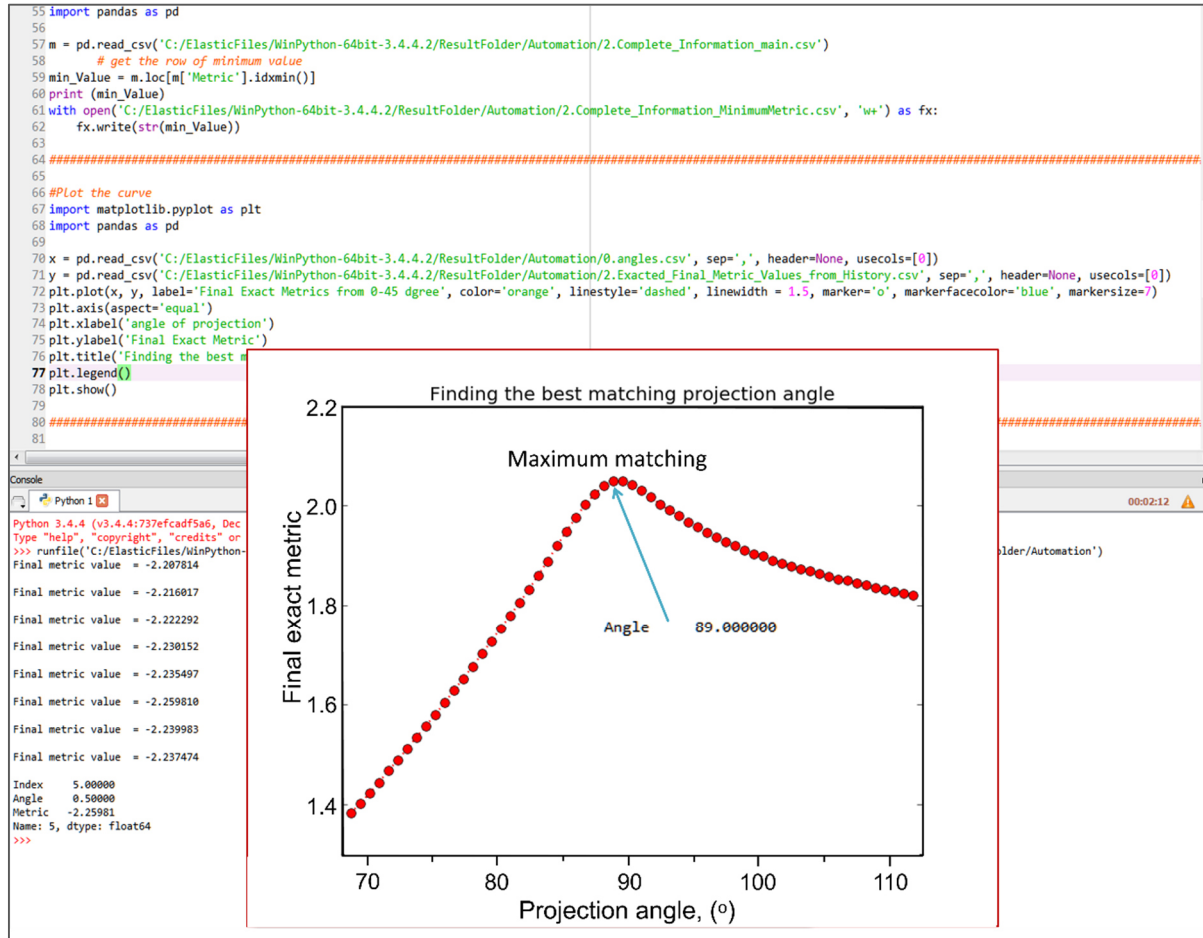


Figure A6. The code developed for automatizing of sample repositioning workflow.

The Python script to perform the search of the global maximum of the registration object function versus the θ value of the radiograph at time t_i was the following:

#Extract final metric value

filename = "C:/ElasticFiles/WinPython-64bit-3.4.4.2/ResultFolder/Hex-21.18.2019/90-(1,1,1,1,1)/1.thetaZ/1.history.log"

with open('C:/ElasticFiles/WinPython-64bit-3.4.4.2/ResultFolder/Hex-21.18.2019/90-(1,1,1,1,1)/1.thetaZ/2.Exacted_Final_Metric_Values_from_History.csv', 'w+') as fx:

with open(fileName) as inputFile:

```
data = inputFile.readlines()

inputFile.close()

for line in data:

    if "Final metric value =" in line:

        fx.write(line [22::]) #the [22::] skips 22 places (eaiter space or character which in this case is
equal to "Final_metric_value__=_", so that I can save only numbers!!)

        print(line)

#####Combine
csv files of the angles and extracted final metric values

import pandas as pd

df1 = pd.read_csv('C:/ElasticFiles/WinPython-64bit-3.4.4.2/ResultFolder/Hex-21.18.2019/90-
(1,1,1,1,1,1)/1.thetaZ/0.angles.csv', header=None)

df2 = pd.read_csv('C:/ElasticFiles/WinPython-64bit-3.4.4.2/ResultFolder/Hex-21.18.2019/90-
(1,1,1,1,1,1)/1.thetaZ/2.Exacted_Final_Metric_Values_from_History.csv', header=None)

combined_csv = pd.concat([df1 , df2], axis=1)

combined_csv.to_csv( "2.Complete_Information.csv", index=True)

#####

#Rename the index names in the CSV file

import csv

import os

inputFileName = "C:/ElasticFiles/WinPython-64bit-3.4.4.2/ResultFolder/Hex-21.18.2019/90-
(1,1,1,1,1,1)/1.thetaZ/2.Complete_Information.csv"

outputFileName = os.path.splitext(inputFileName)[0] + "_main.csv"

with open(inputFileName, newline=") as inFile, open(outputFileName, 'w', newline=") as outfile:

    r = csv.reader(inFile)

    w = csv.writer(outfile)

    next(r, 0) # skip the first row from the reader, the old header

    # write new header
```

```
w.writerow(['Index', 'Angle', 'Metric'])

# copy the rest

for row in r:

    w.writerow(row)

#####

#Extract minimum metric value

import pandas as pd

m      =      pd.read_csv('C:/ElasticFiles/WinPython-64bit-3.4.4.2/ResultFolder/Hex-21.18.2019/90-
(1,1,1,1,1)/1.thetaZ/2.Complete_Information_main.csv')

# get the row of minimum value

min_Value = m.loc[m['Metric'].idxmin()]

print (min_Value)

with      open('C:/ElasticFiles/WinPython-64bit-3.4.4.2/ResultFolder/Hex-21.18.2019/90-
(1,1,1,1,1)/1.thetaZ/2.Complete_Information_MinimumMetric.csv', 'w+') as fx:

    fx.write(str(min_Value))

#####

#Plot the curve

import matplotlib.pyplot as plt

import pandas as pd

x      =      pd.read_csv('C:/ElasticFiles/WinPython-64bit-3.4.4.2/ResultFolder/Hex-21.18.2019/90-
(1,1,1,1,1)/1.thetaZ/0.angles.csv', sep=',', header=None, usecols=[0])

y      =      pd.read_csv('C:/ElasticFiles/WinPython-64bit-3.4.4.2/ResultFolder/Hex-21.18.2019/90-
(1,1,1,1,1)/1.thetaZ/2.Exacted_Final_Metric_Values_from_History.csv', sep=',', header=None,
usecols=[0])

plt.plot(x, -y, label='Final Exact Metrics from 0-45 dgree', color='red', linestyle='dotted', linewidth =
1.5, marker='o', markerfacecolor='red', markersize=7)

plt.axis(aspect='equal')

plt.xlabel('angle of projection')

plt.ylabel('Final Exact Metric')
```

```
plt.title('Finding the best matching projection angle')
```

```
plt.legend()
```

```
plt.show()
```

The same exact procedure for the first step of the iterative workflow was repeated for a broader range of $\theta_z = \theta$ values ($90^\circ \pm 90^\circ$), in order to verify whether the global optimal matching was achieved instead of a local one. The resulting values for the registration objective function are shown in Figure A7, similarly as in Figure A6. It can be observed that the maximum value found in the range $90^\circ \pm 20^\circ$ was indeed a global maximum.

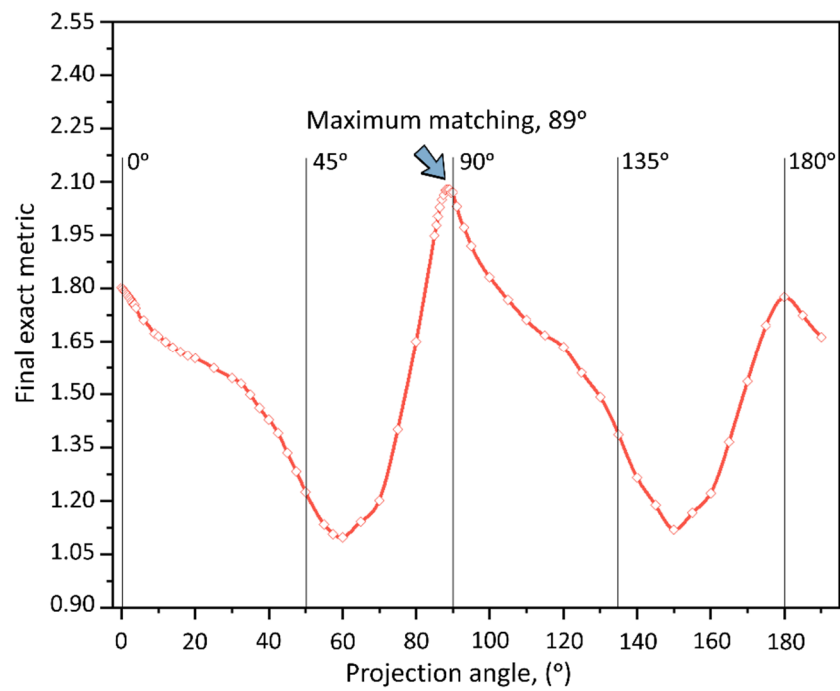


Figure A7. Another example of finding maximum θ_z amongst a larger range of projection angles.

The second step of the workflow was dedicated to correct for the misalignment around the Y-axis, represented by the angle of rotation θ_Y . In this step, only one rigid body registration was performed between the radiograph acquired at t_i at 0° (stage rotation angle around Z-axis) and the radiograph acquired at t_0 at 0° as well. As a result of the latter rigid registration, the specimen was rotated via the hexapod around the Y-axis of a certain value for θ_Y to minimize such type of rotational misalignment. A similar procedure was performed at the third step to correct for the misalignment around the X-axis by rotation of an optimal θ_X angle, except for the fact that the radiographs of the specimen at 90° were used.

The forth step in the workflow was dedicated to correct for translational misalignments, along the X-, Y- and Z-axis. For this purpose, two rigid body registrations were performed between two radiographs acquired at 0° and 90° at t_i and the two corresponding radiographs, taken at 0° and 90° , acquired at t_0 .

In this case, only the translation information from output of the rigid body registration was considered for simultaneously correcting for all the three misalignments, along the X-, Y- and Z-axes. The horizontal translation suggested by the registration of the radiographs at 0° allowed minimizing the misalignment along the X-axis, the one from the registration of the radiographs at 90° allowed minimizing the misalignment along the Y-axis and, finally, the Z-displacement suggested by any of the two registrations was used to minimize the misalignment along the Z-axis. Finally, to control the correctness of the repositioning, the procedure at step four was repeated. If the specimen was properly repositioned with respect to its position at t_0 , the process was dismissed otherwise all the steps had to be repeated from the beginning.

The overall workflow was performed, before each tomography measurement at t_i , $\forall i = 1, \dots N_t$, only with two iterations, to reposition the specimen as close as possible to its t_0 position.

A3. Image processing and analysis of the time-lapse X-ray tomograms

A3.1 Image enhancement

The following values of the parameters of the "Anisotropic diffusion" plugin were used for noise filtering each tomogram, independently of the specimen and time point:

- "Anisotropic diffusion method" = "Tschumperle - Deriche"
- "Max # of complete iterations" = 20
- "Time step" = 10
- "Smoothing number per iteration" = 2
- "A1 diffusion limiter" = 0.5
- "A2 diffusion limiter" = 0.7
- "A3 diffusion limiter" = 0.9
- "Edge threshold" = 5
- "Constrain in case of overflow" = true

A3.2 Correction for specimen misalignments

The parameter text file for the 3D rigid body registration included the following settings:

(FixedInternalImagePixelFormat "short")

(FixedImageDimension 3)

(MovingInternalImagePixelFormat "short")

(MovingImageDimension 3)

(Registration "MultiResolutionRegistration")

(Interpolator "LinearInterpolator")

(ResampleInterpolator "FinalBSplineInterpolator")
(Resampler "DefaultResampler")
(FixedImagePyramid "FixedRecursiveImagePyramid")
(MovingImagePyramid "MovingRecursiveImagePyramid")
(Optimizer "AdaptiveStochasticGradientDescent")
(Transform "EulerTransform")
(Metric "AdvancedMattesMutualInformation")
(AutomaticScalesEstimation "true")
(AutomaticTransformInitialization "true")
(HowToCombineTransforms "Compose")
(NumberOfHistogramBins 64)
(ErodeMask "false")
(NumberOfResolutions 5)
(MaximumNumberOfIterations 1000)
(NumberOfSpatialSamples 20000)
(ImageSampler "RandomCoordinate")
(NewSamplesEveryIteration "true")
(BSplineInterpolationOrder 1)
(FinalBSplineInterpolationOrder 3)
(DefaultPixelValue 0)
(WriteResultImage "true")
(ResultImagePixelFormat "short")
(ResultImageFormat "mhd")

The following is the content of the Python script used to perform the 3D rigid body registration using the SimpleElastix libraries:

```

import SimpleITK as sitk

elastixImageFilter = sitk.SimpleElastix()

elastixImageFilter.LogToConsoleOn()

outDir = "path to output directory"

fixImage = "path to fixed/reference image"

movImage = "path to moving/deformed image"

elastixImageFilter.SetOutputDirectory(outDir)

elastixImageFilter.SetFixedImage(sitk.ReadImage(fixImage))

elastixImageFilter.SetMovingImage(sitk.ReadImage(movImage))

parameterMapVector = sitk.VectorOfParameterMap()

parameterMapVector.append(elastixImageFilter.ReadParameterFile("path to text parameter file"))

elastixImageFilter.SetOutputDirectory(outDir)

elastixImageFilter.Execute()

elastixImageFilter.GetParameterMap()

transformParameterMap = elastixImageFilter.GetTransformParameterMap()

transformix = sitk.SimpleTransformix()

transformix.SetOutputDirectory(outDir)

transformix.LogToConsoleOn()

transformix.SetTransformParameterMap(elastixImageFilter.GetTransformParameterMap())

transformix.ComputeDeformationFieldOn()

transformix.SetMovingImage(sitk.ReadImage(movImage))

transformix.Execute()

transformix.GetComputeDeformationField()

resultFloatImage2 = transformix.GetResultImage()

sitk.WriteImage(resultFloatImage2, 'Result_image.tif')

elastixImageFilter.SetOutputDirectory(outDir)

```

A3.3 Empty crack segmentation

3D, global affine registration. The algorithmic implementation was done also in this case by using the Python API of SimpleElastix. The parameter text file for the 3D affine registration included the following settings:

(FixedInternalImagePixelType "short")

(FixedImageDimension 3)

(MovingInternalImagePixelType "short")

(MovingImageDimension 3)

(Registration "MultiResolutionRegistration")

(Interpolator "BSplineInterpolator")

(ResampleInterpolator "FinalBSplineInterpolator")

(Resampler "DefaultResampler")

(FixedImagePyramid "FixedRecursiveImagePyramid")

(MovingImagePyramid "MovingRecursiveImagePyramid")

(Optimizer "AdaptiveStochasticGradientDescent")

(Transform "AffineTransform")

(Metric "AdvancedMattesMutualInformation")

(AutomaticScalesEstimation "true")

(AutomaticTransformInitialization "true")

(HowToCombineTransforms "Compose")

(NumberOfHistogramBins 64)

(ErodeMask "false")

(NumberOfResolutions 4)

(MaximumNumberOfIterations 1000)

(NumberOfSpatialSamples 20000)

(ImageSampler "RandomCoordinate")

(NewSamplesEveryIteration "true")

(BSplineInterpolationOrder 1)

(FinalBSplineInterpolationOrder 3)

(DefaultPixelValue 0)

(WriteResultImage "false")

(ResultImagePixelFormat "short")

(ResultImageFormat "mhd")

The Python script used to perform the 3D global affine registration was the following:

```
import SimpleITK as sitk

elastixImageFilter = sitk.SimpleElastix()

elastixImageFilter.LogToConsoleOn()

outDir = "path to output directory"

fixImage = "path to fixed/reference image"

movImage = "path to moving/deformed image"

elastixImageFilter.SetOutputDirectory(outDir)

elastixImageFilter.SetFixedImage(sitk.ReadImage(fixImage))

elastixImageFilter.SetMovingImage(sitk.ReadImage(movImage))

parameterMapVector = sitk.VectorOfParameterMap()

parameterMapVector.append(elastixImageFilter.ReadParameterFile("path to text parameter file"))

elastixImageFilter.SetParameterMap(parameterMapVector)

elastixImageFilter.SetOutputDirectory(outDir)

elastixImageFilter.Execute()

elastixImageFilter.GetParameterMap()

transformParameterMap = elastixImageFilter.GetTransformParameterMap()

transformix = sitk.SimpleTransformix()

transformix.SetOutputDirectory(outDir)
```

```

transformix.LogToConsoleOn()

transformix.SetTransformParameterMap(elastixImageFilter.GetTransformParameterMap())

transformix.ComputeDeformationFieldOn()

transformix.ComputeDeterminantOfSpatialJacobianOn()

transformix.SetMovingImage(sitk.ReadImage(movImage))

transformix.Execute()

transformix.GetComputeDeformationField()

transformix.GetComputeDeterminantOfSpatialJacobian()

resultFloatImage2 = transformix.GetResultImage()

sitk.WriteImage(resultFloatImage2, 'Result_U0-3_Local_Affine_1-17.tif')

elastixImageFilter.SetOutputDirectory(outDir)

```

3D, non-affine registration. The Python API of SimpleElastix was used to program also this type of registration. The parameter text file for the 3D affine registration included the following settings:

```

(FixedImageDimension 3)

(MovingImageDimension 3)

(FixedInternalImagePixelType "short")

(MovingInternalImagePixelType "short")

(Registration "MultiMetricMultiResolutionRegistration")

(FixedImagePyramid "FixedSmoothingImagePyramid")

(MovingImagePyramid "MovingSmoothingImagePyramid")

(Interpolator "BSplineInterpolator")

(Metric "AdvancedMattesMutualInformation" "TransformBendingEnergyPenalty" "TransformRigidityPenalty")

(Metric0Weight 1)

(Metric1Weight 0.1)

(Metric2Weight 0.4)

```

(UseLinearityCondition "true")

(UseJacobianPreconditioning "false")

(Optimizer "AdaptiveStochasticGradientDescent")

(ResampleInterpolator "FinalBSplineInterpolator")

(Resampler "DefaultResampler")

(Transform "BSplineTransform")

(ErodeMask "false")

(AutomaticScalesEstimation "true")

(AutomaticTransformInitialization "true")

(AutomaticTransformInitializationMethod "Origins")

(NumberOfResolutions 3)

(FinalGridSpacingInVoxels 64.0)

(MaximumNumberOfIterations 700)

(HowToCombineTransforms "Compose")

(UseFastAndLowMemoryVersion "true")

(NumberOfHistogramBins 64)

(FixedKernelBSplineOrder 3)

(MovingKernelBSplineOrder 3)

(ImageSampler "RandomCoordinate")

(UseRandomSampleRegion "false")

(NumberOfSpatialSamples 10000)

(NewSamplesEveryIteration "true")

(CheckNumberOfSamples "true")

(MaximumNumberOfSamplingAttempts 5)

(BSplineInterpolationOrder 1)

(FinalBSplineInterpolationOrder 3)

(DefaultPixelValue 0)
(SP_a 2000.0)
(SP_A 50.0)
(SP_alpha 0.6)
(GetJacobian "false")
(WriteTransformParametersEachIteration "false")
(WriteResultImage "true")
(CompressResultImage "false")
(WriteResultImageAfterEachResolution "false")
(ShowExactMetricValue "false")
(ResultImagePixelType "short")
(ResultImageFormat "mhd")

The Python script for such 3D non-affine registration was the following:

```
import SimpleITK as sitk

elastixImageFilter = sitk.SimpleElastix()

elastixImageFilter.LogToConsoleOn()

outDir = "path to output directory"

fixImage = "path to fixed/reference image"

movImage = "path to moving/deformed image"

elastixImageFilter.SetOutputDirectory(outDir)

elastixImageFilter.SetFixedImage(sitk.ReadImage(fixImage))

elastixImageFilter.SetMovingImage(sitk.ReadImage(movImage))

parameterMapVector = sitk.VectorOfParameterMap()

parameterMapVector.append(elastixImageFilter.ReadParameterFile("path to text parameter file"))

elastixImageFilter.SetParameterMap(parameterMapVector)
```

```
elastixImageFilter.SetOutputDirectory(outDir)

elastixImageFilter.Execute()

elastixImageFilter.GetParameterMap()

transformParameterMap = elastixImageFilter.GetTransformParameterMap()

transformix = sitk.SimpleTransformix()

transformix.SetOutputDirectory(outDir)

transformix.LogToConsoleOn()

transformix.SetTransformParameterMap(elastixImageFilter.GetTransformParameterMap())

transformix.ComputeDeformationFieldOn()

transformix.ComputeSpatialJacobianOn()

transformix.ComputeDeterminantOfSpatialJacobianOn()

transformix.SetMovingImage(sitk.ReadImage(movImage))

transformix.Execute()

transformix.GetComputeDeformationField()

transformix.GetComputeSpatialJacobian()

transformix.GetComputeDeterminantOfSpatialJacobian()

resultFloatImage2 = transformix.GetResultImage()

sitk.WriteImage(resultFloatImage2, 'Result_U0-3_BS_1-16.tif')

elastixImageFilter.SetOutputDirectory(outDir)
```

Empty crack segmentation: Remarks and segmentation results validation.

The chosen and implemented empty ASR crack segmentation workflow has both advantages and disadvantages compared with any other workflow not relying on non-rigid registration followed by subtraction. The tomogram $\{\tilde{I}(\vec{x}_j, t_i)\}_{j=1, \dots, N}$, $\forall i = 1, \dots, N_t$, output after the B-spline-based registration, does not contain any more the same exact cracks as in the tomogram after rigid-body registration, $\{I_{RB}(\vec{x}_j, t_i)\}_{j=1, \dots, N}$, $\forall i = 1, \dots, N_t$. That is an intrinsic consequence of the non-rigid registration itself. The implemented TS workflow cannot return exactly the same results, especially the orientation of the cracks, as any other crack segmentation workflow using as input only $\{I_{RB}(\vec{x}_j, t_i)\}_{j=1, \dots, N}$, $\forall i = 1, \dots, N_t$. However, this limitation does not necessarily imply that this workflow produces less reliable

results. A segmentation workflow, which uses $\{I_{RB}(\vec{x}_j, t_i)\}_{j=1,\dots,N}$ as the only data and information source for segmentation can also perform worse due, e.g., to image noise and partial volume effects. Since any segmentation approach has a limited degree of reliability, which is, by itself, difficult to assess because a ground truth segmentation result is not available [5], what is important is to understand the differences in errors made by distinct segmentation approaches.

To assess such differences, a test analysis was performed to understand the advantages and disadvantages of the TS-based segmentation of empty cracks. For such analysis, we implemented the crack segmentation workflow based upon the BTH (already used only for segmenting the ASR-pre-existing cracks in the tomogram at t_0 , see Section 3.3, *sssteep* (III)) for segmenting both ASR-induced and pre-existing cracks in a tomogram at t_i , $\{I_{RB}(\vec{x}_j, t_i)\}_{j=1,\dots,N}$. Such alternative segmentation workflow was considered as a benchmark, since it uses as information for the segmentation only the voxel values of the tomogram to be segmented. The latter is a typical feature of the most frequently used segmentation algorithms/workflows. The results of crack segmentation based on the BTH-based approach were then compared with the segmentation results obtained with the TS-based one. There are two important features associated with the quality of the crack segmentation: the volume fraction of segmented cracks (empty crack volume *per* unit volume of tomogram); second, their shape/orientation. Therefore, the comparisons were carried out under two distinct conditions to evaluate both features: (1) segmenting the cracks using both methods applied to exactly the same (non-affinely registered) tomogram; (2) segmenting the cracks by applying the BTH approach to the non-registered tomogram (at time t_i) and using the TS approach for the same tomogram but after non-affine registration. Using the first test allows to quantify the volume fraction of the segmented crack in the exact same tomogram using both techniques. The second test is useful both for evaluating the volume fraction of the segmented cracks and their overall shape/orientation change (due to the non-affine registration).

Figure A8 shows two distinct examples of the segmentation results for a specimen cast with U aggregates and with Cs, at the end of the experimental campaign described in Chapter 5 (250 days). Such results concern the first evaluation procedure. It is observed in such figure that the TS technique resulted in a more accurate segmentation, especially in the case of finer cracks, compared to the one obtained by the BTH-based technique. The TS-based approach led to a relative increase of 25 ± 1.5 % in the estimated empty crack volume fraction, compared with the estimate obtained by the BTH-based approach. This means a remarkable improvement of the segmentation results because, as shown in the two examples of Figure A8, the BTH-based approach systematically missed some crack regions. Furthermore, the overall TS-based segmentation was carried out faster and was easier to implement. The human intervention in the TS segmentation is also less than the one of the BTH.

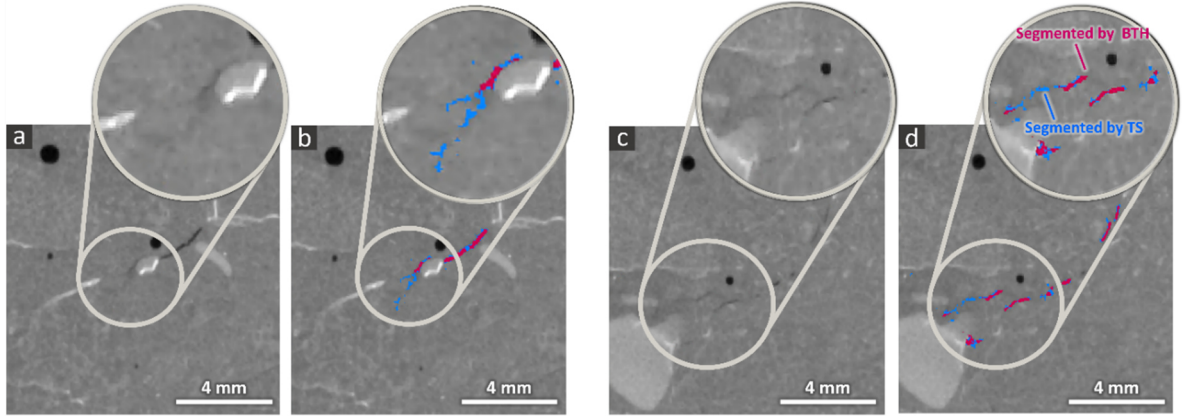


Figure A8. Two distinct examples of segmentation results from two different regions of a U specimen cast with additional Cs for ASR products labeling. The non-affinely registered tomogram at 250 days of such specimen was used. The results were obtained by the BTH-based and by the TS-based approaches, respectively. (a) and (c): two slices from two distinct regions of the tomogram, with, highlighted in the zoom-in insets, some cracks. (b) and (d): comparison of the binary tomograms of the empty cracks obtained with the two distinct approaches. For each region, each binary tomogram is superimposed on top of the non-affinely registered tomogram. The binary tomogram obtained by the TS -based approach is colored in blue, whereas the one obtained by the BTH-based approach is colored in pink.

Figure A9 shows some results for some small volumes of interest (VOIs) of the tomogram of the same U specimen cast with Cs as for Figure A8 and at 250 days. The implemented TS approach segmented crack volumes which were displaced compared with those produced by the reference segmentation based upon the BTH approach, the latter using only $\{I_{RB}(\vec{x}_j, t_i)\}_{j=1, \dots, N}$. However, no significant changes in orientation, shape and sizes were observed. This suggests that the mapping vector field $\vec{x}' = \vec{T}_{N-AFF}(\vec{x})$ represented by the B-spline expansion acted locally, in the crack region, mainly as a translation vector. The translation was typically at the scale of a few voxels. The volume of the segmented cracks, in the chosen VOIs, showed only a subtle difference of $0.7 \pm 0.05 \%$ when obtained by the TS-based approach rather than the BTH-based one.

Such degree of translation in the segmented cracks, compared with where they were actually located, did not have significant negative impact on the analysis. That is because the analysis targets in this project did not require determining quantitatively the absolute positions of the crack regions. On the contrary, the targets included both tracking qualitatively the crack network's spatial-temporal evolution and quantifying some of their features, such as size, volume, shape and orientation. However, the TS workflow may not be useful in applications where the exact spatial position of the cracks needs to be preserved and retrieved.

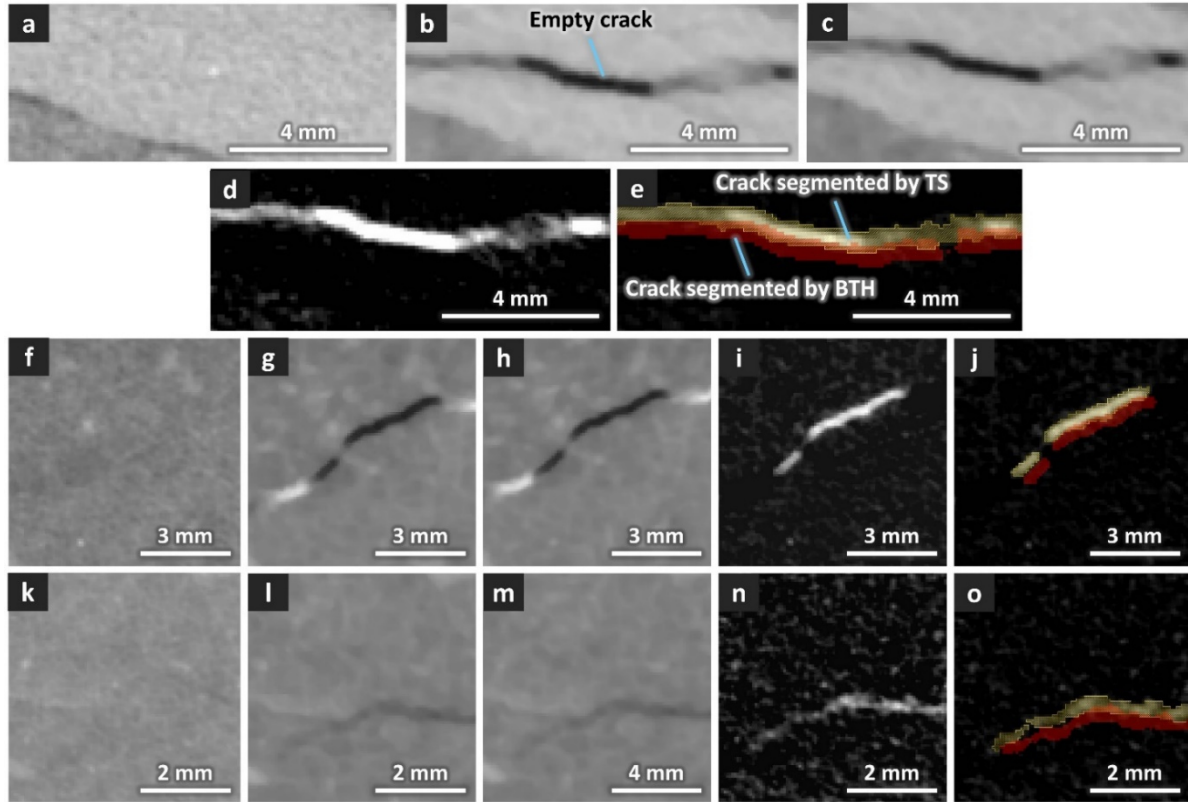


Figure A9. Evaluation of the effects of non-affine registration on the shape and orientation of ASR-induced cracks, in 3 small volumes of interest (VOIs) of a U specimen cast with Cs to label the ASR products and at 250 days. Only one slice from each VOI is shown. (a) One VOI in the reference tomogram, at $t_0 = 1$ day. (b) Same VOI as in (a) but from the rigidly registered tomogram at 250 days. (c) Same VOI as in (a) but from the deformed tomogram at 250 days, obtained after the rigid, affine and non-affine registrations, respectively. (d) Same VOI as in (a) but from the difference tomogram which is the result of subtracting the tomogram shown in (c) from the one in (a), as needed for the TS-based empty crack segmentation. (e) Superimposed results of the crack segmentation over the image in (d). The binary tomogram shown in semi-transparent yellow corresponds to the result of the TS segmentation (thresholding from (d)). The binary tomogram in red shows the results obtained with the BTH-based approach applied directly to the non-registered tomogram shown in (b). The third (insets (f) to (j)) and fourth (insets (k) to (o)) rows present two other examples from other VOIs, with the same order as specified for the first example of insets (a) to (e).

The reason why the shape and size of the cracks segmented by the TS-based workflow were approximately preserved, despite the overall tomogram containing them was deformed, lies, on three intrinsic features of the type of non-rigid registration used (affine + non-affine based on a B-spline expansion):

1. the assumption of "image intensity conservation" (also termed "optical flow equation" [6], see Section 2.4.5.2), i.e., that a portion (i.e., voxel) of the object gets moved as a consequence of the deformation but keeps its image (voxel) value at the two time points (Figure A10); written in equations this means that $I(\vec{T}_{real}(\vec{x}_j), t_i) = I(\vec{x}_j, t_0)$ (see also Eq. (2.19), where $\vec{T}_{real}(\vec{x})$ is the actual mapping vector field which the registration algorithm tries to approximate as accurately as possible;
2. the chosen image similarity metric, whose optimization drives the search for the optimal approximation of $\vec{T}_{real}(\vec{x})$, depends only upon the statistics of voxel values and not on other features of the tomograms;
3. since the ASR cracks exist in the tomogram at t_i but not at t_0 , the regions containing them not only contribute to violate the assumption at point Nr. 1, impairing locally the registration itself, but there is also no possible realization of $\vec{T}(\vec{x})$ which could make their local deformation contribute to increase the image similarity metric; thus, it is as if the registration workflow could not properly deform locally such regions because it lacks the information for doing so. Figure A11 shows, by a very simplified toy case study, this fact. It reports the results of the same crack segmentation procedure based on the TS approach applied to the case where the only difference between the reference image (Figure A11 (a)) and the deformed one (Figure A11 (b)) is a new feature appearing only in the latter and being like a thin dark stripe, simulating an empty crack. No other difference exist between the reference and the deformed images, i.e., no kind of deformation at all. Instead, just a part of the reference image, in the form of a thin rectangular stripe, has been zeroed. It can be observed that the affine + non-affine registration chain preserves all the features common in both the reference and the deformed image. In addition, it perfectly adds the new feature of the deformed image to the registration result, without deforming it at all. This suggests that the mentioned two steps of registration cannot identify any local deformation of the deformed image which could increase the local matching of the registration result with the reference image. Therefore, such feature is exactly reproduced into the resulting, registered image without being modified (Figure A11 (c));
4. the B-spline expansion representation of each vector component of $\vec{T}_{real}(\vec{x})$ can extend (i.e., copy) to the crack regions the same expression determined as optimal for its nearest neighbouring regions, leading to a $\vec{T}(\vec{x})$ which locally is just constant (pure translation) across a crack region. A mapping vector field locally across the crack regions acts as a constant translation which preserves size, orientation and shape.

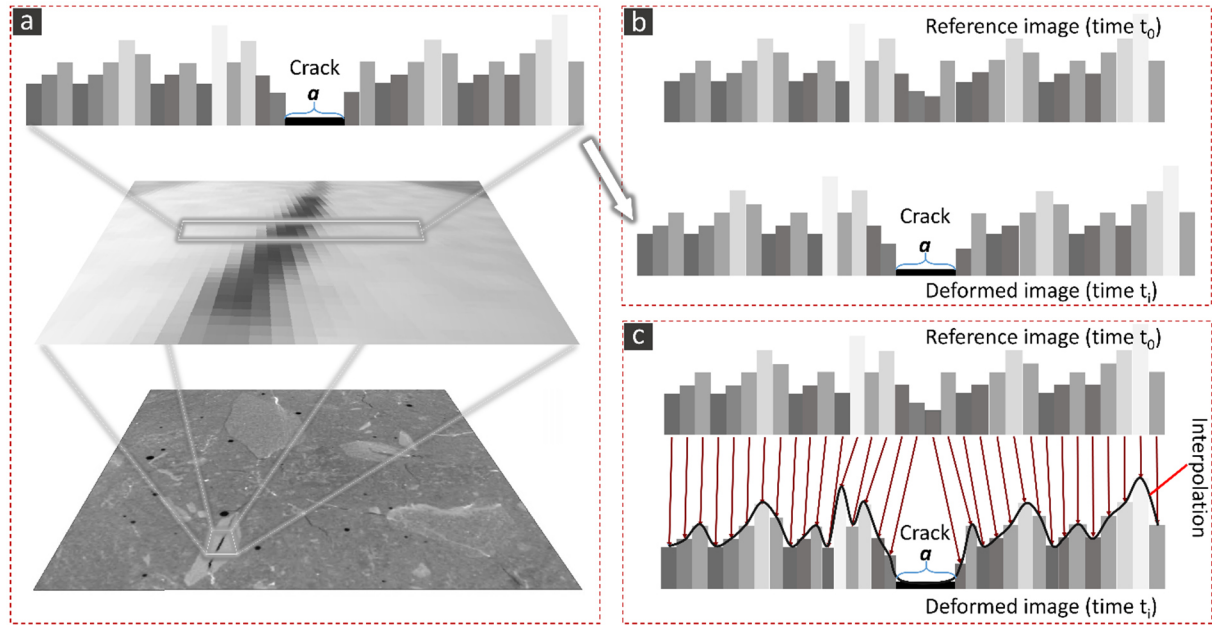


Figure A10. Schematic illustration of the condition expressed by the optical flow equation (see Eq. (2.19)) and of its implications for non-affine image registration: (a) a crack, shown at higher resolution (middle image) in an actual tomogram (slice thereof shown at the bottom) and a one-dimensional, voxel value profile from it along a line crossing the crack thickness (top image, schematic cartoon only); (b) comparing the reference state (time t_0) and the state after cracking (deformed image at time t_i) in the same schematic image and (c) comparing the deformed image to its corresponding image after non-affine (b-spline) registration.

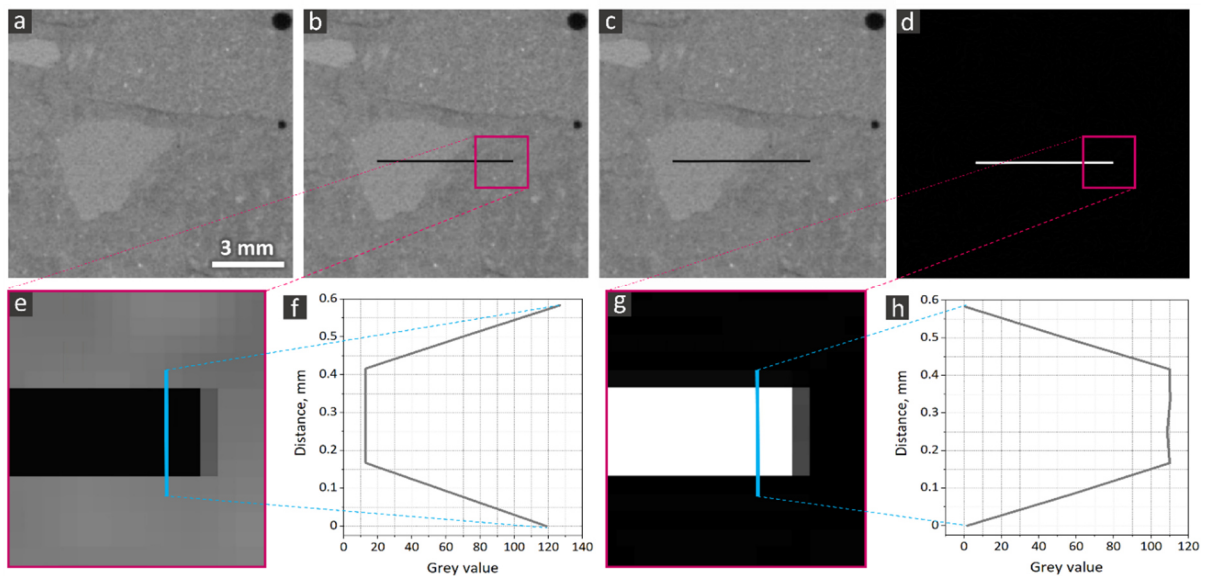


Figure A11. Evaluating the effect of affine + non-affine registrations on a newly emerged feature (a black, crack-like, stripe in this example) in the deformed image, compared with the reference one, without any actual deformation or other change having occurred to produce the deformed image. (a) Reference image (a slice from a small ROI from one of the tomograms). (b) Deformed image, obtained from (a) just by reassigning value = 0 (i.e., black) to some of its pixels, constituting a thin rectangular stripe. (c) Resulting image after affine + B-spline registration of (b) against (a). (d) Result of subtraction of (c) from (a). (e) Zoomed-in view of the stripe in (c). (f) Plot of Distance (mm) vs. Grey value for (c). (g) Zoomed-in view of the stripe in (d). (h) Plot of Distance (mm) vs. Grey value for (d).

from the reference image shown in (a). (e) and (g) Magnified region in the tip of the crack-like feature shown in (b) and (d), respectively. (f) and (h) The corresponding profile of the pixel values along the blue lines shown in figures (e) and (g), respectively, comparing the width of the crack-like feature before and after the image registration.

Figure A12 summarizes the effects of the different registration steps used in the TS-based crack segmentation procedure on the cracks and their surroundings using a simplified model system. Such model system consists of an artificially created, 2D reference image (Figure A12 (a)) which was deformed in a way to simulate (some feature of) the deformations due to ASR cracking, including the crack opening (Figure A12 (b)). The surrogate cracks in this model system are two wedge-like regions with pixel value = 0, introduced in the deformed image of Figure A12 (b). Based on the introduction of such surrogate cracks, the remaining portions of the reference image were displaced, rotated and deformed as to simulate (some features of) ASR cracking and expansion.

The affine registration (Figure A12 (c)) tries to match the deformed image with the reference one globally. To do so, it relies only on the similar portions in both images. Therefore, the deformed texture (a sort-of microstructure), moved in Figure A12 (b) due to the emergence of the two surrogate cracks, has to be sort-of compressed back in a way such that it falls approximately back into the same region occupied by the frame of the reference image. Nevertheless, the cracks remain intact in the resulting final image after the registration is done (Figure A12 (c)). A similar result also applies when the affine registration is followed by the B-spline-based non-affine one (Figure A12 (d)). Only similar portions of the image get involved in the registration, which also tries to correct for the spatially heterogeneous part of the deformations, not accounted for by the global affine registration. The cracks still remain intact in the new resulting image (Figure A12 (d)).

The advantages of the TS-based segmentation workflow can be summarized in the two following points.

- (1) Compared with the reference segmentation workflow based upon the BTH, the amount of small, quasi-spherical voxel clusters falsely classified as belonging to crack regions because of, e.g., partial volume effects was significantly smaller for the TS-based workflow. Although in both cases the final ASR crack binary tomogram was obtained after applying the sphericity-based filter described before, the false positive segmentation rate was still lower with the registration + subtraction workflow. This result is clearly expectable, since the subtraction operation intrinsically contributes to avoid such false positive segmentation results.
- (2) The registration + subtraction workflow could segment regions of cracks with thickness close to the tomogram's spatial resolution, which were missed by the reference segmentation workflow. This result can be ascribed to the stronger and negative influence of partial volume effects on the reference segmentation workflow, while the registration + subtraction one is more immune to them. The latter feature intrinsically stems from the impossibility for the registration to deform the $\{\tilde{I}(\vec{x}_j, t_i)\}_{j=1, \dots, N}$, $\forall i = 1, \dots, N_t$, as such to sort-of close the ASR cracks, since they are features which exist in $\{I(\vec{x}_j, t_i)\}_{j=1, \dots, N}$ but not in $\{I(\vec{x}_j, t_0)\}_{j=1, \dots, N}$ and every performed registration was based only upon the voxel values, as mentioned before. Essentially, an unavoidable error for the type of image registration used could be exploited in this work to improve the segmentation results, in terms of crack volume fraction actually segmented. This is a feature

of image registration already exploited and proposed by Hild *et al.* for locating crack regions in tomograms of concrete specimens undergoing drying shrinkage even when such cracks were not completely resolved at any point in the tomogram time series [7].

Overall, the TS-based segmentation workflow for ASR-generated empty cracks allowed reducing false positive segmentation results due to partial volume effects and increasing the crack volume segmented.

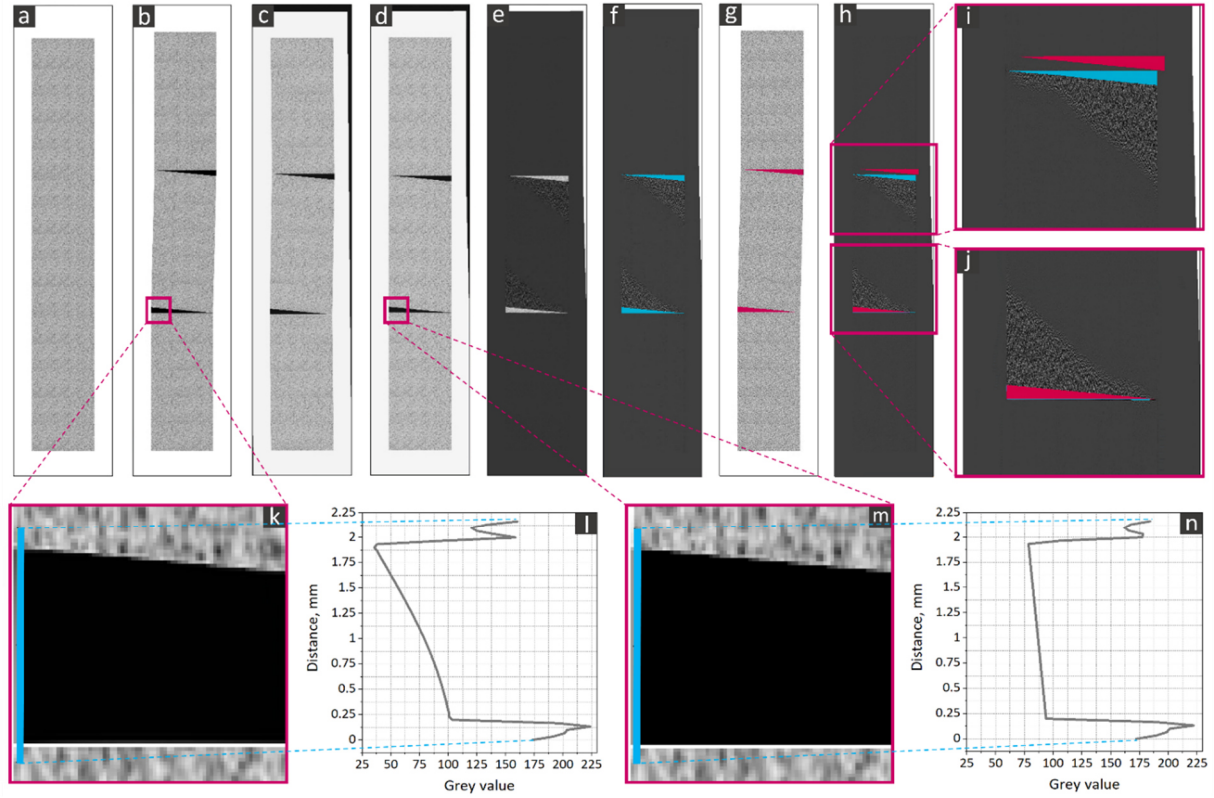


Figure A12. The effects of different registrations (affine and non-affine), used in the TS-based segmentation, as evaluated on a model, 2D case study where a uni-directional expansion occurred as a consequence of the appearance of new, crack-like features. (a) Reference, artificially created, 2D image. (b) Deformed image, artificially obtained from (a) by inserting two new features, each with the shape of a triangular wedge and with pixel values = 0, simulating cracks, and by deforming correspondingly the rest of the image as to simulate the effects of ASR crack opening for such toy case. (c) Resulting image after affine registration. (d) Resulting image after affine + non-affine registration. (e) Result of subtracting the affine + non-affine registered image (shown in (d)) from the reference image (shown in (a)), as done in the TS-based crack segmentation procedure for the real tomograms. (f) Binary image of the segmented model cracks superimposed over the subtracted image after affine + non-affine registration (shown in (e)) and obtained by the TS-based segmentation method. (g) Binary image of the segmented model cracks (the wedges) superimposed over the deformed image (shown in (b)), rendered as semi-transparent in pink and obtained by BTH-based crack segmentation procedure, used in this case as the reference (ground-truth) segmentation method. (h) Superposition of both types of binary images (shown in (f) and (g)) over one image to enable an easier comparison. (i) and (j) Magnification of the regions in (h) containing the segmented model cracks. (k) and (m) Magnified region at the tip of the model crack shown in (b) and (d), respectively. (l) and (n) Profiles of the pixel values of (k) and (m) along the blue lines shown in insets (e) and (g), respectively, comparing the model crack's width before and after the affine + non-affine registration.

A4. Specimen relative length change measurements: customized setup and its statistical characterization

The Mitutoyo mechanical displacement gauge mentioned in Section 3.2 and shown in Figure 3.1 (c) was replaced during the experimental campaign described in Chapter 6 by a commercial optical displacement gauge installed on a customized rig developed during this project. The mechanical gauge required reading the measured ΔL_z values from digital display, without the possibility to automatically store them on file. On the contrary, the new rig with the optical gauge allowed fully digitalized data collection, reducing significantly the overall measurement effort. The new rig was designed and implemented to host specimens with various size (Figure A13), either with prismatic or cylindrical shape.

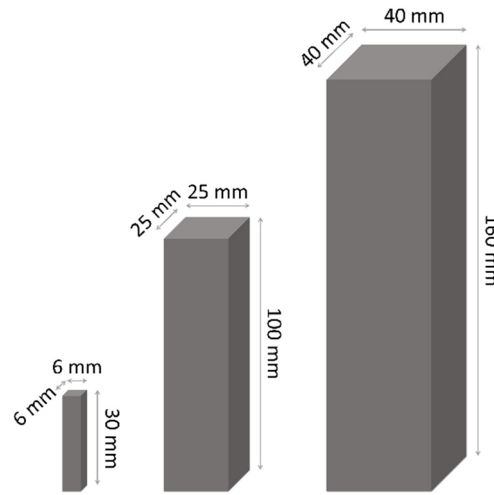


Figure A13. Examples of specimen sizes (schematic) that can be measured (length changes) by new laser tool.

Figure A14 provides an overview of the rig, with its distinct components labelled. The actual displacement gauge is a laser-based optical one manufactured by Micro-Epsilon (Swiss) AG, model Nr. ILD2300-20. It works based upon the basic principle that the displacement along the direction orthogonal to a surface on which a laser beam is shone at a certain angle (to such orthogonal direction) causes a lateral shift of the location where the reflected beam is received on a photodetector. By calibration measurements, the lateral shifts of the reflected beam can be converted into surface orthogonal displacements.

In the rig of Figure A14, the specimens are placed on customized holders screwed on a tilted breadboard whose angle of inclination is adjustable. The tilt allows controlling the constant force, due to Earth's gravitational field, which pushes the specimen against a landing metallic pin (see Figure A15), thus contributing to holding it stably in place. There are three different specimen holder stations screwed on the breadboard, designed to host specimens with similar size as shown in Figure A13. The laser beam spot-size is about 0.5 mm and can be adjusted in order to be focused on the centermost region of the specimen top surface.

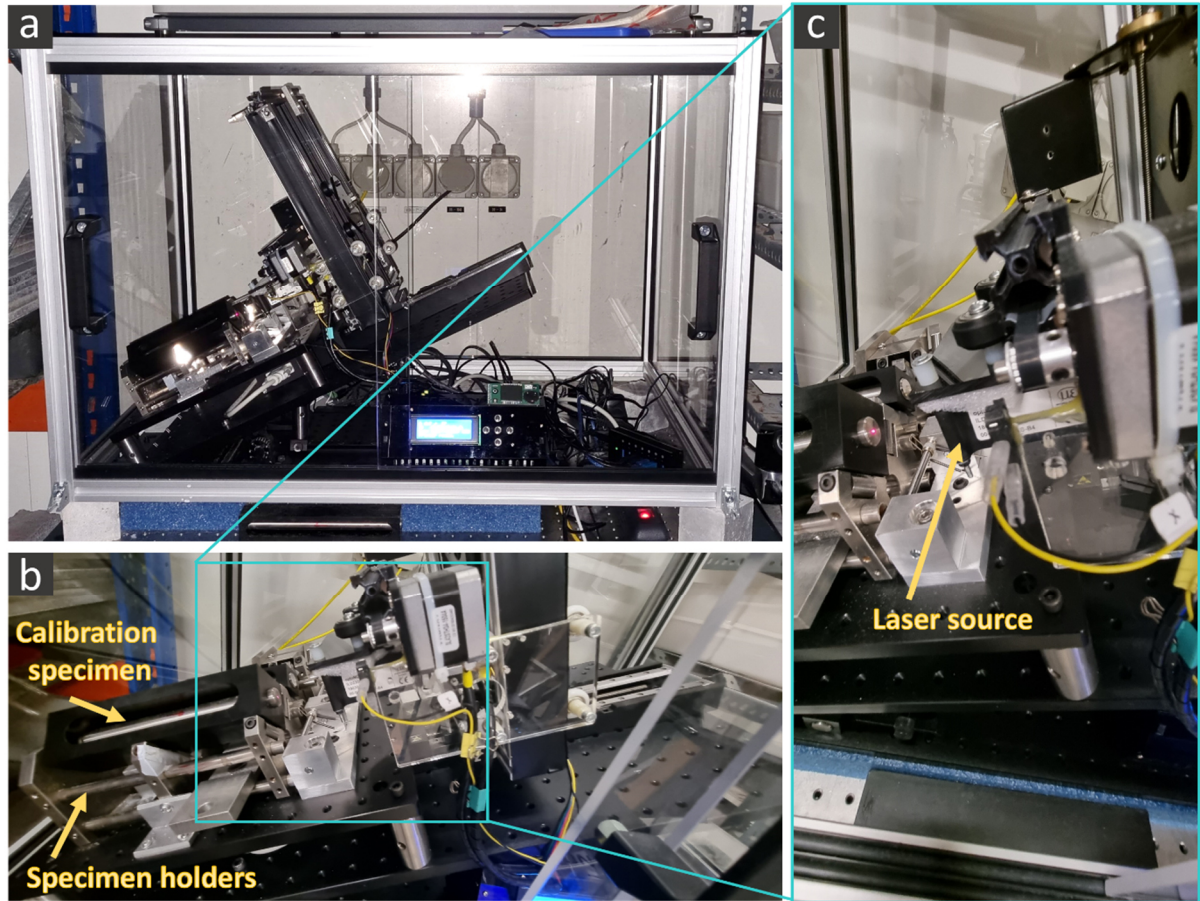


Figure A14. Rig for displacement measurements custom designed and built during this PhD project for the purpose of automating the specimen longitudinal dimensional (relative) changes, $\frac{\Delta L_z}{L_z}$.

Any measurement by the optical displacement gauge requires upfront a reference measurement by which a zero displacement is defined, corresponding to a reference length. Such measurement is performed with a calibration specimen (Figure A15(a)). Such a specimen, for each of the three nominal size values shown in Figure A13, constitutes of an Invar (FeNi36, a nickel–iron alloy) rod of length equal to the nominal one and embedded in a polyethylene frame with lateral size values equal to those of the cast specimen. The polyethylene frame acts only as holder of the central Invar rod, in order to place it in the center region the laser beam should illuminate. Given Invar's very low coefficient of thermal expansion [8], such central rod acts as a stable reference object with an accurate nominal length. After the reference measurement, the target specimen is placed on the holder to measure essentially the difference in distance between the reflecting surface and the laser head, as a consequence of exchanging the reference, Invar specimen with the actual one (Figure A15(b)). By summing up the value provided by the optical gauge to the nominal length of the Invar rod, the length of the specimen is estimated. Finally, upon acquiring time series of such values, the relative length change time series, $\frac{\Delta L_z}{L_z}(t_i)$, $\forall i = 1, \dots, N_t$, can be computed in respect to the reference time point t_0 .

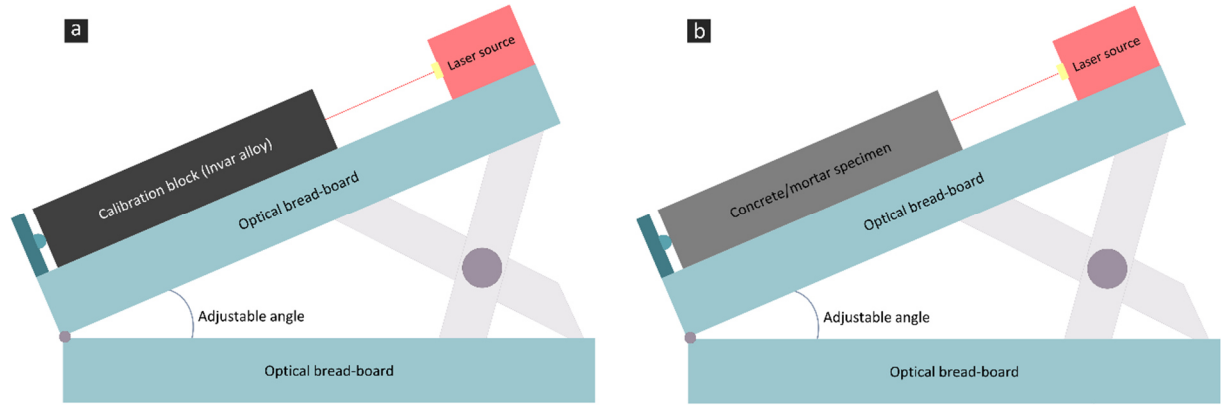



Figure A15. Schematic illustration of measuring (relative) length change of the specimens with custom designed and implemented rig based upon an optical, i.e., laser-based, displacement gauge: (a) first, defining a zero displacement measurement with a reference distance between the reflecting surface and the laser head, using a reference, calibration specimen; (b) following measurement with target specimen.

The optical displacement gauge is equipped with a dedicated, Web-based software interface provided by the manufacturer, through which the acquired displacement/distance difference values can be stored on file, e.g., with CSV format. For computing the $\frac{\Delta L_Z}{L_Z}$ time series, a Matlab function was custom written, accompanied by a respective graphical user interface (GUI, see Figure A16). Such function reads in the displacement values from the CSV files (one for each time point) and provides as output the plot of the $\frac{\Delta L_Z}{L_Z}$ time series.

Menu



acqMode	<input type="text" value="Webinterface"/>	definition	acqMode: option flag indicating whether the raw data from the measurements, saved into .csv files, were collected via the laser systems software installed on the
CSVOrExcel	<input type="text" value="csv"/>	definition	CSVOrExcel: binary option flag indicating which type (.csv or .xlsx) of input files, saved by the software which is running on the laser system and which is accessed via
source_dir	<input type="text" value="K:\SNFSinergiaASR\SubProjekt_5\0.MainCast\0.Resu"/>	definition	source_dir: full or relative path of the folder containing the distance raw data from the measurements, in the format of .csv files. These files are converted into
dest_dir	<input type="text" value="K:\SNFSinergiaASR\SubProjekt_5\0.MainCast\0.Resu"/>	definition	dest_dir: full or relative path of the folder where the .xlsx files with the distance values, for each specimen and each measurement session, are located and where the
skipInitialSamples	<input type="text" value="1000"/>	definition	skipInitialSamples: number of initial samples acquired which should be skipped before considering the actual samples for computing the average values. Integer
samplesNr	<input type="text" value="6000"/>	definition	samplesNr: number of samples of each measured distance which should be considered for computing the average value. Integer number.
xAxisLabel	<input type="text" value="\$ASR\ acceleration\ time\ [days]\$"/>	definition	xAxisLabel: X-axis label of each of the four plots. The X variable is essentially used as the indicator of a distinct and successive dataset acquired at a distinct time point.
NominLengthCalibrSpec	<input type="text" value="160"/>	definition	NominLengthCalibrSpec: nominal length of the calibration specimen, expressed in mm. Integer or floating point number.
relChangeDistUnitFlag	<input type="text" value="1"/>	definition	relChangeDistUnitFlag: flag to specify whether the relative change in distance values are provided in arbitrary units or in % points. Possible values and
MeasSessionLabel	<input type="text" value="[1,3,7,14,21,50,80,100,130,150,200,240,280,320,350]"/>	definition	MeasSessionLabel: 1D array of values of the variable identifying/characterizing each performed measurement session. See the explanation for the input variable
SpecLengthExcelFilename	<input type="text" value="K:\SNFSinergiaASR\SubProjekt_5\0.MainCast\0.Resu"/>	definition	SpecLengthExcelFilename: filename (full or relative path) of the Excel file where to write the specimen absolute length values. Character string. It must end in
figureFilenameTemp1	<input type="text" value="K:\SNFSinergiaASR\SubProjekt_5\0.MainCast\0.Resu"/>	definition	figureFilenameTemp1: template of the figure filename (full or relative path) for the box plot of the relative length change value, one box at each measurement session
figureFilenameTemp2	<input type="text" value="K:\SNFSinergiaASR\SubProjekt_5\0.MainCast\0.Resu"/>	definition	figureFilenameTemp2: template of the figure filename (full or relative path) for the range plot (a vertical bar whose bottom end is located at the minimum value and
figureFilenameTemp3	<input type="text" value="K:\SNFSinergiaASR\SubProjekt_5\0.MainCast\0.Resu"/>	definition	figureFilenameTemp3: template of the figure filename (full or relative path) for the plot of the average value +/- 1 standard deviation of the relative length change as a
figureFilenameTemp4	<input type="text" value="K:\SNFSinergiaASR\SubProjekt_5\0.MainCast\0.Resu"/>	definition	figureFilenameTemp4: template of the figure filename (full or relative path) for the plot of the median value +/- MAD (median absolute deviation from the median value)

Figure A16. A snapshot of the graphical user interface of the Matlab application custom developed for the automatic reading of the data from the optical displacement gauge and the corresponding plotting of the time series of relative length change values ([link to the GUI](#)).

In order to evaluate the uncertainty level of measurements performed with both displacement gauges, 100 repeated measurements, with specimen repositioning were performed by myself on the 160 mm-long calibration specimen and on a mortar specimen with a cast size of $40 \times 40 \times 160 \text{ mm}^3$, for both rigs.

For any given rig, the following statistical modeling and analysis was performed based upon the set of 100 measured values:

- each measured value, called $\langle \Delta L_z \rangle$, was assumed to be the average value of a random variable ΔL_z with fluctuating values due to intrinsic measurement errors; this hypothesis was needed because, in the case of the optical displacement gauge, the output value was actually the average of a time series of values collected over a certain acquisition time, while the mechanical gauge provided one single value for each repositioning;
- the repositioning was assumed to create uncertainty in $\langle \Delta L_z \rangle$, making it a random variable itself; its 100 acquired values were its realizations;
- the standardized version of $\langle \Delta L_z \rangle$, called $\langle \widetilde{\Delta L_z} \rangle = \frac{\langle \Delta L_z \rangle - \mu}{\sigma}$, was computed, where μ is the empirical average value of $\langle \Delta L_z \rangle$ computed from the 100 realizations and σ the corresponding empirical standard deviation of the sample;
- the hypothesis of $\langle \widetilde{\Delta L_z} \rangle$ being a normalized Gaussian random variable was tested by the Kolmogorov-Smirnov (KS) test, in order to decide whether to use or not σ as a well-posed definition of displacement measurement uncertainty.

The KS test quantifies a distance between the empirical cumulative distribution function (CDF) of the acquired statistical sample of the random variable and the cumulative distribution function of a reference distribution, in this case a normalized Gaussian. The test's null hypothesis is that the acquired sample was actually drawn from the reference distribution [9].

The KS test uses as statistic the maximum value of the absolute difference between the two CDFs, the empirical one and the reference one, evaluated on all sampled values. For a pre-selected confidence level of 5%, the p-value for each set of 100 measurements was computed. The p-value is the probability, given the null hypothesis, of observing a value for the KS statistic as large as the one computed from the acquired statistical sample. The lower the p-value, the greater the statistical significance of the observed difference between the empirical CDF and the reference one [10], thus the less likely that the measured value were drawn from the reference distribution. The empirical CDF of the standardized measured values and the CDF of the standardized Gaussian distribution are shown in Figure A17 along with μ , σ and the p-value for each measurement set.

The results shown in Figure A17 indicate that the empirical standard deviation σ of the sets measured with the mechanical gauge could not be adopted as a well-posed definition of measurement uncertainty, because the KS test's null hypothesis could be fully rejected (the case for the calibration specimen set, $p = 0.001$) or almost rejected ($p = 0.06$ for the mortar specimen case). Thus, concerning the mechanical gauge measurement, no actual estimate of uncertainty could be obtained. On the contrary, the KS test's null hypothesis could not be rejected for the measurement sets obtained with the custom built rig ($p > 0.05$), thus the respective σ values could be used as a well-posed estimate of measurement uncertainty, being about 1 μm for the calibration specimen and about 2.5 μm for the mortar one.

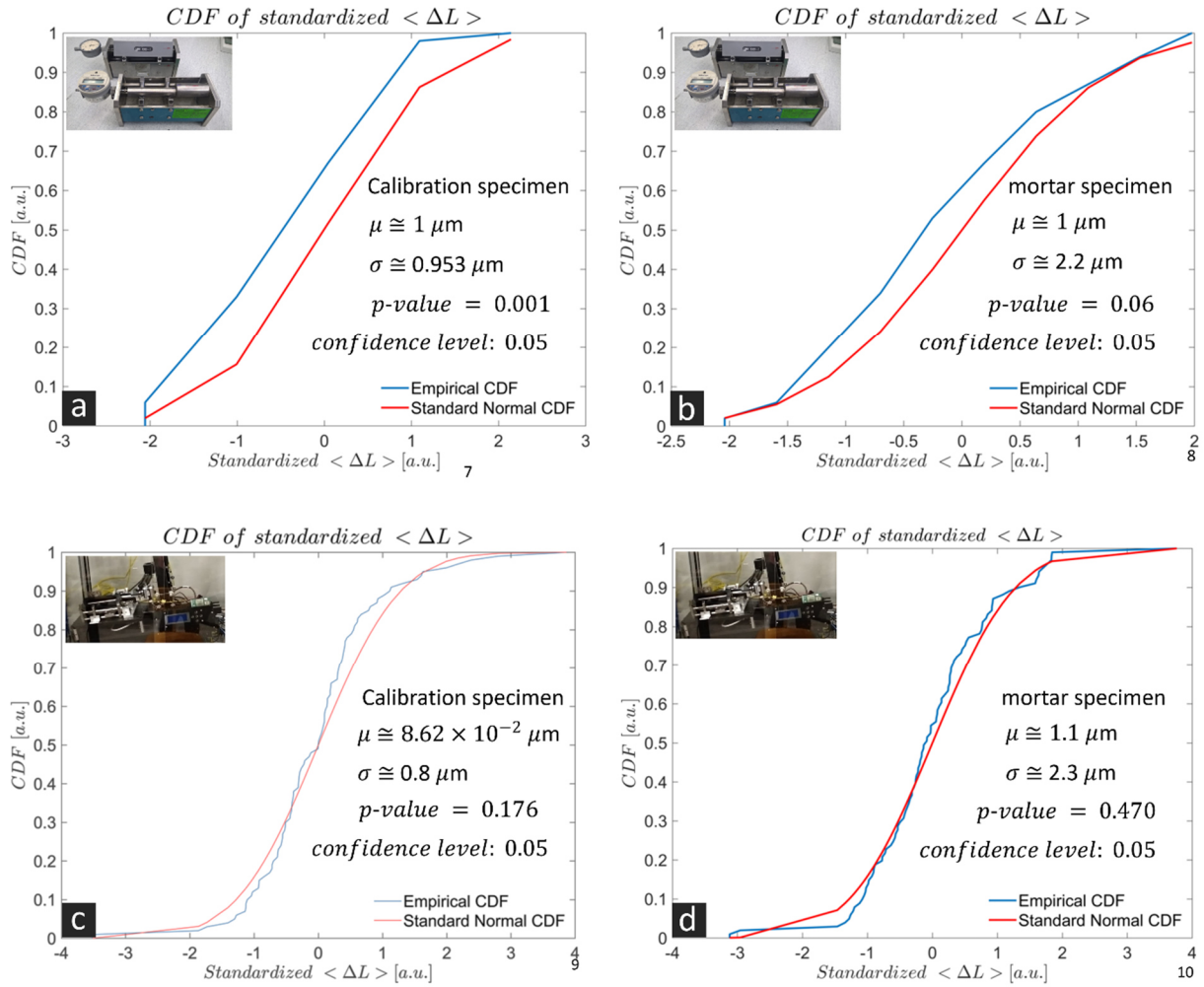


Figure A17. Results of the Kolmogorov-Smirnov test for the distribution of displacement values measured repeatedly 100 times with each rig, the conventional one based on a mechanical gauge, top row, and the one custom built in this project, based upon an optical gauge. The left column shows the results for the Invar, 160-mm long calibration specimen. The right column shows the results for a mortar specimen with cast size of $40 \times 40 \times 160 \text{ mm}^3$. The empirical cumulative distribution function (CDF) of the standardized measured values is shown by the blue curve, while the red one shows corresponding values of a normalized Gaussian distribution, adopted as the reference distribution in the Kolmogorov-Smirnov test. The p -values of the hypothesis test is provided in correspondence of a confidence level of 5%.

Bibliography

- [1] “DIN EN 196-2 : 2013 | METHOD OF TESTING CEMENT - PART 2: CHEMICAL ANALYSIS OF CEMENT | SAI Global.” [Online]. Available: https://infostore.saiglobal.com/en-us/Standards/DIN-EN-196-2-2013-386164_SAIG_DIN_DIN_877353/. [Accessed: 11-Nov-2020].
- [2] “ISO - ISO 10694:1995 - Soil quality — Determination of organic and total carbon after dry combustion (elementary analysis).” [Online]. Available: <https://www.iso.org/standard/18782.html>. [Accessed: 11-Nov-2020].
- [3] I. Fernandes *et al.*, “Alkali-silica reactivity of some common rock types. A global petrographic atlas,” *Q. J. Eng. Geol. Hydrogeol.*, vol. 46, no. 2, pp. 215–220, May 2013, doi: 10.1144/qjegh2012-065.
- [4] S. Klein and M. Staring, “Elastix, The Manual Elastix 4.9.0,” 2018. [Online]. Available: <https://usermanual.wiki/Document/elastix490manual.1389615963/html>. [Accessed: 03-May-2021].
- [5] T. Perciano *et al.*, “Insight into 3D micro-CT data: Exploring segmentation algorithms through performance metrics,” *J. Synchrotron Radiat.*, vol. 24, no. 5, pp. 1065–1077, Sep. 2017, doi: 10.1107/S1600577517010955.
- [6] H. Jin, C. Sciammarella, S. Yoshida, and L. Lamberti, Eds., *Advancement of Optical Methods in Experimental Mechanics, Volume 3*. Cham: Springer International Publishing, 2014.
- [7] F. Hild *et al.*, “ON THE USE OF 3D IMAGES AND 3D DISPLACEMENT MEASUREMENTS FOR THE ANALYSIS OF DAMAGE MECHANISMS IN CONCRETE-LIKE MATERIALS ON THE USE OF 3D IMAGES AND 3D DISPLACEMENT MEASUREMENTS FOR THE ANALYSIS OF DAMAGE MECHANISMS IN CONCRETE-LIKE MATERIALS. VIII,” in *International Conference on Fracture Me-chanics of Concrete and Concrete Structures*, 2013.
- [8] J. R. Davis, *Alloying: Understanding the Basics*. ASM International, 2001.
- [9] M. Naaman, “On the tight constant in the multivariate Dvoretzky–Kiefer–Wolfowitz inequality,” *Stat. Probab. Lett.*, vol. 173, p. 109088, Jun. 2021, doi: 10.1016/j.spl.2021.109088.
- [10] R. L. Wasserstein and N. A. Lazar, “The ASA’s Statement on p-Values: Context, Process, and Purpose,” *American Statistician*, vol. 70, no. 2. American Statistical Association, pp. 129–133, 02-Apr-2016, doi: 10.1080/00031305.2016.1154108.

Appendix B

Supplementary data/materials for chapter 4

B1. Materials characterizations

B1.1. ASR-reactive aggregates: chemical and mineralogical characterizations

Table TB1. Chemical composition obtained by X-ray fluorescence (XRF) analysis for B aggregates performed according to the DIN EN 196-2:2013 standard. ♥ LOI: Loss on Ignition.

Chemical species	Brienz ("B")
	Content (mass-%)
SiO ₂	69.1
Al ₂ O ₃	14.3
CaO	2.9
Fe ₂ O ₃	2.3
MgO	1
K ₂ O	3.4
Na ₂ O	3.7
SO ₃	0.1
LOI♥	3
Total	99.8

Figure B1 below shows CP-OM micrographs from the 200 μm -thick concrete thin sections containing B, P and U aggregates (insets (a), (b) and (c), respectively).

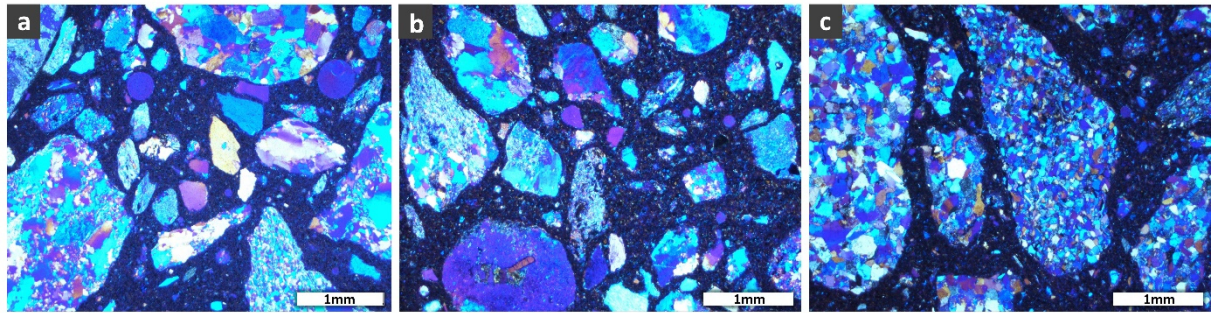


Figure B1. Examples of mineral textures of the three types of aggregates used in laboratory-accelerated specimens, characterized by optical microscopy with cross-polarized light (CP-OM): (a) to (c) thin-section images from specimens cast with B, P and U aggregates, respectively.

B2. Time-lapse X-ray tomography

B2.1. Laboratory specimens

Selected ROIs on tomographic slices of the laboratory specimens, b25, p25 and u25, at three distinct time-points, are shown in Figure B2 (a) – (c), respectively.

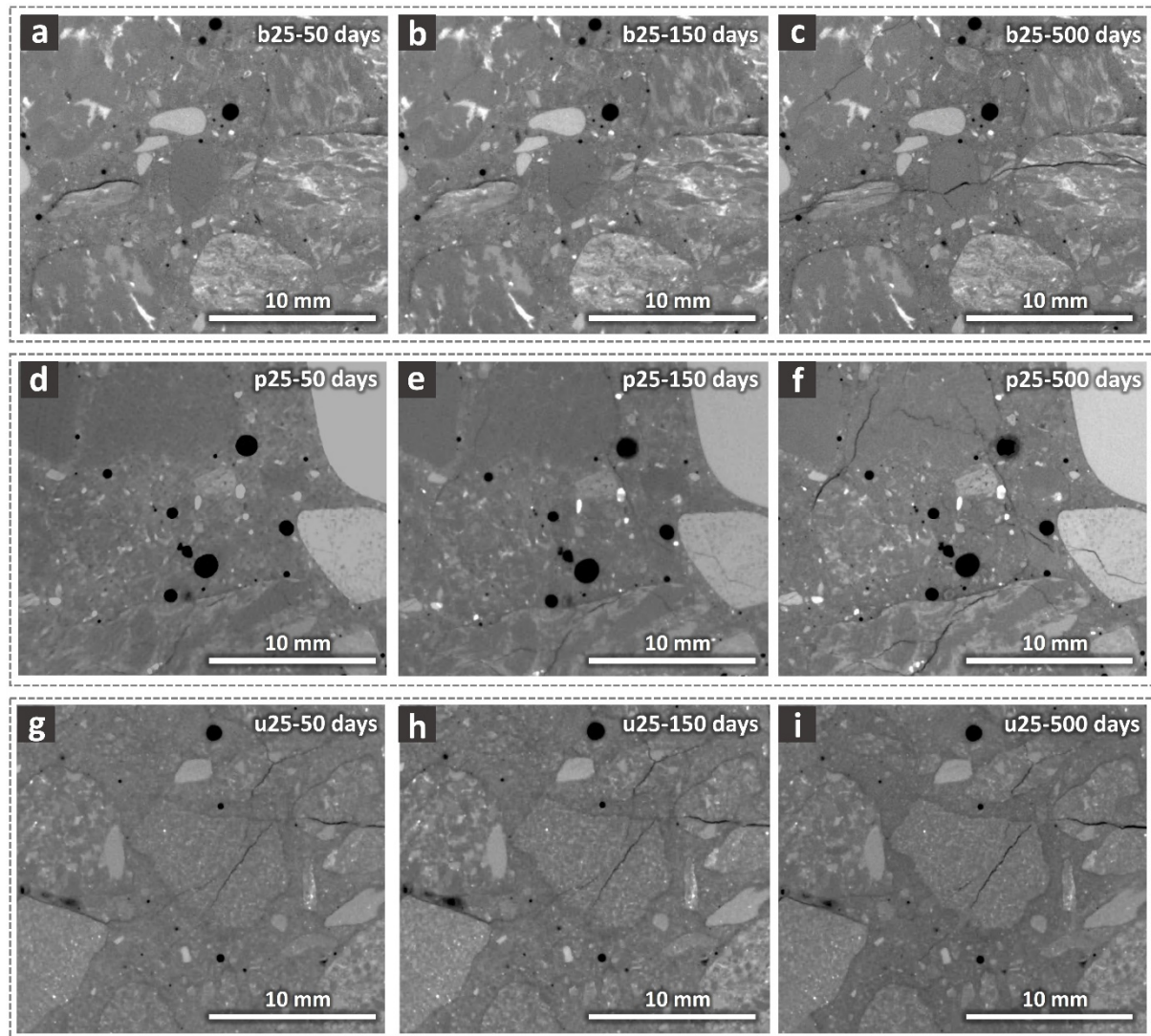


Figure B2. Examples of tomographic slices from ROIs of the b25, p25 and u25 specimens, shown at three different time points to characterize qualitatively the ASR cracking. The first row shows always the slice at the same position from the tomograms of the b25 specimen, acquired at (a) 50 days, (b) 150 days and (c) 500 days. The second row, insets (d) to (f), shows something similar but for the p25 specimen. The last row, insets (g) to (i), shows a similar example but for the u25 specimen.

B3. Time-lapse tomography analysis of ASR cracking

B3.1. Laboratory specimens

The fully segmented crack networks are 3D rendered as solid, colored objects in Figure B3 for the laboratory specimens b25, p25 and u25 at 500 days of ASR acceleration.

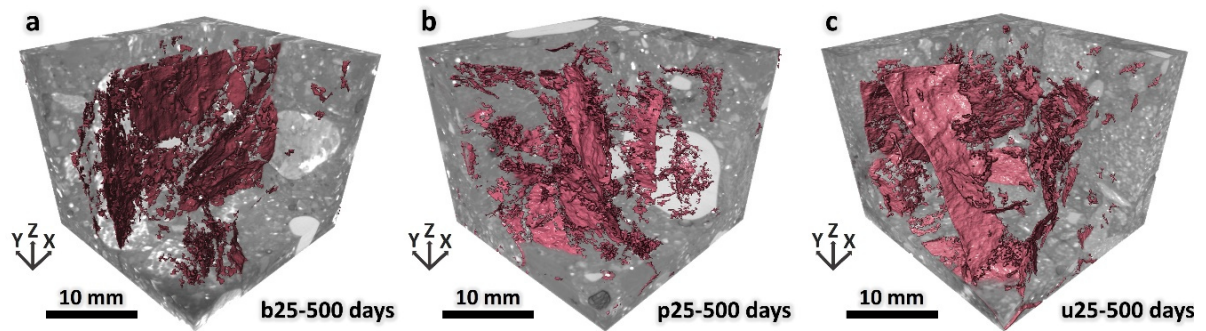


Figure B3. 3D rendering of the segmented cracks binary tomograms at 500 days since the ASR acceleration start for the laboratory specimens (a) b25, (b) p25 and (c) u25. In each inset, a small part of the concrete was also rendered (in grey tones), while the most of it was corner-cut to reveal the segmented cracks inside it.

B4. Empirical evaluation of specimen size effect on the segmentatble crack quantity in tomograms

B4.1. Field-exposed specimens

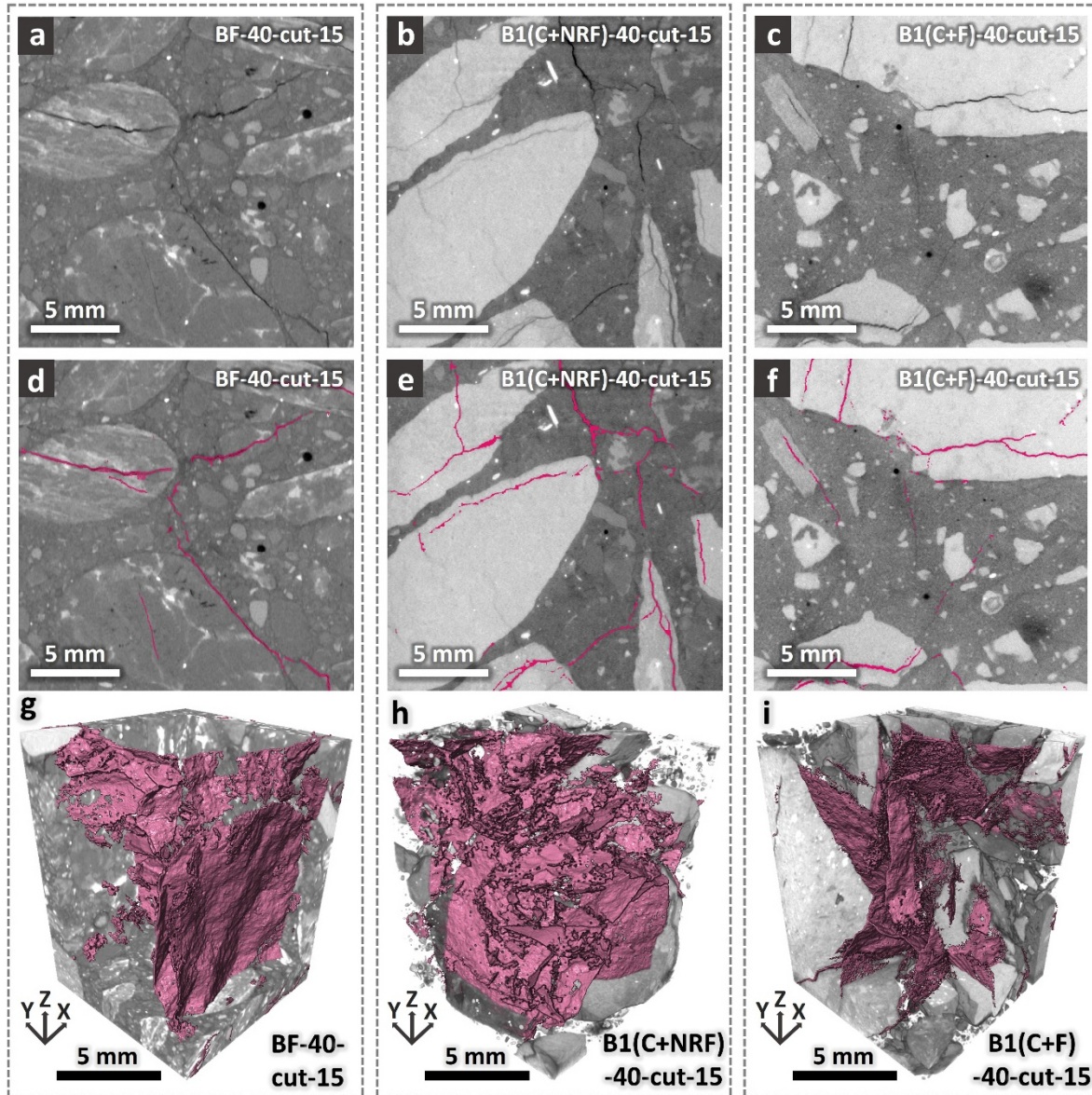


Figure B4. Example tomographic slices from a VOI of (a) the BF-40-cut-15, (c) the B1(C+NRF)-cut-15 and (d) the B1(C+F)-cut-15 specimens, along with (d) to (f) corresponding slices from the binary tomograms of the segmented cracks superimposed over the same slices and (g) to (i) the 3D rendering of the binary tomograms of the segmented cracks of each specimen, respectively.

B5. Shape tensor analysis of the separated cracks

The segmented 3D crack networks were subjected to a 3D connected component labeling procedure to identify and digitally tag distinct crack branches within the network. Figure B5 shows the 3D rendered labeled total crack networks of the six laboratory specimens (at 500 days) and of the three field-exposed specimens. Each individual, disconnected crack is rendered with a different color. Regardless of the crack network complexity, several cracks could be clearly distinguished.

Figure B6 shows an example of the bounding box of an individual crack selected from the labelled binary tomogram of the crack network of the P40 specimen. In this figure, the larger blue box represents the tomographed volume of the specimen, the smaller, orange parallelepiped box encompassing the crack is the bounding box computed by the shape tensor analysis. The *eigenvectors* of that individual crack are rendered as arrows, originating from the center of mass of the crack itself.

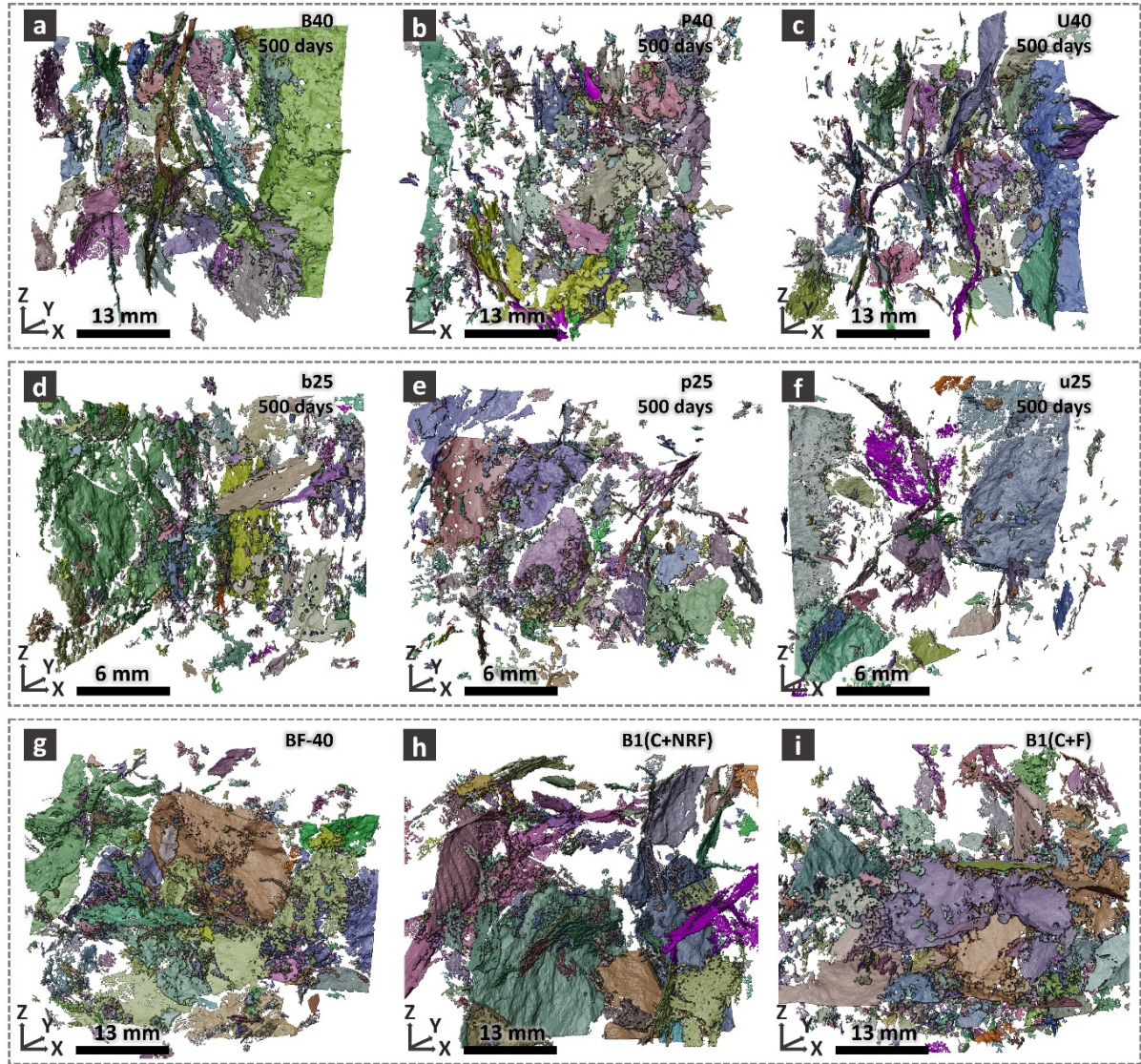


Figure B5. 3D rendering of the segmented and labeled total crack networks of distinct laboratory and field-exposed specimens. Each separated part of the crack network is rendered with a distinct color, to be individually distinguished. The color assignment to each branch was random. (a) to (c): B40, P40 and U40 specimens, respectively, all at $t_f = 500$ days. (d) to (f): b25, p25 and u25 specimens, respectively, all at $t_f = 500$ days as well. (g) to (i): BF-40, B1(C+NRF)-40 and B1(C+F)-40 specimens, respectively.

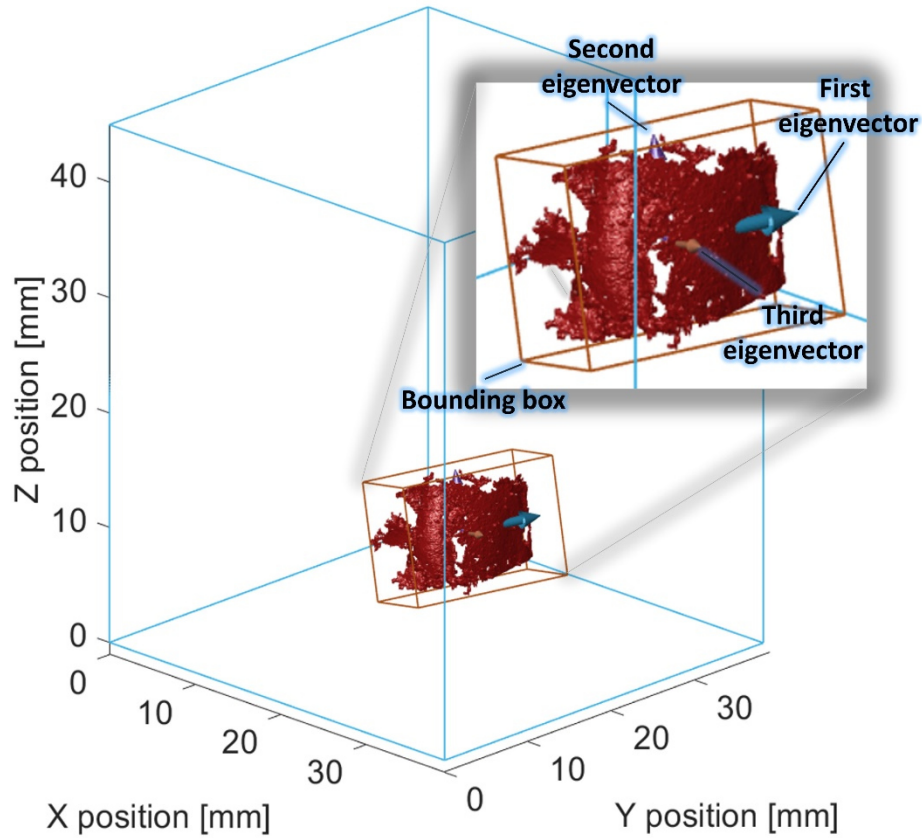


Figure B6. A single separated crack segmented from the tomogram at 250 days of the P40 specimen. The large parallelepiped box in blue delineates the tomographed volume of the specimen. The smaller orange box encompassing the crack (also magnified) indicates the bounding box of that crack, oriented along the three eigenvectors of its shape tensor \mathbf{G} . Each eigenvector is rendered as a solid arrow originating from the center of mass of the crack's region, scaled by half the lateral size of the bounding box along the same direction, distinct colors indicating the distinct eigenvectors. The blue arrow refers to the 1st eigenvector, the purple to the second eigenvector and the orange to the third one.

Appendix C

Supplementary data/materials for Chapter 5

C1. Materials characterizations

C1.2. ASR products: chemical and morphological characterizations by SEM-EDX analysis

SEM-BSE and EDX measurements were performed according with the settings detailed in Section 3.2.

Figures C1 (a) to (d) show the EDX analysis results in the form of ternary diagrams. There, $\text{Na}_2\text{O}_{\text{eq}}$ indicates the sum of atomic percentages of existing alkalis in each system. For the reference specimens, the alkali are only Na and K, while Cs is included for the doped specimens. Each point in such ternary diagrams refers to a small region occupied by ASR products, either crystalline regions located well inside the aggregate volume or amorphous regions at the aggregate boundaries or inside cracks through the cement paste.

In all ternary diagrams the composition of the ASR products was almost identical regardless of the Cs addition and of the aggregate type. This result indicates that Cs replaced part of other alkalis in the products. The only subtle difference between the diagrams is a slight shift towards higher silica in the Cs-doped specimens. This could be related to the higher rate of SiO_2 dissolution in presence of Cs^+ ions, already reported in [5].

Figure C2 (a) shows the products' composition, in terms of alkali-to-silicon molar ratio and calcium-to-silicon molar ratio, at different time points during the ASR acceleration and for Cs-doped specimens. At any time, each molar ratio spanned approximately the same respective range. Such range was similar to what already reported in the literature [5]. No significant difference in such molar ratios was observed when comparing products formed in specimens with or without Cs-doping (Figure C2 (b)). Finally, in the presence of Cs-doping, the contribution of the Cs^+ ions to the ASR products remained almost the same at different ages (Figure C2 (c)).

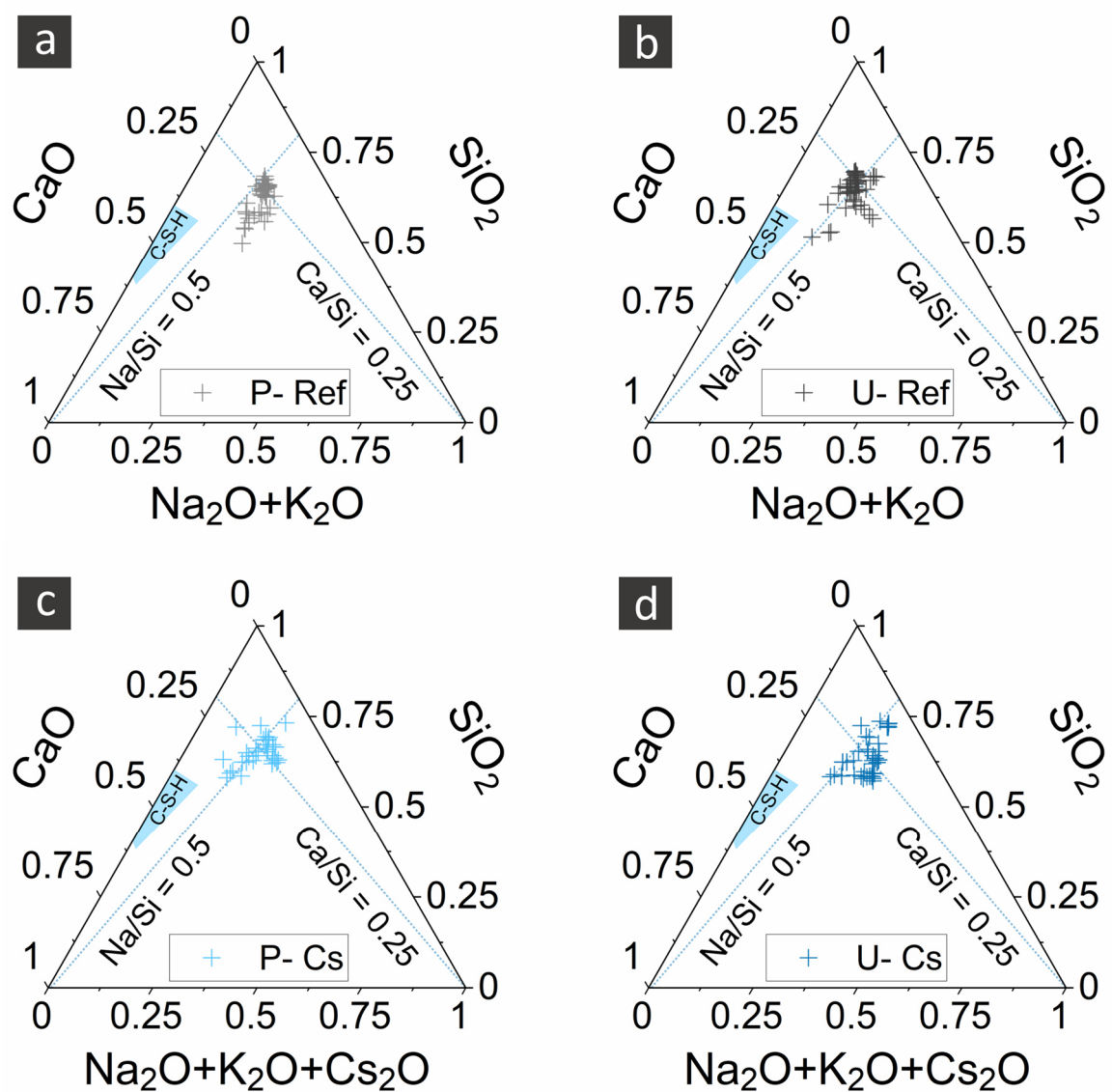


Figure C1. EDX analysis results (atomic percentage) presented in the form of ternary diagrams of the ASR products' composition at more than forty points from both the crystalline (inside the aggregates) and the amorphous (boundary regions of the aggregates and in the cement paste) products for the (a) P-Ref, (b) U-Ref, (c) P-Cs and (d) U-Cs specimens, respectively.

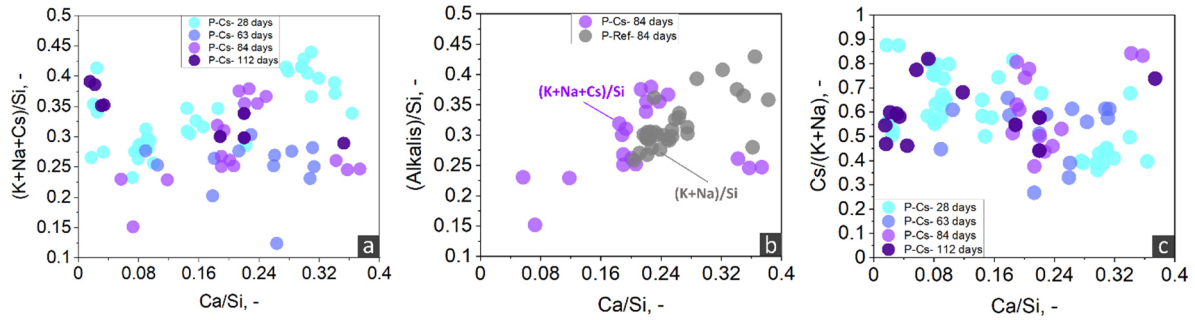


Figure C2. Evolution of the chemical composition of ASR products formed in the specimens with and without Cs-doping: example of EDX analysis results. (a) Evolution of the composition of the products in P-Cs specimens, in terms of alkali-to-silicon $(K+Na+Cs)/Si$ molar ratio and calcium-to-silicon (Ca/Si) molar ratio. (b) Corresponding data as in (a) but at one time point only (84 days) and comparing ASR products formed in P-Cs and P-Ref specimens. (c) Evolution of the molar ratio of Cs^+ to the other alkali ions in the ASR products found in P-Cs specimens. In each scatter plot, each point refers to a location inside a products region.

The SEM-BSE micrographs for distinct specimens at distinct time points, both without and with Cs-doping, exemplify the advantages brought by the Cs-doping. In its absence, ASR products inside cracks could be recognized mainly based upon the characteristic plate-like morphology. The BSE contrast between products and the aggregates or cement paste material phases was and is too small for an easy and always unequivocal detection of the products. See Figure C3 and Figure C4. On the contrary, in the presence of Cs-doping, the BSE contrast itself suffices for unequivocally detecting products and opens up the possibility to observe characteristic spatial distribution patterns, e.g., the prevalence of products in regions close to the aggregate boundaries, at earlier ages, followed by their appearance closer to the center of the aggregates only at later ages (see Figure C4).

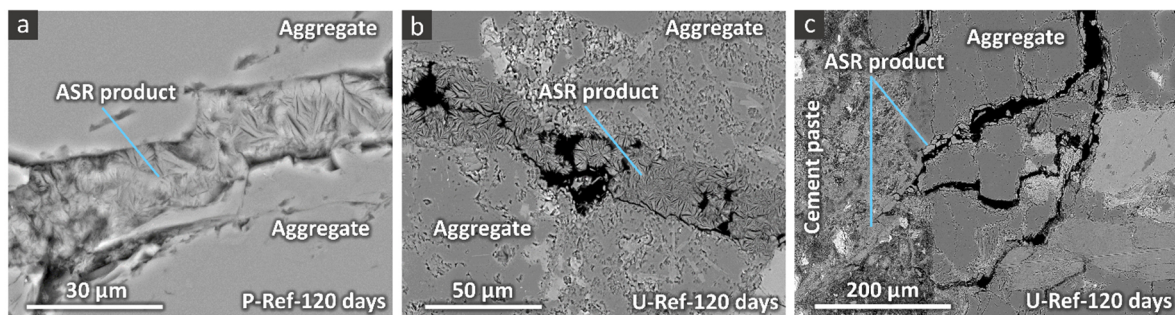


Figure C3. Examples of SEM-BSE micrographs from reference specimens showing the formation of ASR products inside aggregates and cement paste: (a) P-Ref and (b) U-Ref specimens, products within aggregates; (c) a wider view showcasing ASR damage in a U-Ref specimen, both inside aggregates and through the cement paste.

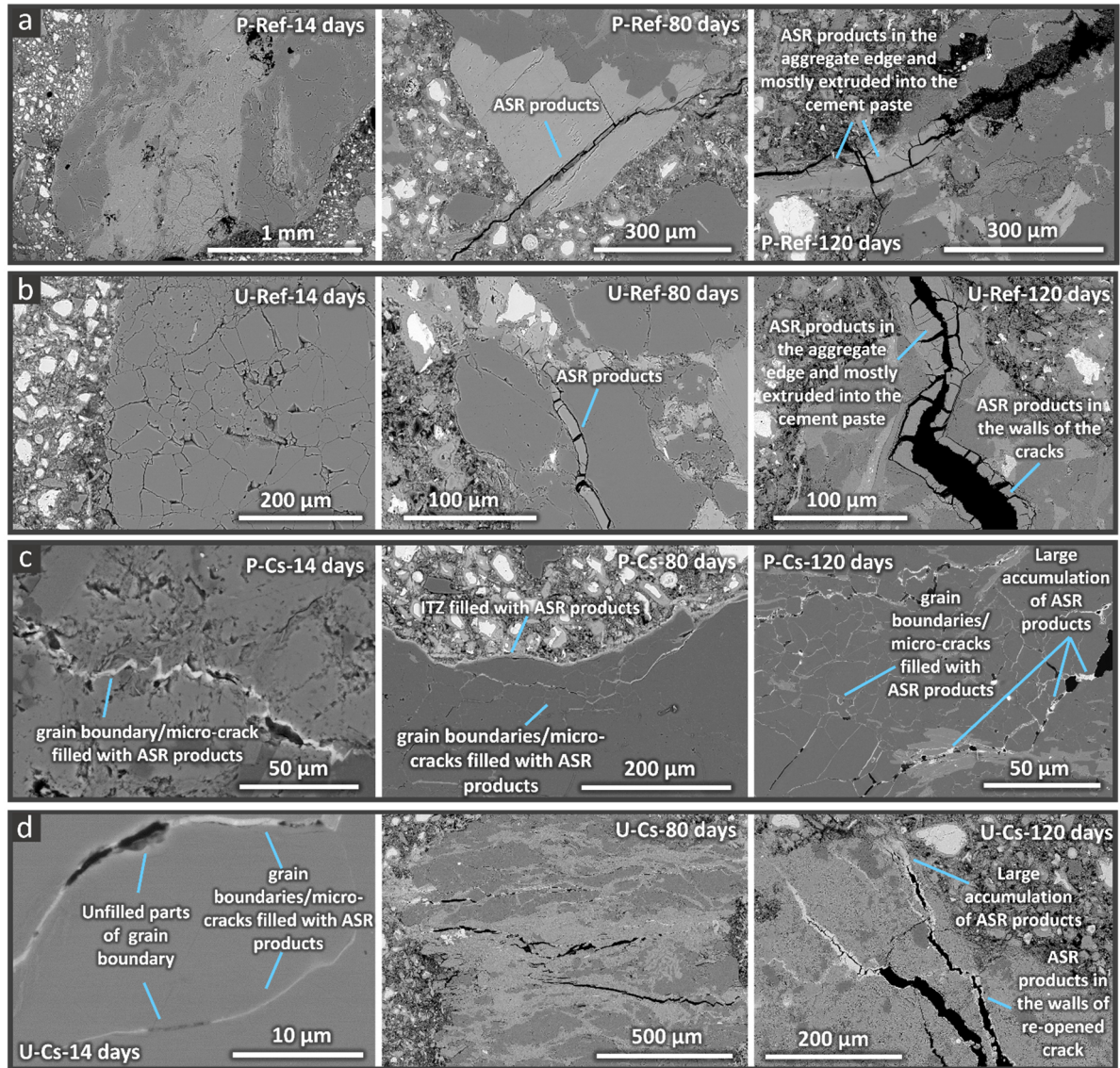


Figure C4. SEM-BSE micrographs providing examples of the distribution of ASR products and cracks in the specimens with and without Cs, cast with P and U aggregates. For every specimen type, the micrographs were acquired at 14, 80 and 120 days. Each column refers to a distinct specimen type. SEM-BSE micrographs for (a) P-Ref, (b) U-Ref, (c) P-Cs and (d) U-Cs specimens, respectively.

C2. X-ray attenuation contrast of ASR products labelled with alkalis. Testing experimental campaign.

In order to assess the degree of X-ray attenuation contrast by the ASR products, when labelled by alkali cations, XT was performed only at the end of a preliminary ASR acceleration experimental campaign. Such campaign involved only specimens cast with P aggregates. Distinct specimens were cast by adding to their mix sources of distinct alkalis, specifically Na, K, Rb and Cs. The compound supplying each alkali element was added to the specimen mix in an amount depending on its atomic number. The specimens were cast and underwent ASR acceleration according to the Swiss standard SIA 2042 [7], developed for assessing the degree of ASR-induced expansion in concrete. The specimens (prisms with size of $70 \times 70 \times 280 \text{ mm}^3$) were subjected to different boundary conditions compared with those used for the time-lapse XT campaign. They were stored in a climatic chamber at 100% RH and at 60°C , for a total of 168 days. They were cast with mix design identical to that of the specimens for the XT campaign. At 112 days of ASR acceleration time, smaller specimens were cut out, with sizes of $20 \times 20 \times 40 \text{ mm}^3$ by using a diamond saw, to perform XT and assess which alkali doping led to the highest X-ray attenuation contrast between the ASR products and the other material phases in the concrete mesostructure.

C3. Effect of the alkali-doping on ASR

The preliminary ASR experimental campaign described in Section C2 included time-lapse measurements of relative length changes and of specimen mass [35]. All types of alkalis boosted up the reference concrete type's normal ASR expansion. However, the extent of such effect varied with the type of alkalis used. For instance, Rb and K increased the expansion the most. Na enhanced it slightly less. Cs produced the least increase.

C4. Dimensional and mass changes during ASR acceleration

C4.1. Dimensional changes

The main difference in the expansion behaviour of the specimens cast with the two aggregate types was quantitative: the P specimens expanded more slowly than the U ones. Compare the results in Fig. 1 with those in Figure C5. This result was independent of Cs-doping.

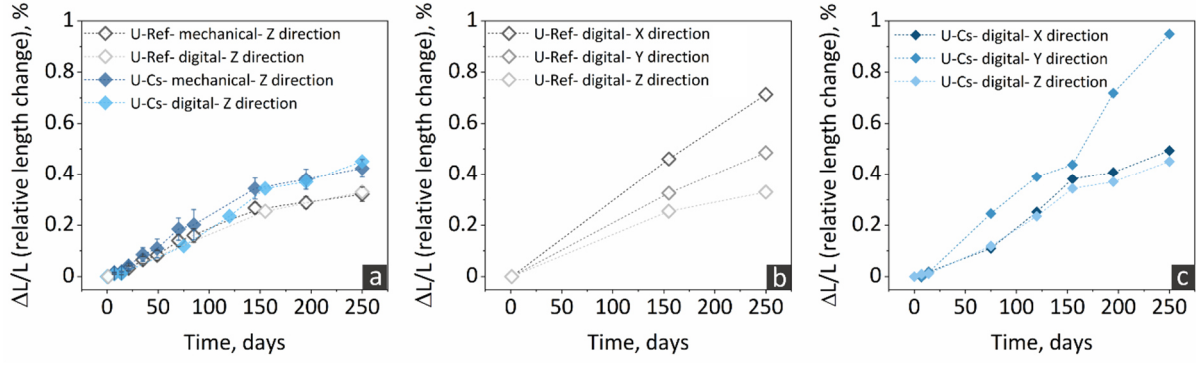


Figure C5. Similar plot as in Figure 5.5 but for the U-Ref and U-Cs specimens.

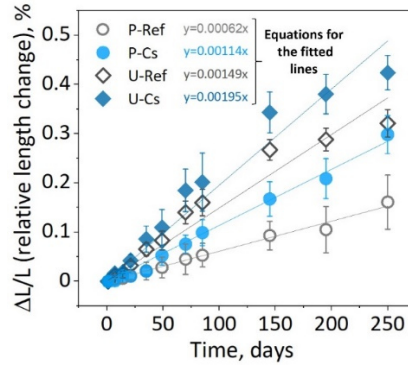


Figure C6. Linear regression analysis (not weighted by error bars) of the experimentally measured relative length change of the Cs-doped and reference specimens. It was performed to estimate and compare overall approximate rates of expansion. The coefficient of determination, R^2 , values are 0.994, 0.994, 0.974 and 0.977, for the P-Ref, P-Cs, U-ref and U-Cs specimens, respectively. The markers correspond to the average values of the relative length change of six distinct specimens, at each time point. The error bar of each marker corresponds to the standard deviation over those six distinct values.

C4.2. Comparison of experimentally measured and global affine registration-based estimates of length changes

In order to compare the experimentally measured relative length change values, $\frac{\Delta L_Z}{L_Z}$, with the respective value obtained by the global affine registration procedure, $\frac{\Delta L_{AFF,Z}}{L_{AFF,Z}}$, the following operative assumptions was made:

1. the six $\frac{\Delta L_Z}{L_Z}$ values, each from a distinct full specimen, were samples from a random variable with Gaussian distribution with mean value estimated by the average of the six samples, $\langle \frac{\Delta L_Z}{L_Z} \rangle$ (reported in Table T2 below), and standard deviation approximated by the empirical standard deviation of the six samples, $\sigma_{\frac{\Delta L_Z}{L_Z}}$ (also reported in Table T2 below); randomness in $\frac{\Delta L_Z}{L_Z}$ values stemmed not only from measurement errors but also from material heterogeneity;
2. if the tomographed volume, belonging to one of those six specimens and being slightly smaller than 30% of the total specimen volume, was representative enough of the whole specimen's volume, in terms of ASR-induced expansion, then the $\frac{\Delta L_{AFF,Z}}{L_{AFF,Z}}$ value (reported in Table TC3 below), obtained from its affine registration to the first tomogram of the same volume in the time series, at the beginning of the ASR acceleration, should be just another sample of the same random variable as at point 1.

Under the assumption at point 2 above, a $\frac{\Delta L_{AFF,Z}}{L_{AFF,Z}}$ value should differ from a $\frac{\Delta L_Z}{L_Z}$ one just by randomness (null hypothesis) with Gaussian statistics characterized by $\langle \frac{\Delta L_Z}{L_Z} \rangle$ and $\sigma_{\frac{\Delta L_Z}{L_Z}}$. As a consequence of such null hypothesis, the probability of measuring, by the affine registration of tomograms with such size, $\frac{\Delta L_{AFF,Z}}{L_{AFF,Z}}$ values differing in absolute value from $\langle \frac{\Delta L_Z}{L_Z} \rangle$ more than 1.96 times $\sigma_{\frac{\Delta L_Z}{L_Z}}$ should be smaller than 5%.

Table TC4 reports, for each specimen type, the absolute value of the difference between $\langle \frac{\Delta L_Z}{L_Z} \rangle$ and $\frac{\Delta L_{AFF,Z}}{L_{AFF,Z}}$, normalized by $\sigma_{\frac{\Delta L_Z}{L_Z}}$. Such values were computed either at identical or close enough times when the two variables, $\frac{\Delta L_Z}{L_Z}$ and $\frac{\Delta L_{AFF,Z}}{L_{AFF,Z}}$, were measured. A value in Table TC4 smaller than 1.96 corresponds to a probability smaller than 5% that the difference in the relative length change estimates was only due to randomness. In such a case, the null hypothesis can be rejected with 95% confidence, which was assume as confidence level. When that happens, it cannot be stated that the tomographed volume expanded in a way representative of the expansion of the whole specimen volume.

Table TC2: time series of relative length change values obtained by experimental measurements with the mechanical gauge, $\frac{\Delta L_Z}{L_Z}$. For each specimen type, only the average (Ave.) and the standard deviation

(Std.) values computed from the six specimens are reported. Such time series are plotted in Fig. 5.5(a) and in Figs. C7 and C8 above.

	U-Ref		P-Ref		U-Cs		P-Cs	
Time [days]	Ave. [%]	Std. [%]	Ave. [%]	Std. [%]	Ave. [%]	Std. [%]	Ave. [%]	Std. [%]
1	0	0	0	0	0	0	0	0
7	0.012	0.004	0.004	0.008	0.016	0.003	0.001	0.006
14	0.014	0.007	0.006	0.009	0.018	0.002	0.011	0.006
21	0.032	0.009	0.011	0.009	0.042	0.012	0.011	0.006
35	0.065	0.013	0.021	0.018	0.086	0.026	0.021	0.007
49	0.083	0.019	0.028	0.021	0.110	0.037	0.053	0.019
70	0.14	0.023	0.045	0.031	0.185	0.043	0.076	0.018
85	0.16	0.027	0.053	0.024	0.202	0.059	0.099	0.026
145	0.267	0.021	0.093	0.029	0.343	0.042	0.168	0.035
195	0.288	0.023	0.105	0.047	0.380	0.040	0.209	0.041
250	0.321	0.028	0.161	0.055	0.424	0.035	0.298	0.039

Table TC3: time series of relative length change values obtained from the global affine registration of the tomograms, $\frac{\Delta L_{AFF,Z}}{L_{AFF,Z}}$. For each specimen type, only one value is available because only one of the three tomographed specimens was analyzed. Such time series are plotted in Fig. 5.5 and in Figs. C7 above.

U-Ref		P-Ref		U-Cs		P-Cs	
Time [days]	Value [%]	Time [days]	Value [%]	Time [days]	Value [%]	Time [days]	Value [%]
1	0	1	0	1	0	1	0
						3	0.001
				7	0.010	7	0.018
				14	0.012	14	0.021
						21	0.03
						30	0.031
						50	0.048
				75	0.119	65	0.067
				120	0.235	85	0.13
155	0.254	155	0.069	155	0.344	145	0.2
				195	0.369	195	0.24
250	0.329	250	0.199	250	0.451	250	0.285

Table TC4: absolute value of the difference between the global affine registration-based relative length change of the tomographed volume and the average value of the experimentally measured relative length

changes, normalized by the standard deviation of the latter, $\frac{|\frac{\Delta L_{AFF,Z}}{L_{AFF,Z}} - \langle \frac{\Delta L_Z}{L_Z} \rangle|}{\sigma_{\frac{\Delta L_Z}{L_Z}}}$, where $\langle \frac{\Delta L_Z}{L_Z} \rangle$ means the average of the six values of $\frac{\Delta L_Z}{L_Z}$ while $\sigma_{\frac{\Delta L_Z}{L_Z}}$ is the empirical standard deviation of such six values.

Time [days]	U-Ref	P-Ref	U-Cs	P-Cs
7			1.89	2.96
14			2.80	1.53
21				3.09
50				0.24
85				1.18
150	0.60	0.83	0.01	0.93
195			0.27	0.77
250	0.30	0.69	0.77	0.34

C4.3. Mass changes

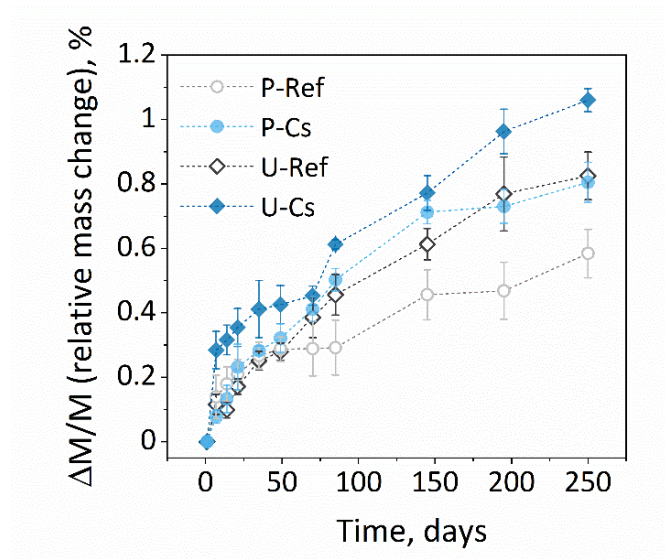


Figure C5. The relative mass changes of the Cs-doped specimens and their corresponding reference specimens during the ASR acceleration. For each mix type, the measurements were performed on the same exact six specimens on which the length was also measured, including among them the specimen being the subject of the tomography analysis. Each marker shows the average of the six values. Each error bars shows their standard deviation.

C5. Evolution of the mechanical properties for the specimens cast with Uri aggregates

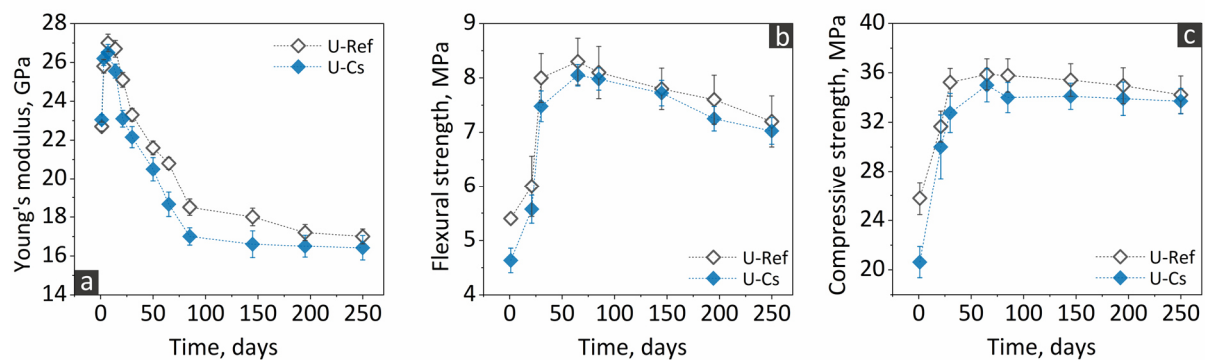


Figure C8. The time series of the (a) quasi-static Young's modulus, (b) the flexural and (c) the compressive strength of specimens with and without Cs addition, cast with U aggregates. In each plot, the markers indicate the average of three values from three distinct specimens, while the error bar indicates the respective empirical standard deviation. In the case of the Young's modulus, the measurements were successively performed always on the same specimens, which were the same used also for XT.

C6. Qualitative analysis of ASR cracking by time-lapse tomography.

Reference specimens

Figure C9 and Figure C10 showcase the crack network segmentation results for the reference specimens. They serve the double goal of (1) showing the quality of the segmentation results and of (2) illustrating some typical features of the cracking evolution in such specimens. For each aggregate type, a small ROI of the respective tomograms at three time points was selected as representative, because containing several evolving cracks. At times 155 and 250 days, the tomograms after the final non-affine registration were used. This choice allowed easier analysis of the temporal evolution, since the main difference between the tomograms is due to the evolving cracks.

The first row in each figure shows, at any time point, a specific 2D digital cross-section ($X - Y$ slice) from the chosen ROI. The position of the cross-section is the same at every time point. The second row shows the same slices as in the first one. However, overlapped on top of them and rendered in solid, blue/purple color, are the corresponding slices from the respective crack network binary tomograms. The overlapping helps with assessing the quality of the segmentation. It provides a qualitative idea about whether the majority of the cracks are segmented, which ones are typically not and to which degree single cracks are segmented (in terms of length and width). The segmented, full crack network is shown in the third row as a 3D solid volume rendering, for any time point. The parallelepiped box containing it indicates the tomographed volume of the specimen. Note that the point of view of the rendering of the 3D scene is the same at any time point, such that it is easier to track the cracking and to compare the crack network at successive time points. The last row shows the rendered crack network at the last time point (250 days) overlapped on top of the 3D rendering of the respective, non-affine registered tomogram, made semi-transparent. Such rendering is shown twice, from two distinct points of view.

On the one hand, the time series of a single slice shows that several parts of the crack network evolved both in length and in width and, in several cases, starting from cracks already existing at 1 day, i.e., before the ASR acceleration started. On the other hand, the time series of 3D renderings of the full crack network shows that the cracks were rather homogeneously distributed inside the tomographed volume. The latter is a feature to be expected since (1) ASR cracking mainly starts inside aggregates and (2) the specimens had stress-free boundary conditions. The 3D rendering of the segmented crack network at time = 250 days also shows that the chosen U-Ref specimen clearly achieved a larger crack volume fraction (total crack volume divided by tomogram volume) than the chosen P-Ref one. Such result was confirmed for all the specimens by the quantitative analysis of their crack networks (see Figure 5.8 and Figure C18).

More details of the ASR cracks are visible in Figure C11, which shows zoom-in ROIs from the $X - Y$ slices shown in insets (a) – (c) of Figure C9 and Figure C10. Such figure is organized exactly as insets (a) – (f) of Figure C9 and Figure C10. In addition to provide a better view of some details of the cracks, the quality level of the crack segmentation can be better appreciated in Figure C11 (d) – (f) and (j) to (l), for the P-Ref and U-ref specimens respectively.

Examples of cracks which appeared to be filled with ASR products are pointed at in Figure C9 (b), Figure C10 (b) and Figure C11 (b) and (h). These examples show the very small X-ray attenuation contrast between the natural products and the other material phases of the aggregate and in the cement paste. Such small contrast and the limited tomographic spatial resolution (in comparison to the thinnest cracks at early and intermediate times) made it challenging, even for the human eye, to detect the products inside the cracks, let alone their systematic segmentation by algorithms.

Figure C12 shows the binary tomograms of the segmented cracks at the three time points of Figure C9 and Figure C10 and for the same specimens. Such binary tomograms are rendered with distinct colors and superimposed on top of each other in the order 250, 150 and 1 days. Its insets (a) and (c) show 2D ROIs from a slice while (b) and (d) show the 3D rendering.

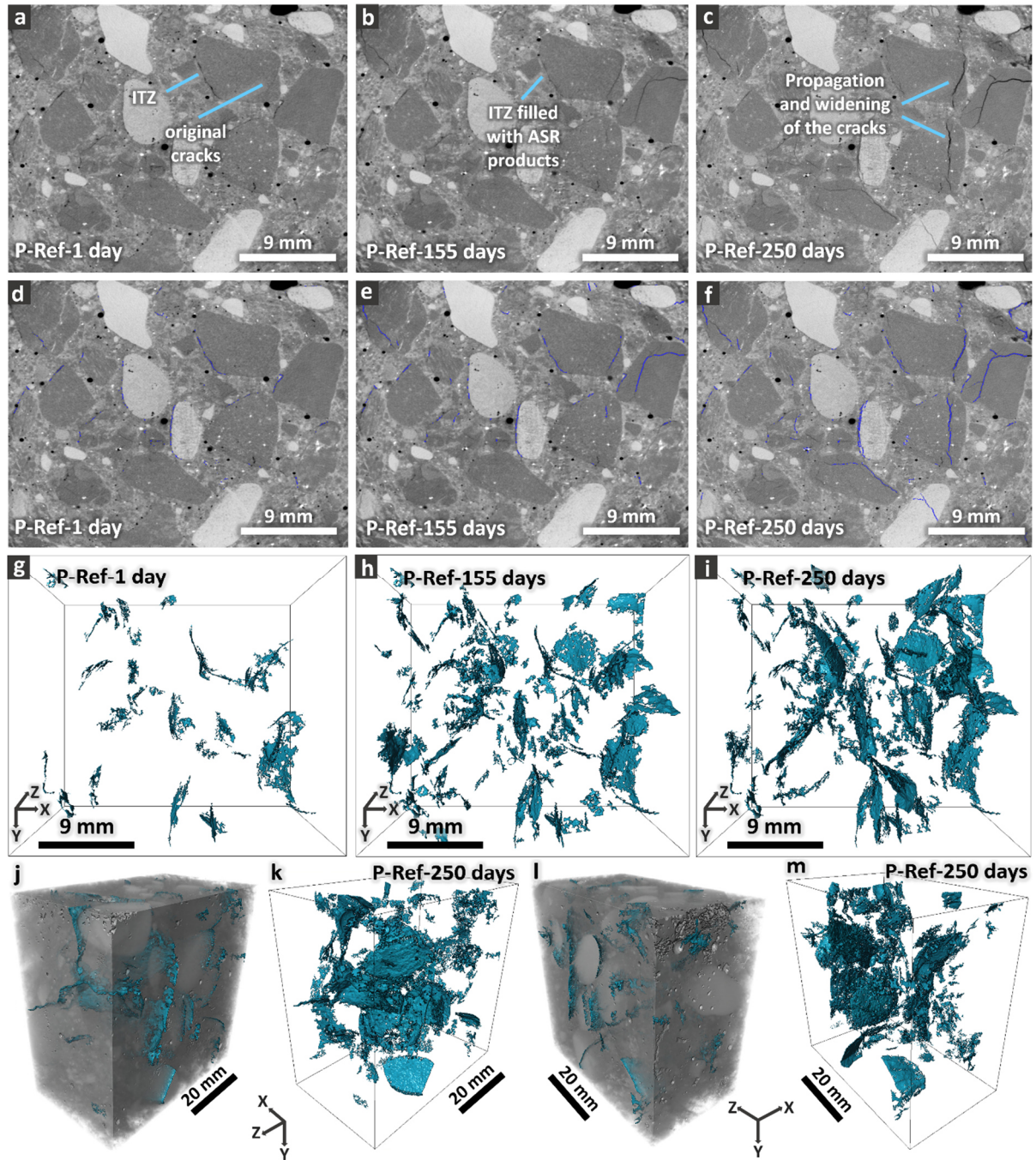


Figure C9. Temporal evolution of the crack network in the P-Ref specimen. (a)-(c): 2D cross-section ($X - Y$ slice) from a small ROI of the tomogram at 1 day, 155 days and 250 days, respectively. The position of the slice and of the ROI is the same at any time point. The tomograms at 155 and 250 days are those obtained as output from the final non-affine registration. (d)-(f): the same slice as in (a)-(c) and, overlapped on top of it and in blue/purple color, the corresponding slice from the corresponding crack binary tomogram. (g)-(i): 3D rendering of the crack binary tomogram for the full tomographed volume of the specimen. (j) and (l): 3D rendering in semi-transparent grey tones of the non-affine registered tomogram at time = 250 days and, overlapped on top of it, the correspondingly segmented crack network, also shown independently in (k) and (m), respectively. Two distinct points of views for rendering the 3D scene.

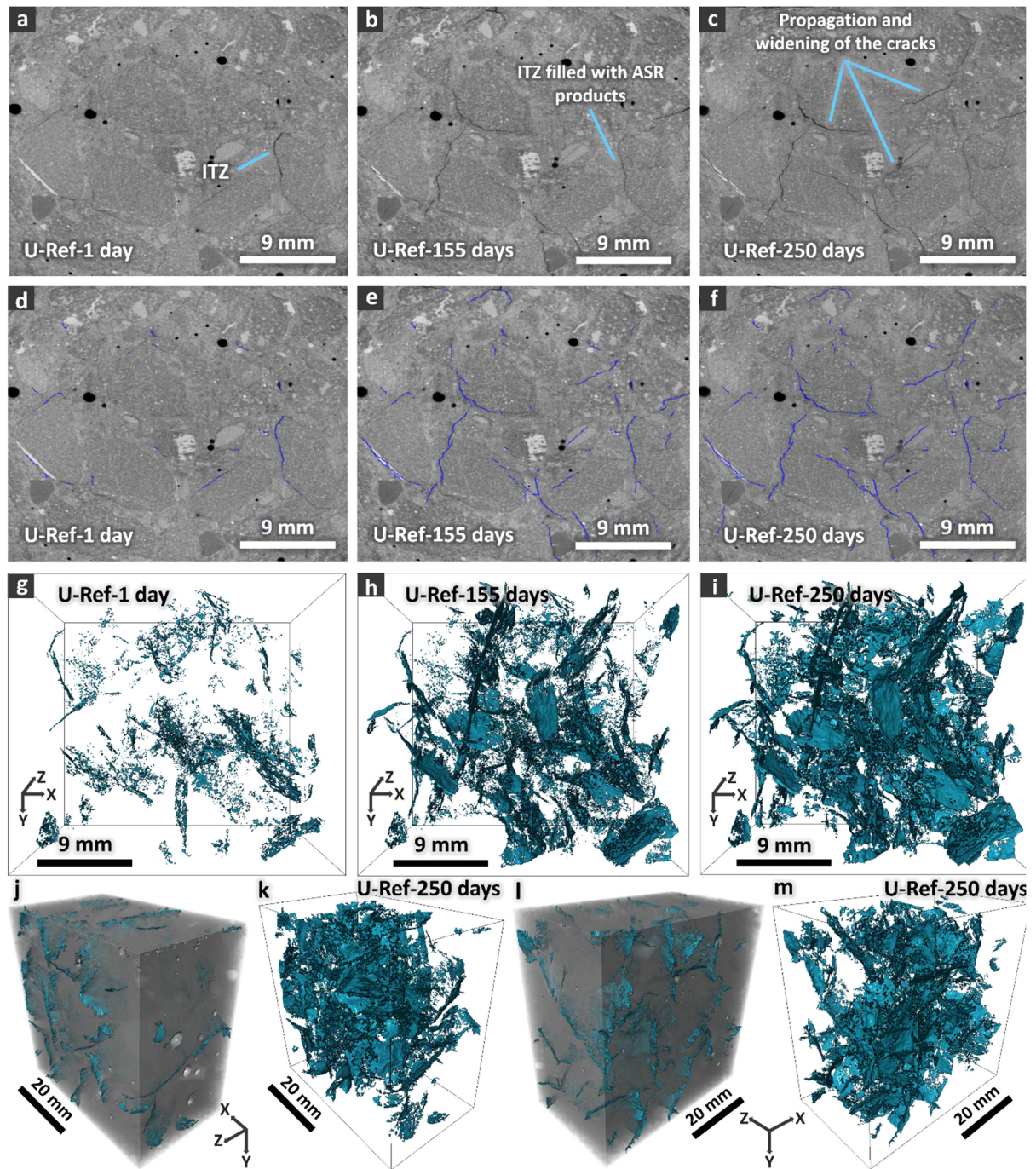


Figure C10. Temporal evolution of the crack network in the U-Ref specimen. (a)-(c): 2D cross-section ($X - Y$ slice) from a small ROI of the tomogram at 1 day, 155 days and 250 days, respectively. The position of the slice and of the ROI is the same at any time point. The tomograms at 155 and 250 days are those obtained as output from the final non-affine registration. (d)-(f): the same slice as in (a)-(c) and, overlapped on top of it and in blue/purple color, the corresponding slice from the corresponding crack binary tomogram. (g)-(i): 3D rendering of the crack binary tomogram for the full "tomographed" volume of the specimen. (j) and (l): 3D rendering in semi-transparent grey tones of the non-affine registered tomogram at time = 250 days and, overlapped on top of it, the correspondingly segmented crack network, also shown separately in (k) and (m), respectively. Two distinct points of views for rendering the 3D scene.

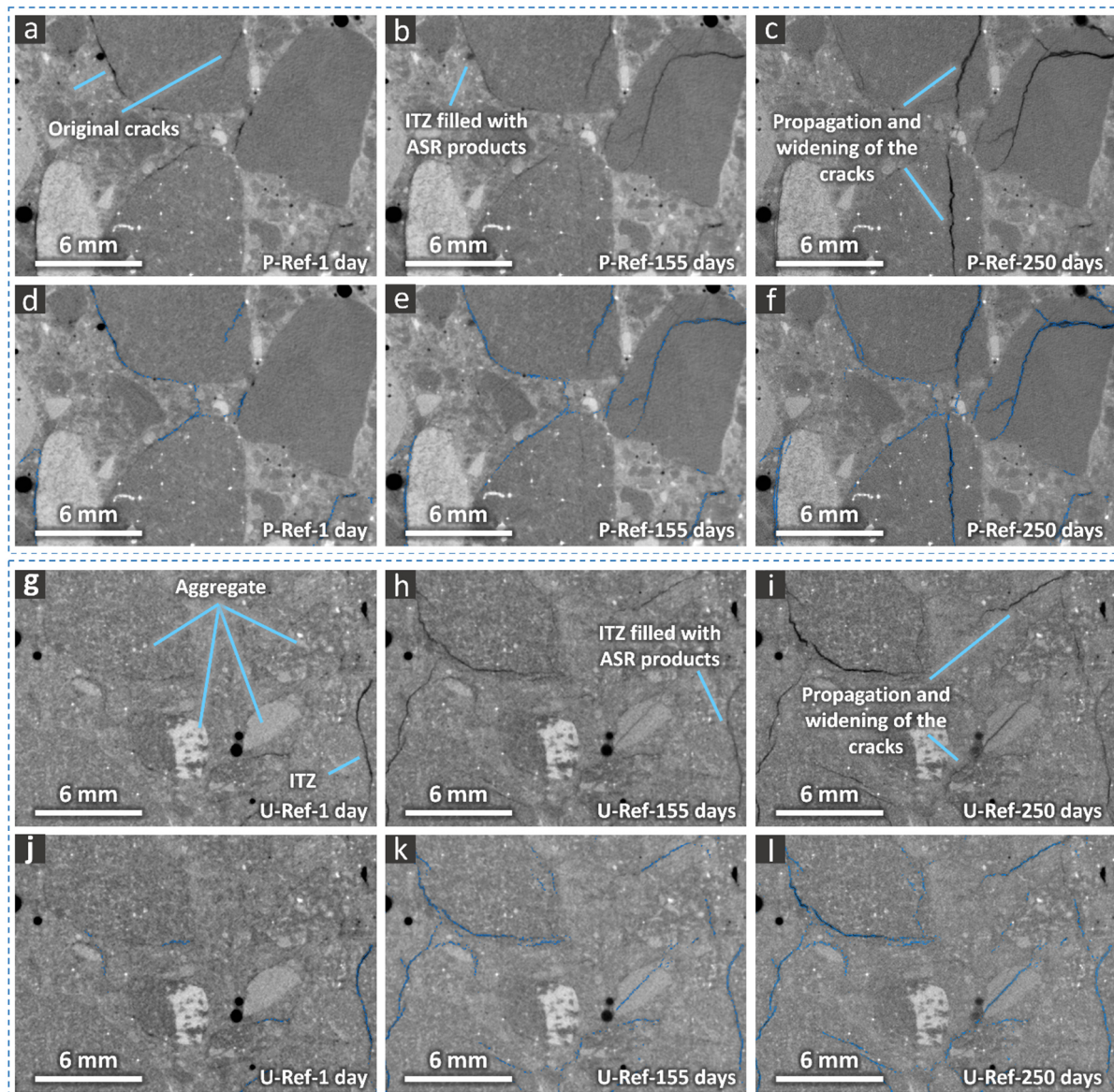


Figure C11. Smaller region of interest (ROI) from the slices shown in Figure C9 and Figure C10 in insets (a)-(f), summarized in a single image to facilitate the visibility and the comparison.

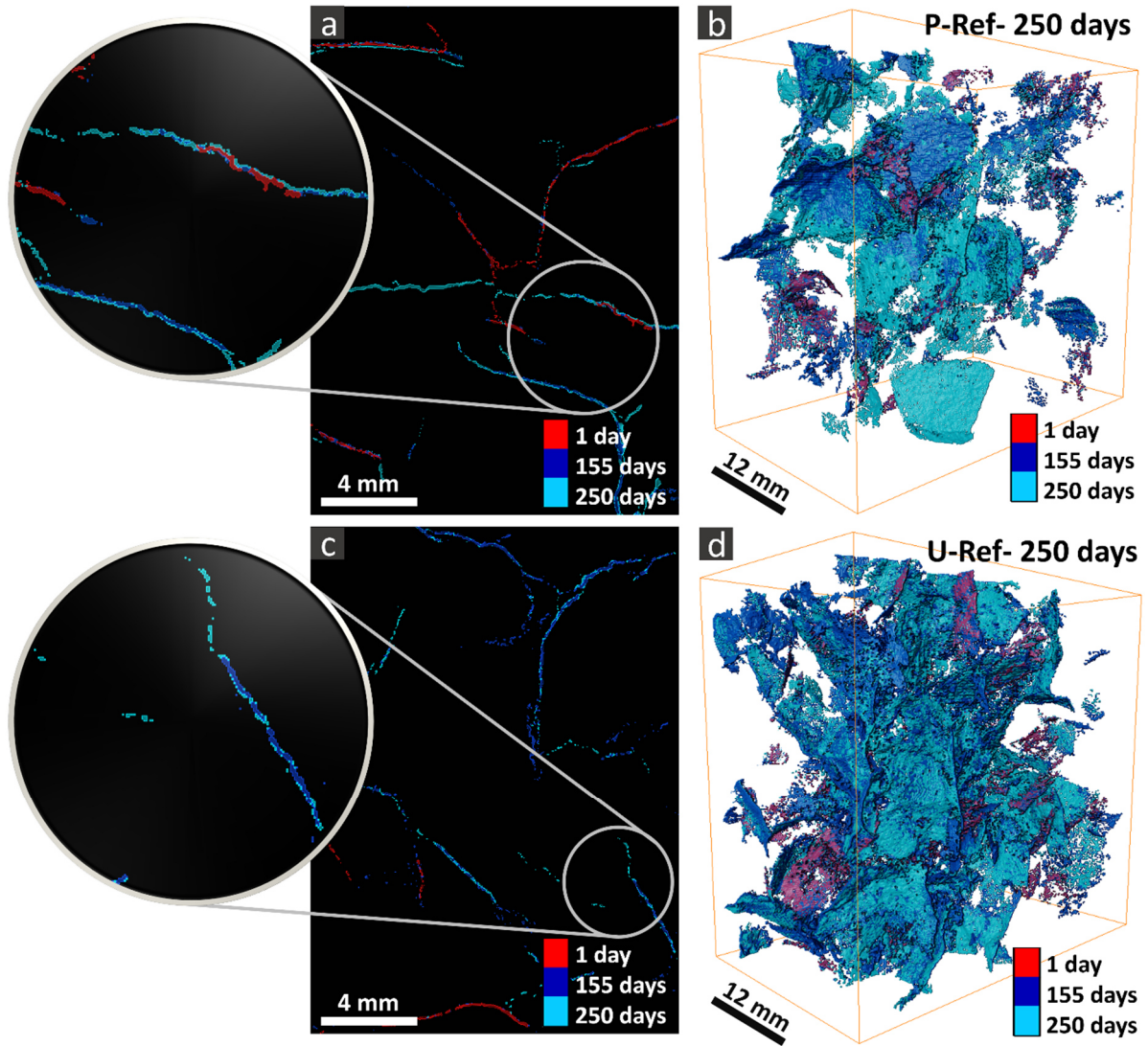
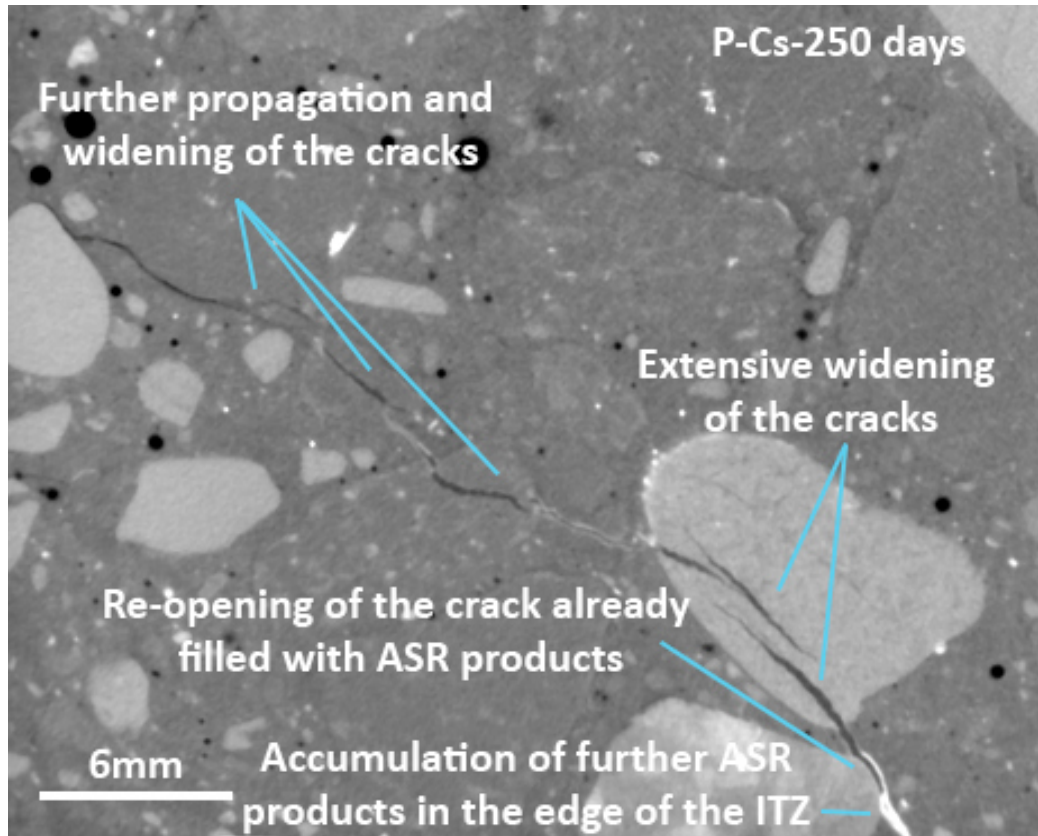


Figure C12. Visualization of the time evolution of crack networks. Examples from the reference specimens. Top row: P-Ref specimen. Bottom row: U-Ref specimen. Left column: in each row, 2D digital cross-section taken from a ROI fixed at the three distinct time points (color coded). The binary tomograms were overlapped in order of decreasing time. Right column: 3D rendering of the overlapped crack network binary tomograms of the two reference specimens, at the same three time points as in insets (a) and (c), respectively.

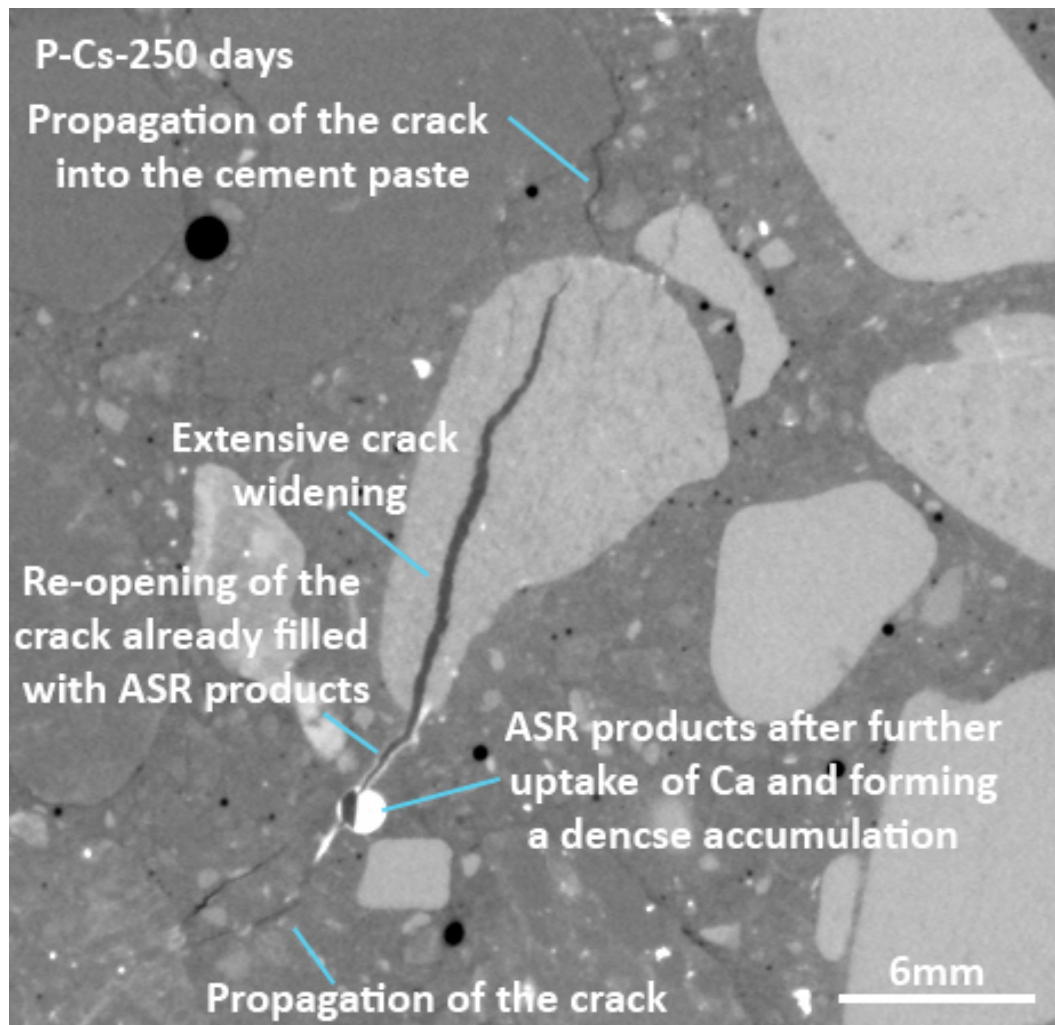
C7. Qualitative analysis of ASR cracking by time-lapse tomography.

Cs-doped specimens

P-Cs specimen



Movie MS1: last frame of a movie simply consisting of the sequence of a ($X - Y$) slice taken from the same ROI of the tomograms of the P-Cs specimen. All the tomograms in the time series of this specimen were used to create the movie. The positions of the ROI and of its slice were always the same, at each time point. At times > 1 day, the "non-affinely" registered tomograms were used to allow full sequential comparability of the slice at the distinct time points. The ROI used for this movie contained the one used for Figure 5.7. The blue line in each frame points to the main aggregate of interest, which is the same aggregate as in the center of the slices shown in Figure 5.7. The slice shown in this movie was not at the same exact position as the one used for Figure 5.7. The movie file is MS1.avi, in the uncompressed AVI format (readable by Microsoft Windows Media Player or any other media player, e.g., VLC), or MS1.mov, in the MPEG4-compressed format (readable by QuickTimeX or Quicktime Pro on Apple's computers) and is available at <https://doi.org/10.5281/zenodo.4813591>.



Movie MS2: last frame of a movie simply consisting of the sequence of a (Z – Y) slice taken from a ROI of the tomograms of the P-Cs specimen, the ROI being different as the one considered in Movie MS1 but containing the ROI of the slice shown in Figure 5.8. All the tomograms in the time series of this specimen were used to create the movie. The positions of the ROI and of its slice were always the same, at each time point. At times > 1 day, the "non-affinely" registered tomograms were used to allow full sequential comparability of the slice at the distinct time points. The blue line in each frame of the movie points to the main aggregate of interest. The movie file is MS2.avi, in the uncompressed AVI format (readable by Microsoft Windows Media Player or any other media player, e.g., VLC), or MS2.mov, in the MPEG4-compressed format (readable by QuickTimeX or Quicktime Pro on Apple's computers) and is available at <https://doi.org/10.5281/zenodo.4813591>.

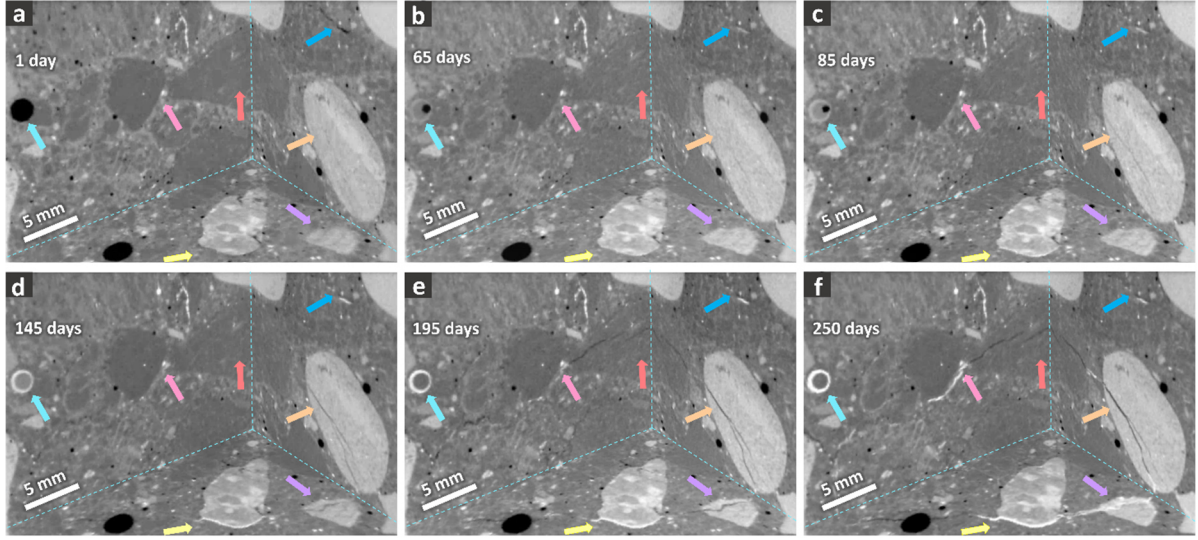


Figure C13. An additional example of tomographic time series showing the corner of three mutually orthogonal 2D cross-sections ("ortho-slices") from another ROI of the P-Cs specimen. The specific time points at which the images are provided include: (a) 1 day, (b) 65, (c) 85, (d) 145, (e) 195 and (f) 250 days. The light cyan arrow refers to an air void which gets filled with ASR products. The blue arrow showcases an ITZ, being filled with ASR products. The orange arrow points to part of an aggregate with a pre-existing crack which started to open up before other regions in this ROI. The purple arrow refers to the tip of the same aggregate, as the one pointed at by the orange arrow, observed in another ortho-slice. It helps to visualize the fact that this aggregate first widened due to small products at its edges. Then, such products acted like a "jack" which pushed the pieces of that aggregate apart. The opened crack then got filled with further ASR products. The pink arrow shows the ASR products being extruded from another aggregate to the ITZ of its neighbouring aggregate. The yellow arrow also shows similar phenomena as those highlighted by the pink arrow but in the ITZ of another aggregate.

Figure C14 below shows, for the P-Cs specimen, a time series of two binary tomograms (only parts thereof) rendered in 3D as solid, colored volumes and overlapped on top of each other. The empty crack binary tomogram, $\{\tilde{I}_{ASR\ crack}^B(\vec{x}_j, t_i)\}_{j=1, \dots, N}$, is rendered in cyan. The ASR product one, i.e., the union of $\{\tilde{I}_{ASR\ prod.-crack}^B(\vec{x}_j, t_i)\}_{j=1, \dots, N}$ and of $\{\tilde{I}_{ASR\ prod.-void}^B(\vec{x}_j, t_i)\}_{j=1, \dots, N}$, is rendered in yellow. What is shown in yellow corresponds to the part of the segmented pore space filled with products, including also the parts of the crack network which are filled.

Not the full binary tomograms are rendered in such figure. For each binary tomogram, each voxel cluster with volume smaller than 10^{-3} mm^3 was excluded from the rendering. Such exclusion allowed for reducing the clutter of 3D objects in the rendered scene while focusing on the most relevant and largest portions of both the crack network and of the ASR products. The insets (g) and (h) show the same

rendering as in inset (f), except for (1) using a different point of view and (2) rendering only the regions filled with ASR products (inset (h)).

The visual comparison of the crack networks rendered in Figure C9 and in Figure C14 provides already qualitative evidence of larger crack volume fraction (crack volume *per* tomogram volume) in the chosen P-Cs specimen compared with the chosen P-Ref one. Notice that, in the case of the P-Cs specimen, the cracks filled with ASR products are colored in yellow and are those 3D objects with high aspect ratio. Such qualitative result is generalized and quantitatively confirmed by the data reported in Figure 5.10.

A general, qualitative feature of the segmented ASR products in the P-Cs specimen is that they could be observed as being distributed in a very uniform way in the tomographed volume, in some cases even far away from the aggregates or the cracks inside them or propagated inside the cement paste. Their extrusion from the aggregates into the cement paste, via opening and propagating cracks, may have not been the only reason for their presence even far away from the cracks themselves. They may have accumulated as well inside aggregate particles with size smaller than or close to the spatial resolution of the tomograms, thus not directly identifiable by visual inspection.

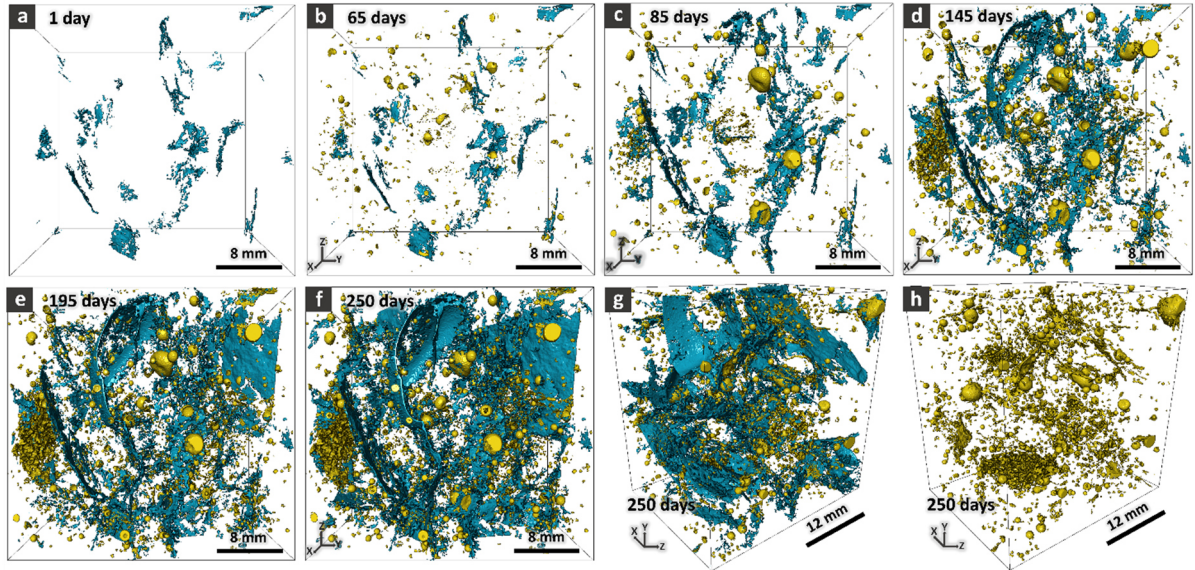


Figure C14. (a)-(f): 3D rendering of the segmented empty crack network $\{\tilde{I}_{ASR\ crack}^B(\vec{x}_j, t_i)\}_{j=1,\dots,N'}$ in cyan) and of the segmented ASR products (both inside cracks, $\{\tilde{I}_{ASR\ prod.-crack}^B(\vec{x}_j, t_i)\}_{j=1,\dots,N'}$ and outside them, $\{\tilde{I}_{ASR\ prod.-void}^B(\vec{x}_j, t_i)\}_{j=1,\dots,N'}$ in yellow) for the tomographed part of the P-Cs specimen. Distinct insets refer to distinct time points: (a) 1 day; (b) 65 days; (c) 85 days; (d) 145 days; (e) 195 days; (f) 250 days. (g) Same as in (f) except for a distinct point of view. (h) Same as in (g) but showing only the ASR products.

U-Cs specimen

Cracking and ASR product extrusion occurred in the U-Cs specimens with similar features and patterns as in the P-Cs specimen.

Figure C15 is the analogue of Figure 5.7 and Figure 5.8 but refers to a small ROI from the U-Cs specimen. It shows few, minor differences compared with the P-Cs specimen. They mainly concerned (1) the ASR product distribution, (2) its quantity and (3) the fraction of ASR-affected aggregates.

For the U-Cs specimens, the observation of ASR products in the aggregate interior regions was more frequent than for the P-Cs specimens, especially at later ASR acceleration times. This was at least the case at a length scales above the tomograms' spatial resolution used in this study. See Figure C15 (c) and (d) for examples. This in general indicates the higher propensity of the U aggregates to ASR. It might be associated with their mineral texture.

Since resolvable ASR product accumulation inside aggregate cracks (in addition to paste cracks and air voids) happened more frequently for the U aggregates than for the P ones, a considerable portion of regions containing ASR products had an elongated, crack-like morphology in the U-Cs specimen. On the contrary, the regions containing ASR products in the P-Cs specimen had mainly a rather isotropic shape. Compare Figure C14 with Figure C16, for some examples. Such difference points at a higher crack filling ratio by ASR products in the U-Cs specimen than in the P-Cs one.

Figure C17 shows, for the U-Cs specimen, more details of the ASR crack propagation and products extrusion by focusing on a single, small ROI containing a single aggregate, just as similarly visualized in Figure 5.9 for the P-Cs specimen.

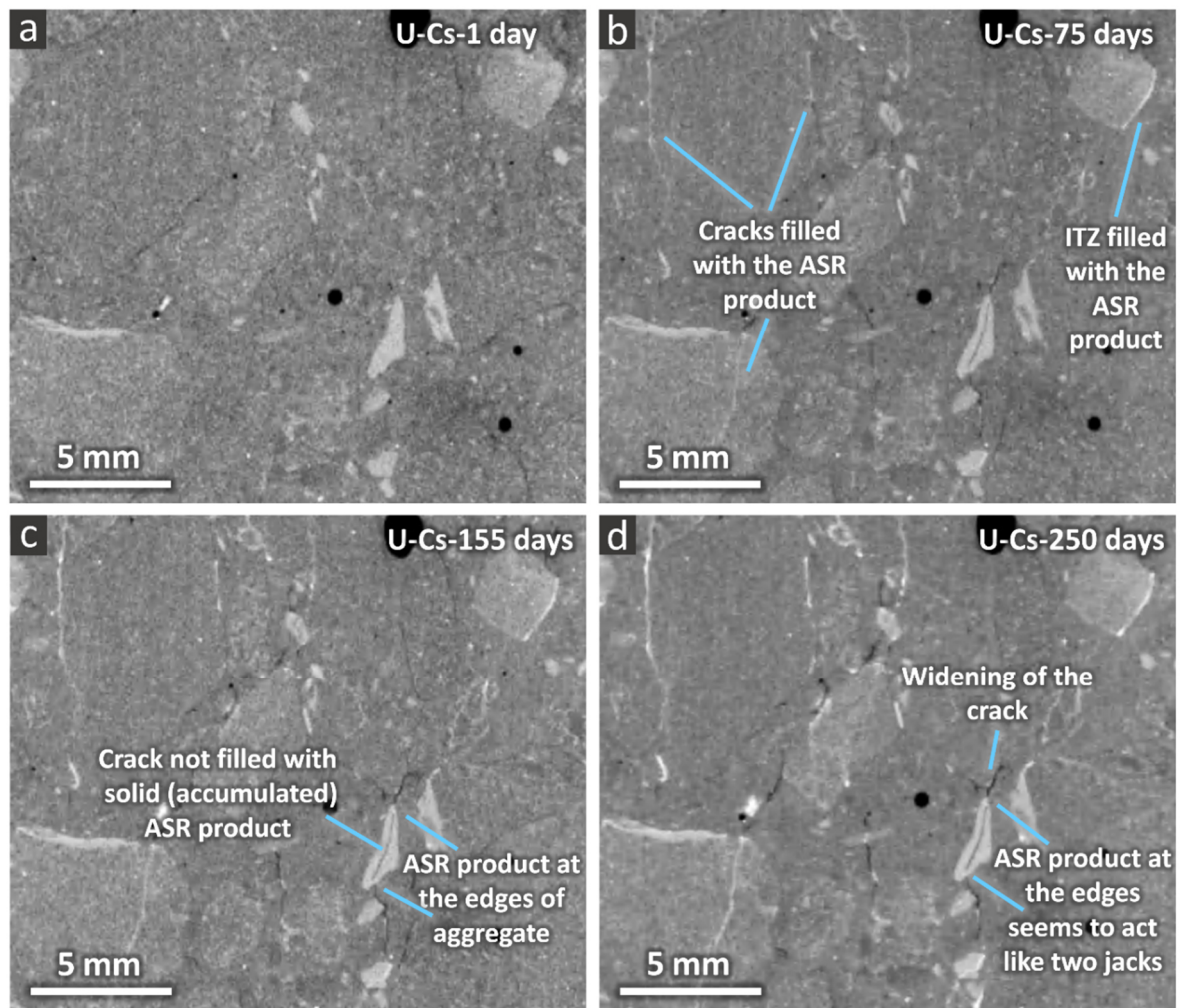


Figure C15. A slice from a ROI of the U-Cs specimen at four different time points. ASR products can be observed as very bright regions within cracks and near the aggregate boundaries. The four slices shown here are from the tomograms at (a) 1 day, (b) 75 days, (c) 155 days and (d) 250 days, respectively.

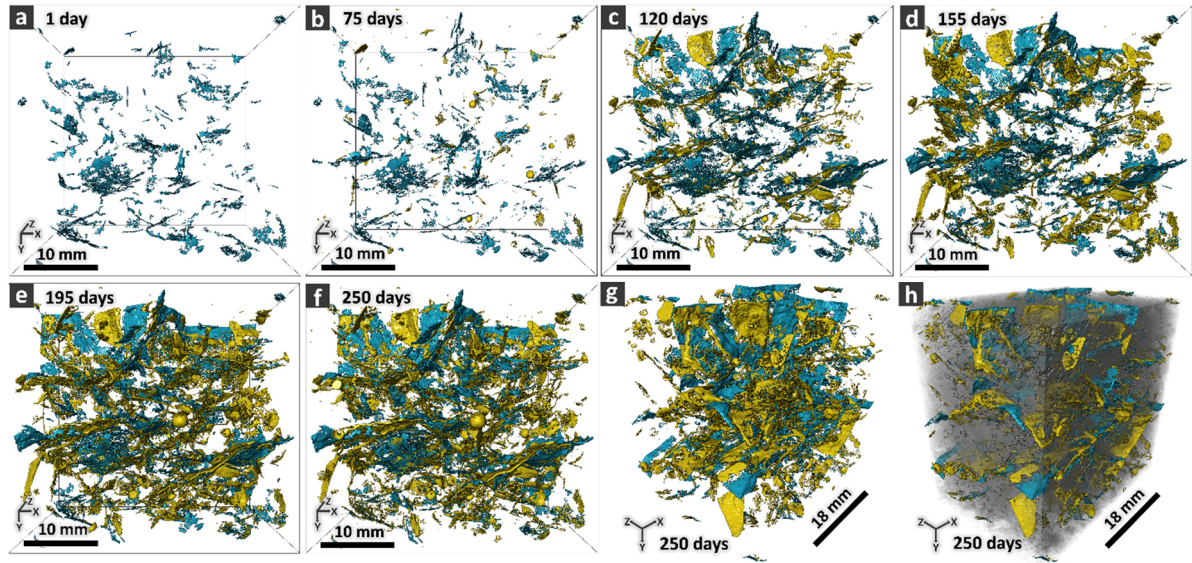


Figure C16. Same as in Figure S 26 but for the tomographed part of the U-Cs specimen. In inset (h), instead of showing only the rendering of the segmented ASR products, also the empty crack network is shown, in addition to the rendering, in semi-transparent grey tones, of the fully registered tomogram at 250 days.

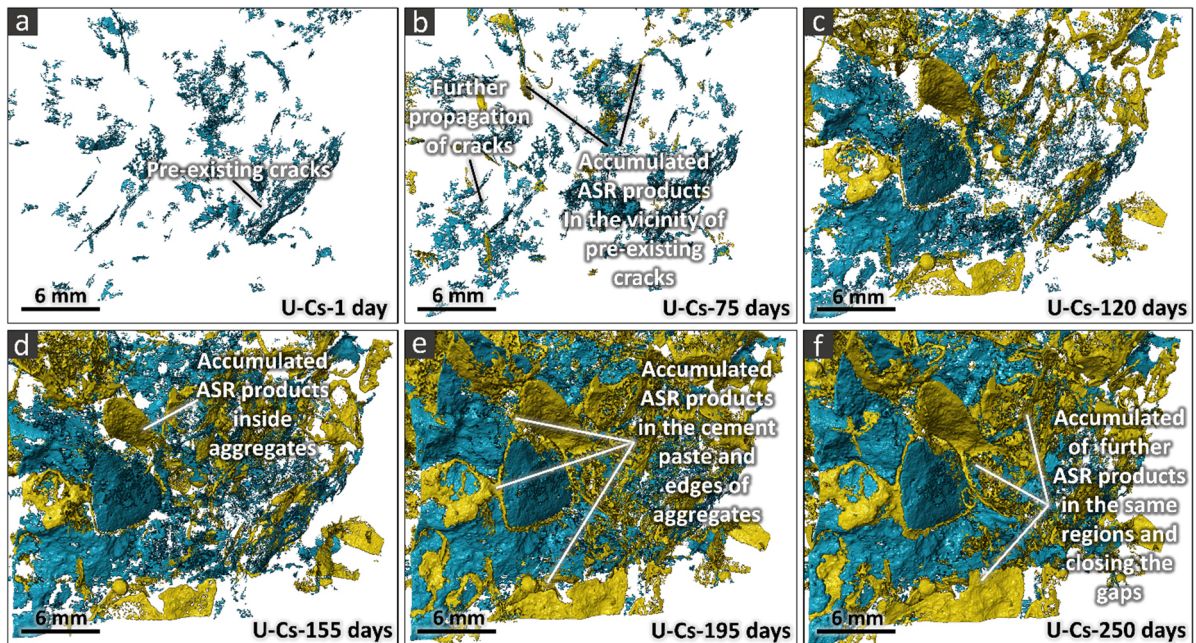


Figure C17. A small ROI of the binary tomograms of empty cracks (in cyan) and of ASR products (both inside and outside cracks, in yellow) is rendered for the U-Cs specimen. Such ROI contained cracks which were nucleated in an aggregate and further propagated into the surrounding cement paste. The insets from (a) to (f) correspond to different time points during the ASR acceleration, including 1 day, 75, 120, 155, 195 and 250 days, respectively.

C8. Quantitative analysis of ASR cracking by time-lapse tomography.

Volume fractions.

The left column of Figure C18 shows the time series of the normalized volume of ASR-generated cracks, $V_{ASR\ cracks}$, as well as the normalized volume of ASR products (inside and outside cracks). The normalization of both volumes was performed by the tomogram's volume, $V_{tomogram}$. In addition to the time series for the P specimens, already shown in Figure 5.10, those of the U specimens are also shown.

The right column of Figure C18 shows the time series of the volume of ASR-generated cracks normalized by the volume of cracks detected at the reference time $t_0 = 1$ day, when the ASR acceleration started. Such normalized volume is defined as

$$\frac{\Delta V_{tot,crack}}{V_{tot,crack}}(t_i) = \frac{V_{tot,cracks}(t_i) - V_{tot,cracks}(t_0)}{V_{tot,cracks}(t_0)}, \forall i = 1, 2, \dots, N_t \quad (EC\ 1).$$

While the $\tilde{V}_{ASR\ cracks}$ time series in the left column allow comparing the ASR crack volume evolution independently of the tomographed volume's size, those in the right column allow comparing its evolution independently of the amount of cracks existing before the ASR acceleration started.

The results shown in Figure C18 and those shown in Figure 5.5 and Figure C5 suggest the existence of a positive correlation between the 1D expansion and the volume of ASR-generated cracks. For example, the U-Ref specimens expanded, along any direction, more than the P-Ref ones (compare Figure 1 with Figure C5). The U-Ref tomographed volume exhibited a larger ASR cracks volume than that of the P-Ref volume (compare Figure C18 (c) with Figure C18 (a)). The same pattern is found when the comparing is performed between the Cs-doped specimens or, for any aggregate type, it is performed between specimens without and with Cs-doping. Such positive correlation is more appreciable by the scatter plot in Figure C19, showing the relative length change, as measured by the mechanical gauge, of the tomographed specimen *versus* its tomographed volume's $\tilde{V}_{ASR\ cracks}$.

The U-Cs specimen exhibited at almost any time point larger values of the normalized volume of ASR products than the P-Cs one. As already observed in Figure C14, in the case of the P-Cs specimen, the majority of the ASR products were located in the air voids or in (low aspect ratio) aggregate pores. Whereas, in the cases of the U-Cs specimen (Figure C16), the products accumulated not only in the low

aspect ratio pores, but also inside cracks in aggregates and in the paste. In order to quantify such difference, the ratio between the volume of ASR products inside cracks and the total volume of cracks (empty or filled) was computed (**ASR cracks filling ratio**, see Figure C20). At 250 days, the U-Cs specimen had about 80% of its crack network filled with products, while the P-Cs specimen achieved 30%. The crack filling was quite slow at the beginning, for both aggregate types (Figure C20). Only at 120 days, the specimens with the two aggregate types started to exhibit a significant difference in cracks filling ratio. After 195 days the cracks filling ratio rate seemed to decline. That may have mirrored the prevalence, from that point on, of product accumulation in the air voids (or in other parts of the pore space) rather than only within the ASR cracks.

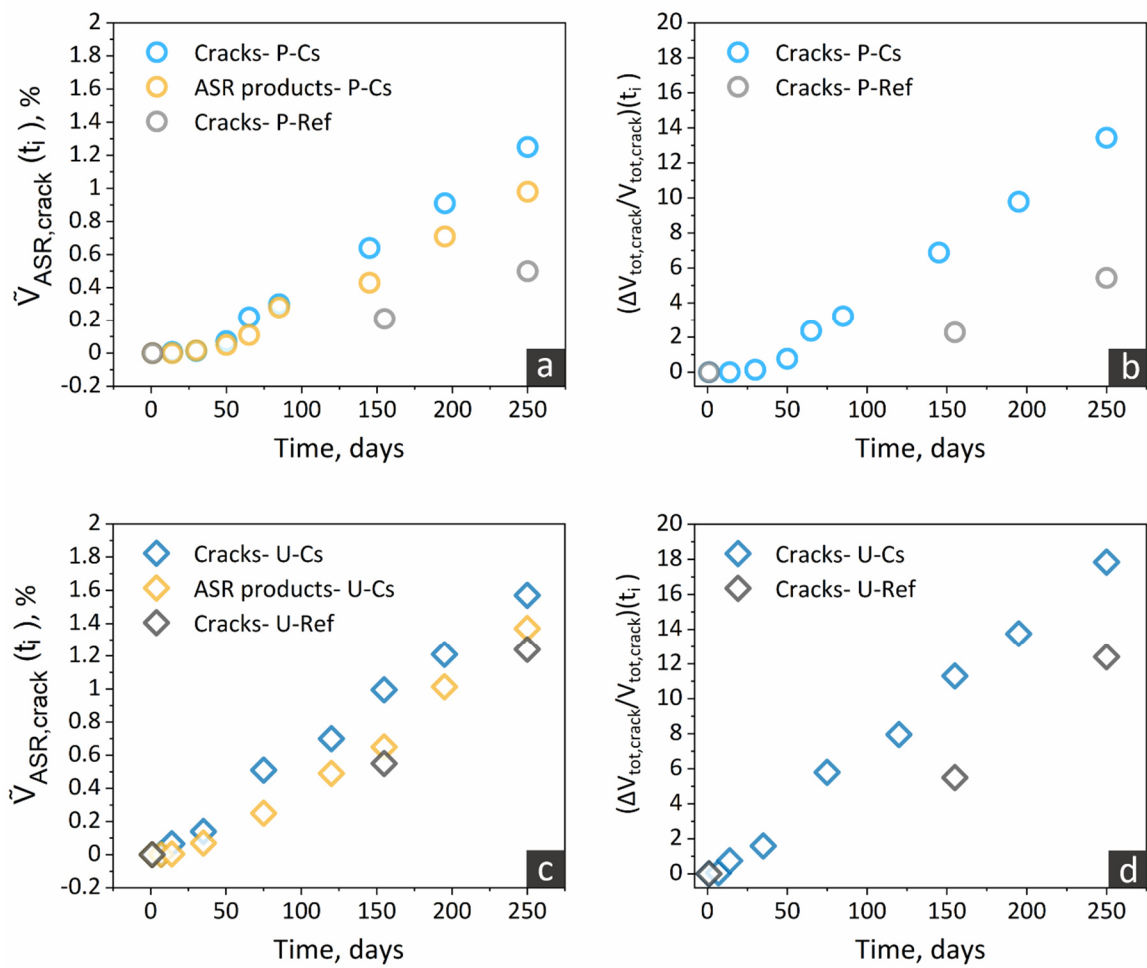


Figure C18. Quantitative comparison of the ASR cracking in different specimens based on the estimates of two variables: (1) the total volume of ASR-induced cracks (with or without ASR products), normalized by the tomogram volume (named as $V_{ASR\ cracks}$) for the (a) P-Cs and (c) U-Cs specimens, respectively. the total volume fraction of ASR products in each specimen is also shown as yellow markers in each corresponding plot; (2) the total volume of ASR-generated cracks normalized by the volume of cracks at the reference time $t_0 = 1$ day, i.e., cracks existing before the start of the ASR acceleration (the latter variable named as $\frac{\Delta V_{tot,crack}}{V_{tot,crack}}$) for the (b) P-Cs and (d) U-Cs specimens, respectively.

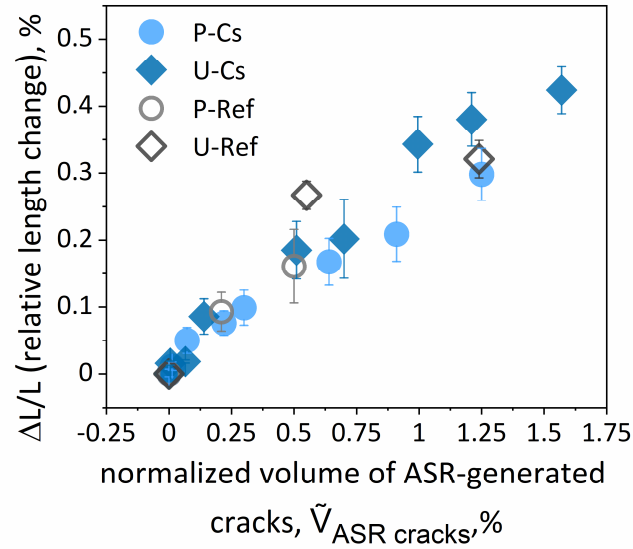


Figure C19. Scatter plot of the ASR-generated crack volume (normalized by the tomogram volume, $\tilde{V}_{ASR \text{ cracks}}$, see Eq. (3.6)) and the whole-specimen relative length change measured with the mechanical gauge (see Figure 5.5 and Figure C5 for the P and U specimens, respectively). Empty markers refer to the specimens without Cs-doping. Solid markers refer to the specimens with Cs-doping. For each specimen type, the relative length change values are the average of experimentally measured values of relative length changes for six specimens (including the one being the subject of the tomography analysis) of each mix type. The error bars show their standard deviations.

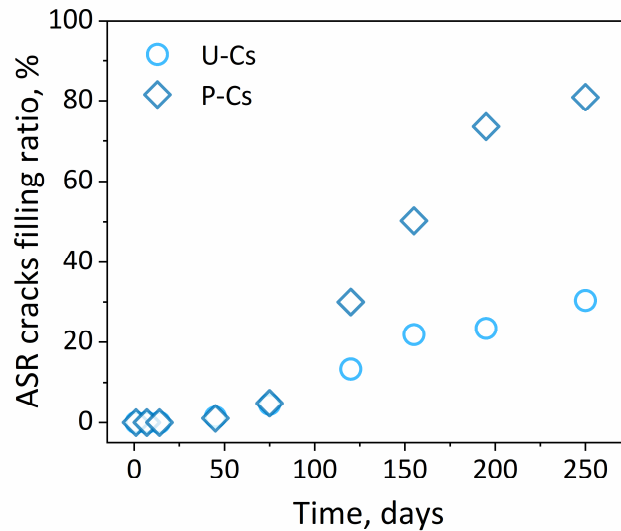


Figure C20. Time series of the ASR cracks filling ratio, defined as the volume of ASR products classified as belonging to cracks divided by the volume of the total crack network (i.e., ASR cracks containing or not products).

C9. Quantitative analysis of ASR cracking by time-lapse tomography: Crack network features.

C9.1. Shape tensor analysis of the separated cracks.

Validation and meaningfulness. Insets (a)-(c) in Figure C21 show 3D renderings of the segmented, total crack network (with or without ASR products) of the U-Cs specimen at three distinct time points (120, 155 and 250 days in insets (a), (b) and (c), respectively). Distinct, disconnected branches of the network (simply termed as separate cracks) are rendered with distinct colors. With time, the color of a branch may change as it becomes connected with other branches and becomes part of a new, distinct crack.

Such 3D renderings provide a qualitative idea about the complex evolution of the overall crack network, characterized by a dynamic reorganization of the relative locations of its distinct and separate branches. Despite such complexity, it is evident that several branches of the network can be clearly distinguished. This feature means that (1) the segmentation captured a significant part of the resolvable crack volume and (2) the crack network labelling managed to recognize as distinct parts the different branches of the network.

Figure C22, Figure C23 (a) to (c) and Figure C24 are analogous to Figure C21 (a) to (c). They refer to the U-Ref, P-Cs and P-Ref specimens, respectively.

The comparison of Figure C22 with Figure S 36 clearly provides qualitative evidence of less cracking in the P-Ref specimen (Figure C24) than in the U-Ref one (Figure C22). The comparison of Figure C21 (a)-(c) with Figure C23 (a)-(c) suggests a higher "fragmentation degree" of the crack network in the P-Cs specimen compared with the U-Cs one.

The shape tensor analysis, performed at each time point for the segmented crack network of each specimen, allowed validating or not qualitative observations like the previous one, which relied only upon visual inspection of the 3D rendering of the labelled crack network.

Figure C21 (d) to (f) shows the 3D renderings of three separate cracks, respectively. They belong to the U-Cs specimen at 250 days. These cracks were selected as examples because they have, from (d) to (f), increasingly complex morphology, e.g., surface folding and fragmentation. While the large, orange box in each inset indicates the tomographed volume, the small blue box is the bounding box of the individual crack, as computed by its shape tensor analysis. Such box is oriented along the three *eigenvectors* of the

shape tensor \mathbf{G} of the crack. The *eigenvectors* are rendered as solid arrows, starting from the center of mass of the crack itself.

Such type of visual analysis allowed validating qualitatively the shape tensor analysis results. The size of an object along the direction of one *eigenvector* of \mathbf{G} may not necessarily provide useful, quantitative information about the object itself. The shape tensor analysis, in this regard, may be hindered or biased just as it happens with other approaches to estimate size and orientation of a 3D object. That is because the definition of size and orientation is an ill-posed problem for 3D highly convoluted and irregularly shaped objects, as separated cracks are. Indeed, there is no unique and unequivocal definitions of size and main orientation of an object with arbitrary shape.

In the specific case of this study, the type of visual analysis mentioned above showed that the directions of the three *eigenvectors* of \mathbf{G} provided, for most of the cracks, the right information about the directions of maximum, intermediate and minimum spatial extent of the crack, despite its eventual complex morphology. Figure C21 (d)-(f), for the U-Cs specimen, and the analogous Figure C23 (d)-(f), for the P-Cs specimen, showcase this result. Correspondingly, the lateral sizes of the mentioned crack bounding boxes (length L , height H and thickness T) could be, for a majority of the cracks, meaningfully used for a quantitative assessment of the crack sizes. That was valid for both the reference and the Cs-doped specimens and for each aggregate type. The exceptions consisted of cracks with rather folded surface, e.g., concave cracks as those shown in Figure C25. For such cracks, the bounding box thickness T achieved values which significantly overestimated the scale of an actual crack thickness. In order to avoid the statistics of an indicative crack thickness being spuriously biased by such overestimated boundary box thickness values, this feature variable was not adopted as indicative crack thickness. Instead, the statistics of the crack network's local thickness field, $T_{local}(\vec{x})$ were analyzed.

Finally it has to be remarked that estimates of crack length and crack height/width more accurate than the computed L and H would need to take into account the actual curvature field of the 3D object, e.g., of its tortuosity [36]. Achieving such more accurate estimates requires more advanced approaches and respective computational techniques and it still presents several challenges. See for example Section 2.6 in [36] and [37] for a description of the open problems and respective approaches. The adoption of such approaches in this work extended beyond the focal points and target of this work, i.e., obtaining meaningful and representative quantitative estimates of crack size even though not the most possible accurate.

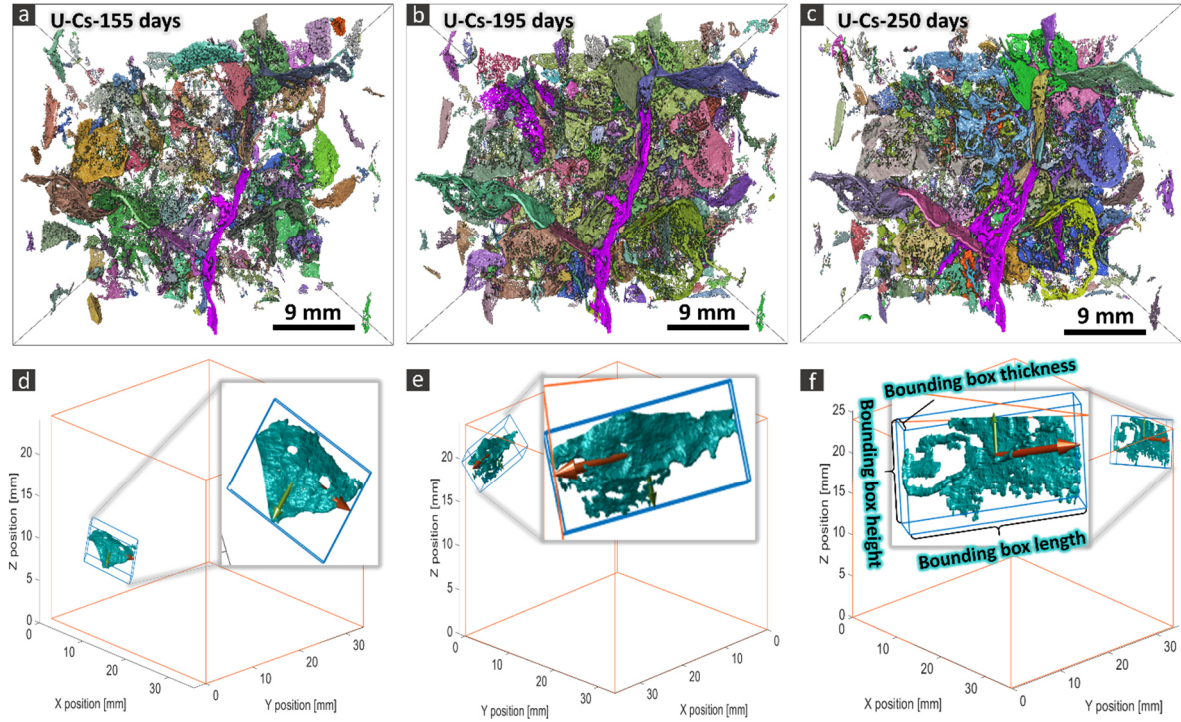


Figure C21. 3D rendering of the segmented, total crack network (containing or not containing ASR products) of the U-Cs specimen, at 155 days, 195 days and 250 days, insets (a), (b) and (c), respectively. In each of insets (a)-(c), each separated part (branch) of the crack network is rendered with a distinct color, just for the purpose of distinguishing them. The color assignment to each branch was random, i.e., did not remain consistent in time, due to the evolution, e.g., merging or splitting, of the crack network branches. Insets (d)-(f) show three examples of separated branches of the crack network at 250 days, for the same specimen. The large parallelepiped box highlighted in orange delineates the tomographed volume. The smaller grey box shows a zoom-in view of the respective crack branch. The blue, parallelepiped box is the crack's bounding box oriented according to the three eigenvectors of the crack's shape tensor \mathbf{G} . Each eigenvector, located at the center of mass of the crack and scaled by half the lateral size of the bounding box along the same direction, is also rendered as a solid arrow. The red arrow refers to the eigenvector associated with the first eigenvalue. The green arrow to the second eigenvector and the blue one to the third.

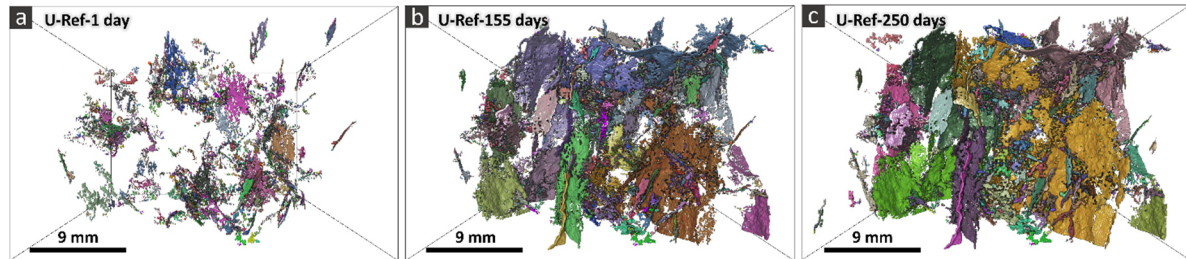


Figure C22. Similar 3D renderings as in Figure C21 (a) – (c) but for the U-Ref specimen.

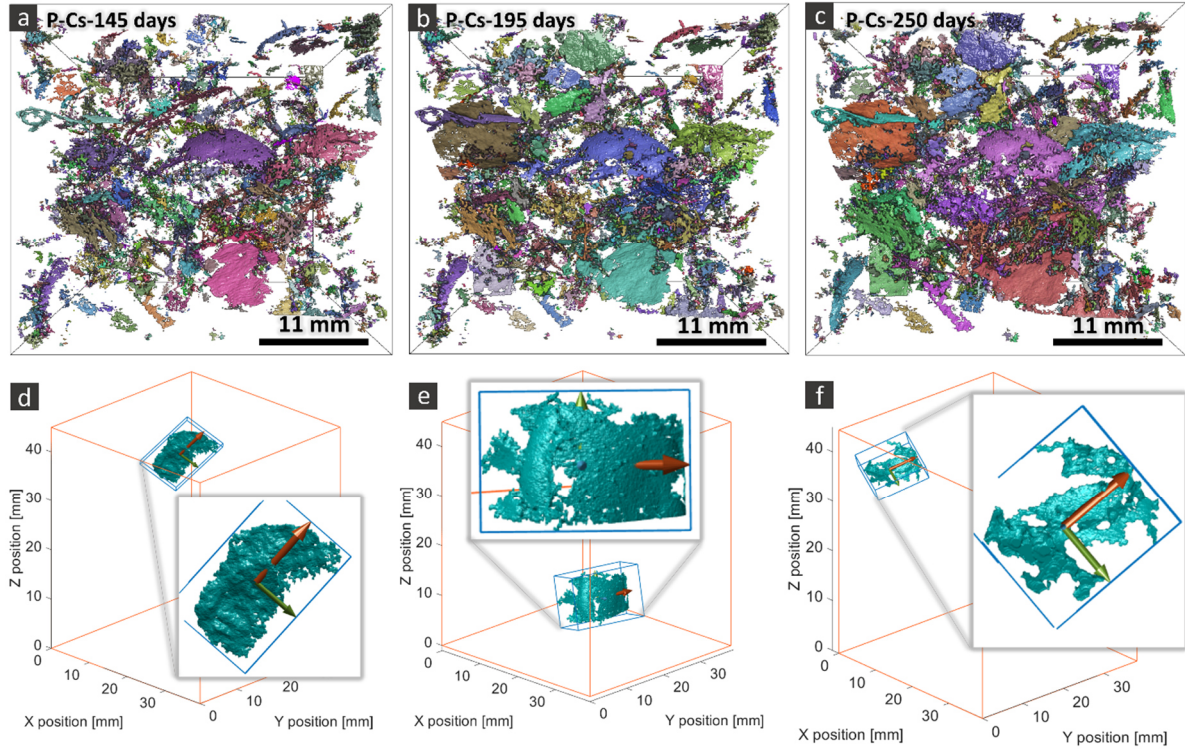


Figure C23. Similar 3D renderings as in Figure C21 but for the P-Cs specimen at three points of its tomographic time series.

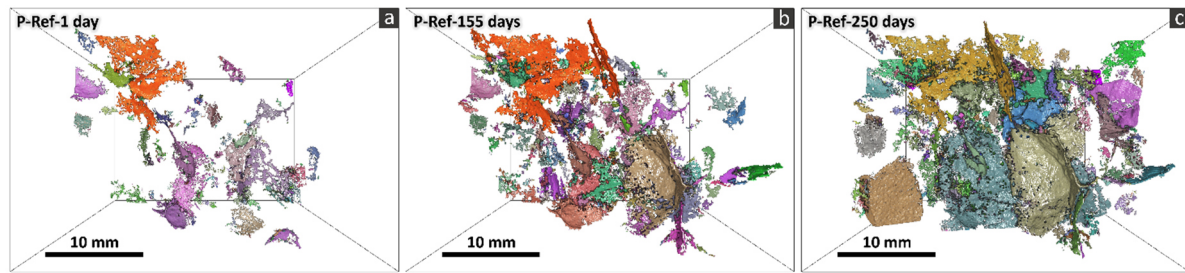


Figure C24. Similar figure as Figure C23 but for the P-Ref specimen.

Crack size analysis results. Figure C25 to Figure C29 show the statistical *ensemble* estimate of the complementary cumulative distribution function (cCDF) of the bounding box length, L , the bounding box height/width, H , and of the separate crack volume, V_{crack} , in insets (a) to (c), respectively. Each cCDF is plotted in \log_{10} - \log_{10} scales, i.e., it is shown in the form of a Zipf's plot, as done in Figure 5.11 in Chapter 5.

Figure C29 and Figure C39 show similar plots as in Figure 5.11 except for adding the corresponding plots for the U specimens. Figure C29 shows the cCDFs of L . Figure C39 shows those of T_{local} .

One remarkable feature shown in the plots of Figure C29 and Figure C39 is that, when comparing the cCDFs at 250 days for the specimens with distinct aggregate types but same mixing (with or without Cs-doping), no dramatic difference in the ranges of L and, more importantly, of T_{local} values is observable. This feature, combined with the results shown in Figure C18, could provide an explanation for the difference in the macroscopic scale expansion observable in Figure 5.1 and Figure C5.

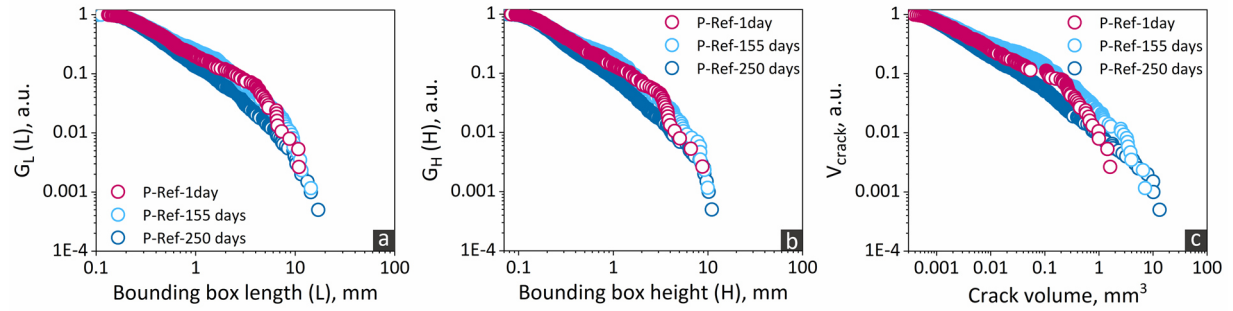


Figure C25. Empirical (i.e., statistical ensemble) complementary cumulative distribution function of (a) the bounding box length, L , $G_L(L)$, (b) the bounding box height (also called width), H , $G_H(H)$, (c) the crack network branch (also called separate crack) volume, V_{crack} . Each complementary cumulative distribution function is plotted in \log_{10} - \log_{10} scales (Zipf'fplot). Each separate crack contributed to one sampled value for each variable.

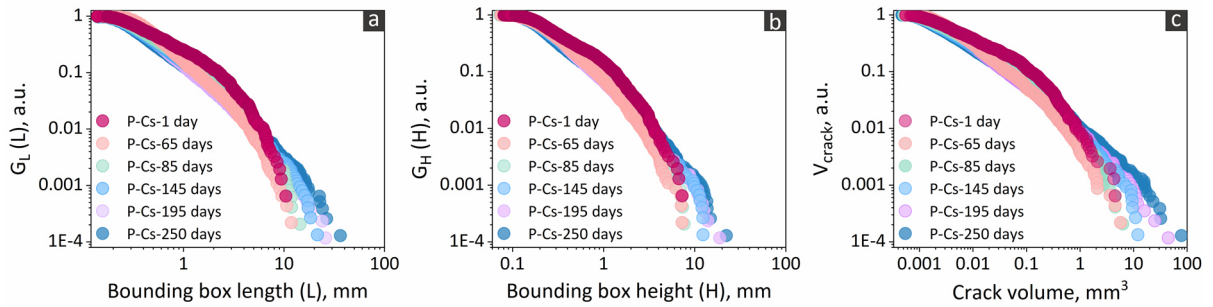


Figure C26. Similar plots as in Figure C25 but for the P-Cs specimen.

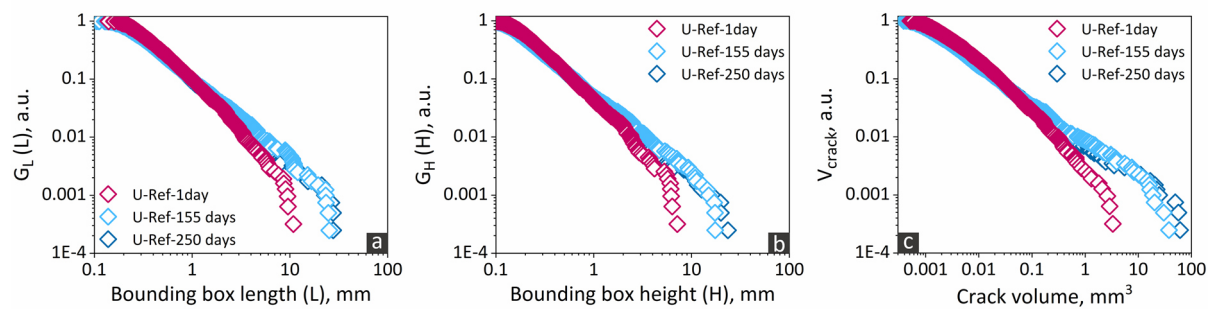


Figure C27. Similar plots as in Figure C25 but for the U-Ref specimen.

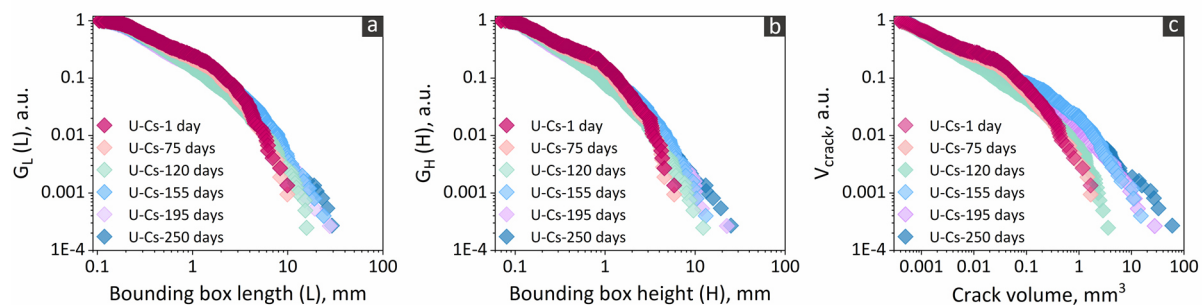


Figure C28. Similar plots as in Figure C25 but for the U-Cs specimen.

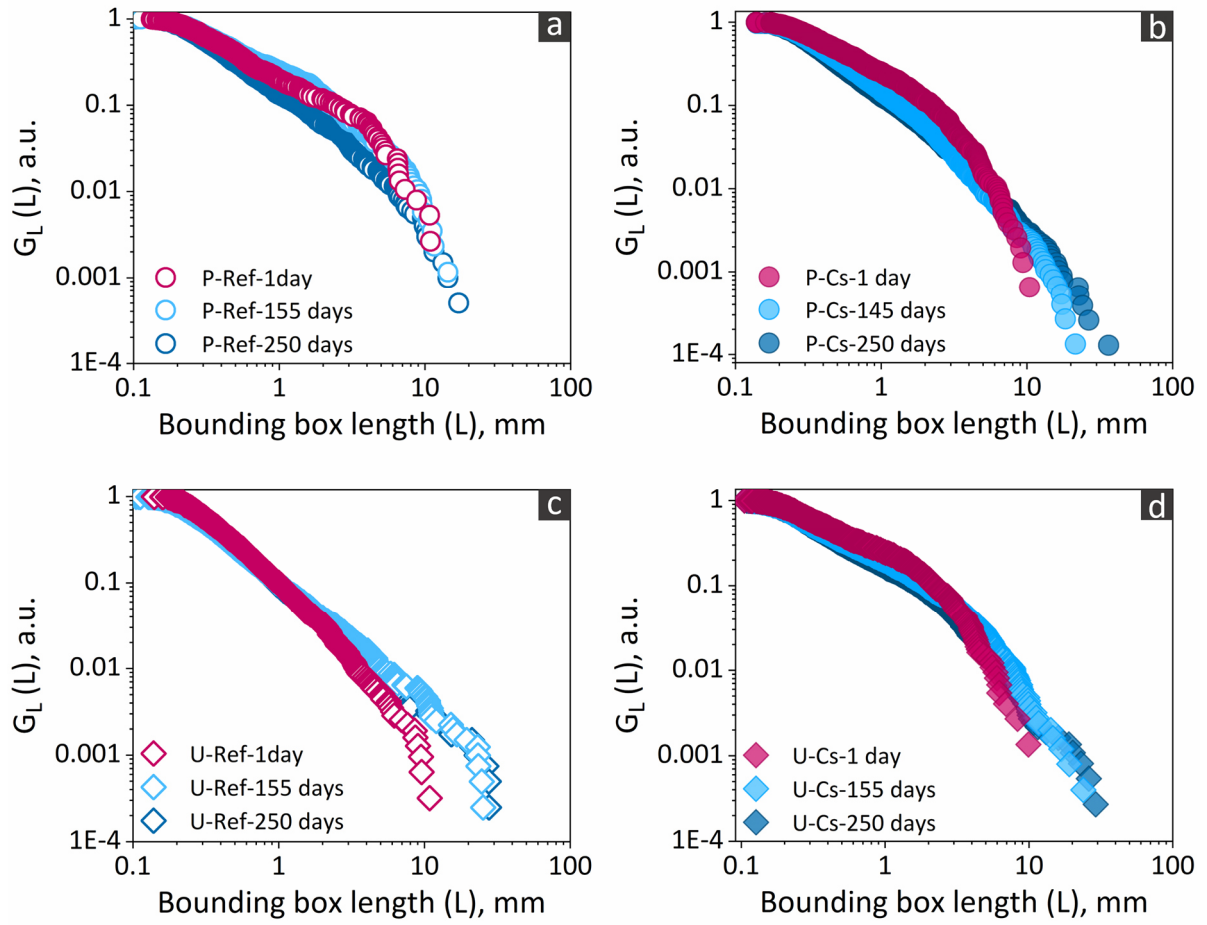


Figure C29. Empirical (i.e., statistical ensemble) complementary cumulative distribution function of the bounding box length, L , $G_L(L)$, in \log_{10} - \log_{10} scales (Zipf plot). Each separate crack contributed to one sampled value for L .

Crack shape analysis results. The 3D rendering of the segmented, total crack networks presented in Figure C21 to Figure C24 show that their distinct separate cracks had a broad range of curvatures and degrees of fragmentation. The shape tensor analysis allowed confirming such visual observation. For a given specimen and a given time point, let C be the total number of independent, disconnected branches of the segmented total crack network (separate cracks, containing or not ASR products). Each of them can be mapped to a point in the $(E; F)$ shape feature space. Notice that, by the E and F definitions themselves, only the $[0; 1] \times [0; 1]$ region of such space can be populated by points. Those points close to the $(0; 0)$ corner correspond to rather spherical separate cracks, while those close to the $(1; 1)$ corner correspond to plate-like cracks. A segmented, total crack network can be thought of corresponding to a statistical sample $\{(E_i; F_i)\}_{i=1, \dots, C}$ of a bi-variate random variable, $(E; F)$.

The plots in Figure C30 to Figure C32 show the kernel density estimate (KDE) of the joint probability density function (PDF) of $(E; F)$, $f_{(E;F)}(E; F)$. The KDE of $f_{(E;F)}(E; F)$ was obtained, for each specimen and at each time point, applying the "2D Kernel Density" function of the OriginPro 2020b (v9.7.5.184) software package (OriginLab®, Northampton, MA, USA). The chosen parameters for such function included: the "Bivariate Kernel Density Estimation" as the method of density estimation, 32 number of Grid Points in X/Y, no point were used for the displaying, the Grid Range of $[-0.05, 1.05]$ for both X and Y and 300 "Interpolate Density Points".

At any time point and for any specimen, the majority of the cracks were mapped to the top-right corner of the region $[0; 1] \times [0; 1]$ in the $(E; F)$ plane (see from Figure C30 to Figure C32). No relevant difference in "shape distribution" could be observed between specimens with distinct aggregate types, with or without Cs-doping, at the beginning of the experimental campaign. The evolution in time also did not seem to alter substantially the shape distribution much. The Cs-doping also did not change much the shape distribution, in comparison with the cases in its absence. Despite the broad degree of curvature and fragmentation, the fact that the separate cracks are predominantly shaped like irregular plates allowed using the shape tensor analysis also for obtaining representative estimates of crack sizes and for a coarse assessment of the overall orientation of the distinct branches of the crack network.

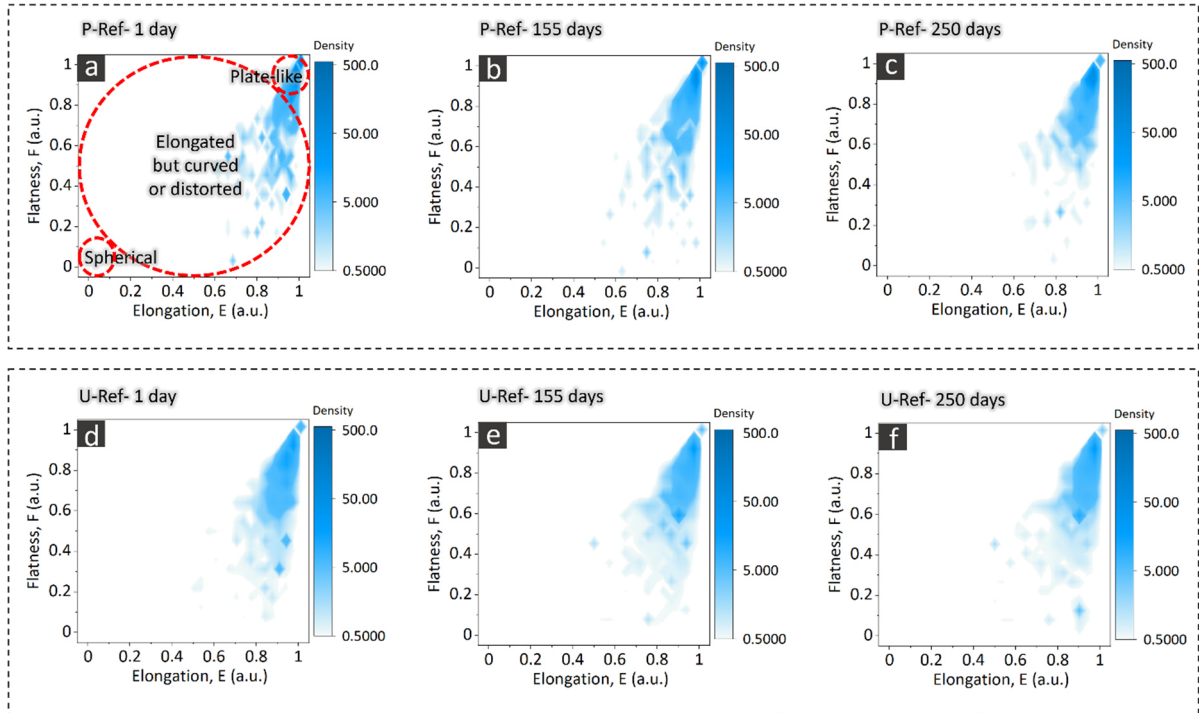


Figure C30. Plot of the kernel density estimate (KDE) of the joint probability density function (PDF) of the two shape feature variables, the elongation E and the flatness F , computed from the shape tensor analysis of the segmented total crack network and treated as a bi-variate random variable, $(\mathbb{E}; \mathbb{F})$. The statistical sample of such PDF was provided, for each specimen and at each time point, by the set of values $\{(E_i; F_i)\}_{i=1, \dots, C}$ obtained from the shape tensor analysis, where C indicates generically the total number of disconnected and independent branches of the segmented, total crack network of a specimen and at a certain time point. (a) to (c): P-Ref specimen, at 1 day, 155 and 250 days, respectively. (d) to (f): U-Ref specimen, at 1 day, 155 and 250 days.

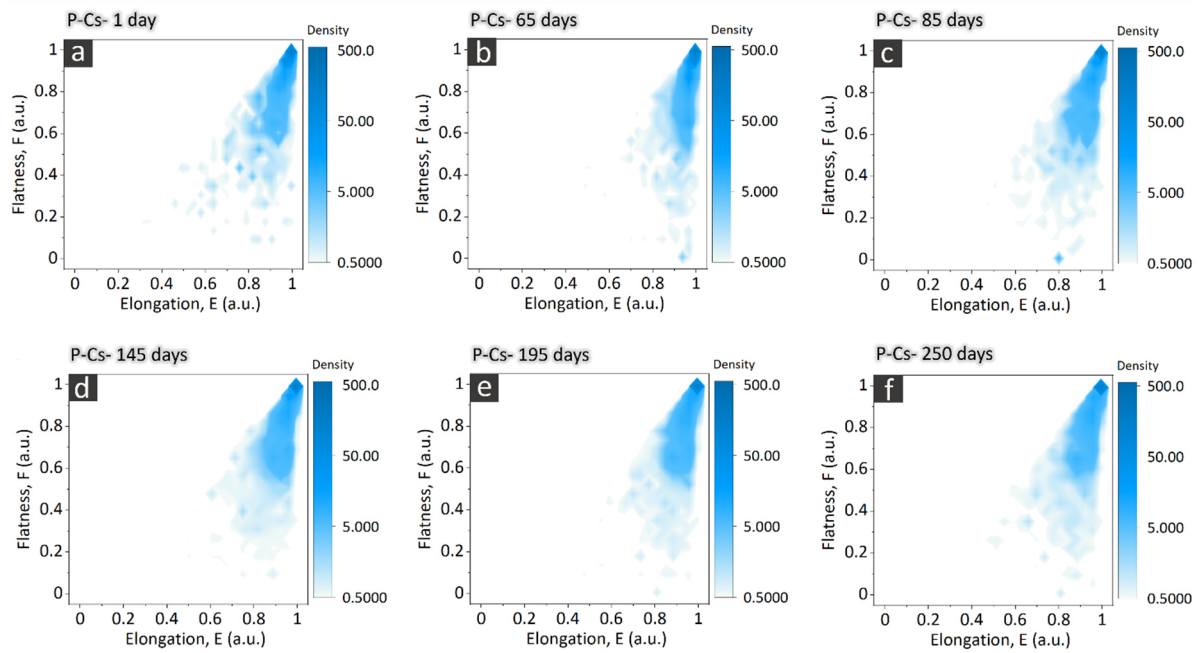


Figure C31. Same plots as in Figure C30 but only for the P-Cs specimen: at (a) 1 day (b) 65 days, (c) 85 days, (d) 145 days, (e) 195 days and (f) 250 days.

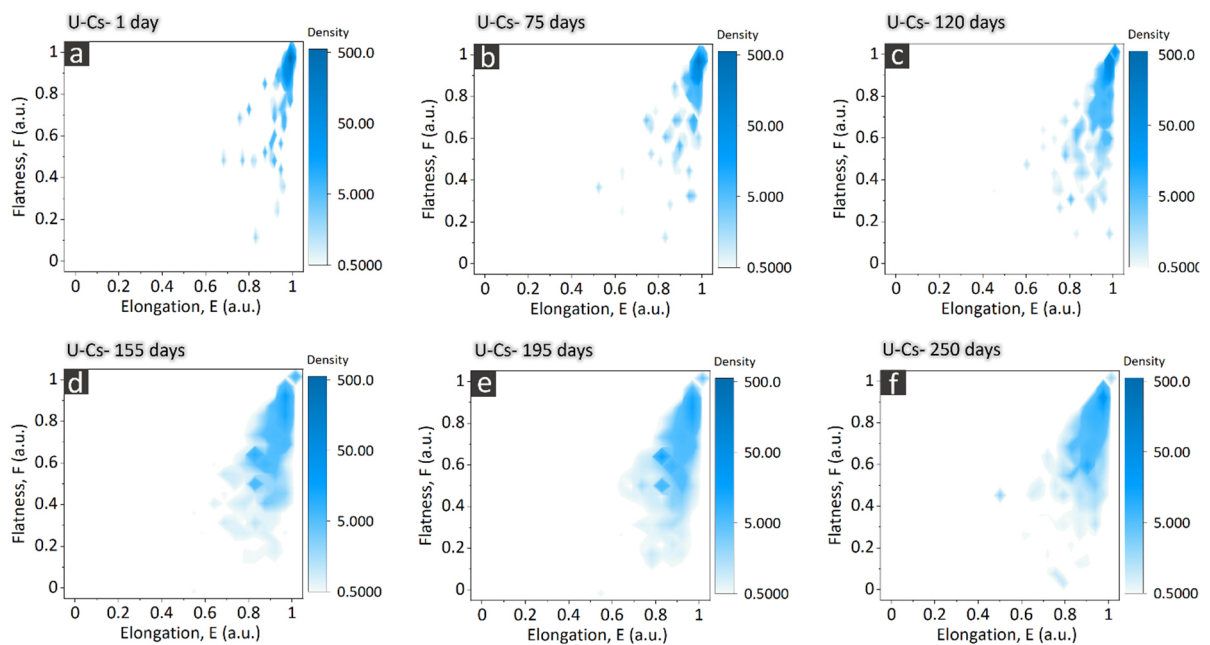


Figure C32. Same plots as in Figure C31 but for the U-Cs specimen.

Crack orientation analysis results. The direction of the first *eigenvector* of \mathbf{G} , \hat{u}_1 , was chosen to define the feature variable "crack orientation". Only a qualitative analysis of the crack orientation of any specimen at any given time point was performed. It was based on plotting the \hat{u}_1 of each separate crack. Given that the *eigenvectors* of \mathbf{G} are unit vectors, the visualization corresponds to mapping the \hat{u}_1 's as points on a unit sphere. The higher the density of points in a portion of such sphere, corresponding to a certain range of spherical coordinate angles ($\varphi; \theta$), the larger the number of separate cracks whose direction of largest extent (i.e., the \hat{u}_1 direction) falls in that angular range.

Figure C33 to Figure C35 show the plots of the full \hat{u}_1 vectors, after rescaling their magnitudes by a factor equal to 0.33 (in order to ensure the visibility of their projections on the $X - Y$, $Y - Z$ and $X - Z$ planes). In all the figures, it can be noticed that, by increasing time, the density of vectors increased more considerably within a cone with symmetry axis approximately equal to the Z axis. No specific region of the sphere was completely empty of points/vectors. This feature indicates lack of strong orientation anisotropy. However, the higher densification towards the positive Z direction was a feature characterizing every specimen, independently of the aggregate type and of the absence or the presence of Cs-doping. It suggests that Cs-doping brought no evident perturbation of the crack networks, in terms of crack orientation.

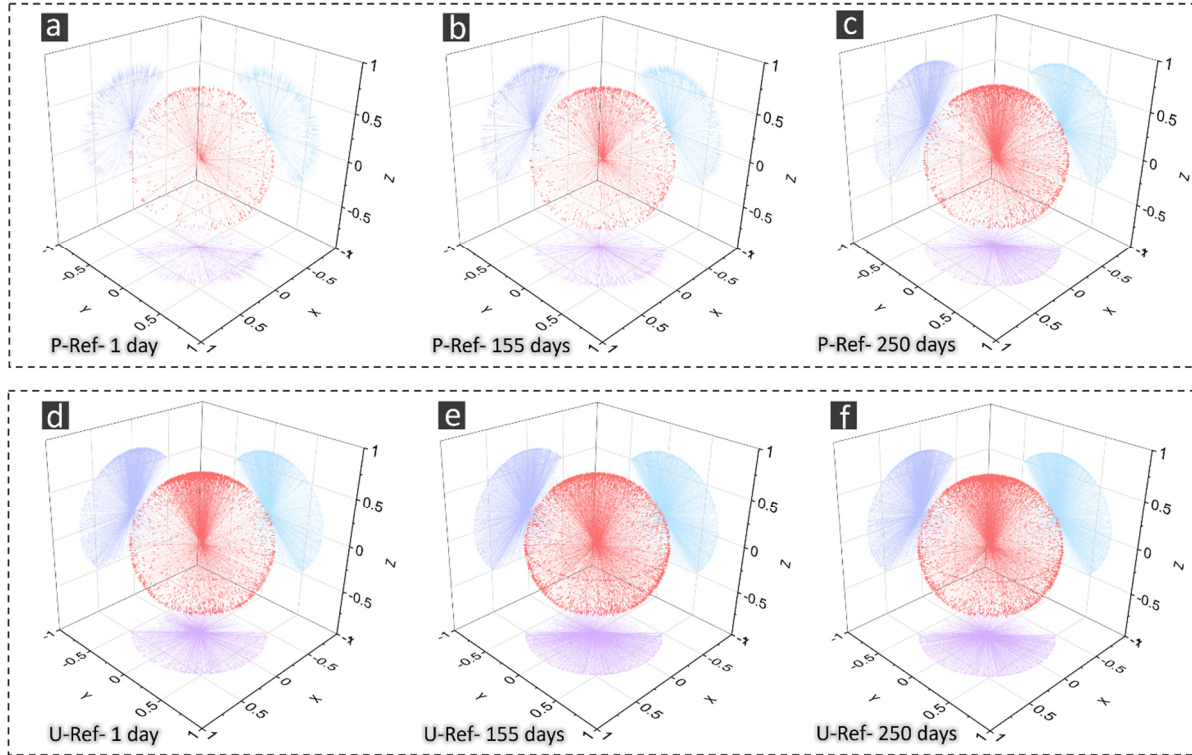


Figure C33. Visualization of the crack orientation analysis results for the reference specimens. The "crack orientation" was operatively defined as the direction of the eigenvector \hat{u}_1 associated with the first and largest eigenvalue of the shape tensor \mathbf{G} . The segmented total crack network of a specimen corresponded to a set of \hat{u}_1 's, one for each independent crack (branch of the network). Each of these vectors are here plotted in red, after rescaling their magnitudes by a factor equal to 0.33, to make their projections on the planes of the Cartesian frame of reference more visible. The projections of \hat{u}_1 on the $X - Y$ plane are in violet, those on the $X - Z$ plane are in dark blue and those on the $Y - Z$ plane are in light blue. (a)-(c): distribution of the \hat{u}_1 eigenvectors for the P-Ref specimen at 1 day, 155 and 250 days, respectively. (d)-(f): distribution of the \hat{u}_1 eigenvectors for the U-Ref specimen at 1 day, 155 and 250 days, respectively.

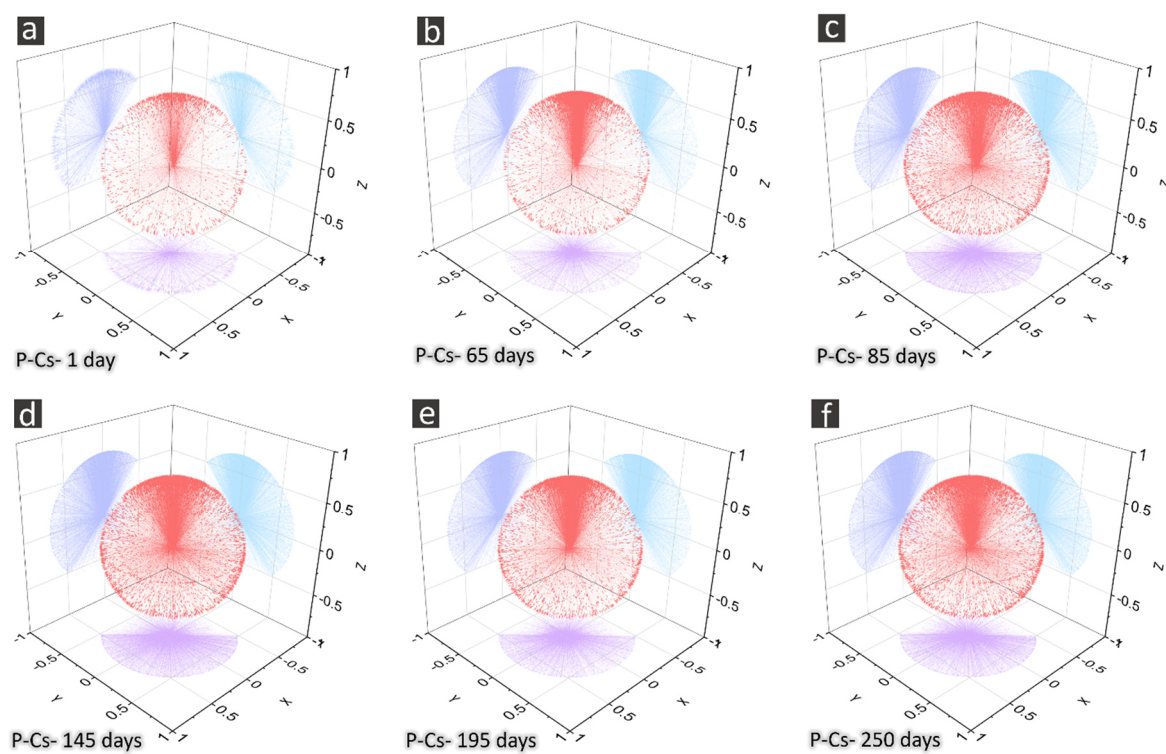


Figure C34. Similar figure as Figure C33 but for the P-Cs specimens at 6 of the 12 time points of measurement. (a)-(f): P-Cs specimen at 1 day, 65, 85, 145, 195 and 250 days, respectively.

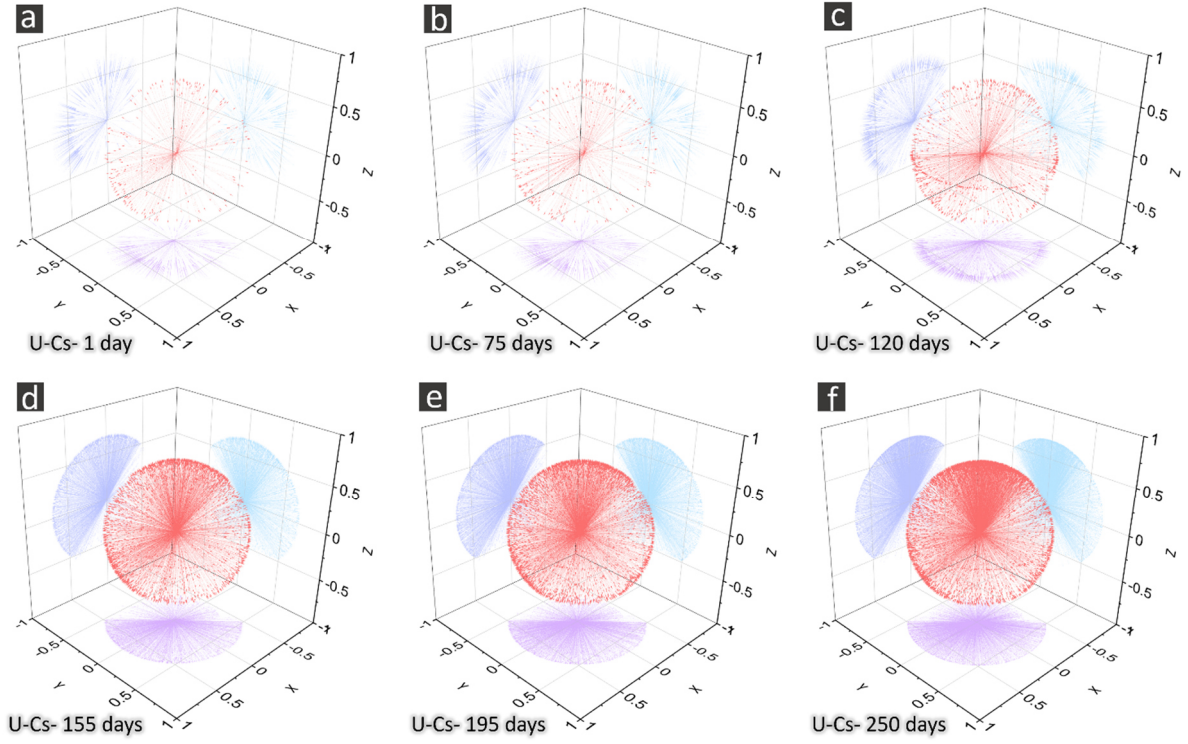


Figure C35. Similar figure as Figure C34 but for the U-Cs specimens.

C9.2. Crack local thickness analysis

Figure C36 and Figure C37 show 3D renderings of the local thickness scalar field, $T_{local}(\vec{x})$, computed for the segmented total crack networks of all the specimens and at certain time points. Figure C36 contains results for the two reference specimens. Figure C37 shows results for the two Cs-doped specimens. $T_{local}(\vec{x})$, by definition, has value equal to 0 outside the segmented total crack network regions. Thus, in Figure C36 and Figure C37, the reader can essentially see 3D renderings of the total crack networks, similar to those in Figure C21 (a)-(c), Figure C22 (a)-(c), Figure C23 (a)-(c) and Figure C24 (a)-(c). However, the difference consists of the fact that each voxel of a network is rendered with a color which is mapped to the value of T_{local} at that voxel's position. The color scale in each inset of Figure C36 and Figure C37 is always the same and is mapped to the same range of T_{local} values. The complementary cumulative distribution function of T_{local} , computed for any specimen (with and without Cs-doping) and (for the Cs-doped specimens) at additional time points, compared with what shown in Figure C39, is shown in Figure C38.

The 3D renderings in Figure C36 and Figure C37 confirm visually what observable in Figure 5.11 and in Figure C38 and Figure C39: a gradual temporal shift of the T_{local} value distributions (especially their right-hand side tails) towards larger values. No significant differences in the spatial-temporal T_{local} distributions of the reference specimens could be noticed.

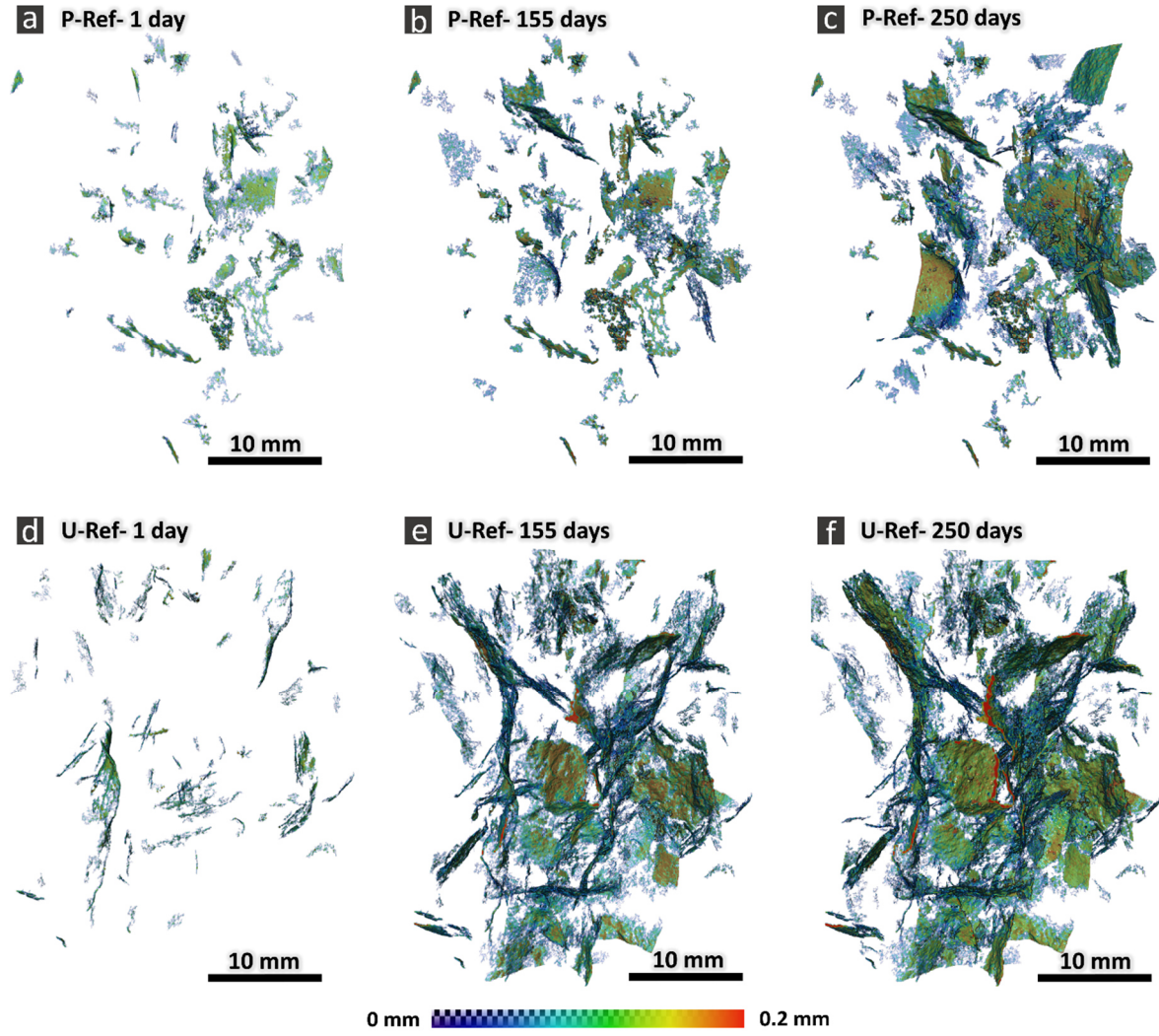


Figure C36. 3D rendering of the local thickness scalar field, $T_{local}(\vec{x})$, computed for the segmented total crack network. (a)-(c): P-Ref specimen at 1 day, 155 and 250 days. (d)-(f): U-Ref specimen at 1 day, 155 and 250 days.

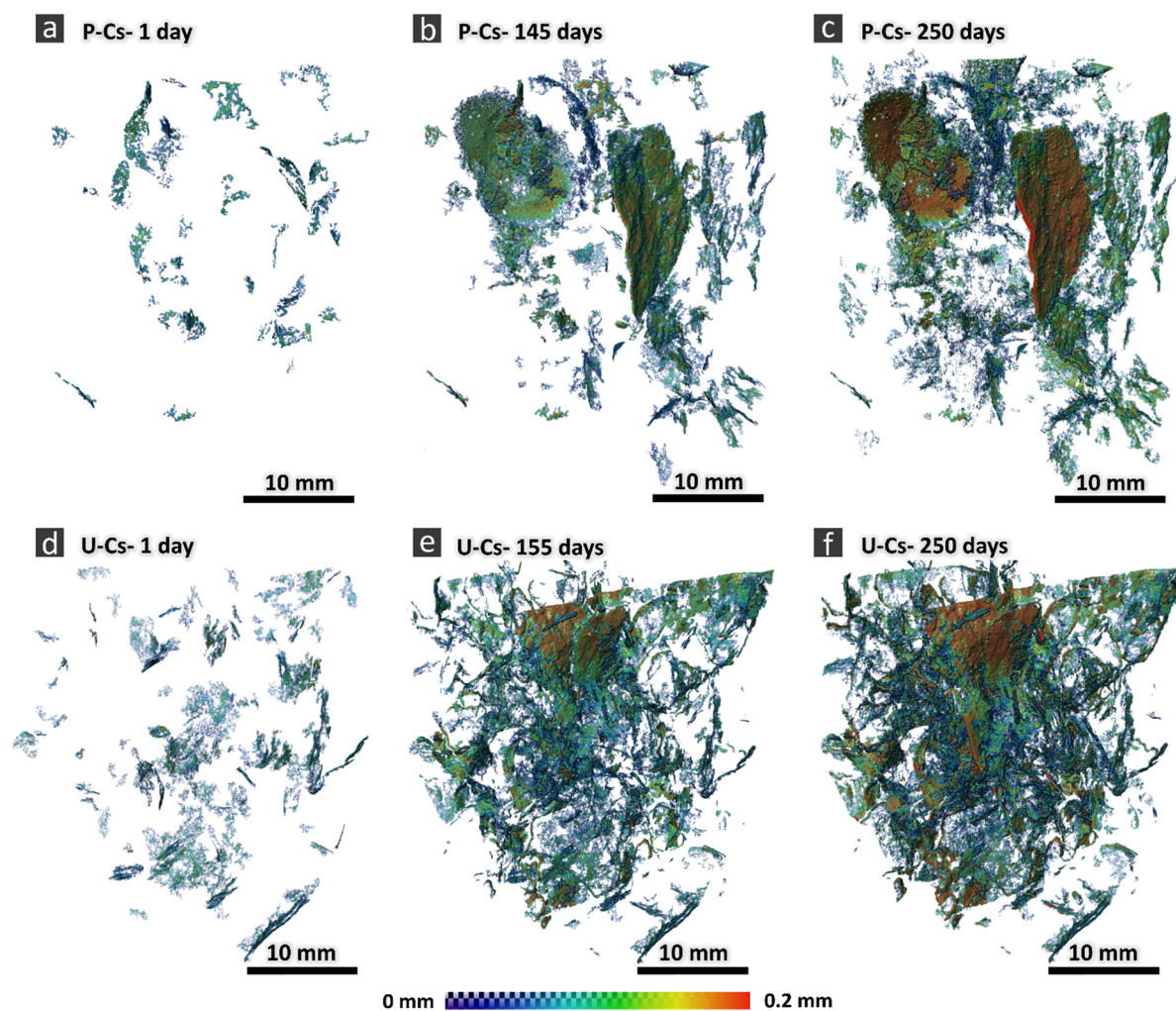


Figure C37. Same figure as Fig. S 49 but for the P-Cs specimen, insets (a) - (b), at 1 day, 145 and 250 days, respectively, and for the U-Cs one, insets (d)-(f), at 1 day, 155 and 250 days, respectively.

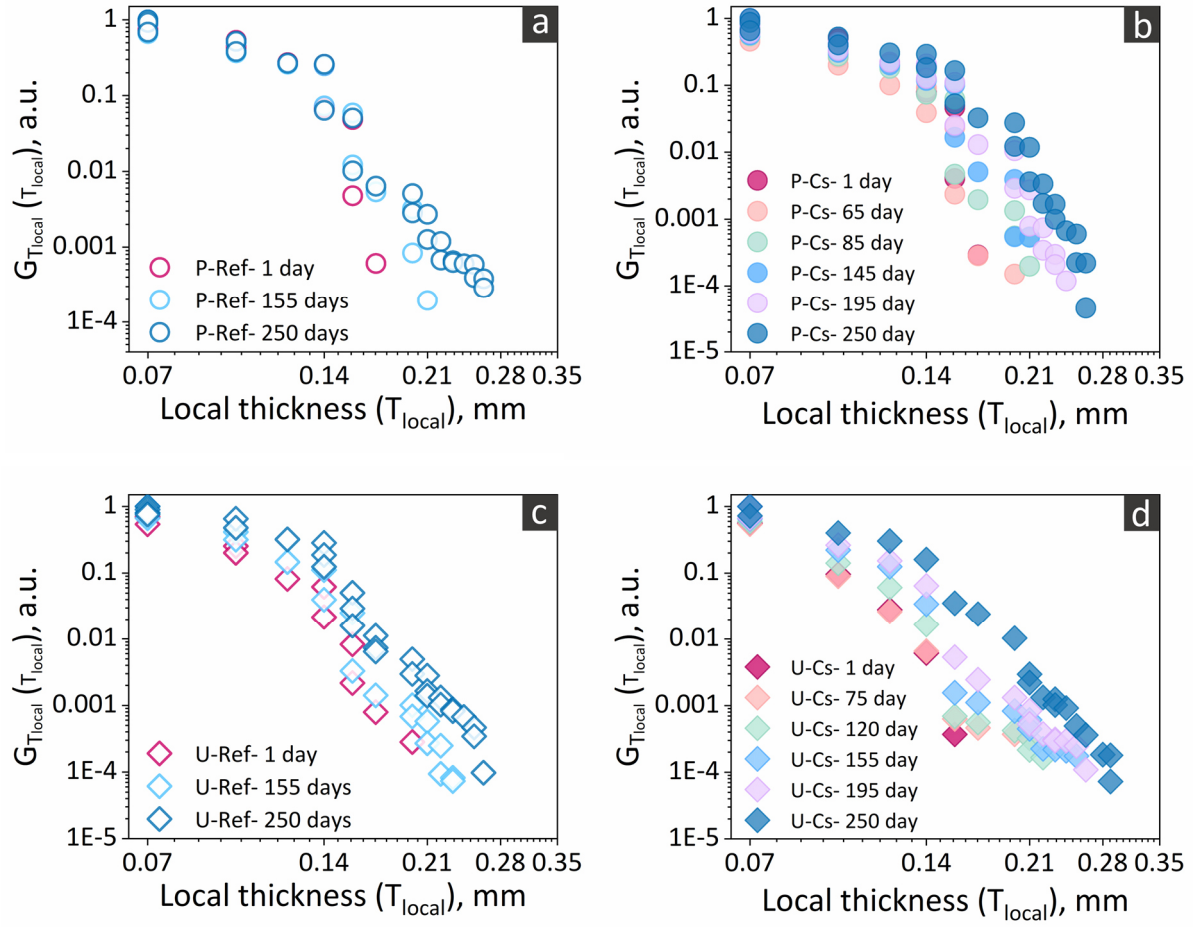


Figure C38. Empirical (i.e., statistical ensemble) complementary cumulative distribution function of the total crack network's local thickness, $T_{local}(\vec{x})$, $G_{T_{local}}(T_{local})$, in \log_{10} - \log_{10} scales (Zipf plot) (a) P-Ref, (b) P-Cs, (c) U-Ref and (d) U-Cs specimens, respectively, at various time points specified on the corresponding plots.

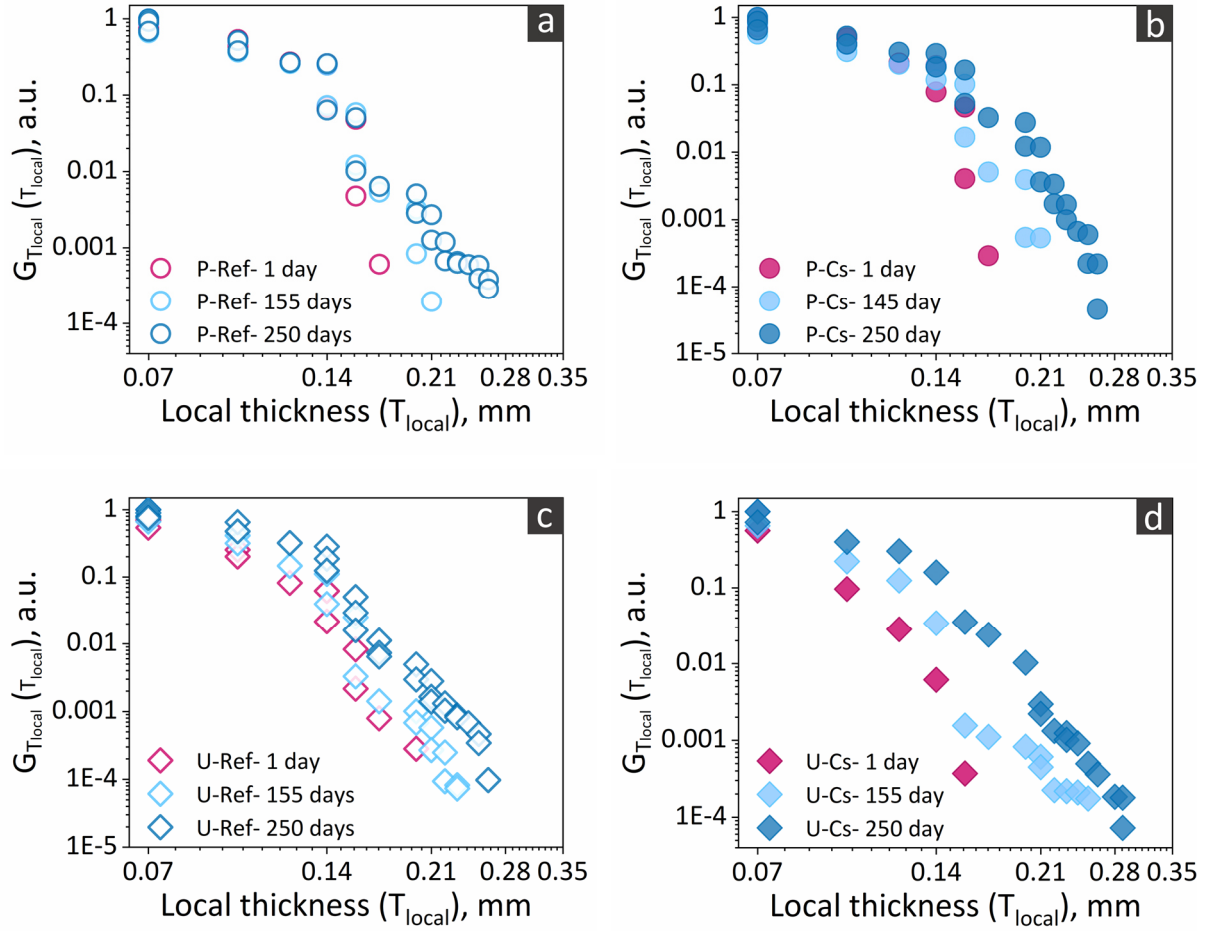


Figure C39. Similar to Figure C38, but comparing only three time points for each specimen.

C10. Quantitative analysis of ASR cracking by time-lapse tomography.

Local deformations analysis

In this Section, further visualizations are reported, both of 2D cross-sections and of smaller sub-volumes, of the two scalar fields, $\|\vec{u}_{N-AFF}\|(\vec{x}, t_i)$ and $J_{\vec{T}_{N-AFF}}(\vec{x}, t_i)$, which was used as 3D maps of where and how the displacement vector due to the ASR deformations was spatially heterogeneous. Both scalar fields, are derived from the displacement vector field, $\vec{u}_{N-AFF}(\vec{x}, t_i)$, generated by the non-affine registration procedure.

It is reminded that such displacement vector field is not the total one due to the ASR deformations. Rather, it is only its component having a spatial dependence, the other component being the one computed from the global affine registration procedure. It should also be noted that the total displacement vector field due to the ASR deformations is not simply the sum of the two fields just mentioned, rather a more complicated nonlinear function of the two. However, from a qualitative point of view, the global affine field captures the overall, bulk effect of the ASR deformations, while the non-affine one describes their local details.

The visualizations in this Section aim at providing examples additional to those shown in Section 5.3.7, concerning the most relevant features of the ASR-induced local deformations. These examples also aim at showing that such features were observed in both the specimens with the P aggregates and in those with the U ones and were essentially independent from the presence or absence of the Cs-doping, except for the different timing at which they appeared.

P-Ref and U-Ref specimens

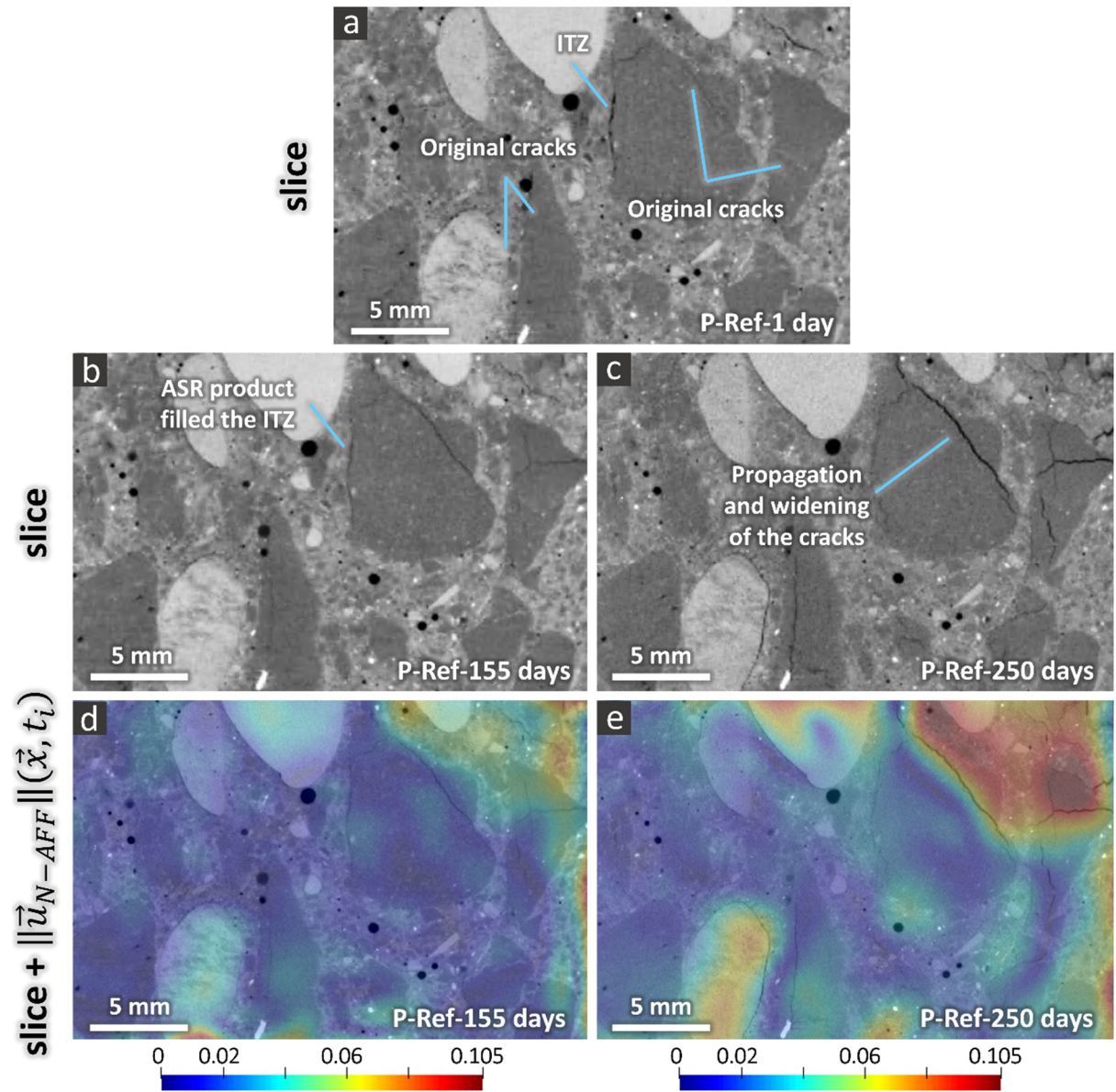


Figure C40. Visualization of the magnitude of the displacement vector field, $\|\vec{u}_{N-AFF}\|(\vec{x}, t_i)$, associated with the transformation vector field, $\vec{T}_{N-AFF}(\vec{x}, t_i)$, of the non-affine registration, for the P-Ref specimen. The scalar field $\|\vec{u}_{N-AFF}\|(\vec{x}, t_i)$ is used as spatial map of the "degree of local heterogeneity" of the ASR deformation. In this figure, only one 2D cross-section from the "tomographed" volume is shown. (a) X-ray tomogram of the P-Ref specimen at the beginning of the ASR acceleration (1 day) and shown only at the position of the chosen 2D cross-section ("slice"). (b) and (c): slice from the X-ray tomograms at 155 and 250 days, respectively. (d) and (e): the

same slices as in (b) and (c), respectively, plus, overlapped on top of them semi-transparently and rendered according to the indicated color scale, the 2D cross-section, at the same position, from $\|\vec{u}_{N-AFF}\|(\vec{x}, t_i)$, at 155 and 250 days, respectively. The color scale bars of insets (d) and (e) are in units of mm.

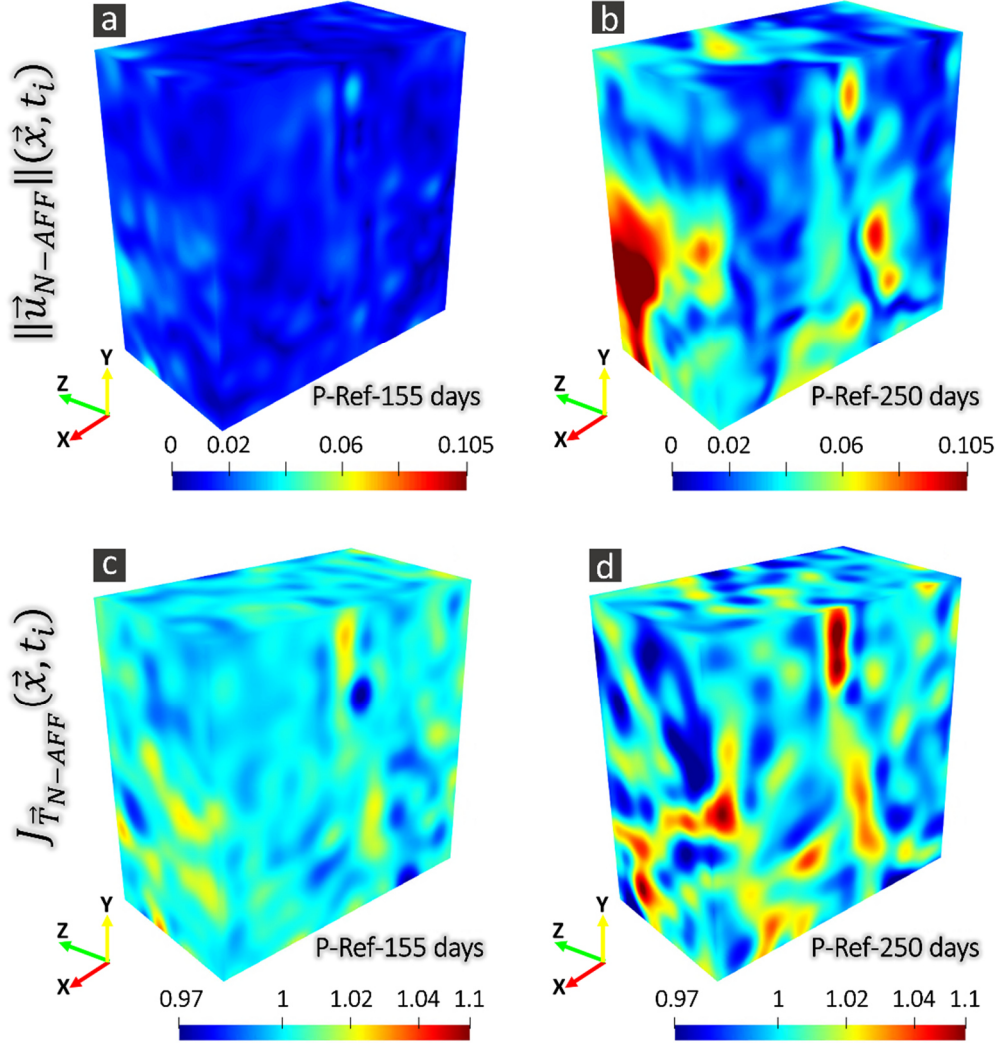


Figure C41. 3D Visualization of the two scalar fields computed from the displacement vector field, $\vec{u}_{N-AFF}(\vec{x}, t_i)$, associated with the non-affine transformation vector field, $\vec{T}_{N-AFF}(\vec{x}, t_i)$, obtained from the non-affine registration and used as indicators of the spatially heterogeneous component of the overall displacement due to the ASR deformations. Case of the P-Ref specimen. Each scalar field is shown on the boundary surfaces of a parallelepiped ROI smaller than the "tomographed" volume of the specimen and it is color-coded. (a) and (b): the scalar field is the magnitude of $\vec{u}_{N-AFF}(\vec{x}, t_i)$, $\|\vec{u}_{N-AFF}\|(\vec{x}, t_i)$. (c) and (d): the scalar field is the determinant of the Jacobian matrix of $\vec{T}_{N-AFF}(\vec{x}, t_i)$, $J_{\vec{T}_{N-AFF}}(\vec{x}, t_i)$. (a) and (c) refer to the time point $t_2 = 155$ days. (b) and (d) refer to $t_2 = 250$ days. In insets (a) and (b) the unit for the color scale bars is mm. The color

scale bars of (c) and (d) have no unit because of the meaning of $J_{\vec{T}_{N-AFF}}(\vec{x}, t_i)$ of a volumetric ratio. Values greater than 1 represent volumetric expansion while smaller than 1 indicate volumetric contraction.

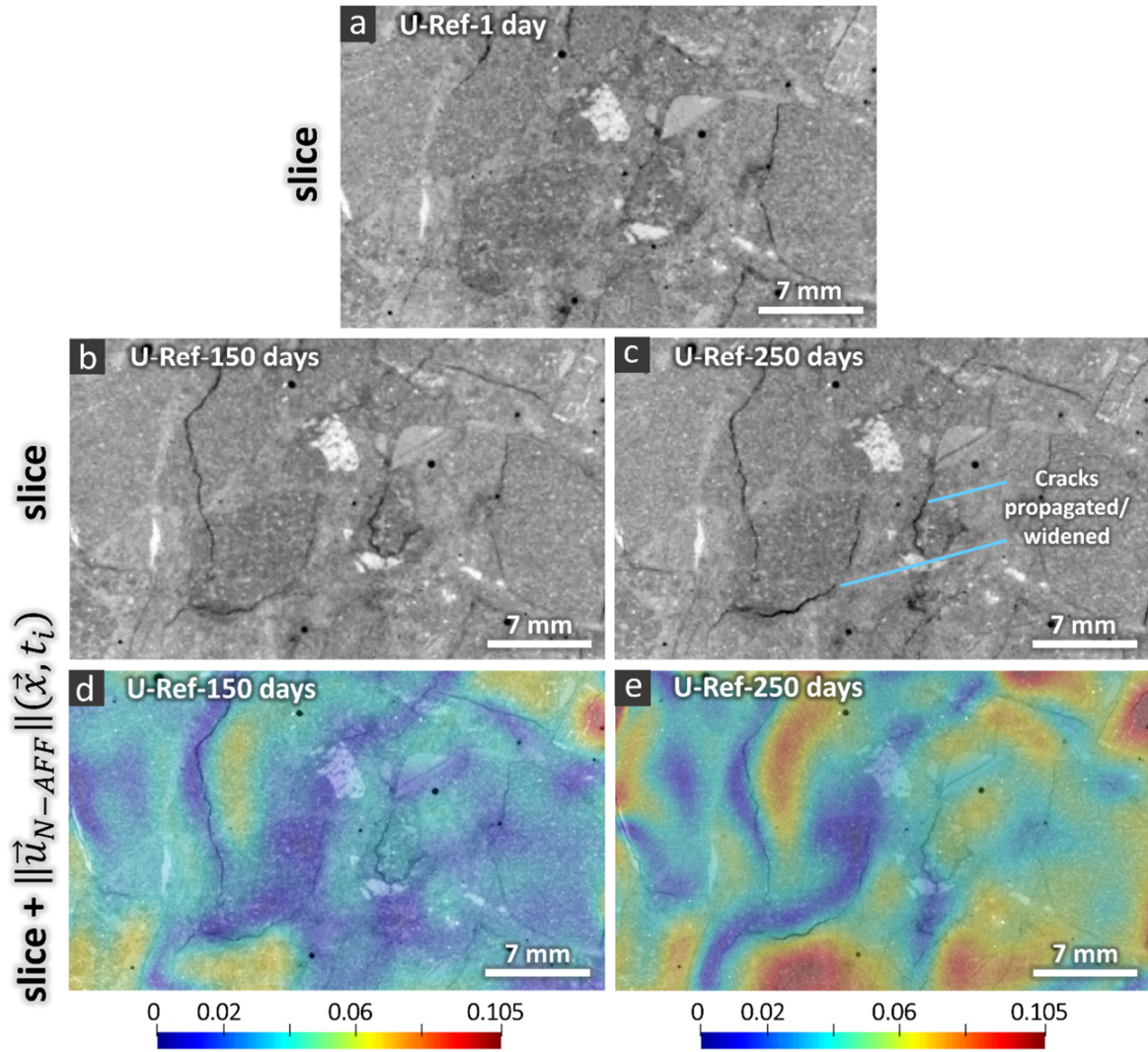


Figure C42. Similar visualization of $\|\vec{u}_{N-AFF}\|(\vec{x}, t_i)$ as in Figure C40 but for the U-Ref specimen. (a): tomographic slice at 1 day. (b) and (c): the same tomographic slices at 155 and 250 days, respectively. (d) and (e): the same tomographic slices as in (b) and (c) plus, overlapped on top of them semi-transparently and according to the color scale indicated below, the values of $\|\vec{u}_{N-AFF}\|(\vec{x}, t_i)$ on the same plane as the one of the tomographic slice and at the respective time points. In (d) and (e) the unit for the color scale bars is mm.

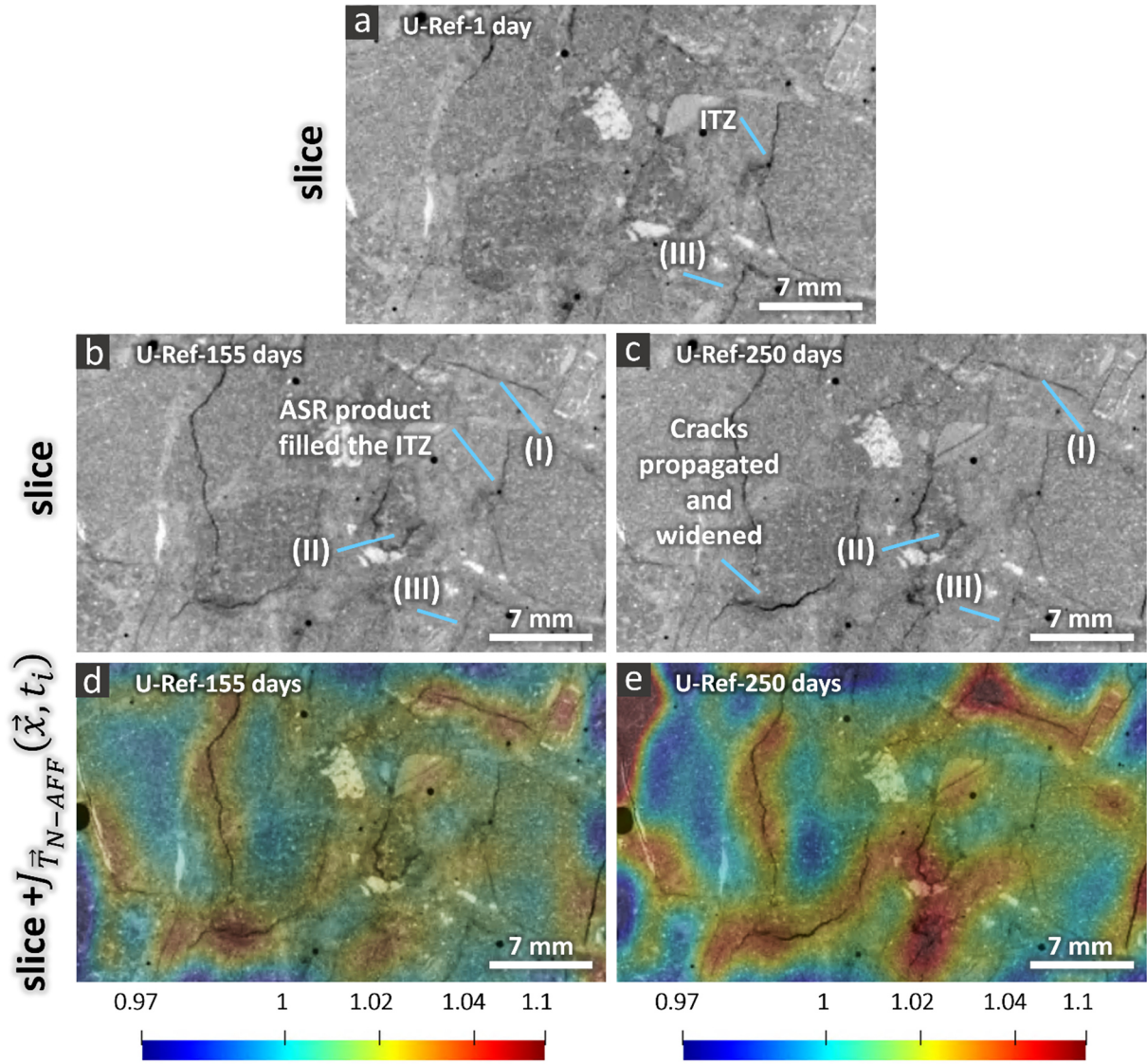


Figure C43. Similar plots as in Figure 5.12 but for the U-Ref specimen. Features (I) and (II) refer to the enlargement (opening) of cracks (zones of high expansion, appearing in red in the $J_{\vec{T}_{N-AFF}}$ map far away from the cracks). Feature labelled by (III) indicate original crack or more porous regions at the aggregate boundaries that did not evolve into an opening and lengthening crack, rather they either remained the same or gradually got closed or filled up.

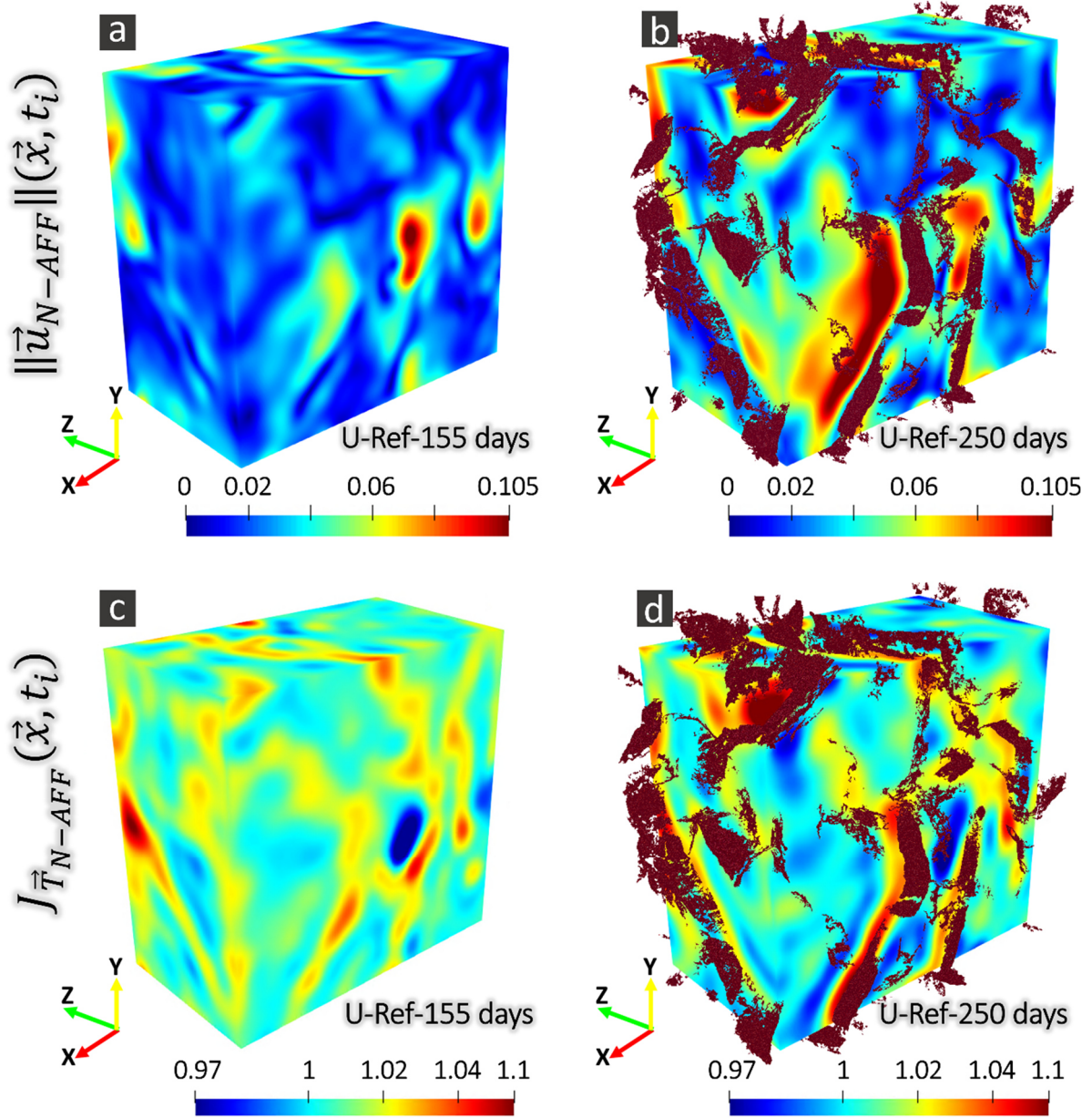


Figure C44. Similar figure as Figure C41 but for the U-Ref specimen. In insets (b) and (d), in addition to the visualization of the two scalar fields, the same small 3R ROI but extracted from the binary tomogram of the segmented total crack network is rendered in dark red solid color in order to show where the crack network was inside such ROI, in comparison with the spatial distribution of the two scalar fields indicating spatially heterogeneous deformations.

P-Cs and U-Cs specimens

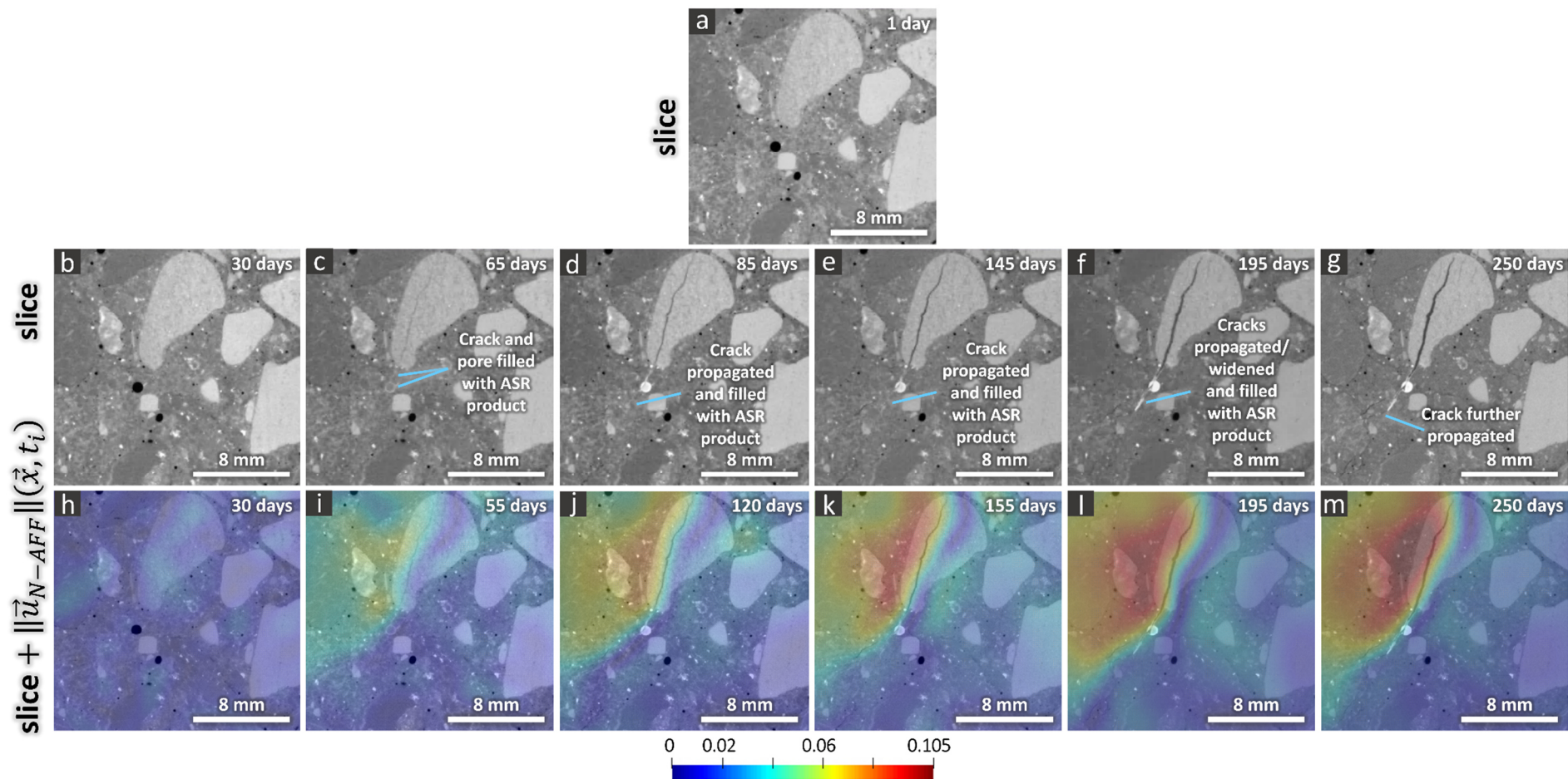


Figure C45. Similar visualization of $\|\vec{u}_{N-AFF}\|(\vec{x}, t_i)$ as in Figure C40 or Figure C42 but for the P-Cs specimen at 7 different time points (1 day, 30, 65, 85, 145, 195 and 250 days).

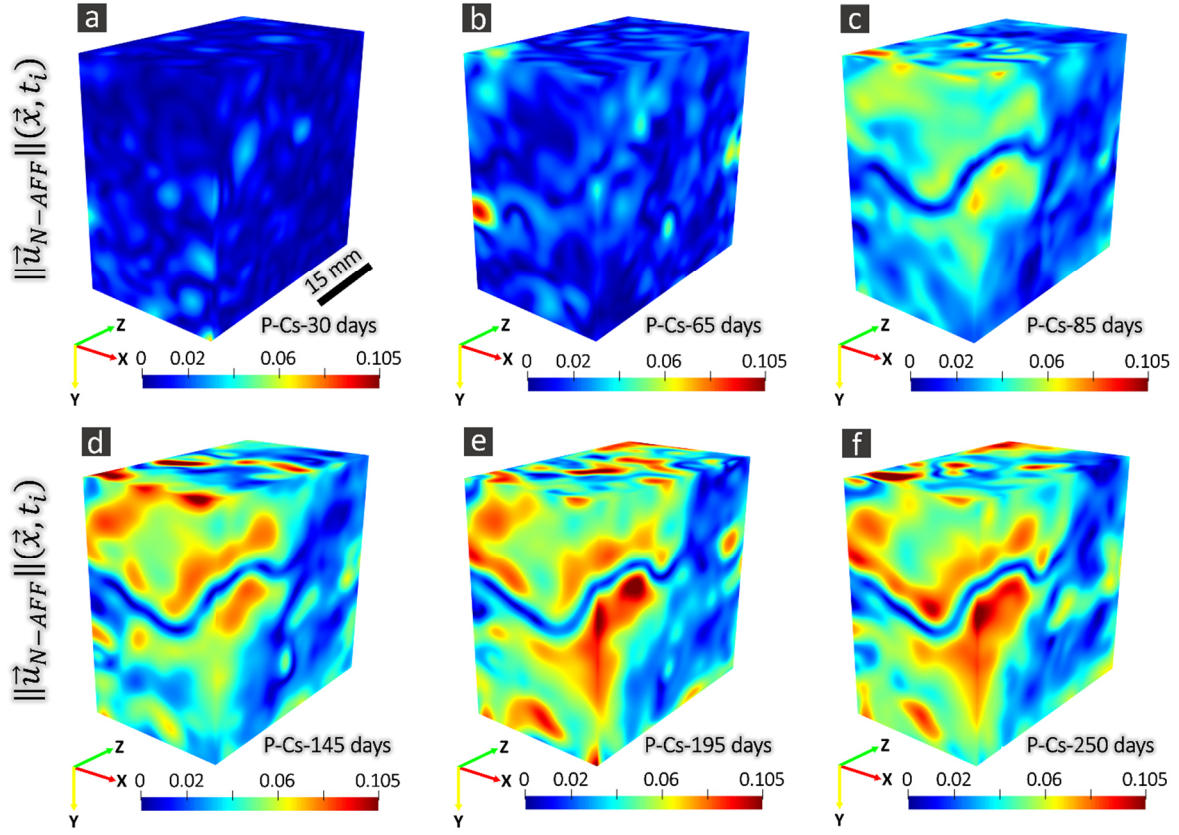


Figure C46. Visualization of the magnitude of $\vec{u}_{N-AFF}(\vec{x}, t_i)$, $\|\vec{u}_{N-AFF}\|(\vec{x}, t_i)$, computed from the displacement vector field, $\vec{u}_{N-AFF}(\vec{x}, t_i)$, associated with the non-affine transformation vector field, $\vec{T}_{N-AFF}(\vec{x}, t_i)$, obtained from the non-affine registration and used as indicator of the spatially heterogeneous component of the overall displacement due to the ASR deformations. Case of the P-Cs specimen. The scalar field is shown on the boundary surfaces of a parallelepiped ROI smaller than the tomographed volume of the specimen and it is color-coded. The insets (a) to (f) show $\|\vec{u}_{N-AFF}\|(\vec{x}, t_i)$ at 6 different time points when the specimen was tomographed, including 1 day 30, 65, 85, 145, 195 and 250 days. In all the insets the unit for the color scale bar is mm.

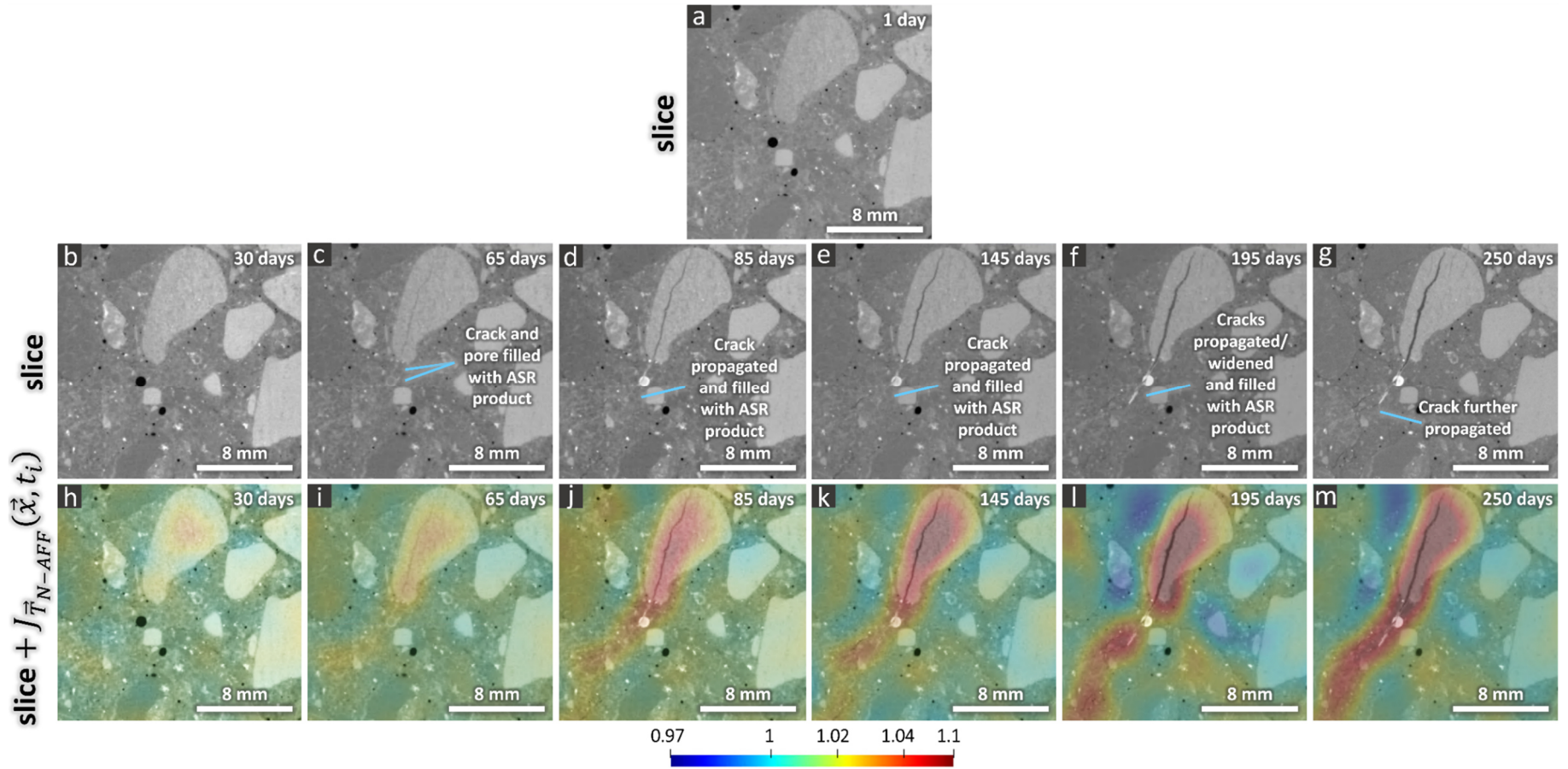


Figure C47. Visualization of the determinant of the Jacobian matrix of $\vec{T}_{N-AFF}(\vec{x}, t_i)$, $J_{\vec{T}_{N-AFF}}(\vec{x}, t_i)$. This scalar field is used as spatial map of the factor by which the volume locally expanded or contracted. In this figure, only one 2D cross-section from the tomographed volume is shown. This figure is an extended version of Figure 5.13. (a) X-ray tomogram of the P-Cs specimen at the beginning of the ASR acceleration (1 day), shown only at the position of the chosen 2D cross-section ("slice"). (b) to (g): slices from the X-ray tomograms at 30, 65, 85, 145, 195 and 250 days, respectively. (h) to (m): the same slices as in (b) to (g), respectively, plus, overlapped on top of them semi-transparently and rendered according to the indicated color scale, the slice, at the same position, from $J_{\vec{T}_{N-AFF}}(\vec{x}, t_i)$, at the same corresponding time points. The color scale bar of insets (h) to (m) has no unit. $J_{\vec{T}_{N-AFF}}$ values greater than 1 represent volumetric expansion, values smaller than 1 mean volumetric contraction.

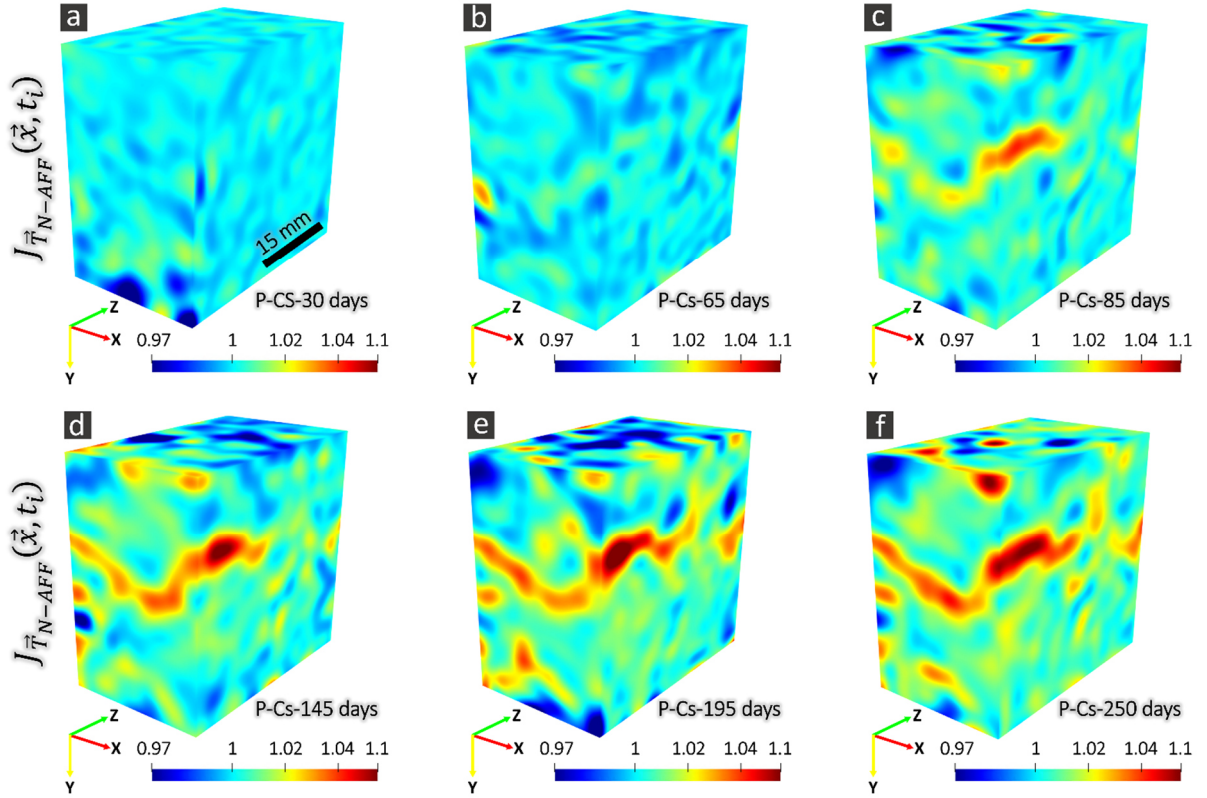


Figure C48. 3D Visualization of the determinant of the Jacobian matrix of $\vec{T}_{N-AFF}(\vec{x}, t_i)$, $J_{\vec{T}_{N-AFF}}(\vec{x}, t_i)$, computed from the displacement vector field, $\vec{u}_{N-AFF}(\vec{x}, t_i)$, associated with the non-affine transformation vector field, $\vec{T}_{N-AFF}(\vec{x}, t_i)$, obtained from the non-affine registration and used as indicator of the spatially heterogeneous component of the overall displacement due to the ASR deformations. Case of the P-Cs specimen. The scalar field is shown on the boundary surfaces of a parallelepiped ROI smaller than the tomographed volume of the specimen and it is color-coded. (a) to (f): time points of 30, 65, 85, 145, 195 and 250 days, respectively. The scale bars of all insets have no unit. $J_{\vec{T}_{N-AFF}}$ values greater than 1 correspond to volumetric expansion, values smaller than 1 to volumetric contraction.

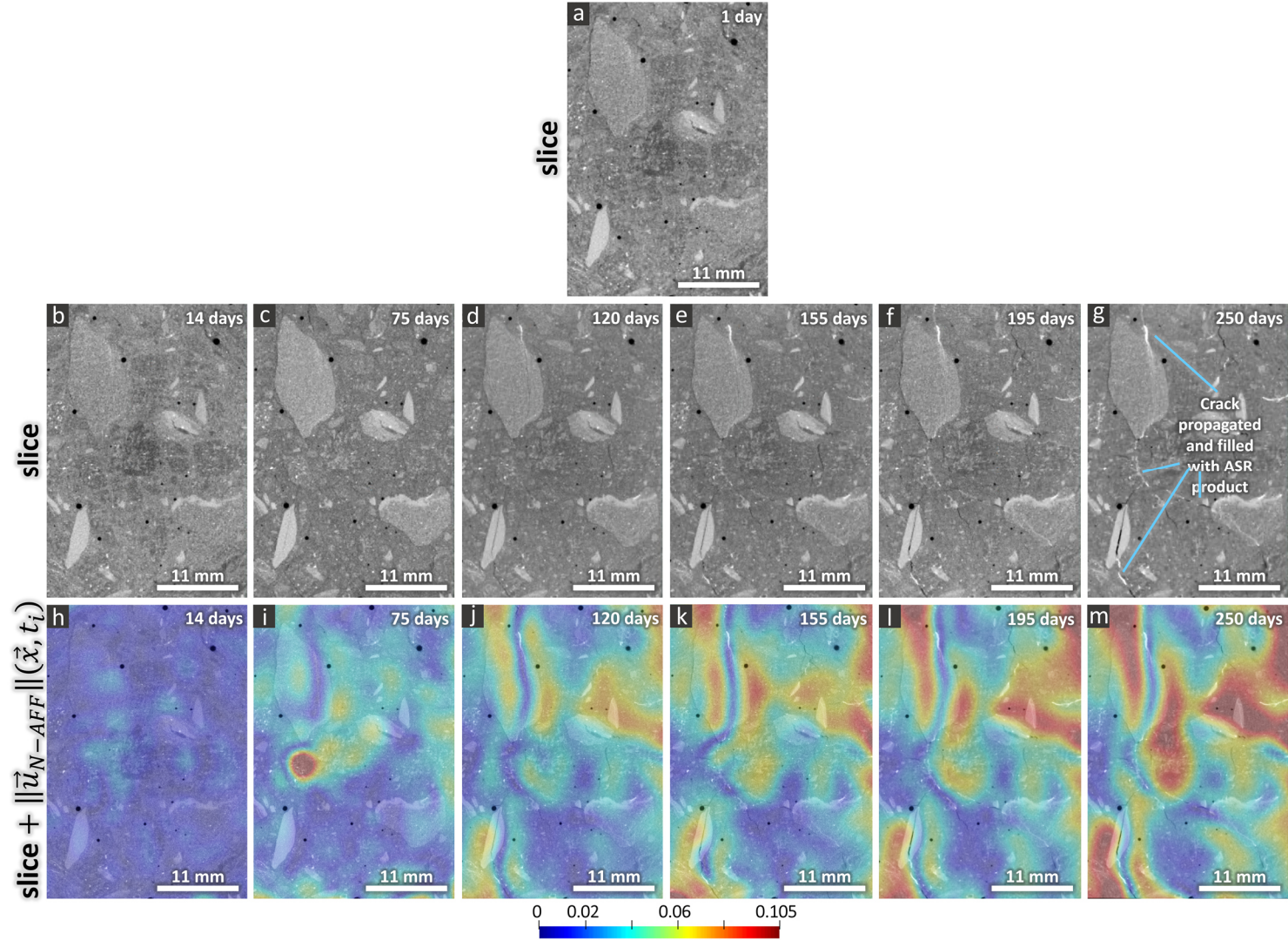


Figure C49. Similar figure as Figure C45 but for the U-Cs specimen.

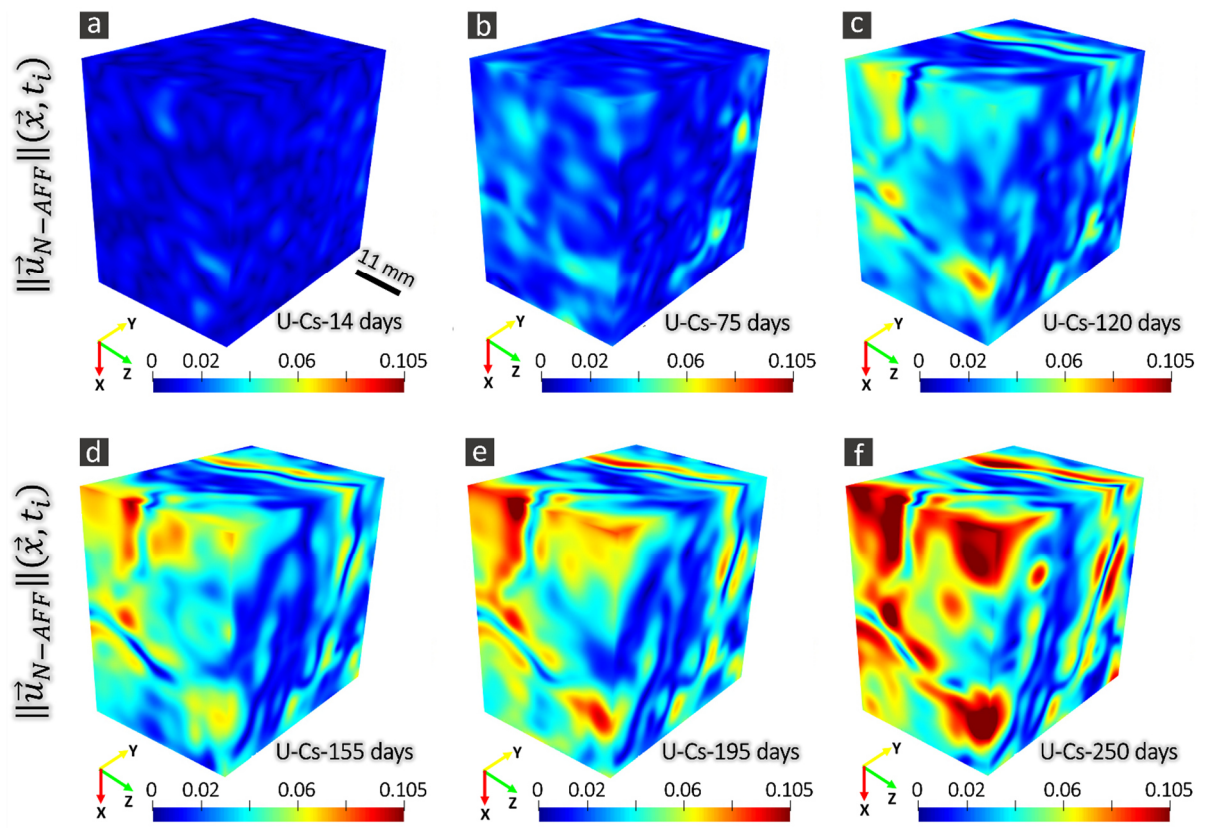


Figure C50. Similar figure as Figure C46 but for the U-Cs specimen.

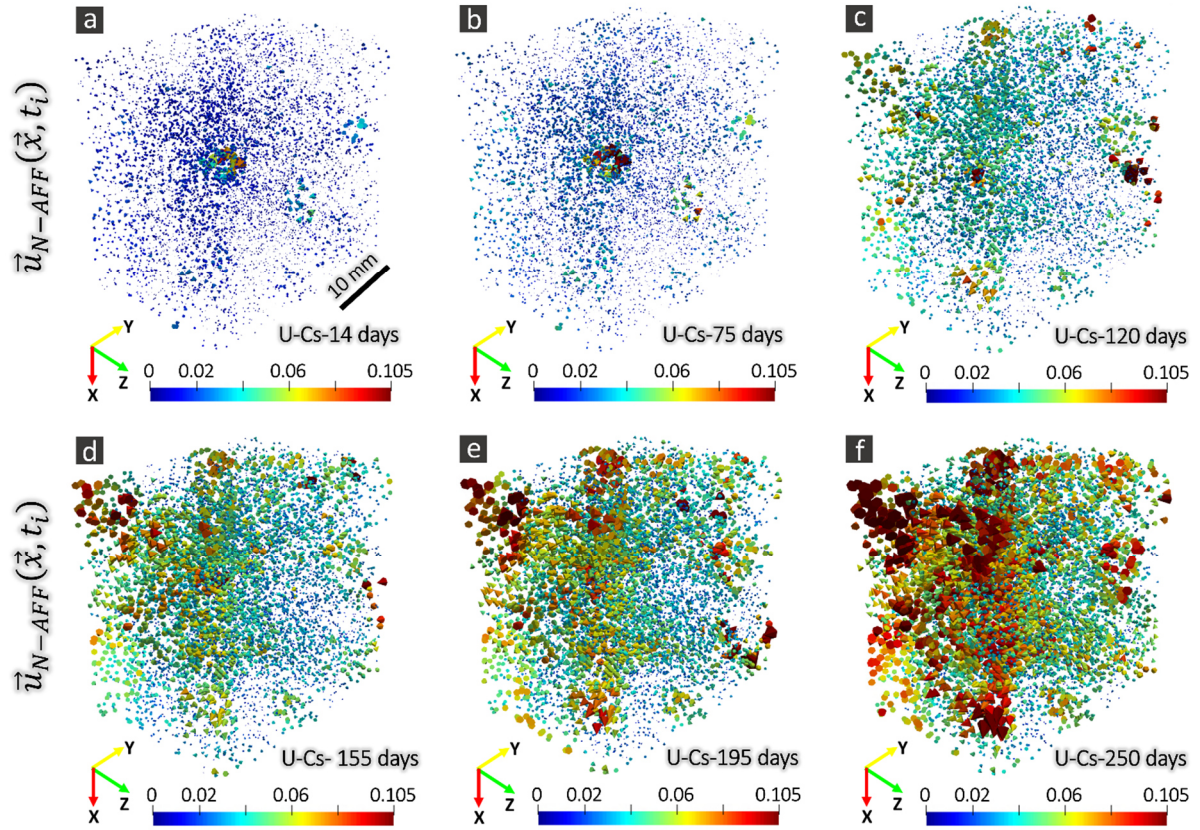


Figure C51. Similar figure as Figure C50 but showing this time the whole $\vec{u}_{N-AFF}(\vec{x}, t_i)$ vector field itself for the P-Cs specimen. $\vec{u}_{N-AFF}(\vec{x}, t_i)$ is represented by conic glyphs rendered at some voxel positions. The size and color of the glyphs represent the corresponding $\|\vec{u}_{N-AFF}\|(\vec{x}, t_i)$ values. In all insets, the unit for the color scale bar is mm.

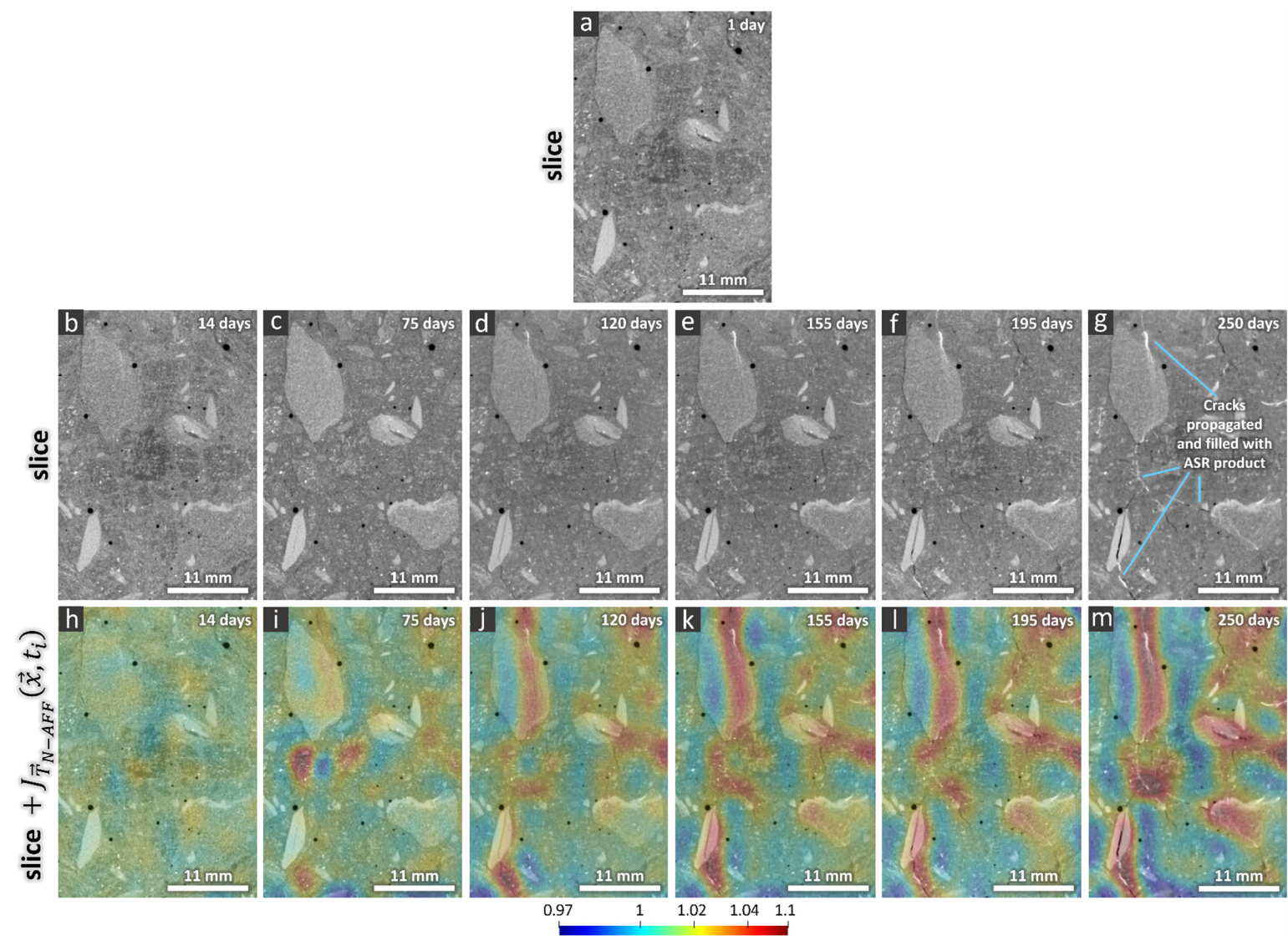


Figure C52. Similar figure as Figure C47Error! Reference source not found. but for the U-Cs specimen.

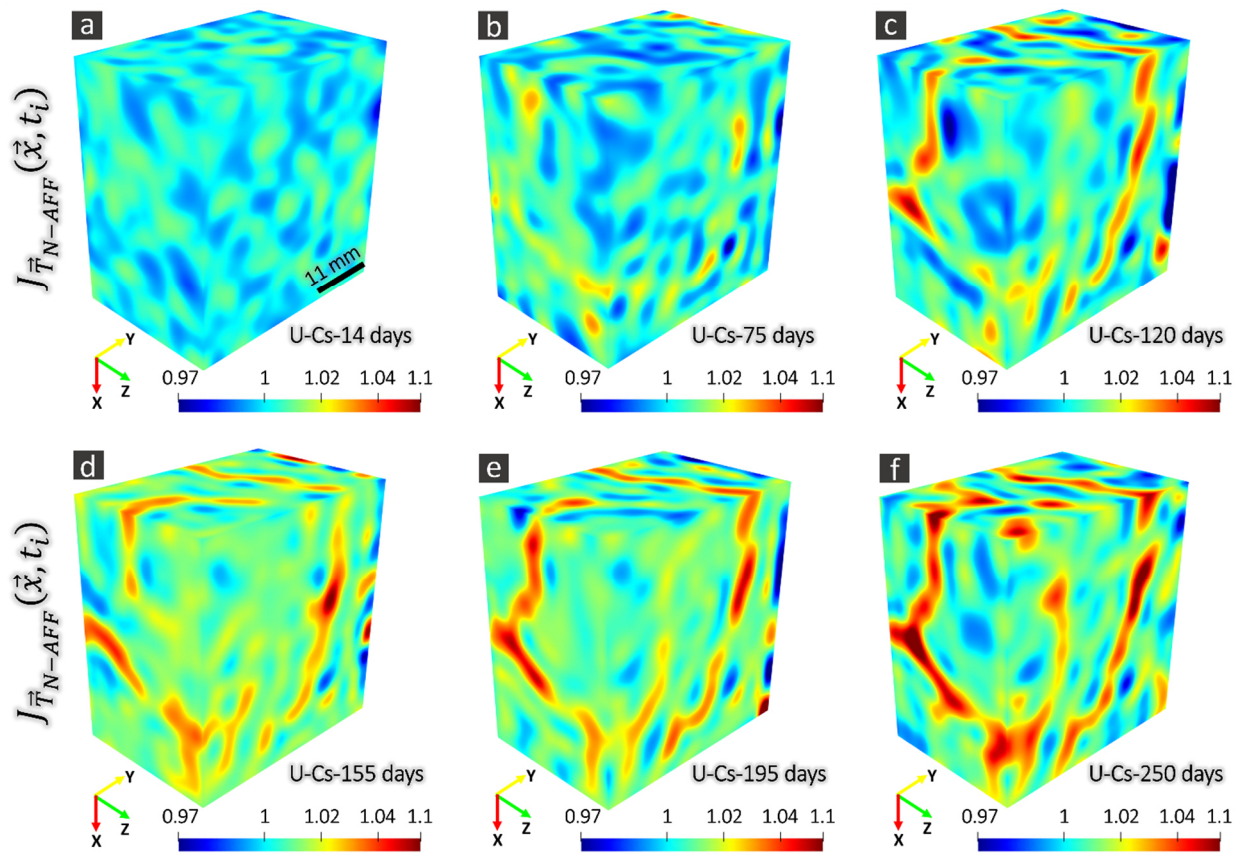


Figure C53. Similar figure as Figure C48 but for the U-Cs specimen.

Bibliography

- [1] “DIN EN 196-2 : 2013 | METHOD OF TESTING CEMENT - PART 2: CHEMICAL ANALYSIS OF CEMENT | SAI Global.” [Online]. Available: https://infostore.saiglobal.com/en-us/Standards/DIN-EN-196-2-2013-386164_SAIG_DIN_DIN_877353/. [Accessed: 11-Nov-2020].
- [2] “ISO - ISO 10694:1995 - Soil quality — Determination of organic and total carbon after dry combustion (elementary analysis).” [Online]. Available: <https://www.iso.org/standard/18782.html>. [Accessed: 11-Nov-2020].
- [3] I. Fernandes *et al.*, “Alkali-silica reactivity of some common rock types. A global petrographic atlas,” *Q. J. Eng. Geol. Hydrogeol.*, vol. 46, no. 2, pp. 215–220, May 2013, doi: 10.1144/qjegh2012-065.
- [4] D. De Paiva Gomes Neto, H. Conceição, V. A. C. Lisboa, R. S. De Paiva Santana, and L. S. Barreto, “Influence of granitic aggregates from Northeast Brazil on the alkali-aggregate reaction,” *Mater. Res.*, vol. 17, pp. 51–58, Aug. 2014, doi: 10.1590/S1516-14392014005000045.
- [5] A. Leemann and B. Münch, “The addition of caesium to concrete with alkali-silica reaction: Implications on product identification and recognition of the reaction sequence,” *Cem. Concr. Res.*, vol. 120, pp. 27–35, Jun. 2019, doi: 10.1016/j.cemconres.2019.03.016.
- [6] A. V. Bronnikov, “Cone-beam reconstruction by backprojection and filtering,” *J. Opt. Soc. Am. A*, vol. 17, no. 11, p. 1993, Nov. 2000, doi: 10.1364/josaa.17.001993.
- [7] “SIA 2042 NOTICE | Prevention of damage from the alkali | SNV.” [Online]. Available: <https://shop.snv.ch/Technische-Regel/Diverses/SIA-2042-MERKBLATT.html>. [Accessed: 11-Nov-2020].
- [8] D. Tschumperlé and R. Deriche, “Anisotropic Diffusion Partial Differential Equations for Multichannel Image Regularization: Framework and Applications,” *Advances in Imaging and Electron Physics*, vol. 145, no. SUPPL. pp. 149–209, 2007, doi: 10.1016/S1076-5670(06)45004-7.
- [9] B. Münch, “Xlib (ImageJ / Fiji plugins),” *ImageJ*, 2019. [Online]. Available: <https://imagej.net>.
- [10] C. A. Schneider, W. S. Rasband, and K. W. Eliceiri, “NIH Image to ImageJ: 25 years of image analysis,” *Nature Methods*, vol. 9, no. 7. Nat Methods, pp. 671–675, Jul-2012, doi: 10.1038/nmeth.2089.
- [11] B. Zitová and J. Flusser, “Image registration methods: A survey,” *Image Vis. Comput.*, vol. 21, no. 11, pp. 977–1000, Oct. 2003, doi: 10.1016/S0262-8856(03)00137-9.
- [12] K. Marstal, F. Berendsen, M. Staring, and S. Klein, “SimpleElastix: A user-friendly, multi-lingual library for medical image registration.”

-
- [13] B. C. Lowekamp, D. T. Chen, L. Ibáñez, and D. Blezek, “The Design of SimpleITK,” *Front. Neuroinform.*, vol. 7, 2013, doi: 10.3389/fninf.2013.00045.
- [14] A. Nan, M. Tennant, U. Rubin, and N. Ray, “DRMIME: Differentiable Mutual Information and Matrix Exponential for Multi-Resolution Image Registration,” PMLR, Sep. 2020.
- [15] S. Klein, M. Staring, K. Murphy, M. A. Viergever, and J. P. W. Pluim, “Elastix: A toolbox for intensity-based medical image registration,” *IEEE Trans. Med. Imaging*, vol. 29, no. 1, pp. 196–205, Jan. 2010, doi: 10.1109/TMI.2009.2035616.
- [16] R. Hagege and J. M. Francos, “Parametric estimation of affine transformations: An exact linear solution,” *J. Math. Imaging Vis.*, vol. 37, no. 1, pp. 1–16, May 2010, doi: 10.1007/s10851-009-0188-4.
- [17] A. Sotiras, C. Davatzikos, and N. Paragios, “Deformable medical image registration: A survey,” *IEEE Trans. Med. Imaging*, vol. 32, no. 7, pp. 1153–1190, 2013, doi: 10.1109/TMI.2013.2265603.
- [18] D. Rueckert, “Nonrigid registration using free-form deformations: Application to breast mr images,” *IEEE Trans. Med. Imaging*, vol. 18, no. 8, pp. 712–721, 1999, doi: 10.1109/42.796284.
- [19] M. Tsuchiya *et al.*, “Temporal subtraction of low-dose and relatively thick-slice CT images with large deformation diffeomorphic metric mapping and adaptive voxel matching for detection of bone metastases: A STARD-compliant article,” *Med. (United States)*, vol. 99, no. 12, 2020, doi: 10.1097/MD.00000000000019538.
- [20] R. Sakamoto *et al.*, “Temporal subtraction of serial CT images with large deformation diffeomorphic metric mapping in the identification of bone metastases,” *Radiology*, vol. 285, no. 2, pp. 629–639, Nov. 2017, doi: 10.1148/radiol.2017161942.
- [21] K. Onoue *et al.*, “CT temporal subtraction improves early detection of bone metastases compared to SPECT,” *Eur. Radiol.*, vol. 29, no. 10, pp. 5673–5681, Oct. 2019, doi: 10.1007/s00330-019-06107-w.
- [22] I. Cruz-Matías *et al.*, “Sphericity and roundness computation for particles using the extreme vertices model,” *J. Comput. Sci.*, vol. 30, pp. 28–40, Jan. 2019, doi: 10.1016/j.jocs.2018.11.005.
- [23] E. R. Dougherty and R. A. Lotufo, *Hands-on Morphological Image Processing*. SPIE, 2003.
- [24] T. Perciano *et al.*, “Insight into 3D micro-CT data: Exploring segmentation algorithms through performance metrics,” *J. Synchrotron Radiat.*, vol. 24, no. 5, pp. 1065–1077, Sep. 2017, doi: 10.1107/S1600577517010955.
- [25] H. Jin, C. Sciammarella, S. Yoshida, and L. Lamberti, Eds., *Advancement of Optical Methods in Experimental Mechanics, Volume 3*. Cham: Springer International Publishing, 2014.
- [26] F. Hild *et al.*, “ON THE USE OF 3D IMAGES AND 3D DISPLACEMENT
-

- MEASUREMENTS FOR THE ANALYSIS OF DAMAGE MECHANISMS IN CONCRETE-LIKE MATERIALS ON THE USE OF 3D IMAGES AND 3D DISPLACEMENT MEASUREMENTS FOR THE ANALYSIS OF DAMAGE MECHANISMS IN CONCRETE-LIKE MATERIALS. VIII,” in *International Conference on Fracture Me-chanics of Concrete and Concrete Structures*, 2013.
- [27] M. R. Teague, “IMAGE ANALYSIS VIA THE GENERAL THEORY OF MOMENTS.,” *J. Opt. Soc. Am.*, vol. 70, no. 8, pp. 920–930, Aug. 1980, doi: 10.1364/JOSA.70.000920.
 - [28] D. N. Theodorou and U. W. Suter, “Shape of Unperturbed Linear Polymers: Polypropylene,” *Macromolecules*, vol. 18, no. 6, pp. 1206–1214, 1985, doi: 10.1021/ma00148a028.
 - [29] S. T. Erdoğan, E. J. Garboczi, and D. W. Fowler, “Shape and size of microfine aggregates: X-ray microcomputed tomography vs. laser diffraction,” *Powder Technol.*, vol. 177, no. 2, pp. 53–63, Aug. 2007, doi: 10.1016/j.powtec.2007.02.016.
 - [30] M. Zemp, O. Y. Gnedin, N. Y. Gnedin, and A. V. Kravtsov, “On determining the shape of matter distributions,” *Astrophys. Journal, Suppl. Ser.*, vol. 197, no. 2, p. 30, Dec. 2011, doi: 10.1088/0067-0049/197/2/30.
 - [31] H. Goldstein, C. P. Poole, and J. L. Safko, “The Rigid Body Equations of Motion: Classical Mechanics, 3rd ed.,” *Pearson*, 2013. .
 - [32] M. C. Cavalli, M. Griffa, S. Bressi, M. N. Partl, G. Tebaldi, and L. D. Poulikakos, “Multiscale imaging and characterization of the effect of mixing temperature on asphalt concrete containing recycled components,” *J. Microsc.*, vol. 264, no. 1, pp. 22–33, Oct. 2016, doi: 10.1111/jmi.12412.
 - [33] T. Hildebrand and P. Rüegsegger, “A new method for the model-independent assessment of thickness in three-dimensional images,” *J. Microsc.*, vol. 185, no. 1, pp. 67–75, 1997, doi: 10.1046/j.1365-2818.1997.1340694.x.
 - [34] M. H. Protter and B. Charles Jr, *Intermediate Calculus*. 2012.
 - [35] A. Leemann, “Impact of different added alkalis on concrete expansion due to ASR,” in *Proceeding of international conference on Alkali-Aggregate Reaction in Concrete, (ICAAR2022)*, 2022, no. 31 May 2021, pp. 175–184.
 - [36] P. M. Adler and J.-F. Thovert, “Analysis and Generation of Random Objects,” in *Fractures and Fracture Networks*, vol. 15, Dordrecht: Springer Science+Business Media, 1999, pp. 15–66.
 - [37] D. C. P. Peacock, C. W. Nixon, A. Rotevatn, D. J. Sanderson, and L. F. Zuluaga, “Glossary of fault and other fracture networks,” *J. Struct. Geol.*, vol. 92, pp. 12–29, Nov. 2016, doi: 10.1016/j.jsg.2016.09.008.

Appendix D

Supplementary data for Chapter 6

D1. Optimization of the BaSO₄ concentration and assessment of its effects on the ASR (cracking)

D1.1. SEM/EDX analysis of raw materials and of ASR products

SEM-BSE was used both to assess the size range of the BaSO₄ grains and to characterize qualitatively their spatial distribution in the concrete specimens cast with it.

Figure D1 shows SEM-BSE micrographs of both the BaSO₄ powder's grains compared against the cement ones, insets (a) and (b), respectively. Insets (c) and (d) show ROIs in the cement paste of one U-3 vol.%Ba specimen at 40 days from casting (i.e., 39 days of ASR acceleration). The BaSO₄ grains had larger BSE pixel value than any other material phase because of their larger electron density, compared with the un-hydrated cement grains, which are by themselves denser than the cement hydrates. From insets (c) and (d), it is possible to assess that the BaSO₄ grains (the brightest, small spots) were homogeneously dispersed throughout the cement paste and seemed not to have interacted at all with the hydrating cement, as expectable based upon what already reported in the literature [1].

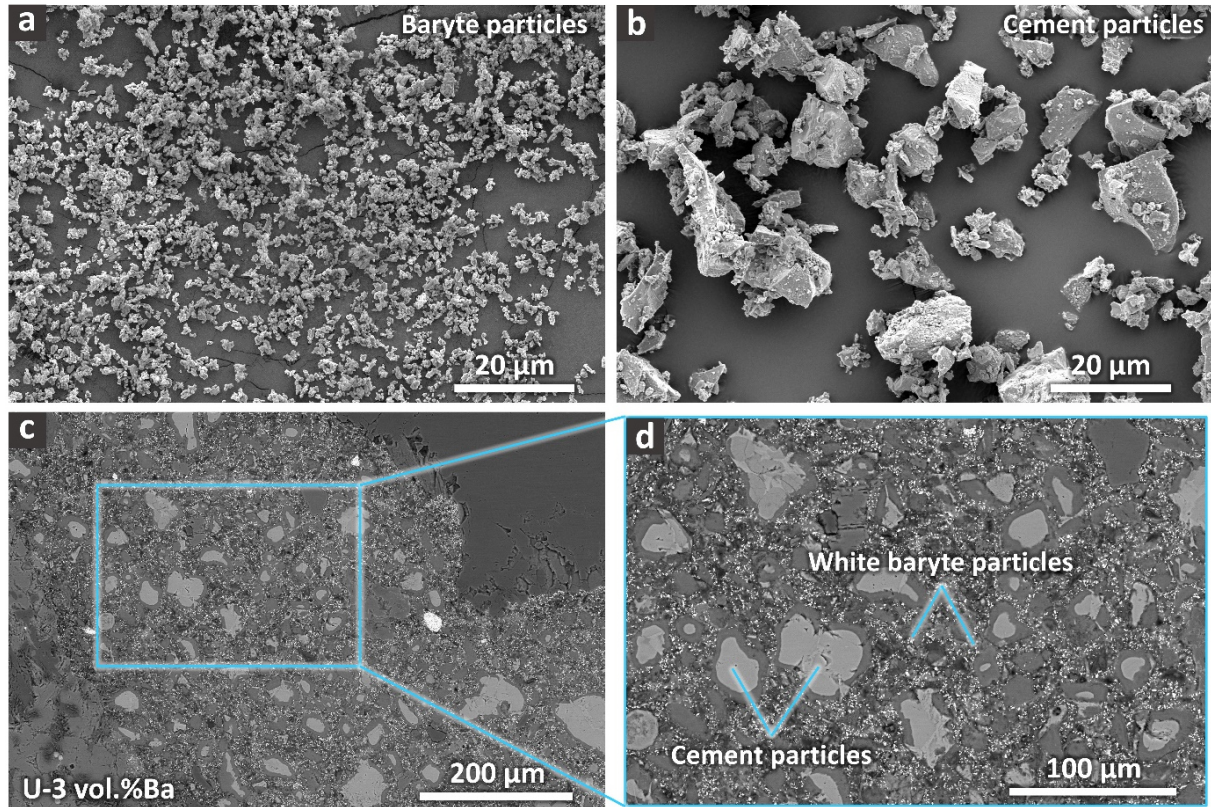


Figure D1. An example of SEM-BSE micrographs of (a) the used BaSO_4 powder, (b) the used cement powder, for comparison, (c) the cross-section of a specimen cast with 3 vol.-% of BaSO_4 at 40 days from casting, and (d) a region of interest of inset (c) to highlight the spatial distribution of the BaSO_4 grains across the cement paste.

SEM-BSE was also exploited to analyse the morphology of the ASR products formed in specimens cast with and without BaSO_4 . Figure D2 shows in some of such micrographs ASR products inside cracks in specimens at 120 days, cast both without and with BaSO_4 at a concentration of 2.5 vol.-%. All micrographs were acquired for aggregate interior regions, where the ASR products are expected to be rather crystalline, with a plate-like morphology. Regardless of the BaSO_4 absence or presence, the ASR products exhibited analogous morphology and BSE contrast inside the aggregates. This result suggests that no significant perturbation of ASR took place because of the presence of BaSO_4 in the cement paste, in agreement with the available knowledge from the literature about its very low solubility in aqueous environments [2].

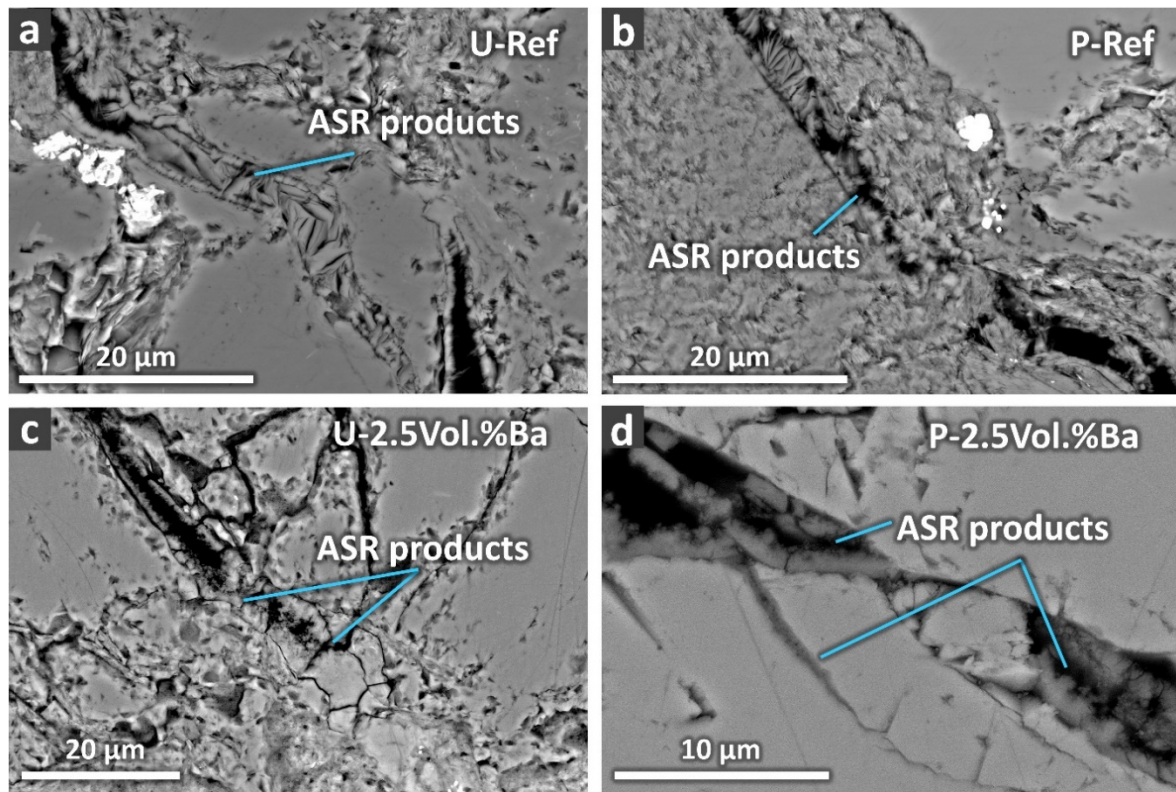


Figure D2. SEM-BSE micrographs providing examples of the distribution of ASR products inside cracks of specimens containing both aggregate types and either without or with BaSO_4 . For every specimen type, the micrographs were acquired at 120 days. Micrographs for (a) U-Ref, (b) P-Ref, (c) U-2.5 vol.-% BaSO_4 , (d) P-2.5 vol.-% BaSO_4 , respectively.

The EDX point analysis of ASR products in different regions of distinct specimens, without and with BaSO_4 , confirmed their similarity in terms of chemical composition. Figure D3 shows ternary diagrams, obtained by such EDX analysis. As it is observed in such ternary diagrams, the ASR products compositions remained almost identical regardless of aggregate type and of the presence or not of BaSO_4 . No sign of Ba^+ or SO_4^- incorporation into the ASR products was detected, providing additional evidence of the BaSO_4 chemical stability in the concrete aqueous environment.

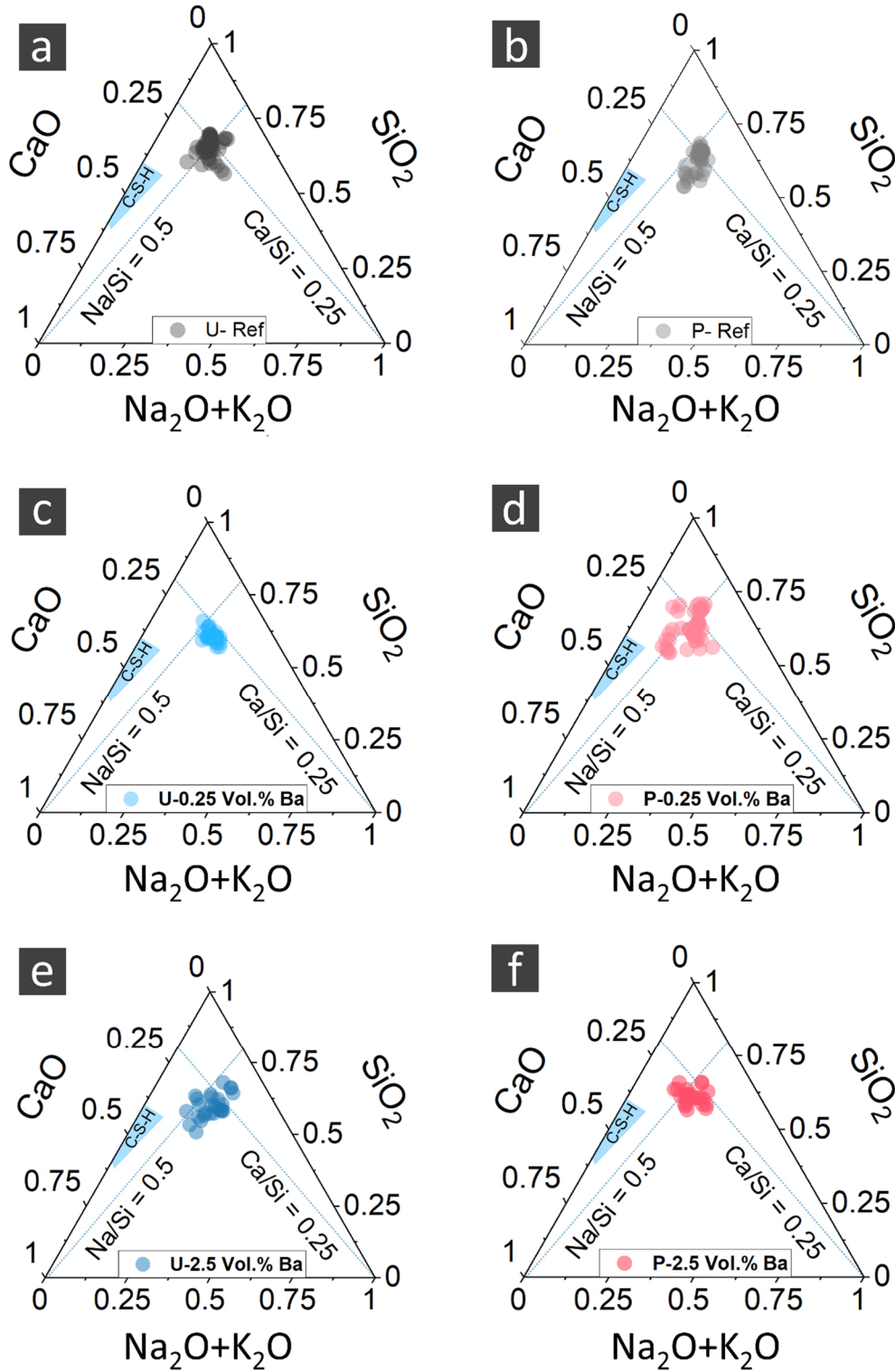


Figure D3. EDX analysis results showing the equivalent sodium oxide ternary diagrams for ASR products located at more than 30 points and both of crystalline type (i.e., inside the aggregates) and of amorphous type (at the aggregate boundary regions and in the cement paste). The investigated specimens were cast with both aggregate types and without or with two BaSO_4 concentrations. (a) U-Ref, (b) P-Ref, (c) U-0.25 vol.-% BaSO_4 , (d) P-0.25 vol.-% BaSO_4 , (e) U-2.5 vol.-% BaSO_4 , (f) P-2.5 vol.-% BaSO_4 specimens, respectively.

D1.2. Time-lapse XT

Reference specimens

Selected ROIs on slices from the tomograms of two U-Ref and P-Ref specimens are shown in Figure D4 (a) and (b), respectively. These two ROIs are shown in order to convey, for each aggregate type, an example of level of X-ray attenuation contrast between aggregates and the cement paste which could be achieved in the absence of BaSO₄. It can be seen that the contrast was extremely low for almost all the U aggregates while it was a bit higher for some but not all the P ones. The latter feature can be explained based upon the higher mineralogical heterogeneity of the P aggregates compared with that of the U aggregates.

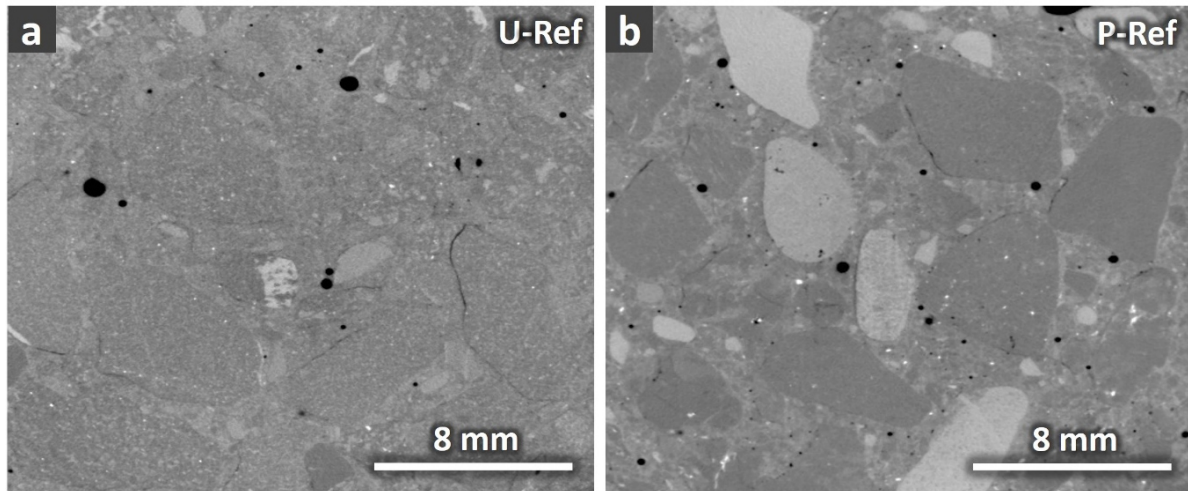


Figure D4. A ROI example on a tomographic slice from (a) one U-Ref specimen and (b) one P-Ref specimen. These tomograms, for both specimens, were acquired at 1 day since the ASR acceleration start.

D1.3. Influence of BaSO₄ addition

By comparing Figure D4 (a) with Figures D5 (a) to (e), it is possible to observe that the addition of BaSO₄ to the mix did not provide any enhancement of the X-ray attenuation contrast in the tomograms of the U specimens when its concentration was smaller than or equal to 0.25 vol.-%. The same result was obtained for the tomograms of the P specimens, as evident when comparing Figure D4 (b) with Figures D6 (a) to (e).

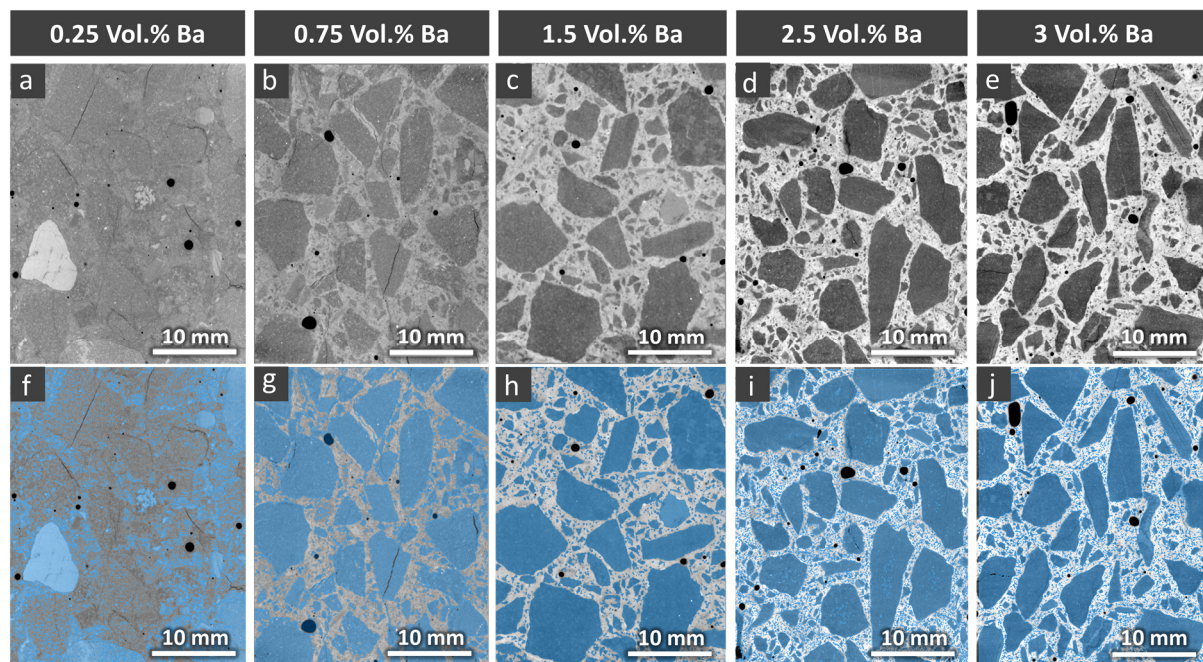


Figure D5. (a) to (e): examples of ROIs on tomographic slices at 150 days of ASR acceleration, from specimens cast with the U aggregates and with various BaSO_4 concentrations. These ROIs are containing also the ones shown in Figure 6.1 in Chapter 6. (f) to (j): the same slices as in (a) to (e) but, additionally, with the corresponding slices from the binary tomograms of the segmented aggregates rendered as semi-transparent, in blue and overlaid on top of the tomographic slices.

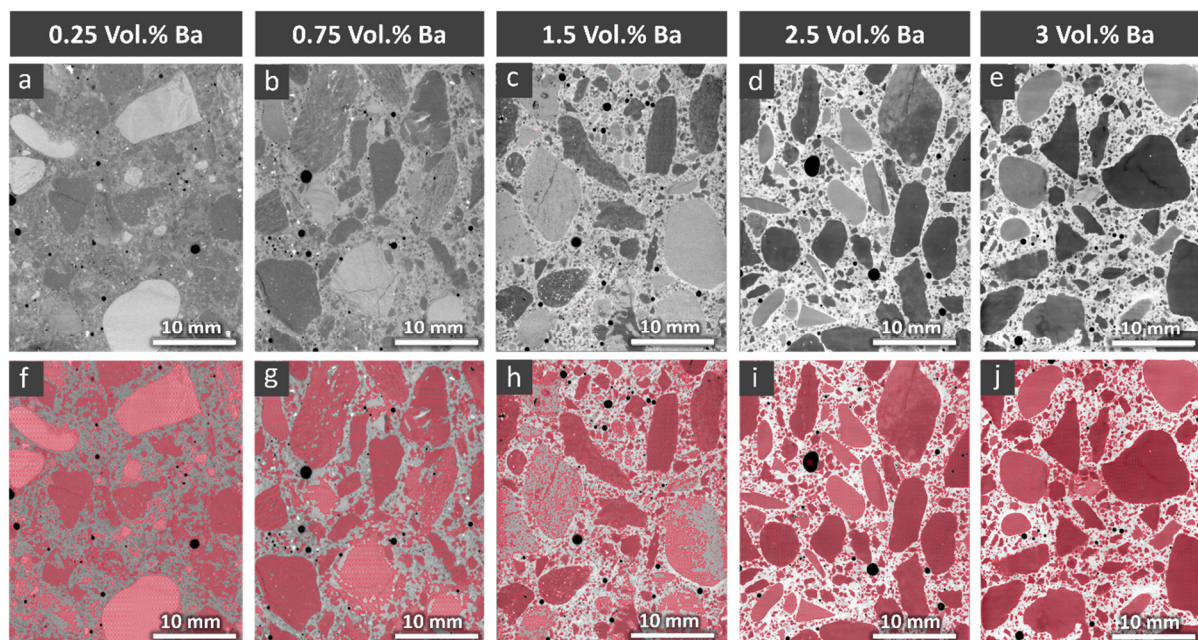


Figure D6. Similar figure as Figure D5 but for the specimens cast with the P aggregates.

D1.4. Local deformations induced by ASR cracking as assessed by time-lapse XT analysis

Reference specimens

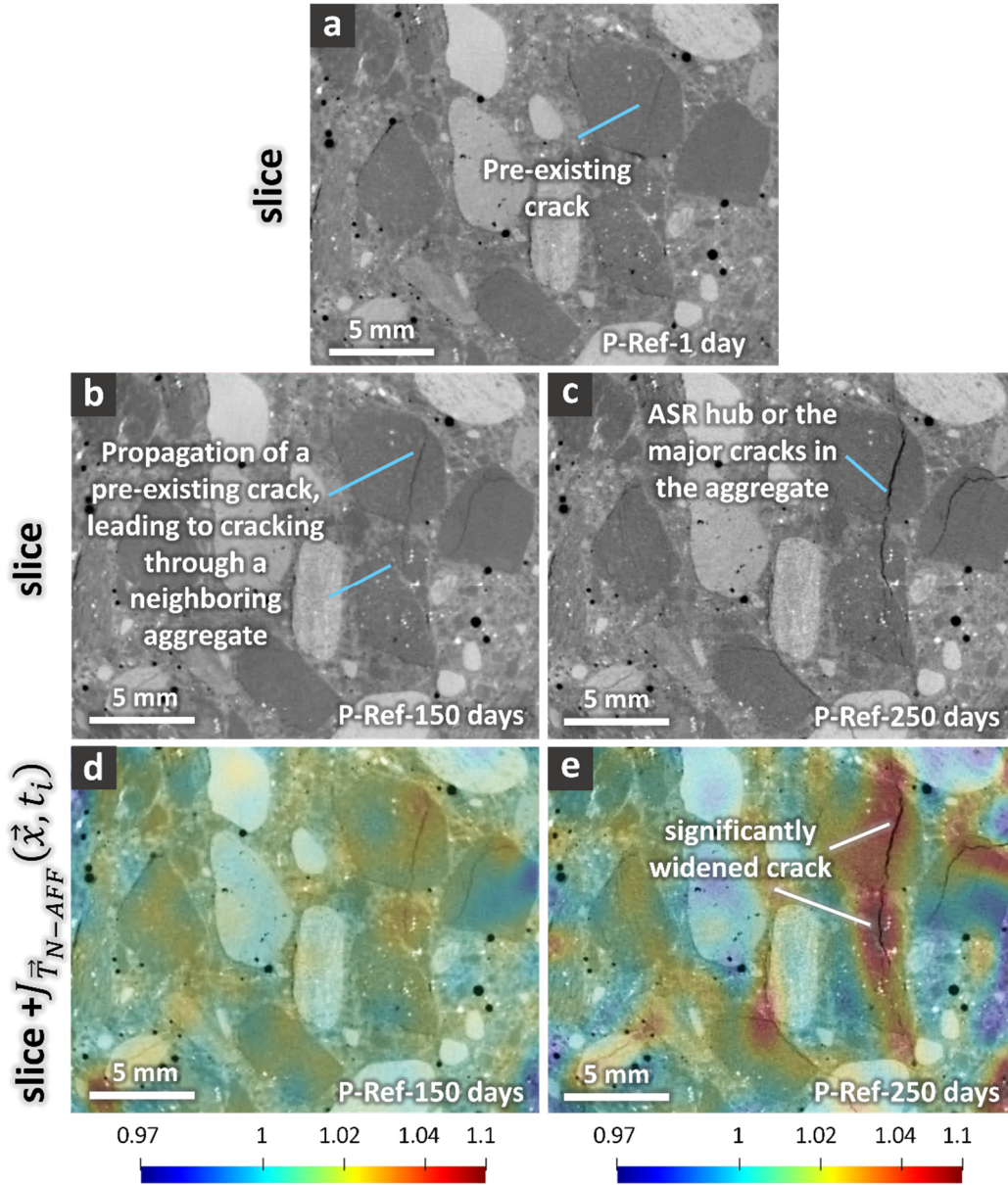


Figure D7. Visualization of the evolution of ASR cracks and associated localized deformations for the P-Ref specimen, by considering one slice from its tomographed volume, at multiple time points. The localized deformations are estimated by the determinant of the Jacobian matrix ($J_{\vec{T}_{N-AFF}}(\vec{x}, t_i)$) of the transformation vector field $\vec{T}_{N-AFF}(\vec{x}, t_i)$ associated with the non-affine registration. Its values larger than 1 indicate local volumetric expansion. Its values smaller than 1 indicate volumetric shrinkage. (a) X-ray tomogram at 1 day since start of the ASR acceleration. (b) and (c): slice at the same position as in (a) but from the tomograms at 150 and 250 days, respectively. (d) and (e): the same slice as in (b) and (c), respectively, and, overlapped on top of them in a semi-transparent way, the slice at the same position but from $J_{\vec{T}_{N-AFF}}(\vec{x}, t_i)$ at the corresponding time points, respectively. The scale bars in (d) and (e) have, by definition of $J_{\vec{T}_{N-AFF}}$ (relative volume), no unit.

Cracks in the reference specimens were segmented following the same TS-based procedure described at point (III) in Section 3.3. Figure D8 and Figure D9 showcase the segmented, full crack networks, as solid objects rendered in 3D, at three distinct time points, for the U-Ref and P-Ref specimens, respectively. The parallelepiped box encompassing the crack networks, indicates the tomographed volume of the specimens. The rendering views are exactly the same in all the rendered binary tomograms. The cracks seemed to be rather homogeneously distributed inside the tomographed volume. As time evolved, a larger crack volume fraction was achieved by both specimens.

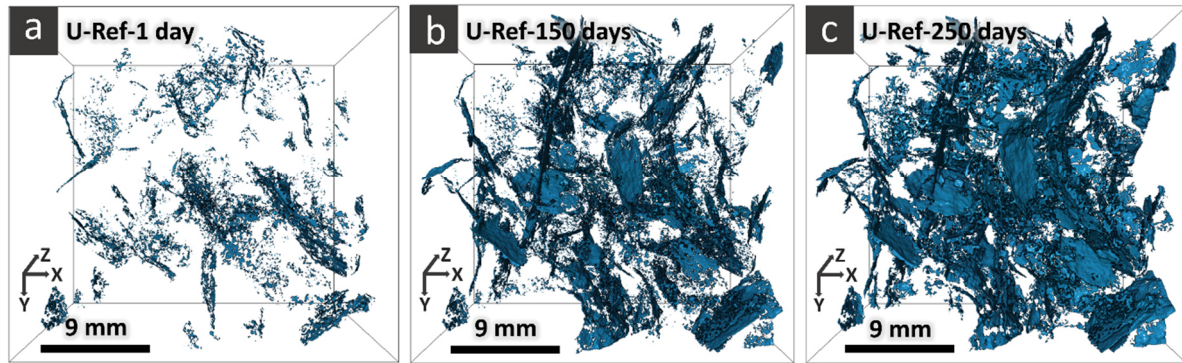


Figure D8. Temporal evolution of the crack network in the U-Ref specimen. (a)-(c): 3D rendering of the crack binary tomogram for the full tomographed volume of the specimen, at 1, 150 and 250 days, respectively

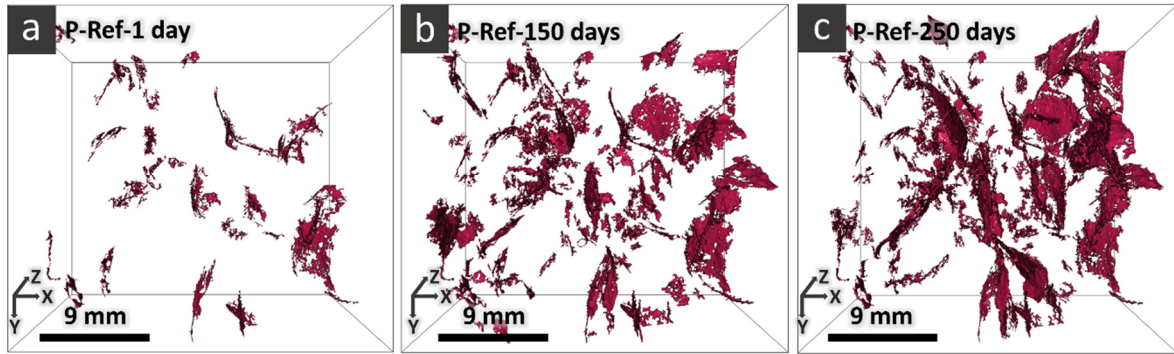


Figure D9. The same images as shown in Figure D8, but for the P-Ref specimen.

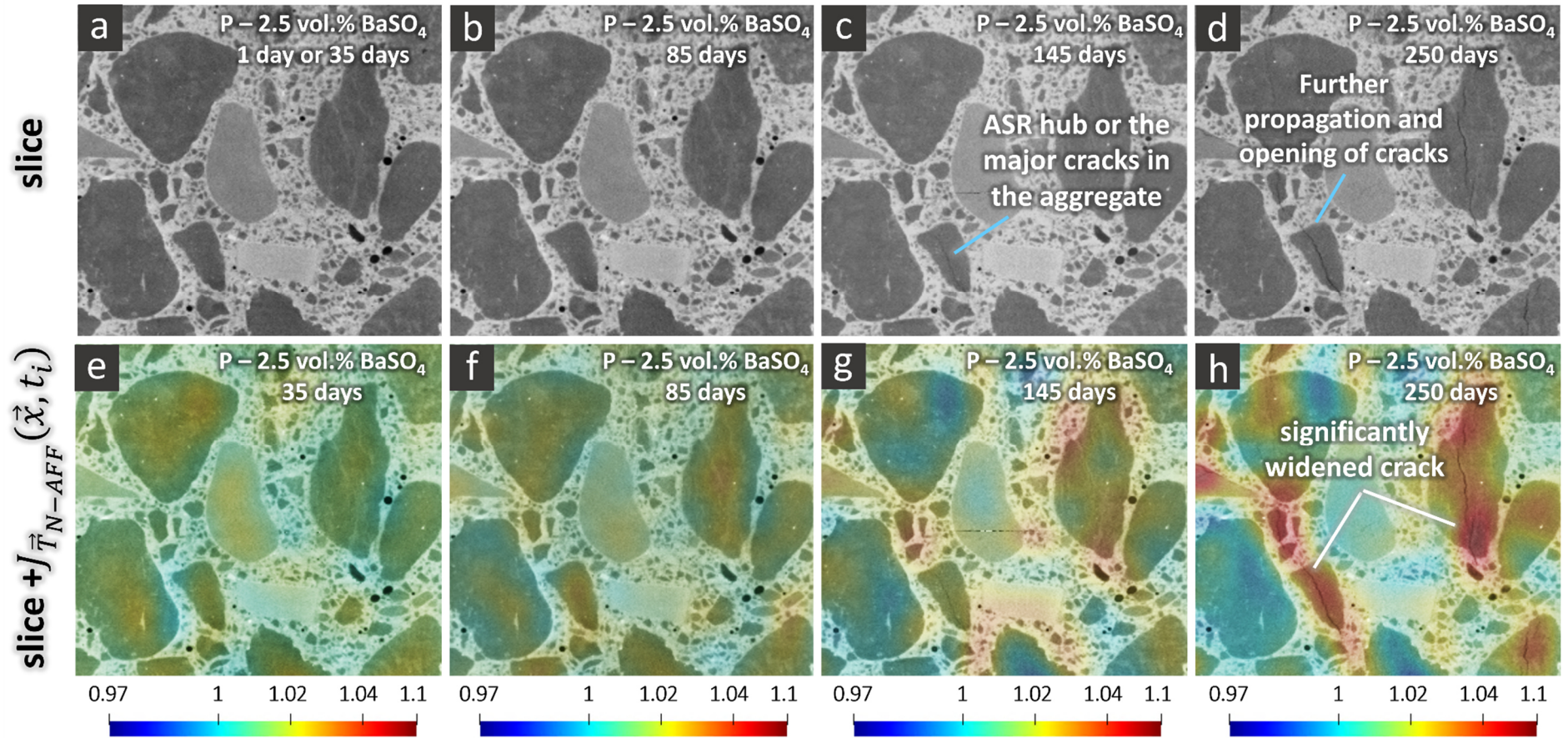
Specimens with BaSO₄

Figure D10. Similar visualization as in Figure 6.7 for the P-2.5 vol.-% BaSO₄ specimen. The chosen time points for the visualization are 35 days (insets (a) and (e)), 85 days ((b) and (f)), 145 days ((c) and (g)), 250 days ((d) and (h)). The tomograms did not change significantly between 1 day and 35 days. Thus, the one at 35 days was representative of the reference tomogram at 1 day.

The cracks in the specimens cast with BaSO_4 were segmented also by following the same TS-based procedure described in Section 3.3. In addition to their segmentation, the availability of an additional label for each voxel, i.e., whether it belonged to aggregates or not, allowed classifying crack voxels also based upon whether they were inside aggregates or outside them.

Figure D11 and Figure D12 show the time series of binary tomograms of cracks distinguishing by color their parts belonging to aggregate regions from their parts within the cement paste, for the U-2.5vol% Ba and the P-2.5vol.% Ba specimens, respectively.

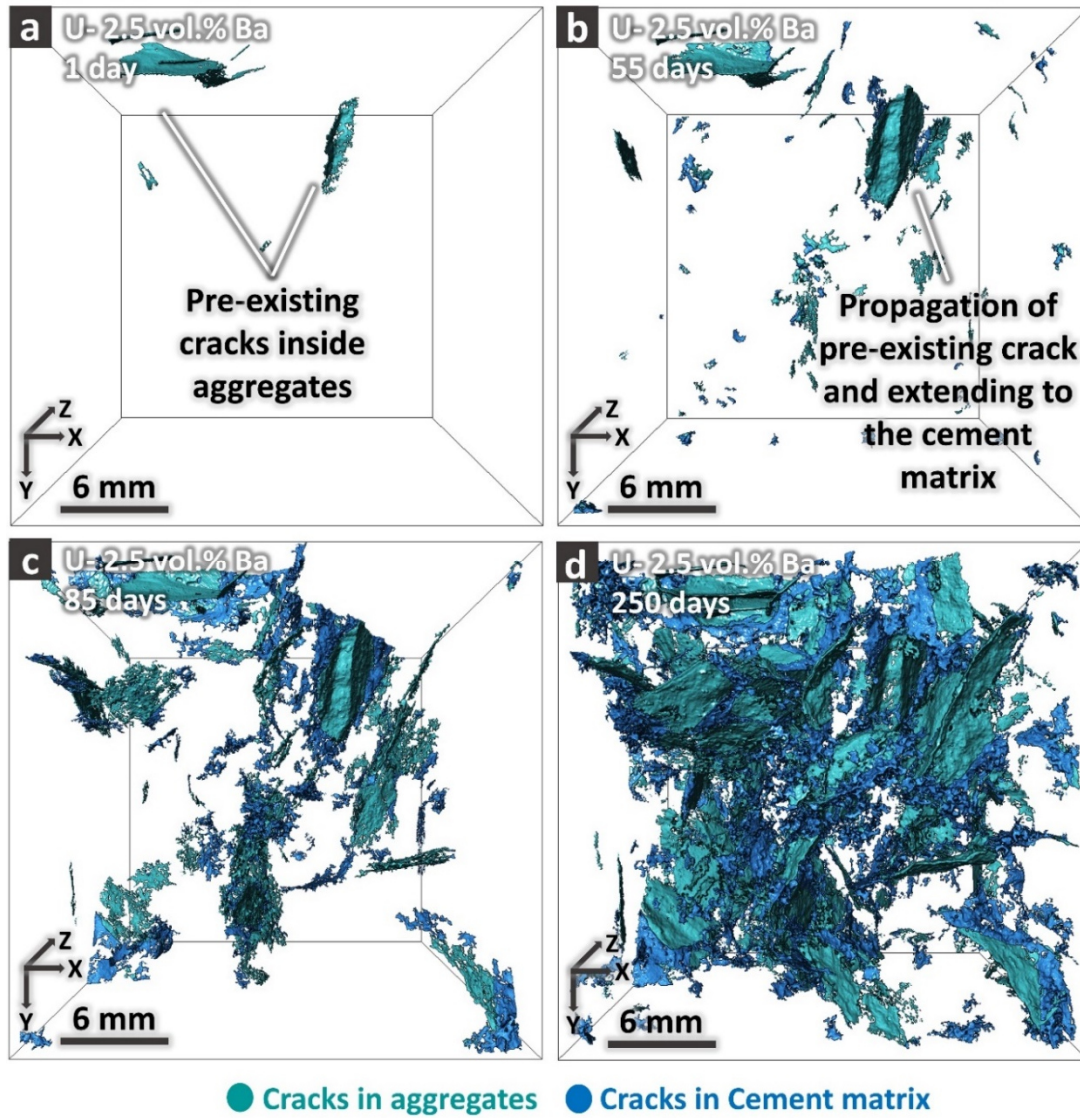


Figure D11. A small ROI of the segmented cracks binary tomograms, distinguishing between cracks inside aggregates (in cyan) and those within the cement paste (in blue), rendered for the U-2.5 vol.-% BaSO_4 specimen. Such ROI contained cracks, which were nucleated in an aggregate and further propagated into the surrounding cement paste. The insets from (a) to (d) correspond to different time points during the ASR acceleration, including 1, 55, 85 and 250 days, respectively.

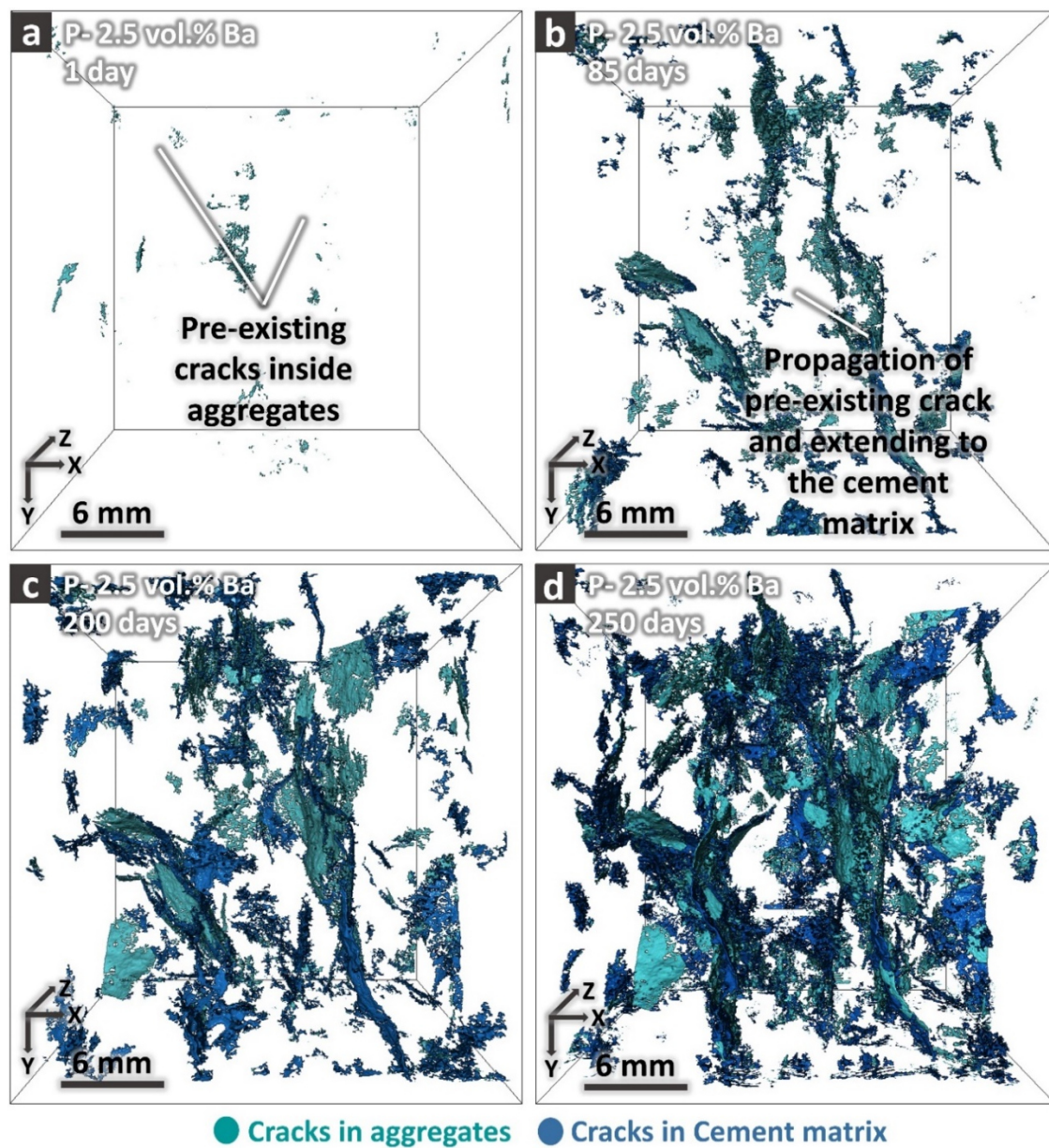


Figure D12. Similar visualization as shown in Figure D11 but for the P-2.5 vol.-% BaSO₄ specimen and at ((a) to (d)) 1, 85, 200 and 250 days, respectively

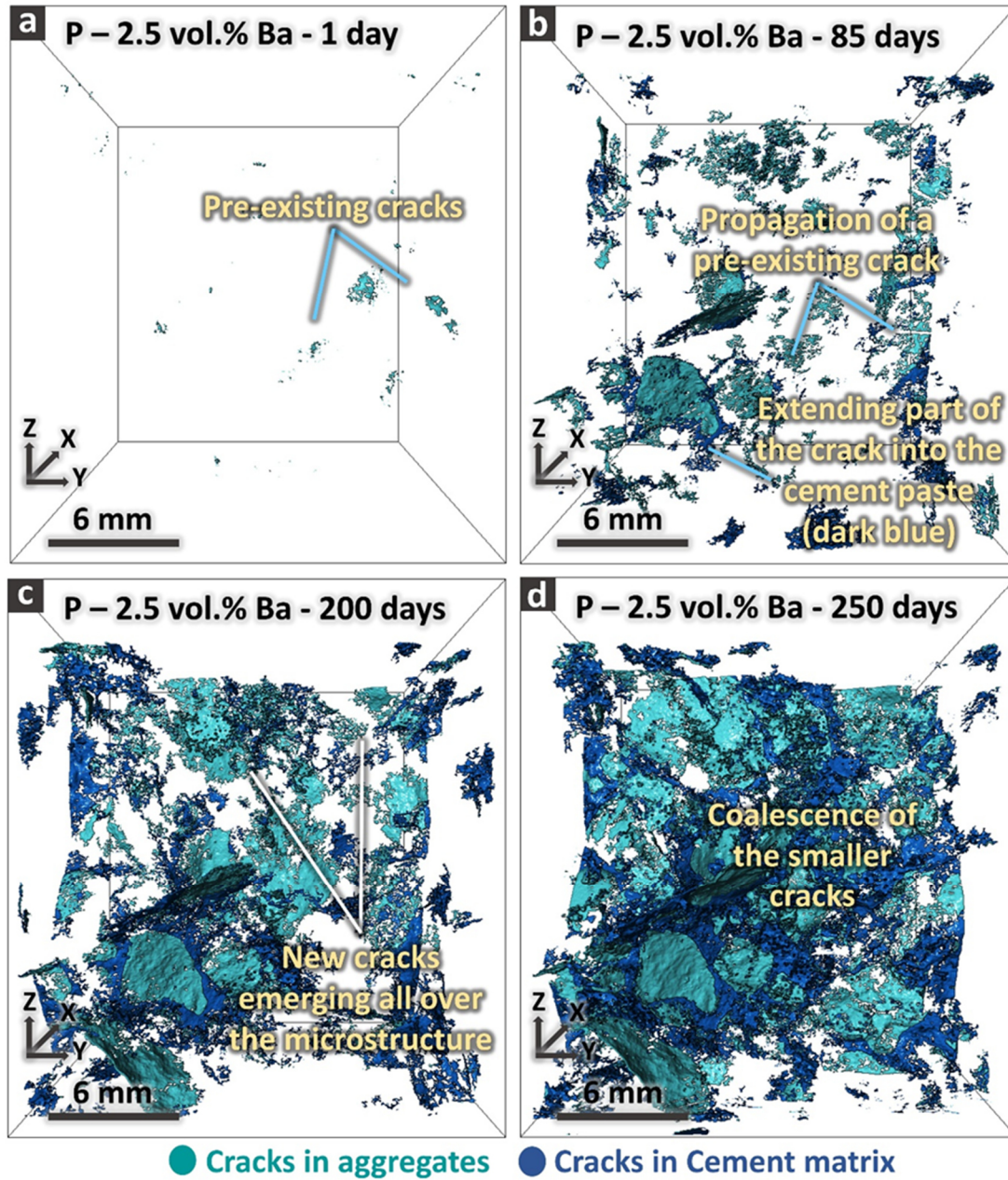


Figure D13. Similar visualization as in Figure D12 but for a distinct ROI.

D1.5. Shape tensor analysis of the separated cracks

Figure D14 (a) shows the 3D rendering of the segmented, total crack network of the U-Ref specimen at 250 days. Distinct, disconnected cracks are rendered with different colors. Despite a great complexity, several cracks could be clearly distinguished, which indicates that the crack network labelling managed to recognize the distinct cracks.

As mentioned in Section 6.3.25, the shape tensor analysis was carried out at distinct time points on the segmented cracks of each tomographed specimen, to quantitatively characterize their shape and orientation. Figure D14 (b) shows the 3D rendering of a single crack extracted from the labelled binary tomogram of the total crack network rendered in inset (a), to serve as an example for the shape of an isolated ASR crack and its shape tensor. The three *eigenvectors* of the crack are also rendered as solid arrows, starting from the center of mass of the crack itself.

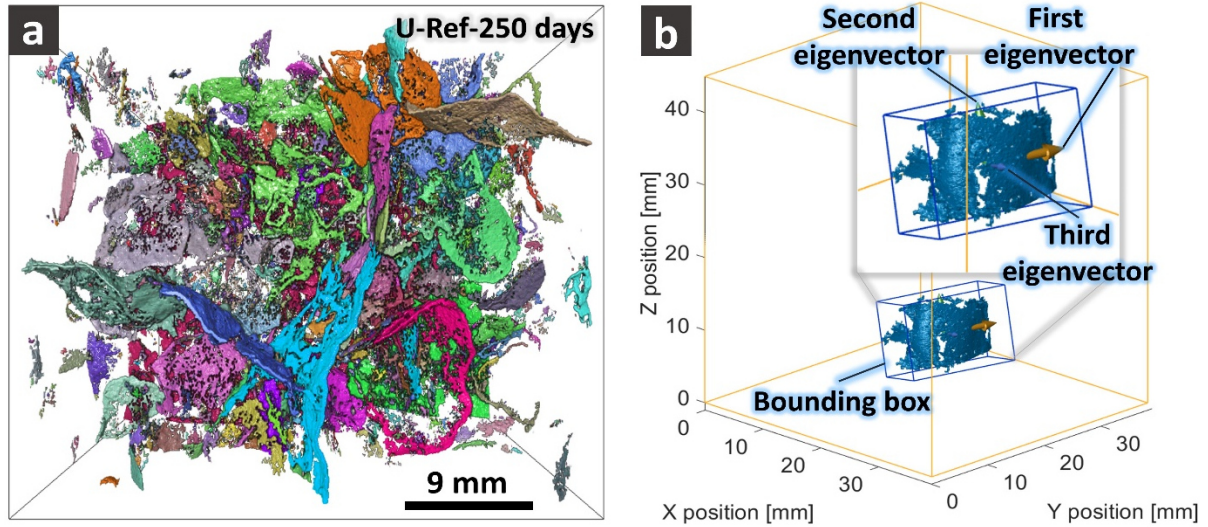


Figure D14. (a): 3D rendering of the segmented, total crack network of the U-Ref specimen, at 250 days. Each separated part (branch) of the crack network is rendered with a distinct color, just for the purpose of distinguishing them. The color assignment to each branch was random. (b) A single separated crack from the networks shown in (a). The large parallelepiped box highlighted in orange delineates the tomographed volume. The smaller grey box shows a zoom-in view of the respective crack. The blue, parallelepiped box is the crack's bounding box oriented according to the three eigenvectors of the crack's shape tensor \mathbf{G} . Each eigenvector, located at the center of mass of the crack and scaled by half the lateral size of the bounding box along the same direction, is also rendered as a solid arrow. The red arrow refers to the eigenvector associated with the 1st eigenvalue. The green arrow to the second eigenvector and the blue one to the third.

D2. Extensive quantitative analysis of specimens with optimal BaSO₄ concentration

D2.1. Mass and length evolution

Relative length and mass change measurement results

The relative length and mass changes of the specimens with size $25 \times 25 \times 100 \text{ mm}^3$, cast with both aggregate types, U and P, are compared in insets (a) and (b) of Figure D15, respectively. It is observed for both specimen types that the relative length changes increased faster for the specimens cast with the U aggregates (labelled as *u* in inset (a)) after the initial shrinkage period, i.e., after about 56 days. The mass gain was only slightly higher/comparable for the *u* specimens after 110 days. As observed in chapter 5, the ASR-reactivity of U aggregates are higher than the P ones.

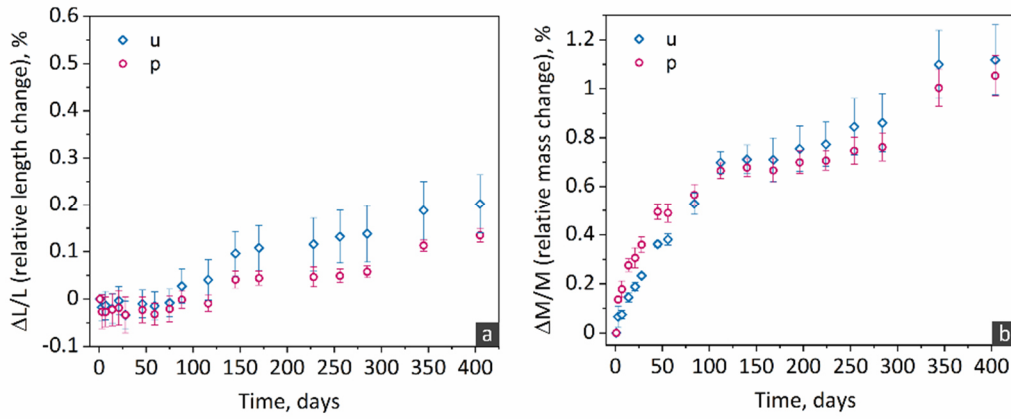


Figure D151. Comparison of the time series of the relative (a) length and (b) mass changes of the *u* and *p* specimens. The relative length changes were measured by the expansion measurement setup 2 shown in Figure 3.1 (e) and described in details in Section A4 of the Appendices. At each time point, the same 10 specimens were measured upon. In each plot, each marker shows the average of the 10 values, while the error bar was defined as the empirical standard deviation of such ensemble of sampled values.

D2.2. Mechanical properties

The time series of the three mechanical properties (quasi-static compressional Young's modulus, along the specimen longitudinal direction, flexural and compressive strengths, the latter also along the longitudinal direction) are shown in Figure D16 (a) to (c), respectively, for specimens cast with both aggregate types (*U* and *P*, labelled correspondingly). It is reminded here that, contrary to the *u* specimens, used for the time-lapse XT measurements and with size $25 \times 25 \times 100 \text{ mm}^3$, the specimens for these mechanical properties measurements had size $40 \times 40 \times 160 \text{ mm}^3$.

It can be observed that, regardless of slightly higher mechanical properties at the peaks, the specimens cast with the *U* aggregates (*U*) exhibited a faster, post peak decline, compared with those cast with the *P* aggregates (*P*). This faster decline can be attributed to the higher ASR reactivity of the *U* aggregates, mirrored in the faster expansion shown in Figure D15, and the associated more extensive cracking (shown already in Figure 4.8 (a) and Figures C18 (a) and (c), in terms of ASR cracks volume fraction, $\tilde{V}_{ASR,cracks,tot}$). Of special remark is the fact that while the Young's modulus and flexural strength continued decreasing in the *P* specimens case, a recovery of the same properties was observed after about 244 days for the *U* specimens. The compressive strength for both types of specimens remained after 244 days almost steady.

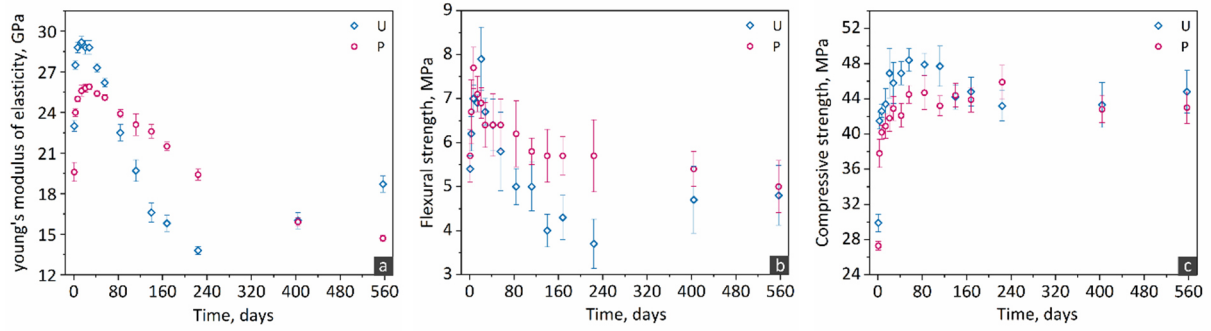


Figure D162. Comparison of the time series of the (a) quasi-static, compressional Young's modulus measured along the specimen longitudinal direction, (b) the flexural strength, and (c) the longitudinal compressive strength of the U and P specimens. In each plot, the markers show the average while the error bar the empirical standard deviation of an ensemble of values from distinct specimens, the ensemble size being 3, 3 and 6 for insets (a), (b) and (c), respectively. For the Young's modulus measurements, the specimens were always the same at each time point.

As discussed in Section 6.4, the apparent recovery, at very late stages, in Young's modulus and flexural strength of the U specimens could be associated with, on the one side, the significant accumulation of ASR products within the cracks of these specimens. On the other side, the increasing stiffening of the ASR products with increasing Ca^{2+} ions uptake, discussed already in Section 5.4, may also contribute to the observed recovery.

In Chapter 5, it was observed that more ASR products accumulated within cracks in the specimens cast with U aggregates than it happened in those cast with the P aggregates. Compare, for example, Figure C18 (a) *versus* (c), for a quantitative example. An additional qualitative example of such difference due to the aggregate type is provided in Figure D17, where the segmented crack networks and the ASR products of the two specimens belonging to the experimental campaign described in Chapter 5 are rendered in 3D with distinct two distinct colors. It is reminded that those two specimens were cast with similar mix design as the *u* specimens, except for the absence of BaSO_4 and the presence of CsNO_3 .

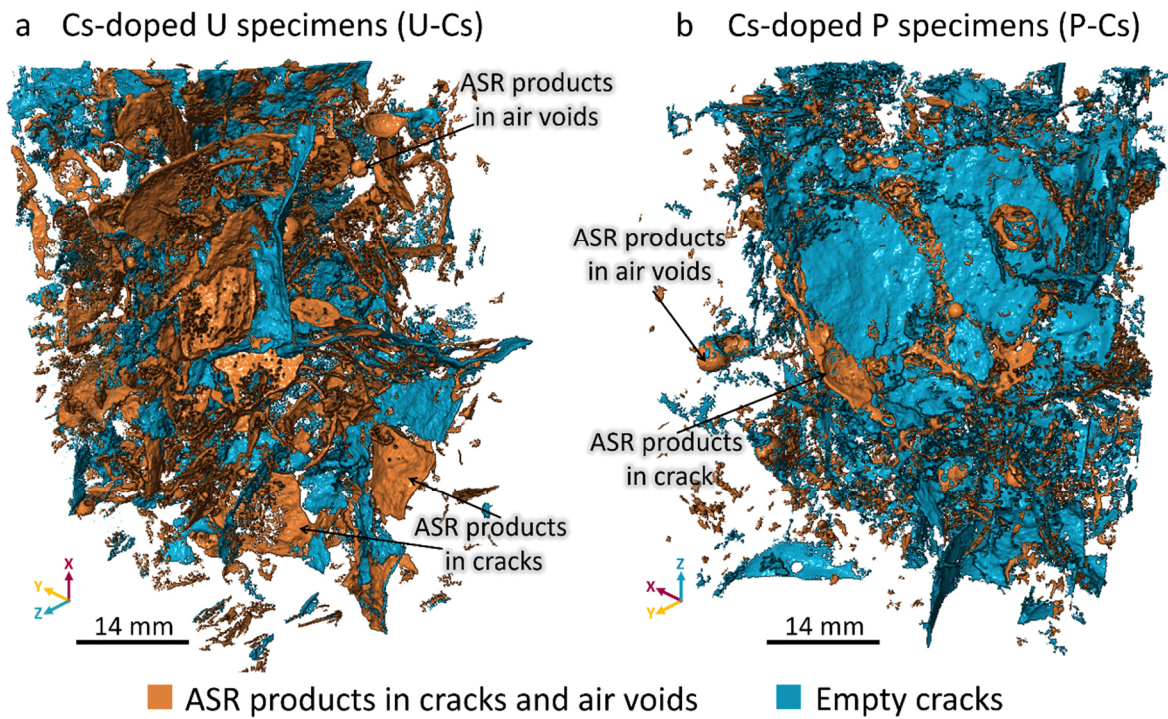


Figure D17. 3D rendering of the segmented empty crack network (in aquamarine) and of the segmented ASR products (both inside cracks and in other types of pores, in orange), for specimens cast with CsNO_3 and with (a) the U aggregates or with (b) the P aggregates.

D2.3. Time-lapse XT

Cracks and local deformations

This Subsection provides additional/complementary visualizations both of tomographic slices from the VOIs of the registered tomograms and of the two scalar fields used to map out the local deformations as estimated from the non-affine registration, namely magnitude of the displacement vector field computed from the non-affine registration results, $\|\vec{u}_{N-AFF}\|(\vec{x}, t_i)$, and the determinant of the Jacobian matrix of the non-affine transformation field, $J_{\vec{T}_{N-AFF}}(\vec{x}, t_i)$. The visualization of these two scalar fields includes both single slices as well as their visualization on the lateral faces of the tomographed volume.

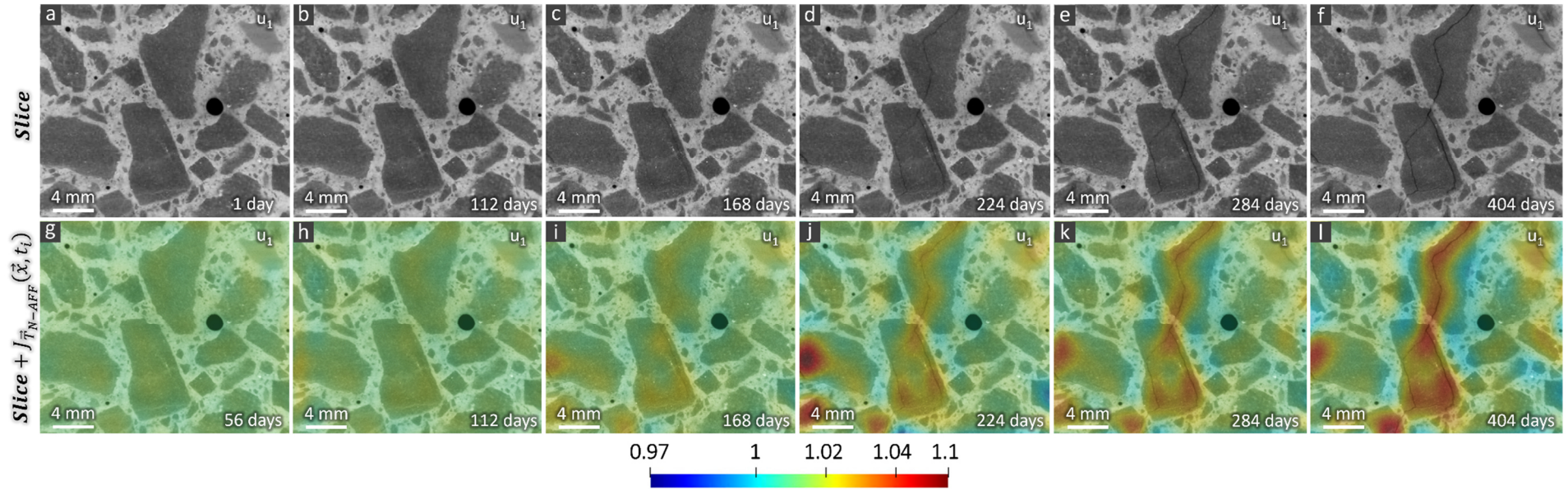


Figure D18. Visualization of the determinant of the Jacobian matrix, $J_{\vec{T}_{N-AFF}}(\vec{x}, t_i)$, of the transformation vector field $\vec{T}_{N-AFF}(\vec{x}, t_i)$ associated with the non-affine registration, as computed from the tomographic time-series of the u_1 specimen. Only a few time points from the series are shown. $J_{\vec{T}_{N-AFF}}(\vec{x}, t_i)$ is used as a spatial map of the factor by which the volume locally expanded or shrunk due to the spatially heterogeneous components of the ASR-induced displacement vector field. This Figure is identical to Figure 6.18, except for considering two additional time points from the tomographic series. (a) to (f): a ROI of one slice from the fully registered X-ray tomogram, shown at 1 day, 112 days, 168 days, 224 days, 284 days and 404 days, respectively. (g) to (l): the same slices as in (a) to (f), except for the one in (g) being the slice from the tomogram at 56 days instead of at 1 day, to showcase that the two tomograms were essentially identical; in addition, the corresponding slices from $J_{\vec{T}_{N-AFF}}(\vec{x}, t_i)$ are overlapped on top of the tomographic slices and rendered semi-transparently and color coded with the same color map used in Figure 6.18. The scale bar of the insets (e) to (h) has no unit. $J_{\vec{T}_{N-AFF}}(\vec{x}, t_i)$ values greater than 1 represent volumetric expansion, values smaller than 1 indicate volumetric shrinkage.

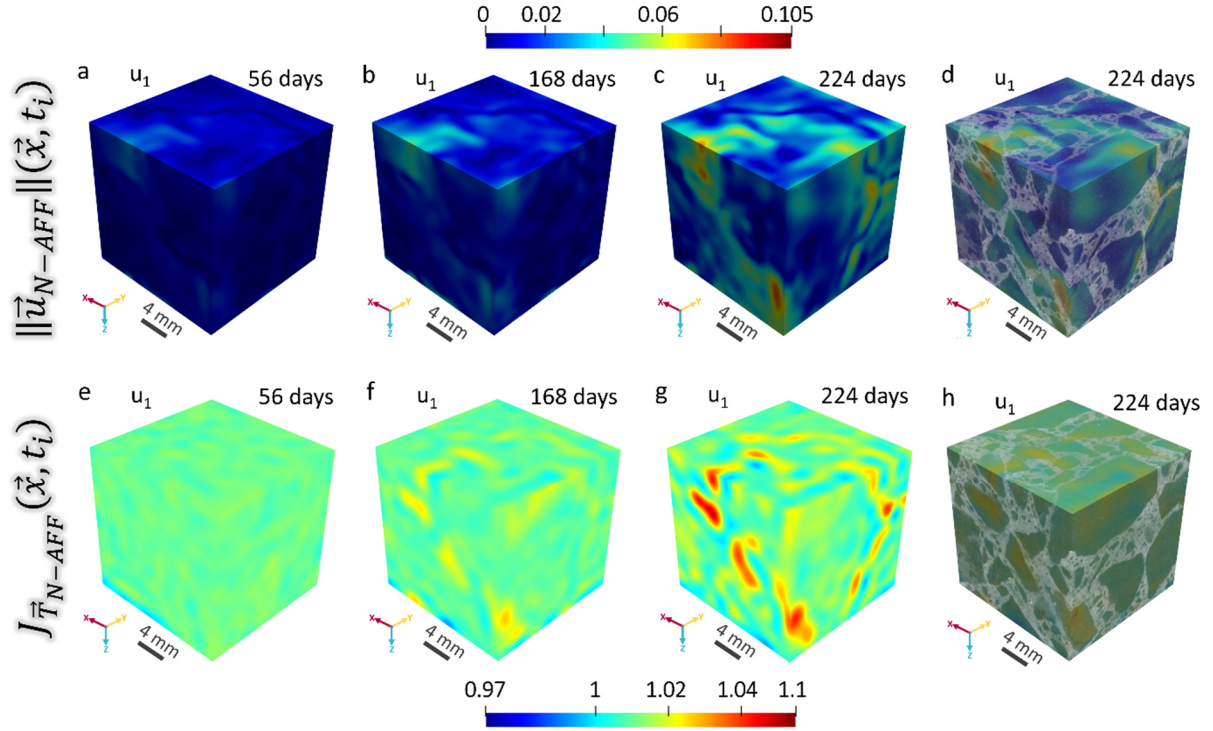


Figure D19. Visualization of the localized deformations in the u_1 specimen, using different approaches. (a) to (c): 3D visualization of $\|\vec{u}_{N-AFF}\|(\vec{x}, t_i)$ at 3 distinct time points, 56, 168 and 224 days, respectively. Inset (d) shows $\|\vec{u}_{N-AFF}\|(\vec{x}, t_i)$ at 224 days superimposed on top of the semi-transparent 3D rendering in the same grey scale as in (c) of the tomographed volume. (e) to (g): 3D visualization of the determinant of the Jacobian matrix, $J_{\vec{T}_{N-AFF}}(\vec{x}, t_i)$, of the non-affine transformation function, $\vec{T}_{N-AFF}(\vec{x}, t_i)$, shown at the same 3 time points as for the visualizations in the other insets. (h): same visualization as in (g) but for $J_{\vec{T}_{N-AFF}}(\vec{x}, t_i)$ instead for $\|\vec{u}_{N-AFF}\|(\vec{x}, t_i)$.

D2.4. Additional visualizations of the segmented cracks

This part is dedicated to further examples of the cracking in the three distinct u specimens, at eight distinct time points.

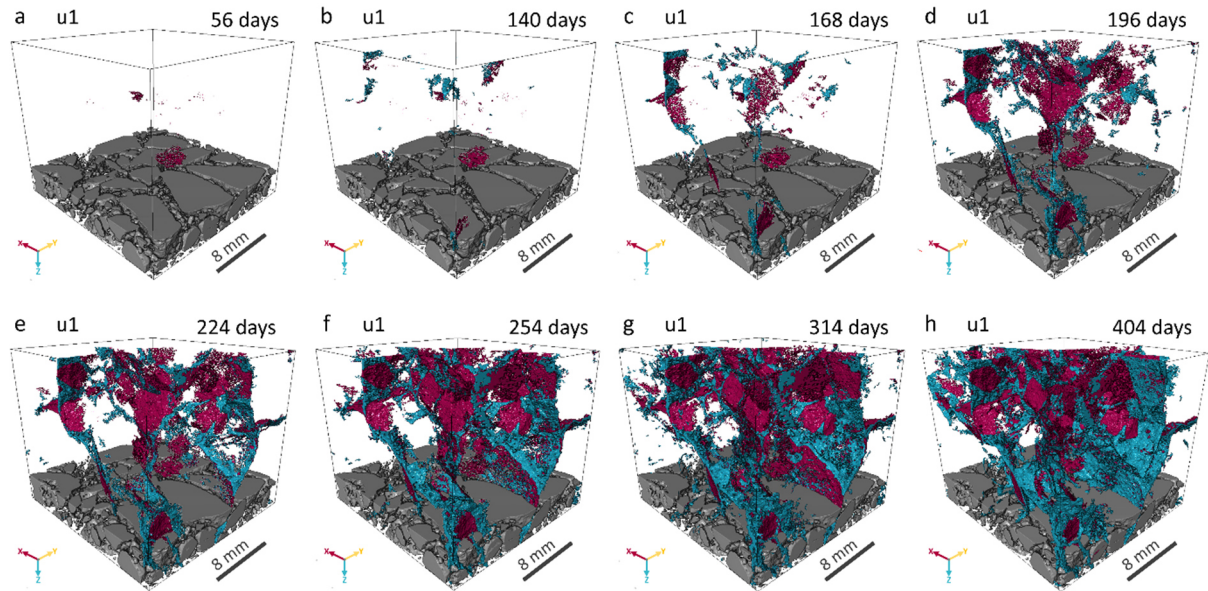


Figure D20. Binary tomograms of cracks in aggregates (purple) and in cement paste (aquamarine), rendered for the u_1 specimen. The insets from (a) to (h) correspond to different time points during the ASR acceleration, including 56, 140, 168, 196, 224, 254, 314 and 404 days, respectively. A small part of the segmented aggregates has been rendered in dark grey, visible at the bottom of each volume.

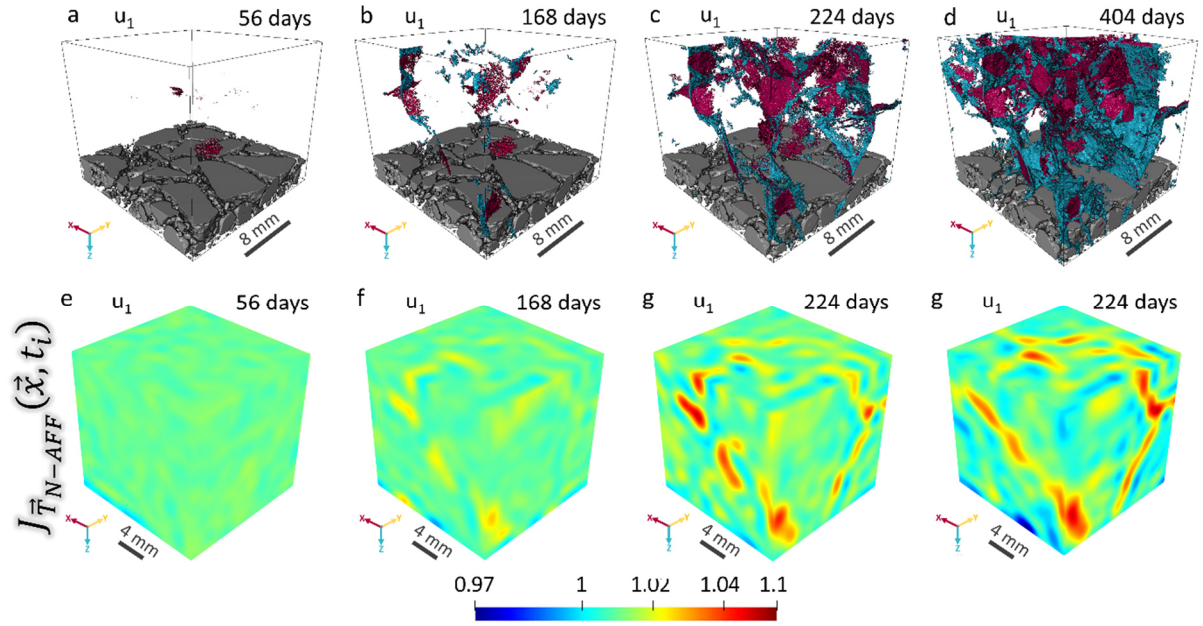


Figure D21. An example of spatial correlation between regions of local maximum for the volumetric expansion and regions of cracking, using the case of the u_1 specimen. (a) to (d): 3D rendering of the segmented cracks binary tomograms of cracks, with a color distinct between cracks inside aggregates (in purple) and cracks within the cement paste (in aquamarine). The insets correspond to different time points during the ASR acceleration, including 56, 168, 224 and 404 days, respectively. (e) to (h): 3D rendering on the lateral surfaces of the tomographed region of the determinant of the Jacobian matrix, $J_{\vec{T}_{N-AFF}}(\vec{x}, t_i)$, of the non-affine transformation vector field $(\vec{T}_{N-AFF}(\vec{x}, t_i))$, shown at the corresponding time points. It can be noted that some regions characterized by local maxima of $J_{\vec{T}_{N-AFF}}(\vec{x}, t_i)$, with values well above 1 (meaning local volumetric expansion) were also regions where cracks propagated. As an example, consider the front bottom corner of the parallelepiped indicating the tomographed region, where cracks were visible at 168 days and, at the same time, local volumetric expansion concentrated there.

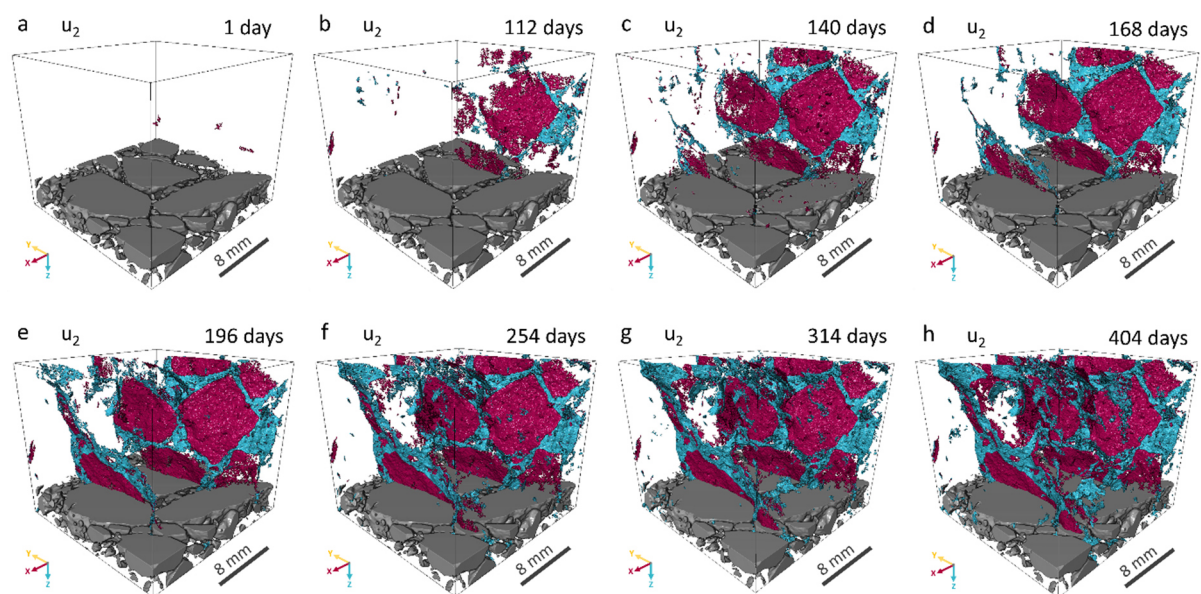


Figure D22. Same figure as Figure D20 but for the u_2 specimen.

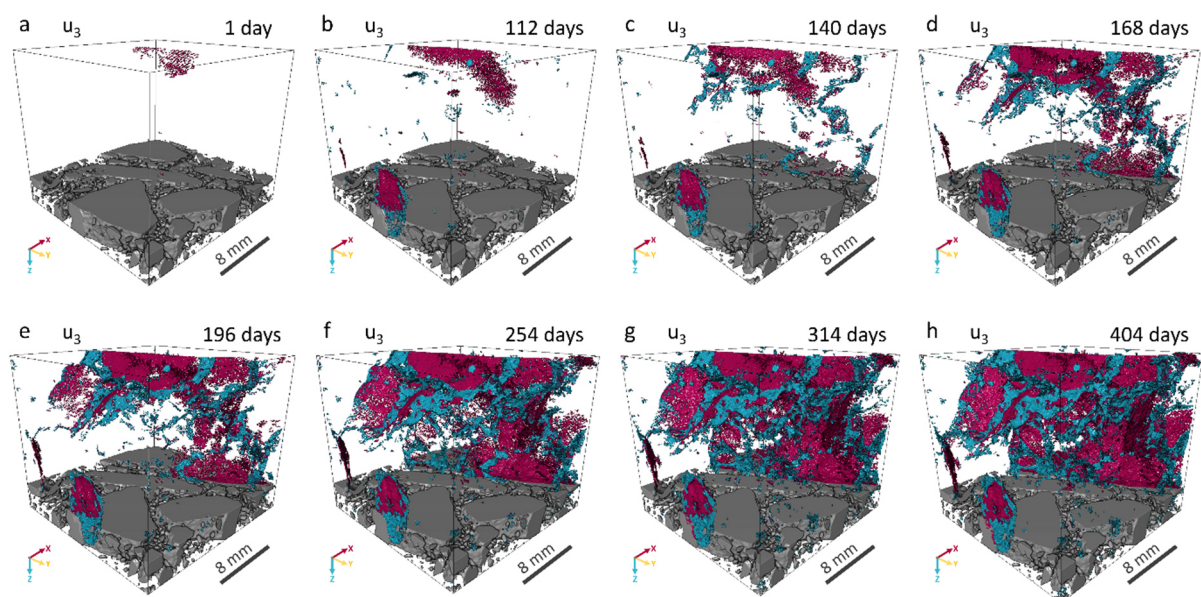


Figure D23. Same figure as Figure D22 but for the u_3 specimen.

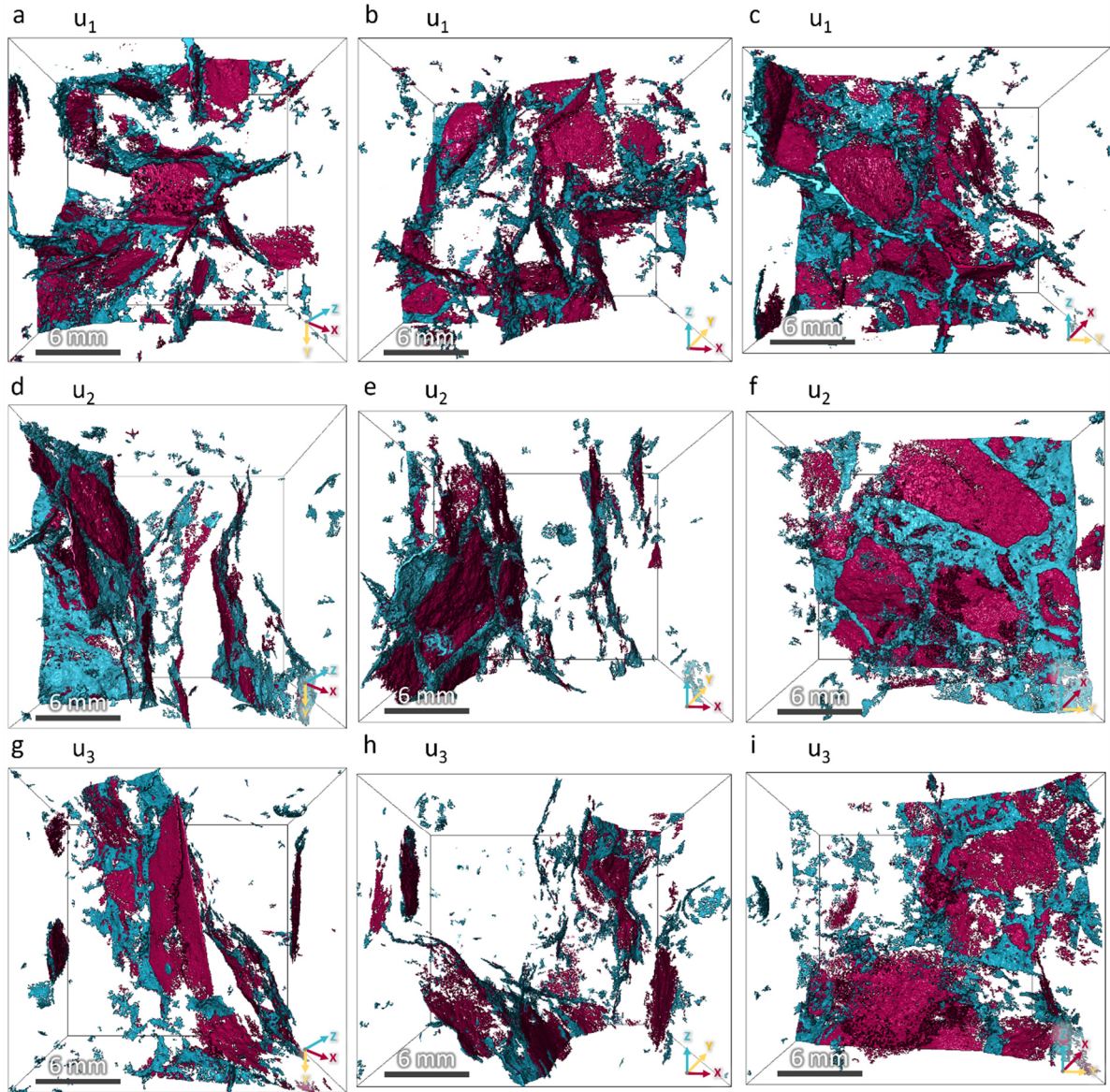


Figure D24. 3D rendering of the segmented cracks binary tomograms, with distinction between cracks inside aggregates (in purple) and within the cement paste (in aquamarine), shown only at 254 days and from three distinct viewpoints, indicated by the axes in each inset: (a) to (c) for the u_1 specimen, (d) to (f) for the u_2 specimen and (g) to (i) for the u_3 specimen.

D2.5. Quantitative analysis of ASR cracking

ASR cracks segmentation by an inverse temporal subtraction approach

It is remarked at point (III) in Section 3.3 that the empty crack segmentation based upon the TS-based approach is affected by a systematic error consisting of a displacement of a few voxels for the segmented cracks compared with their actual positions in a tomogram. A detailed analysis and characterization of such systematic error is reported in Section A3.3 of the Appendices, where it is also shown, by use of case studies from the actual tomograms or artificially created model images and cracks, that other crack

features, e.g., size and orientation, are not perturbed by the segmentation procedure. In Section 3.3, it is thus mentioned that the segmentation's systematic error is not relevant unless the position of the crack network in the frame of reference of the tomographed volume needs to be preserved as much as possible because of specific meaning to the analysis, which was not the case for this PhD project. However, a modification of the TS-based approach was tested and adopted in the experimental campaign with the u specimens, in order to avoid the mentioned systematic error completely.

The modification simply consisted of using, at each time point t_i , $\forall i = 1, \dots, N_t$, the respectively acquired tomogram as the reference one for the image registration while the tomogram at the reference time point t_0 as the one to be registered to match the newly defined reference tomogram. The registration and subtraction steps described at point (III) in Section 3.3 were then still followed exactly in the same way, except with the new definition of the reference and deformed tomograms. Given this only change, this alternative way of implementing the TS-based segmentation procedure is here labelled as inverse TS-based segmentation (inverse TS, in short), while the one described in Section 3.3 is labelled direct TS.

Since the tomogram to be deformed by the three distinct and successive registration types is the tomogram at t_0 , the subtraction from its registered version of the original tomogram at t_i bears no deformation at all of the ASR crack regions. However, it has to be remarked that original cracks, existing already at t_0 may be deformed, for the same reasons mentioned in Section 3.3 for the ASR cracks. Thus, the inverse TS approach allows segmenting ASR cracks without introducing any displacement. However, it may not allow removing completely, by subtraction, the contribution of the original cracks, existing already at t_0 , to the final region of segmented ASR cracks.

In order to evaluate and compare the performances of the inverse TS *versus* the direct TS approaches, the ASR empty crack segmentation was performed at any time point with both of them on the tomograms of all the u specimens. The total ASR crack volume fraction, $\tilde{V}_{ASR,cracks,tot}$, was computed correspondingly for all specimens. For one specimen only (u_3) and at one one time point only (168 days) several crack features were evaluated and compared.

The segmented crack network of the u_3 specimen at 168 days was chosen as an example for the qualitative comparison of the segmentation results. Figure D25 (a) shows the 3D rendering of the cracks segmented by the direct TS approach. Figure D25 (b) shows the 3D rendering of the cracks segmented by the inverse TS approach. The visual inspection of both 3D rendered networks highlighted no easily noticeable difference. When superimposing the two networks, as shown in Figure D25 (c), it was possible to notice some displacement and/or misalignment of one with respect to the other, at some locations. Such displacements/misalignments were at the scale of a few voxels, as visible on a single slice and for a small ROI in Figure D25 (d).

In order to achieve a more informative and meaningful comparison, the shape tensor analysis of both crack networks was performed for the mentioned specimen at the mentioned time point and the size, shape and orientation features were analyzed. No significant difference between the two crack networks was found in terms of distribution of both crack local thickness (T_{local}) values (see Figure D25 (e)) and crack bounding box length (L) ones (see Figure D25 (f)). Differences in the crack orientation distributions, visualized with the same approach described in Section 6.3.3.3, are clearly observable in Figure D25 (h) and Figure D25 (e). However, it can be noticed by the comparison of those two polar coordinates plots that the density of points in corresponding regions was approximately the same, despite the absence of points located at the same exact positions. This result indicates that the two crack networks differed

on average only slightly in crack orientation. Finally, the KDE of the joint PDFs of the two shape feature variable, $(E; F)$ also exhibited very small differences, as it can be seen by comparing Figure D25 (j) with Figure D25 (k).

In summary, no major differences were found for the two crack networks of the u_3 specimen at 168 days obtained by the two distinct TS-based segmentation approaches, respectively. Since the inverse TS approach leads to no deformation at all of ASR cracks but only of original cracks at t_0 and since such original cracks were typically in a rather small amount in any tomogram, such approach was adopted instead of the direct TS one for the quantitative crack network analysis for the three u specimens. However, very similar results of such analysis would have been expected, had the direct TS approach been used. The latter approach would be preferable in the cases where the tomogram at t_0 would show an extensive presence of original cracks, whose deformation by the registration might introduce a not too small systematic error in the segmentation results.

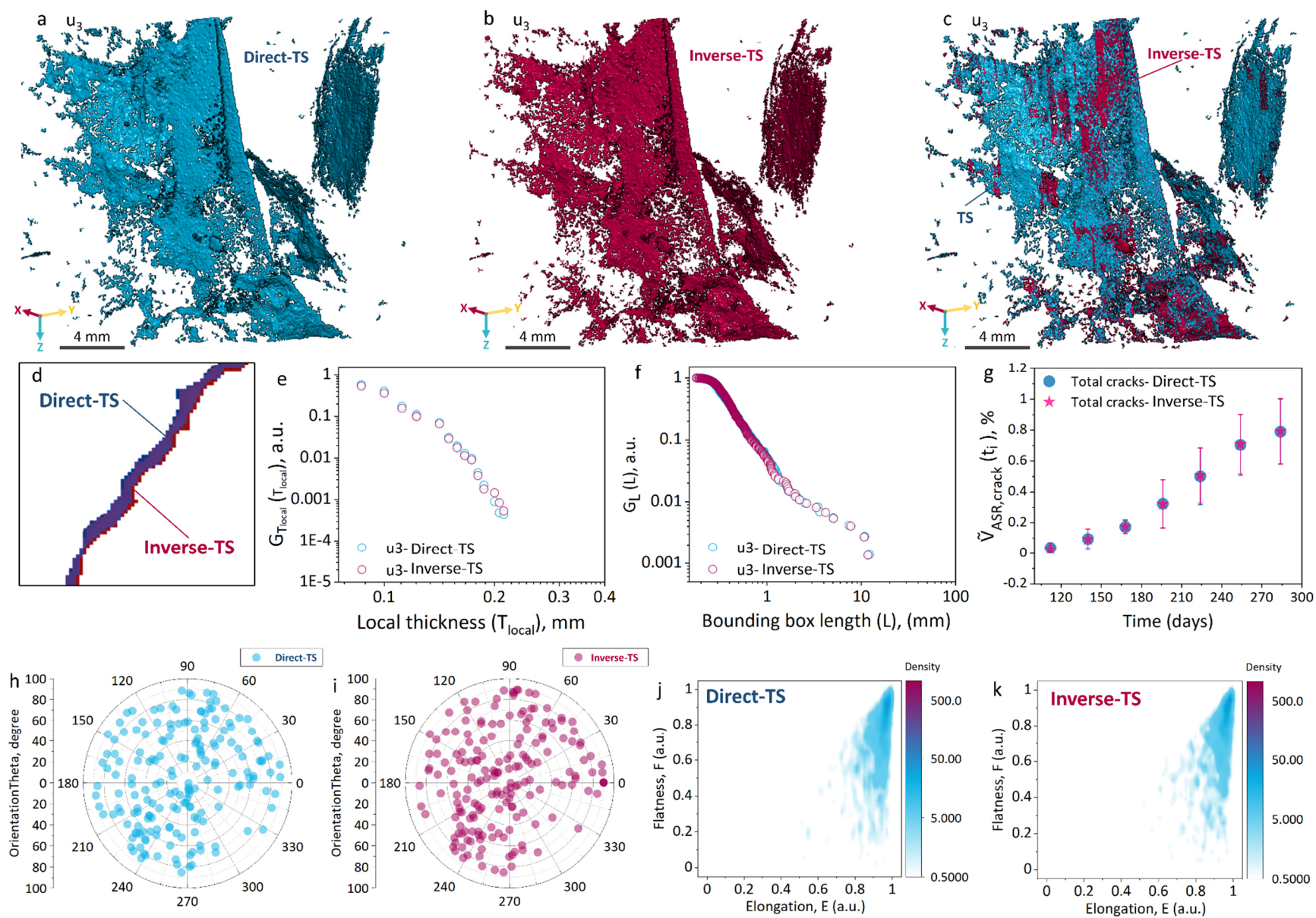


Figure D25. Comparison of the crack networks segmented with the direct and inverse TS approaches for the u_3 specimen at 168 days. (a) to (c): binary tomograms of the total crack network, rendered in 3D with distinct colors and obtained (a) by the direct TS approach and (b) by the inverse TS one; the two rendered networks are shown overlapped on top of each other in (c) to ease their visual comparison. (d): a small ROI on one slice from the volume shown in (c) is provided here, to showcase the difference between the two segmented crack networks. (e): comparison of the empirical complementary cumulative distribution functions, $G_{T_{\text{local}}}(T_{\text{local}})$, of the crack local thickness, T_{local} , shown in the form of Zipf's plots (f): same as in (e) but for the crack bounding box length, L . (g): time series of the ASR total crack volume fraction ($\tilde{V}_{\text{ASR,cracks,tot}}$) computed for both crack networks of all three u specimens. The markers indicate the average value from the three specimens while the error bar was calculated as the respective empirical standard deviation. (h) and (i): comparison of the crack orientation distributions for the two crack networks of the u_3 specimen at 168 days, visualized by the polar coordinates of the projections of the \hat{u}_1 eigenvector on the equatorial plane of the respective unitary sphere on which they lie. (j) and (k): comparison of the kernel density estimates (KDEs) of the joint probability density functions (PDFs) for the crack elongation E and flatness F .

Crack thickness and bounding box length

Insets (a) to (c) in Figure D26 present the evolution of the crack bounding box length distribution for the three u specimens. The insets (d) to (f) in Figure D26 show the evolution of the distribution of crack local thickness values, T_{local} for the same specimens.

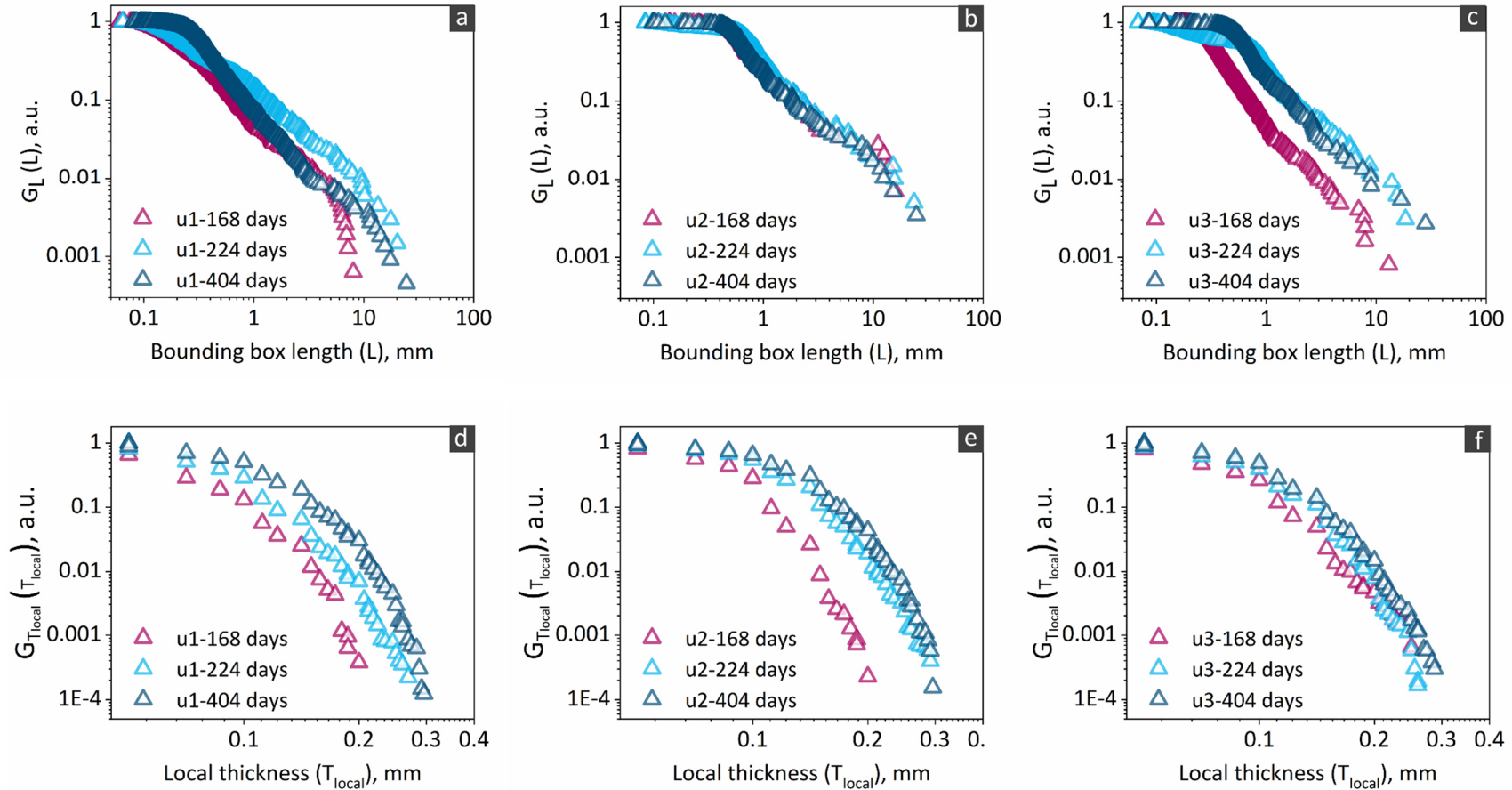


Figure D26. (a) to (c): empirical (i.e., statistical ensemble) complementary cumulative distribution function, $G_L(L)$, of the crack bounding box length, L , in \log_{10} - \log_{10} scales (Zipf's plot), for the u_1 , u_2 and u_3 specimens, respectively, at three time points (168, 224 and 404 days). (d)-(f) corresponding Zipf's plots for the crack local thickness, T_{local} .

Crack shape and orientation

Figure D27 shows the shape phase diagrams (elongation *versus* flatness maps, (E; F)) of all the three tomographed u specimens, at three distinct time points. Figure D28 shows the crack orientation distributions of the three u specimens, at three distinct time point.

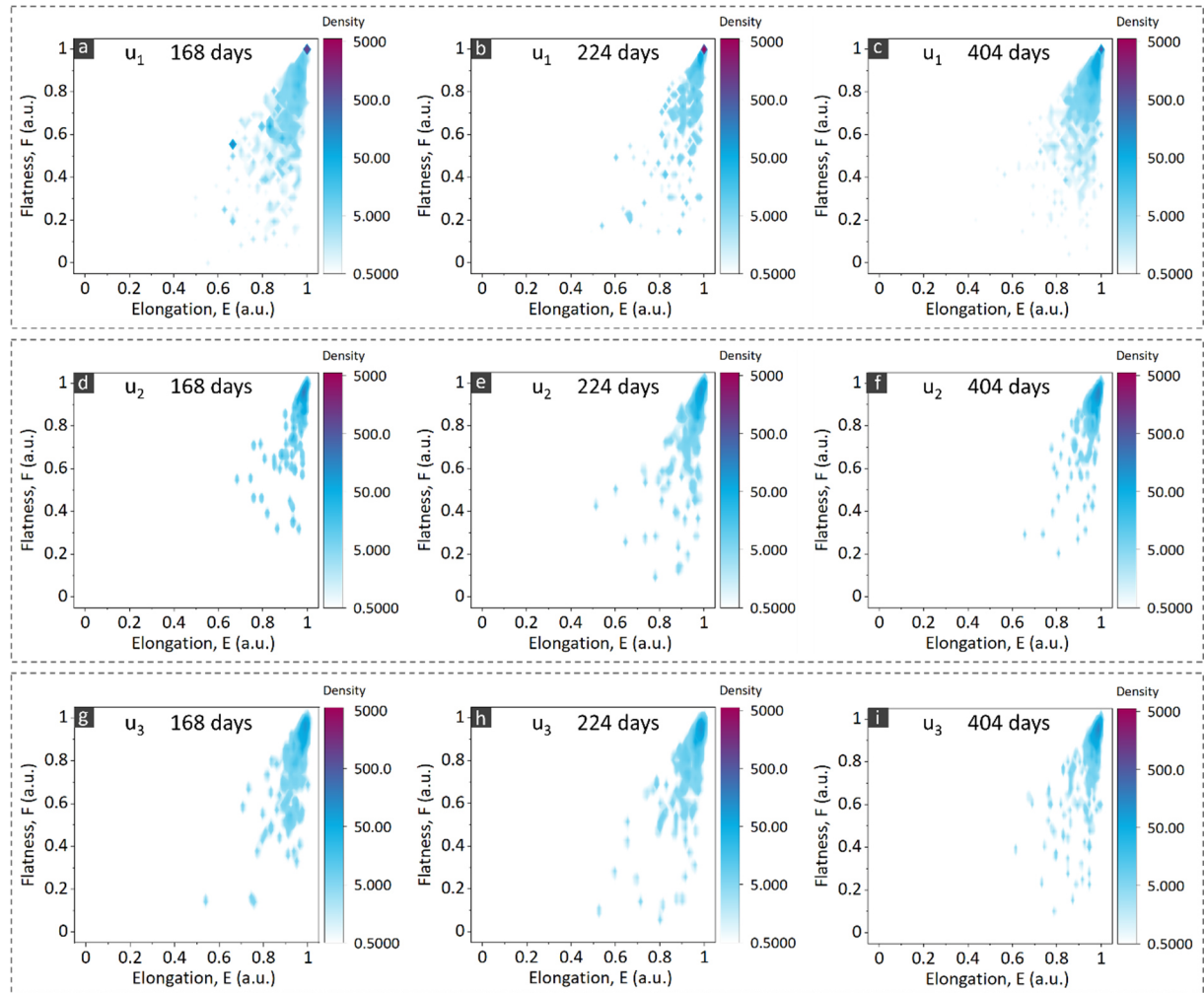


Figure D27. The kernel density estimate (KDE) plots of the joint probability density function (PDF) for the elongation E and the flatness F , computed from the shape tensor analysis of the segmented total crack network and treated as a bi-variate random variable, $(E; F)$. (a) to (c): u_1 specimen, at 168, 224 and 404 days, respectively. (d) to (f): u_2 specimen, at 168, 224 and 404 days, respectively. (g) to (i): u_3 specimen, at 168, 224 and 404 days, respectively.

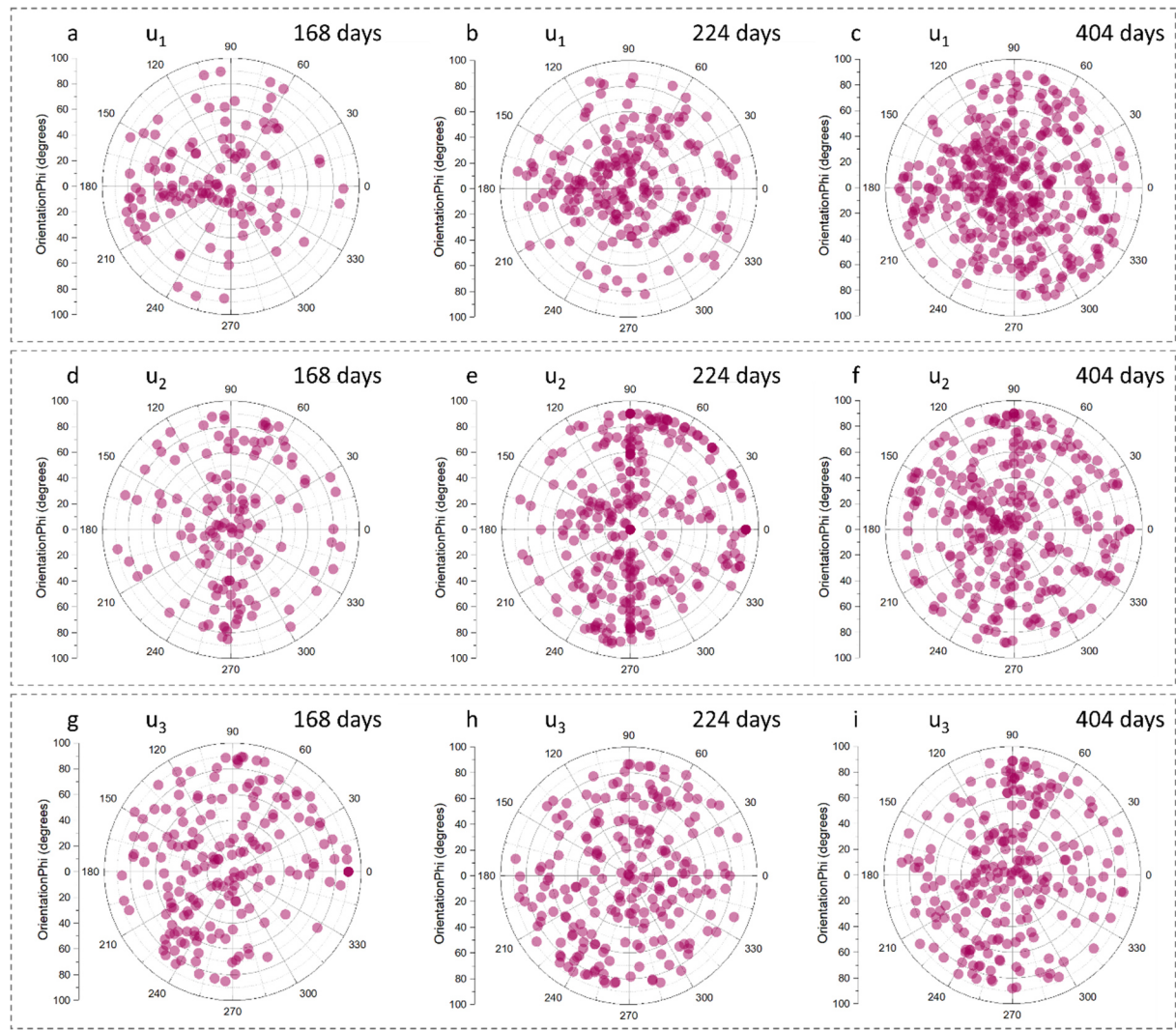


Figure D28. Visualization of the crack orientation analysis results for (a)-(c) the u_1 specimen, (d)-(f) the u_2 specimen and (g)-(i) the u_3 specimen, respectively. Each column refers to a distinct time point, 168, 224 and 404 days, respectively. Instead of visualizing by an arrow the first eigenvector \hat{u}_1 of a crack's shape tensor, it was first represented as a point on the unit sphere, with spherical coordinates $(\theta; \varphi)$, $\theta \in [0^\circ; 360^\circ]$ and $\varphi \in [-90^\circ; 90^\circ]$. Then, such a point was projected on the shown equatorial plane, which corresponds to the $X - Y$ plane of the Cartesian frame of reference of the specimen. The radial distance of a point from the origin is mapped to the elevation angle φ axis according to the vertical scale, such that the distance between two successive circles in such polar coordinates framework corresponds to 10° distance on the φ axis.

Bibliography

- [1] P. Carrara *et al.*, “Improved mesoscale segmentation of concrete from 3D X-ray images using contrast enhancers,” *Cem. Concr. Compos.*, vol. 93, pp. 30–42, Oct. 2018, doi: 10.1016/j.cemconcomp.2018.06.014.
- [2] R. Kresse *et al.*, “Barium and Barium Compounds,” *Wiley-VCH Verlag GmbH Co. KGaA (Ed.), Ullmann’s Encycl. Ind. Chem. Wiley-VCH Verlag GmbH Co. KGaA, Weinheim, Ger.*, pp. 621–640, 2007, doi: 10.1002/14356007.A03_325.PUB2.

Appendix E

Supplementary data for Chapter 7

E1. Relative mass changes

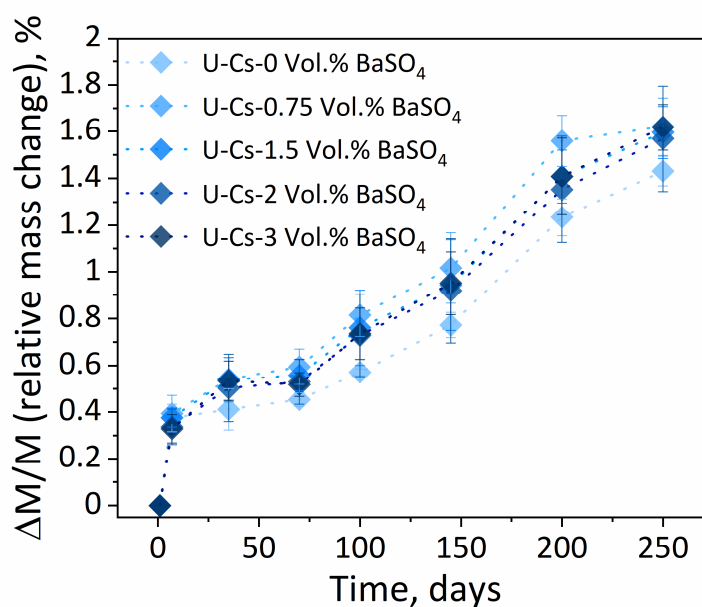


Figure E1. Evolution of the relative mass change of distinct specimens cast with U aggregates, CsNO_3 and various BaSO_4 concentrations. The markers indicate averages while the error bars size is the standard deviation of six values from an ensemble of six distinct specimens, for each specimen set.

E2. Time-lapse XT

Figure E2 and Figure E3 provide two examples of selected ROI slices from the tomogram of the U-Cs-1.5vol.% Ba specimen, at four distinct time points specified on each slice.

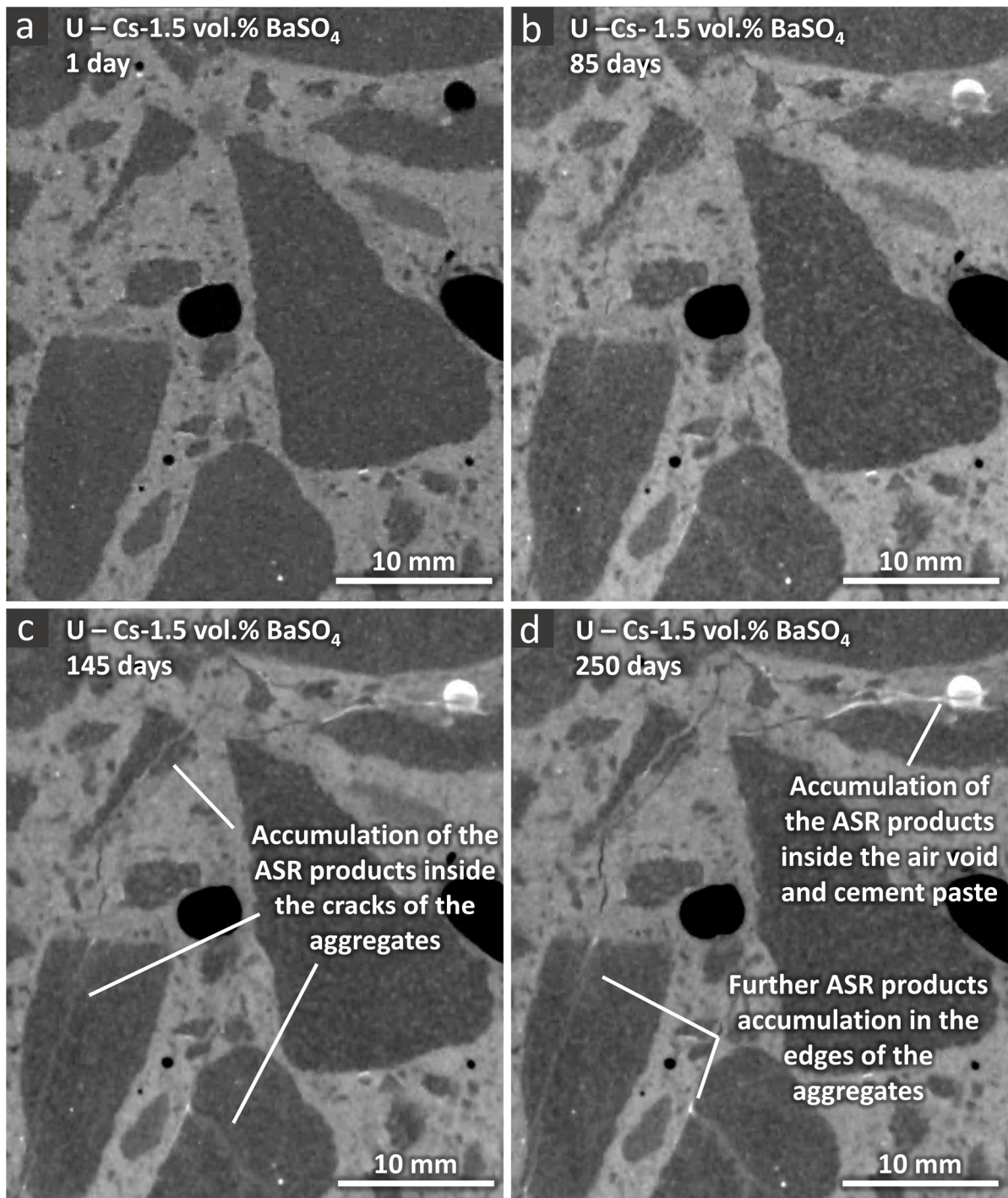


Figure E2. Temporal evolution of the crack network in the U-Cs-1.5 vol.-% BaSO₄ specimen. (a)-(d): on one (X – Y) slice of the tomograms at 1, 85, 145 and 250 days, respectively. The position of the slice and of the ROI on it is the same at any time point.

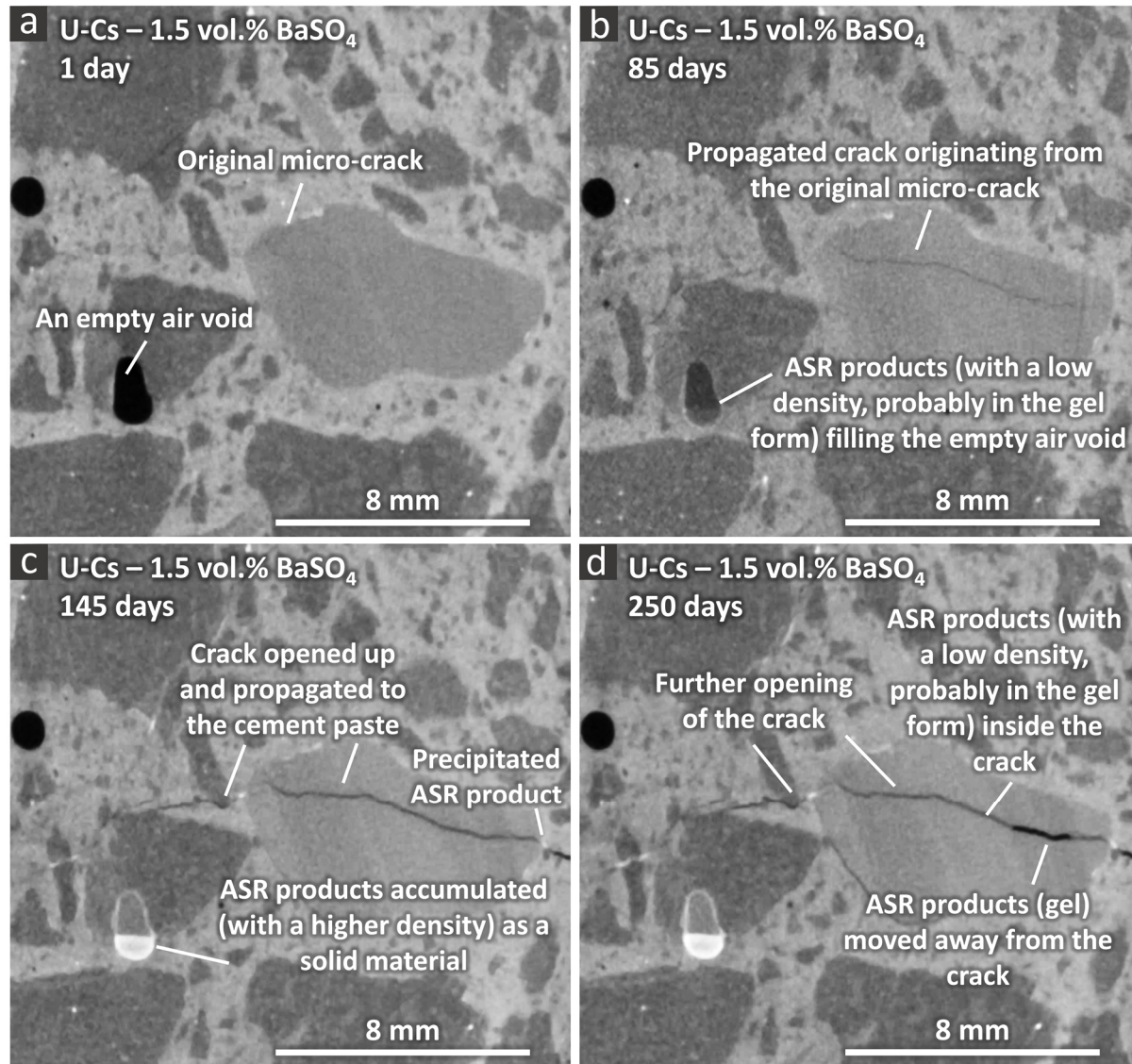


Figure E3. Similar figure as E4 but considering another ROI on a distinct slice of the tomograms of the U-Cs-1.5 vol.-% BaSO₄. The dynamic range of the visualization of the slices was different from the one in Figure E2 to better highlight certain features.